BUBBLES IN VISCOUS LIQUIDS:

SHAPES, WAKES AND VELOCITIES

by

Dahya Bhaga

A Thesis Submitted to the Faculty of Graduate Studies and Research

in Partial Fulfillment of the Requirements for the Degree of

Doctor of Philosophy

Department of Chemical Engineering
McGill University
Montreal, Canada

September 1976

"Modern science strives to construct its picture
of the world not from speculations but so
far as possible from facts. It verifies its
constructs by recourse to observation."

Ernst Mach (1943)

ABSTRACT

The behaviour of bubbles (volume — 0.08 - 139 cm^3) rising in viscous (μ — 0.62 - 28.2 Poise) Newtonian liquids was studied. A detailed classification of bubble shape regimes was presented and a method for predicting the bubble shape and the shape of its wake was developed. The available theoretical models and correlations were tested and their limits of validity were pointed out.

The hydrogen bubble flow visualization technique was modified for use in viscous liquids thus permitting measurement of the velocity field around bubbles of different shapes, including the velocities in the wake. Streamlines were obtained for 0.087 < Re < 296 and, where possible, were compared with existing theories. The transition from a closed toroidal wake carried with the bubble to an open unsteady wake occurred at Re $\approx$ 110.

Interaction of two vertically aligned bubbles was observed and the principle of velocity superposition was verified directly using the measured velocity field.

The skirt incipience theory of Wegener et al (1971) was extended to indented oblate-ellipsoidal-cap bubbles and drops. A theory for skirt thickness was developed which predicts decreasing skirt thickness with skirt length, as observed experimentally. A simple theory to predict the length of the skirt was also formulated and verified experimentally.

It was found that the proximity of the container walls reduces the bubble rise velocity, elongates the bubble in the vertical direction, alters the liquid flow field, reduces the volume of the toroidal wake and the rate of circulation within it, delays skirt formation and promotes the formation of waves on the skirt. The wall effect theory of Collins (1967) was shown to be valid for bubbles in viscous liquids for Re as low as 10.

RESUME

Le comportement des bulles (de 0.08 - 139 cc) dans des liquides Newtoniens (de 0.62 - 28.2 Poise) a été étudié. Une classification détaillée de la forme des bulles selon leur regime est présentée et une méthode est developpée pour la prédiction de la forme des bulles et de leur sillage. Les quelques modèles théoriques et corrélations existants ont été testés et leur domaine de validité déterminé .

La téchnique de visualisation par des bulles d'hydrogène a été modifiée pour permettre la détermination du champ de vitesse dans des liquides visqueux autour des bulles de différentes formes et autour des sillages accompagnant ces bulles. Les lignes de courant ont été obtenus dans le domaine du nombre de Reynolds de 0.087 à 296, et si possible, ces lignes sont comparées avec des théories existantes. La transition d'un sillage "fermé" de forme toroidale à un sillage "ouvert" transitoire est observée à un nombre de Reynolds d'environ 110.

L'interaction de deux bulles alignées verticalement a été étudiée, et le principe de superposition des vecteurs de vitesse a été verifié directement à l'aide du champ de vitesse mesuré.

La théorie de Wegener et al (1971) sur la formation des "jupes" a été étendue à des bulles et gouttes de la forme d'un ellipsoide applatie dont la base est echancrée. Une théorie sur l'épaisseur des "jupes", a été developpée, celle-ci prédit, en accord avec les observations, que l'épaisseur de la "jupe" décroit avec la longueur. Aussi, une théorie simple pour la prédiction de la longueur de la "jupe" a été formulée et verifée experimentalement.

Il a été trouvé que l'effet de paroi réduit la vitesse ascensionnelle, allonge la bulle dans la direction verticale change le champ de

vitesse, diminue le volume et la vitesse de circulation du sillage toroidal, retarde la formation de la "jupe" et favorise en elle l'apparition des instabilités. La théorie de Collins (1967) sur l'effet de paroi a été prouvée valide pour des bulles dans un liquide visqueux ayant un nombre de Reynolds aussi bas que 10.

ACKNOWLEDGEMENTS

TABLE OF CONTENTS

LIST OF FIGURES

LIST OF TABLES

CHAPTER 1

INTRODUCTION

Bubbles play an important role in many processes encountered in chemical and metallurgical engineering. Operations such as absorption, desorption, fermentation, mixing, floatation, sewage treatment, vacuum degassing and metal refining all involve the motion of dispersed gas bubbles in liquids. Most industrial processes usually involve swarms of bubbles created by a large number of nozzles or by a perforated plate. Nevertheless, it is essential to understand the behaviour of a single bubble before a complete knowledge of interacting bubbles can be achieved. Recognition of this has motivated a number of investigations dealing with the fundamental aspects of bubble phenomena such as bubble formation, bubble shape and movement, interaction with another bubble or a plane surface, and mass transfer to and from the liquid. (Sideman et al 1966; Calderbank 1967; Soo 1967; Valentin 1967; Gomezplata and Regan 1968; Regan and Gomezplata 1970; Bischoff and Himmelblau 1968; Gal-or et al 1969; Gill et al 1969-70; Tavlarides et al 1970). Despite these efforts many challenging problems still remain as pointed out in recent reviews (Harper 1972 ; Wegener and Parlange 1973; Clift, Grace and Weber 1976).

The formation mechanism of a bubble may vary from process to process, however, once a bubble has attained terminal velocity its behaviour is independent of the formation mechanism and depends only upon its volume, the physical properties of the liquid, and the size of the

container. A complete description of the behavior of a single bubble requires the knowledge of its shape, rise velocity, the motion induced in the surrounding liquid and the effect of the container wall on these variables.* The present work is directed towards obtaining this knowledge for single bubbles rising in relatively viscous (0.8 to 28.0 Poise) Newtonian liquids. Since a large number of variables were investigated and each has its own literature, the results of this work are presented in five relatively self-contained chapters, Chapters 3 through 7. Each chapter contains a review of the relevant literature, lists the specific objectives and then presents and discusses data obtained in this study.

In order to measure the external liquid motion an experimental technique was developed to provide the velocity distribution over an extended region around the bubble without disturbing the bubble or the flow and to provide, simultaneously, a vivid picture of the flow field. This experimental technique is described in Chapter 2. The study of bubble shape and rise velocity is presented in Chapter 3. The review of literature in this chapter is longer than that in the other chapters and serves as a general introduction to the phenomena of bubble motion. Chapter 4 contains extensive results on the liquid flow field around all of the different shapes of bubbles encountered in this work together with a detailed examination of the nature of bubble wakes. The results

---

* Since the velocity field within the bubble has relatively little effect on bubble shape, liquid phase controlled mass transfer rate, bubble interaction and coalescence no attempt was made to study this internal motion. Accurate interval circulation measurements are very difficult to obtain for gas bubbles though some attempts have been made. (Garner and Haycock 1959; Davidson and Kirk 1969; Filla et al 1976).

of Chapters 3 and 4 are used in Chapter 5 to explain the interaction and coalescence of two bubbles rising in line. Chapter 6 is devoted to the elucidation of the factors which control the onset, thickness and length of skirts trailing behind bubbles moving in viscous liquids. The results of other workers on skirted bubbles and drops are incorporated wherever possible to support the theories developed in this chapter. The effect of the proximity of the container wall on bubble shapes, wakes and velocities is the subject of Chapter 7. Finally, the important contributions of this study are presented in Chapter 8, and suggestions are offered for further work.

CHAPTER 2

EXPERIMENTAL EQUIPMENT AND PROCEDURES

2.1 The Technique for Measuring Velocity Distribution in the Liquid

2.1.1 Selection of the experimental technique

To measure the velocity field in the liquid around a rising bubble, it was necessary to have an experimental technique which would provide the velocity distribution over an extended region around the bubble without disturbing the bubble or the flow, and which would simultaneously provide a visual record of the flow field. These requirements ruled out the use of conventional probe instruments such as pitot tubes and liquid film anemometers and also the recently developed technique of laser-doppler anemometry. This left the flow visualization techniques, such as injection of dye or neutrally buoyant particles into the liquid, electro-chemical luminescence, schlieren and shadow photography and electrolytic hydrogen-bubble generation. For a more detailed discussion and comparison of the various techniques of flow visualization the reader should refer to the comprehensive reviews on the subject (Lippisch 1958; Clutter et al 1959; ASME 1960; Clayton and Massey 1967; Macagno 1969; Kline 1972; Werlé 1975; Merzkirch 1974; Hyzer 1974).

After a review of the various flow visualization methods the hydrogen-bubble technique was selected for the present investigation because it is the most versatile, as can be seen from its application in a variety of rather complex, steady as well as time-dependent flows (Lukasik and Grosh 1959; Hama 1962; Hama and Nutant 1963; Schraub et al

1965; Hansen 1968; Weinberg and Heiser 1968; Lennemann and Howard 1969; Maxworthy 1970; Mattingly and Criminale 1972; Rice and Thomas 1973; Mattingly and Chang 1974; Offen and Kline 1974).

Basically the technique utilizes the electrolysis of water to introduce hydrogen bubbles into the flow. In a typical installation a very fine wire which acts as cathode is stretched across the region of flow that is to be investigated. A pulse of d.c. voltage is applied to the wire and the hydrogen formed is swept off the wire by the passing flow. The gas leaves the wire in the form of very small bubbles. Careful illumination makes these bubbles visible. Oxygen is formed at an anode which is located out of the field of view. Hydrogen bubbles rather than oxygen are selected as tracers since volumetrically twice as much hydrogen is formed as oxygen in the electrolysis of water.

The technique was first used by Geller (1954), who in turn was stimulated by the work of Wartmann (1953) on injection of tellurium by electrolysis. A review of this early work and an excellent exposition of the hydrogen bubble technique is given by Clutter et al (1959,1961), Schraub et al (1965) Asunuma and Takeda (1965) and Mattingly (1966). The evaluation of this technique for quantitative measurements has been dealt with by Schraub et al(1965), Davis and Fox (1967), Tory and Haywood (1971), Somerscales (1971) and Gerrard (1972). Studies of the factors affecting the size of the hydrogen bubble have been made by Blandamer et al (1967) and by Tory and Haywood (1971).

The hydrogen-bubble technique was used in this study for the following reasons:

(1) The tracer bubbles are easily produced in the flow at any location and, because of the electrical nature of the generation, they may be pulsed and timed, and their number and size are easily controlled.

(2) The technique allows multiple point observation at the same instant, thus providing complete velocity information.

(3) The cathode wire may be made so small that it causes negligible disturbance to the flow.

(4) By suitably designing the cathode (see Section 2.2.4.1) the tracer bubbles can be introduced into the wake of the bubble* without breaking the bubble.

(5) The tracer bubbles are relatively easy to photograph because they are highly reflective, giving good contrast against the flow medium when side lighting is used. Also for photography the technique is superior to those methods of flow visualization that suspend the tracer particles throughout the liquid.

(6) The effect of tracer particles on the physical properties of the liquid and on the flow under observation is minimized because the tracer bubbles are generated in a single plane in the desired quantity at a desired instant.

---

* Throughout this thesis, the term "bubble" refers to the air bubble around which the flow is being investigated whereas the terms "tracer bubble" or "hydrogen bubble" are used interchangeably to refer to the small, electrolytically generated hydrogen bubbles used to trace the flow field.

(7)   Unlike filaments of dye the tracer bubbles do not lose

their identity and do not discolor or contaminate the

liquid thus permitting repeated use of the same liquid.

(8)   The technique can be adapted (see Section 2.1.2) for use

in very viscous liquids of aqueous solutions.

(9)   The technique is relatively inexpensive.

A major drawback of the technique is the considerable time and

effort required to analyse the film data.

2.1.2   Modification of the conventional hydrogen-bubble technique

In the conventional application of the hydrogen-bubble technique

to study flow behind a bluff body, rows of hydrogen bubbles are generated

at a thin wire (usually made of platinum or its alloys) placed downstream

of the body. By pulsing the current to the wire a regular pattern of

hydrogen bubbles is formed; the subsequent distortion or displacement of

this pattern gives the picture of the flow (see Tory and Haywood 1971 for

an example). By applying d.c. pulses to a partly insulated wire or by

using two cathodes, one of which is a kinked or partly insulated straight

wire that is connected to a continuous d.c. supply and the other a

straight bare wire to which d.c. pulser are applied, so called "time and

streak line" patterns can be formed to provide qualitative as well as

quantitative information on steady and time-dependent flow (Schraub et al

1965; Mattingly 1966).

Because it is difficult to hold a bubble steady* and observe the flow of the liquid past it, the conventional technique had to be modified before it could be used in the present investigation. Preliminary experiments showed that the most convenient method of visualizing the flow relative to a stationary observer was to generate isolated hydrogen tracer bubbles at reasonable spacing in a plane passing through the axis of the bubble and then to photograph the path of these tracer bubbles with a stationary ciné-camera. The observed motion at a fixed point in space would, of course, be unsteady with time. To visualize the flow in the immediate neighbourhood of the bubble, the tracer bubbles were injected as above and their motion around the bubble was photographed with a camera travelling upward at the same speed as the bubble. Here the observed motion appeared steady with time. To observe the liquid motion in the closed wake trailing the bubble, it was necessary to develop a cathode that could introduce tracer bubbles into the wake without breaking the bubble. The description of the successful cathode is given in Section 2.2.4.1.

To date, all of the studies employing the hydrogen-bubble

---

* A bubble can be held steady by a downward flow as demonstrated by Davidson and Kirk (1969), Moo-Young et al (1971) and Kojima et al (1975), but the experimental difficulty in doing this for the large number of different sizes and shapes of bubbles studied in the present work would have been formidable. Further, the liquid velocity profile necessary to hold the bubble steady distorts the bubble shape from that obtained in a free rise in a quiescent liquid.

technique have used water as the working medium* to which a small quantity of an ionic solute such as sodium chloride or sodium sulphate is added to enhance the conductivity. It was felt that the technique could be applied to any aqueous liquid, even of considerably higher viscosity, if sufficiently high voltage could be applied. Consequently, a special high voltage (750 volts d.c. max.) electronic circuit was built that could generate hydrogen tracer bubbles in sugar solution of viscosity as high as 30 Poise. The details of this circuit can be found in Section 2.2.3.

2.2 Experimental Equipment

2.2.1 Liquid column and accessories

A schematic diagram of the experimental set-up is shown in Figure 2.1. The test liquid was contained in a transparent plexiglass column ①**of height 182.9 cm., outside diameter 30.5 cm., and inside diameter 29.2 cm. To avoid radial optical distortion a square plexiglass box ② of wall thickness 1 cm. and outside cross-section 38.1 cm. x 38.1 cm. was placed around the upper 121.9 cm. of the column, and was filled with the test liquid.

A hemi-spherical plexiglass dumping cup ③ of 7.62 cm. inside diameter was mounted on a brass shaft ④ which passed through a liquid-

---

* Recently the author has discovered that Nowell (1965) had used 200 watt (2 amp. max.) pulses to generate hydrogen bubbles in water-glycerine mixtures with concentration of glycerine up to 40% (viscosity = 0.036 Poise).

** Numbers in circles correspond to those indicated in Fig. 2.1.
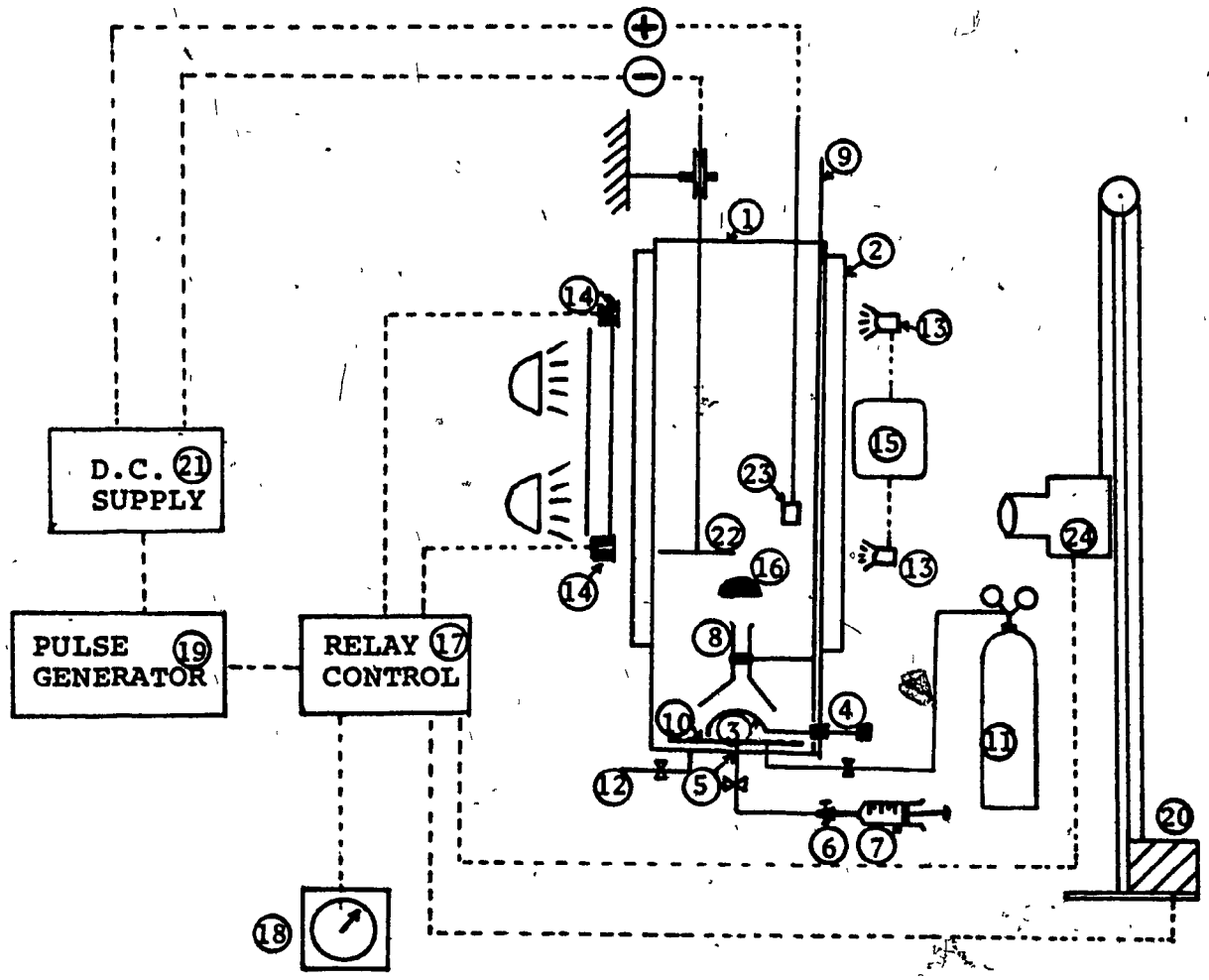
1	TEST COLUMN	13	FLASHLIGHTS
2	SQUARE BOX	14	PHOTOCELLS
3	DUMPING CUP	15	LOW VOLTAGE D.C. SUPPLY
4	ROTATING SHAFT	16	RISING BUBBLE
5	AIR INLET	17	RELAY UNIT
6	LUER VALVE	18	CLOCK
7	SYRINGE	19	PULSE GENERATOR
8	INVERTED FUNNEL	20	CAMERA MOVING DEVICE
9	FUNNEL HOLDING ROD	21	HIGH VOLTAGE D.C. SUPPLY
10	AIR SPARGER	22	CATHODE
11	COMPRESSED-AIR BOTTLE	23	ANODE
12	LIQUID OUTLET	24	16 MM BOLEX CINE-CAMERA

FIGURE 2.1 Schematic diagram of the experimental apparatus

tight rubber O-ring seal placed on the column wall 10 cm. above the
bottom of the column. The cup was fixed to the rotating shaft in such
a way that it could be rotated along its diameter thus causing minimum
disturbance in the liquid. Air was introduced into the cup via a 0.64 cm.
I.D. copper tube (5) located at the center of the base of the column.
To the other end of the copper tube was fixed a Luer valve (6) which
ensured a tight fit with the nozzle of a syringe (7) used to inject the
air bubble.

An inverted glass funnel (8) attached to a stainless steel rod
(9) 214 cm. long and 0.95 cm. diameter was placed above the cup and care-
fully centered on the axis of the column so that the bubble after leaving
the cup passed through the funnel and thus was centered. Three funnels
of varying neck diameters (2.8 cm., 3.7 cm. and 4.9 cm.) and 36 cm. height
were used for effective centering of bubbles of different sizes.

For easy mixing of the liquid after diluting the solution air
could be dispersed by means of a copper sparger (10) connected to a
compressed air bottle (11). For withdrawing a liquid sample or emptying
the column, a 1.27 cm. I.D. outlet (12) was provided at the base of the
column.

2.2.2 Photocell activation system

Two ordinary flashlights (13) were placed dimetrically opposite
two photocells (14) (National Semiconductor Model NSL-364) at approximately
120 cm. apart along the column. The high sensitivity of the photocell

required that the intensity of incident light be maintained very steady.
This was achieved by connecting the flashlights to a steady low voltage
d.c. power supply (15). The photocell responded to the interruption in
light caused by a rising bubble (16). When the light falling on the
bottom photocell was interrupted a relay unit (17) simultaneously switched
on the clock (18) (Standard Electric Time Co. Model S-1), the pulse genera-
tor (19) (Hewlett Packard Model 8005A), and the camera moving device (20).
The same circuit switched off these instruments when the bubble interrupted
the light falling on the top photocell.

The circuit diagram of the photocell activation system is shown
in Figure 2.2. It was built from several Motorola integrated circuits.
The change in the light intensity falling on the photocell changed its
resistance which in turn was used to trigger a relay which had three inde-
pendent contacts. The output of the photocells was applied to an electronic
switching arrangement via the two Schmidt Triggers (SN 7413) and then to
the relay driver (SN 75451). These Schmidt Triggers were specifically
selected to increase the response time of the circuit. The sensitivity
of the photocells could easily be adjusted using the two potentiometers.
This enabled ready triggering for different sizes of bubbles. The circuit
could be reset by a switch. The photocells were protected from stray
light by the photocell holders shown in Fig. 2.3(a). These devices
permitted only the light from the flashlights to fall on the photocells.

2.2.3 Electronic equipment for tracer bubble generation

The hydrogen tracer bubbles were produced by the electronic
circuit shown in Fig. 2.4. It consisted of a specially designed amplifier
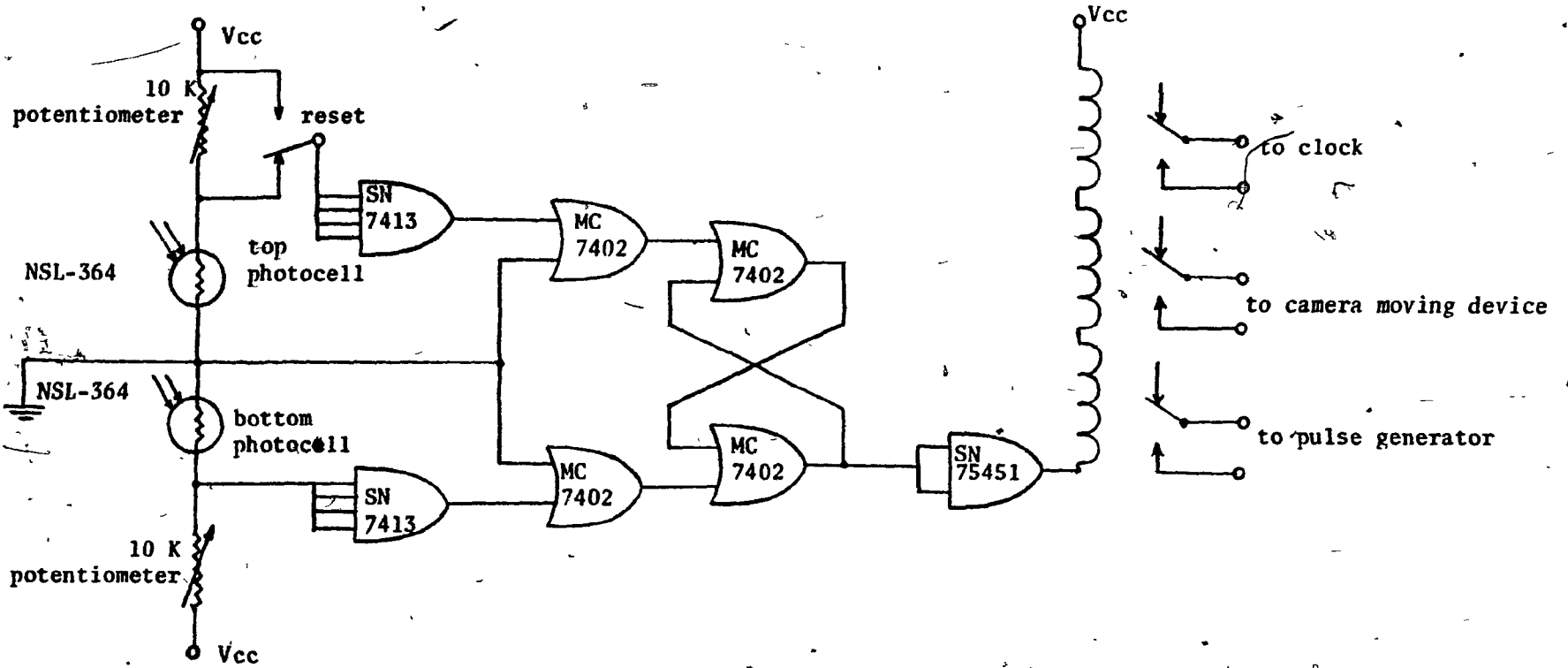
FIGURE 2.2 Circuit Diagram of the Photocell Activation System

(a)

mounting rod

blackened plexiglass block

light from flashlight

photocell

PHOTOCELL HOLDER

(b)

probe

K1

K2

K3

wall

platform

slot for inserting & withdrawing probe

slotted brass rod

brass nut with a teflon insert
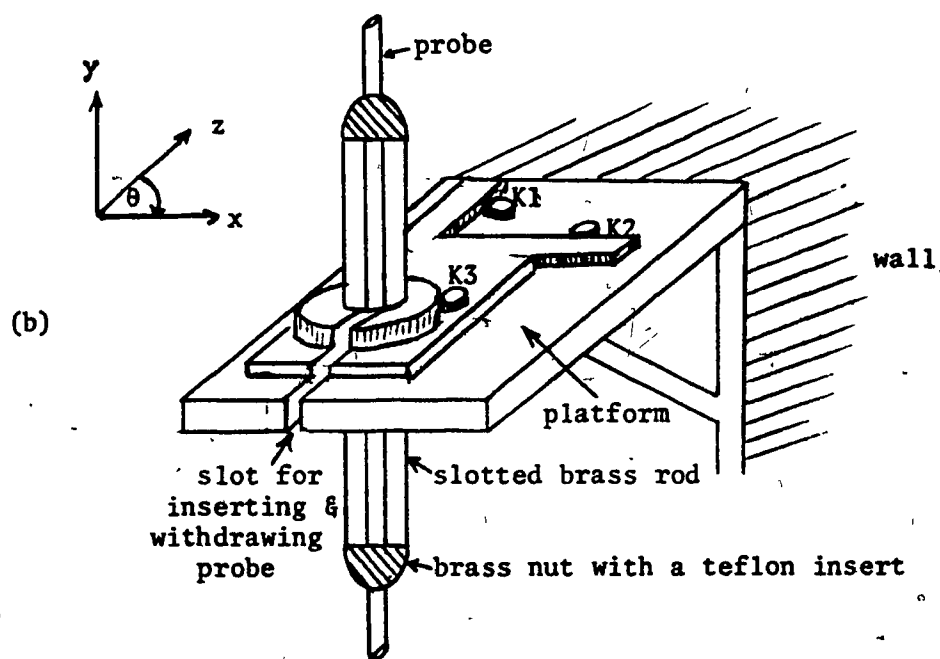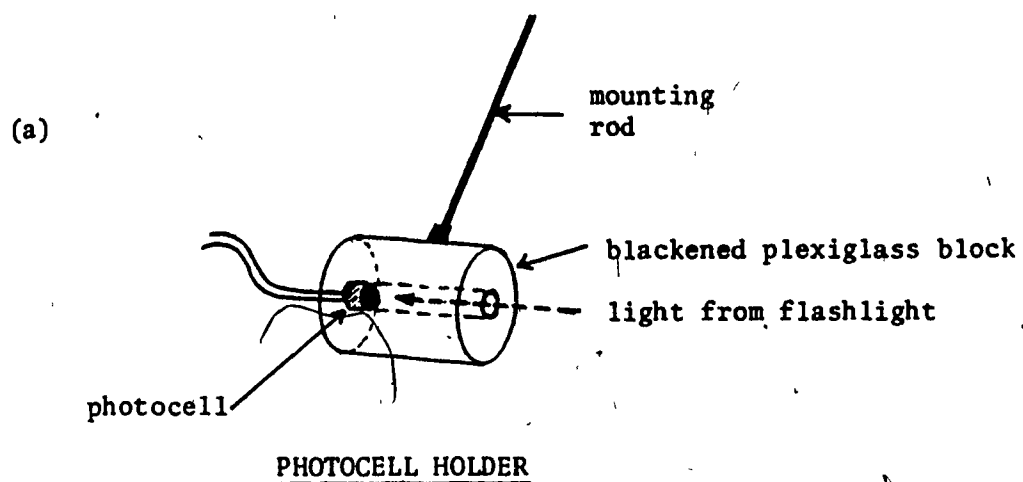
K1, K2, and K3:knobs for moving probe in z, x and θ directions, respectively.

CATHODE PROBE HOLDER

FIGURE 2.3(a)   Details of Photocell Holder

(b)   Details of Cathode Probe Holder

line input
120 volts a.c. 60 cps

variac
transformer

rectifier

F R1

R6

pulse generator
Hewlett Packard
model 8005A

relay

C1 C2 C3 C4 C5

R2 R4

V

R7

PRS

R3 R5

C6 C7 C8 C9 C10

R8

output to bubble
generating wire
(0-750v pulsed d.c.)

output to oscilloscope

resistors: R1   10Ω , 10ω
            R2,R3   100 kΩ, 1ω
            R4,R5   10 kΩ, 30ω
            R6   100Ω, 50ω
            R7   30kΩ, 1ω
            R8   332Ω, 3ω

capacitors: C1–C10   40 μf , 500 volts
fuse   F   1·5 amp
voltmeter   V   0 - 750 volts
polarity reversing switch   PRS

FIGURE 2.4   Electronic Circuit for Hydrogen Bubble Generation

powered from a variac (Superior Electric Co.; Powerstat type 2PF136).
The power from the variac was transformed using a step-up transformer
(Hammond type EN7P), rectified by means of four diodes (IN 1120) and
accumulated in a bank of capacitors. The energy was released as negative
pulses with voltage range of 0 to 750 volts triggered by a pulse generator
(Hewlett Packard Model 8005A) which in turn could be triggered at the
desired moment either automatically by the photocells or manually. The
very high amplification was necessary to pulse enough current through the
wire to create hydrogen bubbles of acceptable size in the viscous liquids
used in the present work.

The output signal (max. 5 volts) of the pulse generator had a
reversible polarity and a 0.3 cps to 10^7 cps continuously adjustable
repetition rate with a variable pulse width ranging from $3x10^{-8}$ sec. to
3 sec.. The sharply rising and falling voltage pulse enabled essentially
instantaneous triggering of the d.c. voltage. The characteristics of the
output of the pulse generator, such as pulse width, period and amplitude
could be accurately monitored on an oscilloscope.

The provision of a switch in the output of this power supply
permitted an easy polarity reversal which was used when necessary to clear
the cathode and thereby improve the quality of the tracer bubbles (i.e.
smaller and more uniform bubbles).

2.2.4 Configuration of electrodes

2.2.4.1 Cathode

The conventional cathode consisting of a platinum 13% Rhodium wire (0.001 to 0.010 in. thick) mounted on a glass frame (see Fig.2.5(a)) was tested in preliminary experiments. The wire was aligned with the diametric plane of the bubble. Upon passage of a bubble, thin wires were often broken; whereas, thicker wires ($\geq$ 0.005 in. thick) broke the bubble into two equal size bubbles which rose side by side to the top of the column. Consequently, it was necessary to construct a probe that would let the bubble pass without breaking it and that would remain rigid.

Since the bubble and the flow field were axisymmetric only half of the diametric plane needed to be considered. Based on this idea the cathode probe shown in Fig.2.5(b) was designed. It consisted of a bent glass tube of 0.8 cm. O.D. and 0.6 cm. I.D.. A tungsten rod 7 cm. long and 0.2 cm. diameter was held at the lower end of the glass tube by melting the glass around the rod. Mercury placed at the bottom of the glass tube provided the electric contact between the tungsten rod and copper wire led from the power supply. Across the tip of the tungsten rod a 0.0254 cm. thick tungsten wire was soldered. Because only half or slightly more than half of the bubble passed over the tungsten wire, the bubble did not break. By sending an electrical pulse to the wire triggered by the photocell when the bubble had just passed the cathode, tracer bubbles could be introduced into the wake.

Approximately equal sections ($\sim$ 0.2 cm.) of the cathode wire were insulated to generate sufficient hydrogen-bubbles. The method of
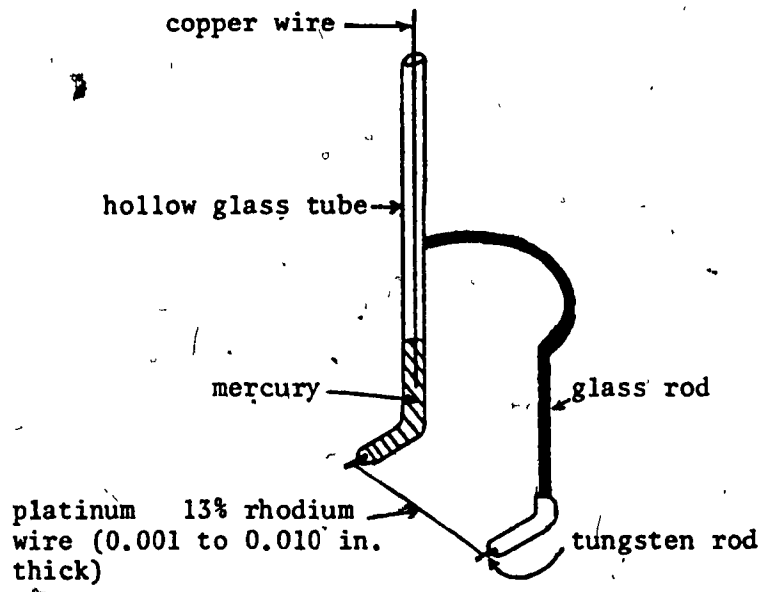
(a) Initial Version of Cathode
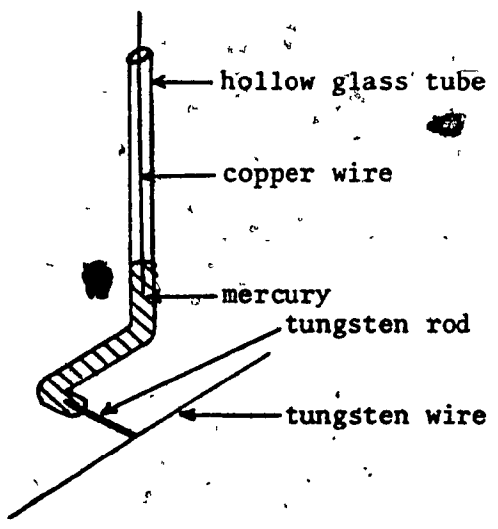
(b) Final Version of Cathode
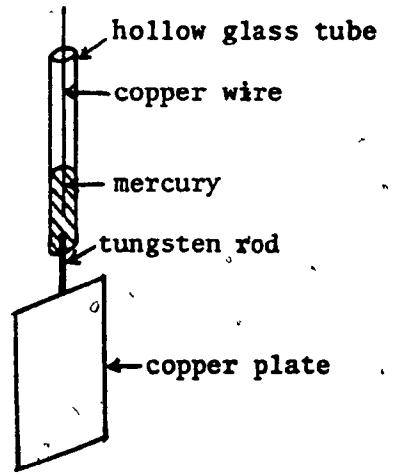
(c) Anode

FIGURE 2.5 Configuration of Electrodes

masking the wire by "sandwiching" it between cardboard cut-outs and then
spraying with several thin coats of paint as suggested by Schraub et al
(1965) was tried but it was unsuccessful as indicated by an uneven produc-
tion of hydrogen bubbles. The method finally adopted involved applying a
thin coat of red enamel paint (Krypton manufactured by Borden Inc.) or a
high voltage corona dope (manufactured by General Electric) with a small
brush over the entire length of the wire and, after drying, dissolving
off the unwanted insulation by applying drops of acetone to the wire.

The cathode probe was steadied by a probe holder (see Fig.2.3(b))
which allowed accurate positioning. It consisted of a slotted brass rod
2 cm. diameter and 15 cm. long fixed to a platform which was rigidly
mounted on a wall. The platform could be moved in two perpendicular
directions in the horizontal plane and could also be rotated. A brass
nut with a teflon insert was used to fasten the glass probe to the slotted
brass rod.

2.2.4.2 Anode

The anode terminal is shown in Fig.2.5(b). It consisted of a
0.05 cm. thick rectangular (5 cm. x 8 cm.) copper plate attached to a 2.5
cm. long 0.2 cm. diameter tungsten rod that was fixed to a glass tube
similar to one used for the cathode. The copper plate provided suf-
ficiently large area to reduce the resistance of the circuit. The anode
was fixed in the column at the same level as the cathode terminal but
near the wall out of the field of view.

2.2.5 Camera moving device

A sketch of the camera moving device is given in Fig.2.6. It consisted of a platform attached to a system of pulleys. This platform, on which the camera was mounted, could move up or down at any speed between 0 - 200 cm./sec., with the use of a variable speed electric motor. The power to this electric motor was switched on and off automatically by means of the photocell controlled relay. Two guide rods were provided to prevent vibrations when the platform was in motion. The variable motor speed controller was calibrated to allow the desired speed to be selected.

2.2.6 Lighting and photography

The lighting arrangement is shown in Fig.2.7. Two types of lighting were employed: back-lighting and side-lighting. The back-lighting was provided by a 116 cm. long Sylvania fluorescent tube light which was chosen over the conventional flood lights to avoid generation of excessive unwanted heat because the viscosity of the test liquid was very sensitive to temperature. For the shape study, the wall effect study, the skirt formation study and the coalescence study only back-lighting was used, since it gave excellent photographs of bubbles with a sharp, dark outline silhouetted against the bright background. (See typical photographs in Chapter 3, 5, 6 and 7.)

The most successful lighting for photographing the tracer bubbles was by illumination with a sharply collimated sheet of light from the side obtained using two slits in series. The light source consisted of two 1000 watt self cooled spot lights (Naren Industries Ltd., Model N-103) placed about 60 cm. apart. The thickness of the sheet of

pulley

limit
switch

cable
wire

camera

platform

FRONT
VIEW

counter
weight

variable speed
motor

felt pad

guide rod

camera

SIDE
VIEW

motor speed
controller

base
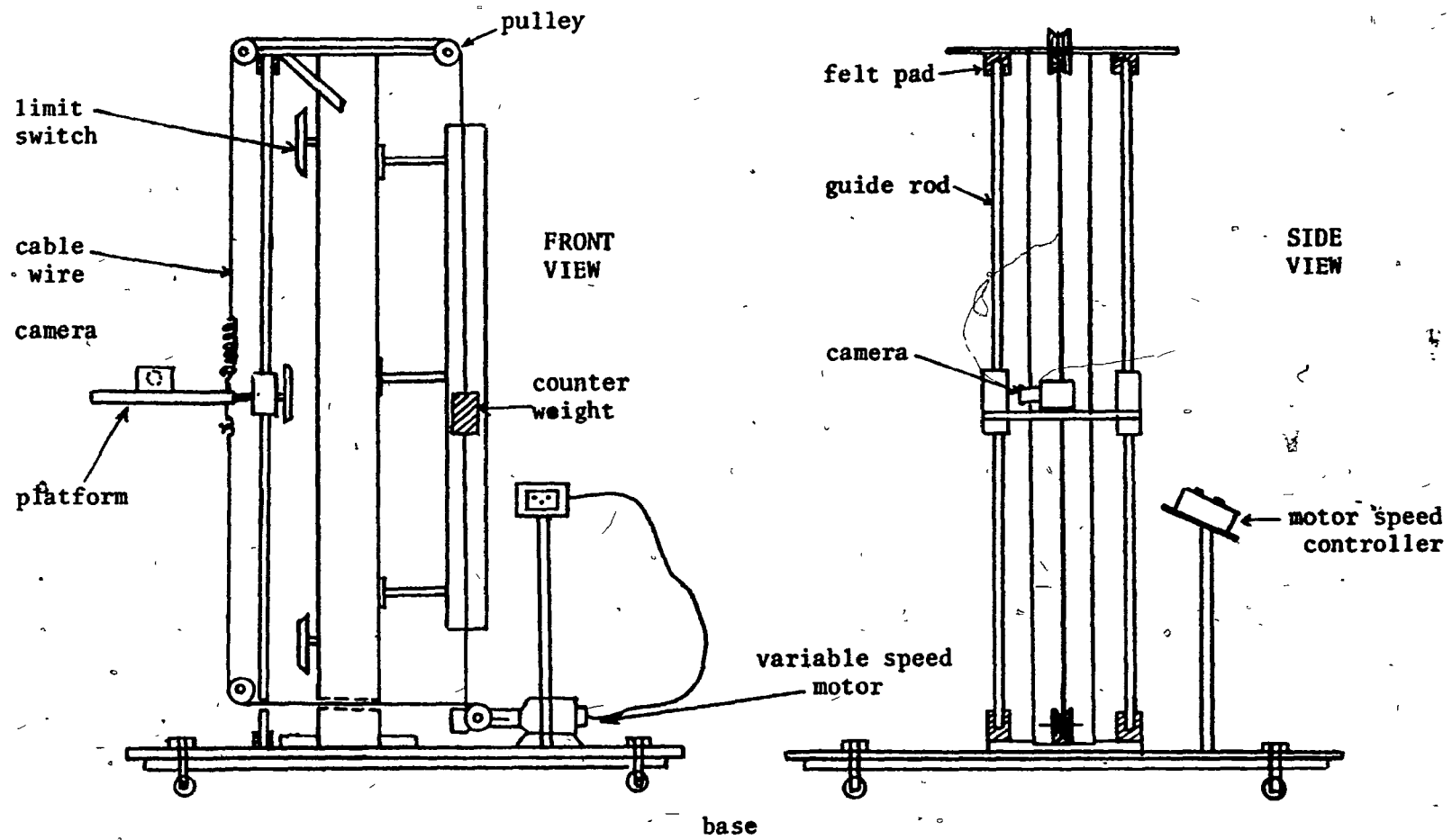
FIGURE 2.6 Camera Moving Device
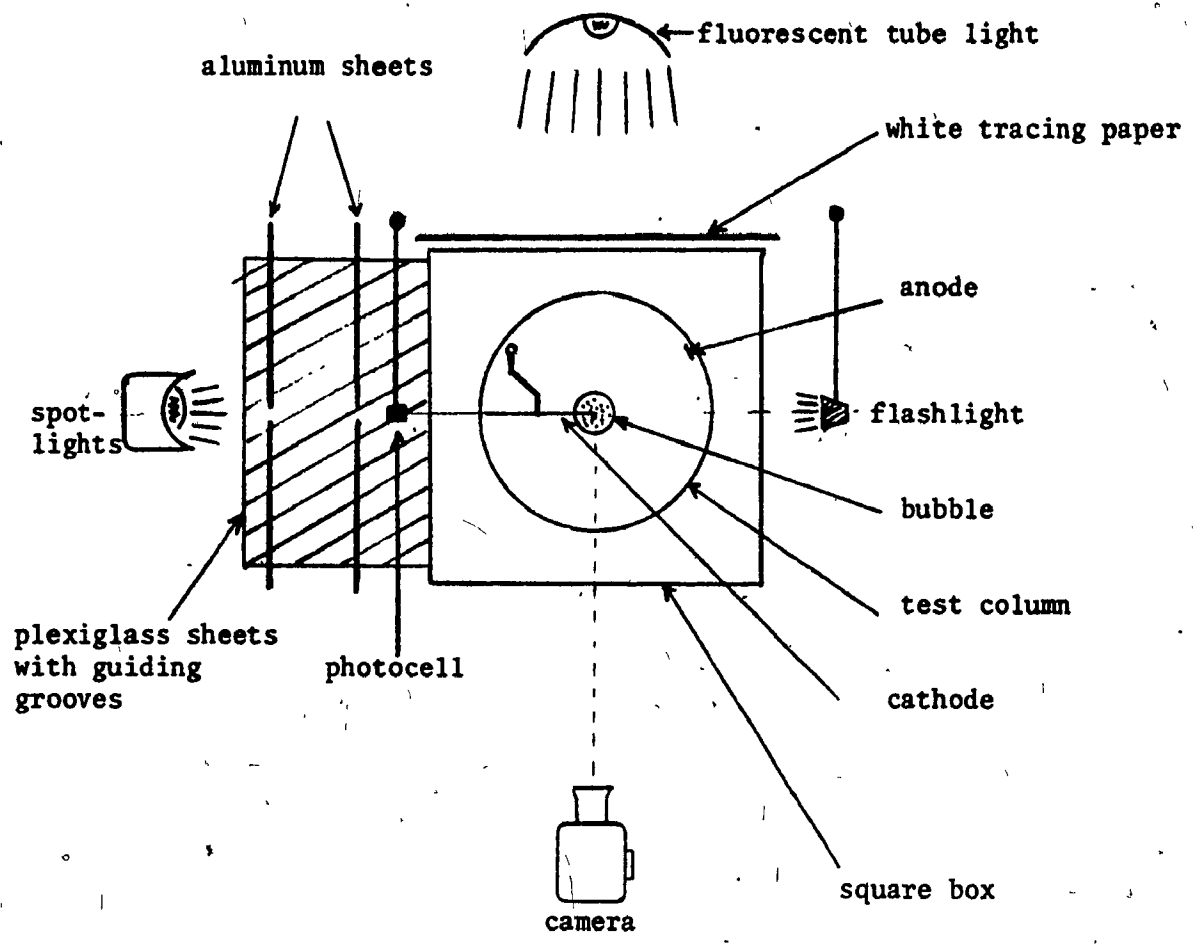
FIGURE 2.7 Lighting Arrangement (Viewed from the Top)

light could be varied by adjusting the gap between two aluminum sheets, and was maintained at 2-3 mm.. The aluminum sheets slid in grooves machined in two plexiglass plates, one mounted at each end of the square box surrounding the column. A plane of illumination at slightly more than 90° to the optical axis of the camera gave the best results. To prevent excessive heating of the liquid, the spotlights were left on only when photographs were being taken. In the flow field study it was necessary to photograph the bubble, as well as the tracers, hence a combination of back and side illumination had to be employed. This resulted in photographs showing a black bubble surrounded by white tracer bubbles on a gray background (see Fig. 4.4).

Photographic records of the various types of experiments were obtained on 4-X 16 mm. reversal films ASA 400 with a 16 mm. Bolex reflex ciné camera that could operate at 12 to 64 frames/sec.. Various lenses and filming speeds were employed. The speed of the camera was independently determined by filming a clock accurate to 0.01 sec. for about 4 sec. at the beginning of each film.

2.3 Range of Variables Studied

The hydrogen-bubble flow visualization technique requires the presence of water in the liquid medium. An aqueous sugar solution was chosen as the liquid because it satisfied this requirement and because its viscosity could be varied over a wide range by dilution. The concentrated sugar solution ("sugar invert") was obtained in bulk from a local sugar refinery.* Although pale yellow in colour it was sufficiently clear for

---

photography. Since the properties of the gas do not play an important role in the behaviour of bubbles, air was used as the dispersed phase. The range of the variables studied in the present work are summarized in Table 2.2.

2.4 Experimental Procedures

The test column and the surrounding square box were filled with the concentrated sugar solution. Initially a small quantity of distilled water containing some sodium sulphate was added to the liquid to enhance its conductivity. Air was dispersed in the liquid for some time to achieve good mixing and the liquid was left overnight to clear the dispersed air. The physical properties of the liquid were then measured. The density of the liquid was determined with calibrated hydrometers, the viscosity with a Cannon-Fenske Capillary viscometer and the surface tension with a ring tensiometer. Since the viscosity of the liquid was very sensitive to temperature, the temperature variations in the vertical direction were minimized by circulating the air in the laboratory with three fans. The various procedures employed for the different measurements are described below.

2.4.1 Shape and rise velocity measurements

The required volume of bubble was introduced into the liquid column by means of a calibrated syringe and caught in the dumping cup. The accuracy of the volume measuring technique is discussed in Section 3.4.1.1. After the disturbance in the liquid due to the bubble injection had subsided, the bubble was released by rotating the cup. The bubble motion was photographed using back-lighting with a stationary 16 mm Bolex ciné camera positioned at 330 cm from the centre of the column and 110 cm

TABLE 2.1

Range of Variables Studied

Continuous Phase: AQUEOUS SUGAR SOLUTION

μ = 0.62 - 28.2 Poise

ρ = 1.30 - 1.39 g/cm^3

σ = 76.7 - 80 dynes/cm

M = 2.39x10^{-4} - 8.75x10^2

Dispersed Phase: AIR

μ = 1.84x10^{-4} - 1.85x10^{-4} Poise

ρ = 1.18x10^{-3} - 1.20x10^{-3} g/cm^3

Bubble Volume: 0.08 - 139 (cm^3)

Temperature: 20.8 - 25.3 ^{o}C

Column Diameter: 29.2, 14.4, 7.06 cm. I.D.

above the bubble generating cup. The time of passage of a bubble through

the column was obtained automatically by a clock activated by photocells.

The ciné film was projected onto the lower surface of a trans-

parent screen and the shape of the bubble was traced on a semi-transparent

paper. To obtain the appropriate magnification factor, an accurate scale

(25.4 cm x 25.4 cm) was suspended in the liquid in the central plane

containing the axis of bubble rise and photographed. The projection of

the photograph of this scale also showed that the square box surrounding the

cylindrical column was successful in eliminating the radial optical

distortion. Errors due to the oblique viewing of bubbles were avoided

by tracing the bubble image when its position coincided with the optical

axis of the camera. To allow ready comparison of shapes of bubbles of

different volumes and in different liquids the images of the bubble were

always projected at a fixed magnification. The accuracy of the shape

measuring technique is discussed in Section 3.4.1.3.

The velocity was determined from the bubble displacement data

obtained from the ciné film or from the photocell actuated clock. The

accuracy of these two techniques is discussed in Section 3.4.1.2.

2.4.2 Liquid velocity field measurement

For the flow field study a combination of back and side-

lighting (see Section 2.2.6) was used. The ciné camera was mounted on the

platform of the camera moving device and moved to the same level as the lower

photocell. The electronic equipment for generation of tracer bubbles

(see Section 2.2.3), the lighting system and the camera moving device

were all prepared for use. Sufficient hydrogen bubble tracers were

generated in the lighted, central plane, perpendicular to the viewing

axis of the camera. The bubble was introduced into the liquid and

released as described earlier. When the bubble reached the level of the bottom photocell the activation system (see Section 2.2.2) switched on the clock, the pulse generator and the camera moving device. The motions of the bubble and the tracer bubbles in the surrounding liquid were simultaneously recorded by the ciné-camera moving at the same speed* as the bubble. When the bubble reached the level of the upper photocell the various instruments were automatically switched off.

The above procedures were used to study the flow field in the immediate neighbourhood of the bubble. For the flow far away from the bubble and specifically behind the bubble the same experimental procedure was followed except that the ciné camera was kept stationary while filming.

Two camera speeds, about 12 and 32 frames/sec, were employed. At the low filming speed the exposure was long enough for the tracer bubbles to appear as streaks. These streaks represent velocity vectors, thus showing the overall features of the velocity field in a single photograph (see Figs. 4.4-4.8). Details of the liquid motion were obtained from frame-by-frame analysis of the film taken at the higher speed.

2.4.3 Bubble interaction and coalescence observation

The interaction and coalescence of two vertically aligned bubbles were studied as follows. The volume of the leading bubble was

---

* At the beginning of each experiment, the speed of the camera moving device was preset at the rise velocity of the bubble under study.

introduced into the dumping cup by means of the calibrated syringe. When the disturbance in the liquid had died, a desired volume for the trailing bubble was measured into the syringe and the syringe was connected to the air inlet via the Luer valve. The first bubble was released from the cup and the second was injected from the syringe into the column. The initial separation distance of the bubbles could be adjusted by varying the time between inverting the cup and injecting the second bubble. Both bubbles went through the inverted funnel above the dumping cup and were thereby vertically aligned. The motion of the bubble pair was recorded by a stationary ciné camera.

2.4.4 Wall effect measurements

The influence of the wall was examined by studying the behaviour of bubbles rising in columns of smaller diameters. For these experiments smaller plexiglass tubes were inserted from the top into the large column and aligned over the inverted funnel. The experiments were performed using the procedure described earlier.

CHAPTER 3

SHAPE AND RISE VELOCITY OF BUBBLES

3.1 Introduction

In many mass transfer devices gas-liquid contacting is facilitated by dispersing the gas in the liquid. The purpose of this subdivision of the gaseous phase into small bubbles is generally two-fold; it increases the interfacial area and it produces relative motion between the phases. . Both of these effects contribute to an increase in overall mass transfer rate.

Several investigators have studied mass transfer for a single bubble in order to obtain information which might ultimately aid in the design of large scale contactors. An estimate of the overall rate of mass transfer in a bubble column can be obtained by considering the mass transfer for a single bubble. To do this it is necessary to predict the terminal velocity and the shape of the bubble from its volume, since the residence time of the bubble is dependent on the terminal velocity and the mass transfer coefficient is dependent on the terminal velocity and the shape.

This chapter reports the study of bubble shape and terminal velocity in relatively viscous Newtonian liquid media. It is well known that the shape as well as the rise velocity of the bubble is strongly affected by the proximity of the container wall. In this chapter the bubbles are considered to rise in an infinite medium. The wall effect is dealt with in Chapter 7.

3.2 Literature Review

3.2.1 Dimensional analysis

Any body rising or falling under gravity reaches a terminal velocity when the forces acting on it are in equilibrium, i.e.

$$\text{drag force} + \text{buoyancy force} + \text{weight} = 0 \qquad (3.1)$$

For rigid bodies the drag is a function of the shape of the body, the terminal velocity and the physical properties of the medium. However, for fluid bodies such as a gas bubble the situation is further complicated by the fact that:

  (i) the bubble can be deformed under the action of hydrodynamic forces, and

  (ii) a vortex motion may ensue inside the bubble due to momentum transfer across the interface.

Thus, the shape of the bubble and therefore the drag force acting on it will, in general, be a complex function of the hydrodynamic, viscous and interfacial forces.

Since a general analytical solution for the "drag" of a bubble is not possible except for special cases which will be discussed later, various workers (Schmidt 1934; Rosenberg 1950; Haberman and Morton 1953 and 1956; Wegener and Parlange 1973; Grace 1973) have tried to correlate experimental results by dimensional analysis.

The relevant physical quantities for a single bubble rising at its terminal velocity in an infinite liquid are:

U — terminal velocity of bubble

g — acceleration due to gravity

ρ — density of the liquid

ρ' — density of the gas

μ — viscosity of the liquid

μ' — viscosity of the gas

σ — surface or interfacial tension

d_e — equivalent sphere diameter

It is usual in the studies of bubbles and drops to employ the equivalent sphere diameter, d_e, as the relevant length parameter because it is independent of the bubble shape and is related directly to the bubble volume:

$$d_e = (\frac{6V}{\pi})^{1/3} \tag{3.2}$$

For gas bubbles rising in liquids the number of variables to be considered is usually reduced by assuming that the motion of the enclosed gas has a negligible effect on the flow.* Thus the density and the viscosity of the dispersed gas can be dropped from the above list. With the remaining six variables and the three dimensions of mechanics, we can form three dimensionless groups which will describe the motion of the bubble. Various combinations of dimensionless groups have been used, for example:

---

* This assumption is justified because the ratio of the pressure and the viscous forces exerted by the gas on the interface to the same forces exerted by the liquid on the interface are ρ'/ρ and μ'/μ respectively, which are usually smaller than 10^{-3} and 10^{-2}, respectively.

$$F_1(C_D, Re, M) = 0 \qquad (3.3)$$

$$F_1(C_D, We, M) = 0 \qquad (3.4)$$

$$F_1(Re, E\ddot{o}, M) = 0 \qquad (3.5)$$

$$F_1(Fr, Re, M) = 0 \qquad (3.6)$$

The definitions of these dimensionless numbers and their physical significance are listed below:

$$Re = \frac{\rho d_e U}{\mu} \propto \frac{\text{inertial force}}{\text{viscous force}} \qquad \text{(Reynolds Number)} \quad (3.7)$$

$$We = \frac{\rho U^2 d_e}{\sigma} \propto \frac{\text{inertial force}}{\text{surface tension force}} \qquad \text{(Weber Number)} \quad (3.8)$$

$$E\ddot{o} = \frac{g d_e^2 \rho}{\sigma} \propto \frac{\text{buoyancy force}}{\text{surface tension force}} \qquad \text{(Eötvos Number)} \quad (3.9)$$

$$Fr = \frac{U^2}{g d_e} \propto \frac{\text{inertial force}}{\text{buoyancy force}} \qquad \text{(Froude Number)} \quad (3.10)$$

$$C_D = \frac{4 g d_e}{3 U^2} \propto \frac{\text{buoyancy force}}{\text{inertial force}} \qquad \text{(drag coefficient)} \quad (3.11)$$

$$M = \frac{g \mu^4}{\rho \sigma^3} = \text{liquid property parameter (Morton Number)} \quad (3.12)$$

Only three of these dimensionless numbers are independent since:

$$We = \left(\frac{4 M Re^4}{3 C_D}\right)^{1/3} \qquad (3.13)$$

$$Fr \; = \; \frac{4}{3C_D} \qquad\qquad (3.14)$$

and

$$E\ddot{o} \; = \; \frac{3}{4} \, WeC_D \qquad\qquad (3.15)$$

The Morton Number, M, is extensively used in the literature to correlate experimental data since it is only a function of liquid physical properties and the acceleration of gravity. M varies over a wide range; in highly viscous oils it can be as high as 10^5 and in liquid metals it can be as low as 10^{-14}. The variations in M are principally due to the factor μ^4, since ρ and σ do not vary much from liquid to liquid.*

3.2.2 Classification of liquids according to Morton Number

There have been many studies of the rise velocity of bubbles in liquids. Most of the early work is summarised by Haberman and Morton (1953,1956). They have made an exhaustive study of the literature, collecting data of the previous experimenters and integrating these data with their own. These workers have demonstrated that the Morton Number, M, has a profound influence on the behaviour of rising bubbles. Their results show that the liquids can be classified into two broad categories according to the Morton Number: low M liquids $(M < 10^{-8})$ and high M liquids $(M > 10^{-3})$; each exhibiting radically different bubble behaviour.

For low M liquids the terminal velocity at first increases rapidly as the bubble volume increases, achieves a maximum and after falling to a minimum rises again gradually. The bubble shape is at first

---

* Liquid metals are exceptions. They are reported to have surface tensions in the range 200-2000 dynes/cm (Slaughter 1967) as compared to ordinary liquids having the range of 20-80 dynes/cm.

spherical, then increasingly oblate, then, at about the volume corresponding to the maximum velocity, the shape fluctuates rapidly about an oblate form until, for very large volumes, the bubbles attain a spherical-cap shape with a steady frontal surface and a fluctuating base. The bubble trajectory is at first rectilinear, then at about the bubble volume for maximum velocity, zig-zag or spiral trajectories are observed. Finally, the spherical cap bubbles rise nearly rectilinearly.

For high.M liquids, the terminal velocity increases steadily with bubble volume, although the rate of increase decreases with volume. Small bubbles are spherical. At larger volumes distortion from the spherical shape occurs, but the corresponding instability and decrease in rise velocity do not appear; the spherical cap shape is achieved without the bubble surface ever becoming unsteady. The bubble trajectories are rectilinear for any volume.

In attempting to correlate bubble rise velocity data many authors (Peebles and Garber 1953; Haberman and Morton 1953 and 1956; Tadaki and Maeda 1961; Jones 1965; Angelino 1966; Kojima et al 1968; Harper 1972) have plotted experimental results in terms of C_D versus Re at constant M as suggested by Equation (3.3). The main features of these plots can be summarised as follows:

(i)   The·C_D versus Re curves have a nearly universal form for very small and very large Re.

(ii)   For small bubbles the drag coefficient falls between the drag curve of Stokes for rigid spheres and the drag curve of Hadamard for fluid spheres. A transition from the solid to the fluid curve takes place at a different Re for different liquids, e.g. it occurs at Re $\approx$ 40 for pure

water and Re $\approx 10^{-3}$ for olive oil (Haberman and Morton 1953).

(iii) For large Re, when the bubbles are spherical caps, C_D is independent of Re and has a constant value of about 2.6.

(iv) The variation of C_D with M is mainly in the range Re $\approx$ $0(10^2)$ for low M liquids where these curves exhibit a sharp minimum. It is this minimum which corresponds to the maximum velocity, and to the onset of oscillation for the ellipsoidal bubble.

(v) For high M liquids the minimum in the C_D versus Re curve is very shallow or altogether absent.

From the above discussion it is evident that the behaviour of bubbles in high M liquids is distinctly different from that in low M liquids.

3.2.3 **Bubble regimes**

A plot of C_D versus Re is not completely satisfactory for predicting the rise velocity and the shape a bubble of given volume adopts in a liquid. An additional drawback of this plot is that both C_D and Re contain the variable U, which generally is unknown. Recently, Grace (1973) pointed out that it is more convenient to have only one dimensionless group containing the terminal velocity U, namely Re and to plot Re versus Eotvos Number, Eö, for constant M. Using such a plot he successfully correlated data for 21 different liquids with physical properties as diverse as mercury (M $= 3.6 \times 10^{-14}$) and a very viscous liquid used to simulate a glass melt (SA1B, M $= 1.0 \times 10^7$). Three distinct regimes of bubble shape, namely

spherical, ellipsoidal and spherical-cap were delineated. (See Fig.3.13.) It is convenient to discuss the previous work in terms of these regimes.

3.2.3.1 Spherical_bubbles

It is widely recognized that interfacial tension forces tend to minimize the surface area of a fluid particle; thus bubbles of sufficiently small Eo (and hence small We) tend to be spherical no matter how large the value of Re. (See Fig.3.13.) Although first pointed out by Saito (1913), it is not widely appreciated that when viscous forces predominate over inertia forces a bubble will also tend to be spherical; thus bubbles are spherical at low Re, no matter how large the value of Eo. (See Fig.3.13.)

For Re << 1, when inertial forces are negligible, the drag coefficient, C_D, has been shown to be

$$C_D = \frac{24}{Re} \qquad (3.16)$$

for a solid sphere (Stokes 1851), and

$$C_D = \frac{16}{Re} \qquad (3.17)$$

for fluid sphere (Hadamard 1911, Rubczynski 1911) with $\mu' << \mu$ and $\rho' << \rho$, the conditions appropriate to a gas bubble. The former equation applies to spherical bubbles with a rigid interface, i.e. when surface-active impurities are present in quantities sufficient to prohibit internal circulation (Levich 1962). The latter applies to a bubble with a completely mobile interface, corresponding to a very pure liquid. Recently, Golovin

and Ivanov (1973) used the asymptotic matching technique* to obtain higher order approximation for the drag coefficient of a gas bubble:

$$C_D = \frac{16}{Re} + 2 + \frac{2}{5} Re \, \ln(\frac{Re}{2})$$

(3.18)

For Re >> 1, Fig. 3.13 shows that bubbles can be spherical providing that the Morton Number is sufficiently small. Here one expects the effects of fluid viscosity to be important in the viscinity of the bubble surface but of little importance in the bulk of the fluid. At high Re, Levich (1949) evaluated the energy dissipation in irrotational flow past a sphere and obtained

$$C_D = \frac{48}{Re}$$

(3.19)

as a first approximation to the drag coefficient of a spherical bubble, as did Ackeret (1952) and Chan and Prince (1965) later but independently. Moore (1963) improved Levich's result by solving the boundary layer equations analytically. By extending the energy dissipation calculation to include the contribution from the boundary layer and wake he obtained

$$C_D = \frac{48}{Re}(1 - \frac{2.21}{Re^{1/2}})$$

(3.20)

* Golovin and Ivanov's solution is the gas bubble analogue of the well known Proudman and Pearson (1957) expansion for a rigid sphere. It matches the Oseen solution, which takes account of the convective terms as Re → 0 and correctly describes the velocity distribution at large distances (van Dyke 1964), to the Hadamard-Rybczynski solution for a freely circulating gas sphere in the neighbourhood of the bubble surface.

Winnikao and Chao (1966), Harper and Moore (1968) and Parlange (1970) have extended the theory to account for the internal as well as external flow. The theoretical treatment of boundary layers is beyond the scope of the present work. The interested reader should refer to Harper's (1972) review paper.

3.2.3.2 Ellipsoidal bubbles

Ellipsoidal bubbles are found at relatively high Reynolds Number and intermediate Eötvos Number. Grace's (1973) boundary between the ellipsoidal and spherical regime is somewhat arbitrary because of paucity of data and the amount of eccentricity which can be tolerated before a bubble is considered ellipsoidal. The presence of surface active impurities has a significant effect on bubble deformation and this further complicates the issue. Ellipsoidal bubbles commonly undergo periodic dilations or random wobbling motions which also make characterization of shape difficult. Grace classified bubbles as ellipsoids when the ratio of minor to major axis was less than 0.9. The term "ellipsoidal" was used to refer to bubbles which are oblate concave (viewed from inside) around the entire surface, and it did not necessarily imply fore and aft symmetry.

Taylor and Acrivos (1964) showed by a perturbation technique for Re << 1 and We << 1 that a spherical bubble would deform into an oblate ellipsoid and finally approach a shape somewhat similar to that of a spherical cap bubble with further increase in We. These authors derived the following equation for the drag of a bubble at low Re:

$$C_D = \frac{16}{Re} + 2 + \frac{2}{5} Re \ln\frac{Re}{2} + 1.33\frac{We}{Re} + \ldots\ldots \qquad (3.21)$$

The second and third terms of the right-hand side of the equation are the contributions of the inertial effect and the fourth, of the deformation of the bubble.

Moore (1965) and El Sawi (1974) have shown for gas bubbles in steady flow at Re >> 1 in low M liquids that the minimum and subsequent rise in C_D with Re can be explained in terms of a transition from a spherical to an oblate ellipsoidal shape.

Finally, the instability of bubbles, generally encountered in low M liquids has been studied experimentally and theoretically by Saffman (1956) and Harturian and Sears (1957). These later workers collated previous results on onset of instability and also experimented on a number of liquids. No experiments were reported with $M > 10^{-8}$ in which the motion became unstable. Instability was found to set in either when Re reached a value of about 200 or when We (as defined by Equation (3.8))* reached about 3.2, with the former criteria applying to impure viscous liquids and the latter to purer liquids of low viscosity. It was postulated that oscillations originated from a surface instability generated by interaction of surface tension and hydrodynamic pressure forces. Other workers have obtained experimental critical values of We ranging from 2.96 to 4.24 for bubbles and drops (Winnikow and Chao 1966).

---

* Note that Hartunian and Sears have employed a different definition for Weber Number.

3.2.3.3 Spherical-cap bubbles

Most of the previous work on spherical-cap bubbles is summarised in recent reviews by Harper (1972) and Wegener and Parlange (1973).

Grace (1973) has shown that conditions for the occurance of spherical-cap bubbles are: (see Figure 3.12)

(i)   Eö ≥ 40. This condition assures that interfacial tension forces play a negligible role in determining the behaviour of bubbles; and

(ii) Re ≥ 1.2

For low M liquids condition (ii) is satisfied well before (i). However, for high M liquids, bubbles pass directly from the spherical regime to spherical-cap regime, exhibiting no ellipsoidal regime. Condition (ii) then becomes the limiting condition. It should be emphasized that in what Grace refers to as "spherical-cap regime", he has included all bubbles with flat or indented (dimpled) bases without fore and aft symmetry. Such bubbles may look very similar to segments cut from spheres or from oblate ellipsoids. In the present work the former will be referred to as "spherical-caps" and the latter as "oblate-ellipsoidal-caps", respectively.

There has been considerable controversy regarding the exact nature of wakes below spherical-cap bubbles*, but now there is enough evidence to support the proposition that at low Re (often encountered in high M liquids) these bubbles carry along with them closed laminar wakes while at high Re (usually in low M liquids) the wakes are unconfined and turbulent (Wegener and Parlange 1973). Spherical cap bubbles in highly

---

* This point is discussed in Chapter 4.

viscous liquids have also been reported to trail very thin sheets of gas referred to as "skirts".* (Harper 1972; Wegener and Parlange 1973)

On the theoretical side Davies and Taylor (1950) were first to advance a fluid mechanical model to determine the rise velocity of spherical-cap bubbles without regard to the nature of the wake. Assuming that:

(i) the flow around the bubble-cap is potential flow over the forward part of a sphere of the same radius as the bubble-cap, and

(ii) constant pressure condition inside the bubble can be satisfied near $\theta = 0$ to order θ^2, where θ is the polar angle measured from the front stagnation point,

these authors related the bubble velocity, U, to the radius of curvature at the bubble nose, R_o, by the simple equation:**

$$U = \frac{2}{3} \sqrt{gR_o} \tag{3.22}$$

It is interesting to note that this relation has been found to agree well with experiments both in low M liquids where one expects a turbulent wake (Davies and Taylor 1950; Rosenberg 1950) and in high M liquids where a closed laminar wake is expected (Davenport 1964; Guthrie 1967; Sundell 1971).

Collins (1966) obtained the second approximation to the Davies and Taylor expression by using a linear perturbation of the spherical shape. The constancy of the surface pressure was satisfied to terms of order θ^4 giving:

---

* The subject of skirted bubbles is dealt with in Chapter 6.

** According to Siemes (1954), Prandtl had also derived the same equation independently as seen in his unpublished notes on bubble research.

$$U = 0.652 \sqrt{g\bar{R}} \tag{3.23}$$

where $\bar{R}$ is the average radius of curvature over the front 75° (i.e. $\pm 37.5^{\circ}$ around front stagnation point) of the bubble. Recently, Harper (1972) repeated Collin's analysis with the well known irrotational flow past a spheroid and found that the spheroid must be oblate with eccentricity $= 1/2$ and the corresponding rise velocity is given by

$$U = 0.643 \sqrt{g\bar{R}} \tag{3.24}$$

Since the last three equations do not differ significantly from each other, Equation (3.22) is usually used.

In order to obtain a relationship between the bubble velocity, U, and the bubble volume, V, the semi-angle subtended by the spherical-cap, θ_m, must be known. For spherical-cap bubbles with Re $\geqslant$ 100, Grace (1970) has shown that θ_m is approximately constant at 50°. Using this experimental observation together with the geometric relationship (see Equation (3.40)) which gives the volume of the spherical-cap segment, Equation (3.22) can be transformed into

$$U = 25V^{1/6} \tag{3.25}$$

This relation is in good agreement with the experimental data on low M. liquids (Davies and Taylor 1950; Haberman and Morton 1953; Guthrie 1967; Slaughter 1967).

Moore (1959) suggested a free-streamline model which assumed that the spherical cap bubble is followed by an infinite axi-symmetric wake and predicted values of $\theta_m = 39°$ and $C_D = 2.1$. However, these values were in poor agreement with the observed values of $\theta_m = 50°$ and $C_D = 2.6$. This is not surprising since Moore's assumption misrepresents the actual wake. Moore's model was improved by Rippin and Davidson (1967), who predicted the shape and the velocity by a numerical method. They found that the shape is indeed close to spherical cap with $\theta_{max} = 50°$ which is in excellent agreement with the observed value. However, their velocity predictions were about 20% higher than the values observed experimentally.

Mendelson (1967) tried to draw an analogy between spherical-cap bubbles rising in liquid and waves travelling along a plane free surface. His equation* agrees reasonably well with large bubbles moving through low M liquids but fails to predict correctly the transition between large spheroidal and spherical-cap bubbles (Harper 1972).

Parlange (1969) has given a solution for the case of spherical cap bubbles with closed laminar wakes in high M liquids. He assumed that for Re >> 1 (but small enough to still have a laminar wake) the flow consists of a Hill's (1894) spherical vortex, surrounded by an irrotational flow excepting a thin boundary layer. To zeroth order the volume of the bubble was ignored compared with the volume of the enclosed wake. The role of the bubble was primarily to furnish, by its buoyancy, the energy necessary for the rise of the wake. The theory gave for the rise velocity

$$U = \frac{1}{3}(\frac{2}{5\pi})^{1/3} g^{2/3} (\frac{\rho}{\mu})^{1/3} V^{1/3} \tag{3.26}$$

* By replacing the wave length in the well known Kelvin's equation (Lamb 1932) for wave velocity by the equatorial circumference, πd_e, of the equivalent sphere Mendelson obtained: $U = \sqrt{\frac{2\sigma}{\rho d_e} + \frac{g d_e}{2}}$

where it should be noted that the rise velocity can be calculated from a known bubble volume and the physical properties of the liquid,unlike Davies and Taylor expression, Equation (3.22).

Assuming that the boundary layer corrections computed by Harper and Moore (1968)[*] can be applied, Parlange (1969) also gave a second approximation for the rise velocity:

$$U = U_o\left[1 + (6.6 - 0.14 \ln Re_o)(9\,Re_o)^{-1/2}\right] \qquad (3.27)$$

where U_o is given by the zeroth order result of Equation (3.26) and
$Re_o = \dfrac{2\rho R_o U_o}{\mu}$.

Davidson (1974)[**] showed that viscous flow around a spherical-cap bubble results in a different radial pressure distribution within the fluid from that obtained for potential flow. In order to maintain constant pressure within the bubble, he calculated that the radius of curvature was decreased with increasing viscosity, and was related to the bubble's velocity by:

$$R_o = \frac{9}{8}\frac{U^2}{g}\left[1 + \sqrt{\frac{128}{27}\frac{\mu g}{\rho U^3}}\right] \qquad (3.28)$$

---

[*] In a later paper Parlange (1970) presented his own version of the boundary layer correction (see Section 4.3 for details). However, both theories yield essentially the same numerical result for viscous dissipation and rise velocity.

[**] The author is grateful to Professor J. Davidson of Cambridge University, who graciously provided his research notes on this subject. Since Equations (3.28) and (3.29) have not been published elsewhere, a brief outline of Davidson's derivation is presented in Appendix A.

and $\qquad U = \frac{2}{3}\sqrt{gR_o - \frac{6\mu U}{\rho R_o}}$ (3.29)

Note that by putting $\mu = 0$ in the above expression Davies and Taylor's relationship, Equation (3.22), is recovered.

3.2.3.4 Oblate-ellipsoidal-cap bubbles

It will be shown later in this chapter that for $1.2 \lesssim Re \lesssim 45$ and $Eo \gtrsim 14$ bubbles adopt an oblate-ellipsoidal-cap shape. Recently, Wairegi and Grace (1976) have developed an equation that relates the rise velocity of an oblate-ellipsoidal-cap fluid particle to its shape:

$$U = \frac{\sin^{-1}e - e\sqrt{1-e^2}}{e^3}\sqrt{\frac{(\rho-\rho')}{\rho}gb}$$ (3.30)

Here e is the cap eccentricity defined as $e = \sqrt{1-(b/a)^2}$ where b and a are the semi-minor and the semi-major axis, respectively. Their derivation essentially uses the Davies and Taylor assumptions, but with the pressure distribution derived assuming the cap is a portion of an oblate ellipsoid of revolution. Note that for bubbles, where $\rho' \ll \rho$, Equation (3.30) simplifies to Equation (3.22) as $e \to 0$. A favourable agreement with experimental data for drops and bubbles was reported.

3.2.4 Bubble deformation and shape parameters

Most of the early experimental work dealing with bubble deformation was concentrated on bubbles rising in low M liquids (Rosenberg 1950; Harmathy 1960; Tadaki and Maeda 1961; Calderbank and Lochiel 1964; Calderbank 1967; Aybers and Tapucu 1969). Of these studies that of Tadaki

and Maeda (1961) is the most extensive, covering 14 different liquids with $3.94 \times 10^{-11} < M < 2.54 \times 10^{-4}$. They correlated the deformation index, defined as the ratio of the equivalent spherical diameter to the major axis of the bubble, with Re and M and proposed empirical formulae for approximately predicting the bubble shape for low viscosity liquids.

Experimental studies on the shapes of bubbles rising in high M liquids have been published only in the last decade. These are summarised in Table 3.1.

The first successful theoretical treatment of the deformation of a spherical fluid particle was carried out by Taylor and Acrivos (1964) for low Re and small deformation. These authors used a singular perturbation solution of the axisymmetric equation of motion and obtained the first order and the second order deformation equations describing the surface of the fluid particle. For air bubbles their second order deformation equation, which takes into account the perturbation due to deformation, simplifies to:

$$R^* = 1 - \frac{5}{24} We P_2(\cos\theta) - \frac{5}{56} \frac{We^2}{Re} P_3(\cos\theta) \qquad (3.31)$$

where R^* is the dimensionless radial distance, r/r_e describing the bubble surface, θ is the angle measured from the front stagnation point and $P_2(\cos\theta)$ and $P_3(\cos\theta)$ are the Legendre polynomials of 2nd and 3rd order, respectively. Brignell (1973) extended the Taylor and Acrivos solution to higher order and derived the following equation to describe the bubble surface:

TABLE 3.1 Summary of Bubble Shape Measurements in High M Liquids

Author	Liquid Used	Approx. * Bubble Size	Shape Parameters Measured
Angelino (1964,1966)	propylene glycol mineral oil glycerine	M,L	maximum width
Jones (1965)	sucrose solutions of diff. conc. paraffin oil glycerol at diff. temps.	S,M,L	maximum width for spherical and ellipsoidal caps only
Hayashi & Matumobu (1967)	syrup glycerine	S	aspect ratios (height/width)
Davenport (1964) Davenport et al (1967)	polyvinyl alcohol solutions of diff. conc.	M,L	radius of cap, θ_m height, basal radius
Slaughter (1967)	glycerine	M,L	radius of cap, θ_m height, basal radius
Guthrie (1967) Guthrie & Bradshaw (1973)	polyvinyl alcohol solution of diff. conc.	M,L	radius of cap, θ_m height, basal radius
Kojima et al (1968)	caster oil glycerine corn syrup	S,M	aspect ratio
Calderbank (1970)	aq. glycerol	S,M,L	inverse of aspect ratio
Grace (1970)**	various liquids	M,L	included angle
Sundell (1971)	mineral oil	M,L	radius of cap, θ_m
Hnat (1973)	mineral oil	M,L	radius of cap, θ_m, skirt length, etc.
Wairegi (1974)	sugar solution paraffin oil	S,M,L	radius of cap, θ_m, skirt length, etc.
Bonato (1971)	glycerine of diff. conc.	S,M	maximum width and height

* S approx. size 0.1 - 1 cm^3
  M approx. size 1 - 10 cm^3
  L approx. size > 10 cm^3

** Data of other workers on included angle, θ_m, correlated.

$$R^* = 1 - \frac{5}{24}WeP_2(\cos\theta) - \frac{5}{56}\frac{We^2}{Re}P_3(\cos\theta) + WeRe\left\{\frac{1}{16}P_2(\cos\theta)\right.$$

$$\left. - \frac{1}{1400}P_3(\cos\theta)\right\} - \frac{1}{24}WeRe^2(\log Re)P_2(\cos\theta) \qquad (3.32)$$

However, this result is of little practical value as shown later in Section 3.4.2.2. Pan and Acrivos (1968) extended the Taylor and Acrivos solution to the more general case where the Reynolds number pertaining to the motion inside of a bubble is unrestricted. They demonstrated that the internal circulation does not affect the shape of a gas bubble, whereas it contributes in a minor, but significant, way to the deformation of a liquid drop.

At smaller Re where small deformations from spherical shape are encountered the theoretical approach of Taylor and Acrivos has been successful in predicting the deformation of bubbles and drops (Wellek et al 1966; Hayashi and Matunobu 1967; Kojima et al 1968; Pan and Acrivos 1968). On the other hand, at larger Re and for more extensive deformations analytical approaches have not been successful primarily because of the non-linearities in the equation of motion and the a priori unknown geometry of the bubble surface. In addition, numerical solutions to the full Navier-Stokes equation in which the shape, as well as the flow is unknown are not economic on present computers. Faced with these difficulties, several simple predictive models have been proposed. Savic (1953) suggested a procedure whereby the shape is determined by a balance of the normal stresses at the interface. Savic's approach has been extended by Prappacher and Pitter (1971) for water drops falling through air and by Wairegi (1974) for drops and bubbles in liquids. Unfortunately, the external dynamic pressure distribution (which in turn depends on the

shape one wishes to deduce) must be known to apply the method. Thus, this method is of limited practical value for predicting shapes from first principles.

3.3 Objectives

From the foregoing discussion it is clear that there is no satisfactory theoretical solution available to predict the shape for the wide range of Re and the associated complex flow conditions encountered in practice. Despite the wealth of data now available (see Table 3.1), no unified way of presenting and predicting bubble deformation has been reported. The present work on bubble shape was, therefore, directed towards collecting more experimental data in viscous-liquids, integrating them with previously reported data and devising a scheme to predict bubble shape.

Another objective of the present research was to determine the conditions at which the bubbles change from spherical to oblate-ellipsoidal to oblate-ellipsoidal-cap and then to spherical-cap. It was also desired to delineate on Grace's plot (i.e., Re versus Eö plot) other possible sub-regions such as spherical-cap with closed steady wake, spherical-cap with open unsteady wake, skirted bubble with smooth skirts, wavy skirts, etc..

In his review paper Harper (1972) points out that: "More experimental results are desirable for Re > 10 and M > 10^{-6}; there seems to be a change in the character of the C_D versus Re curves between M — 10^{-5} and M — 10^{-2} but no transitional cases are available." The present experiments were performed on high M liquids ($2.39 \times 10^{-4} < M < 7.11 \times 10^2$) in order to fill some of the gaps present in the existing experimental data.

It appears that no systematic experiments have been reported in liquids of intermediate values of M to determine the value of M for which there will be no bubble instability and maximum rise velocity. If this critical value of M could be located precisely, one could use this as the boundary between the low M liquids and the high M liquids. In the present investigation an attempt was made to locate this critical value of M.

The final objective was to test the available theoretical models predicting rise velocity and to point out their limitations.

3.4 Experimental Results and Discussion

The results obtained on shapes and rise velocities of bubbles are presented and discussed in the following sections.

3.4.1 Evaluation of measuring techniques

3.4.1.1 Volume measurement

The simple method of introducing a desired volume of gas into the liquid column by means of calibrated syringe as described in Chapter 2 was checked as follows. For large syringes, the volume was checked by catching the bubble at the top of the column with a funnel leading to a graduated cylinder. For the smallest syringe (1 cm^3 capacity) the volume introduced was compared with that calculated from photographic measurement of the bubbles which were either perfectly spherical or oblate ellipsoidal. Both of these checks verified that the volume introduction technique used in the present work was accurate within ± 1%. The volume was corrected to the local hydrostatic pressure at the midpoint of the test section where all shape and velocity measurements were made.

(a) Oblate
Ellipsoidal Cap
$(\theta_m > 90)$

$w = 2a$

(b) Oblate
Ellipsoidal Cap
$(\theta_m < 90)$

$w = 2a'$

(c) Spherical Cap

$a = b = R$

$w = 2a'$
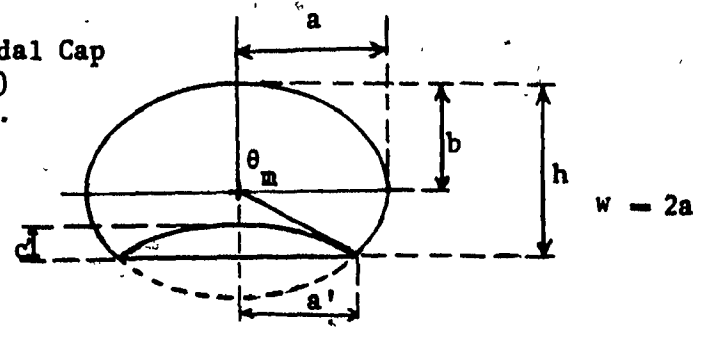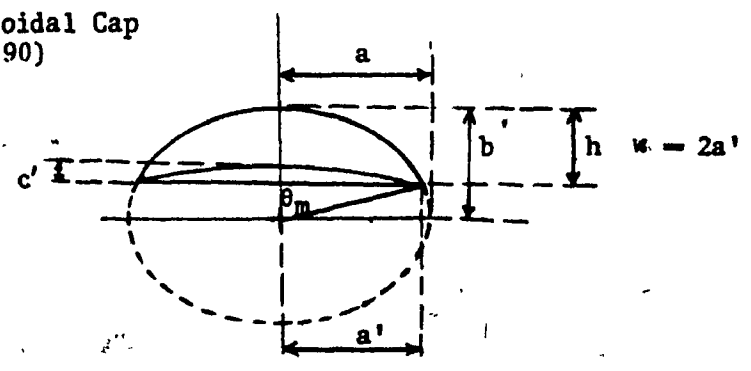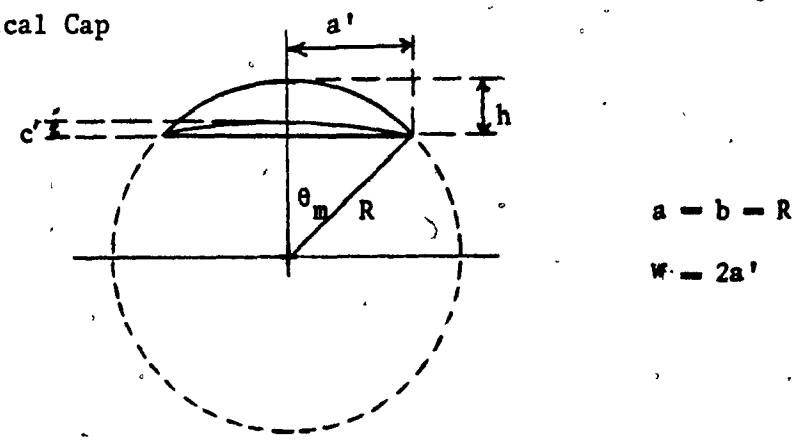
FIGURE 3.1 Definition of Bubble Shape Parameters

3.4.1.2 Velocity measurement

Using the ciné-photography technique described in Chapter 2, the instantaneous rise velocity of a bubble could be determined within ± 0.5% accuracy. Typical results of bubble displacement with time showed a linear relationship indicating that the possible increase in velocity due to the change in hydrostatic head was negligible. The average rise velocity measured using the two photocells was accurate within ± 0.9%. The agreement between the results of these two techniques was found to be excellent.

3.4.1.3 Measurement of shape parameters

The shapes of the bubbles were obtained with the photographic method described in Chapter 2. Careful analysis of a great number of tracings from the films indicated that an oblate ellipsoidal or spherical shape described the whole of the contour of the bubble except the base of the bubble which was slightly convex for small bubbles and flat for larger bubbles. To determine the ellipsoid or sphere which fits the shape, the following procedures were used.

(i) Oblate-ellipsoidal-cap bubbles as shown in Fig.3.1(a)

On the tracing of a bubble a vertical axis of symmetry was determined by folding the tracing such that the left and the right halves of the bubble coincided. The horizontal symmetry was similarly obtained by folding the tracing along the maximum width of the bubble. By superpositioning the top half of the bubble on to the bottom, the ellipse which fits the bubble was completed.

(ii) Oblate-ellipsoidal-cap bubbles as shown in Fig.3.1(b)

The vertical symmetry was found as before. Assuming the origin of the co-ordinate system at the nose of the bubble the equation

of the ellipse is given by:

$$\frac{x^2}{a^2} + \frac{(y+b)^2}{b^2} = 1$$

(3.33)

where a and b are the major and minor semi-axis of the ellipse, respectively.

The value of a and b could be obtained by solving Equation (3.33) using any two co-ordinate points lying on the bubble boundary. To increase the accuracy and avoid subjective error introduced when drawing the bubble shape, several co-ordinate points on the bubble boundary were obtained to give several estimates of a and b from Equation (3.33). Provided that the co-ordinates were sufficiently widely spaced, five co-ordinate points were found to be satisfactory in giving values of a and b with ± 6.5% accuracy.

(iii) Spherical-cap bubbles as shown in Fig.3.1(c)

The vertical axis of symmetry was found as before. The centre of the sphere that fits the bubble was located by superimposing on the bubble tracing a transparent plexiglass plate (1 mm. thick) on which circles of varying radius at intervals of 2 mm. were inscribed. The values of radius of curvature, R, using this method were determined with ± 5.0% to ± 3.0% accuracy for the smallest to largest radius, respectively. The values of the measured radius of curvature were found to be in good agreement with those calculated geometrically from measurements of the basal radius, a', and the height, h, of the bubble.

Having determined the ellipsoid or sphere that fits the shape the following shape parameters defined in Fig.3.1 were measured.

a — semi-major axis

b — semi-minor axis

h — bubble height

w — bubble width

a' — basal radius

c' — indentation

R — radius of spherical cap

θ_m — semi-included angle

3.4.2 Bubble shape results

3.4.2.1 Qualitative description

The photographs in Fig.3.2 show all of the shapes encountered in the present work. The change in the bubble shape with the variation of liquid properties is illustrated by the series of photographs in Fig.3.3 for a 9.3 cm^3 bubble in eight different sugar solutions. The viscosity was varied from 28 to 0.85 Poise giving Re — 2.47 to 151. To facilitate visual comparison the bubble is shown at the same magnification in all the photographs. The effect of bubble volume and liquid properties on bubble shape is demonstrated in Fig.3.4(a) & (b). The horizontal series of tracings in these figures depict the gradual transformation of the bubble shape with increase in volume, from sphere to skirted bubble or to spherical-cap bubble depending upon the physical properties of the liquid. The progressive stages in these transformations are summarised schematically below.

FIGURE 3.2 <u>Photographs of Typical Shapes of Bubbles</u>

	Liquid Properties									
No.	μ (Poise)	ρ (g/cm³)	σ (dynes/cm)	M	V (cm³)	U (cm/sec)	Re	Eö	We	Shape*
1	26.80	1.390	80.0	7.11×10^2	0.19	2.12	0.078	8.67	0.056	S
2	"	"	"	"	0.56	4.37	0.232	17.7	0.339	OE
3	0.84	1.315	76.8	8.20×10^{-4}	1.39	25.49	55.3	32.2	15.4	OED
4	20.84	1.384	79.0	2.66×10^3	27.8	31.12	7.77	243	63.8	OEC
5	1.30	1.326	77.0	4.63×10^{-3}	9.3	35.33	94.0	115	130	SCC
6	0.84	1.315	76.8	8.20×10^{-4}	27.8	43.93	259	237	124	SCO
7	13.15	1.378	79.1	4.30×10	46.3	39.12	18.3	339	119	SKS
8	"	"	"	"	120.3	47.14	30.3	641	237	SKW

* S - spherical
OE - oblate ellipsoidal
OED - oblate ellipsoidal disc-like
OEC - oblate ellipsoidal cap
SCC - spherical cap with closed toroidal wake
SCO - spherical cap with open unsteady wake
SKS - skirted bubble with steady smooth skirt
SKW - skirted bubble with wavy skirt

<u>Note:</u> Bubbles are not shown at the same magnification. The grid in the background is approximately 2 cm x 2 cm.
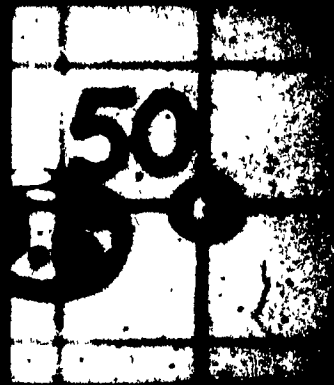
FIGURE 3.3 <u>Effect of Liquid Property on Bubble Shape</u>

Bubble volume — 9.3 cm^3; d_e — 2.61 cm.

No.	Liquid Properties			M	U (cm/sec)	Re	Eö	We	Shape†
	μ (Poise)	ρ (g/cm^3)	σ (dynes/cm)						
1	28.00	1.389	80.0	8.48×10^3	19.10	2.47	116	17.3	OEC
2	20.84	1.384	79.9	2.66×10^3	20.61	3.57	116	19.3	OEC
3	13.00	1.378	79.1	4.11×10^1	25.92	7.16	116	36.0	OEC
4	7.81	1.370	78.5	5.51	29.15	13.3	116	48.4	OEC
5	5.42	1.361	78.0	1.31	31.15	20.4	116	61.2	OEC
6	2.85	1.346	77.6	1.03×10^{-1}	34.28	42.2	116	89.3	OEC
7	1.30	1.326	77.0	4.63×10^{-3}	35.33	94.0	115	130	SCC
8	0.85	1.314	76.8	8.60×10^{-4}	37.55	151	114	170	SCO

* OEC - oblate ellipsoidal-cap
SCC - spherical-cap with closed toroidal wake
SCO - spherical-cap with open unsteady wake

<u>Note:</u> All bubbles shown at the same magnification. The grid in the background is approximately 2 cm x 2 cm.

μ (Poise) M (-)

26.80 7.11×10³   0.19   0.36   0.66   1.39

13.98 5.55×10   0.63   1.11   1.98   3.92

7.30 4.17   1.84   3.25   5.13   9.28

2.89 1.09×10⁻¹   7.86   10.43   16.13   27.12

1.00 1.64×10⁻³   28.13   38.53   60.47   92.76

Volume (cm³) ⟶   0.46   0.93   1.85   4.63

Eo(-) ⟶   15.6   24.8   39.4   72.6
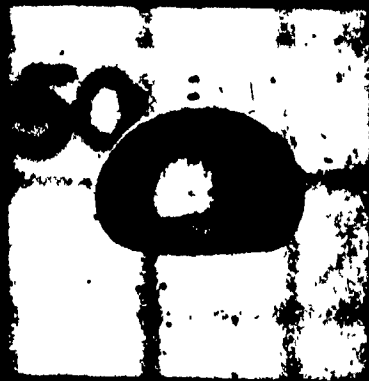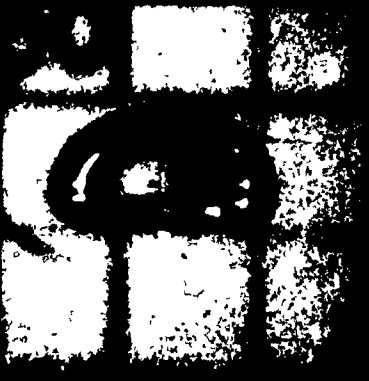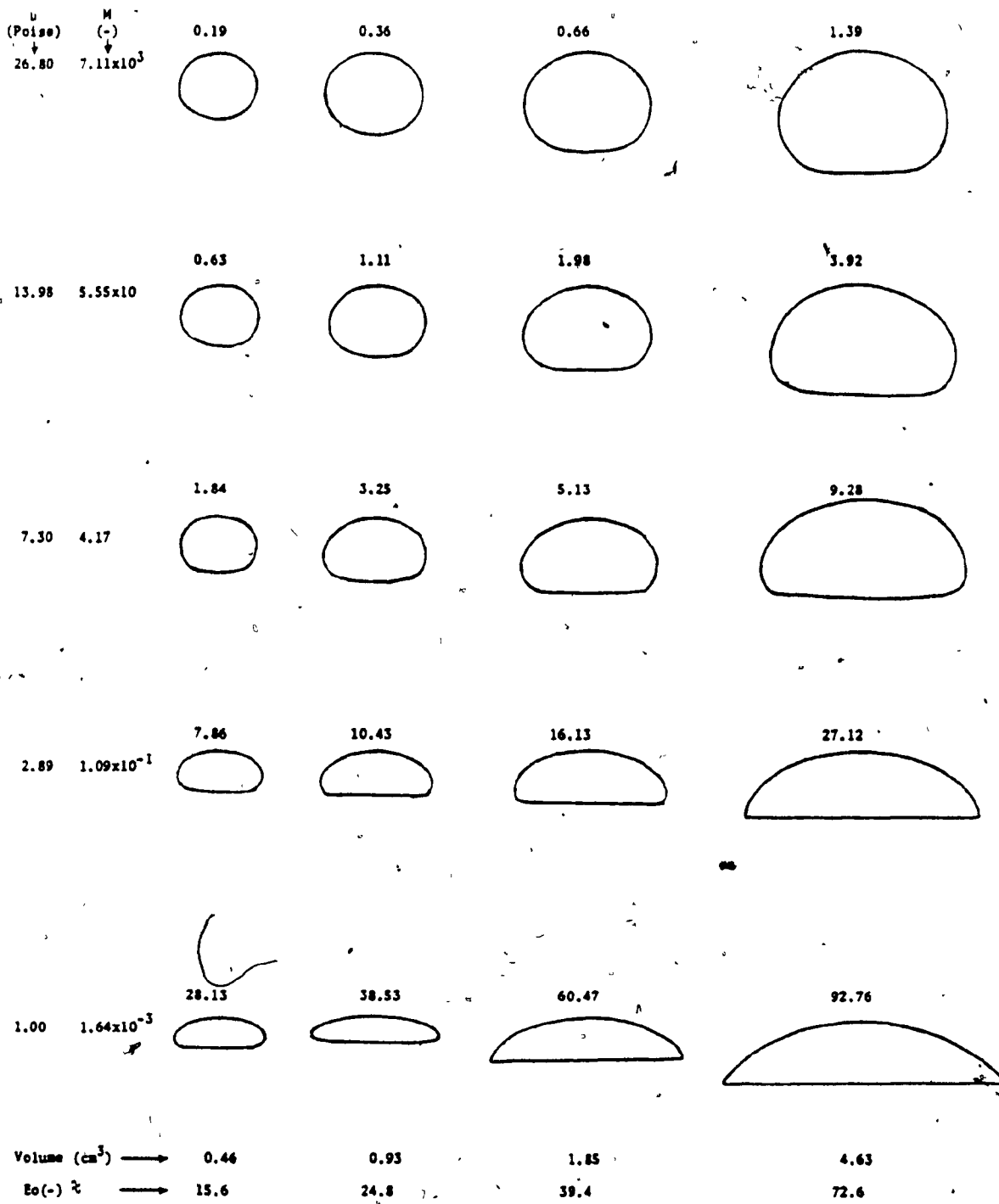
2 cm

FIGURE 3.4(a) Tracings Illustrating the Effect of Bubble Volume and Liquid Properties on Bubble Shape (The number at the nose is the corresponding Re; indentation at the bubble base is not shown; for other liquid properties see Table 3.3)

μ (Poise) ↓	M (-) ↓				
		2.46	4.84	7.61	14.64
26.80	7.11x10³				
		6.43	11.27	17.17	30.40
13.98	5.55x10				
		14.15	23.96	35.44	62.84
7.30	4.17				
		40.21	65.67	91.94	161.7
2.89	1.09x10⁻¹				
		128.5	196.6	266.5	491.2
1.00	1.64x10⁻³				
Volume (cm³) →		9.3	23.2	46.3	139.0
Eo(-) →		115	242	337	705

5 cm
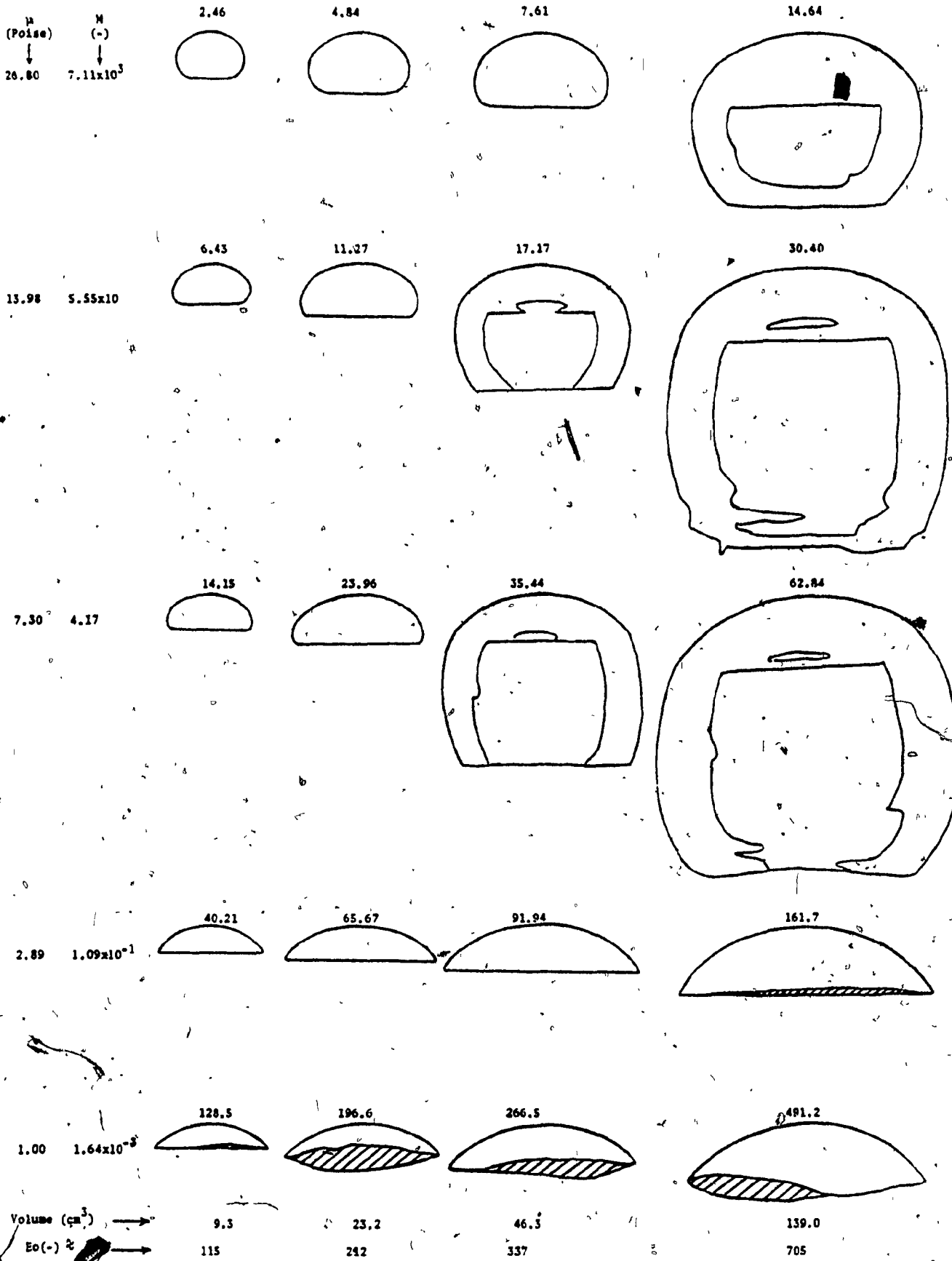
FIGURE 3.4(b) Tracings Illustrating the Effect of Bubble Volume and Liquid Properties on Bubble Shape (The number at the nose is the corresponding Re; indentation at the bubble base is not shown; for other liquid properties see Table 3.3)

spherical
↓
oblate-ellipsoidal
↓
oblate-ellipsoidal-cap

INCREASING
VOLUME

spherical-cap (open unsteady wake)　　spherical-cap (closed toroidal wake)　　steady skirt

steady skirt
↓
wavy skirt　　　　　　wavy skirt

$M \lesssim 0.7$　　　　$0.7 \lesssim M \lesssim 3$　　　　$M \gtrsim 3$
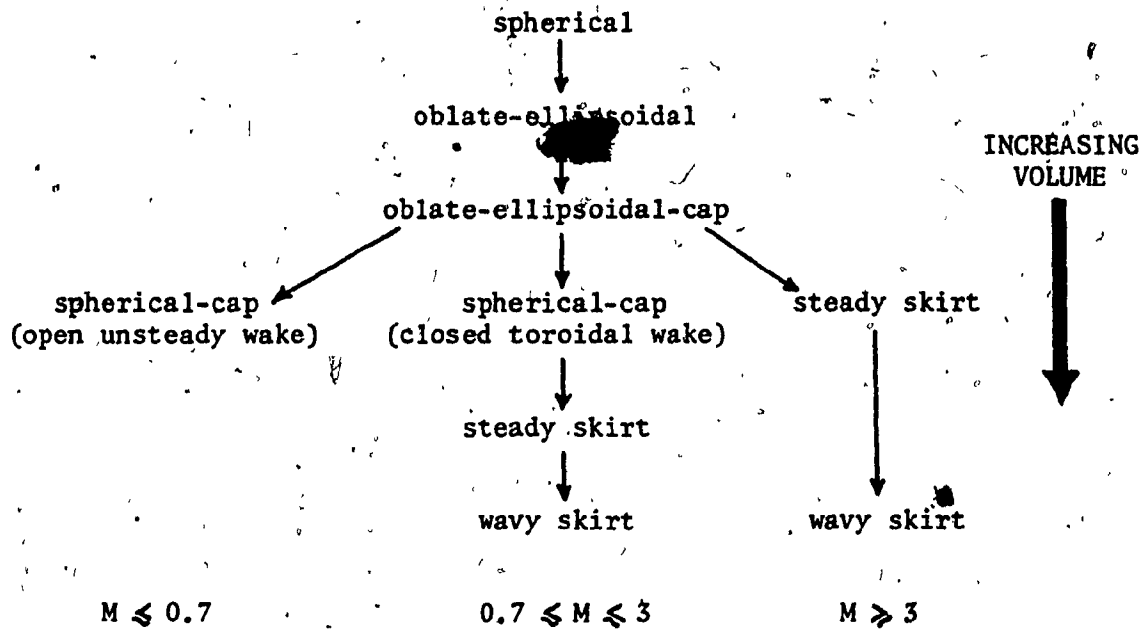
It is often reported in the literature (Haberman and Morton 1953, 1956; Grace 1973) that with increasing volume bubbles in viscous (or high M) liquids change directly from spherical to spherical cap shape without going through an ellipsoidal regime. The present photographs indicate that this is clearly not true. The transformation from spherical to spherical-cap shape is a gradual process via ellipsoidal and ellipsoidal-cap shapes. In fact, in fairly high M liquids $(M \gtrsim 3)$ ellipsoidal bubbles do not change into spherical caps* but instead around Re $\approx$ 12 develop thin skirts at the periphery of their bases. For intermediate M liquids $(3 \gtrsim M \gtrsim 0.7)$ the ellipsoidal-cap bubbles change into

---

* This was found to be true for volumes up to 139 cm^3. At considerably larger volumes with higher Re, skirts would be unstable and it is conjectured that at very high volumes bubbles will be spherical-cap even in liquids of high M.

spherical-cap bubbles and then develop skirts. For liquids with $M \leq 0.7$ no skirts were observed for bubble volumes up to 139 cm^3. For skirted bubbles the length of the skirt was found to increase with bubble volume and above a certain volume the skirt became wavy and its bottom edge showed some instability (see Fig.3.2(8)). In the remainder of this chapter, only bubbles without skirts are considered. The interesting topic of skirted bubbles is taken up again in Chapter 6.

The vertical series of tracings in Figs.3.4(a) & (b) show the profound effect of liquid properties on bubble shape for a fixed volume. It is observed that as the viscosity of the liquid decreases the bubble deformation for a fixed volume increases making it progressively flatter. For bubbles of all shapes the front surface was always smooth. The edge of the bubbles changed from being rounded for the small sizes to being quite sharp for the larger ones. The bottom of the ellipsoidal cap and spherical cap bubbles for Re < 110 appears flat on side-view photographs but is actually indented. This indendation was readily observed visually and it was also seen on photographs of bubbles with Re < 50.(see Fig.3.2(4), Fig.3.3(1) to Fig.3.3(6)). Similar indentations have also been reported by other workers (see end of Section 3.3.2.2). For spherical-cap bubbles with Re $\gtrsim$ 110, where the bubbles have open unsteady wakes (see Chapter 4), the lower surface does not remain steady but fluctuates as can be seen from Fig.3.2(2) and Fig.3.3(8).

3.4.2.2 Comparison of deformation from the spherical shape with theoretical predictions

The experimental shapes of slightly deformed bubbles rising in 28.23 Poise sugar solution are compared with the theory of Taylor and

FIGURE 3.5 Comparison of Deformation of Bubbles in 28.23 Poise
Sugar Solution with Theoretical Predictions

liquid properties: μ = 28.23 Poise
ρ = 1.390
σ = 80.00
M = 8.82x10^2

No.	V (cm^3)	U (cm/sec)	Re (-)	Eö (-)	We (-)
a	0.46	3.94	0.19	15.7	0.26
b	0.74	4.82	0.27	21.5	0.45
c	0.93	6.63	0.40	25.9	0.93
d	1.39	8.00	0.55	32.7	1.54
e	1.85	8.17	0.61	39.6	1.77
f	2.78	10.00	0.86	51.8	3.03

left half → experimental shape   ▬▬ ▬▬

right half → theoretical predictions

For bubbles (a) to (e): the theoretical predictions of Taylor and
Acrivos (1964) and Brignell (1973) are
indistinguishable. (Maximum difference
less than 2%.)

For bubble (f): ------- Taylor & Acrivos' prediction, Equation (3.31)

—·— Brignell's prediction, Equation (3.32)

(a)

(b)

(c)

(d)

(e)
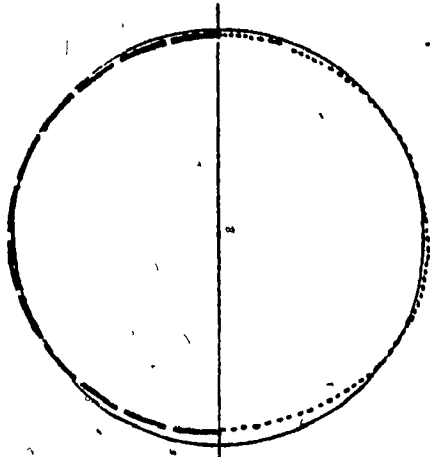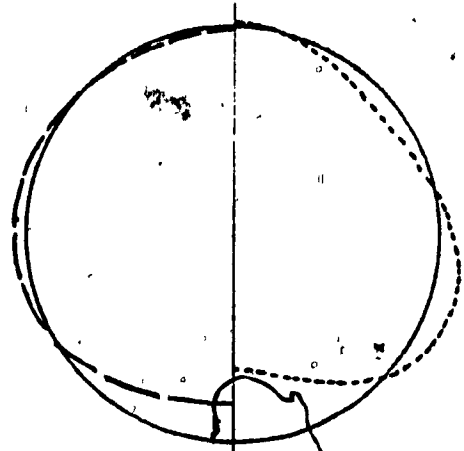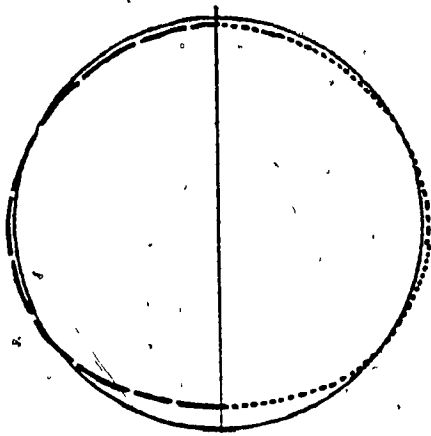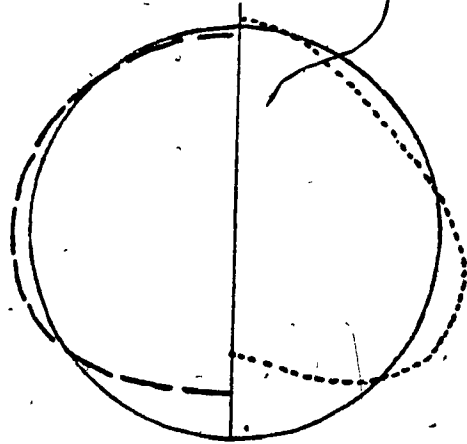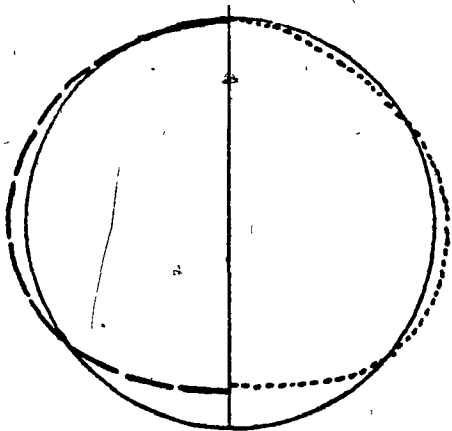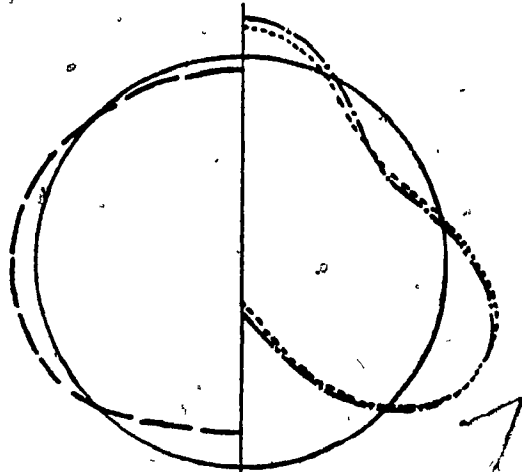
(f)

Acrivos (Equation (3.31)) and Brignell (Equation (3.32)) in Figure 3.5. The theory successfully predicts the flattening of the bubble and development of the indentation at the rear as bubble volume increases. It is noteworthy that for low Re (see Fig.3.5(a) to (e)) Brignell's higher order theoretical predictions do not differ significantly (less than 2%) from those of Taylor and Acrivos until We exceeds~2 (see Fig.3.5(f)). However, at this point the basic assumptions of the theory are violated and both equations fail to represent the observed shape. Hence, it is concluded that the theory of Taylor and Acrivos is accurate enough for predicting very small deformations and that the higher order theory of Brignell is of little practical value.

3.4.2.3 Correlations for bubble deformation

In the present work b/a, h/w, h/d_e and w/d_e and θ_m are selected as deformation indices to give a measure of the deviation from spherical shape. The reason for their choice will become obvious in the following discussion. The shape parameters h, w, a, b, and θ_m have been defined in Figure 3.1. The physical properties of the liquids employed in the shape study are listed in Table 3.3. Only data on bubbles of d_e < 4.3 cm.* rising in the 29.2 cm I.D. column are shown to insure that the wall effect was negligible.

(a) Dependence of bubble shape on Reynolds Number

The deformation indices, w/d_e and h/d_e, are plotted against

---

* The reason for selecting this as a criteria is given in Section 3.4.3.5.

Re in Fig. 3.6 for seven sugar solutions with M varying from 1.64×10^{-3} to 7.11×10^{2}. On these co-ordinates the data collapse onto a single curve which suggests that for high M liquids, deformation is function of Re only. This confirms the observation of Kojima et al (1968) for high M liquids up to Re $\approx$ 25.

As expected, both w/d_e and h/d_e tend toward unity as Re decreases, whereas an asymptotic mean value of 1.79 and 0.4 respectively is approached at Re $\geqslant$ 100.

The radius of curvature, height and width of a perfect spherical-cap segment (i.e. with flat base without any indentation) is given by:

$$R = \frac{d_e}{2(\cos^3\theta_m - 3\cos\theta_m + 2)^{1/3}} \qquad (3.34)$$

$$h = R(1 - \cos\theta_m) \qquad (3.35)$$

$$w = 2R \sin\theta_m \qquad (3.$$

Using these equations and the mean experimentally observed value of the semi-included angle, $\theta_m = 48^\circ$, for Re $\geqslant$ 100 we predict $w/d_e = 1.792$ and $h/d_e = 0.399$. Both of these values are in excellent agreement with the experimentally observed values of 1.79 and 0.4, respectively.

The deformation indices b/a and θ_m or h/w give a complete description of bubble shape except the indentation at the base. These deformation indices are plotted against Re in Figure 3.7. The various shape regimes (except skirted bubbles) are also indicated. All three deformation indices are well correlated and are found to be a function only of Re for these high M liquids. This is in contrast to experimental observations in low M
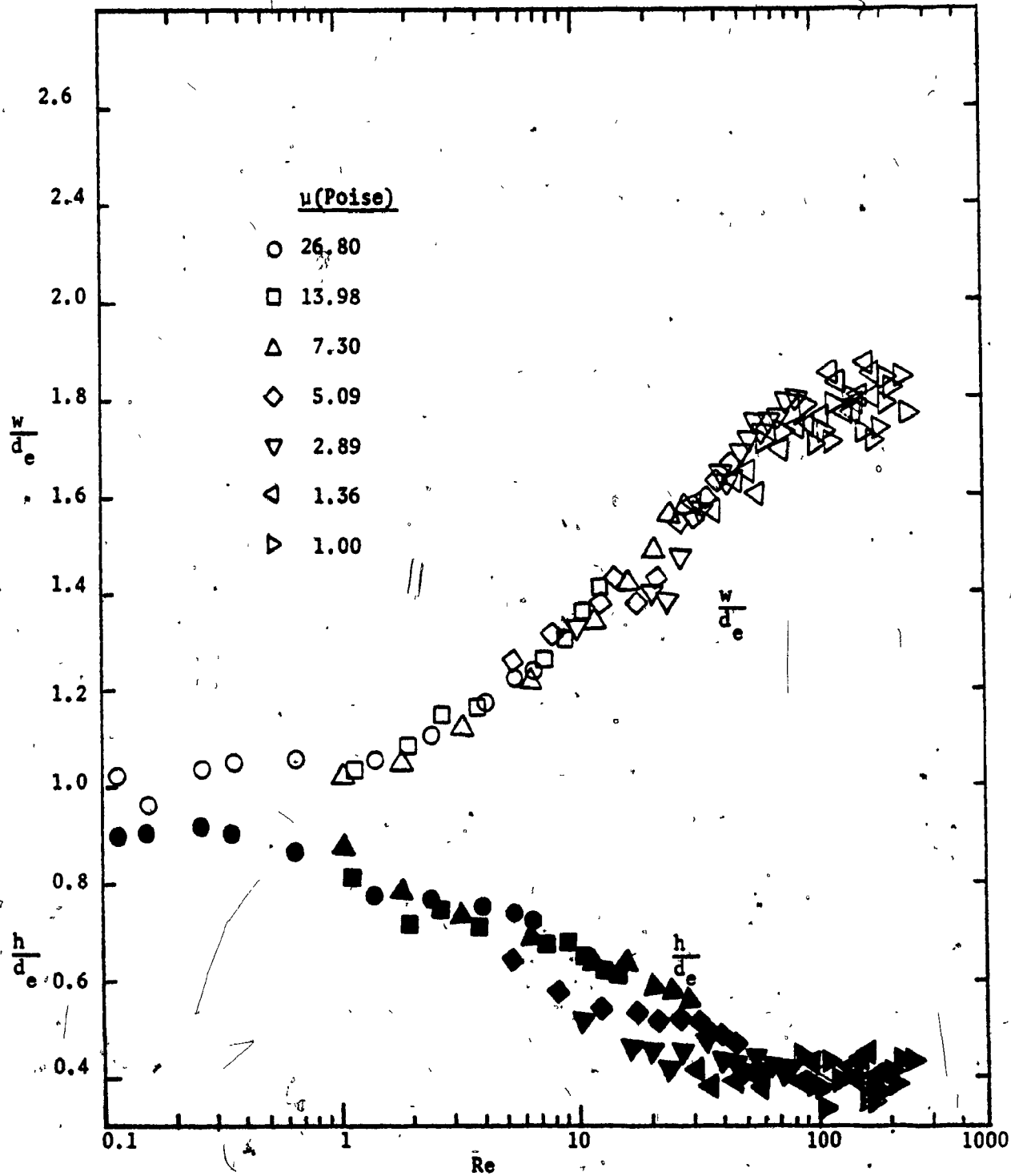
FIGURE 3.6　Effect of Re on bubble width and height
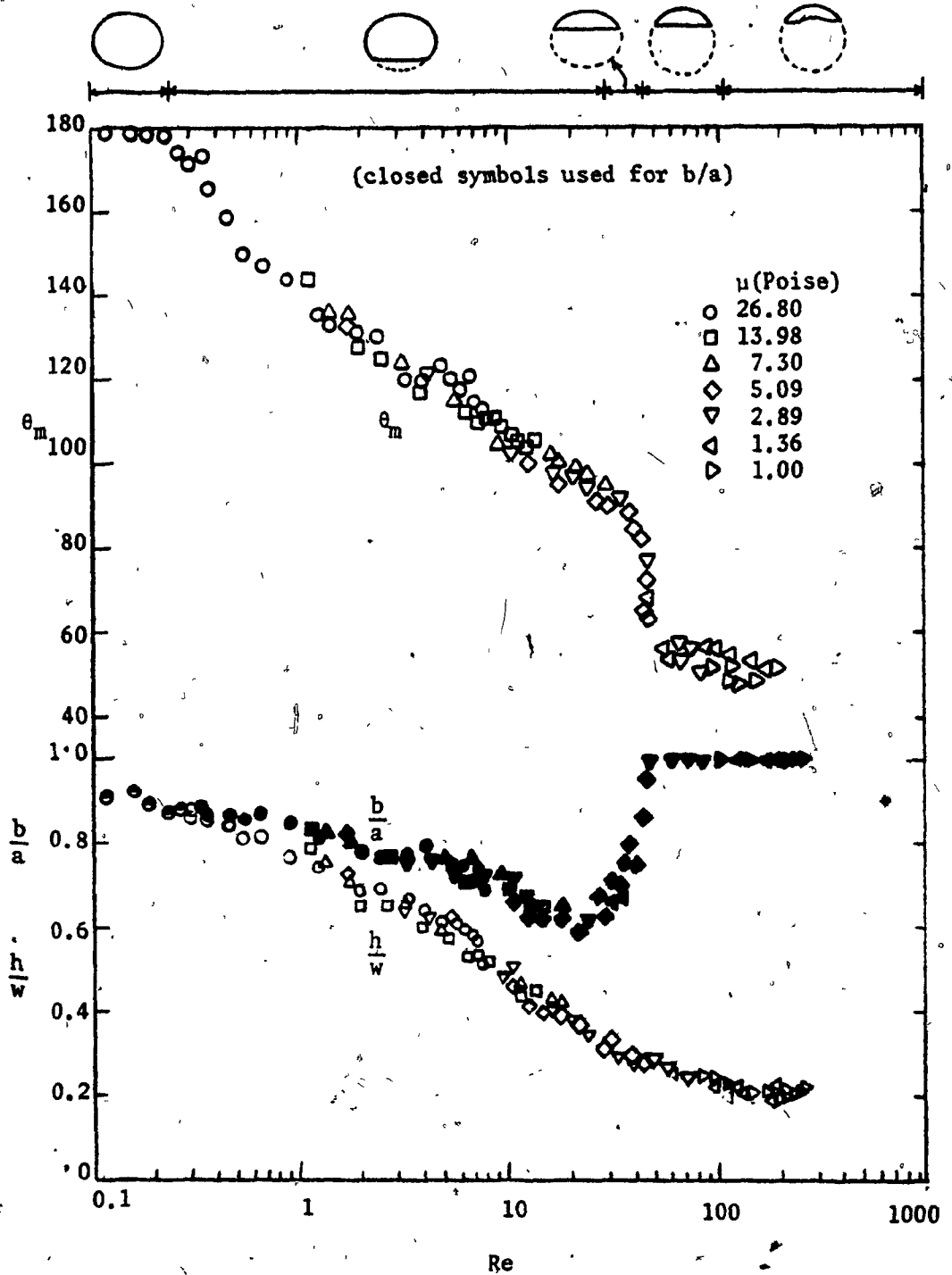
FIGURE 3.7 Generalized correlation for the bubble deformation

liquids where Tadaki and Maeda (1961) found the deformation to be function of both Re and M.

In Figure 3.8 the present correlations are compared with the shape data of other workers for 25 high M liquids. The agreement is excellent bearing in mind the different experimental techniques and the wide variety of liquids used.

Kojima et al (1968) presented the following empirical correlation for high M liquids and for $0.1 < Re < 20$.

$$\frac{h}{w} = 0.81 - 0.217 \log \cdot Re - 0.084 (\log Re)^2 \qquad (3.37)$$

This equation, also shown on Figure 3.8, is in good agreement with the present data.

Parlange's theory (1969), which was reviewed in Section 3.2.3.3, can also be used to predict the shape of spherical-cap bubbles with laminar wakes. The lower order and higher order rise velocities can be calculated for a known volume and liquid properties using Equations (3.26) and (3.27), respectively. The radius of curvature, R, can then be found by Davies and Taylor's expression, Equation (3.22). Further, neglecting the indentation at the rear θ_m, h and w can be computed by Equations (3.34) to (3.36). The values of h/w so calculated were found to be independent of liquid properties, and were only functions of Re as depicted in Figure 3.8. For $45 \gtrsim Re \gtrsim 110$ where the basic assumptions of Parlange's Theory are reasonably justified the experimental data are found to lie between the two theoretical lines.

FIGURE 3.8 <u>Comparison of present correlation with</u>
<u>previous work</u>

<u>Experiments</u>

◇ Wairegi (1974)

◁ Haberman & Morton (1953)

○ Angelino (1964)

△ Jones (1965)

□ Wegener <u>et al</u> (1971)

———— R Rosenberg (1950)

———— DT Davies & Taylor (1950)

— — — — — Davenport (1964)

·············· Guthrie (1967)

ᕽᕽᕽᕽᕽᕽᕽᕽᕽᕽ Slaughter (1967)

—— — —— Kojima <u>et al</u> (1968)

▨▨▨▨▨ Experimental data of many previous workers (see Fig. 3.9)

━━━━━ Present correlation (from Fig. 3.7)

<u>Theory</u>

———— M Moore (1959)

———— RD Rippin & Davidson (1967)

— x — x — Parlange's zeroth order theory (1969)

— · — · — Parlange's first order theory (1969)
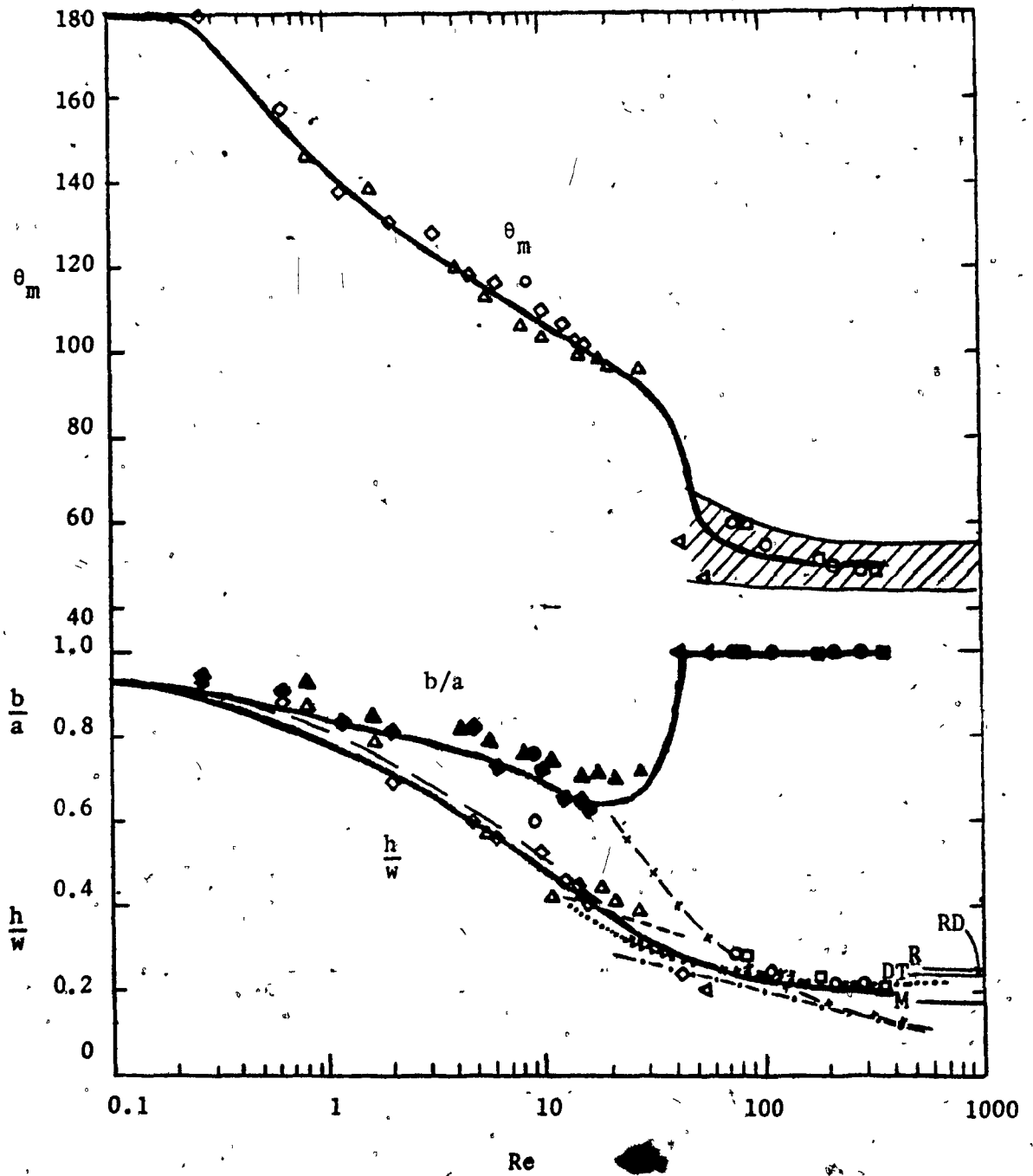
Above Re $\geqslant$ 110 spherical-cap bubbles have unsteady open wakes*

and are dynamically similar in shape with $\theta_m \approx 48^o$. When this value of

θ_m is substituted into Equations (3.35) and (3.36) we obtain h/w — 0.223.

This value compares well with h/w — 0.23 observed in Figure 3.8.

Previous workers have classified bubbles as spherical-caps for

Re as low as 1.2 (Jones 1965; Grace 1970). Careful re-examination of the

same data revealed that the bubbles were actually oblate-ellipsoidal-caps

and that the spherical-cap classification was used as a crude approximation.

Present classification using method (iii) described in Section 3.4.1.3

indicates that the bubbles are of spherical-cap shape for Re $\geqslant$ 45. How-

ever, if Collins' (1966) suggestion of fitting the sphere only over the

front 75° of the bubble cap is adopted then bubbles with Re as low as 10

can be treated as spherical-caps for the sake of simplicity.

Using this simplified classification the semi-included angle,

θ_m, for the spherical-cap bubbles is plotted in Figure 3.9 and compared

with previous experimental data. The agreement is very good, with the

scatter in the present data being no more than reported by other workers.

Parlange's theory can be used to predict θ_m for spherical-caps

as described earlier in this section. The values of θ_m so calculated were

also found to be independent of liquid-properties and were only a function

of Re as depicted in Figure 3.9. For $10 \leqslant Re \leqslant 110$ the experimental data

are bounded by the lower and the higher order theoretical predictions.

Above Re $\approx$ 110 both theories are very close and predict a decrease in θ_m

---

* This is shown in Chapter 4.
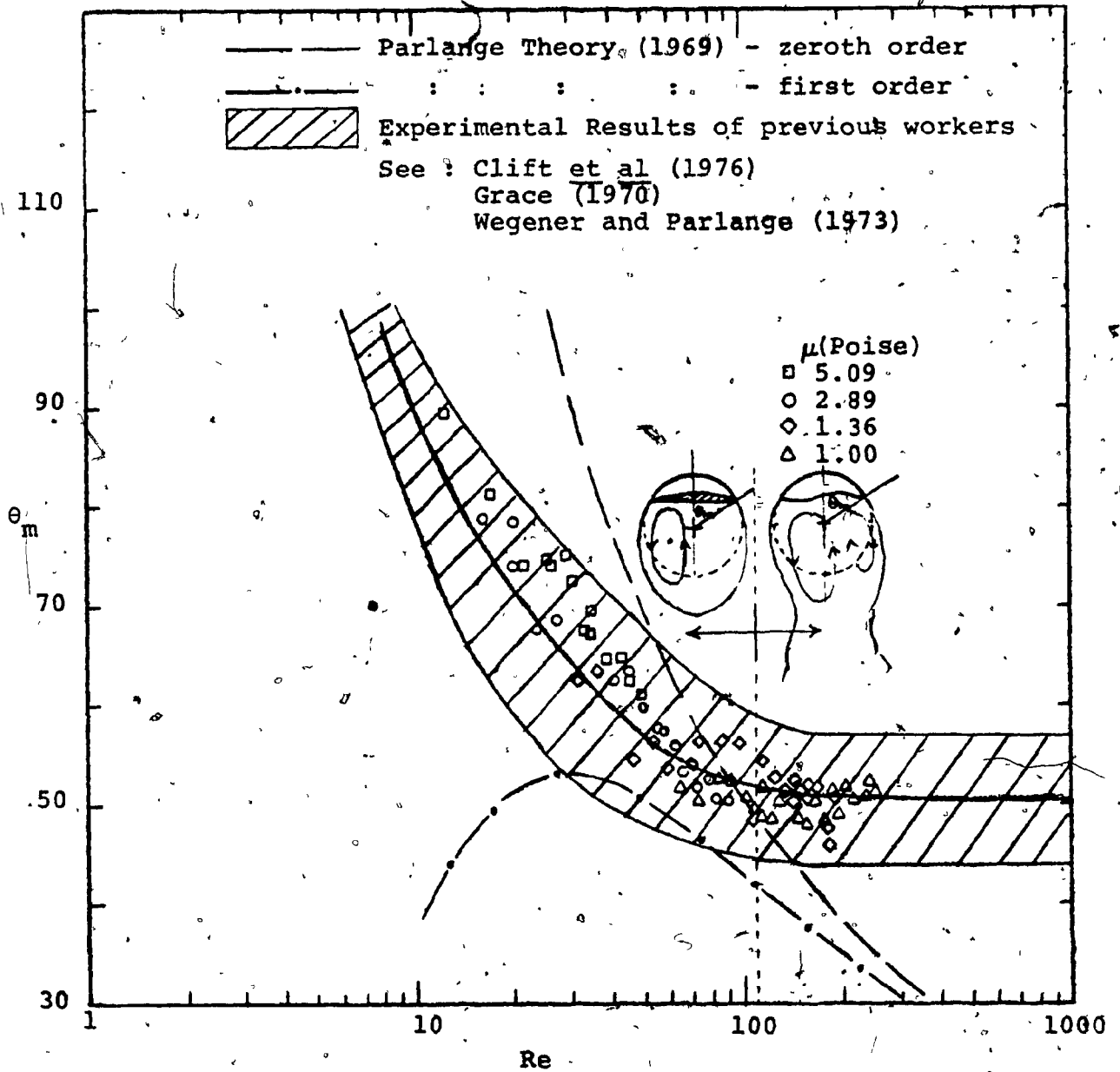
FIGURE 3-9 : <u>Variation of semi-included angle, Θm for spherical-cap bubble with Reynolds number</u>

while the experiments show an approximately constant value. This is not surprising since beyond this point the wake is no longer closed and laminar, and thus the very basic assumption of the theory is violated. On the other hand as Re is lowered below about 45 increasing deviation from the other assumptions* of the theory is expected thus explaining the increasing disagreement between theory and at lower Re.

It should be pointed out that there has been some debate regarding the application of Parlange's theory (Parlange 1972; Grace 1972). This confusion is avoided here by calculating θ_m from the complete equations of Parlange's theory rather than from the simplified equations relating θ_m to Re which require series expansion and then truncation.

(b) Dependence of bubble shape on other parameters

The deformation in terms of h/d_e of bubbles and drops has often been correlated with respect to Eotvos Number, Eö (Harmathy 1960; Wellek et al 1966; Reinhart 1964) and Weber Number, We (Hayashi and Matunobu 1967; Kubota et al 1967; Aybers and Tapucu 1969; Wellek et al 1966). Unlike the h/d_e versus Re plot, Figure 3.6, the data for the various liquids did not collapse onto a single curve when plotted against Eö or We but were represented by different curves with liquids of higher M exhibiting smaller deformation. Thus we conclude that in high M liquids the bubble deformation is well correlated against Re in contrast to low M liquids where the deformation is reported to be well correlated by We (Kubota et al 1967; Aybers and Tapucu 1969) or Eö (Harmathy 1960).

---

* At lower Re the external flow deviates from potential flow and the bubble volume become comparable to the wake volume as will be shown in Chapter 4.

(c) Indentation of bubbles

It was pointed out in Section 3.4.2.1 that under certain conditions the base of the bubble is indented. Similar indentations (or dimples) have been reported by other workers for bubbles (Davenport 1964; Slaughter 1967; Guthrie 1967; Kojima et al 1968; Jones 1965; Calderbank et al 1970; Sundell 1971; Hnat 1973) and for drops (Garner et al 1957; Fararaui and Kinter 1961; Shoemaker and Chazal 1969; Wairegi 1972). However, no measurement of the size of the indentation has been reported.

With proper lighting conditions this indentation is clearly seen on photographs of bubbles (see Fig.3.3) and drops (see Fig. 6.17(1)) (Garner et al 1957; Shoemaker and Chazal 1969; Wairegi 1972), however the curved surface of the dimple is displaced on the photographs due to the difference in refractive indices of the two phases. Hence it is not possible to calculate the actual volume of the indentation from the apparent shape of the indentation, except where the error due to refraction is small such as in liquid drops in continuous liquids of similar refractive index.

In the present work an estimate of the volume of the indentation was made by calculating the total volume of the bubble cap from the close-up photograph (assuming axisymmetry) and subtracting from this volume the measured volume of the bubble.

The volume of the ellipsoidal-cap bubble, V_{EC}, was calculated using the following geometrical relationship (see Fig.3.1(a) for the definition of the variables):

$$V_{EC} = \frac{4}{3}\pi a^2 b - \pi a^2 \left[(2b-h) - \frac{b^3 - (h-b)^3}{2b^2} \right] \qquad (3.38)$$

The volume of the spherical-cap bubbles, V_{SC}, was calculated using two different geometrical relations which are shown below, and the average value was taken (see Fig.3.1(c)).

$$V_{SC} = \frac{\pi}{6}(3a'^2h + h^3) \qquad (3.39)$$

$$V_{SC} = \pi R^3(\frac{2}{3} - \cos\theta_m + \frac{\cos^3\theta_m}{3}) \qquad (3.40)$$

Close agreement between the volumes calculated using these two formulae was found.

The volume of the indentation, V_i, is given by

$$V_i = V_C - V \qquad (3.41)$$

where V_C = total volume of the ellipsoidal cap, V_{EC}, or the spherical-cap, V_{SC}

and V = measured volume of the bubble corrected for the appropriate hydrostatic pressure.

The dimensionless indentation volume, V_i/V_C, is plotted against the Reynolds Number in Figure 3.10. From this graph it is seen that the indentation begins to appear about Re $\approx$ 1.5, and increases to a maximum at around Re $\approx$ 40, then begins to decrease. Note that the indentation is quite significant for intermediate Reynolds Number with a maximum value of V_i/V_C of 0.4. Similar values have been found recently by Hnat (1973) using shadowphotography for spherical-cap bubbles rising in mineral oil.
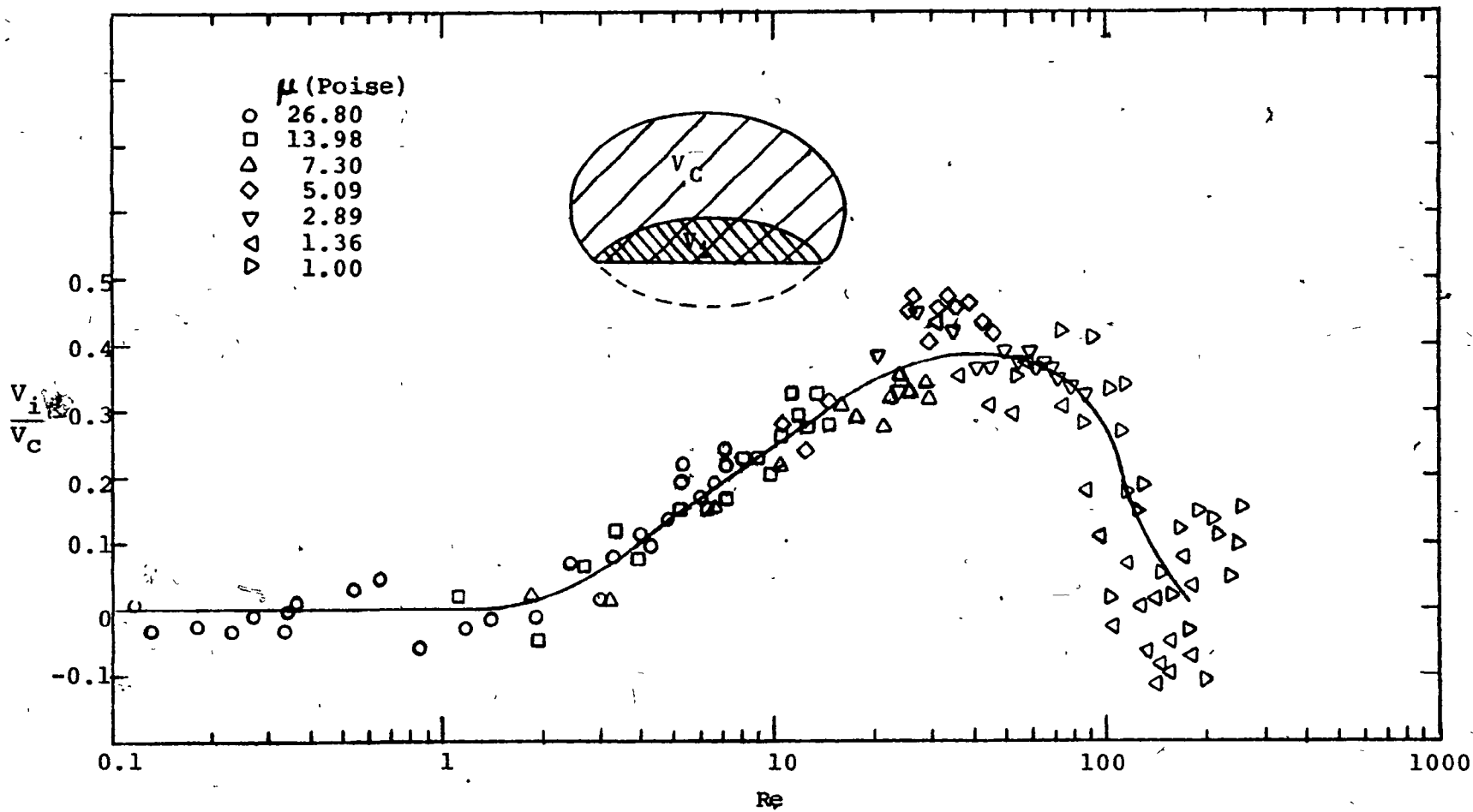
FIGURE 3-10: Dimensionless indentation volume as function of Reynolds number.

Above Re $\geqslant$ 110 the bubble wake is open which causes the bottom surface to fluctuate. This makes the indentation calculation inaccurate, as shown by the increased scatter in the data. Nevertheless, the trend of the data does indicate that the indentation for this regime is negligible as was found by Davenport (1964) and Guthrie (1967).

3.4.3 Rise velocity results

The terminal rise velocities of bubbles of volumes 0.08 to 139 cm^3 in various sugar solutions were measured using the methods described in Chapter 2. The accuracy of these techniques has already been discussed in Section 3.4.1.2. The physical properties of the sugar solutions are given in Table 3.3.

3.4.3.1 Correlation between drag coefficient and Reynolds Number

The rise velocity results are presented in terms of the drag coefficient, C_D, and the Reynolds Number, Re, in Figure 3.11. Various theoretical equations that were reviewed in Section 3.2.3 are also presented on the same figure. The drag coefficients for bubbles of all sizes and shapes for all high M liquids with M > 5.48x10^{-3} fall on a single curve, which also compares very well with the data of other workers (Haberman and Morton 1953 and 1956; Jones 1965; Redfield and Houghton 1965; Angelino 1966; Kojima et al 1968).

At low Re the data correspond to the Hadamard-Rybczynski theory (Equation (3.17)) for gas spheres which suggests that internal circulation was present for these bubbles. The drag curve begins to deviate from the Hadamard-Rybczynski equation around Re $\geqslant$ 0.5, indicating that the inertial effects and the deformation of bubbles begin to affect the drag. Up to
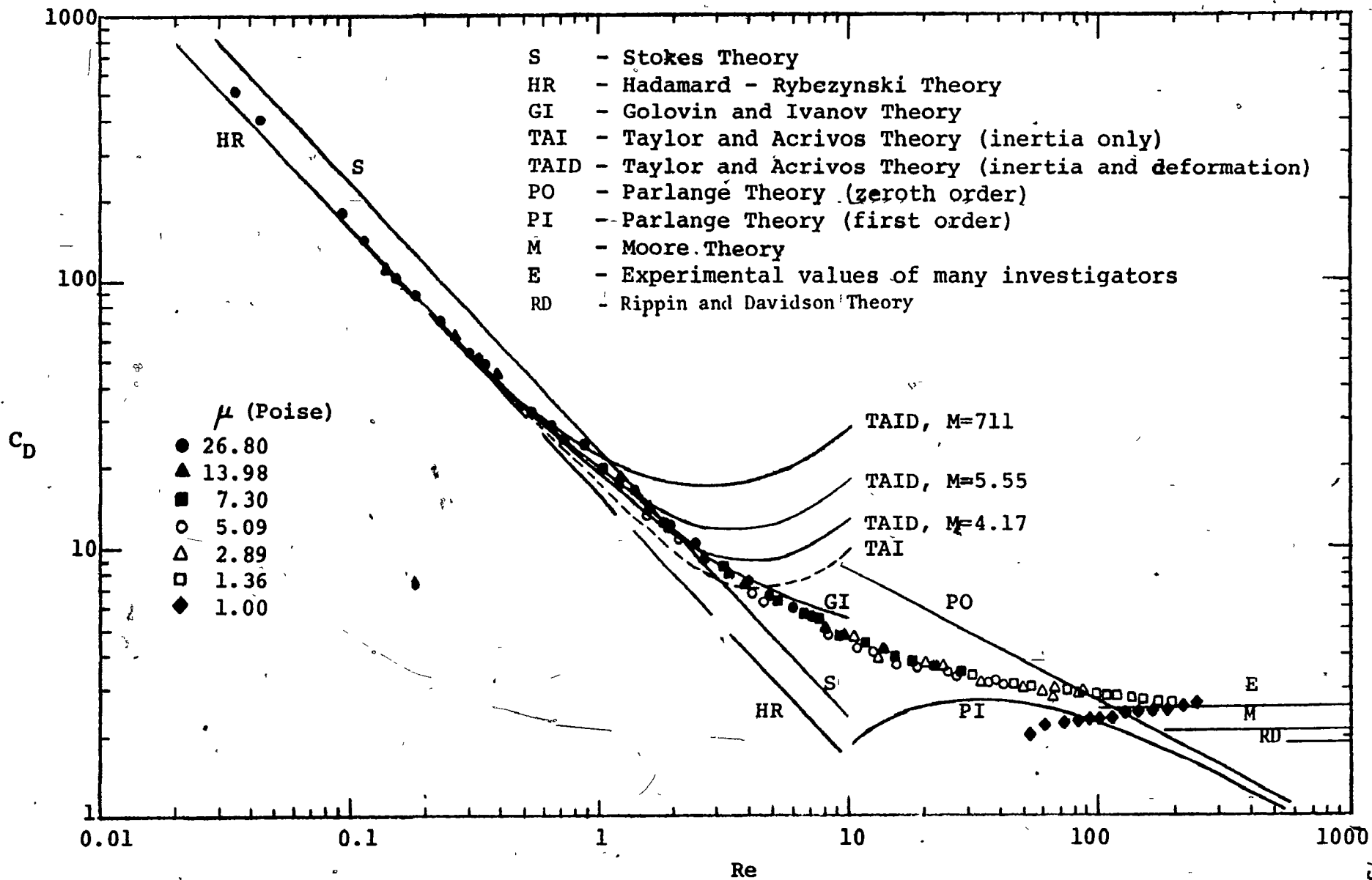
FIGURE 3-11 : <u>Variation of Drag coefficient with Reynolds Number</u>

The figure legend contains:

S   - Stokes Theory
HR   - Hadamard - Rybezynski Theory
GI   - Golovin and Ivanov Theory
TAI - Taylor and Acrivos Theory (inertia only)
TAID - Taylor and Acrivos Theory (inertia and deformation)
PO   - Parlangé Theory (zeroth order)
PI   - Parlange Theory (first order)
M   - Moore Theory
E   - Experimental values of many investigators
RD   - Rippin and Davidson Theory

μ (Poise)
● 26.80
▲ 13.98
■ 7.30
○ 5.09
△ 2.89
□ 1.36
◆ 1.00

Axis labels: C_D (vertical), Re (horizontal)

Curve labels: TAID, M=711; TAID, M=5.55; TAID, M=4.17; TAI; GI; PO; S; HR; PI; E; M; RD

Re $\simeq$ 1.5 the data follow the Taylor and Acrivos theory (Equation (3.21))
which accounts for the inertia effects as well as the effect of the bubble
deformation. Golovin and Ivanov's theory (Equation (3.18)), which takes
into account only the inertial effects, conforms to the data to a larger
value of Re $\simeq$ 5. However, this agreement is fortuituous since the bubble
shape is far from spherical at this value of Re (see Fig. 3.4(a)).

At increasing Re the drag coefficient decreases and tends to-
wards a fairly constant value of about 2.6 for Re $\gg$ 110 where the bubbles
are dynamically similar spherical-caps. In the range 45 $\lesssim$ Re $\lesssim$ 110 where
the bubbles are truly spherical-cap shape with a closed toroidal wake the
drag data are backed by Parlange's zeroth order and first order theories
(Equations (3.26) and (3.27)). Outside this range the predictions show
increasing divergence from the data because the assumptions of Parlange's
theory are not justified as discussed earlier (see Section 3.4.2.3).

For liquid having Morton Number, M, larger than 5.48×10^{-3} the
drag coefficient curve is universal, i.e. it is independent of M, and
hence it can be used to predict the rise velocity of bubbles of any shape.

The drag data for the sugar solution with $M = 1.64 \times 10^{-3}$ do not
follow the general trend for the higher M liquids which suggests that a
change in bubble behaviour sets in somewhere in the Morton Number range
of $1.64 \times 10^{-3} < M < 5.48 \times 10^{-3}$. The minimum in the drag curve for the least
viscous liquid ($M = 1.64 \times 10^{-3}$) corresponded to the bubbles having almost
disc-like shape (see photograph in Fig.3.2(3)) and wobbling motion. The
range of values of M obtained from the data of previous investigators for
the transition in the drag curve are compared in Table 3.2. It is clear
that the present data provide the closest estimate of the Morton Number
for this transition.

TABLE 3.2 <u>Morton Number for Transition in Drag Curve</u>

Reference	Critical M
present work	$1.64 \times 10^{-3} < M < 5.48 \times 10^{-3}$
Haberman & Morton (1953 & 1956)	$4.18 \times 10^{-8} < M < 1.54 \times 10^{-2}$
Jones (1965)	$3.53 \times 10^{-4} < M < 3.76$
Redfield & Houghton (1966)	$1.39 \times 10^{-3} < M < 2.32 \times 10^{-1}$
Tadaki & Maeda (1961)*	$2.54 \times 10^{-4} < M$
Angelino (1966)**	$M < 2.93 \times 10^{-2}$
Kojima et al (1968)**	$M < 1.87 \times 10^{-2}$

*   only lower limit available
** only upper limit available

3.4.3.2 Modification of Grace's plot

Following the method of Grace (1970) the present velocity data
are plotted as Reynolds Number versus Eötvos Number in Figure 3.12. Also
shown in the figure are the boundaries of the three shape regimes distin-
guished by Grace. The measured rise velocities of bubbles larger than
$d_e \sim 4.3$ cm. were corrected for the wall effect using the method described
in Chapter 7, before including them on this plot.

Grace transformed the Stokes and Hadamard-Rybczynski equations
for spherical bubbles in terms of dimensionless groups and gave:

$$Re = \frac{E\ddot{o}^{1.5}}{k'M^{0.5}} \qquad (Re \leqslant 0.2) \qquad\qquad (3.37)$$

where $k' = 18$ and 12 for the Stokes and Hadamard-Rybczynski equations,
respectively. The present data are well-bounded by these two equations
for small spherical and even slightly ellipsoidal bubbles. The data for
small bubbles in the most viscous liquid (M = 711) show very good agree-
ment with the Hadamard-Rybczynski equation, implying that these bubbles
were fully circulating. This can be explained by the fact that these
experiments were performed on a freshly prepared sugar solution thus
ensuring minimal chance for contamination.

For dynamically similar spherical-cap bubbles with $Re \geqslant 100$,
Grace also showed that:

$$Re = \frac{0.70(E\ddot{o})^{0.75}}{M^{0.25}} \qquad (E\ddot{o} \geqslant 40, \ Re \geqslant 100) \qquad (3.38)$$

The present data also conform to this equation in the specified regime.
In the intermediate range, the data showed excellent agreement with the
curves presented by Grace on his generalized plot (similar to Fig. 3.12).

FIGURE 3.12 Experimental Rise Velocity[*] of Bubbles Plotted
on a Grace Plot (i.e. Re versus Eö)

EXPERIMENTAL SHAPES (see Fig. 3.2)

O S   spherical

◐ OE   oblate ellipsoidal

⊕ OED oblate ellipsoidal disc-like (wobbling)

◖ OEC oblate-ellipsoidal-cap

◑ SCC spherical-cap with closed steady wake

◑ SCO spherical-cap with open unsteady wake

● SKS skirted bubble with smooth steady skirt

◎ SKW skirted bubble with wavy unsteady skirt

PROPOSED REGIME BOUNDARIES

━━━━━ Present work

╌╌╌╌ Grace (1973)

THEORETICAL PREDICTIONS

──●── Stokes law

──·── Hadamard-Rybczynski

──×── Davies and Taylor

*In order to delineate the "oblate ellipsoidal disc-like (wobbling)"
regime some additional experiments were performed in sugar solution
of $\mu = 0.615$ Poise; $\rho = 1.301$ g/cm^3; $\sigma = 76.7$ dynes/cm; $M = 2.39 \times 10^{-4}$.
These are also included here. The physical properties of all the
other liquids are listed in Table 3.3.
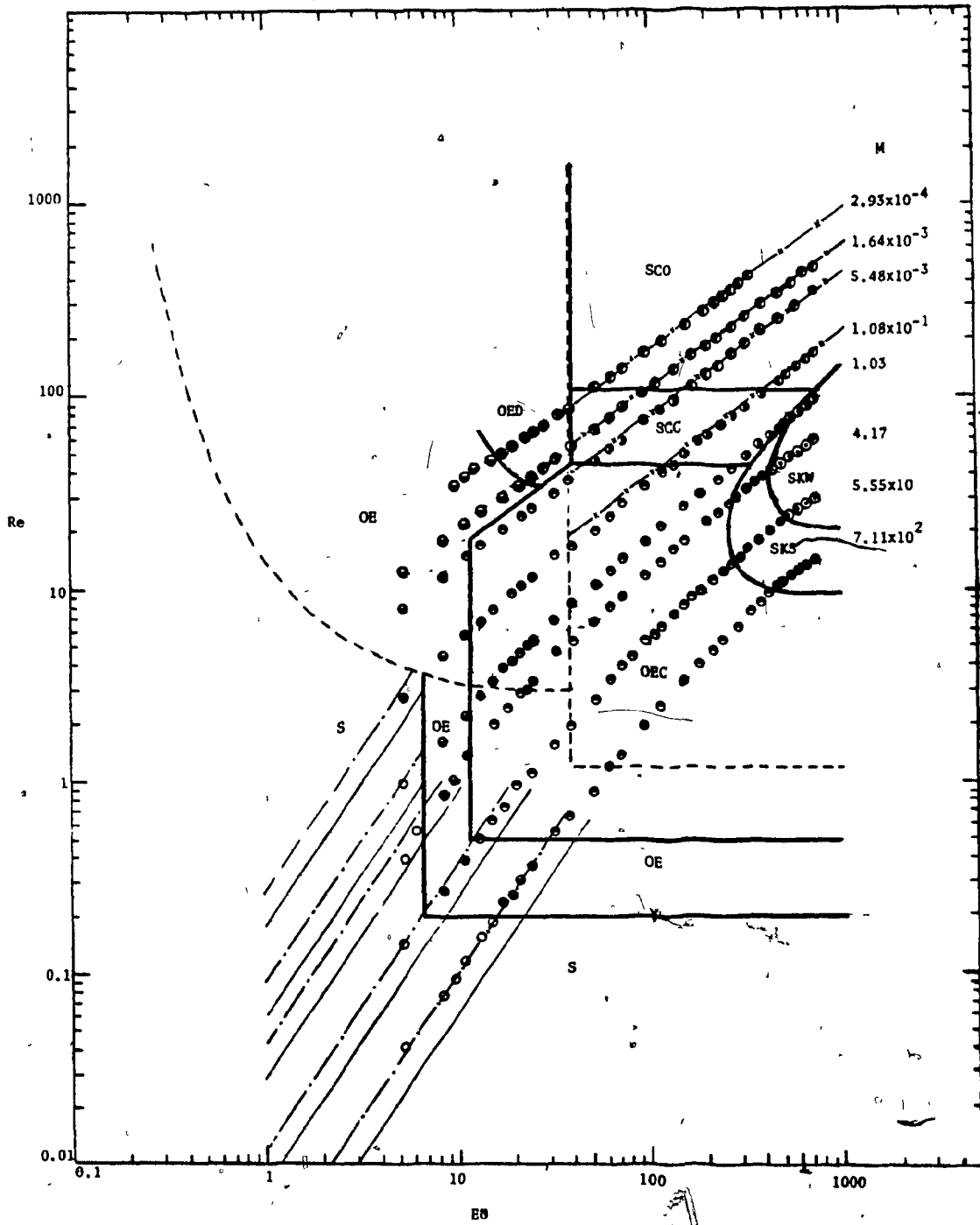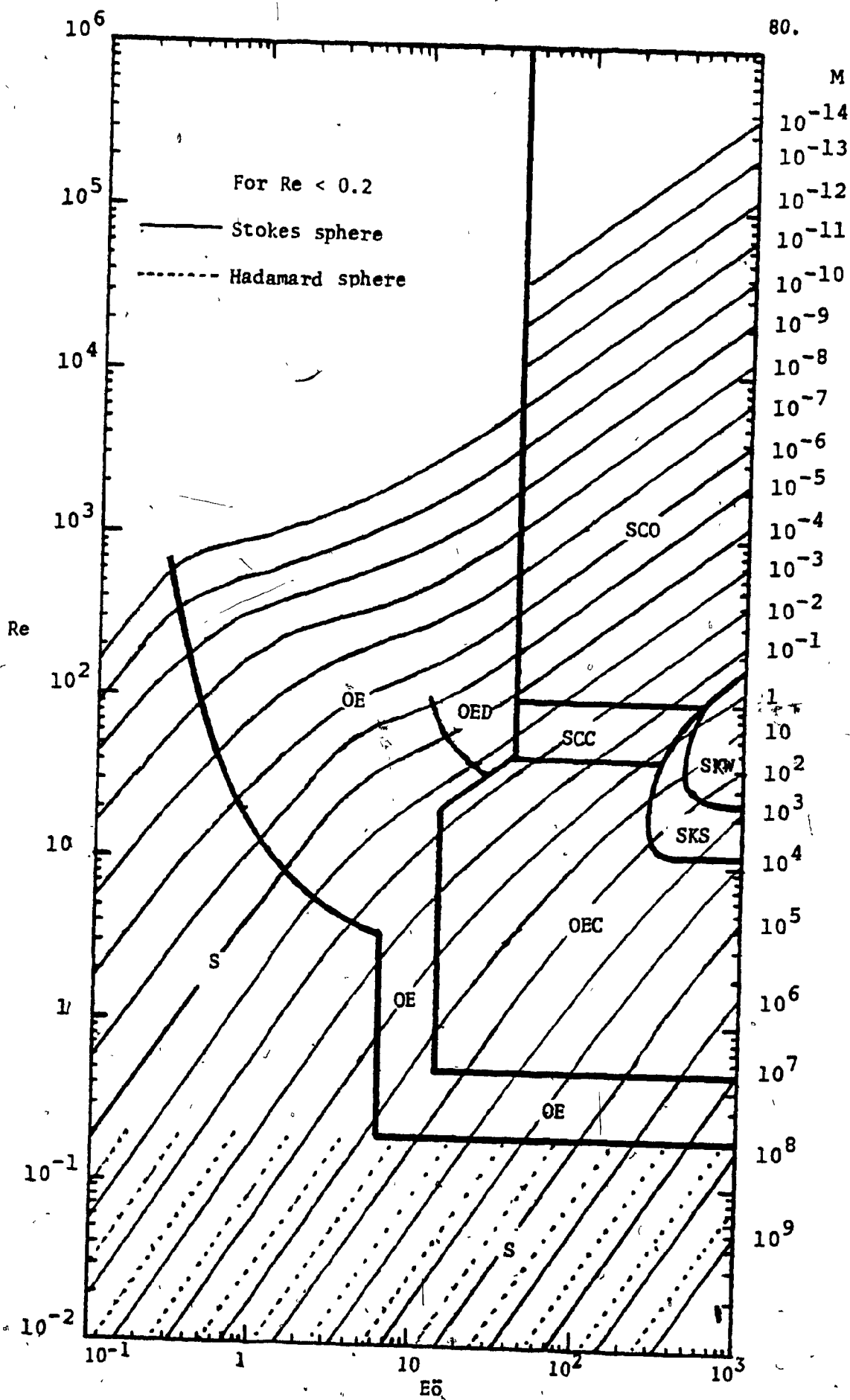
FIGURE 3.13 Modified Grace Plot Showing Bubble Regimes
(data points removed)

Detailed photographic observation of shapes together with the additional information obtained from the studies reported in Chapters 4 and 6, has enabled us to delineate six additional shape regimes on the plot. The modified version of this generalized plot* is shown in Fig. 3.13 with the experimental points removed. It allows the prediction of the terminal rise velocity and the bubble shape, given only the volume of the bubble and the liquid properties; namely viscosity, density and surface tension.

3.4.3.3 Velocity correlation for large bubbles ($E\ddot{o} \geqslant 40$)

For large bubbles ($V > 2$ cm^3) Angelino (1966) suggested the relation $U = KV^m$ between the rise velocity U and the bubble volume V, where K and m are constants which depend only upon the physical properties of the liquid. The present velocity data in a 29.2 cm I.D. column were plotted on log-log paper (see Fig.3.14(a)) and from the straight line graph the value of K and m were calculated. The departure of the data from the straight line corresponds to the point where wall effects begin to become significant. This point is very well demonstrated in Fig.3.14(b) where the data of Wegener et al (1971) for air bubbles of volumes as high as 320 cm^3 rising in two columns of 150 cm and 30 cm diameter are shown.

The present data as well as data of previous investigators covering some 49 liquids in all confirm the relation $U = KV^m$. The physical properties of the liquids and the corresponding values of K and m are given in Table 3.3. The plot of K and m versus M is shown in Fig.3.15. This correlation is entirely empirical, but quite useful. The

---

* Compared with the recent correlation of Wallis (1974), the present modified version of Grace's correlation is based on greater range of data, is easier to use, and provides more information regarding shape regimes. Very recently, the latter correlation has also been extended and verified for drops (Grace et al 1976).

The plot axes and legend:

- Y-axis: Bubble Velocity, U (cm/sec), ranging from 1 to 100
- X-axis: Bubble Volume, V (cm³), ranging from 1 to 100

Column Diameter = 29.2 cm

μ (Poise)

△	26.80
○	13.98
◁	7.30
□	5.09
◇	2.89
▽	1.36
▷	1.00
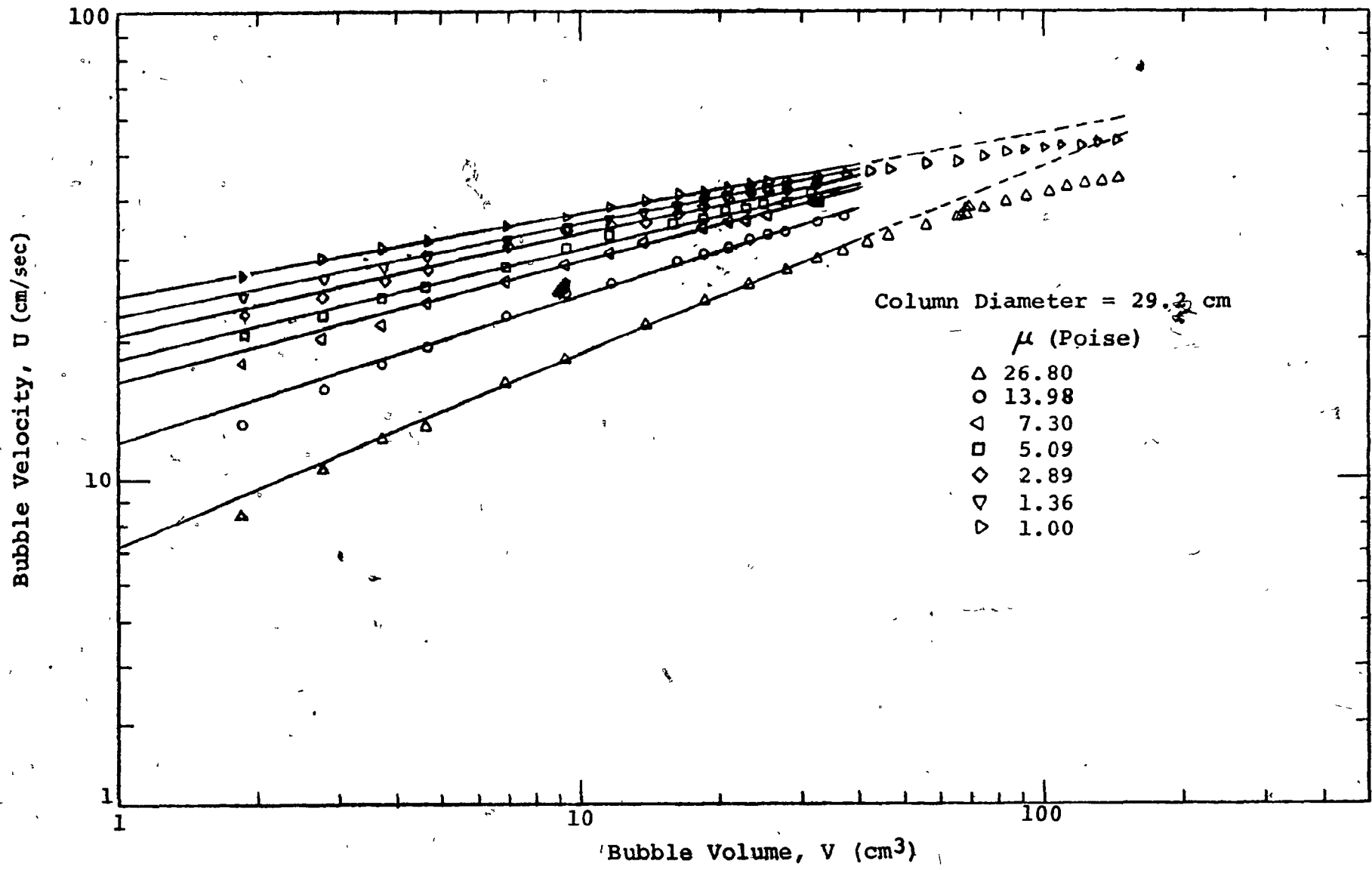
FIGURE 3-14 (a): Variation of bubble rise velocity with volume
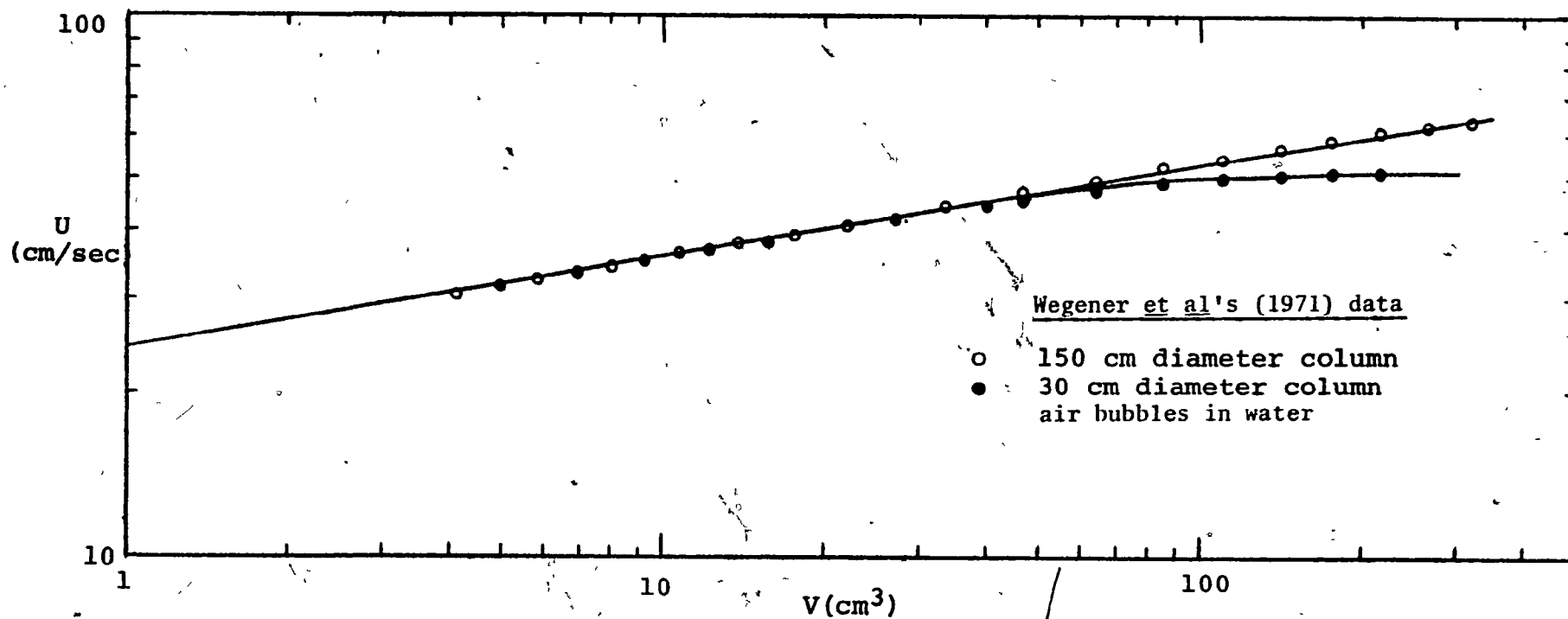
FIGURE 3-14(b): Variation of bubble rise velocity with volume showing the wall effect.

Legend within figure:

Wegener et al's (1971) data

o 150 cm diameter column
● 30 cm diameter column
air bubbles in water

Axis labels: U (cm/sec), V(cm³)
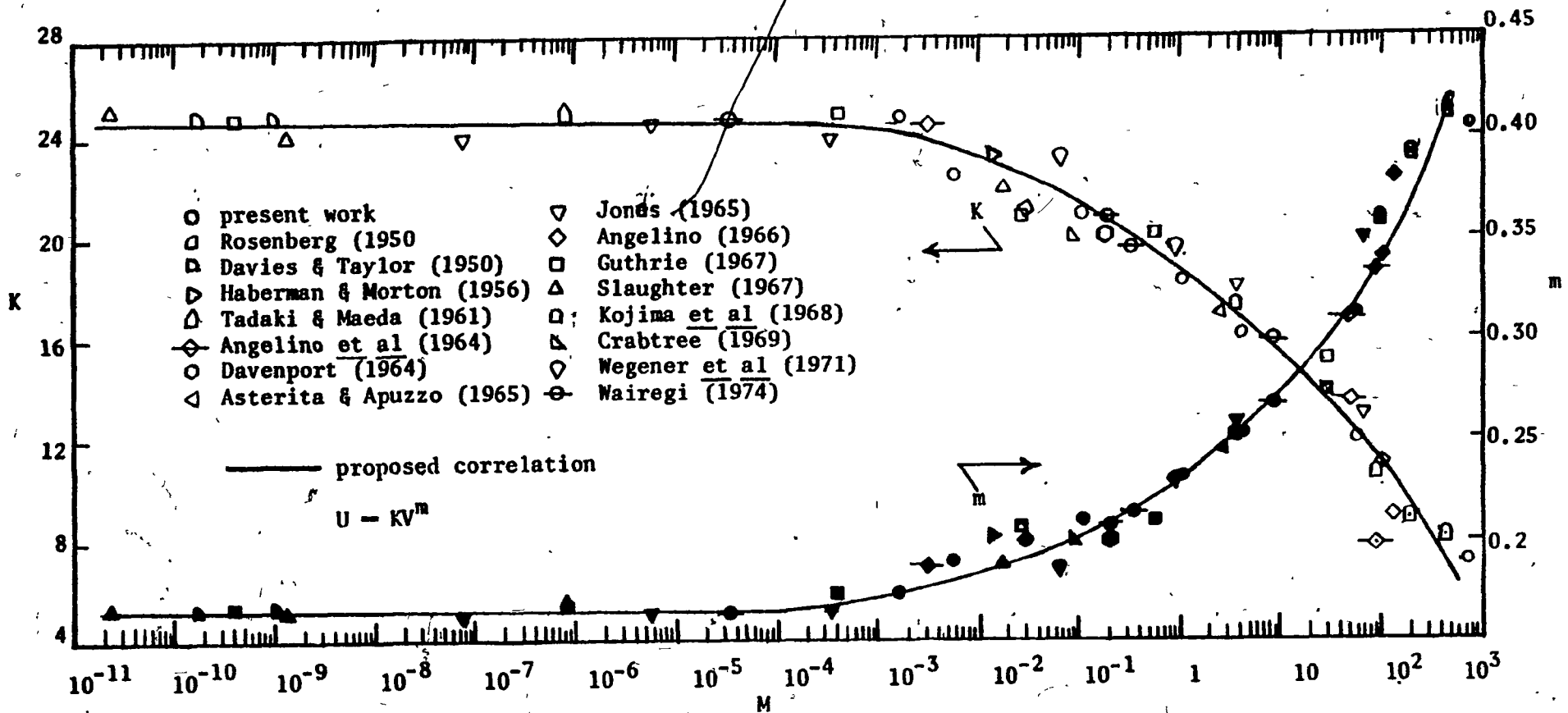
FIGURE 3.15 Variation of the parameters K and m with Morton number, M

TABLE 3.3 _Liquid Physical Properties and Values of K and $_m$ for the Velocity Correlation, $U = KV^m$_

Author	Liquid	μ (Poise)	ρ (g/cm^3)	σ (dynes/cm)	M	K	m
Present work	sugar solution	26.80	1.390	80	7.11×10^2	7.21	0.405
	"	13.98	1.379	78.8	5.55×10	12	0.312
	"	7.30	1.370	78.7	4.17	16.2	0.253
	"	5.09	1.358	77.7	1.03	18.3	0.231
	"	2.89	1.347	77.6	1.08×10^{-1}	20.5	0.209
	"	1.36	1.325	77.3	5.48×10^{-3}	22.5	0.190
	"	1.00	1.320	76.8	1.64×10^{-3}	24.8	0.174
Wairegi (1974)	paraffin oil	2.00	0.883	37.5	3.37×10^{-1}	19.9	0.215
	sugar solution	13.35	1.392	79.1	8.76×10	15.9	0.269
	"	3.40	1.366	76.2	2.17×10^{-1}	20.5	0.209
	"	0.37	1.300	73.6	3.55×10^{-5}	24.5	0.165
Angelino (1966)	glycerine	14.40	1.260	63.72	1.33×10^2	8.9	0.38
	mineral oil	7.40	0.882	31.85	1.03×10^2	11.0	0.34
	glycol	1.05	1.023	34.15	2.93×10^{-2}	21.0	0.20
Davies & Taylor (1950)	water	0.016	1.0	73.00	1.65×10^{-10}	24.8	0.167
	nitrobenzene	0.018	1.2	43.9	1.01×10^{-9}	24.7	0.166
Crabtree (1969)	sugar solution	2.63	1.333	77.4	7.59×10^{-2}	20	0.199
Guthrie (1967)	PVA solution	7.35	1.02	46.0	2.88×10	15.2	0.272
	"	2.76	1.01	46.5	5.61×10^{-1}	20.2	0.210
	"	1.30	1.01	46.9	2.69×10^{-2}	20.8	0.207
	"	0.46	1.01	47.7	4.01×10^{-4}	24.9	0.174
	"	0.015	1.01	50.0	3.93×10^{-10}	24.8	0.168
	tap water	0.011	1.00	73	3.69×10^{-11}	24.8	0.167
Wegener et al (1971)	mineral oil	2.29	0.9	32	9.15×10^{-1}	19.5	0.229
	"	1.19	0.9	32	6.67×10^{-2}	23.0	1.840
Slaughter (1967)	87% glycerol	1.57	1.228	65.5	1.73×10^{-2}	22.0	0.201
	heat transfer salt	0.0458	1.965	118.9	1.31×10^{-9}	24.2	0.166
	water	0.00936	0.998	72.3	2.34×10^{-11}	25.1	0.168
Jones (1965)	99% glycerol	12.00	1.261	62.5	6.60×10	13.0	0.350
	paraffin oil	2.935	0.88	28	3.77	18.0	0.256
	60% sucrose	0.678	1.286	76.95	3.53×10^{-4}	23.5	0.166
	50% sucrose	0.237	1.23	75.85	5.76×10^{-6}	24.5	0.164
	40% sucrose	0.0783	1.176	74.85	7.47×10^{-8}	24.0	0.161
Astarita (1965)	glycerol	5.48	1.246	64.2	2.68	17.0	0.244
Davenport (1967)	PVA solution	2.16	1.00	46.2	2.16×10^{-1}	20.2	0.201
	"	1.15	1.00	46.9	1.66×10^{-2}	23.5	0.166
	"	0.54	1.00	47.0	8.03×10^{-4}	24.5	0.163
	water	0.01	1.00	73.00	2.52×10^{-11}	25.0	0.166
	mercury	0.0155	13.55	48.7	3.6×10^{-14}	25.0	0.166
Haberman & Morton (1956)	mineral oil	0.58	0.866	20.7	1.45×10^{-2}	23.3	0.201
Rosenberg (1950)	water	0.01	0.988	72.8	2.57×10^{-11}	24.9	0.167
Kojima et al (1968)	corn syrup	19.40	1.38	81.0	1.89×10^2	8.8	0.410
	glycerine	19.60	1.27	63.5	4.43×10^2	8.0	0.390
	glycerine	13.30	1.26	63.4	9.54×10^1	10.8	0.358
	caster oil	3.76	0.953	38.8	3.52	17.3	0.251
Tadaki & Maeda (1961)	isoamyl alcohol	0.056	0.813	24.5	8.06×10^{-7}	24.9	0.170
Angelino et al (1964)	glycerine	12.87	1.169	63.72	8.90×10	7.9	0.333
	mineral oil	6.23	0.89	31.85	5.14×10	13.5	0.310
	glycol	0.60	1.015	34.15	3.15×10^{-3}	24.8	0.2

rise velocity of a large bubble in an infinite extent of any liquid can be calculated from this correlation.

It is interesting to note that the value of K approaches 25 and the value of m approaches 1/3 for a low M liquid as predicted by the semi-empirical theory of Davies and Taylor, Equation (3.25). Note also that the values of K and n remain approximately constant for $10^{-14} \leqslant M \leqslant 10^{-4}$ which implies that, for this range of M, liquid properties have no significant effect on the rise velocity of large bubbles.

3.4.3.5 Comparison of rise velocity of oblate-ellipsoidal-cap bubbles with theory

The velocity data for oblate-ellipsoidal-cap bubbles are shown in Fig.3.16(a)-(c). Sundell (1971) reported that the velocity of bubbles rising in water is reduced by the presence of the wall in a 30 cm. diameter column (same as that used in present work) at bubble volumes in excess of about 43 cm^3. (see Fig.3.14(b)). Assuming the same criteria to apply for viscous liquids, the point at which "wall effects" set in, is indicated on each graph (i.e., $d_e \approx 4.3$).

The velocity predicted using the measured shape data (i.e., semi-major axis a, semi-minor axis b) and the theoretical result of Wairegi and Grace, Equation (3.30), is in very good agreement with the experimental values. The theory slightly overpredicts the velocity, especially at very low Re; however, as Re is increased, the predictions approach the experimental values. This is expected since the theory assumes a potential flow around an oblate ellipsoid. It is noteworthy that the theory is successful in predicting the rise velocity for oblate skirted bubbles as well.

FIGURE 3.16 Comparison of the Rise Velocity of Oblate
Ellipsoidal-Cap Bubbles with Theoretical
Predictions

No.	μ(Poise)*
a	26.80
b	13.98
c	7.30

O   experimental data (shaded symbol indicates bubbles with skirt)

—— —— ——Parlange's zeroth order theory (1969)

——.——.——Parlange's first order theory (1969)

——————Wairegi & Grace's theory (1976)

* Other liquid properties are listed in Table 3.3.

FIGURE 3-16(a)

μ — 13.98 Poise

U (cm/sec)

50

40

30

20

10

wall effect

0   1   2   3   4   5   6

de (cm)

0   1   5   10   15

Re
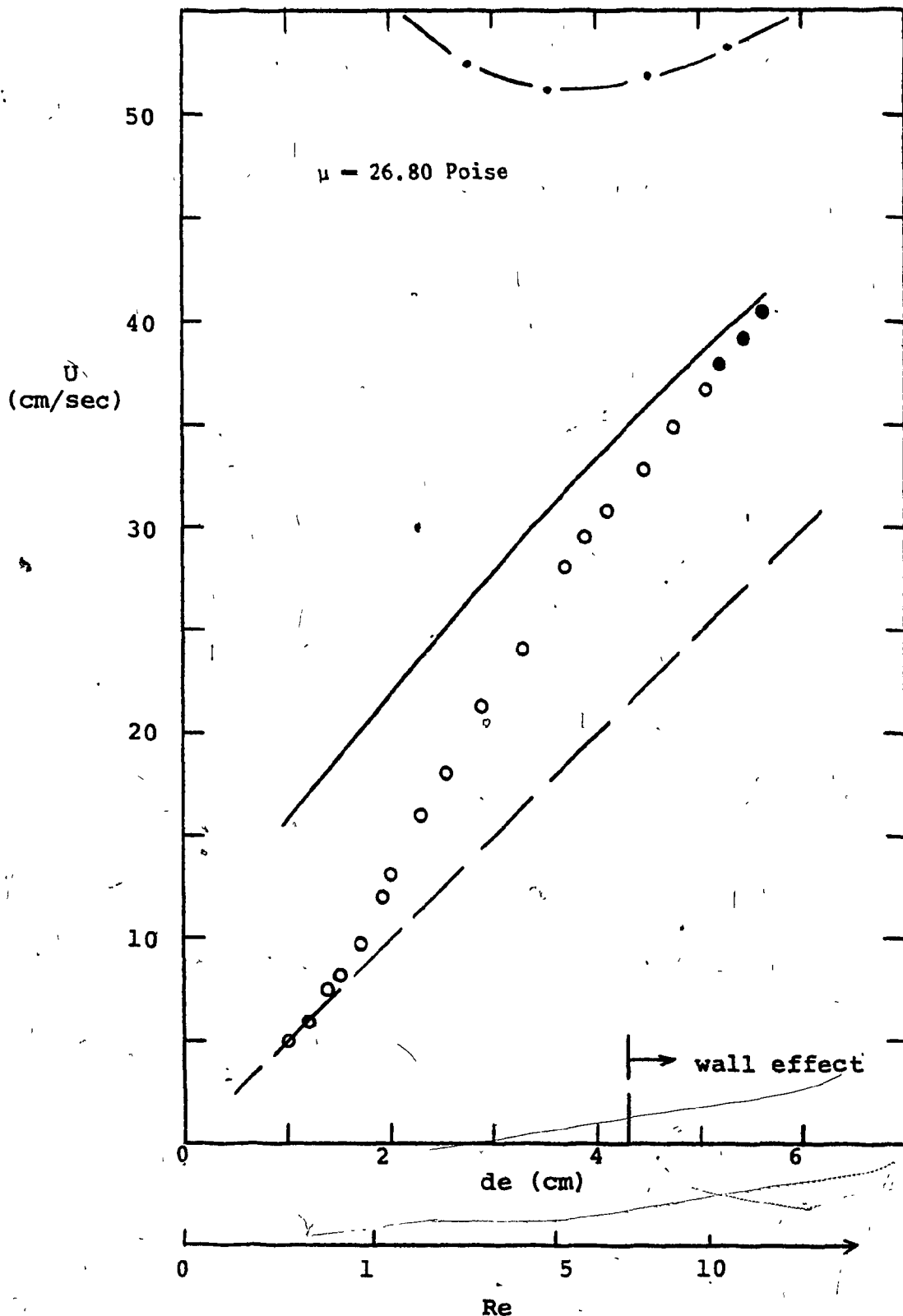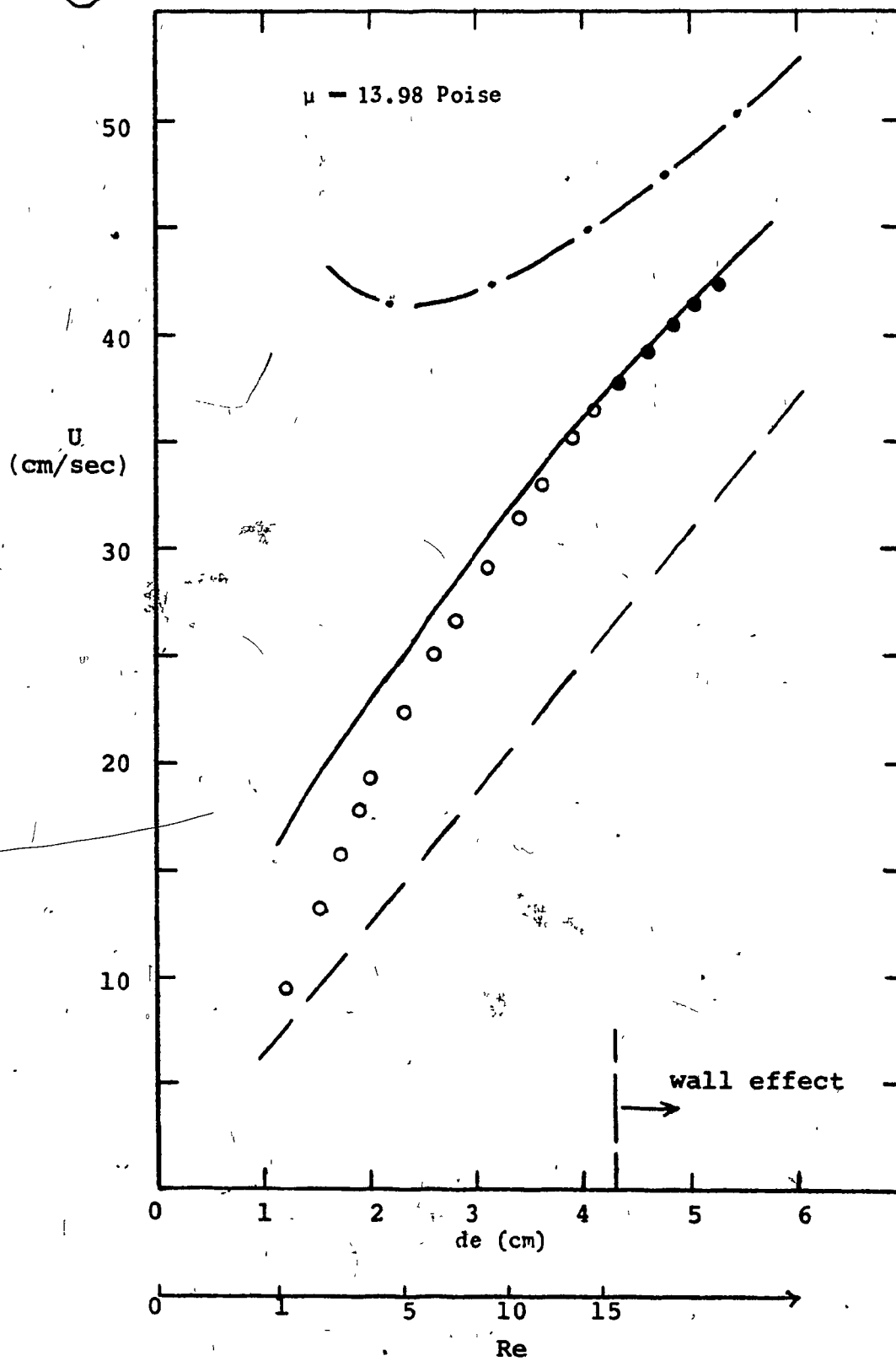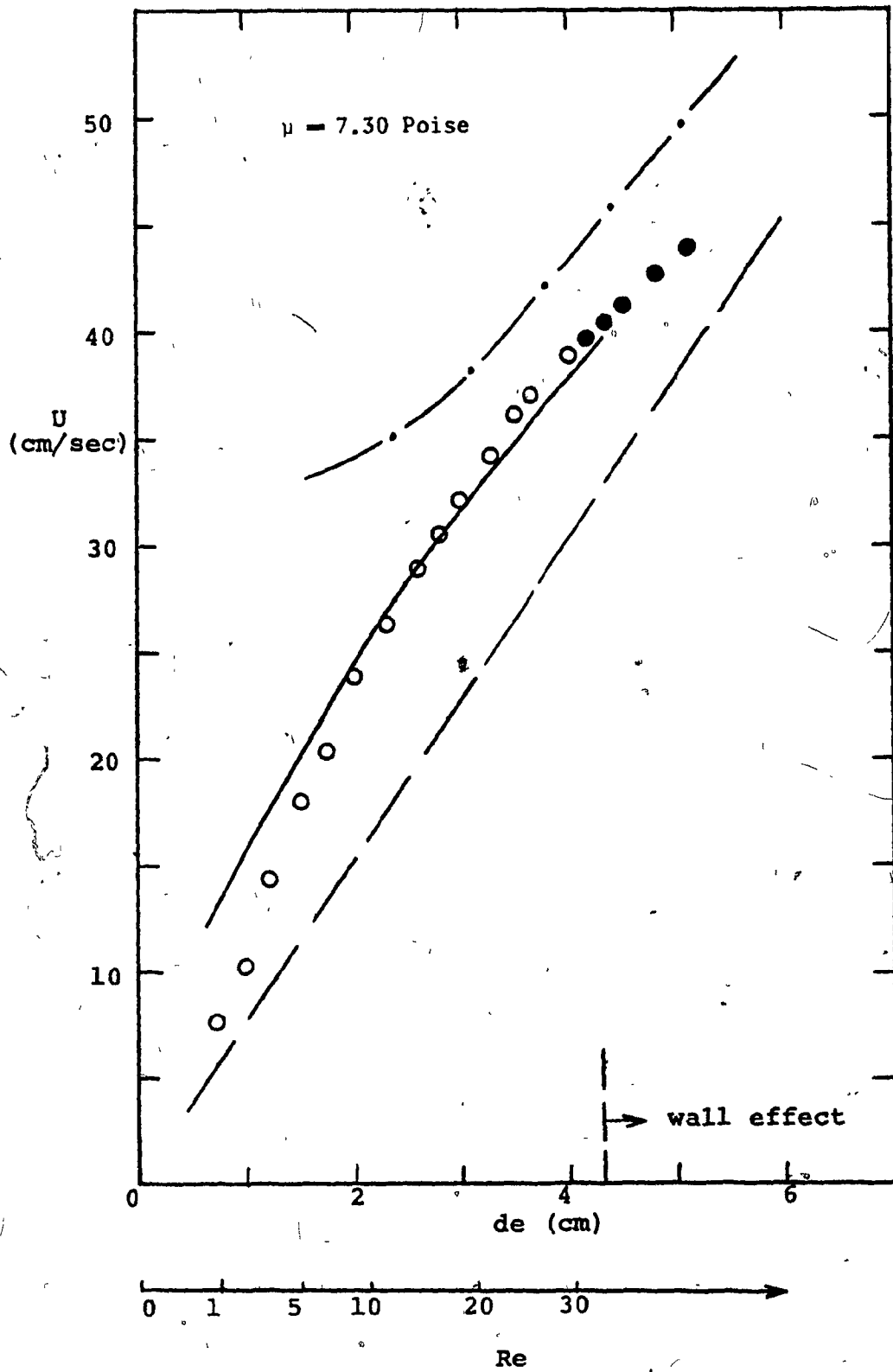
FIGURE 3-16(b)

FIGURE 3-16(c)

The theory of Parlange, Equations (3.26) and (3.27), which is only applicable for spherical-cap bubbles with relatively high Re, is also shown for comparison. The experimental data are bracketed by the theoretical curves, the spread between the curves decreasing with increasing Re. For Re $\gtrsim$ 10 the data are approximated by the average value of the zeroth and first order predictions.

3.4.3.5 Comparison of rise velocity of spherical-cap bubbles with theory

In Fig.3.17(a) - (d) velocity data for the spherical-cap bubbles* are compared with existing theoretical models. We find that the data compare fairly well with Davies and Taylor theory (Equation (3.22)), provided there is no appreciable wall effect.

Davidson's theory (Equation (3.29)), which claims to incorporate the viscous effects into the Davies and Taylor equation, predicts the velocities fairly well despite the fact that the analysis is incorrect as pointed out in Appendix A. The Parlange theory exhibits the trends discussed in the last section and, as expected, the theory begins to disagree with the data for Re $\gtrsim$ 110, where the spherical-cap bubble no longer has a closed toroidal wake. Mendelson's theory agrees reasonably well with the data of spherical-cap bubbles in low viscosity liquid but overpredicts the velocity for bubbles in high viscosity liquids (compare Fig. 3.17(a) with Fig. 3.17(d)).

---

* Bubbles at Re $\leq$ 45 were not spherical-cap in the strictest sense but were classified as spherical-caps as discussed earlier in Section 3.4.2.3.

FIGURE 3.17 Comparison of the Rise Velocity of
Spherical-Cap Bubbles with
Theoretical Predictions

No.	μ(Poise)*
a	5.09
b	2.89
c	1.36
d	1.00

O   experimental data (shaded symbol indicates bubble with skirt)

———— Davies & Taylor's theory (1950)

------------ Mendelson's theory (1967)

— — — — — Davidson's theory (1974)

——— ———Parlange's zeroth order theory (1969)

——— • ——— Parlange's first order theory (1969)

* Other liquid properties are listed in Table 3.3.

μ = 5.09 Poise

U (cm/sec)

d_e (cm)

Re
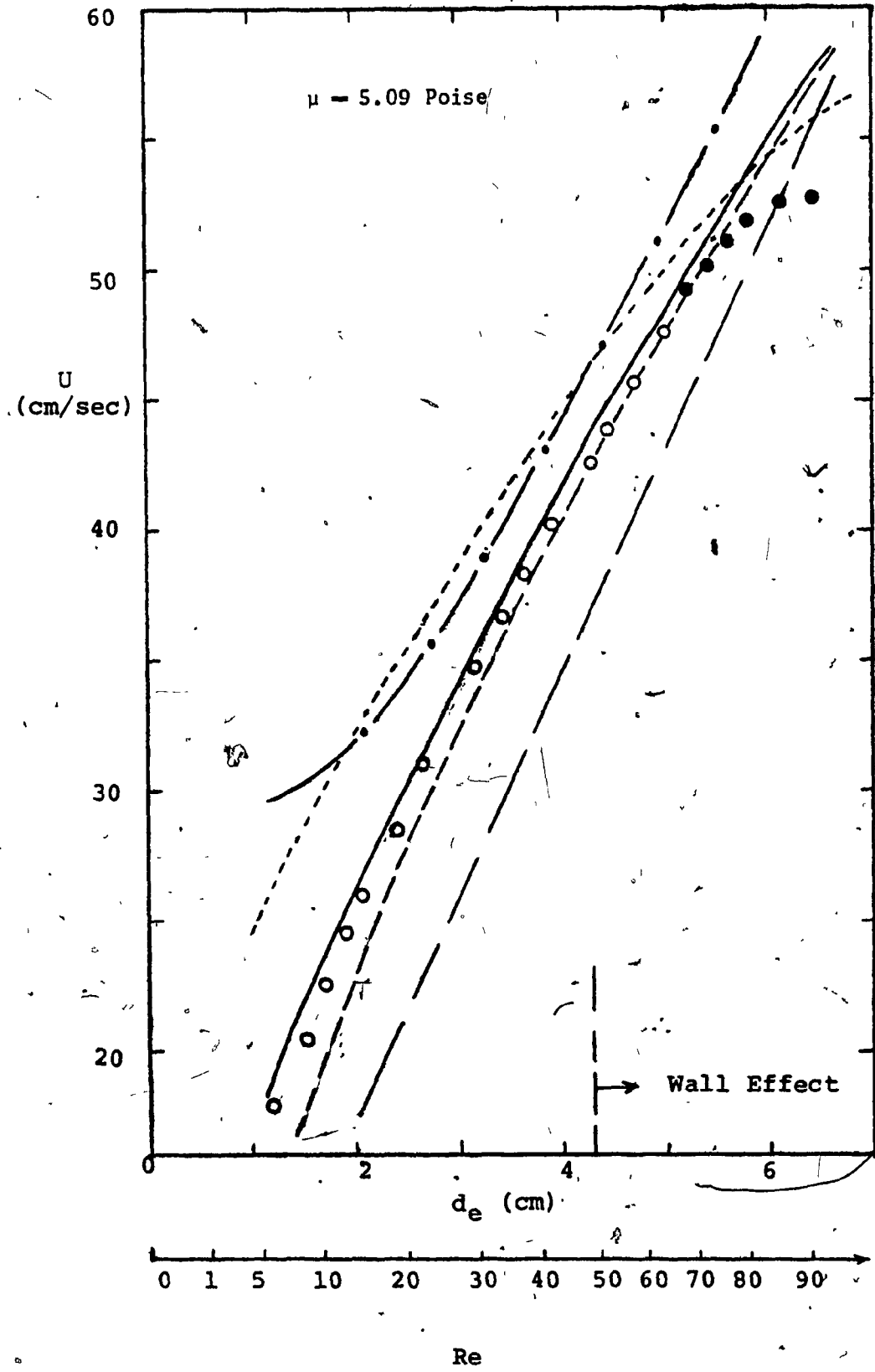
FIGURE 3-17(a)

FIGURE 3-17 (b)

FIGURE 3-17(c)

μ = 1.00 Poise

U (cm/sec)

→ Wall Effect

d_{e}(cm)

Re
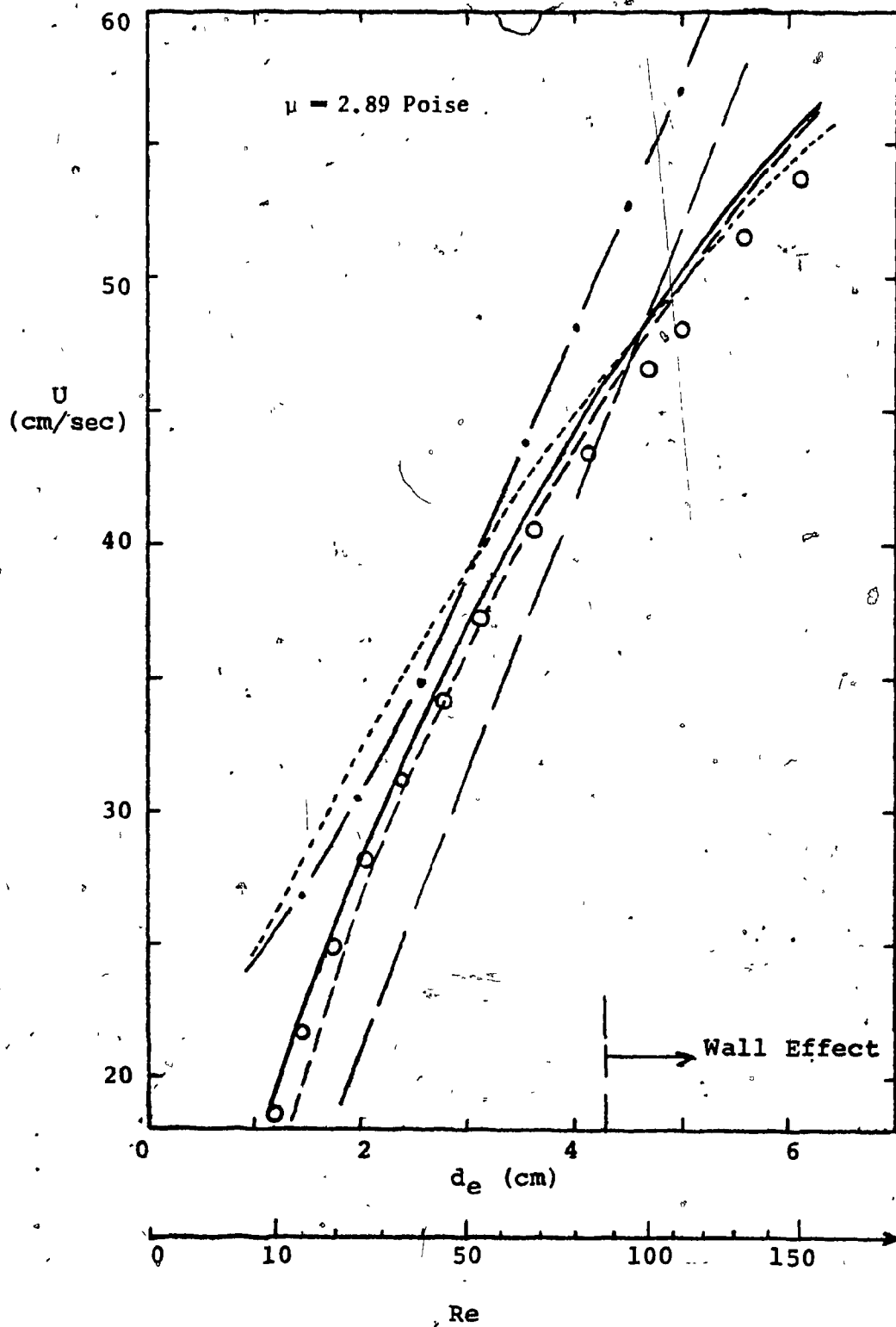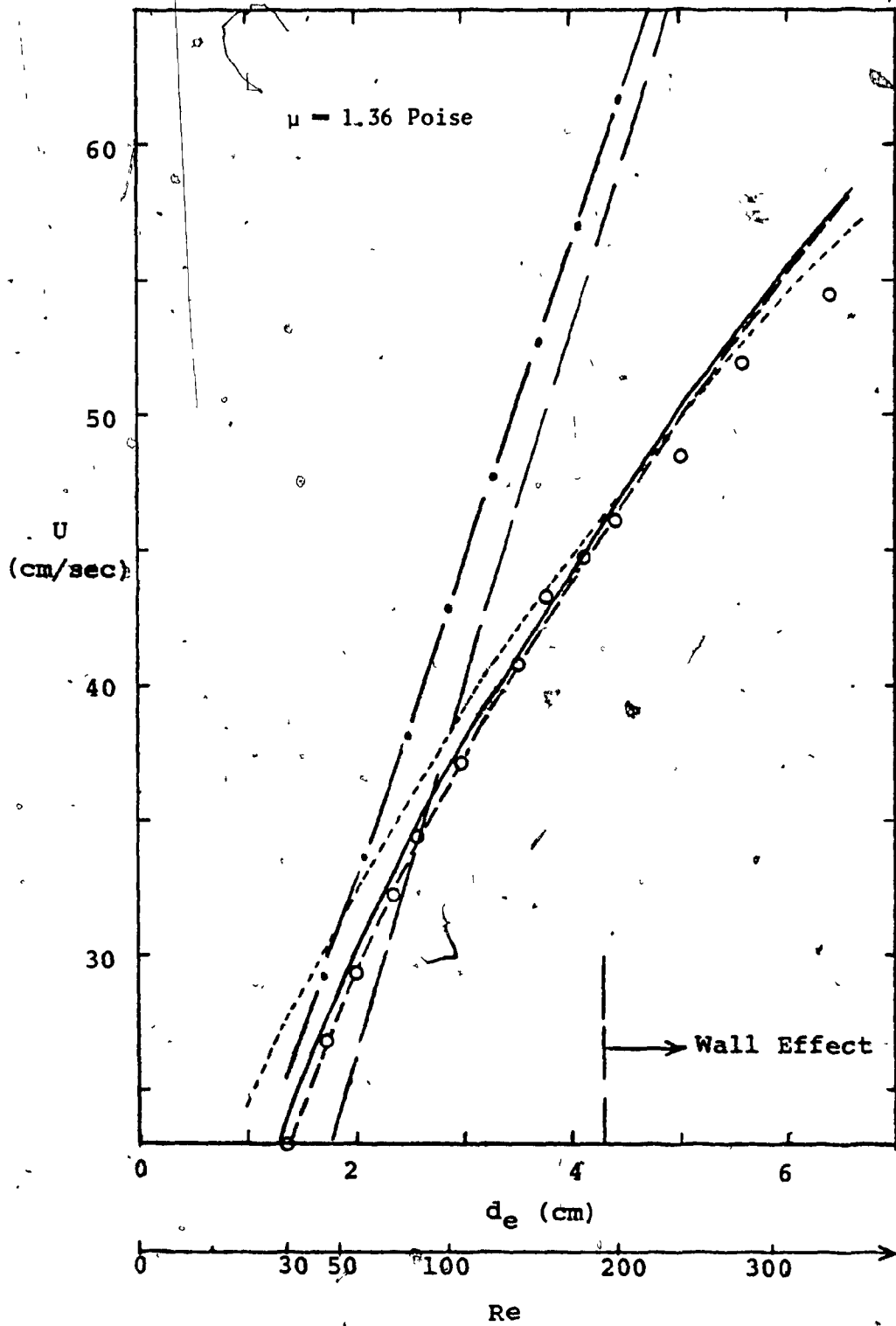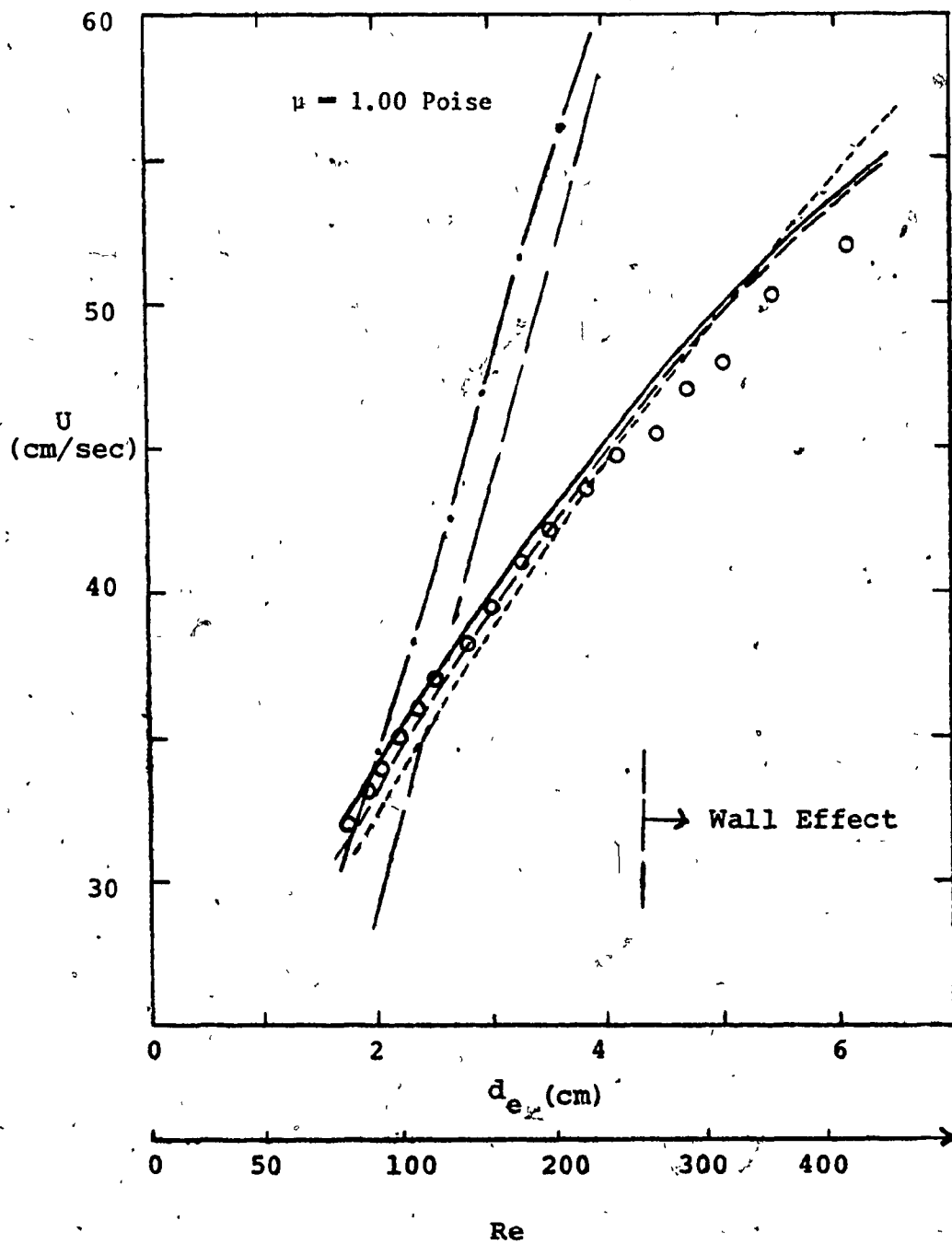
FIGURE 3-17(d)

3.5 Conclusions

1. The physical properties of the liquid have a profound effect on the bubble shape. As the viscosity (or Morton number, M) of the liquid decreases the bubble deformation for a fixed volume increases, becoming progressively flatter.

2. The critical value of M separating the so-called high-M liquids from low-M liquids lies between 1.64×10^{-3} and 5.48×10^{-3}. Bubbles in high-M liquids exhibit no instability or wobbling motion and the drag coefficient curve (C_D versus Re) is independent of M.

3. The small deformation of bubbles from spherical shape at low Re is predicted by the theory of Taylor and Acrivos (1964). The higher order theory of Brignell (1973) is of little practical value.

4. With increase in bubble volume in high-M liquids, the bubble shape does not change directly from spherical to spherical-cap but goes through oblate ellipsoidal and oblate ellipsoidal-cap shapes with the possibility of skirt formation. In these liquids bubble deformation depends only upon Re. The shape parameters of the bubble, such as width, height, indentation, etc. can be predicted from the generalized correlations presented in Figs. 3.6, 3.7 and 3.10.

5. Six additional shape regimes have been added to the Re versus Eö plot, namely: oblate ellipsoidal-cap, wobbling disc-like oblate ellipsoidal, skirted bubbles with smooth steady laminar skirts, skirted bubbles with wavy unsteady skirts, spherical-cap with closed toroidal wake and spherical-cap with open unsteady wake (see Figs. 3.12 and 3.13).

6. The equation of Wairegi and Grace (1976) relating the bubble shape and rise velocity is valid for oblate ellipsoidal-cap and oblate skirted bubbles provided Re $\geqslant$ 5.

7.   For spherical-cap bubbles the Davies and Taylor (1950) equation gives a good prediction of the rise velocity for Re as low as 10.* Parlange's (1969) zeroth order and first order theories give good upper and lower bounds on the rise velocity of spherical-caps provided 10 $\gtrsim$ Re $\gtrsim$ 110. Mendelson's wave analogy predicts the rise velocity of spherical-cap bubbles in low viscosity liquids ($\mu \leqslant 1.0$ Poise) with fair accuracy. Davidson's (1974) attempt to incorporate viscous effects into the Davies and Taylor treatment seems to give good prediction of the velocity of spherical-cap bubbles despite an error in his analysis (see Appendix A).

8.   The rise velocity of large bubbles ($V \gtrsim 2$ cm^3; Eö $\gtrsim$ 40), in an infinite media is predicted by $U = KV^m$ where the values of K and m can be obtained from Fig. 3.15 for any liquid.

9.   For liquids with $M < 10^{-3}$, the rise velocity of large bubbles ($V \gtrsim 2$ cm^3) is independent of liquid properties, and is given by Equation (3.25).

---

* For Re $\leqslant$ 45 the bubbles are not spherical-cap in the strictest sense. However, if Collins' (1966) suggestion of fitting a sphere over the front 75° of the bubble cap (i.e. 37.5° around the front stagnation point) is adopted then bubbles with Re as low as 10 can be treated as spherical-caps.

CHAPTER 4

LIQUID FLOW FIELD INDUCED BY A RISING BUBBLE

4.1 Introduction

The rate of mass, momentum and heat transfer between a moving bubble and the surrounding liquid is dependent upon the details of the velocity field near the bubble. In addition, a rising bubble may carry with it a wake of the continuous fluid. This wake plays a key role in transport processes, mixing, as well as bubble interaction and coalescence.

Due to non-linearity in the equations governing the flow and the a priori unknown shape of the bubble no theoretical solutions exist which accurately describe the flow field, except at very low Re where the inertia effects can be neglected and the bubble adopts a spherical or almost spherical shape. Therefore, for our understanding of the flow field we must rely on the results of systematic experimental investigations in which the significant parameters are varied over a wide range. In this chapter, experimental measurements of the entire velocity field around bubbles of different shapes are presented and discussed. An attempt has been made to cover a wide range of Re (0.087 to 296) where all the major shape transitions and the associated changes in the flow field are encountered; where possible the experimental results are compared with the existing theories.

4.2 Literature Review

4.2.1 Development of the flow field around a moving body

When a body moves through an infinite amount of quiescent fluid, the non-dimensional quantities describing the flow field depend only upon

the Reynolds Number, Re (Rosenhead 1963; Batchelor 1967). The following description of the development of the flow field around a solid sphere will illustrate the dependence of the flow field on Re.

As Re tends to zero the vorticity generated at the surface of the sphere is diffused radially to the bulk of the liquid and the flow is axi-symmetric. By neglecting the inertia terms of the Navier-Stokes equations, Stokes (1851) obtained an analytical solution for the flow. Oseen (1910) took the inertia terms partly into account and obtained solutions valid for small, but finite, Re. In Oseen's approximation the streamlines close less rapidly behind the sphere, the flow does not display fore-aft symmetry and vorticity is convected downstream to form the wake.

As Re increases convection becomes more and more effective in sweeping the vorticity downstream where it is eventually dissipated by viscous motion. The action of convection countering diffusion of vorticity gives rise to a boundary layer around the body which becomes thinner with increasing Re. The liquid in the region outside the boundary layer and outside the wake has negligible vorticity and its motion can be described by the potential (or inviscid) flow equation.

At some critical Re* boundary layer separation occurs leading to a recirculating toroidal standing eddy at the back of the sphere. The

---

* The precise Re at which recirculation starts has been a matter of considerable debate. Clift, Grace and Weber (1976) have reviewed all the available experimental data and numerical solutions and have found the best estimate for the critical Re to be 20.

separation is caused by the retardation of the fluid particles in the
boundary layer during their passage towards the rear stagnation point
where an adverse pressure gradient is encountered.

With further increase in Re the size of the toroidal wake grows
as a result of increasing vorticity generation. Up to Re $\approx$ 130 the wake
remains steady as the vorticity generation is balanced by the rate of
transfer to the fluid outside the wake with no net vorticity accumulation
in the wake. At around Re $\approx$ 130, a weak long-period oscillation becomes
apparent in the tip of the wake. The amplitude increases with Re, but
the flow behind the eddy remains laminar to Re about 200 (Taneda 1956).
At still higher Re (Re $>$ 270) diffusion and convection can no longer keep
pace with vorticity generation so that pockets of vorticity are shed
periodically from the wake (Goldberg and Florsheim 1966). This wake
shedding is the cause of oscillatory motion of a freely falling sphere.
Eventually, at very high Re, $O(10^5)$, the wake becomes turbulent.

A similar sequence of changes has been observed in the flow
past a solid body of other shapes as Re is increased (Batchelor 1967;
Goldberg and Florsheim 1966). The critical value of Re for the various
transitions in the wake is found to depend on the shape of the body.*

The behaviour of a bubble (or drop) differs from a solid sphere
in three ways. Firstly, the velocity of the external fluid relative to

---

* For example, Masliyah and Epstein (1970) has reported a decrease in the
critical Re for the appearance of a recirculating eddy behind spheroids
with decreasing aspect ratio. The results of their numerical solutions
gave the critical Reynolds Number, Re_a (based on semi-major axis, a) of
20, 9, and 3 for the spheroid of aspect ratio (major axis/minor axis) of
1, 0.5 and 0.2, respectively. These values of Reynolds Number correspond
to Re (based on d_e) of 20, 7.14, 1.75, respectively.

the bubble (or drop) is not usually zero at the interface as would be
the case for the solid body. Since this results in less vorticity
generation, wake formation is delayed and thinner boundary layers and
smaller wakes are formed at equal Re.(Le Clair 1970; Le Clair and Hamielec
1971; Hamielec et al 1967; Rivkind et al 1972; Garner and Skelland 1955;
Garner and Tayeban 1960; Elzinga and Banchero 1961). Secondly, a bubble
(or drop) deforms with increasing Re. Since in most systems it deforms
to an oblate spheroid and then to a spherical-cap, the formation of an
attached toroidal wake and the subsequent onset of wake shedding are pro-
moted by the deformation (Satapathy and Smith 1961). Thirdly, surface
active materials may affect the velocity at the surface and hence the
internal circulation (Savic 1953; Garner and Haycock 1959; Levich 1962)
and the shape (Garner and Haycock 1959; Winnikow and Chao 1966; Edge and
Grant 1971).

4.2.2 Flow fields and wakes of bubbles

Several workers have done experiments on wakes behind bubble
rising in two-dimensional liquid beds because it is easier to photograph
the wakes behind two-dimensional bubbles (Collins 1965; Calderbank 1967;
Crabtree and Bridgewater 1967; Lindt 1971 a and b; Lazarek and Littman
1974). However, these results are not directly applicable to three-
dimensional bubbles because the gap width between the plates has a strong
effect on the wake (Crabtree and Bridgewater 1967).

Miyagi (1925) was the first to notice a wake following a three-
dimensional bubble. By close inspection of single oblate spheroidal air
bubbles zig-zagging through water he noticed an upward current of water
behind the bubble; and the larger the bubble the larger was this upward

current. Haberman and Morton (1953) and Saffman (1956) suggested that the zig-zagging (or oscillating) motion is due to the periodic shedding of vortices. Saffman (1956) carried out the most comprehensive study of the unstable motion of bubbles in water and concluded that up to $d_e = 0.14$ cm. the stable motion is rectilinear. For $0.14 < d_e < 0.2$ cm. the zig-zagging motion is stable and is the only motion that occurs. Above $d_e > 0.2$ cm. zig-zagging motion is unstable and spiralling motion can occur in the presence of a disturbance. The cause of the zig-zagging motion was attributed to the interaction between an oscillating wake and an instability in the liquid near the front of the bubble provided that the bubble is sufficiently oblate. No evidence concerning the cause of spiralling motion was presented, except the suggestion that it may be due to the onset of turbulence in the wake.

Subramanian and Tien (1970) photographed the wakes carried by small bubbles (0.1 cm. $\leq d_e \leq$ 0.4 cm., $20 \leq$ Re $\leq$ 600) in water using a dye tracer technique.* Their photographs of the wake and the trailing dye filaments are very similar to those observed for drops (Magarvey and Bishop 1960, 1961a, 1961b; Magarvey and Maclatchy 1968; Al Dimian and Ruckenstein 1970; Winnikow and Chao 1966). The small bubbles of Subramanian and Tien retained their spherical shape and rose rectilinearly with a wake followed by a single trail, the intermediate size bubbles had a slightly distorted oblate shape but moved rectilinearly with a wake followed by a

---

* These authors also attempted to measure the volume of the wake carried by the bubbles but their results are unreliable because their assumed shape of the wake was unrealistic and their method of calculating the volume was in error. Further, the dye used by these authors might have been surface active thus yielding bubbles with more solid-like surfaces.

double trail. The larger bubbles rose with zig-zag motion leaving a haphazard trail. This general description should apply to small bubbles rising in low M liquids.

A great number of studies have been devoted to the nature of the wake behind large spherical cap bubbles. Some confusion arose in the literature from the spark photographs of spherical-cap bubbles in nitrobenzene presented by Davies and Taylor (1950). These photographs, which seemed to indicate a closed turbulent wake at rather large Re (Re $\approx$ 6200), led some authors to assume that around the spherical region, made up of the cap of the bubble and the closed wake, the flow is a potential flow, which closes behind the spherical region. That the bubble formed only a "closed" wake and the combined unit travelled as a potential body was refuted by Maxworthy (1967). His argument was that as a bubble rises with constant velocity it must experience a finite drag and that this drag will be seen behind the bubble as a momentum defect in the liquid. Maxworthy (1967) demonstrated the presence of an extended turbulent wake by letting a 2.5 cm^3 bubble (Re $\approx$ 4800) rise in a clear water above a pool of dye. A significant discharge of vorticity from the wake was found. Similar observations have been reported by Guthrie (1967); Guthrie and Bradshaw (1973) and Lindt (1971). Excellent schlieren photographs of spherical cap bubbles (Re — 8300 to 38,000) and their wakes have recently appeared in the literature.(Wegener et al 1971; Wegener and Parlange 1973). These photographs clearly demonstrate that at high Re the wake is turbulent and extends far downstream from the bubble.

A wake structure entirely different from the turbulent one has been observed for spherical cap bubbles at low Re ($\lesssim$ 100) that are normally encountered in high M liquids. In this case the bubble is followed by a

toroidal vortex. O'brian and Gosline (1935) were the first to observe
such a vortex below a spherical cap bubble rising in livestock oil using
small entrained air bubbles caught in the wake. Similar observations
were reported by Davenport et al (1967), Crabtree (1969) and Narayanan
et al (1974). Schlieren photographs by Slaughter and Wraith (1968) and
Wegener and Parlange (1972) have provided, to date, the best photographic
evidence of a stable laminar wake which consists of a toroidal vortex
with a streaming cylindrical tail extending below it. The latter authors
also showed that the closed laminar wake behind spherical cap bubbles
exists up to about Re $\sim$ 100 above which unsteadiness in the wake sets in
and at higher Re the wakes become turbulent.

4.3 Objectives

From the foregoing review it is evident that the available
information on bubble wakes is very limited, and mainly qualitative.
There is virtually no information available on wakes behind bubbles at
low Re* in high M liquids. Many authors have assumed a particular velo-
city field around a bubble and used it to predict mass transfer rates
(Baird and Davidson 1962; Lochiel and Calderbank 1964; Calderbank et al
1970; Brignell 1974), bubble interaction (Crabtree and Bridgewater 1972;
Wah-on 1971; Wairegi 1974; Narayanan et al 1974) and terminal velocity
from observed bubble shapes (Davies and Taylor 1950; Collins 1966; Grace
and Harrison 1967; Wairegi and Grace 1975). However, the actual velocity

---

* Re $\sim$ 56 appears to be the lowest Re for bubbles in high M liquids,
at which experimental evidence regarding nature of the wake is reported
(Slaughter and Wraith 1968). At the time of writing this chapter the
paper of Hnat and Buckmaster (1976) was not published. Their finding
is discussed in the "addendum", Section 4.6.

field has never been measured experimentally to confirm these assumptions. The aim of the work described in this chapter is to measure the entire velocity field around the bubble, and the size and the shape of the wake behind the bubble of all the different shapes in viscous (high M) liquids.

4.4 Theory
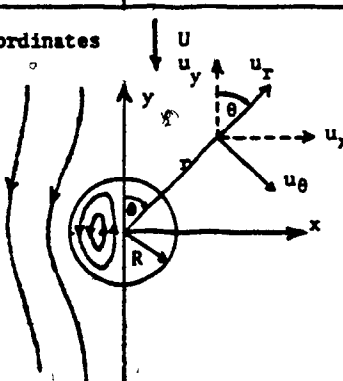
For a fluid sphere moving in another fluid an analytical solution describing the internal as well as external flow field was derived, independently, by Hadamard (1911) and Rybczynski (1911). The key assumption was that the inertial effects were negligible in both phases, i.e. Re → 0. The following boundary conditions were used:

(i)   uniform flow remote from the sphere,

(ii)   no flow across the interface between the fluids,

(iii) continuity of the tangential velocity across the inter-
       face, and

(iv)   continuity of the tangential stress across the interface.

A detailed derivation of this solution is available elsewhere (Levich 1962; Happel and Brenner 1965; Batchelor 1967). The resulting stream function and the velocity components describing the flow field, together with the appropriate co-ordinate system, are summarised in Table 4.1. The Stokes' (1851) solution for a rigid sphere is recovered by putting the viscosity ratio $\kappa = \frac{\mu'}{\mu} = \infty$ into these equations while the solution for a gas bubble rising through liquid can be obtained by setting $\kappa = 0$.

A very important conclusion follows if one considers the normal stresses at the interface. It can be shown that the components of normal stress at the interface differ by a constant amount (Batchelor 1967) and

TABLE 4.1 <u>Hadamand-Rybczinki Solution for a Sphere</u>

	External Fluid	Internal Fluid
stream function, ψ	$\frac{U}{2}r^2\sin^2\theta\ 1 - \left[\frac{(2+3\kappa)}{2(1+\kappa)}\frac{R}{r} + \frac{\kappa}{2(1+\kappa)}\left(\frac{R}{r}\right)^3\right]$	$\frac{Ur^2\sin^2\theta}{4(1+\kappa)}\left[1 - \left(\frac{r}{R}\right)^2\right]$
radial velocity, u_r	$-U\cos\theta\left[1 - \frac{(2+3\kappa)}{2(1+\kappa)}\frac{R}{r} + \frac{\kappa}{2(1+\kappa)}\left(\frac{R}{r}\right)^3\right]$	$\frac{U\cos\theta}{2(1+\kappa)}\left[1 - \left(\frac{r}{R}\right)^2\right]$
tangential velocity, u_θ	$U\sin\theta\left[1 - \frac{(2+3\kappa)}{4(1+\kappa)}\frac{R}{r} - \frac{\kappa}{4(1+\kappa)}\left(\frac{R}{r}\right)^3\right]$	$\frac{U\sin\theta}{2(1+\kappa)}\left[1 - 2\left(\frac{r}{R}\right)^2\right]$
spherical polar co-ordinate system with frame of reference fixed to the sphere	relations with cartesian coordinates and velocity components: $x = r\sin\theta$ $y = r\cos\theta$ $u_x = u_\theta\cos\theta + u_r\sin\theta$ $u_y = u_r\cos\theta - u_\theta\sin\theta$ where $u_r = -\frac{1}{r^2\sin\theta}\frac{\partial\psi}{\partial\theta}$ $u_\theta = \frac{1}{r\sin\theta}\frac{\partial\psi}{\partial r}$	
terminal velocity, U	$\frac{2gR^2(\rho-\rho')}{3\mu}\frac{(1+\kappa)}{(2+3\kappa)}$	

* for Stoke's solution for a rigid sphere viscosity ratio, $\kappa = \frac{\mu'}{\mu} = \infty$
for freely circulating gas bubble, $\kappa = 0$

that if the interfacial tension is constant over the surface (as. it will
be in absence of surface active agents) the curvature will be constant.
In other words, a fluid particle (bubble or drop) moving at its terminal
velocity with very low Re should be spherical, whatever its size (see
Chapter 3, Fig.3.12). It is only when inertial forces become significant
that bubbles and drops deform from the spherical shape. Taylor and Acrivos
(1964) used a singular perturbation procedure analogous to that employed
by Proudman and Pearson (1957) for a solid sphere, and matched a solution
satisfying the Oseen equation at infinity and the Hadamard-Rybczynski
equation in the neighbourhood of the sphere. The partial inclusion of
the inertial effects was shown to be responsible for the deformation.
It was demonstrated that to a first approximation the sphere deformed into
an oblate rather than a prolate spheroid. Having determined the deforma-
tion (i.e. shape of the oblate spheroid) these authors also investigated
the effect of the deformation on the flow field by assuming creeping flow
around the oblate ellipsoid. The stream functions for the flow field
external to the bubble for the two cases cited above can readily be obtained
by setting the viscosity ratio $\kappa = 0$ in the Equations(17) and (24) of
Taylor and Acrivos (1964) and substituting these in their Equation (12a).
The radial and angular velocity components are readily obtained using the
relationships between the stream function and the velocity components
shown in Table 4.1. The final results are summarised in Table 4.2. Taylor
and Acrivos also persued a higher order approximation which predicted a
flattening of the underside of rising bubbles at increased Weber Number, We.

Recently, Golovin and Ivanov (1971) considered only the case
of gas bubbles, i.e. $\kappa = 0$ and used the asymptotic matching technique to
obtain a solution for the external flow field around a spherical bubble

up to terms of order $Re^2 \ln Re$. However, at Re large enough for these higher order terms to become important, the bubble deformation is sufficiently large for the assumption of a slightly deformed spherical shape to be invalid. Further development of these solutions appears fruitless.

At higher Re where the bubble takes on an oblate ellipsoidal-cap shape no theoretical solutions are available. The flow field around the bubble, at least in front of the bubble up to its base, is expected to be between two limiting cases: the creeping flow around a solid oblate ellipsoid and the potential flow around an oblate ellipsoid which fits the bubble shape. A detailed derivation of the stream function for creeping flow and potential flow past an oblate spheroid can be found in Happel and Brenner (1965) and Milne-Thomson (1968), respectively. The results are summarised in Tables 4.3 and 4.4. The co-ordinate system together with transformation relationships and a geometric interpretation of the oblate ellipsoidal co-ordinates ξ and η are presented in Table 4.5.

For Re large with respect to 1 but below the critical Re for which unsteady motion sets in, the bubble assumes a spherical-cap shape and carries with it a closed laminar wake. Parlange (1969) modelled this situation by considering the flow to be irrotational outside the complete sphere of which the bubble formed the cap. The bubble was assumed to have little effect on the dynamics of the flow in the wake except causing it to exist. The vorticity was then confined to the enclosed wake region which was treated as a Hill's (1894) spherical vortex. The stream function and velocity components for the external potential flow and internal Hill's vortex are summarised in Table 4.6.

Parlange (1969) also pointed out that at the streamline separating the wake and the outside flow, the viscous stress must be continuous. As a result, a boundary layer must grow on both sides of the separating

TABLE 4.2 <u>Taylor-Acrivos Solution for a Slightly Deformed Circulating Gas Bubble</u>

	External Flow Field	
	Model I Inertia Effects Included; Assumes Spherical Shape	**Model II** Deformation Effect Included; Assumes Creeping Flow Around an Oblate Ellipsoid
stream function, ψ	$\dfrac{UR^2\sin^2\theta}{2}\left[\left(\dfrac{r}{R}\right)^2 - \dfrac{r}{R}\right]\{1+\tfrac{1}{8}Re(1-\cos\theta)\}$	$\dfrac{UR^2\sin^2\theta}{2}\left[\left(\dfrac{r}{R}\right)^2 - \dfrac{r}{R}\right] + \dfrac{UR^2We\,\sin^2\theta}{24}\left[\dfrac{4r}{R} - \dfrac{3R}{r}\right]$ $- \dfrac{UR^2We\,\sin^2\theta(1-5\cos^2\theta)}{16}\left[\dfrac{9R}{7r} - \dfrac{2R^3}{7r^3}\right]$
radial velocity, V_r	$-U\cos\theta\left[1 - \dfrac{R}{r}\right]\{1 + \tfrac{1}{16}Re(2+2\cos\theta-\sin\theta\tan\theta)\}$	$-U\cos\theta\left[1 - \dfrac{R}{r}\right] - \dfrac{UWe\cos\theta}{48}\left[\dfrac{4R}{r} - 3\left(\dfrac{R}{r}\right)^3\right]$ $- \dfrac{UWe(\cos\theta-5\cos^3\theta+5\sin^2\theta\cos\theta)}{32}\left[\dfrac{9}{7}\left(\dfrac{R}{r}\right)^3 - \dfrac{2}{7}\left(\dfrac{R}{r}\right)^5\right]$
tangential velocity, u_θ	$U\sin\theta\left[1 - \dfrac{R}{2r}\right]\{1 + \tfrac{1}{8}Re(1-\cos\theta)\}$	$U\sin\theta\left[1 - \dfrac{R}{2r}\right] + \dfrac{UWe\sin\theta}{96}\left[\dfrac{4R}{r}+3\left(\dfrac{R}{r}\right)^3\right]$ $- \dfrac{UWe\sin\theta(1-5\cos^2\theta)}{64}\left[\dfrac{9}{7}\left(\dfrac{R}{r}\right)^3 + \dfrac{6}{7}\left(\dfrac{R}{r}\right)^5\right]$
terminal velocity, U	$\dfrac{gD^2(\rho-\rho')}{3\mu}\dfrac{1}{(1+\tfrac{Re}{8})}$	$\dfrac{gR^2(\rho-\rho')}{3\mu}\dfrac{1}{(1+\tfrac{We}{12})}$
co-ordinate system	same as in Table 4.2 with R being radius of equivalent sphere and the origin of the co-ordinate system coinciding with the center of mass of the dispersed fluid	

TABLE 4.3 **Creeping Flow Past a Solid Oblate Ellipsoid**

stream function, ψ	$\frac{1}{2}Ux^2\left\{1-\dfrac{\lambda/(\lambda^2-1) - (\lambda_0^2-1)/(\lambda_0^2+1)\cot^{-1}\lambda}{\lambda_0/(\lambda_0^2+1) - (\lambda_0^2-1)/(\lambda_0^2+1)\cot^{-1}\lambda_0}\right\}$ where $\lambda = \sinh\xi$, $\lambda_0 = \sinh\xi_0$
velocity component, u_η	$\dfrac{Uc^2\sin^2\eta}{x^2c(\cosh^2\xi-\sin^2\eta)^{1/2}}\left\{\cosh\xi\sinh\xi-\dfrac{\cosh\xi-2(1-2e^2)\cosh\xi\sinh\xi\cot^{-1}\sinh\xi+(1-2e^2)\cosh\xi}{2[e\sqrt{1-e^2}-(1-2e^2)\sin^{-1}e]}\right\}$
velocity component, u_ξ	$\dfrac{Uc^2\sin\eta\cos\eta}{x^2c(\cosh^2\xi-\sin^2\eta)^{1/2}}\left\{\cosh^2-\dfrac{\sinh\xi-(1-2e^2)\cosh^2\xi\cot^{-1}\sinh\xi}{2\,e\sqrt{1-e^2}-(1-2e^2)\sin^{-1}e}\right\}$
co-ordinate system	see Table 4.5

TABLE 4.4 <u>Potential Flow Past an Oblate Ellipsoid</u>

stream function, ψ	$\dfrac{Uc^2\sin^2\eta}{2}\cosh^2\xi\left[\dfrac{(\sinh\xi-\cosh^2\xi\cot^{-1}\sinh\xi)}{e\sqrt{1-e^2}-\sin^{-1}e}\right]$
velocity component, u_η	$\dfrac{U\sin\eta}{(\cosh^2\xi-\sin^2\eta)^{1/2}}\left[\sinh\xi-\dfrac{1-\sinh\xi\cot^{-1}\sinh\xi}{e\sqrt{1-e^2}-\sin^{-1}e}\right]$
velocity component, u_ξ	$-\dfrac{Uc^2\sin\eta\cos\eta}{x(\cosh^2\xi-\sin^2\eta)^{1/2}}\left[\cosh^2\xi-\dfrac{(\sinh\xi-\cosh^2\xi\cot^{-1}\sinh\xi)}{e\sqrt{1-e^2}-\sin^{-1}e}\right]$
co-ordinate system	see Table 4.5

TABLE 4.5 Oblate Ellipsoidal Co-ordinates
and Transformation Relationships
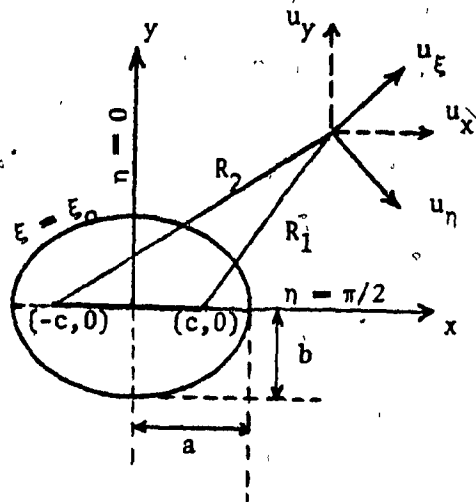
Transformation $y + ix = c \sinh(\xi + i\eta)$ for $c > 0$ gives:

$$y = c \sinh\xi \cos\eta \quad \text{and} \quad x = c \cosh\xi \sin\eta$$

Spheroid surface is given by $\xi_0 = \tanh^{-1}(b/a)$

where $a = c \cosh\xi_0$ and $b = c \sinh\xi_0$ are the semi-axis;

focal length, $c = \sqrt{a^2 - b^2}$; eccentricity, $e = \sqrt{1 - \dfrac{b^2}{a^2}} = \dfrac{c}{a}$.

The ellipsoidal co-ordinates (ξ, η) are related to the cartesian co-ordinates (x, y) by:

$$\xi = \cosh^{-1}\left[\frac{R_2 + R_1}{2c}\right] \quad \text{and} \quad \eta = \sin^{-1}\left[\frac{R_2 - R_1}{2c}\right]$$

where $R_1 = \left[y^2 + (x-c)^2\right]^{1/2}$ and $R_2 = \left[y^2 + (x+c)^2\right]^{1/2}$

The velocity components u_x and u_y are related to the velocity components u_ξ and u_η by: (see Appendix B for detailed derivation).
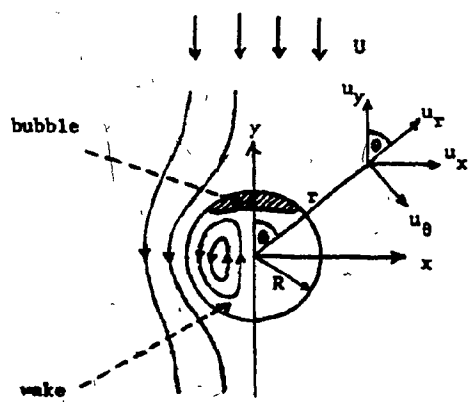
$$u_x = \frac{u_\xi \sinh\xi \sin\eta + u_\eta \cosh\xi \cos\eta}{(\cosh^2\xi \cos^2\eta + \sinh^2\xi \sin^2\eta)^{1/2}}$$

and

$$u_y = \frac{u_\xi \cosh\xi \cos\eta - u_\eta \sinh\xi \sin\eta}{(\cosh^2\xi \cos^2\eta + \sinh^2\xi \sin^2\eta)^{1/2}}$$

TABLE 4.6 Parlange's Model for Wake of Spherical Cap Bubble

	External Flow, $r \geqslant R$	Internal Flow (in Closed Wake), $r \leqslant R$
Theoretical Model	Irrotional (Potential) Flow	Hill's Spherical Vortex
stream function, ψ	$\dfrac{Ur^2\sin^2\theta}{2}\left[1-\left(\dfrac{R}{r}\right)^3\right]$	$\dfrac{3Ur^2\sin^2\theta}{4}\left[\left(\dfrac{r}{R}\right)^2-1\right]$
radial velocity, u_r	$-U\cos\theta\left[1-\left(\dfrac{R}{r}\right)^3\right]$	$-\dfrac{3U\cos\theta}{2}\left[\left(\dfrac{r}{R}\right)^2-1\right]$
tangential velocity, u_θ	$U\sin\theta\left[1+\dfrac{1}{2}\left(\dfrac{R}{r}\right)^3\right]$	$\dfrac{3U\sin\theta}{2}\left[2\left(\dfrac{r}{R}\right)^2-1\right]$
spherical polar co-ordinate system with frame of reference fixed to the spherical wake		

For relationships between co-ordinates and velocity components in spherical-polar and Cartesian system, see Table 4.1.

streamline. The boundary layer theory of Harper and Moore (1968) was incorporated to correct for viscous dissipation in the boundary layer. In his later paper, Parlange (1970) presented his own treatment of the boundary layer which differed from Harper and Moore's.

The essential difference between the two treatments is the assumption regarding the nature of the boundary layer inside the sphere. When the vorticity layer inside the sphere reaches the rear stagnation point it must climb back along the axis. Harper and Moore assume that, as it does so, the structure of the layer is unchanged. The resulting circulation is less than that of the inviscid Hill's vortex and is given by:

$$\frac{\text{actual strength of the vortex}}{\text{strength of unperturbed Hill's vortex}} = 1 - \frac{2.5(2+3\kappa)}{\sqrt{Re_D}} \frac{1+2\sqrt{\kappa\gamma}}{2+3\sqrt{\kappa\gamma}}$$

$$\ldots\ldots(4.1)$$

where $\kappa = \frac{\mu'}{\mu}$; $\gamma = \frac{\rho'}{\rho}$ and $Re_D = \frac{2ReU}{\mu}$, R being the radius of the sphere. The above equation is expected to be valid when $\kappa < 2$, $Re > 50$ and the ratio predicted by Equation (4.1) is greater than 0.5 (Harper 1972). In contrast, Parlange (1970), assumed that viscous diffusion obliterates the inside boundary layer before it reaches the fron stagnation point. Like Harper and Moore's treatment, the internal circulation is less than the inviscid Hill's vortex but by a significantly smaller amount as can be seen from his prediction:

$$\frac{\text{actual strength of the vortex}}{\text{strength of unperturbed Hill's vortex}} = 1 - \frac{4}{3}\sqrt{\frac{6}{\pi Re_D}}\left[1+\frac{3}{2}\kappa\right]$$

$$\ldots\ldots(4.2)$$

It is worth noting that despite these differences in predicted internal circulation, both the theories yield essentially the same numerical results for the viscous dissipation and hence the drag coefficient (Parlange 1970).

To a first approximation the internal flow pattern inside a gas bubble has negligible effect on the external flow (Harper and Moore 1968); hence, any deviation from potential flow around a spherical-cap bubble may be predicted using the boundary layer theory of Moore (1963)*. The theoretical equations for obtaining the radial and angular velocity components for this case are tabulated in Table 4.7.

The external boundary layer enveloping the closed toroidal wake stretches near the rear stagnation point into a long thin wake in which the velocity perturbation gradually decays to zero but the momentum defect remains finite. This momentum defect accounts for the relatively narrow trail extending from the rear of the toroidal wake observed by Slaughter and Wraith (1968) and Wegener and Parlange (1973).

Far downstream from the bubble the vorticity is dissipated by viscosity and the streamlines in the wake become nearly parallel to those in the external irrotational flow. By assuming that the pressure in the wake is nearly equal to the free stream pressure outside the wake, it is possible to evaluate the assymptotic wake velocity distribution. The wake structure is here independent of the geometry of the bubble generating the wake and is determined by the drag, D', exerted on the liquid by the bubble, the liquid density, ρ, and the liquid viscosity, μ. For a steady

---

* Moore's boundary layer theory applies to a gas bubble and is a special case of a more general theory for a fluid sphere later developed by Harper and Moore (1968).

TABLE 4.7   Moore's Boundary Layer Solution for a Spherical Gas Bubble

The angular and radial velocity components for boundary layer solution are:

$$\bar{u}_\theta = u_\theta + u'_\theta \qquad \text{and} \qquad \bar{u}_r = u_r + u'_r, \text{ respectively}$$

where u_θ and u_r are the velocity components for potential flow given in Table 4.6 and

u'_θ and u'_r are the perturbation velocity components given by:

$$u'_\theta = U\delta p \qquad \text{and} \qquad u'_r = U\delta^2 q$$

where $\delta = \sqrt{\dfrac{2}{Re}}$; $Re = \dfrac{\rho U R}{\mu}$

$$p = -6 \sin\theta \, X^{1/2} f(s/2X^{1/2})$$

$$s = \frac{r-R}{R\delta}$$

$$X(\theta) = \frac{2}{3} \csc^4\theta \left(\frac{2}{3} - \cos\theta - \frac{1}{3}\cos^2\theta\right)$$

$$f(z) = \frac{1}{\sqrt{\pi}} \exp(-z^2) - z \, \mathrm{erfc} z$$

$$q = \frac{2\sqrt{X}}{\sin\theta}\left\{ h'(\theta)\int_0^{y/2\sqrt{X}} f(z)dz + h(\theta)\left[2\cot\theta - \frac{1}{3X\sin\theta}\right]\int_0^{y/2\sqrt{X}} z \, f'(z)dz \right\}$$

and

$$h(\theta) = 6\sqrt{X} \sin^2\theta$$

The co-ordinate system is the same as that defined in Table 4.6.

viscous wake, Batchelor (1967) has shown that the asymptotic wake velocity, W_a, is given by:

$$W_a = \frac{D'}{4\pi\mu L} \exp - \frac{Ux^2\rho}{4\bar{\mu}L} \tag{4.3}$$

in the region in which $W_a \ll U$. Here L is the vertical downstream distance from the body to the point considered and x is the horizontal distance to the point from the vertical axis along which the bubble rises. Noting that the drag force acting on a bubble is given by $V\rho g$, where V is the bubble volume, Crabtree and Bridgewater (1971) obtained the axisymmetric asymptotic wake velocity distribution:

$$W_a = \frac{V\rho g}{4\pi\mu L} \exp - \frac{Ux^2\rho}{4\mu L} \tag{4.4}$$

For the turbulent wake behind a spherical cap bubble a free streamline theory which assumes an infinite stagnant wake have been proposed by Moore (1959) and Rippin and Davidson (1967). While this physical model is unrealistic, it is interesting to note that it gives a reasonable approximation for the drag coefficient and for the bubble shape.

4.5 Experimental Results and Discussion

The flow field in the immediate neighbourhood of the bubble was investigated by ciné-photographing the bubble together with the surrounding hydrogen tracer bubbles with a moving camera, where as the flow field far away from the bubble and specifically behind the bubble was ciné-photographed by a stationary camera. The findings of these experiments are presented in Sections 4.5.2 and 4.5.3, respectively.

4.5.1 Evaluation of flow field measuring technique

For both sets of experiments extreme care was taken to insure the alignment of the cathode, the illuminating sheet of light, and the bubble directing funnel such that the tracer bubbles photographed were located in the central plane containing the axis of bubble rise. Any misalignment could easily be detected because the tracer bubbles did not remain in the photographic plane. Only a small number of experiments showed such three-dimensional effects and these were rejected.

It was also necessary to control the size of the tracer bubbles; if they were too small the amount of light reflected was insufficient for satisfactory photographs, whereas, if they were too large, the tracer bubbles would not follow the flow with sufficient accuracy. The size of the tracer bubbles and hence their terminal velocity was expected to be a function of applied voltage, pulse width, cathode wire diameter, liquid properties, liquid velocity past the cathode and the type and concentration of the electrolyte added (Asanuma and Takeda 1965; Tory and Haywood 1971). In the present work the size of the tracer bubbles was controlled by varying the applied voltage and the duration of the pulse. The rise velocity of typical tracer bubbles was estimated by generating a row of hydrogen bubbles in a stagnant liquid and measuring the time taken by these bubbles to rise a fixed distance.* Their size was also calculated using both Stokes and Hadamard equation. The following table shows the results for the tracer bubbles in the most and the least viscous aqueous sugar solution used in the present study.

---

* In order to avoid interference from the cathode these measurements were done above a distance greater than 100 wire diameters, which is larger than the distance of 70 wire diameters recommended by Schraub et al (1965).

Liquid Properties				Tracer Bubble Velocity (cm/sec)	Tracer Bubble Diameter (cm.)	
(Poise)	(g/cm^3)	(dynes/cm)	Temp. ($^\circ$C)		Stokes Spheres	Hadamard Spheres
28.00	1.389	80.0	20.6	0.013	0.069	0.057
0.82	1.314	76.8	23.9	0.018	0.014	0.012

The tracer bubbles removed from the wire by the shear of the flowing liquid were considerably smaller than those detached by buoyancy force in a stagnant liquid, thus, the rise velocity of the tracers may safely be neglected compared to the liquid velocity measured in this present work.

4.5.2 Liquid flow field close to a bubble

The experimental streamlines around various shaped bubbles were obtained from frame-by-frame analysis of the ciné-films as described in Chapter 2. The streamlines predictions of the theoretical models, described in Section 4.4 were computed using the method outlined in Appendix C.

4.5.2.1 Flow field around a spherical bubble

Fig.4.1 compares the experimentally measured equatorial velocity distribution with the three different theoretical predictions (potential flow, Hadamard-Rybczynski solution for a gas sphere and Stokes solution for a solid sphere) for a spherical gas bubble at Re — 0.087. The greatest difference in the velocity field for the three theories is expected at the bubble interface where the Stokes model predicts zero velocity, the Hadamard-

Dimensionless Distance, x/R

0   1   2   3   4   5   6   7   8   9   10   11

● Experimental Results
— — Stokes Theory
——— Hadamard-Rybczynski Theory
----- Potential Flow Theory

Dimensionless Equatorial Velocity, u_{ee}/U

0.5

1.0

1.5

V (cm³)	R (cm)	U (cm/sec)	μ (Poise)	ϱ (gm/cm³)	σ (dynes/cm)
0.224	0.377	2.313	27.83	1.389	80.0

M (-)	Re (-)	Eö (-)
827.5	0.087	9.68
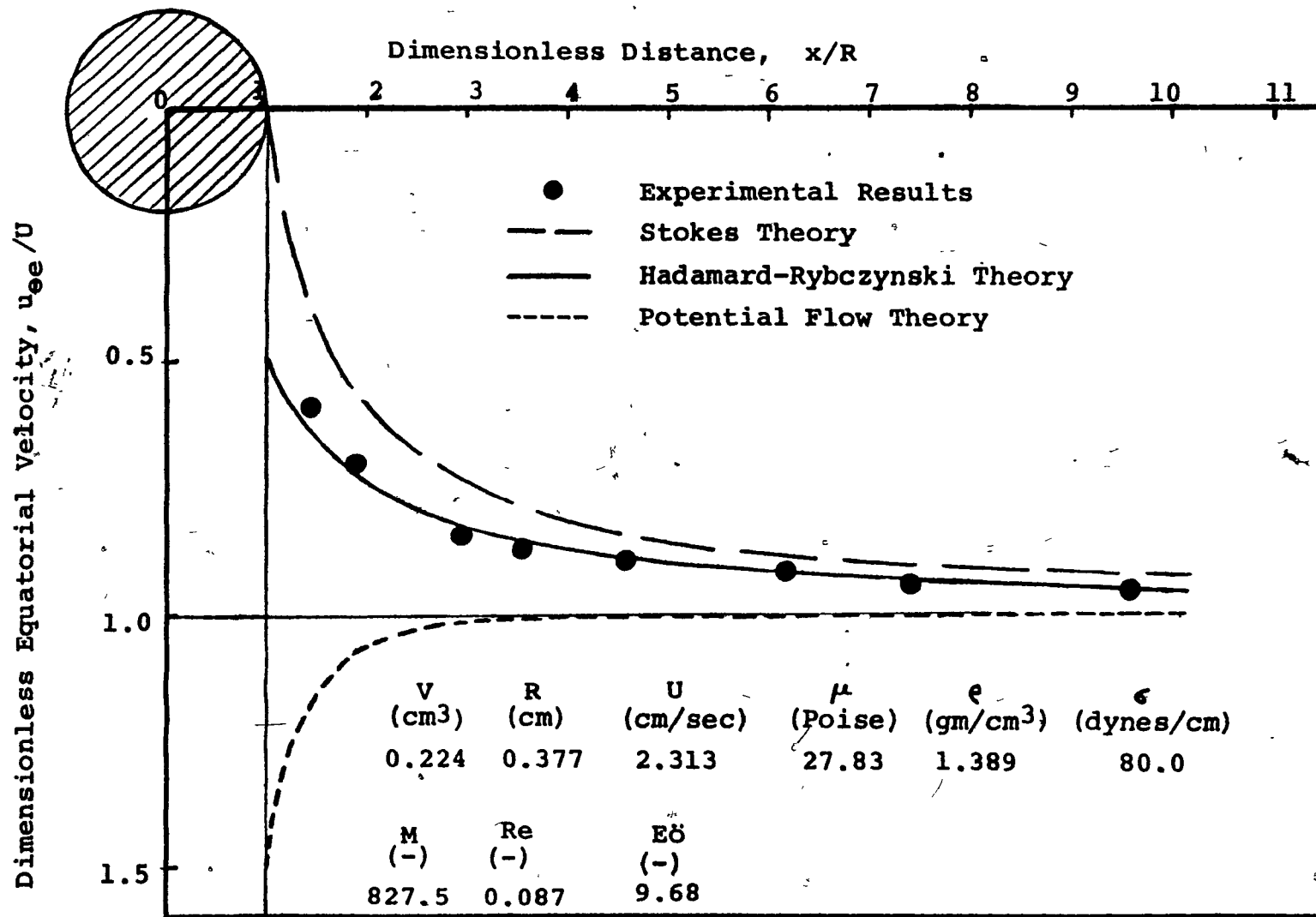
FIGURE 4-1: Comparison of equatorial velocity distribution for a spherical bubble with theoretical predictions.

Rybczynski model predicts a dimensionless equatorial velocity of 0.5 and the potential flow model predicts a value of 1.5. Further, the differences between the predictions of the three models diminish as the distance from the bubble increases. The experimental results are in excellent agreement with Hadamard-Rybczynski theory. The theoretical predictions of the bubble rise velocity is 2.32 cm/sec and 1.54 cm/sec. for the Hadamard-Rybczynski and Stokes models, respectively. The former value agrees very well with the experimental value of 2.31 cm/sec. This experimental run was conducted in a fresh aqeous sugar solution with minimal chance of surface active impurities being picked up by the solution, and this explains why the bubble behaved as a freely circulating sphere.

A comparison of an experimental and theoretical streamline is displayed in Fig.4.2. Each of three theoretical predictions was started from the topmost experimental position. The ticks on the theoretical streamlines indicate the predicted position at the same time interval used in plotting the experimental positions. Again, there is favourable agreement with the Hadamard-Rybczynski model. The combination of the excellent agreement between the measured and the Hadamard-Rybczynski terminal rise velocity plus the excellent agreement between the measured and the predicted streamlines is a convincing proof of the suitability and accuracy of the hydrogen-bubble tracer technique used in this study.

4.5.2.2 Flow field around an oblate ellipsoidal bubble

An experimental streamline close to an oblate bubble is compared with theoretical predictions in Fig.4.3. It clearly demonstrates that for a slightly deformed bubble the deviation from the Hadamard-Rybczynski

1 cm

o Experimental positions at 0.417 sec.
  intervals

✦ Theoretical predictions at 0.417 sec.
  intervals

(experimental conditions as in Fig.4-1)

(a) Potential Flow   (b) Hadamard—Rybczynski   (c) Stokes
        Model   Model   Model
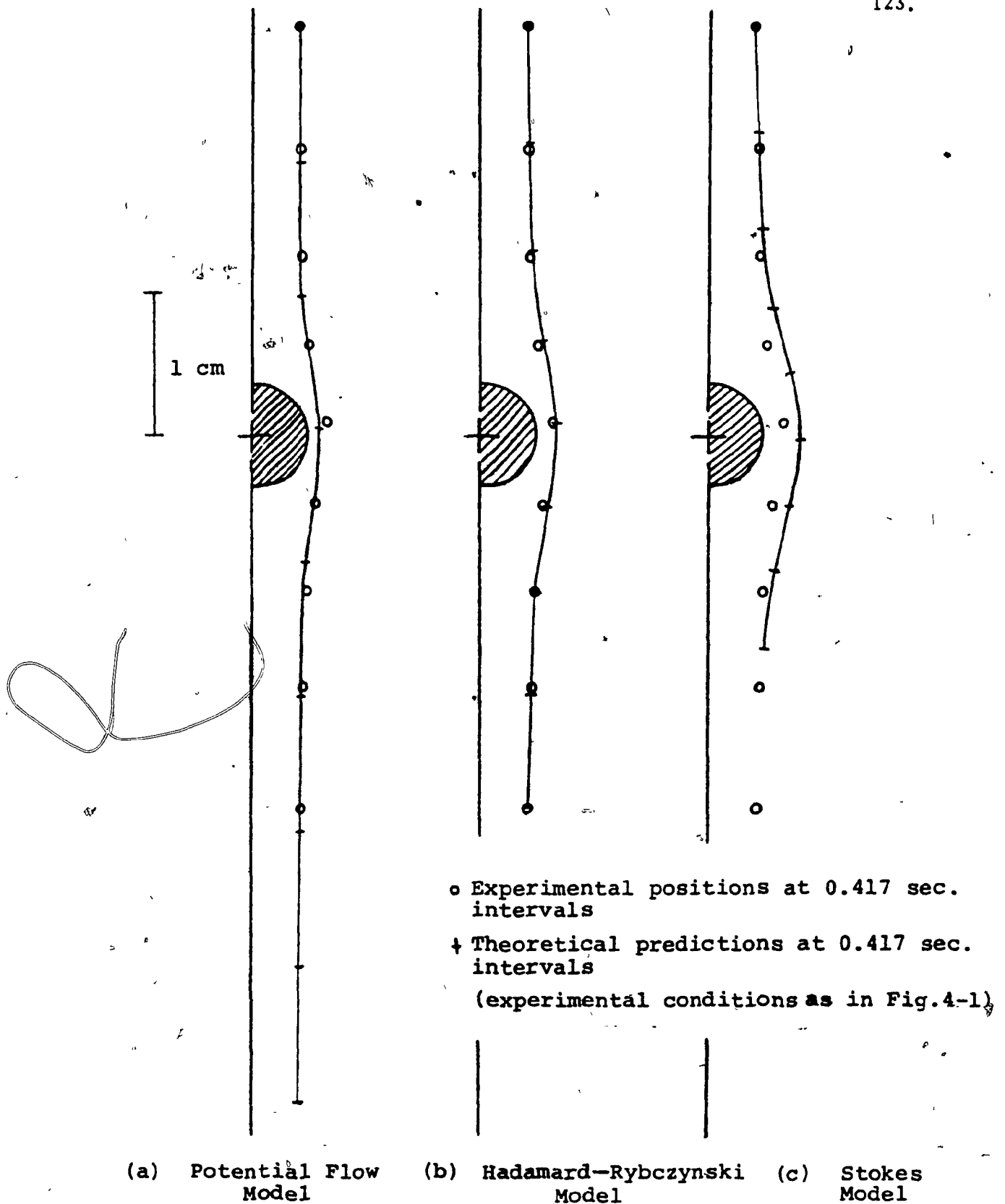
FIGURE 4-2: Comparison of experimental streamline with theoretical

streamline around a spherical bubble.

FIGURE 4.3 Comparison of Experimental Streamline with Theoretical
Streamlines Around an Oblate Ellipsoidal Bubble

O   Experimental - positions at intervals of 0.0417 sec

———+——— Theoretical predictions:

(a) Hadamard-Rybczynski model - assumes creeping flow
     around an equivalent sphere

(b) Taylor-Acrivos Model I - inertia effects taken into
     account with assumption of spherical shape, i.e.
     deformation neglected.

(c) Taylor-Acrivos Model II - assumes creeping flow around
     an oblate ellipsoidal bubble, i.e. inertial effects
     neglected.

Bubble Rise Velocity, cm/sec			
Experimental	Theoretical Predictions		
	(a)	(b)	(c)
5.56	5.89	5.62	5.52

Experimental Conditions:

$V = 0.91$ cm^3
$\mu = 27.83$ Poise
$\rho = 1.389$ g/cm^3
$\sigma = 80$ dynes/cm
$M = 827.5$
$Re = 0.37$
$We = 0.81$
$Eo = 24.90$
$b/a = 0.87$

1 cm

(a)   (b)   (c)
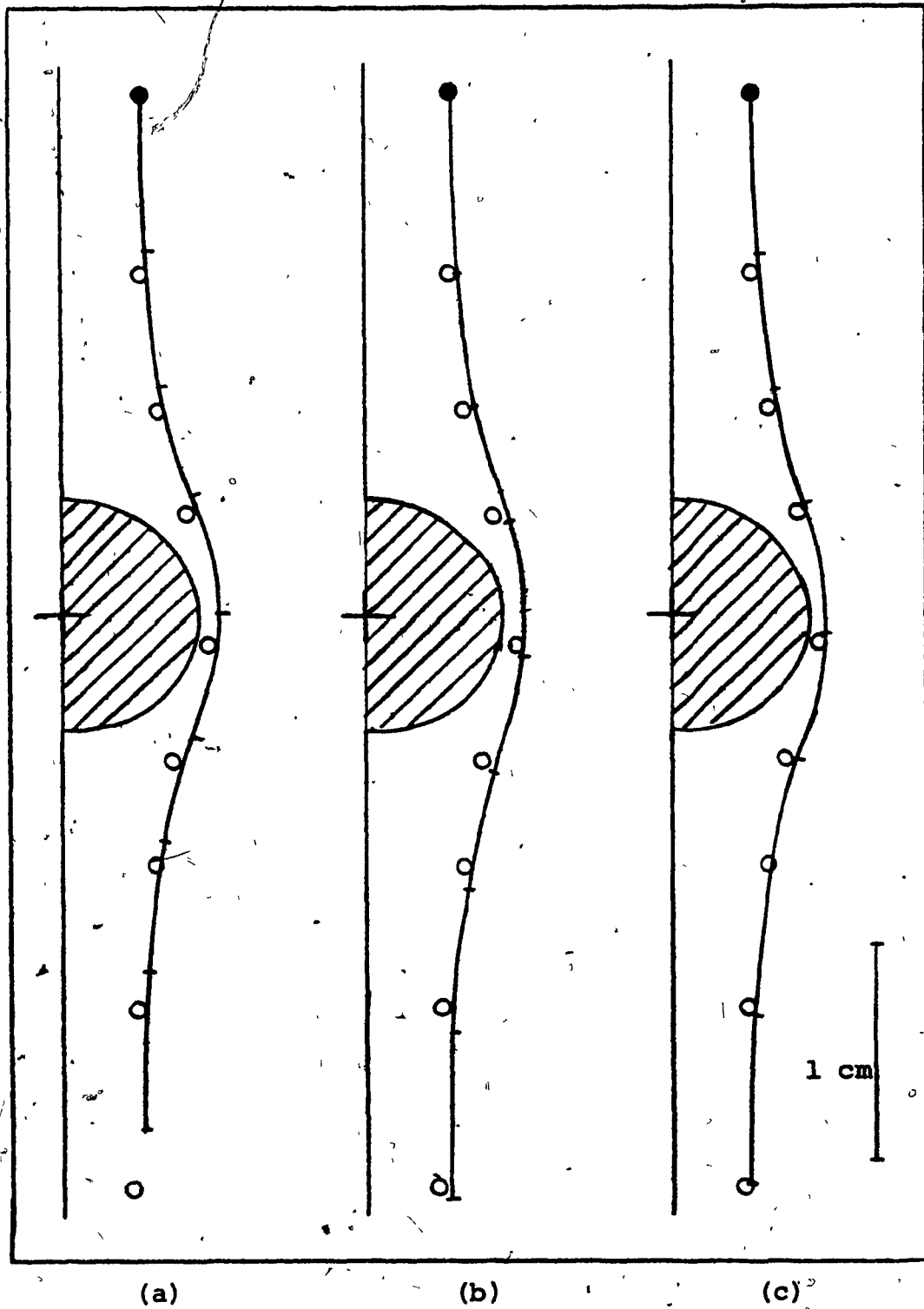
FIGURE 4-3

theory can be explained by the analysis of Taylor and Acrivos (1964).
Their Model II (see Table 4.2) which assumes creeping flow around an
oblate ellipsoidal bubble appears to agree with the data somewhat better
than their Model I which simply takes inertial effects into account while
neglecting the bubble deformation from spherical shape.

Taylor and Acrivos (1964) pointed out that their analysis is
applicable only if the following conditions are met:

(1) the interface be free from surface active impurities

(2) $\frac{Re}{2} < O(1)$

(3) $\frac{We}{2} < O(1)$

(4) $\frac{\mu^2}{\rho R \sigma} \gg 1$

(5) $(\frac{\rho'\mu}{\rho\mu'})\frac{Re}{2} < O(1)$

The experimental run reported in Fig.4.3 satisfied all but the
last condition which requires that Re pertaining to the internal gaseous
phase, i.e., based on gas properties, be small. However, Pan and Acrivos
(1968) extended the Taylor-Acrivos (1964) analysis and demonstrated that
for gas bubbles restriction No.5 can be relaxed because the inertial forces
of the internal circulation do not significantly affect the bubble shape
and the external flow. Therefore, it is concluded that the present data
support the theory of Taylor and Acrivos, within the limits of experimental
error.

4.5.2.3 Description of flow field around bubbles at Re > 1

A. Overall features of the flow field

Typical long-exposure photographs of bubble wakes , taken using
the experimental technique described in Chapter 2, are reproduced in

Figs.4.4 to 4.7 which span the Re range from 12 to 296. In many of the photographs the right-hand portion shows the wake boundary and the position of the vortex ring somewhat better than the left because the probe introduced the tracer bubbles largely in the right-hand half of the wake.

Fig.4.4 illustrates the effect of liquid properties and bubble size on the bubble shape and its wake for Re — 18.2 to 159. The top, the middle and the bottom rows , show bubbles in three different sugar solutions of viscosity 5.00, 3.10 and 1.30 Poise, whereas the left, the middle and the right column show bubbles of three different volumes of 7.0, 9.3 and 27.8 cm^3. All the bubbles except for Fig.4.4(9) are shown at the same magnification to facilitate visual comparison. Note that bubbles No.1 to 8 are at Re < 92 and trail closed, steady, axisymmetric, toroidal wakes while bubble No.9 at Re — 159 has an open, unsteady, asymmetric wake. Eddies or vortices of scale similar to bubble size are observed for the open, unsteady wake while in the turbulent wake observed at much higher Re (of order 10^3 - 10^5) by Wegener et al (1971, 1973) for spherical-cap bubbles in water, the scale of the eddies is much smaller than the bubble.

The development of the wake with increasing bubble size and hence Re in a low viscosity sugar solution is depicted in the series of photographs of Fig.4.5. In Fig.4.5(1) a closed wake trailing an oblate-ellipsoidal-bubble with an aspect ratio (width/height) of 0.25 is illustrated. This almost disc-like shape was observed over a narrow Re range from 42 to 69 in the least viscous solution (μ — 0.84 Poise) investigated in the present work. Bubbles of this type wobbled along their axis of rise, however, the enclosed wakes trailing these bubbles remained attached to the bubbles during the entire rise. The same results were obtained even when the experiments were repeated in the absence of the probe and with

FIGURE 4.4 <u>Effect of Liquid Properties and Bubble Size on the Bubble Shape and Its Wake</u>

	Liquid Properties								
No.	μ (Poise)	ρ (g/cm^3)	σ (dynes/cm)	M	V (cm^3)	U (cm/sec)	Re	Eö	We
1	5.00	1.359	77.7	9.62×10^1	7.0	28.25	18.2	96.2	33.1
2	5.00	1.359	77.7	9.62×10^1	9.3	31.12	22.0	116.5	44.1
3	5.00	1.359	77.7	9.62×10^1	27.8	38.80	39.6	202.4	99.0
4	3.10	1.349	77.6	1.44×10^1	7.0	31.12	32.1	95.6	34.9
5	3.10	1.349	77.6	1.44×10^1	9.3	33.01	37.4	151.8	66.8
6	3.10	1.349	77.6	1.44×10^1	27.8	41.21	67.4	240.9	111.0
7	1.30	1.326	77.3	4.58×10^{-3}	7.0	32.26	77.9	94.5	42.3
8	1.30	1.326	77.3	4.58×10^{-3}	9.3	34.48	91.6	114	53.2
9	1.30	1.326	77.3	4.58×10^{-3}	27.8	43.30	159	238	121

All bubbles shown at magnification of 0.506* except bubble No.9, which is at magnification of 0.316.

*i.e. 1 cm actual corresponds to 0.506 cm on the photograph.
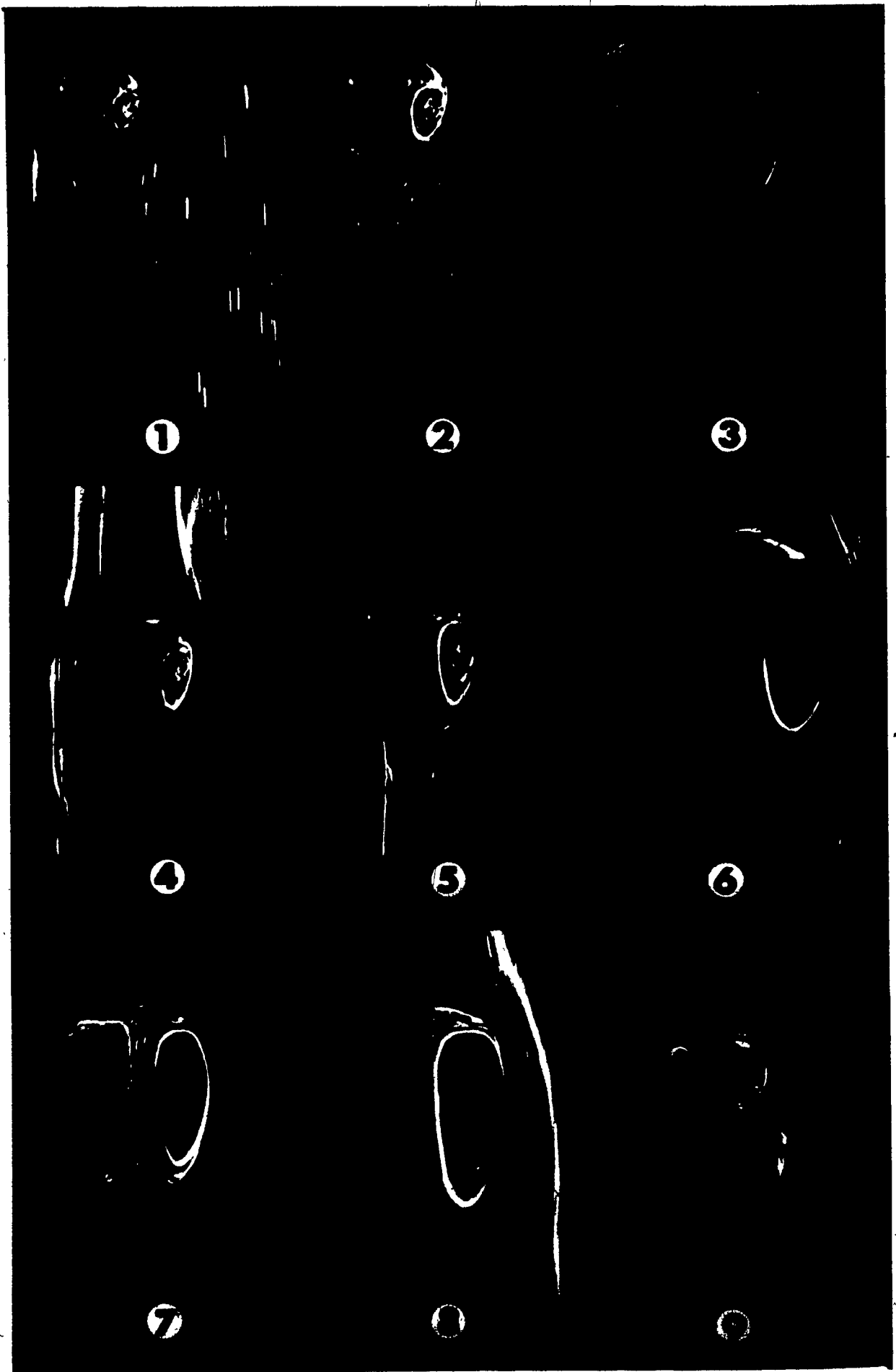
FIGURE 4.5   Wake Development with Increasing Bubble Size
(or Re) in a Low Viscosity Sugar Solution

No.	V (cm^3)	U (cm/sec)	Re	Eö	We
1	0.74	24.14	42.4	21.2	10.3
2*	0.74	24.14	42.4	21.2	10.3
3	2.8	32.00	87.4	51.1	30.6
4	3.7	33.10	99.5	61.9	36.0
5	4.6	33.95	110	71.8	40.8
6**	4.6	33.95	110	71.8	40.8
7	5.6	34.98	120	81.2	46.1
8	27.8	43.93	258	237	124
9	37.2	45.61	296	288	147

*   Same bubble as No.1 but after a rise of 20 cm.

**   Same bubble as No.5 but after a rise of 65.1 cm.

All bubbles shown at magnification of 0.503 except Nos.8 and 9, which are
at magnification of 0.314.

Liquid properties: $\mu = 0.84$ poise
$\rho = 1.315$ g/cm^3
$\sigma = 76.8$ dynes/cm
$M = 8.20 \times 10^{-4}$
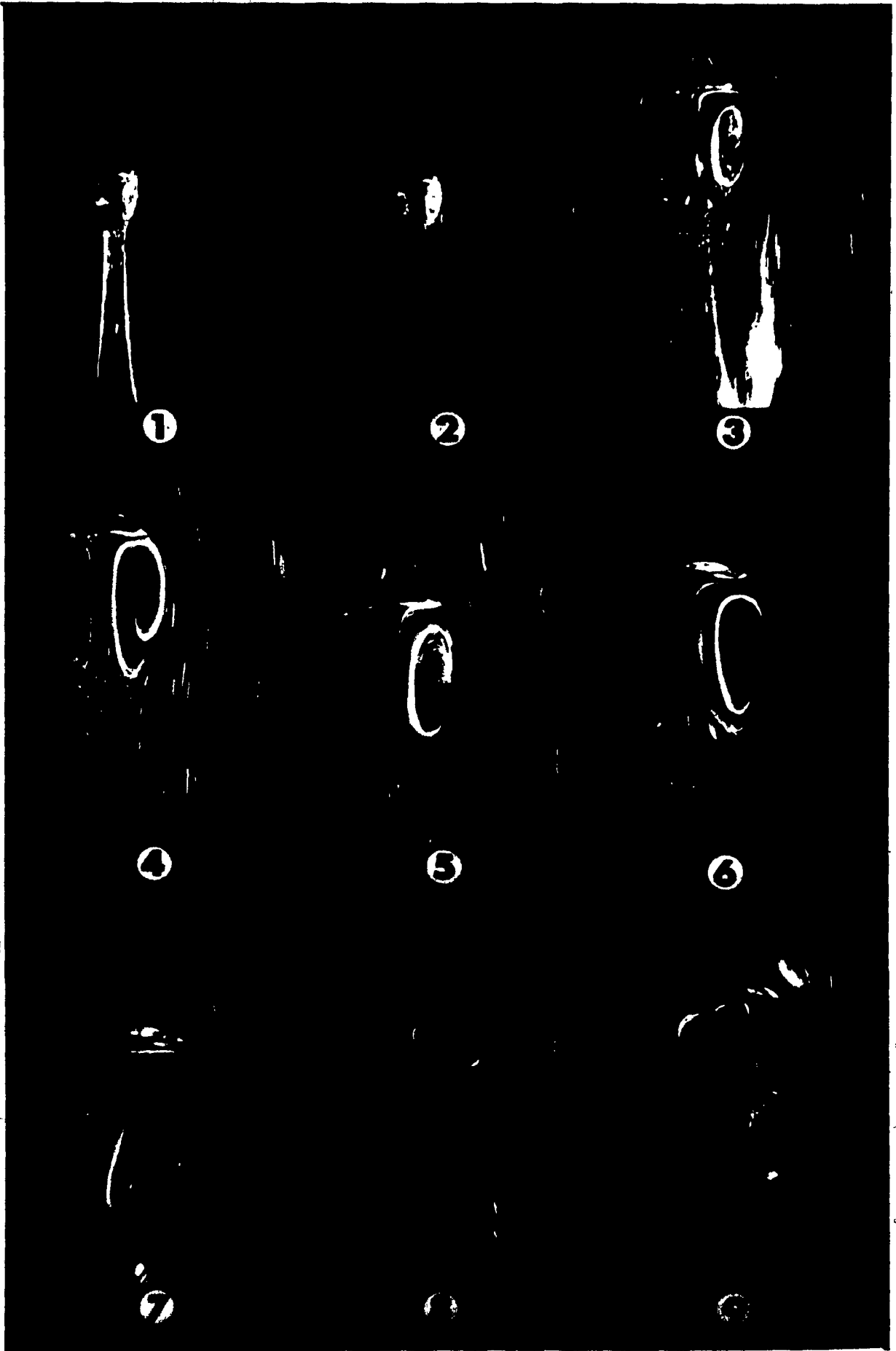
FIGURE 4.6   Different Stages of Unsteady Open
             Wake behind a Spherical Cap Bubble

Experimental conditions: $V = 23.2$ cm^3

$U = 42.22$ cm/sec

$\mu = 1.3$ poise

$\rho = 1.315$ g/cm^3

$\sigma = 76.8$ dynes/cm·

$M = 4.58 \times 10^{-3}$

Re $= 146$

Eö $= 210$

We $= 108$

Photographs taken at intervals of 0.0417 sec. with

moving camera at shutter speed of 1/33 sec.

All photographs shown at magnification of 0.235.
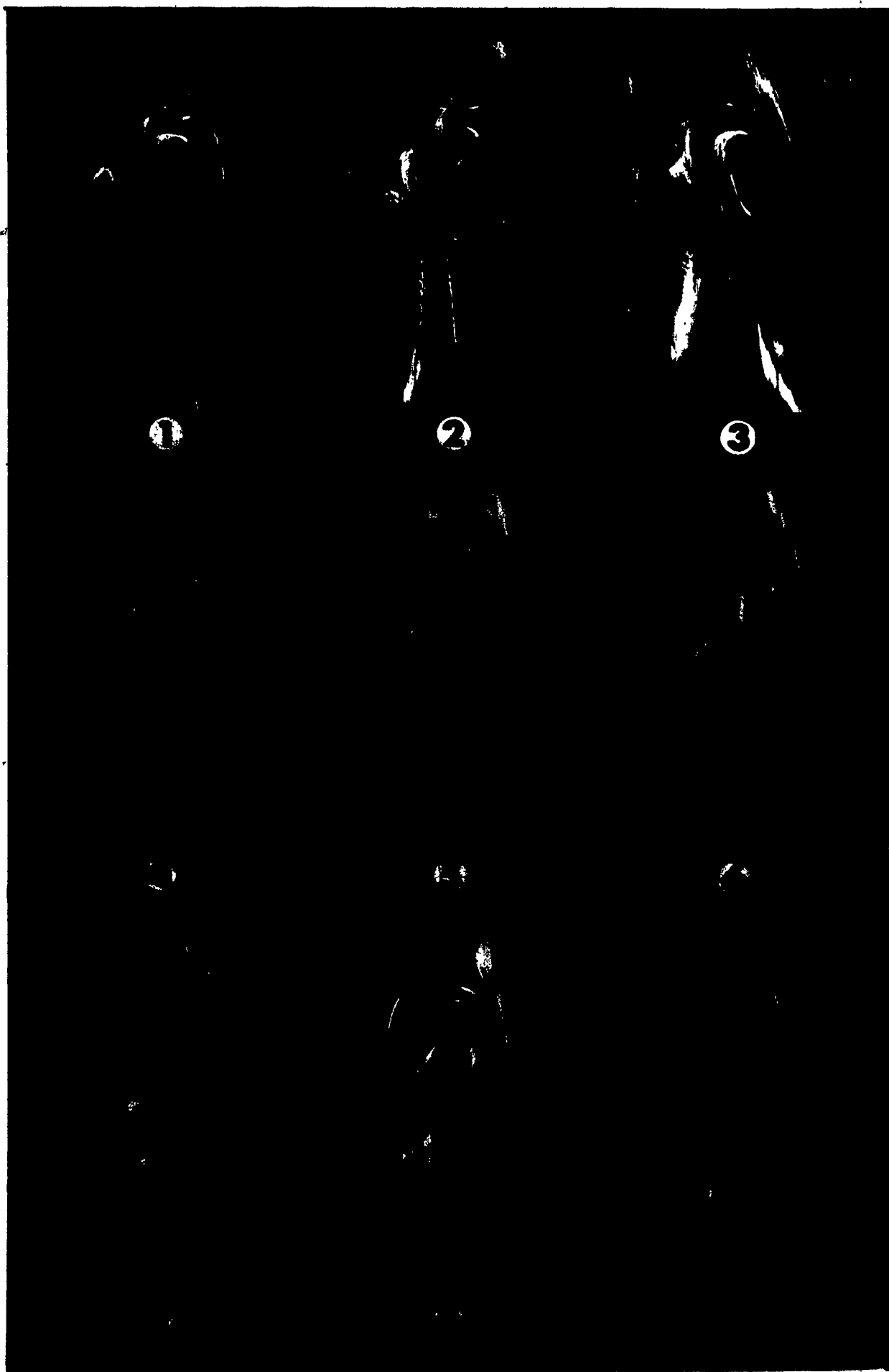
FIGURE 4.7 Wakes Behind Oblate Ellipsóidal
Cap and Skirted Bubbles

No.	Liquid Properties			M	V (cm^3)	U (cm/sec)	Re	Eö	We
	μ (poise)	ρ (g/cm^3)	σ dynes/cm						
1*	20.80	1.390	80.0	2.58×10^2	55.6	38.65	12.2	382	123
2*	20.80	1.390	80.0	2.58×10^2	61.2	39.78	13.0	407	134
3	13.44	1.387	79.8	4.54×10	36.1	36.91	15.6	287	97
4	11.71	1.385	79.3	2.67×10	37.0	40.32	22.1	292	117
5**	11.71	1.385	79.3	2.67×10	37.0	40.32	22.1	292	117
6	13.44	1.387	79.8	4.54×10	37.0	37.55	16.0	292	101
7	10.30	1.382	79.3	1.60×10	33.3	38.04	20.4	275	101
8	10.30	1.382	79.3	1.60×10	42.2	41.24	23.9	319	128
9	7.4	1.370	78.7	4.41	27.80	37.29	26.0	241	91

*   Slight wall effects may have been present for these bubbles.

** Same bubble as No.4 but after a rise of about 40 cm. where a skirt
    had developed.

Note: Bubbles are shown at different magnifications. All photographs
       taken with a Nikon camera at shutter speed of 1/15 or 1/2
       sec. except No.1, 2 and 9 which were taken with a 16 mm Bolex
       camera. The camera was kept stationary only in the case of
       bubble No.6.
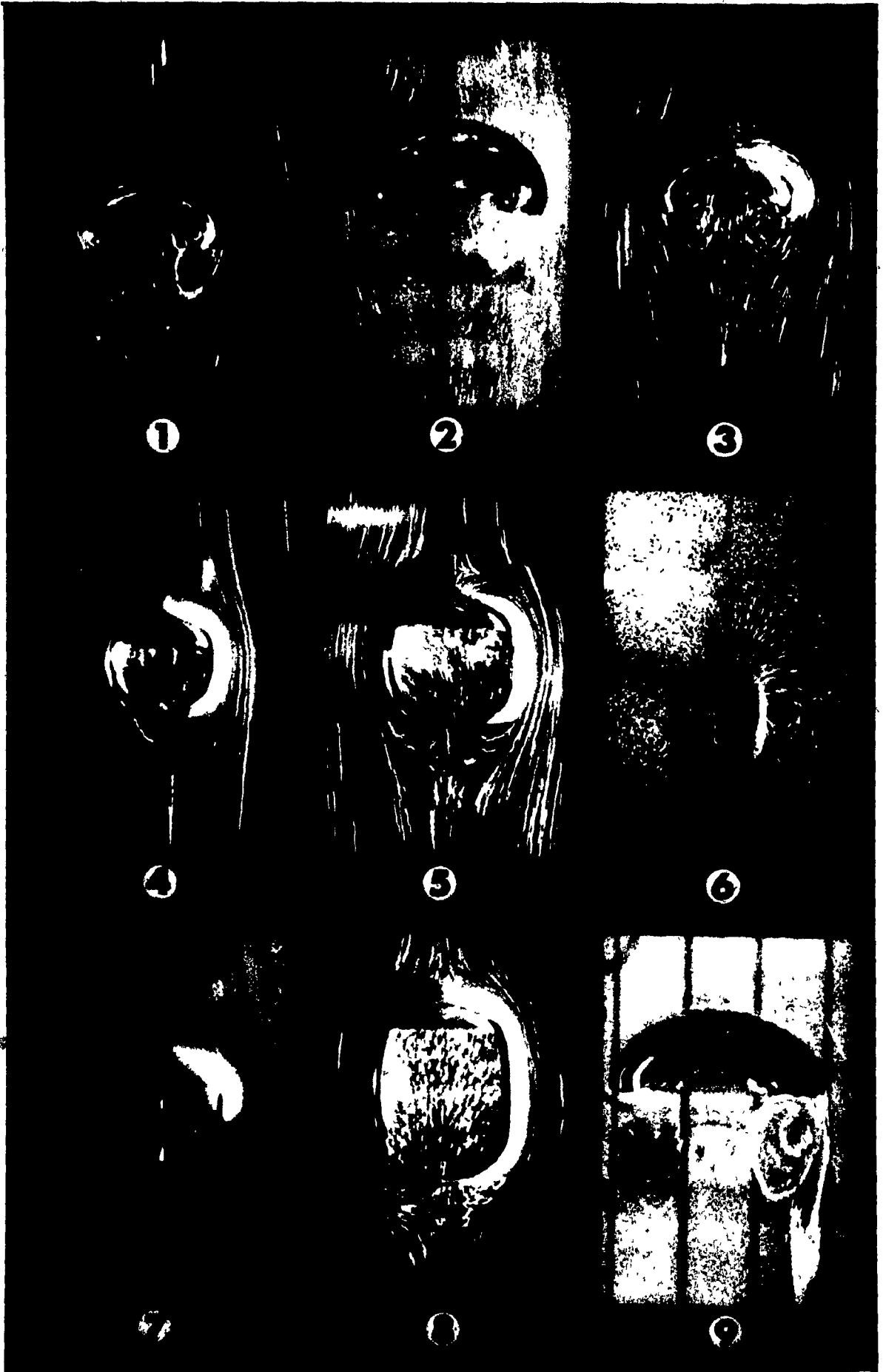
very long time lapse between successive experiments for the residual disturbance in the field liquid to die out. Jones (1965) also observed similar wobbling motion for disc-like bubbles in liquids of similar physical properties although he did not observe the wake behind such bubbles in his experiments. Since the wakes remained attached to the bubbles throughout their rise, the wobbling motion of their bubbles cannot be attributed to vortex shedding phenomena. It should be emphasized that at higher Re (but less than about 110) in the same solution bubbles adopt spherical-cap shapes, rise rectilinearly without wobbling and trail a closed toroidal wake (see Fig.4.5(3), (4) and (5)).

Another noteworthy point is that when a bubble passes by the row of tracer bubbles generated at the probe, the line of tracers is stretched out to indicate the familiar drift* of the surrounding liquid (see Fig.4.23) caused by the passage of the bubble. The widening tail (or two tails) behind the enclosed wake seen in Fig.4.5(1) is part of this drift. It gives the impression that the wake may be spilling out, however, this is not the case as can be seen from Fig.4.5(2) which shows that the trail has disappeared after the bubble has travelled about 20 cm.

With increasing Re, the closed wake grows in both the transverse and the streamwise directions until Re ≈ 110 when the onset of instability in the wake is observed. Figs.4.5(5) and 4.5(6) represent such a situation. Both figures show the same bubble observed at a time lapse of 1.918 sec. during which the bubble had risen 65.1 cm. Note that the wake symmetry observed in Fig.4.5(5) is destroyed in Fig.4.5(6) as the instability

---

*. See the footnote on page 200.

sets in. Further increase in Re results in periodic shedding of vortices which causes the bubble to wobble and its base to oscillate (see Fig.4.5(7) to (9)).

The different stages of a typical unsteady open wake behind a spherical cap bubble (Re - 146) at intervals of 0.0417 sec. are presented in Fig.4.6. The difference between the unsteady and open nature of the wake as compared to a closed laminar wake is quite striking. Although the bubble wobbles around its axis of rise in harmony with the shedding of the vortices, its rise is always rectilinear as indicated from the position of the bubble nose which is always in line with the vertical scale in the photographs.

The nature of the wake behind oblate-ellipsoidal-cap and behind skirted bubbles is illustrated in Fig.4.7 for Re - 12 to 26. The indentation of the bubble base can clearly be seen in Fig.4.7(1) and (2) where the part of the tracer bubble motion is obscured by the indentation and instead a reflection of the streamline is observed on the indented surface. Fig.4.7(3) shows a bubble with a volume just too small to have a skirt while Fig.4.7(4) shows a bubble just large enough for a skirt to exist. The wake of a skirted bubble at Re $\approx$ 21 observed with a moving camera and with a stationary camera is presented in Fig.4.7(5) and 4.7(6), respectively. The presence of a circulating eddy in the wake enclosed by the skirt is obvious in Fig.4.7(5). Ciné-film of this experiment clearly showed that the liquid in the wake contained within the skirt is not stagnant but moves as a toroidal vortex. Fig.4.7(5) shows that some of the circulation occurs outside the skirt with a single toroidal vortex partly inside and partly outside the skirt. The circulation rate of the vortex was observed to be somewhat slower than that observed in the absence

of the skirt for a slightly smaller bubble volume. This is not surprising since the rate of momentum transport from the external liquid to the enclosed wake is expected to be lowered by the presence of the surrounding skirt. Close inspection of Fig.4.7(6) reveals that the induced motion of liquid behind the bubble is significantly greater than ahead of it. Fig.4.7(7) shows an example of a poor photograph that can result due to use of a rather wide sheet of light that shows excessive three-dimensional effects. A wake protected by a fairly long skirt is displayed in Fig.4.7(8) which suggests that the centre of the vortex is shifted towards the end of the skirt as the skirt lengthens. This implies considerable slowing down of the liquid enclosed by the skirt. Finally, the wake behind a bubble which is almost an oblate semi-ellipsoid is shown in Fig.4.7(9).

B. Detailed experimental streamlines

The experimental streamlines describing the detailed motion of liquid around the different shapes of bubbles for Re = 2.5 to 293 are presented in the series of tracings in Figs.4.8 to 4.12. A legend which is common to all of these figures is explained in Table 4.8.

The change in the bubble shape and the corresponding change in the flow field with the variation of liquid properties is shown in Figs.4.8(a) to (g) for a 9.3 cm^3 bubble in seven different sugar solutions. Similar changes for a 27.8 cm^3 bubble in four different solutions are presented in Fig.4.9(a) to (d).

The variation in bubble shapes and the surrounding liquid flow field with the change in bubble volumes is illustrated in Figs.4.10(a) to (e), Figs.4.11(a) to (f) and Figs.4.12(a) to (d) for three different sugar solutions of viscosity 20.84, 7.81 and 1.30 Poise.

TABLE 4.8   Legend for Figures 4.8 to 4.12

●   starting position of tracer particle

o   position of tracer bubble at every frame

●   position of tracer bubble at every 5th frame*

⊕   vortex centre,and wake stagnation point

+   centre of a sphere or an ellipsoid that fits the
    bubble cap

—⊥—·——·—   boundary of a sphere or an ellipsoid that fits the
    bubble cap

—— —— —   boundary of closed toroidal wake

————————— indentation of bubble base

Note: For streamlines in the closed-wake smaller symbols are used and
        for some streamlines, tracer positions only at every 5th frame
        are shown to preserve clarity.

*   Figure 4.8(g) is an exception where the shaded circles represent
    another set of streamlines from the same experimental run but 1 sec.
    later.

Direction of flow of liquid with respect to the bubble is shown below:
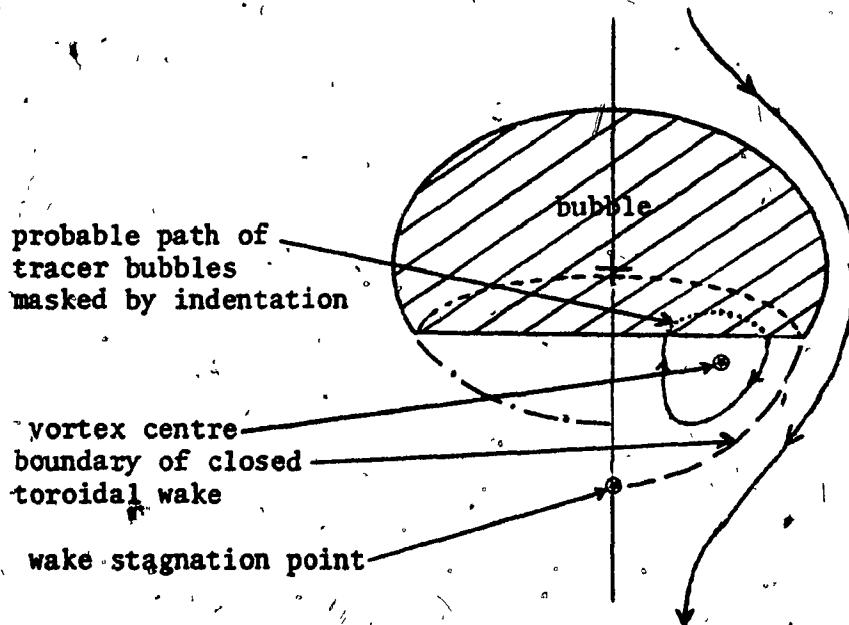
FIGURE 4.8 Effect of Liquid Properties on Bubble Shape and Flow Field

Bubble Volume = 9.3 cm^3; d_e = 2.61 cm.

No.	Liquid Properties			M	U cm/sec	Re	Eö	We	S frame/sec	shape*
	μ (poise)	ρ (g/cm^3)	σ (dynes/cm)							
a	28.00	1.389	80.0	8.48×10^3	19.10	2.47	116	17.3	35.00	OEC
b	13.00	1.378	79.1	4.11×10^4	25.92	7.16	116	36.0	35.67	OEC
c	7.81	1.370	78.5	5.51	29.15	13.3	116	48.4	35.00	OEC
d	5.42	1.361	78.0	1.31	31.15	20.4	116	61.2	35.67	OEC
e	2.85	1.346	77.6	1.03×10^{-1}	34.28	42.2	116	89.3	34.38	OEC
f	1.30	1.326	77.0	4.63×10^{-3}	35.33	94.0	115	130	33.60	SCC
g	0.85	1.314	76.8	8.60×10^{-4}	37.55	151	114	170	34.67	SCO

For legend see Table 4.8.

All bubbles shown at same magnification.

* OEC - oblate ellipsoidal cap
  SCC - spherical cap with closed toroidal wake
  SCO - spherical cap with open unsteady wake

1 cm.

Re = 2.47

FIGURE 4.8(a)

1 CM.

Re — 7.16

FIGURE 4.8(b)

1 cm.

Re = 13.3

FIGURE 4.8(c)

139.

1 cm.

Re — 20.4

FIGURE 4.8(d)

1 cm.

centre of
ellipsoid

centre of
sphere

Re = 42.2

FIGURE 4.8(e)

1 cm.

Re = 94.0

FIGURE 4.8(f)

142.

1 cm.

Re — 151
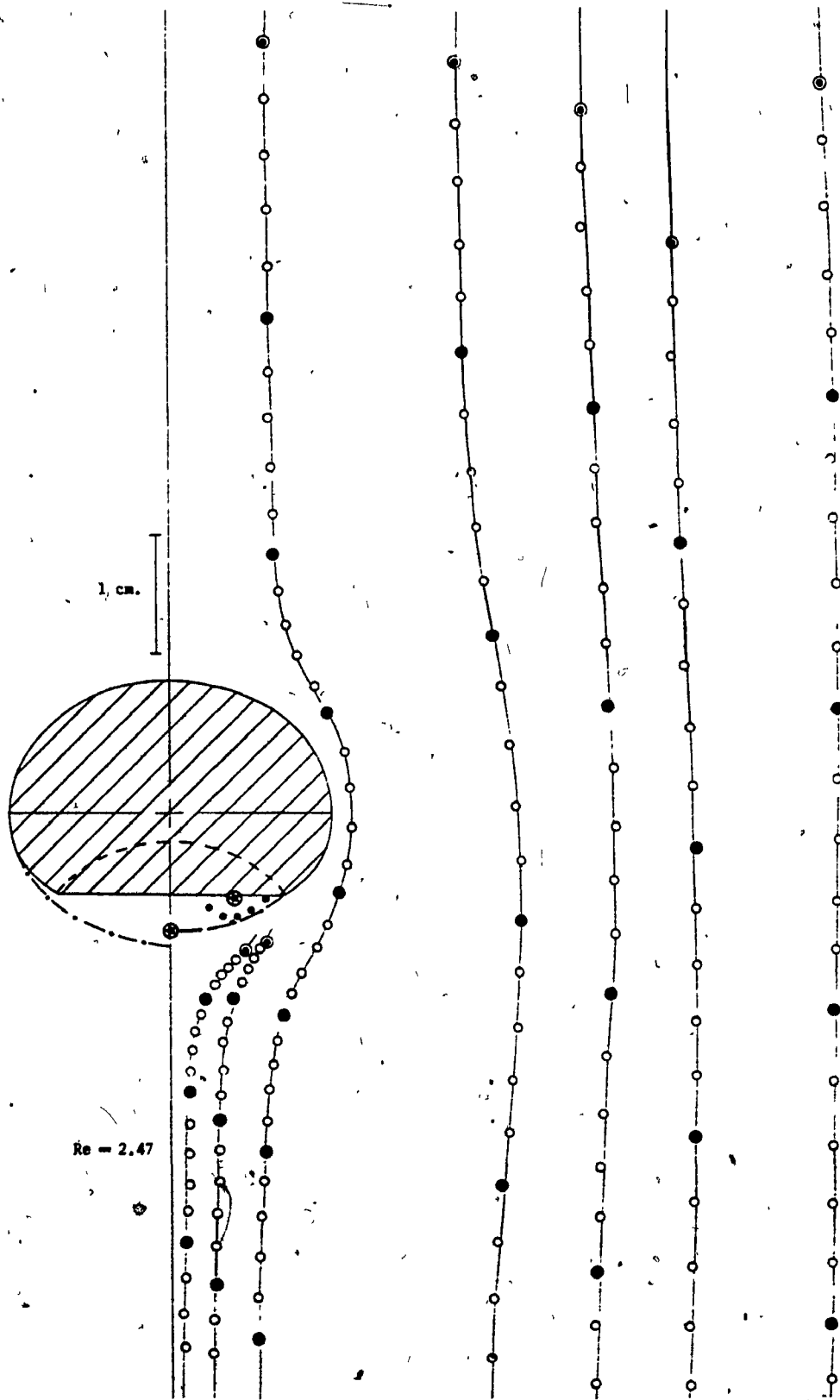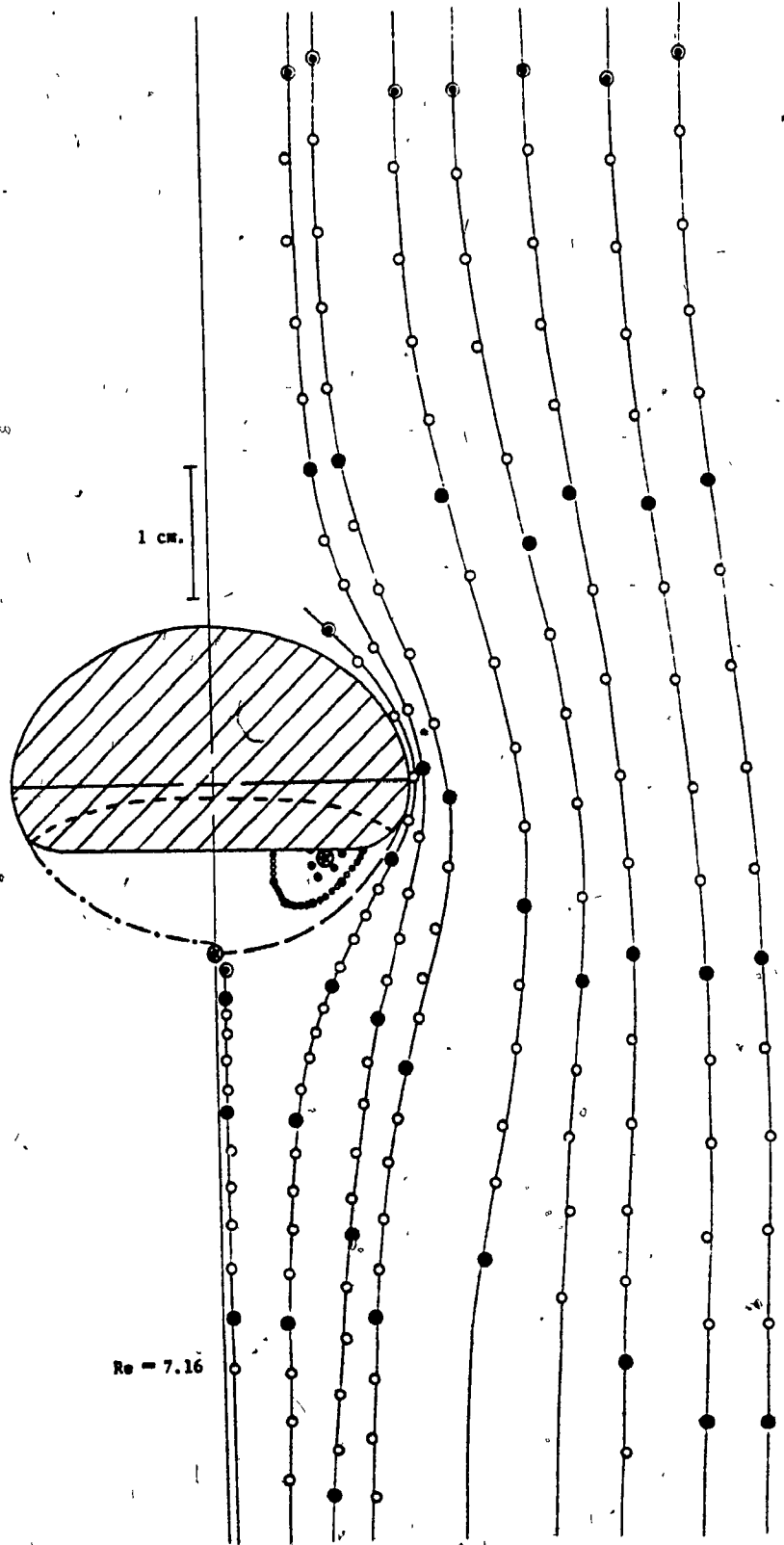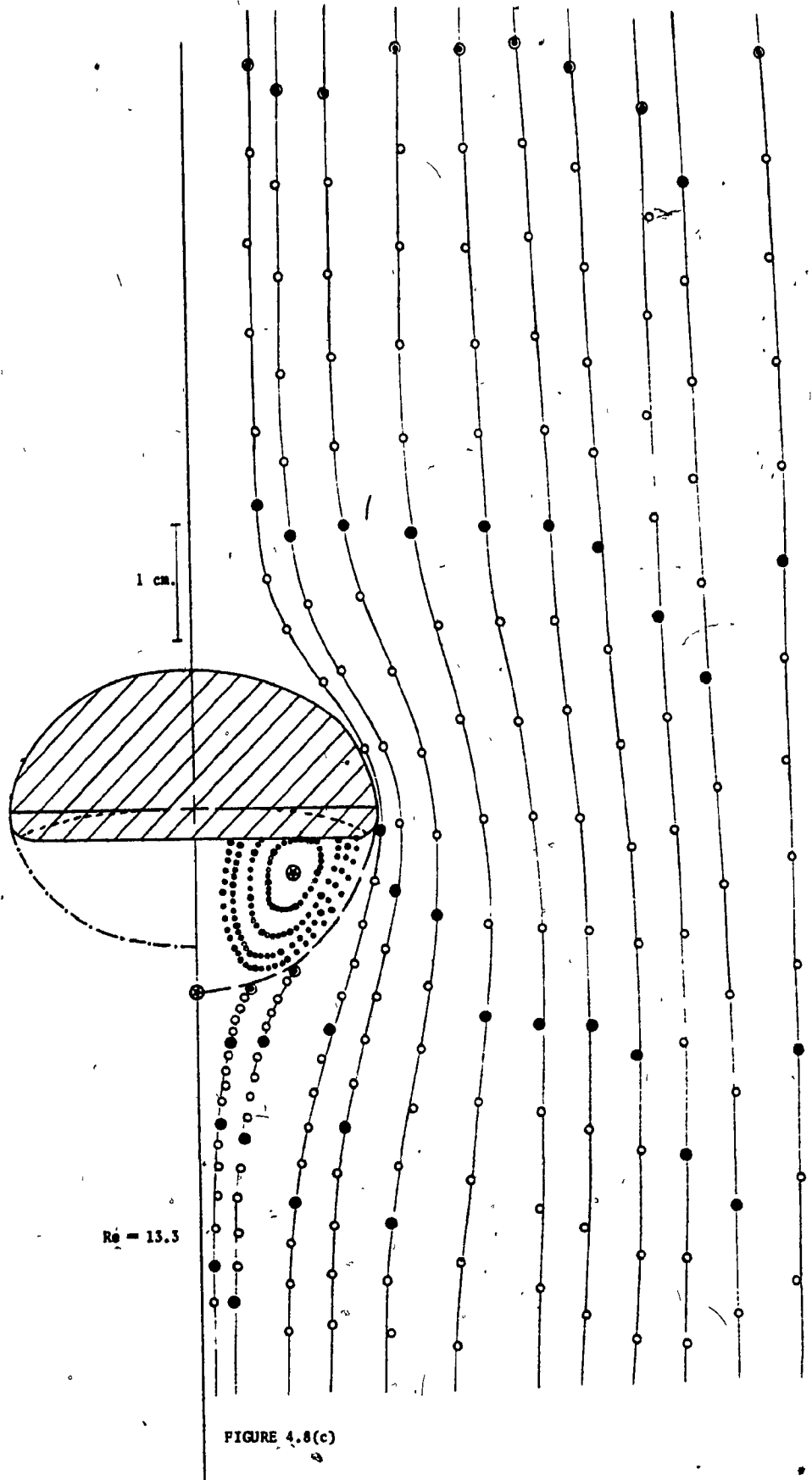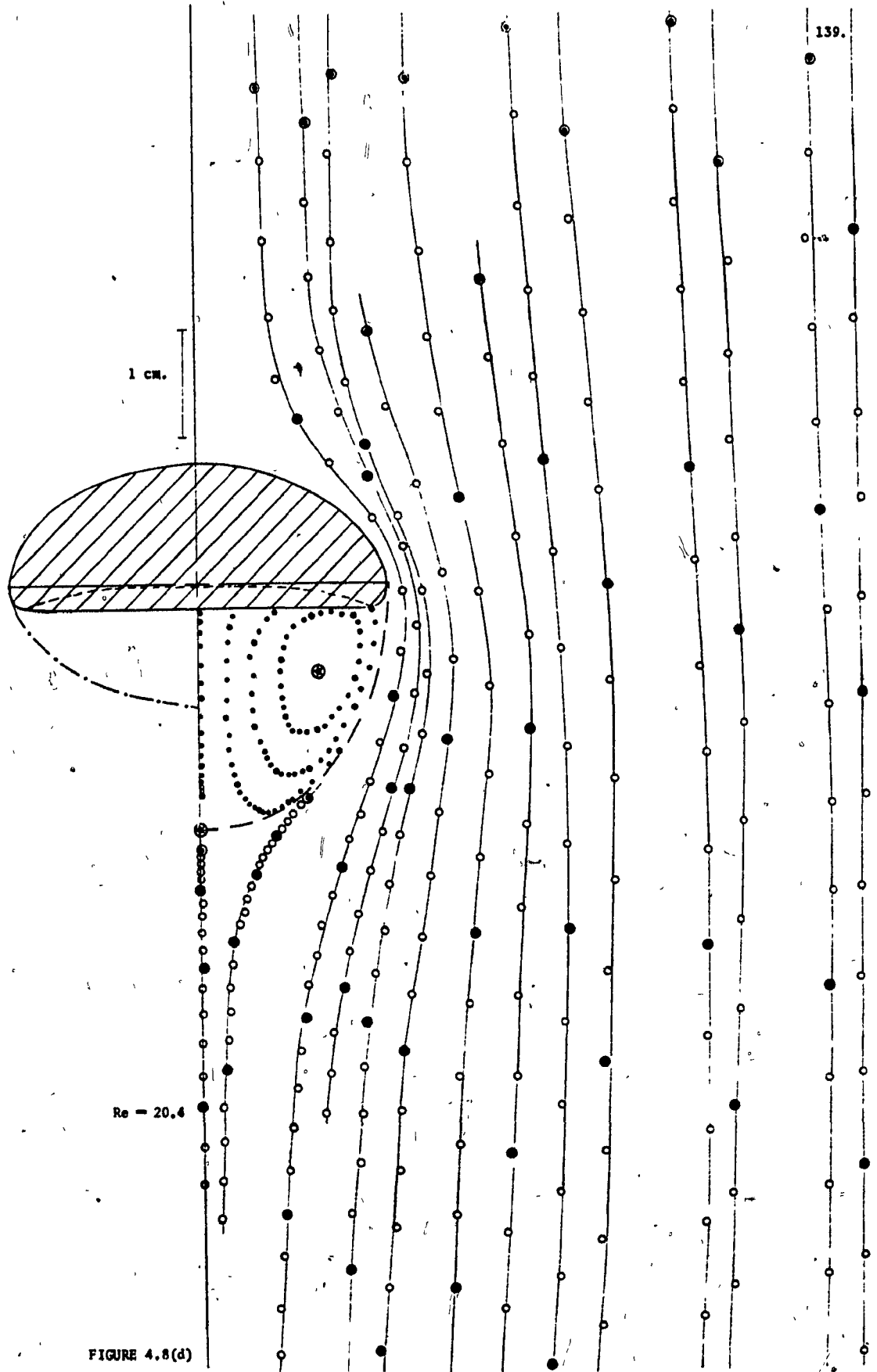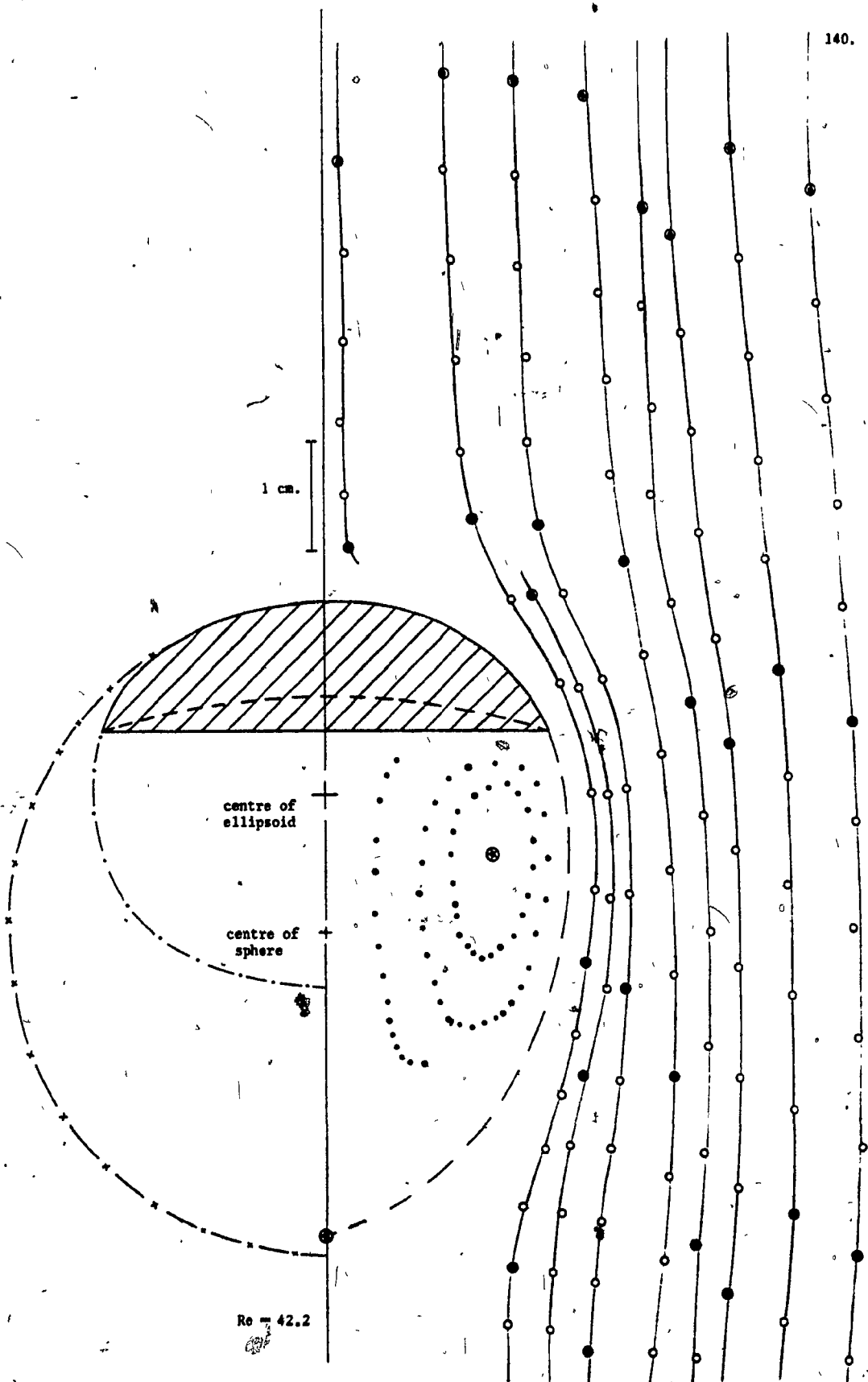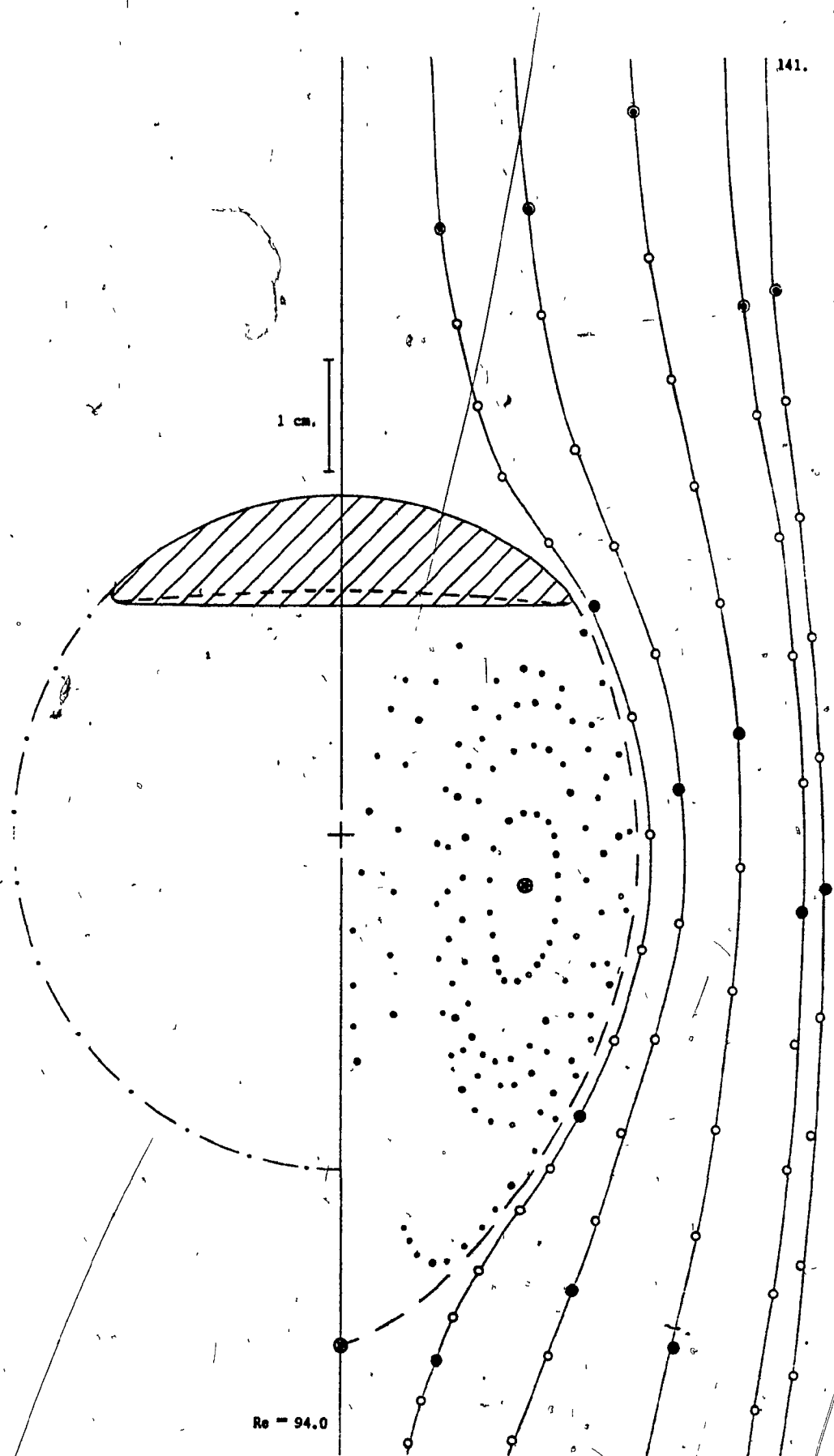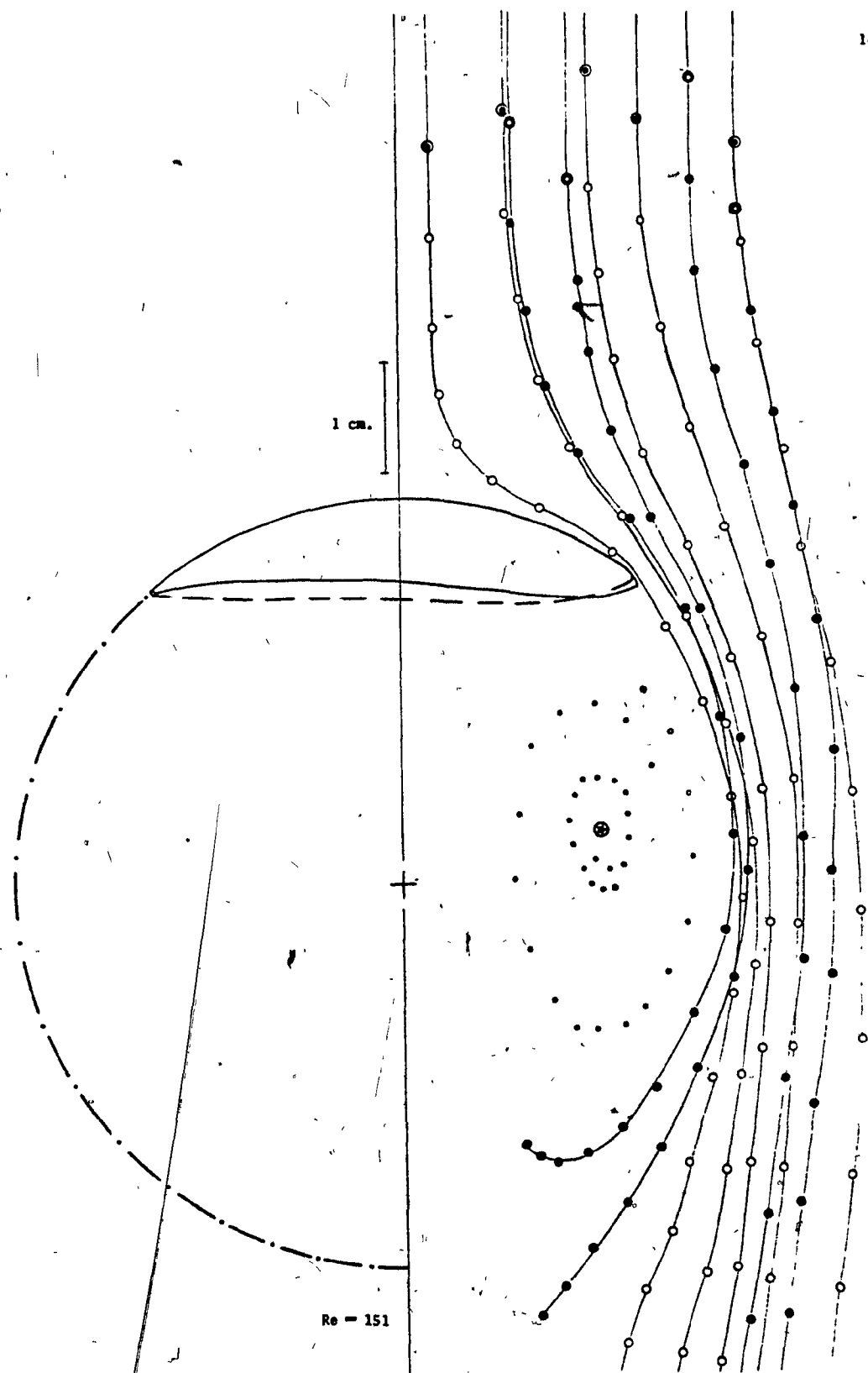
FIGURE 4.8(g)

FIGURE 4.9 Effect of Liquid Properties on Bubble Shape and Flow Field

Bubble Volume = 27.8 cm^3; d_e = 3.76 cm

No.	Liquid Properties			M	U cm/sec	Re	Bo	We	S frame/sec	shape*
	μ (poise)	ρ (g/cm^3)	σ (dynes/cm)							
a	13.70	1.378	79.1	5.07x10	34.24	12.9	241	103	34.00	OEC
b	7.81	1.570	78.5	5.51	37.34	24.6	242	134	35.00	OEC
c	5.42	1.361	78.0	1.31	39.18	37.0	242	159	35.67	OEC
d	0.82	1.315	76.9	7.40x10^{-4}	43.93	265	237	276	35.00	SCO

For legend see Table 4.8.

All bubbles shown at same magnification, except (d).

* OEC - oblate ellipsoidal cap
  SCO - spherical cap with open unsteady wake

144.

1 cm.

Re = 12.6

FIGURE 4.9(a)

1 cm.

Re = 24.6

FIGURE 4.9(b)

1 cm.

146,

Re = 37.0

FIGURE 4.9(c)

1 cm.

Re = 265
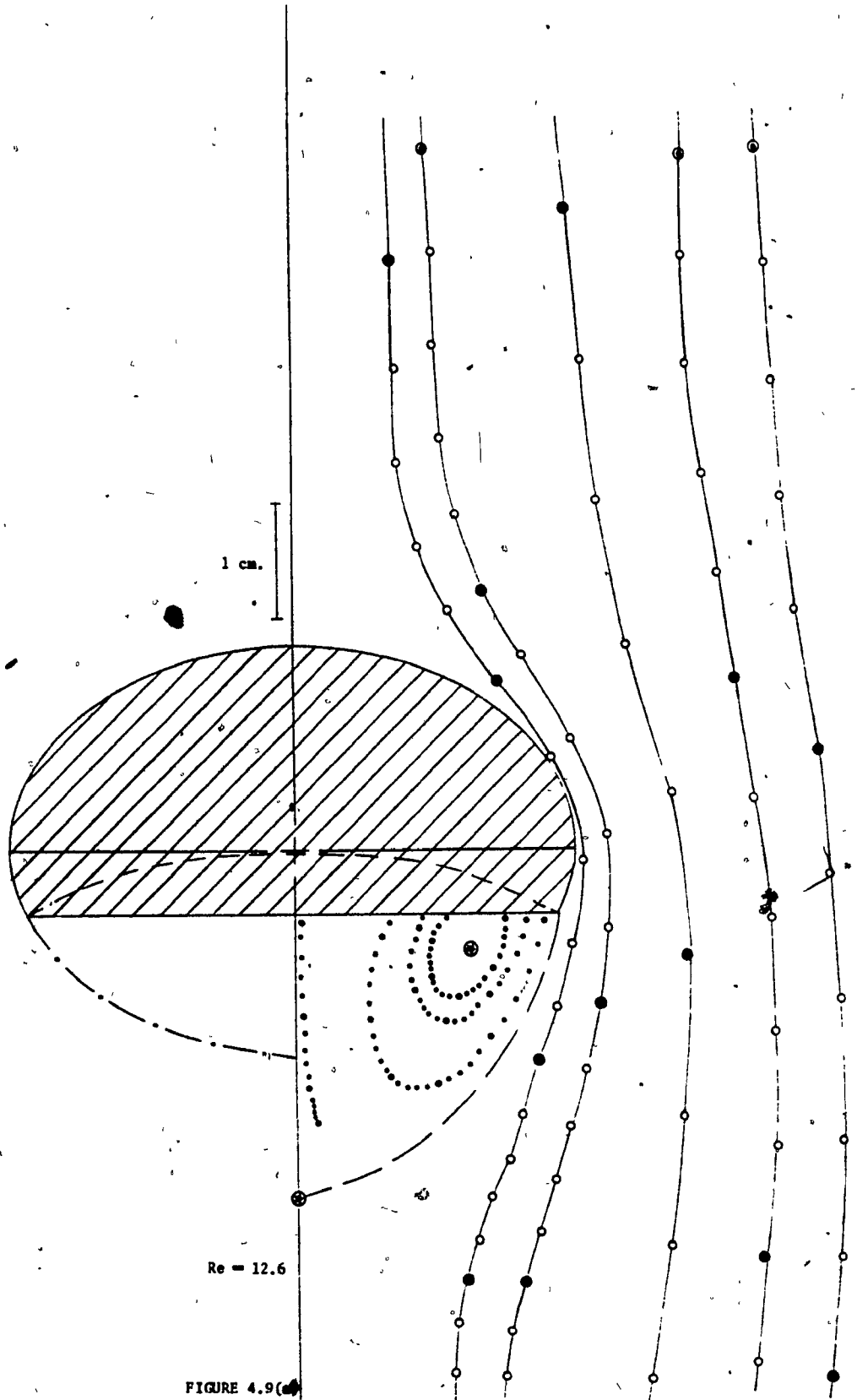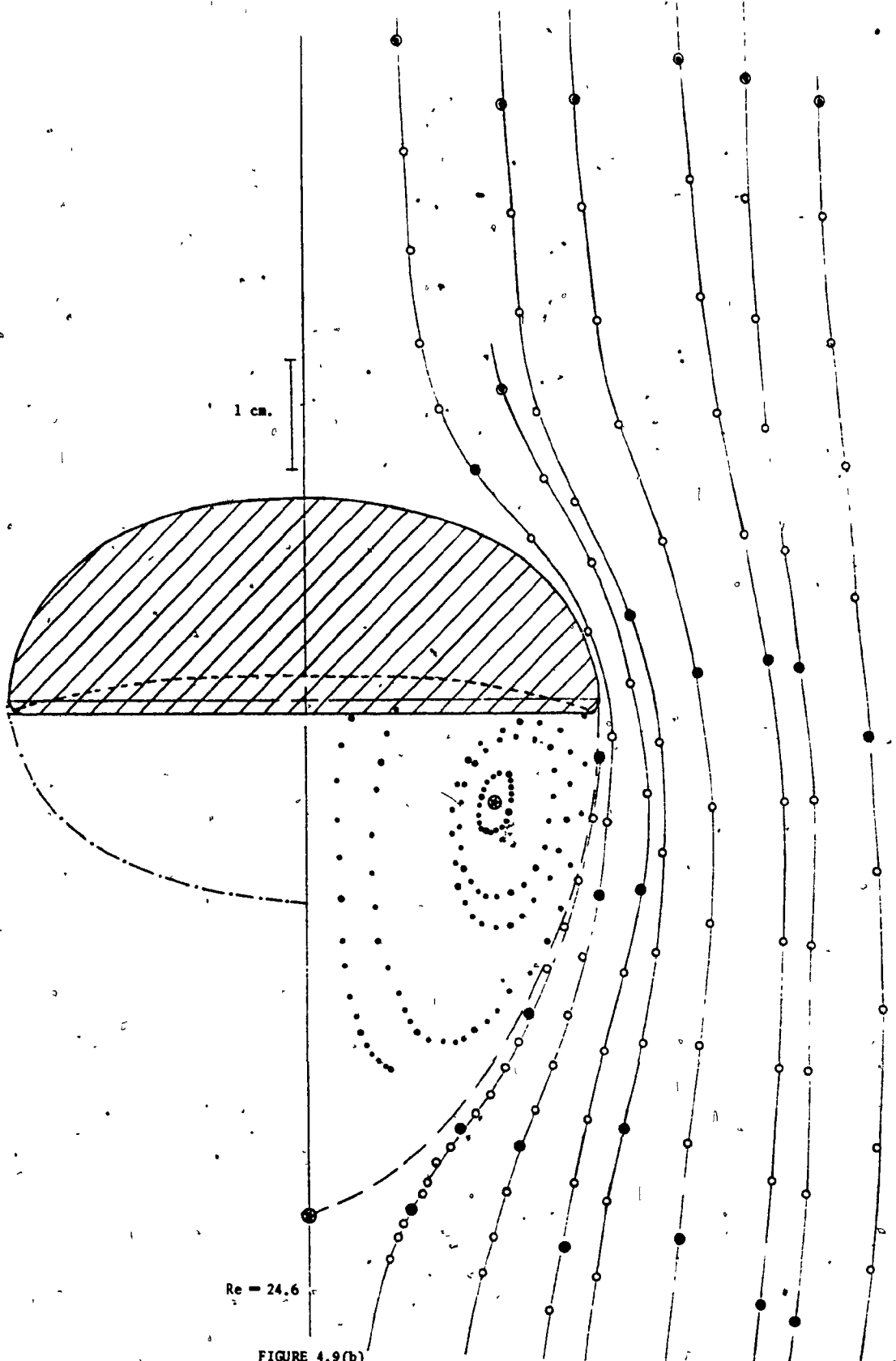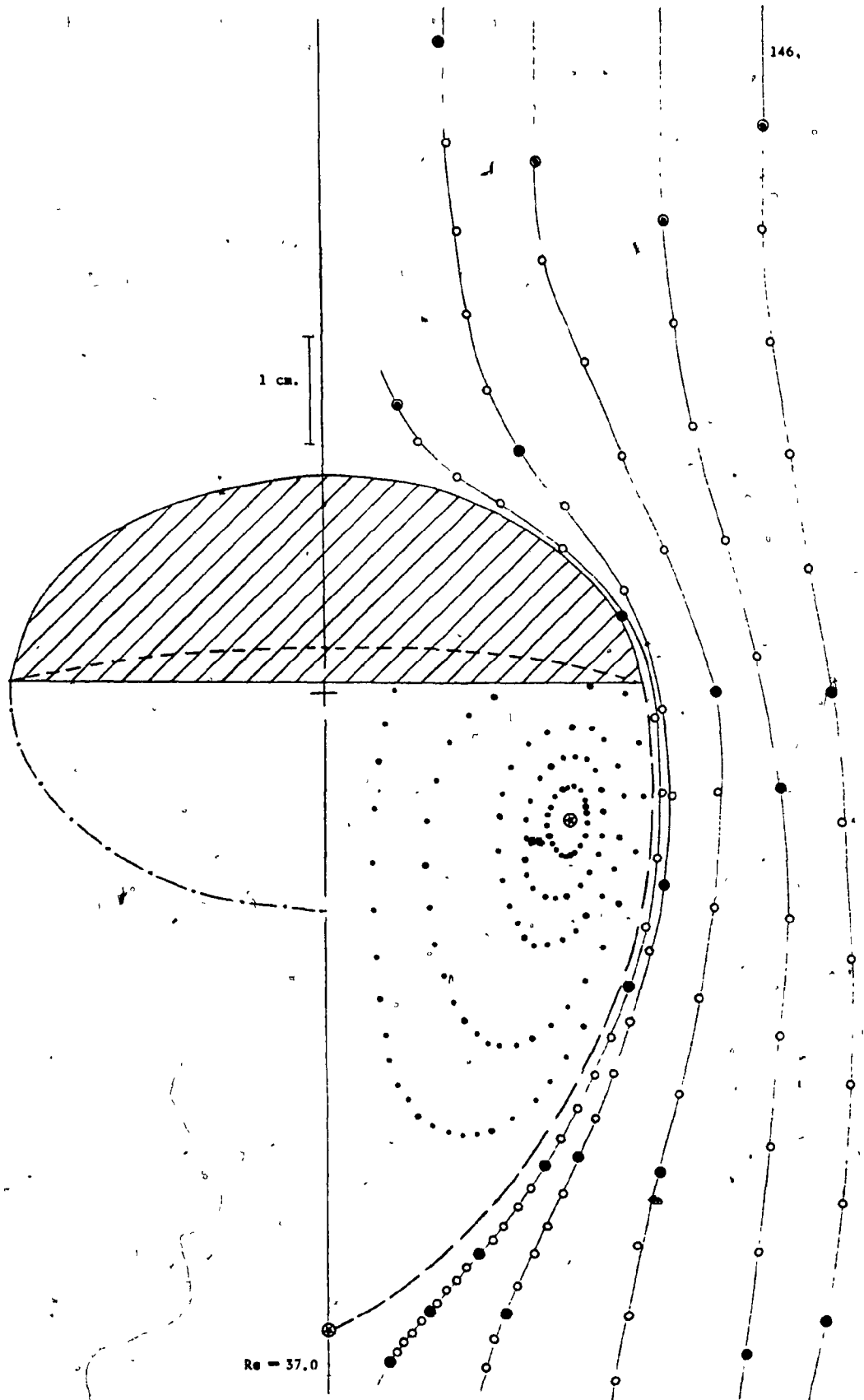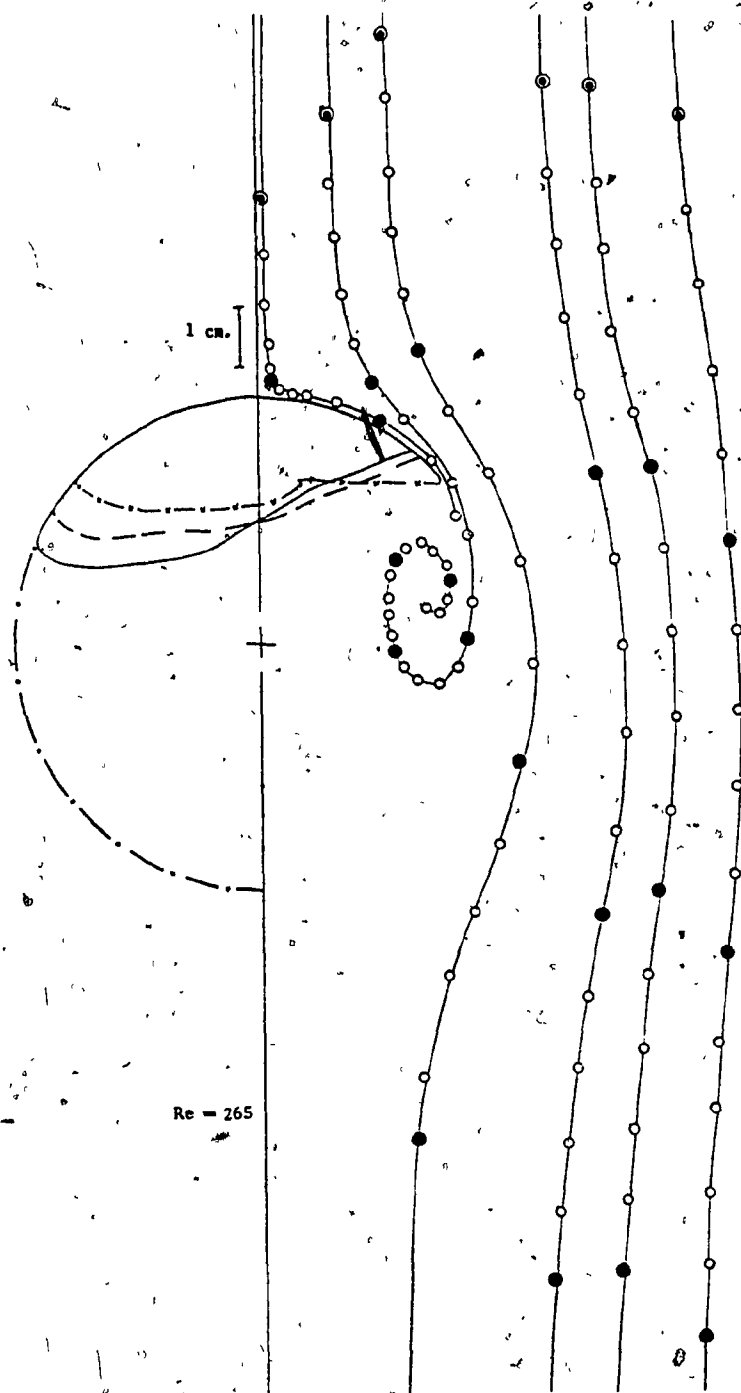
FIGURE 4.9(d)

FIGURE 4.10 Variation of Bubble Shape and Flow Field
with Bubble Volume in High Viscosity Sugar
Solution

No.	V (cm^3)	U (cm/sec)	Re	Eö	We	S frame/sec	shape*
a	13.9	22.85	4.53	152	31.8	36.5	OEC
b	23.1	27.92	6.56	213	59.1	36.5	OEC
c	37.0	32.33	8.88	292	97.5	36.0	OEC
d	46.3	34.19	10.1	339	110	36.0	OEC
e**	55.5	38.65	12.2	383	168	37.0	OEC

For legend see Table 4.8.

All bubbles shown at same magnification.

* OEC - oblate ellipsoidal cap
** Slight wall effects may have been present for this case.

Liquid properties: μ = 20.84 poise
ρ = 1.384 g/cm^3
σ = 79.5 dynes/cm
M = 266

1 cm.

Re — 4.53

FIGURE 4.10(a)

1 cm.

Re = 6.56

FIGURE 4.10(b)

1 cm.

Re = 8.88

FIGURE 4.10(c)

1 cm.

Re — 10.1

FIGURE 4.10(d)

153.

1 cm.

Re = 12.2
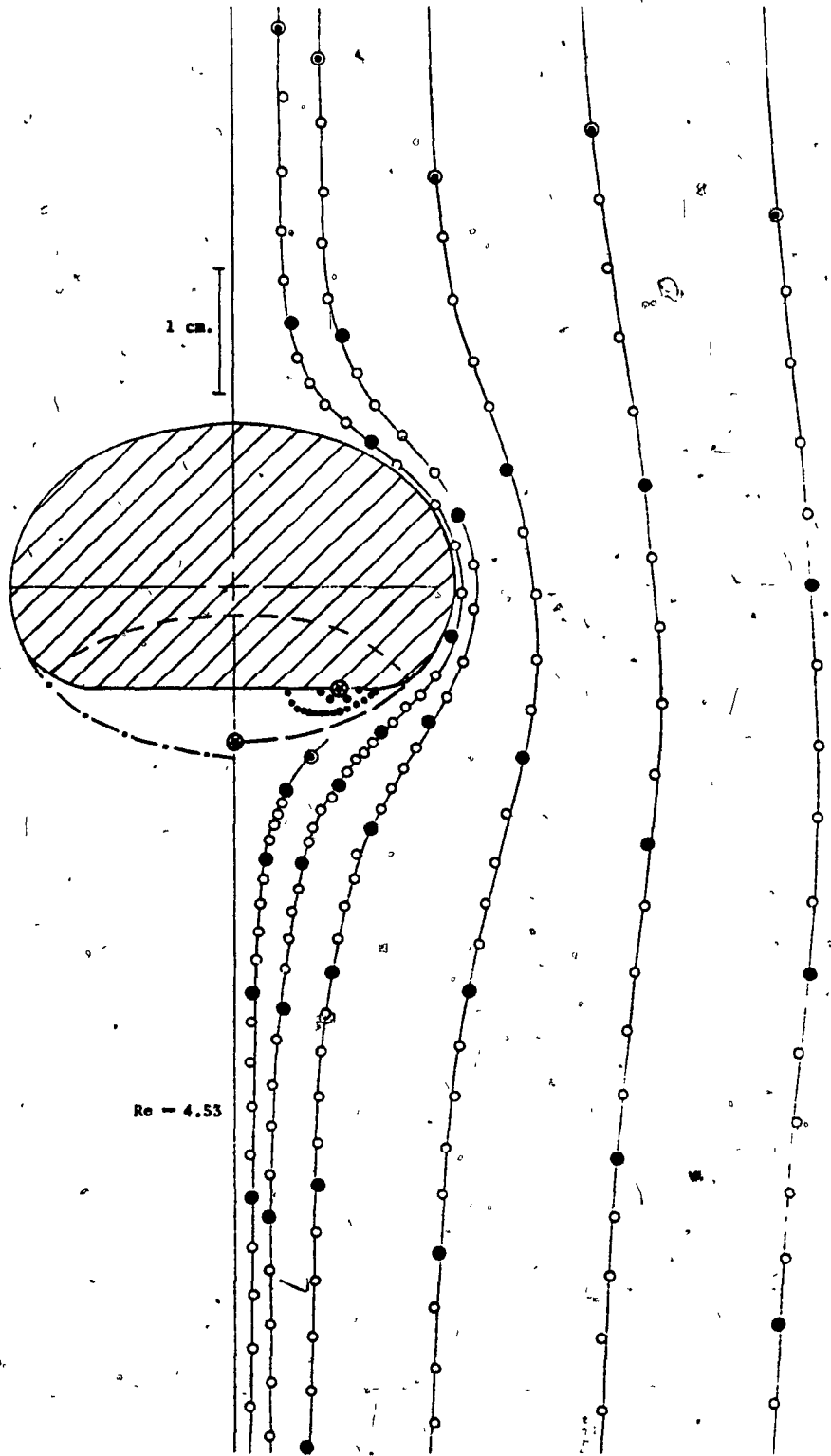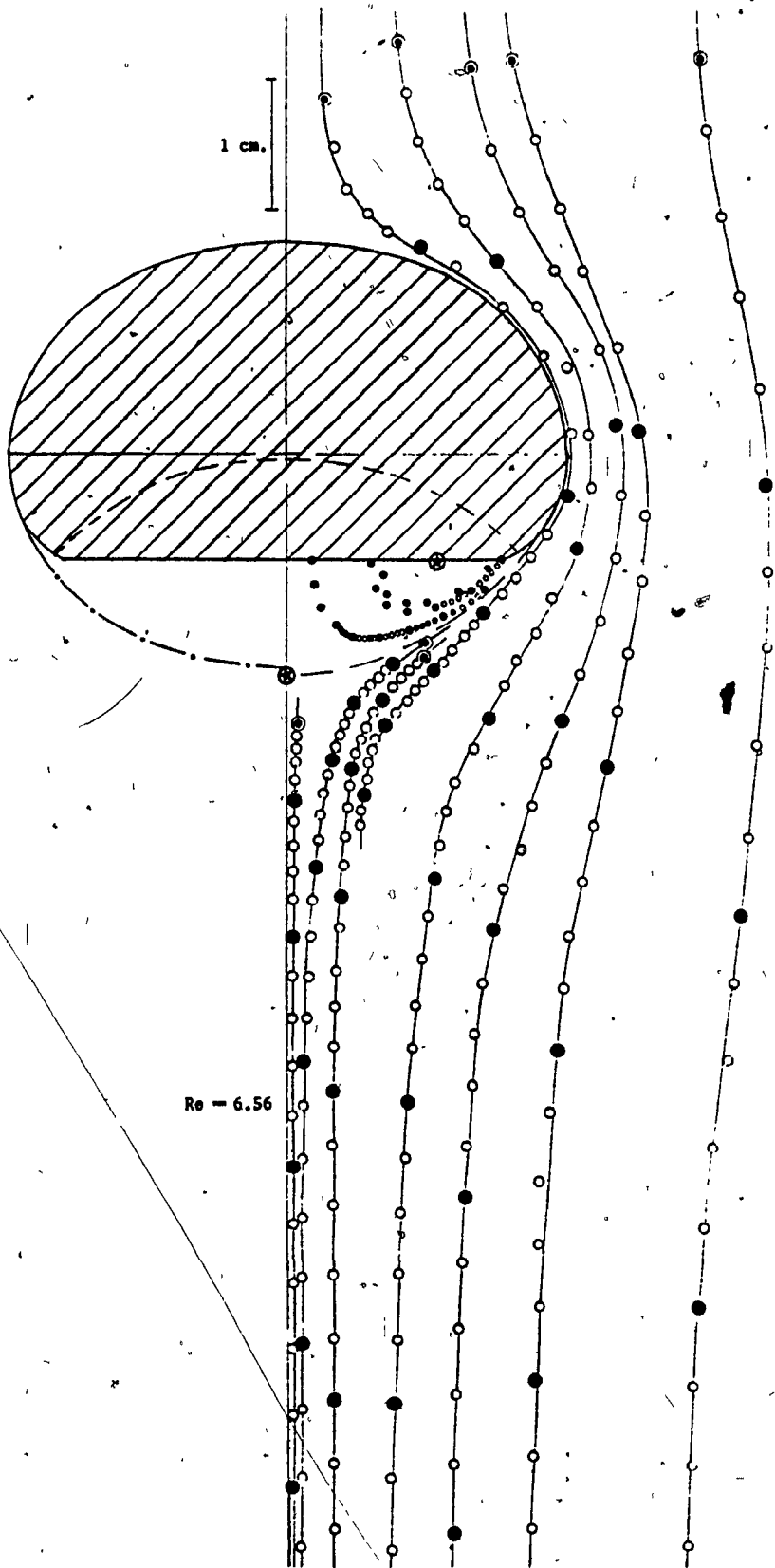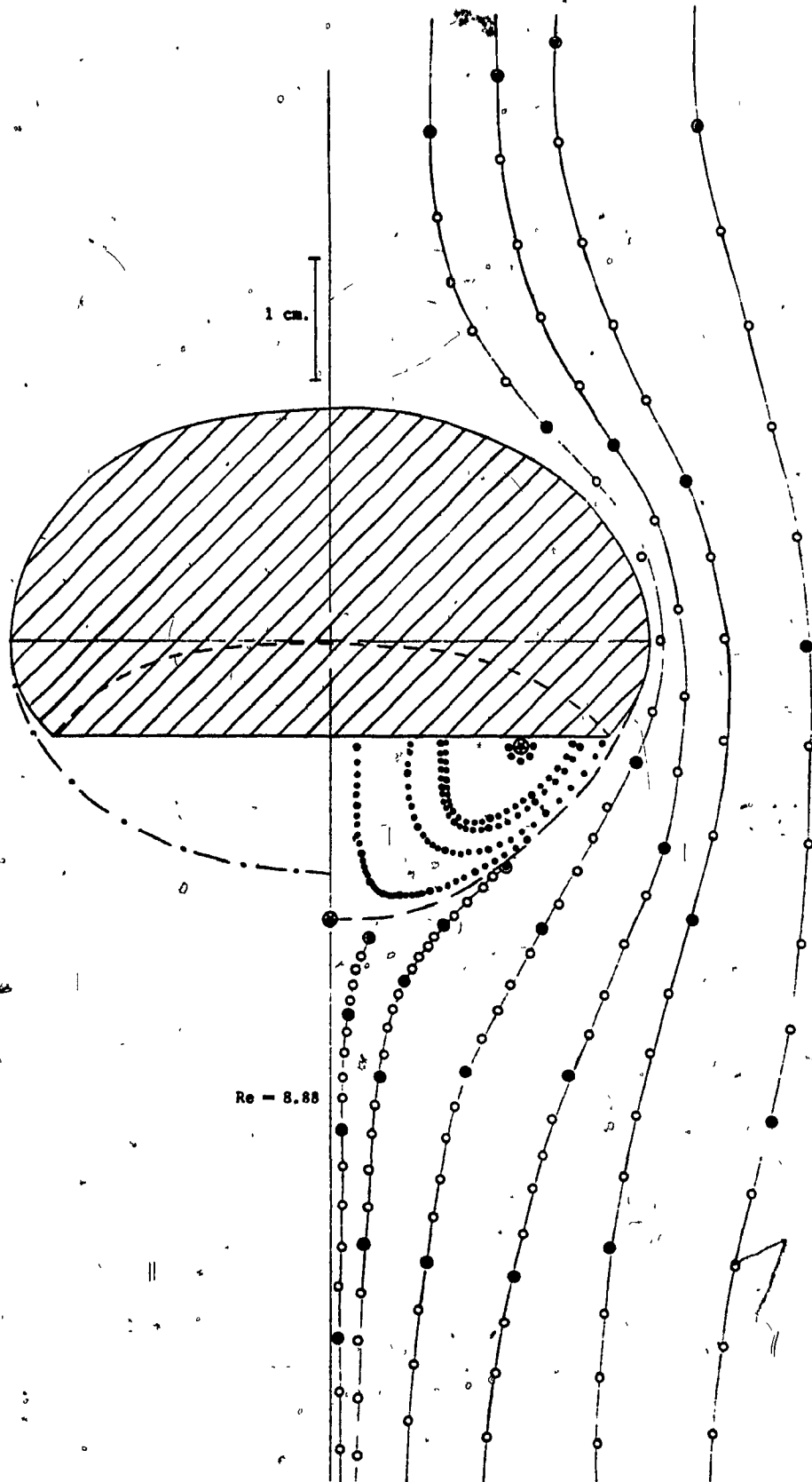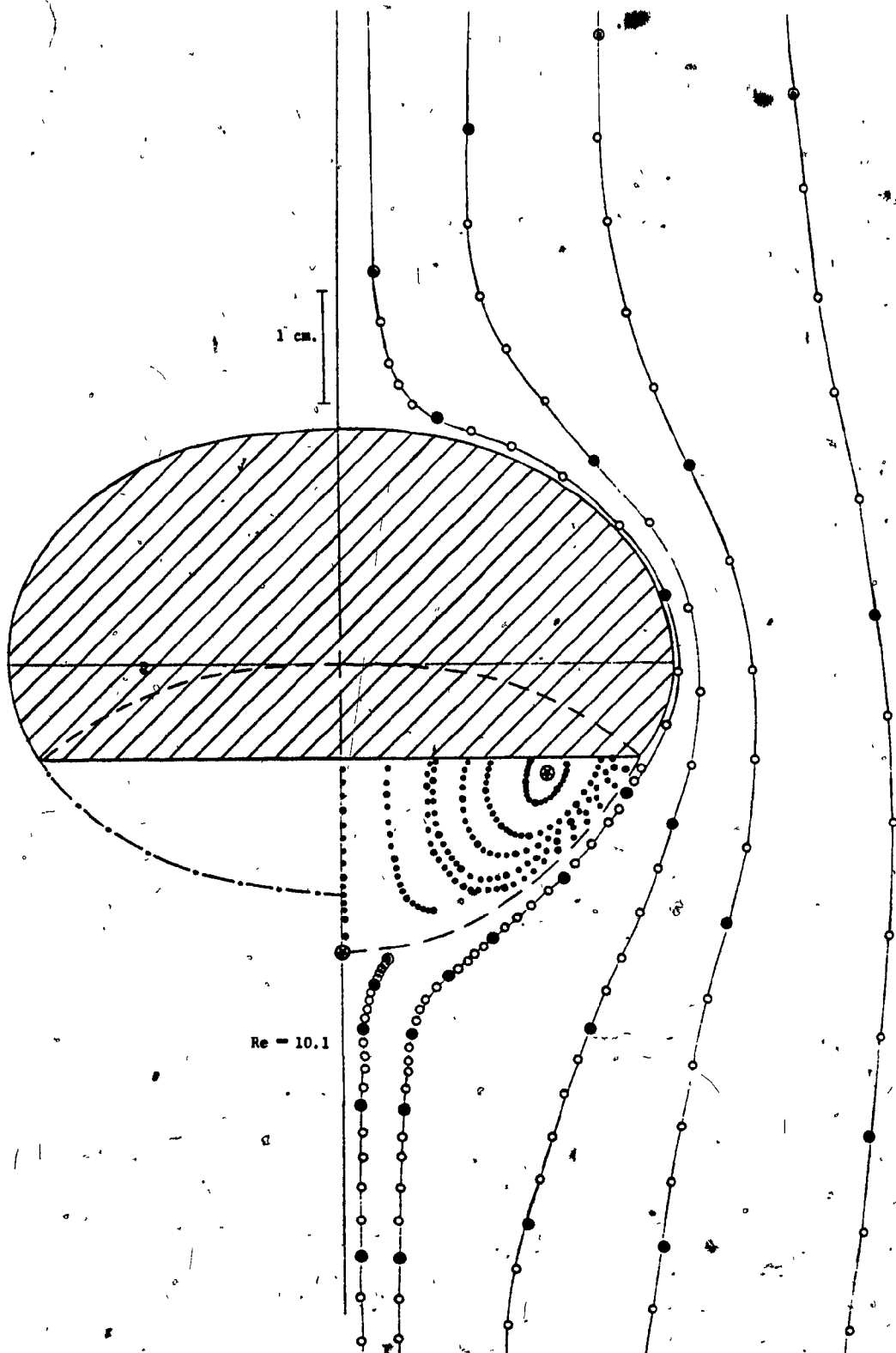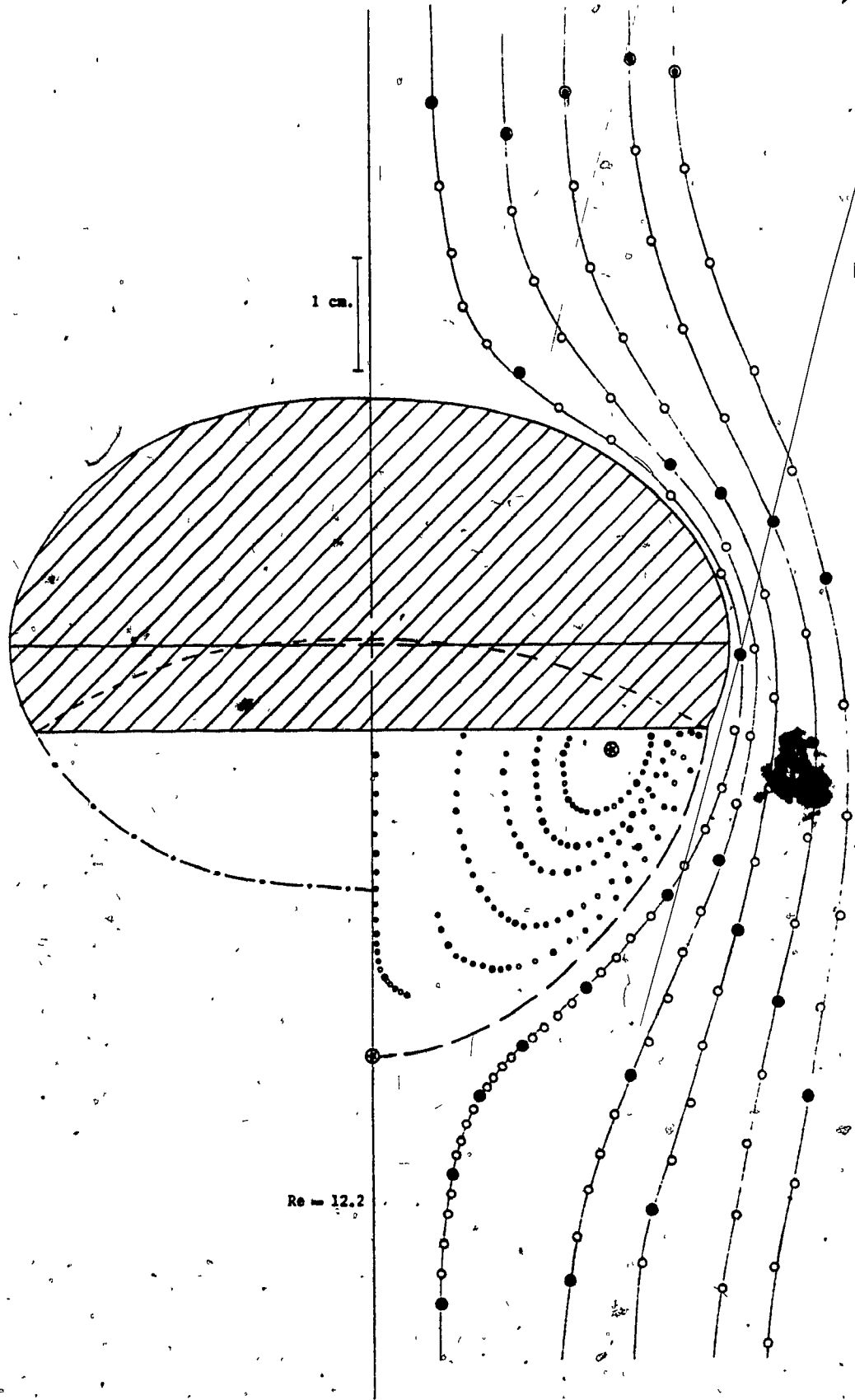
FIGURE 4.10(e)

FIGURE 4.11 Variation of Bubble Shape and Flow Field with Bubble Volume in Intermediate Viscosity Sugar Solution

No.	V (cm^3)	U (cm/sec)	Re	Eö	We	S frame/sec	shape*
a	6.9	27.53	11.4	95.9	38.8	35.00	OEC
b	9.3	29.15	13.3	116	48.4	35.00	OEC
c	18.5	36.43	21.0	184	106	35.00	OEC
d	27.8	37.34	24.6	242	134	35.00	OEC
e	37.0	39.50	28.7	293	174	35.00	OEC
f	37.1	39.77	28.9	293	188	35.00	SKS

For legend see Table 4.8.
All bubbles shown at same magnification.

* OEC - oblate ellipsoidal cap
  SKS - skirted bubble with steady smooth skirt

Liquid properties: μ = 7.81 poise
ρ = 1.370 g/cm^3
σ = 78.5 dynes/cm
M = 5.51

1 cm.

Re — 11.4

155.

FIGURE 4.11(a)

156.

1 cm.

Re — 13.3

FIGURE 4.11(b)

1 cm.

Re = 21.0

FIGURE 4.11(c)

1 cm.

Re — 24.6

FIGURE 4.11(d)

1 cm.

FIGURE 4.11(8)

1 cm.
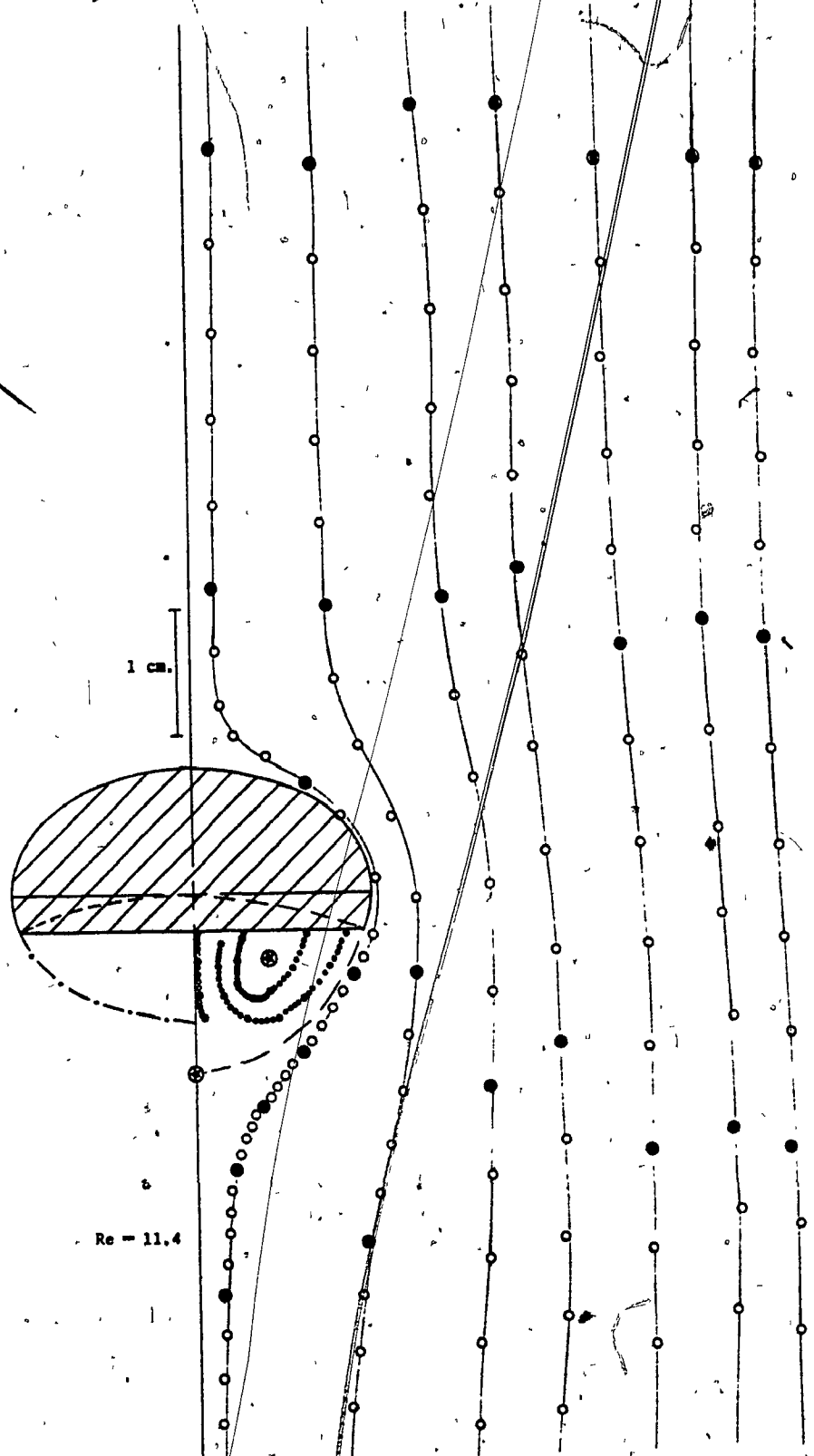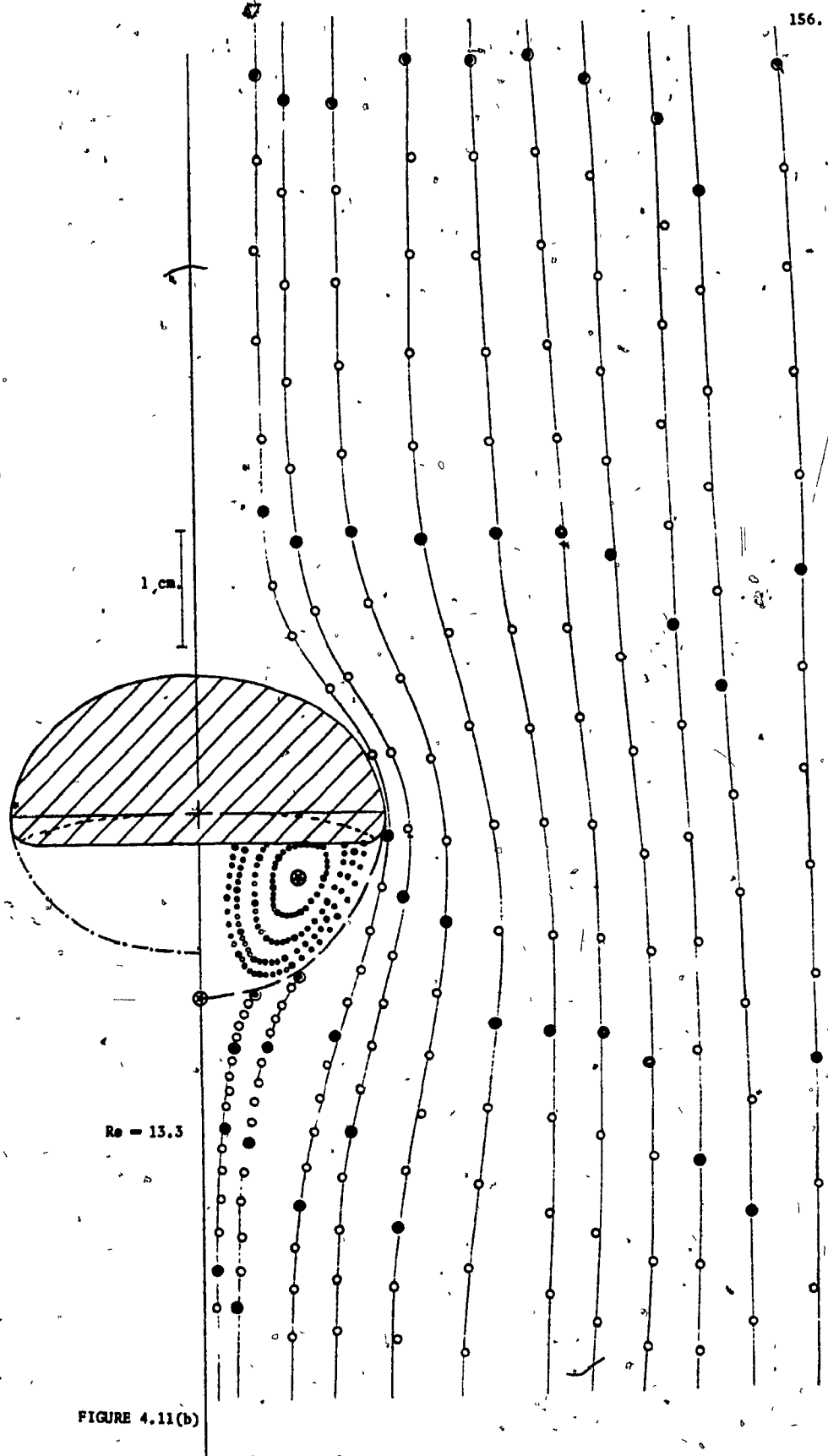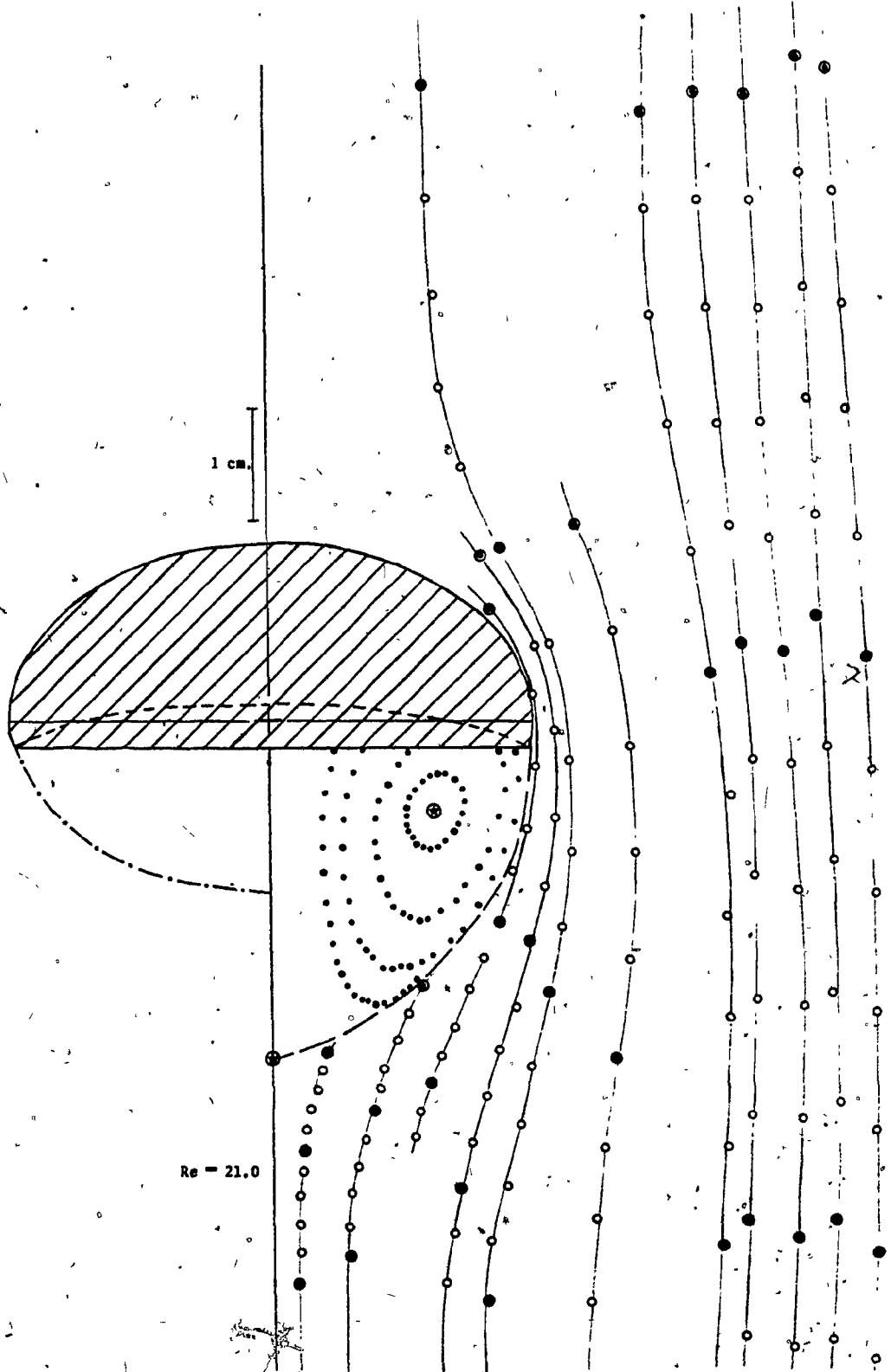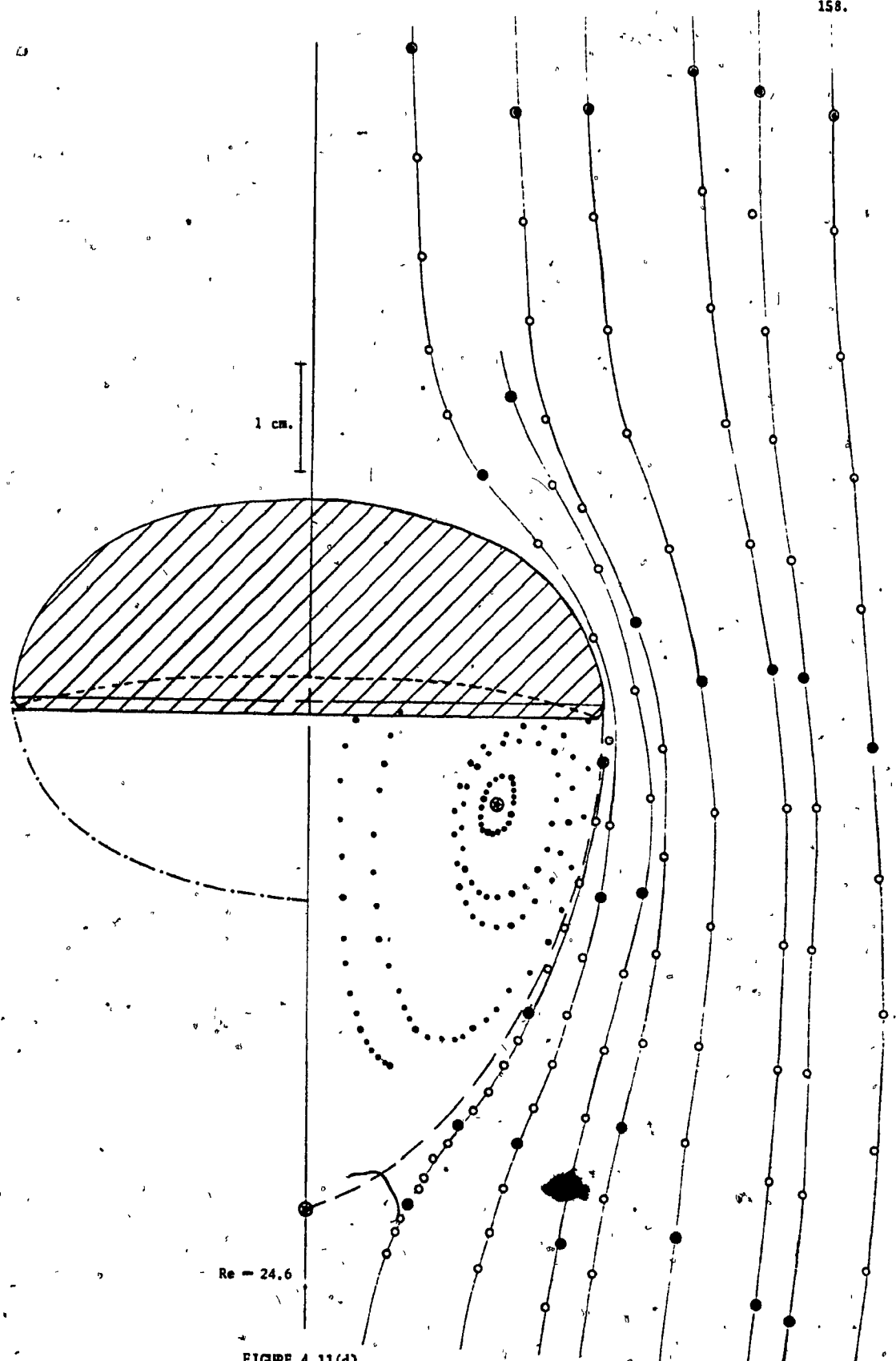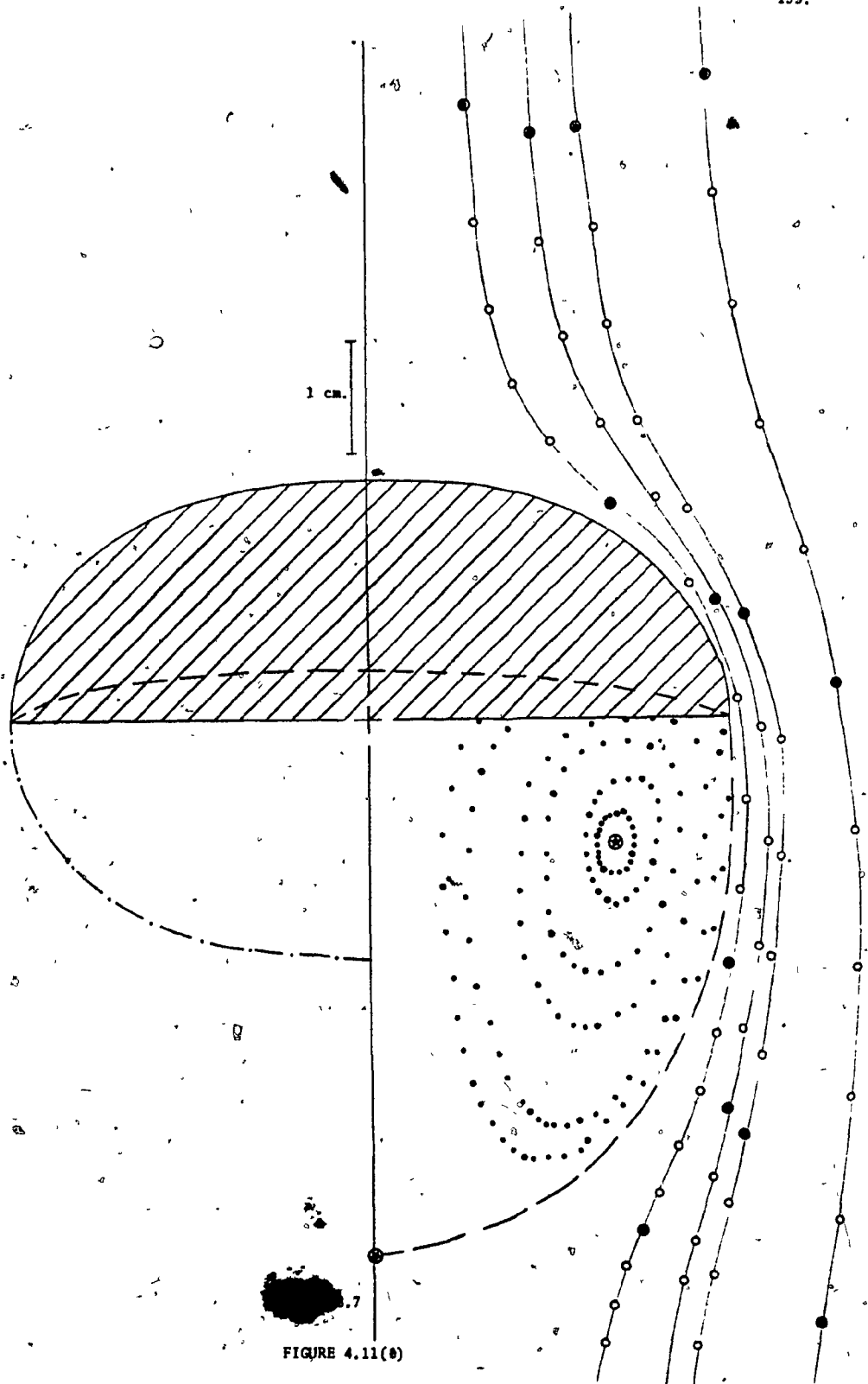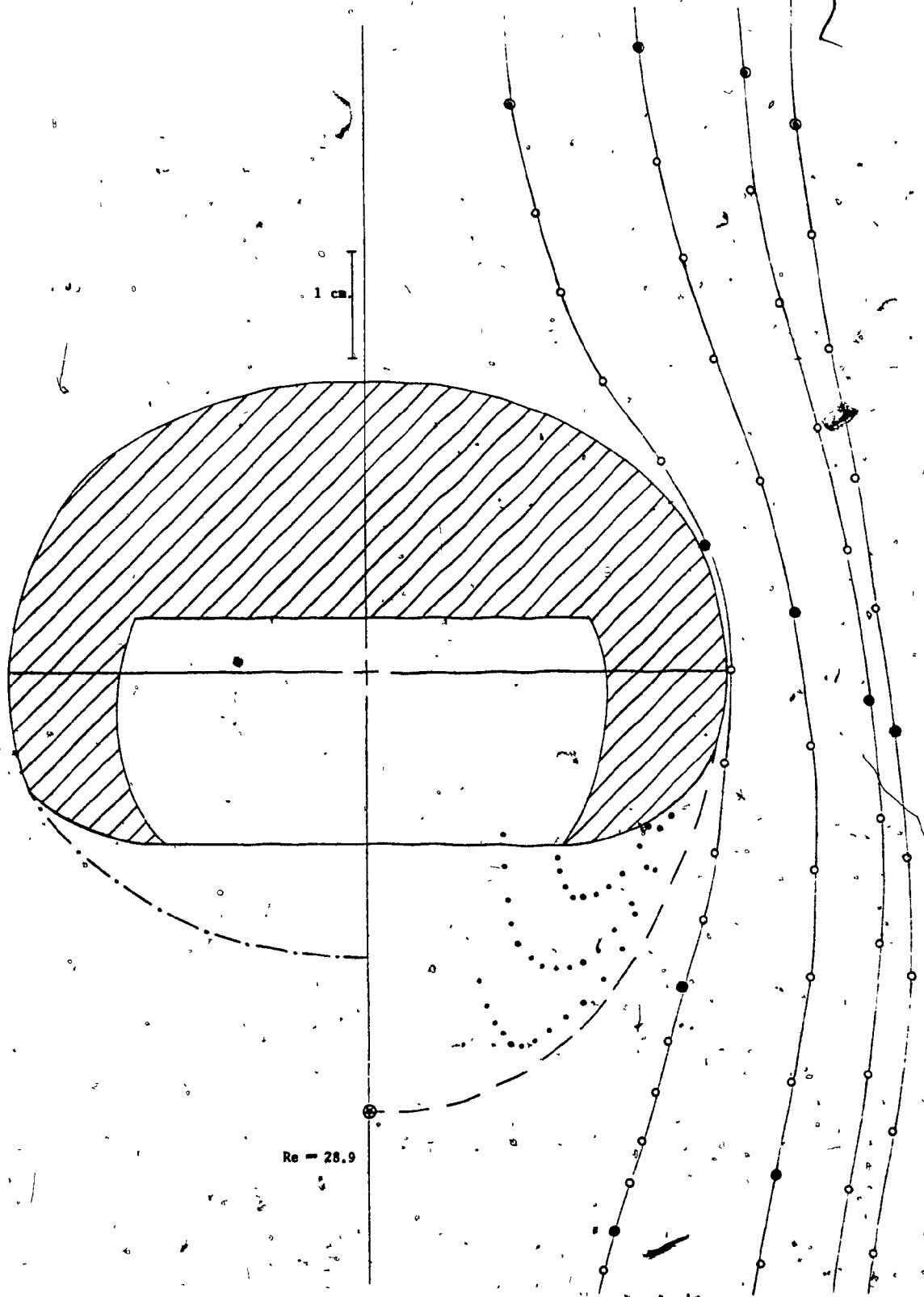
Re = 28.9

FIGURE 4.11(f)

FIGURE 4.12 Variation of Bubble Shape and Flow Field with
Bubble Volume in Low Viscosity Sugar Solution

No.	V (cm^3)	U (cm/sec)	Re	Eö	We	S frame/sec	shape*
a	2.3	27.13	45.5	45.6	48.4	33.60	SCC
b	4.6	30.20	60.9	72.3	87.8	34.00	SCC
c	7.0	33.85	81.8	94.8	118	33.60	SCC
d	9.3	35.33	94.0	115	130	33.60	SCC

For legend see Table 4.8.
All bubbles shown at same magnification.

* SCC - spherical cap with closed toroidal wake

Liquid properties: $\mu = 1.30$ poise
$\rho = 1.326$ g/cm^3
$\sigma = 77.0$ dynes/cm
$M = 0.00463$

1 cm.

Re = 45.5

FIGURE 4.12(a)

163.

1 cm.

Re = 60.9

FIGURE 4.12(b)

1 cm.

Re = 81.8

FIGURE 4.12(c)

1 cm.
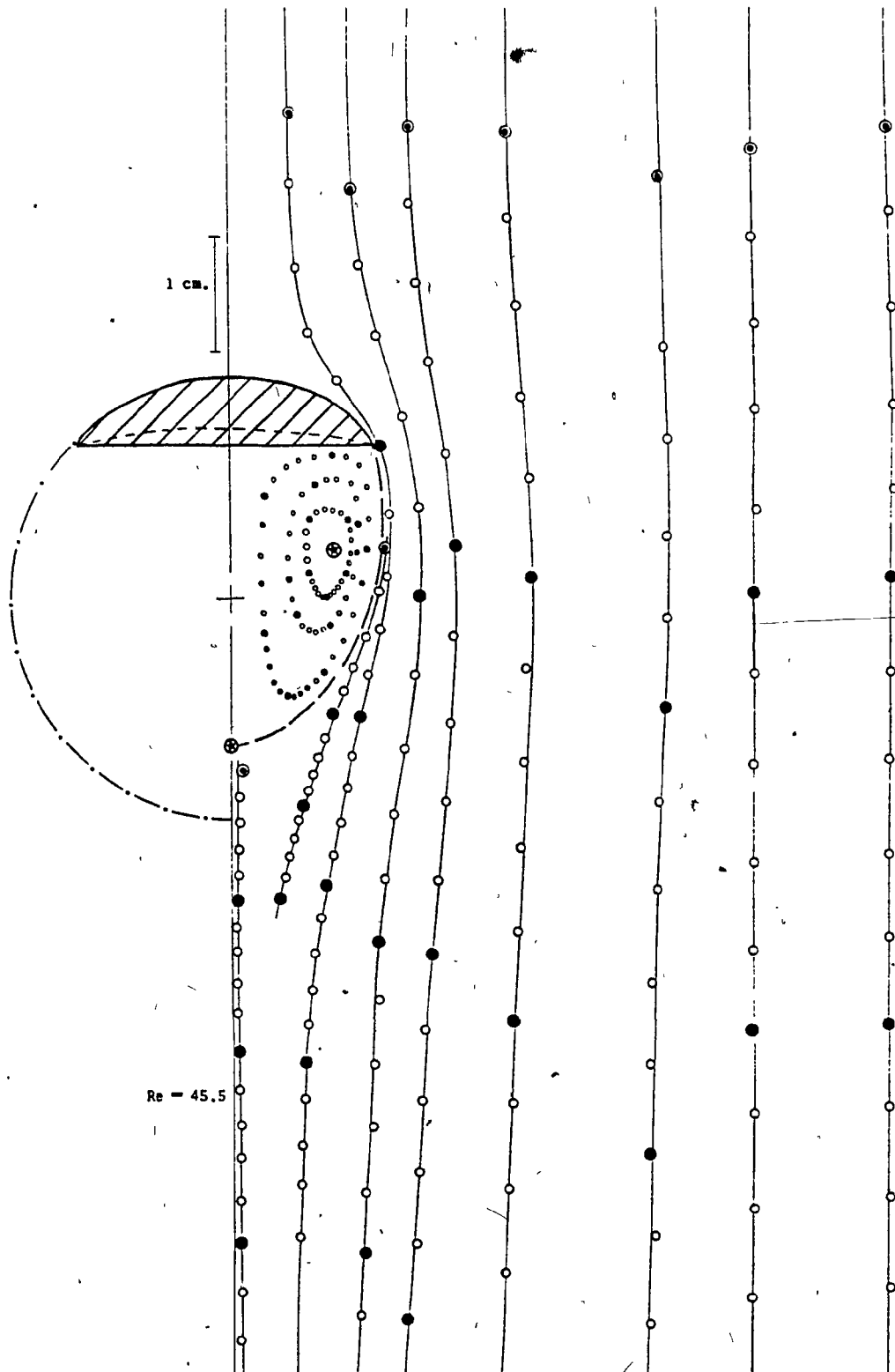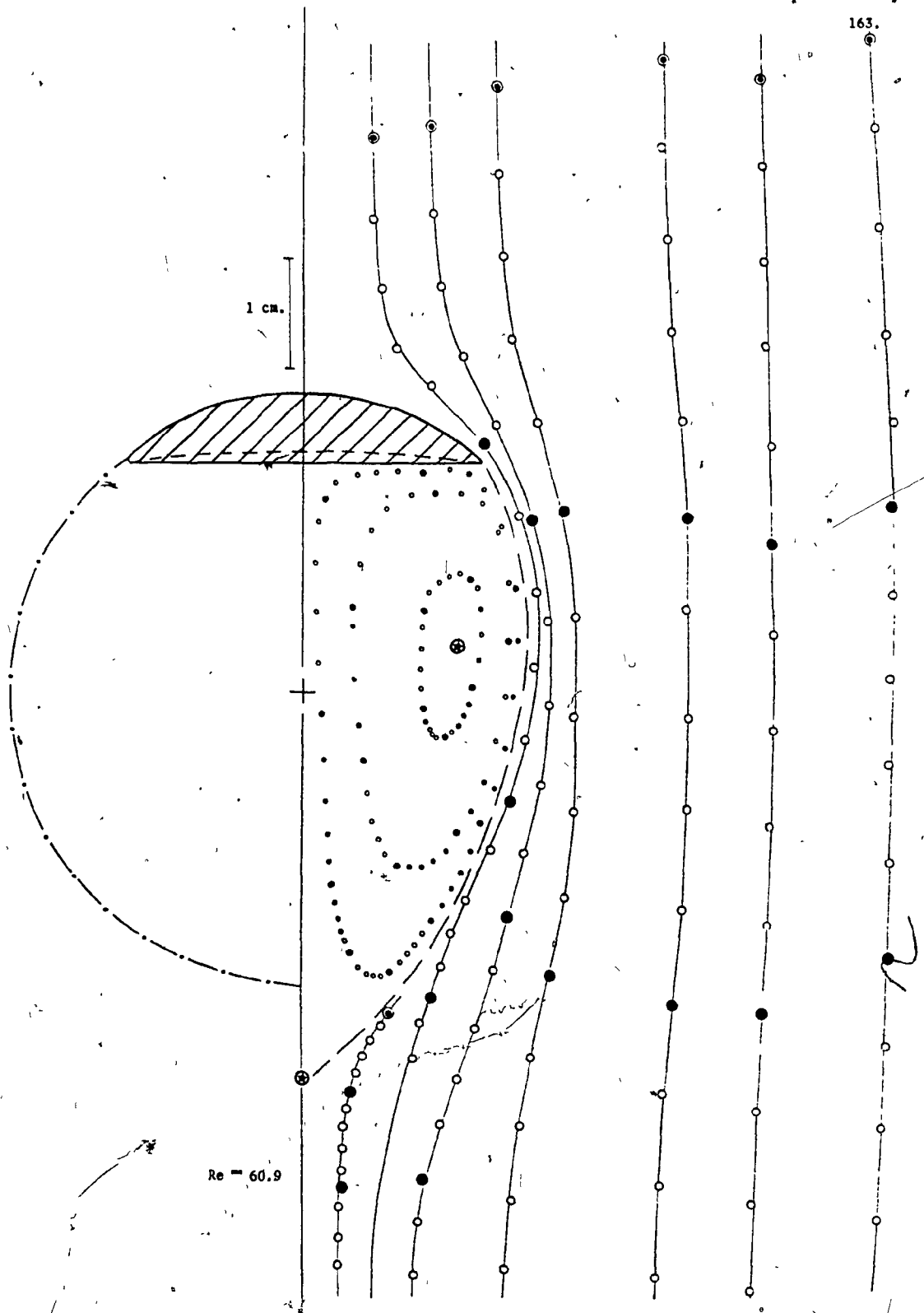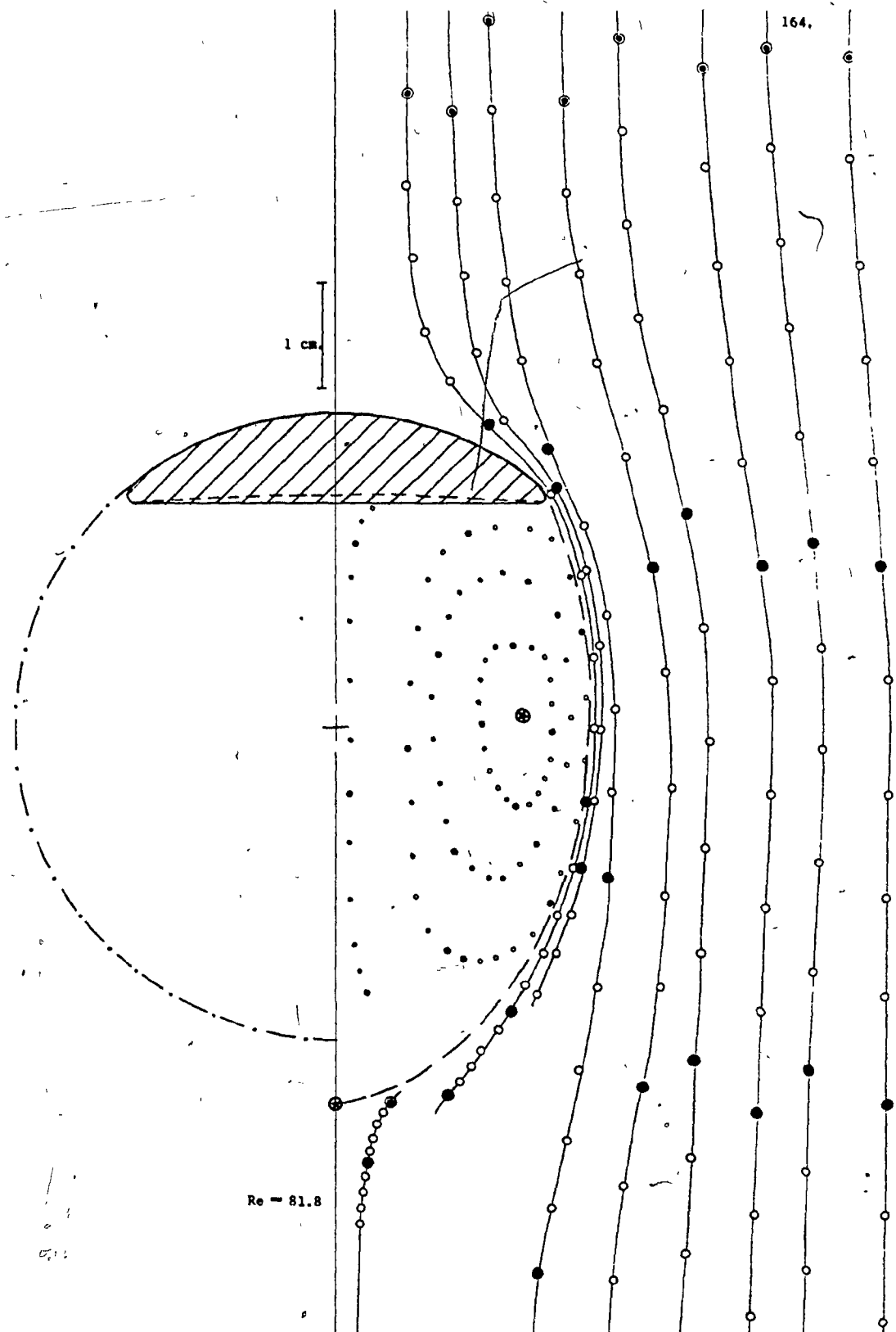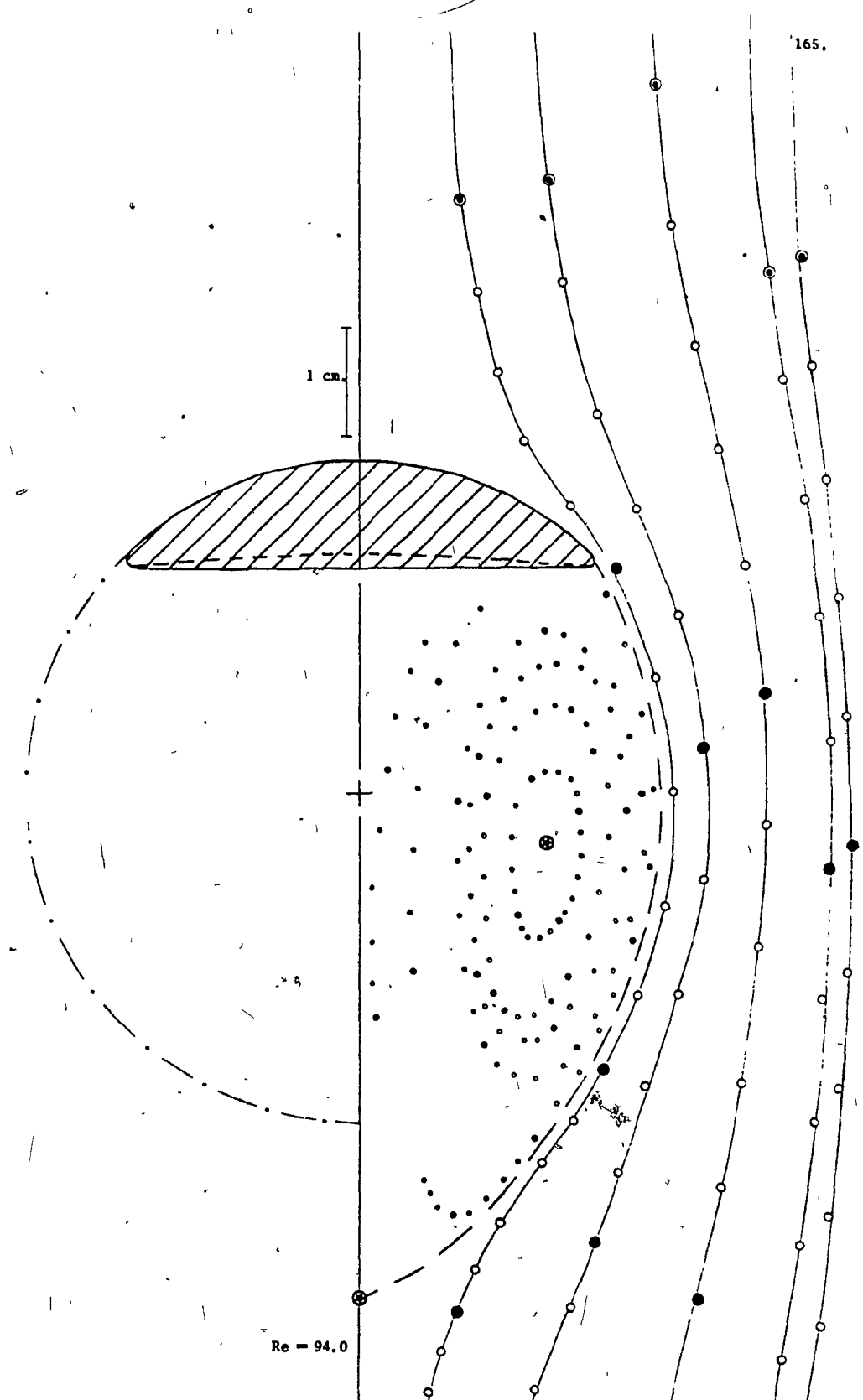
Re = 94.0

FIGURE 4.12(d)

From careful observation of ciné-films, long-exposure photographs of wakes presented on the preceeding pages and the streamline tracings shown in Figs.4.8 to 4.12, the following conclusions emerge regarding bubbles with closed toroidal wakes.

The bubble wake attains a steady state fairly rapidly after passing through the probe. The size of the wake remains constant with no exchange of liquid with the external liquid. Within the toroidal wake the tracer bubbles remain on a single streamline. During their upward motion they disappear into the indentation, but reappear moving downwards and follow the same streamline again. The flow always separates at the edge of the bubble base. The liquid within the closed wake moves considerably slower than the terminal bubble rise velocity. As the external liquid flows around the bubble its velocity decreases, especially once past the base of the bubble (see the streamlines adjacent to the bubble in any of Figs.4.8 to 4.12). As the fluid flows over the surface of the bubble the shear stress at the bubble-liquid surface is very small since the viscosity of the liquid is very much greater than that of the gas. However, on the boundary between the closed wake and the external fluid the shear stress is significant because the wake fluid and the external fluid have the same viscosity. The slowing down of the external fluid is less noticeable at higher Re and lower viscosity; for example, compare Fig.4.8(f) and Fig.4.10(d).

The streamlines of the external flow widen behind the bubble at increasing Re as the size of the closed wake grows (see Fig.4.8(a) to (f), for example). It is also evident that the fore and aft symmetry present at Re << 1 is destroyed rapidly as Re is increased above 1.

A comparison of the boundary of the closed wake with the boundary of an oblate-ellipsoid or of a sphere which fits the bubble-cap shows that these do not match except at Re around 5 (see Fig.4.8(a) and (b) or Fig.4.10 (a) and (b)).   For Re < 5 the wake is smaller and above it is larger than the spheroid that fits the cap.

It is also clear from these figures that the transition from an oblate-ellipsoidal-cap to a spherical-cap bubble occurs around Re ≈ 44 (see Fig.4.8(e) and Fig.4.12(a)) in accord with the shape study presented in Chapter 3. For spherical-cap bubbles close to this transition point the shape of the wake is far from spherical and is more like a part of prolate ellipsoid (see Fig.4.12(a)). As Re is increased further the wake widens in the transverse direction with the maximum width coinciding with the horizontal plane that contains the vortex centres. The wake becomes more nearly spherical as Re approaches 100 (see Fig.4.8(f)), but it is still elongated in the streamwise direction.

Finally, for spherical-cap bubbles with unsteady open wakes, the liquid flow ahead of the bubble base is essentially steady (see photographs of Figs.4.4(9), 4.5(8) and (9) and 4.6). Further evidence of this is provided in Fig.4.8(g) which shows two sets of streamlines. The shaded and unshaded circles represent the streamlines for the same bubble at 1 sec. apart. It is clear that the motion is unsteady only below the base of the bubble.

4.5.2.4   Flow field around oblate-ellipsoidal-cap bubbles

Figs.4.13(a), (b) and (c) compare the experimental streamlines and the theoretical streamlines around oblate ellipsoidal-cap-bubbles at Re = 2.47, 13.3 and 42.2. The theoretical predictions are made for potential

FIGURE 4.13   Comparison between Experimental and Theoretical
              Streamlines around Oblate Ellipsoidal Cap Bubble

No.	Re	For complete experimental data and details refer to
a	2.47	Figure 4.8(a)
b	13.3	Figure 4.8(c)
c	42.2	Figure 4.8(e)

o   experimental position of tracer bubble at every frame

———+———   theoretical predictions - potential flow past an oblate
             ellipsoid

———•———   theoretical predictions - creeping flow past an oblate
             ellipsoid

--------   apparent indentation of bubble base

— — —   boundary of closed toroidal wake

—·—·—   boundary of ellipsoid that fits the bubble cap

⊕   stagnation point

1 cm

Re = 2.47

FIGURE 4-13(a)

.170.

1 cm
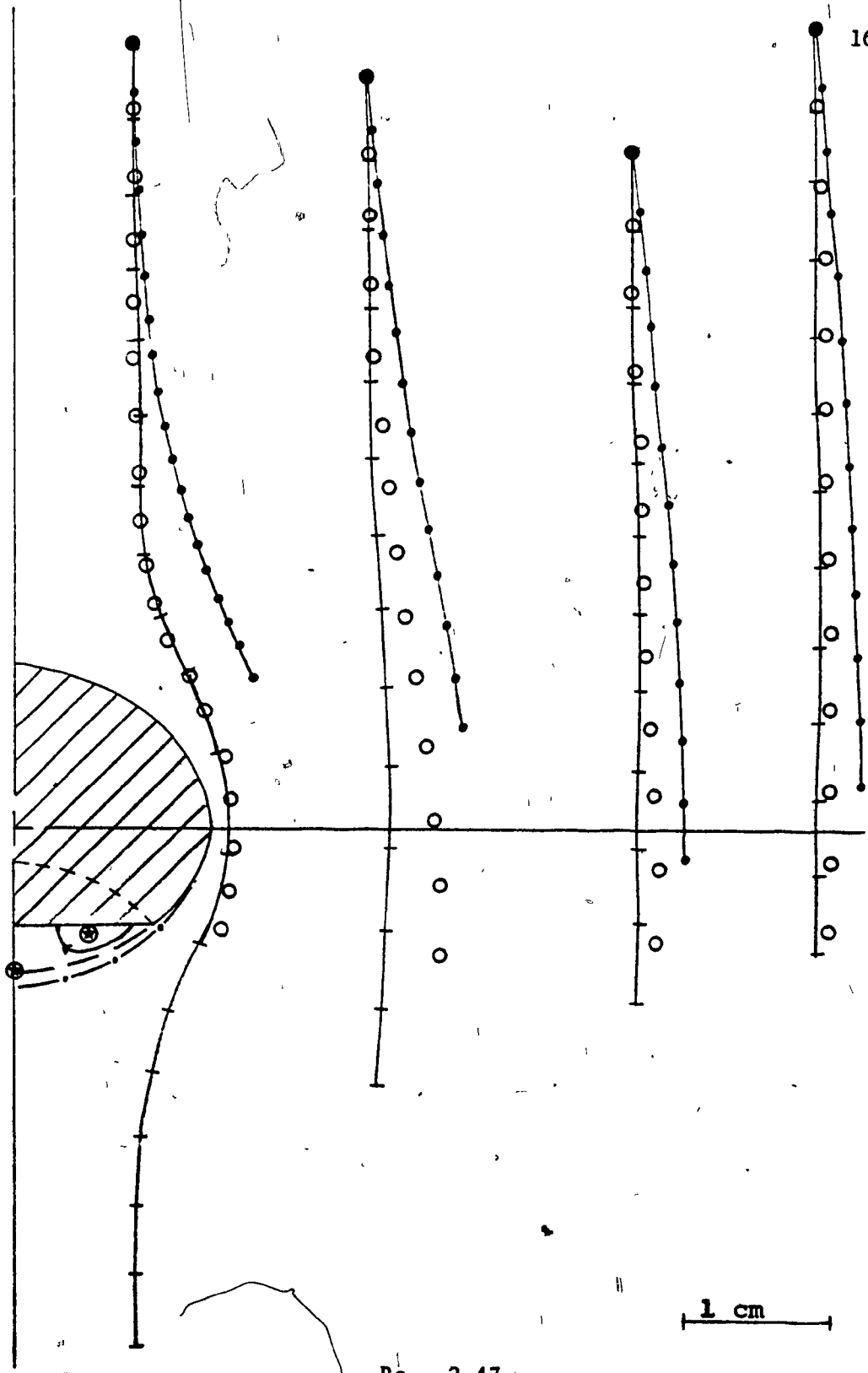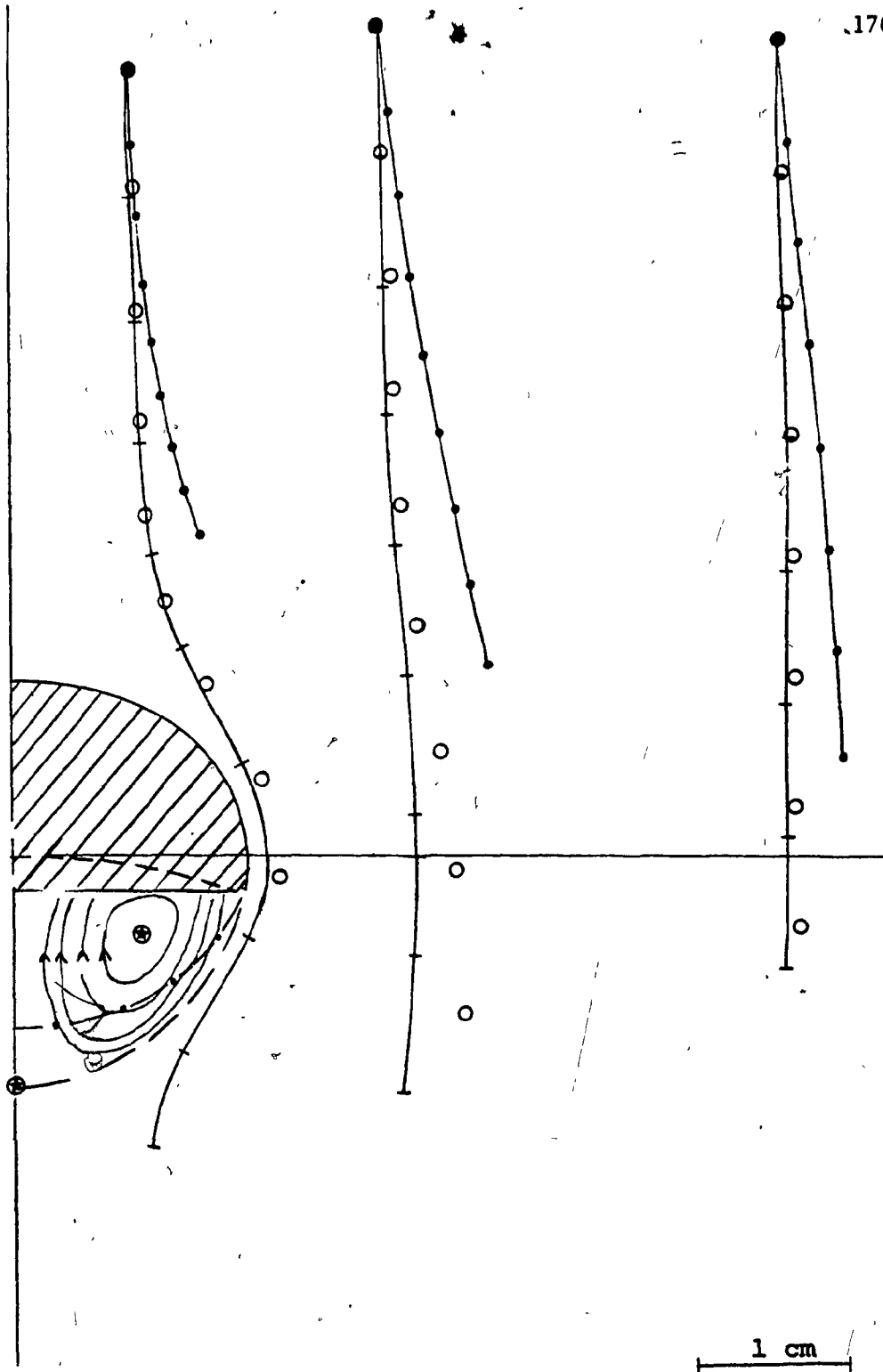
Re — 13.3

FIGURE 4-13(b)

Re = 42.2

1 cm
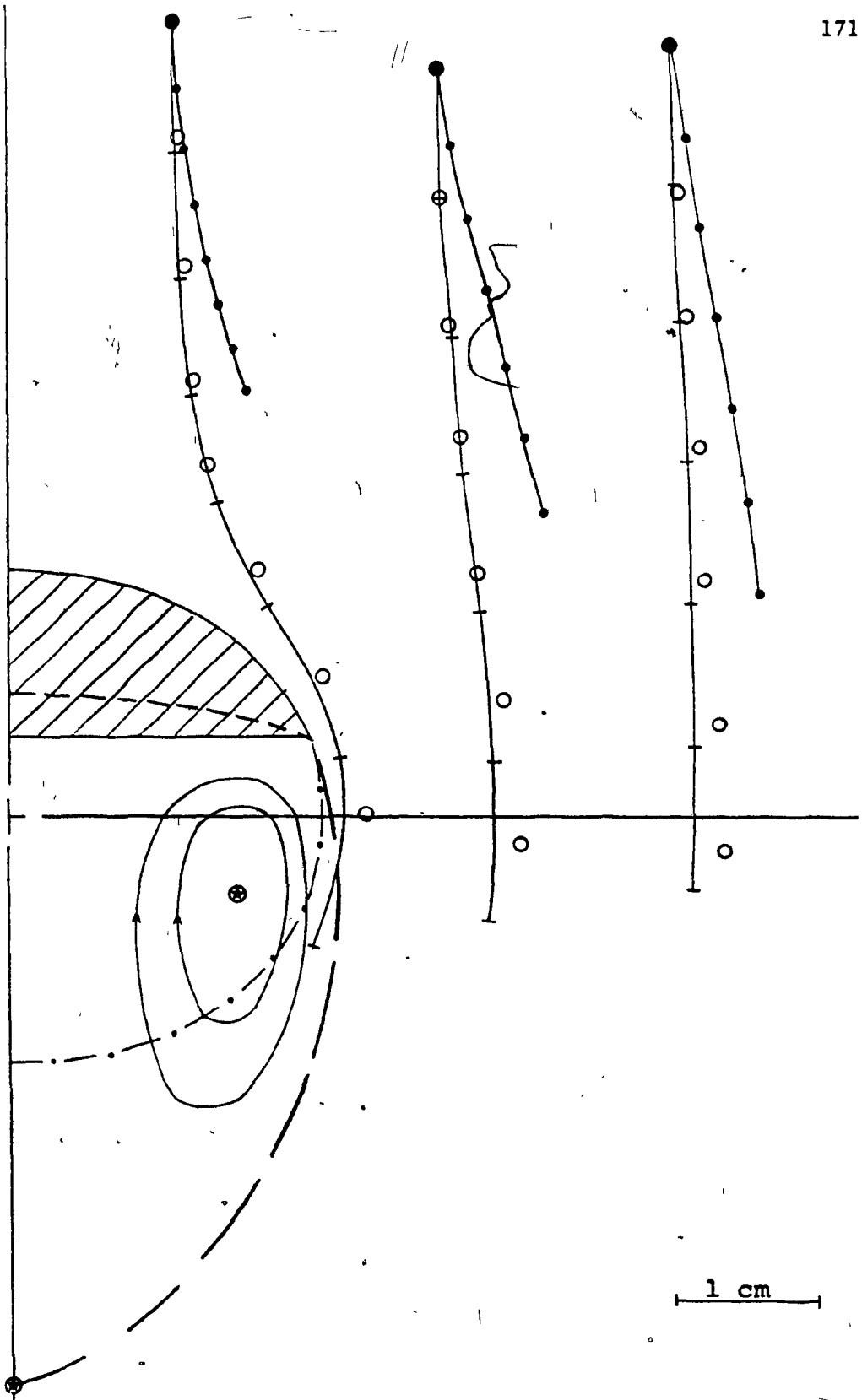
FIGURE 4-13(c)

flow and creeping flow around a solid oblate ellipsoid. Since the shape of the closed wake does not agree with the boundary of the spheroid that fits the cap, one should not expect any agreement between the data and the theory below the base of the bubble. Therefore, the comparison is made for the flow around the bubble cap only up to its base. For all three cases the experimental data lie between the potential flow and the creeping flow predictions with the potential flow showing better agreement. The deviation from the potential flow diminishes with increasing Re. At about 2 to 3 semi-major axes away from the bubble the flow field is well represented by potential flow. This explains why even at Re as low as 5 the rise velocity model for an ellipsoidal cap bubble (Wairegi and Grace 1976), which is based on assumption of potential flow around an oblate ellipsoid, is successful in predicting the rise velocity (see Section 3.4.3.5).

In Fig.4.14 the experimental equatorial velocity distributions for five ellipsoidal-cap bubbles at Re — 2.5 to 42.2 are compared with the predictions of potential flow and creeping flow past solid oblate ellipsoids. The following conclusions emerge.

(i) All the velocity profiles approach the potential flow model rather than the creeping flow.

(ii) As expected, these velocity profiles are ordered systematically with increasing Re.

(iii) The deviation from potential flow extends to a distance of about 3.5 semi-major axis for Re — 2.47, and this distance decreases with Re to about 1.6 semi-major axis at Re — 42.2. At the two highest Re a slight peak in the velocity profile is observed. The velocity approaches the $u_{\theta e}/U = 1$ limit from above. Similar velocity maxima
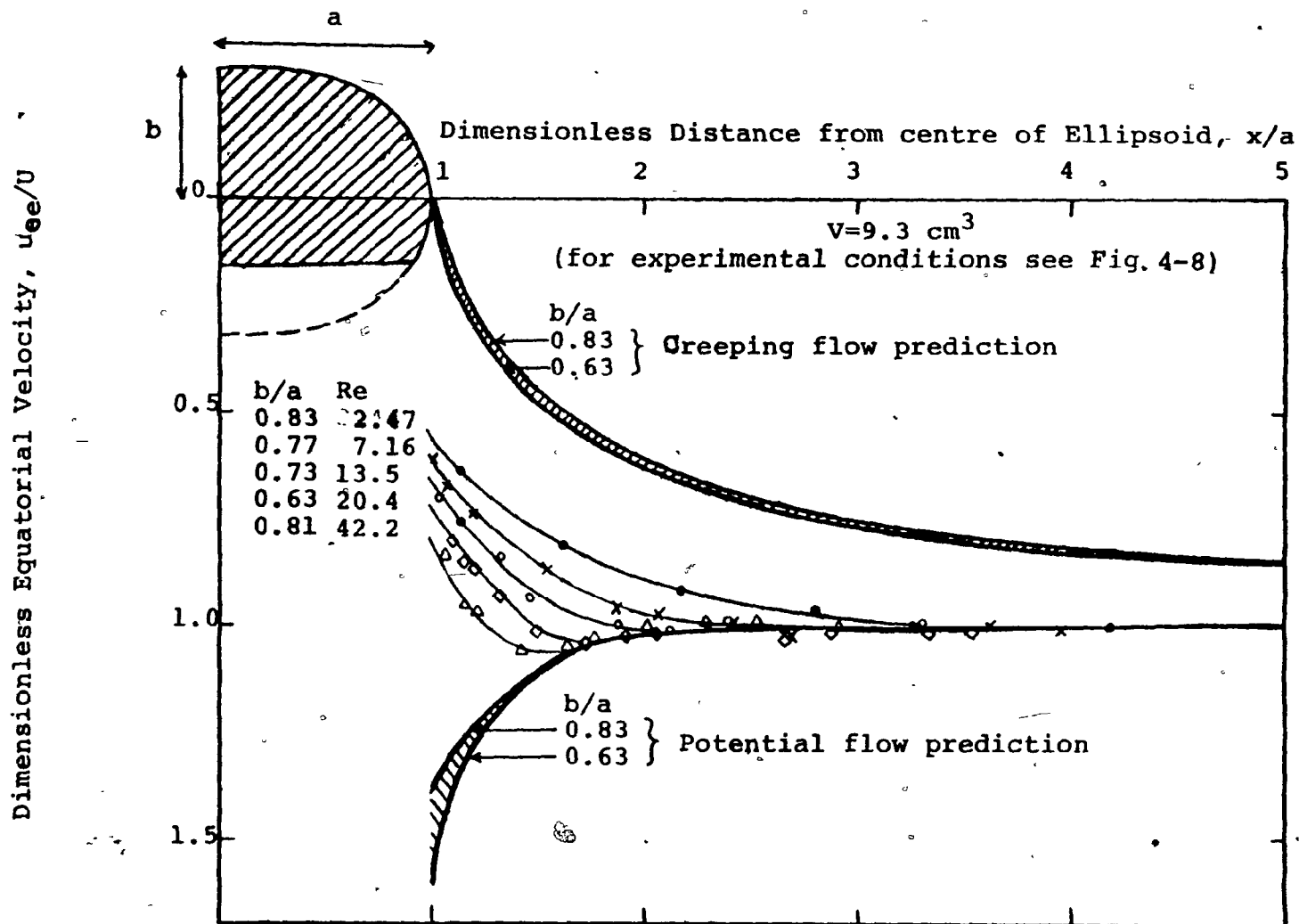
FIGURE 4-14 : Equatorial Velocity Distribution for Oblate Ellisoidal-cap Bubbles

have also been observed by Seeley (1972) for flow

external to solid spheres at Re > 290.

(iv) The dimensionless equatorial velocity at the bubble

surface increases from about 0.56 to 0.81 for Re =

2.47 to 42.2, respectively.

4.5.2.5 Flow field around spherical-cap bubbles

In Fig. 4.15 the experimental streamlines around spherical-cap bubbles are compared with the predictions based upon potential flow around a sphere that fits the bubble cap for Re ranging from 45.5 to 265. The agreement is remarkably good up to the bubble base. It can be seen from Figs. 4.15(a) and (g) that beyond the bubble base the agreement is poor for streamlines fairly close to the toroidal wake because the wake shape does not coincide with the sphere that fits the cap. However, at distances greater than about $2d_e$ the influence of the wake shape on the flow field diminishes and the potential flow prediction is surprisingly close to the experimental measurements, especially at high Re.

An experimental streamline very close to a spherical-cap bubble* is compared with the theoretical predictions of Moore's (1963) boundary layer model and of potential flow in Fig. 4.16. In accord with expectation, the predictions of these theories are almost identical far from the bubble, but differ in the vicinity of the bubble surface where the viscous effects

---

* Since the boundary layer is very thin, only a few tracer bubbles were found which were close to the bubble surface yet whose position within the boundary layer could be determined accurately. The experimental run shown in Fig. 4.16 is one of the few which met these criteria.

FIGURE 4.15 Comparison between Experimental and Theoretical
Streamlines around Spherical Cap Bubbles

No.	Re	For complete experimental data and details refer to
a	45.5	Figure 4.12(a)
b	60.9	Figure 4.12(b)
c	81.8	Figure 4.12(c)
d	94.0	Figure 4.12(d)
e	151	Figure 4.8(g)
f	265	Figure 4.9(d)

o experimental positions of tracer bubble at every frame

———+——— theoretical prediction - potential flow around a sphere

——————— apparent indentation of bubble base

—— —— —— boundary of closed toroidal wake

——·——·—— boundary of sphere that fits the bubble cap

⊕ stagnation point

1 cm

Re = 45.5

FIGURE 4-15(a)

1 cm
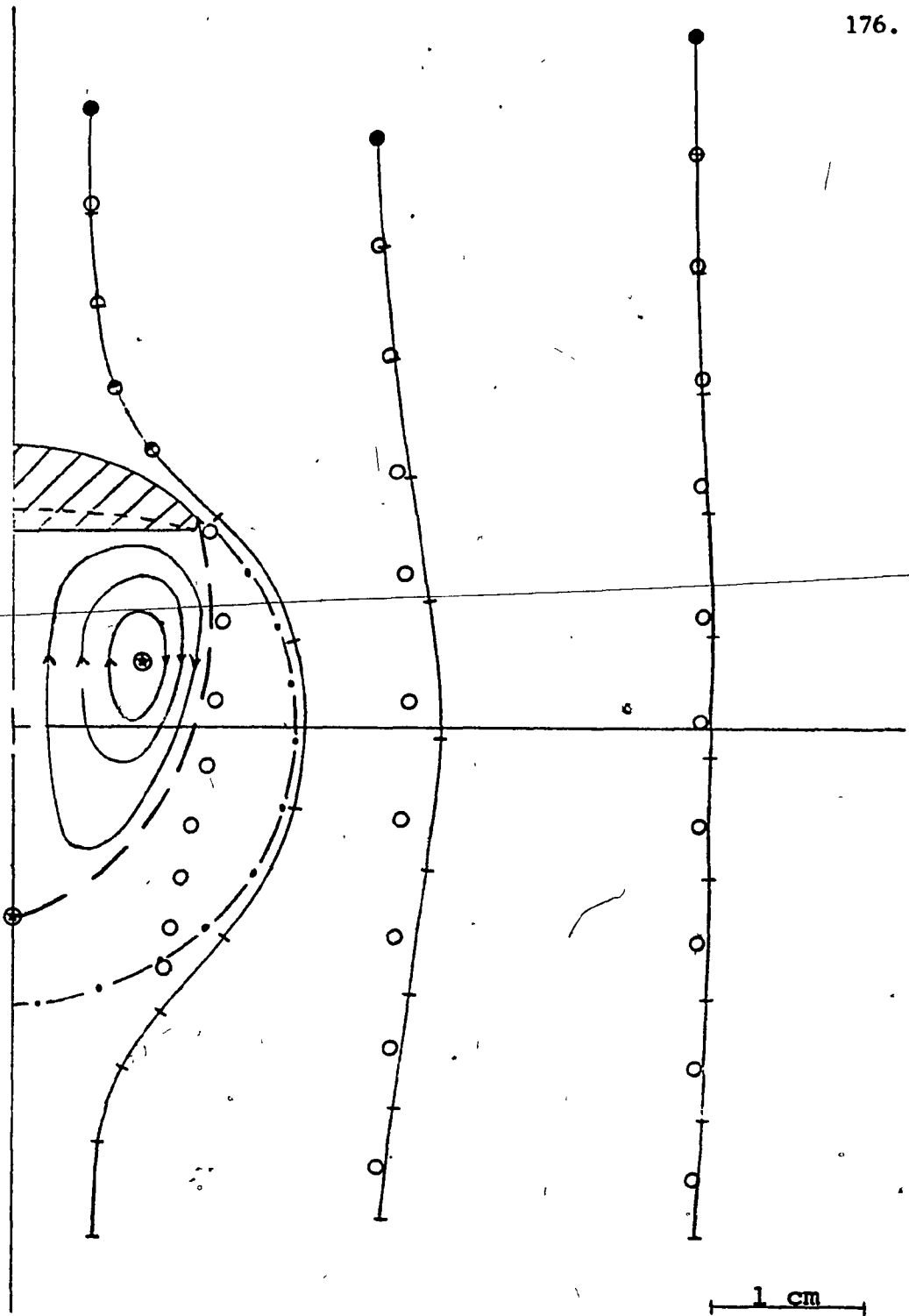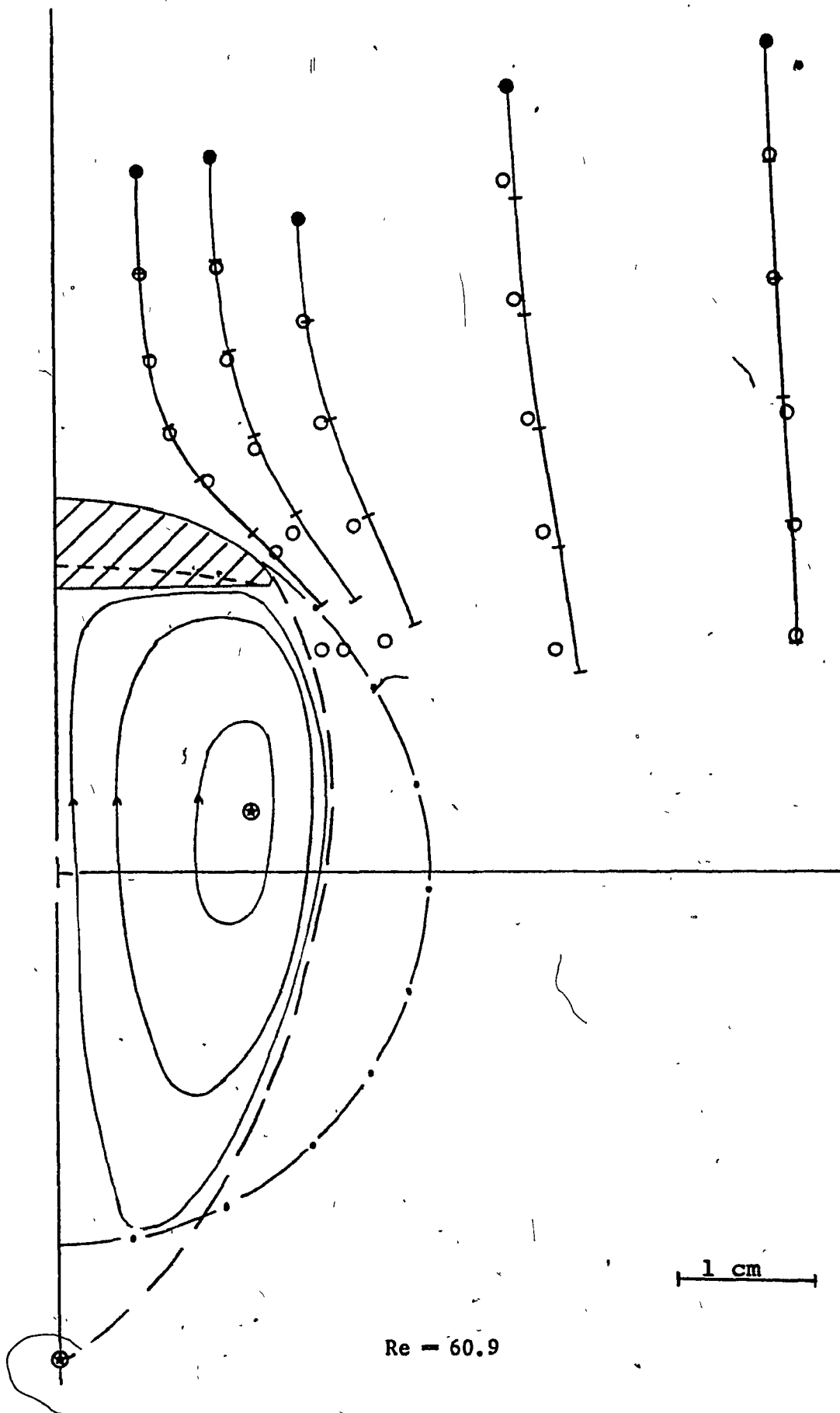
Re = 60.9
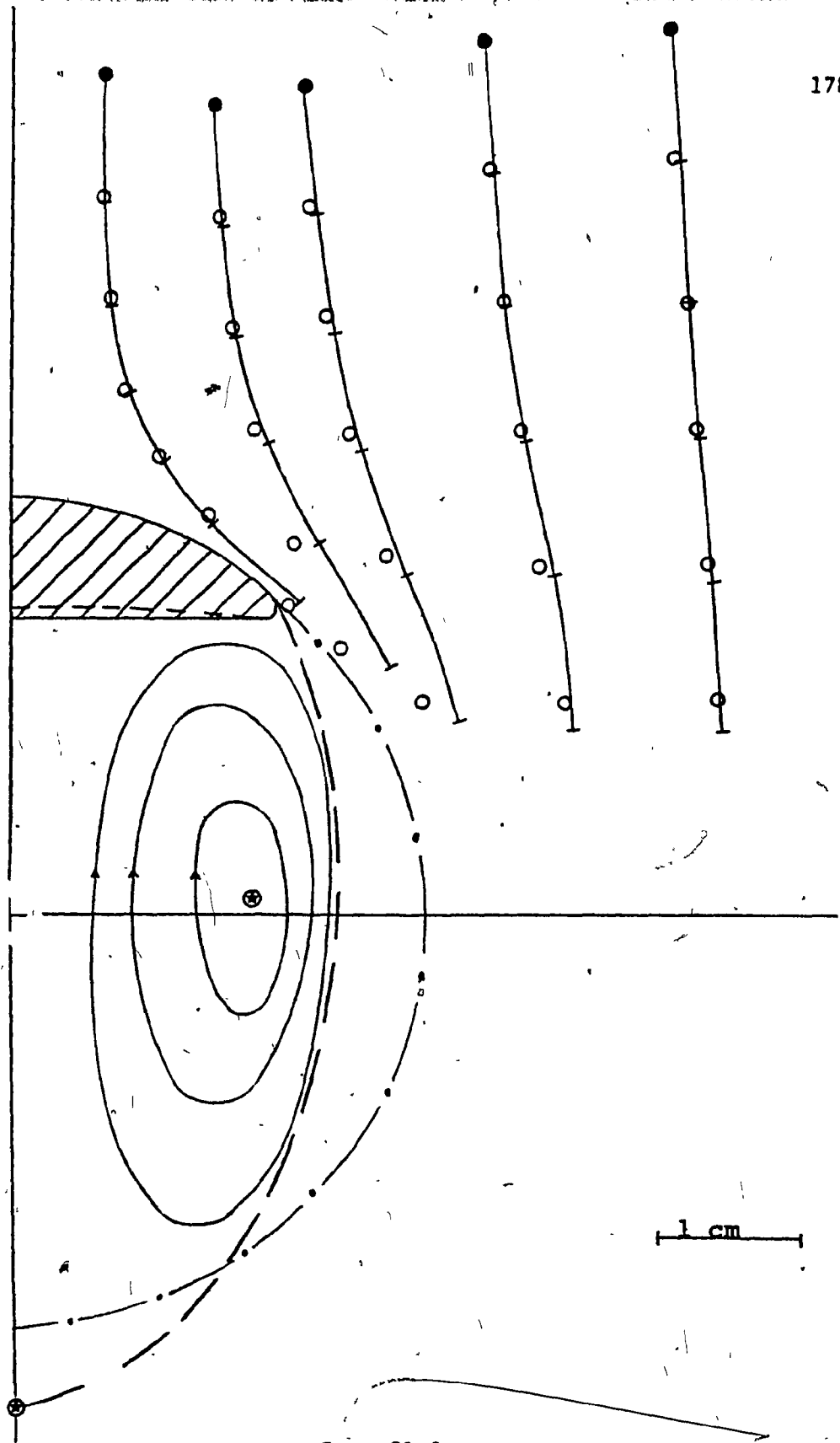
FIGURE 4-15(b)

Re = 81.8

FIGURE 4-15(c)
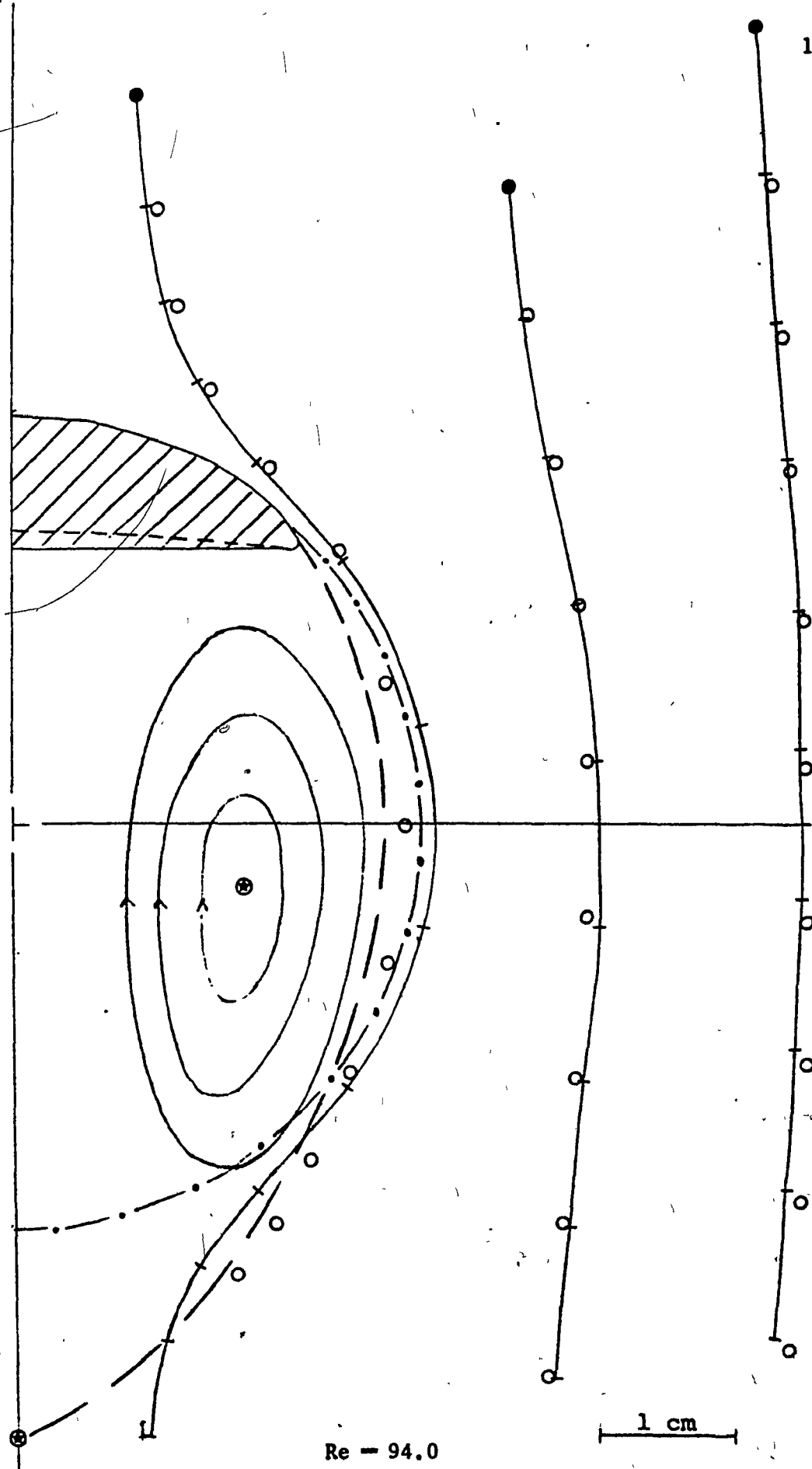
Re = 94.0

1 cm

FIGURE 4-15(d)

Re = 151

FIGURE 4-15(e)

1 cm

1 cm
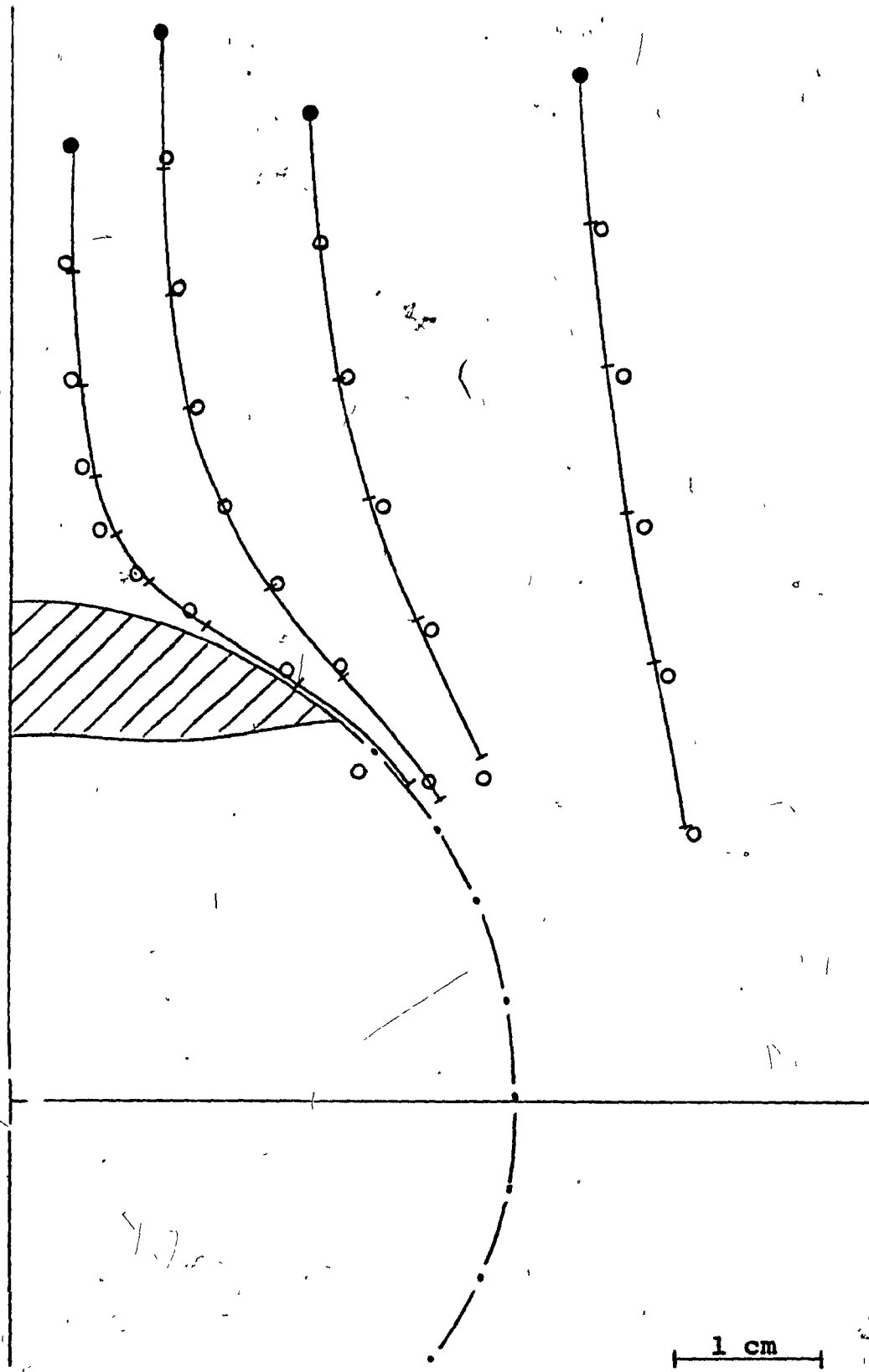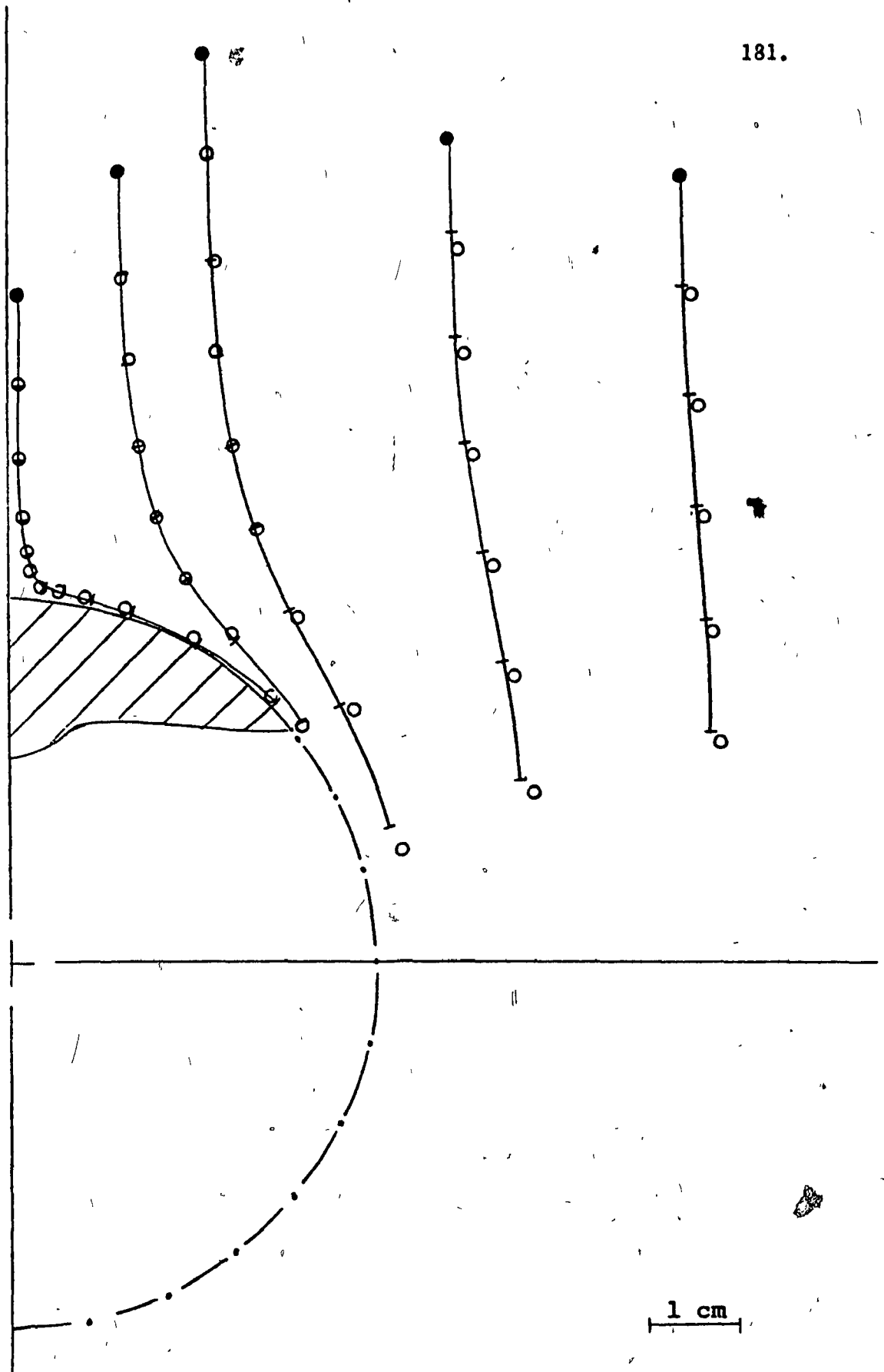
Re = 265
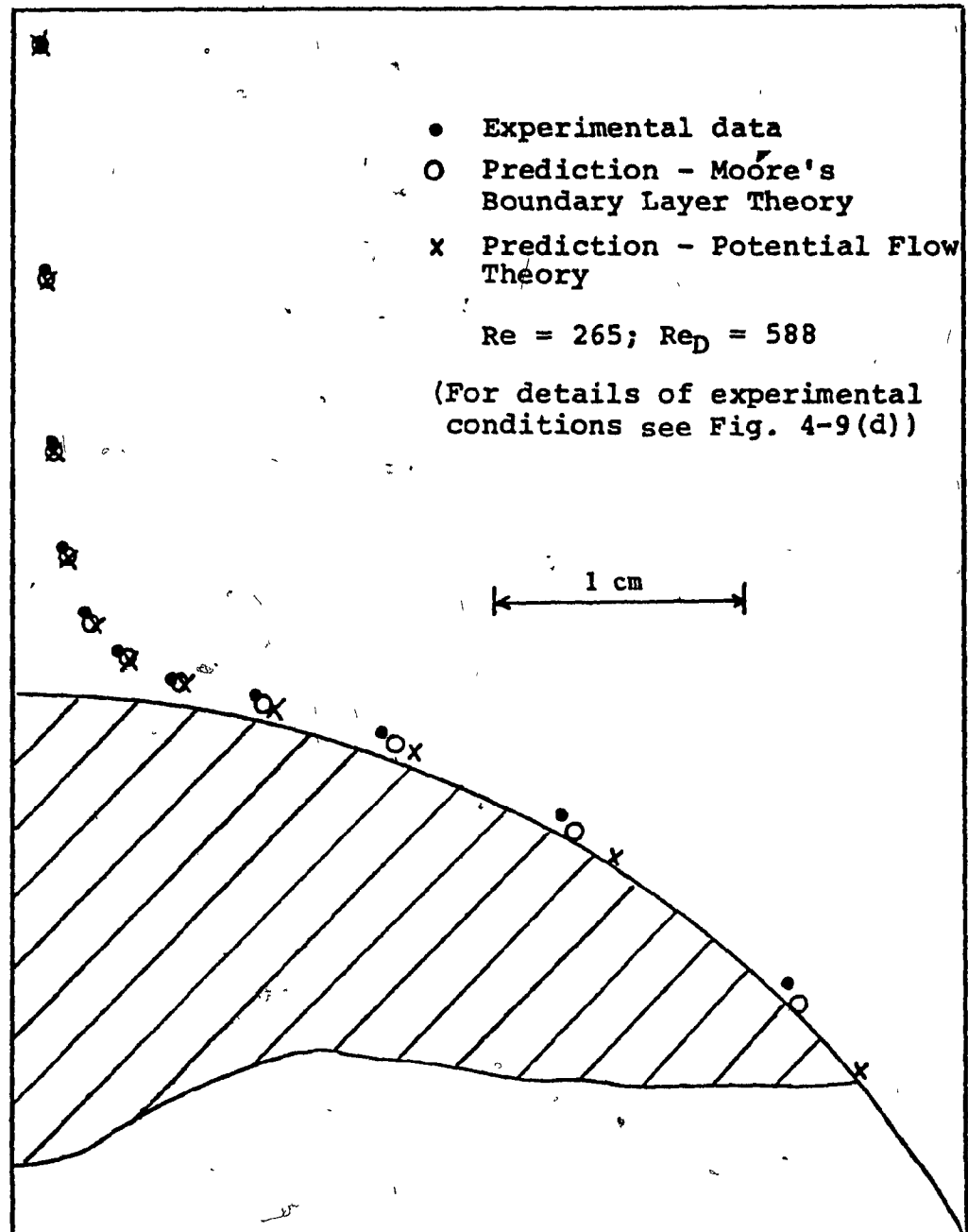
FIGURE 4-15(f)

FIGURE 4-16: <u>Comparison of experimental and theoretical stream-lines very close to the surface of a spherical-cap bubble.</u>

Legend within figure:

• Experimental data
O Prediction – Moore's Boundary Layer Theory
X Prediction – Potential Flow Theory

Re = 265; Re$_D$ = 588

(For details of experimental conditions see Fig. 4-9(d))

1 cm

FIGURE 4.17 Comparison between Experimental and Theoretical Streamlines around Oblate Skirted Bubbles

No.	Liquid Properties			M	V (cm^3)	U (cm/sec)	Re	Eö	We	S frame/sec
	μ (poise)	ρ (g/cm^3)	σ (dynes/cm)							
a	13.00	1.378	79.1	41.08	40.7	37.94	17.2	311	162	35.67
b	7.31	1.370	78.5	5.51	37.1	39.77	28.9	293	188	35.00

o   experimental position of tracer bubble at every frame

———┼——— theoretical predictions - potential flow past an oblate ellipsoid

———•——— theoretical predictions - creeping flow past an oblate ellipsoid

— — — boundary of closed toroidal wake

—•—•—boundary of ellipsoid that fits the bubble cap

1 cm

Re — 17.2

FIGURE 4.17(a)

185.

Re = 28.9

FIGURE 4-17(b)

1 cm
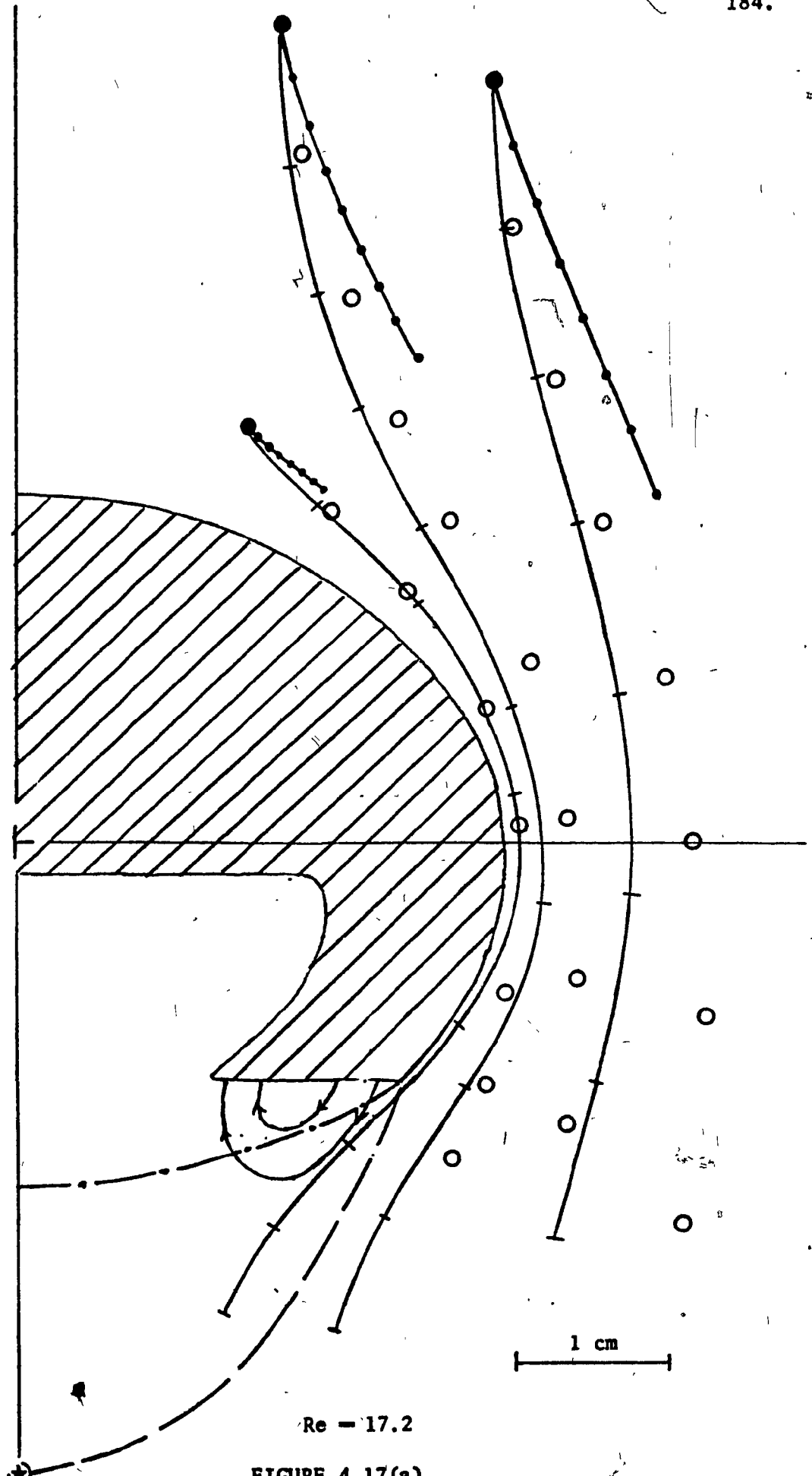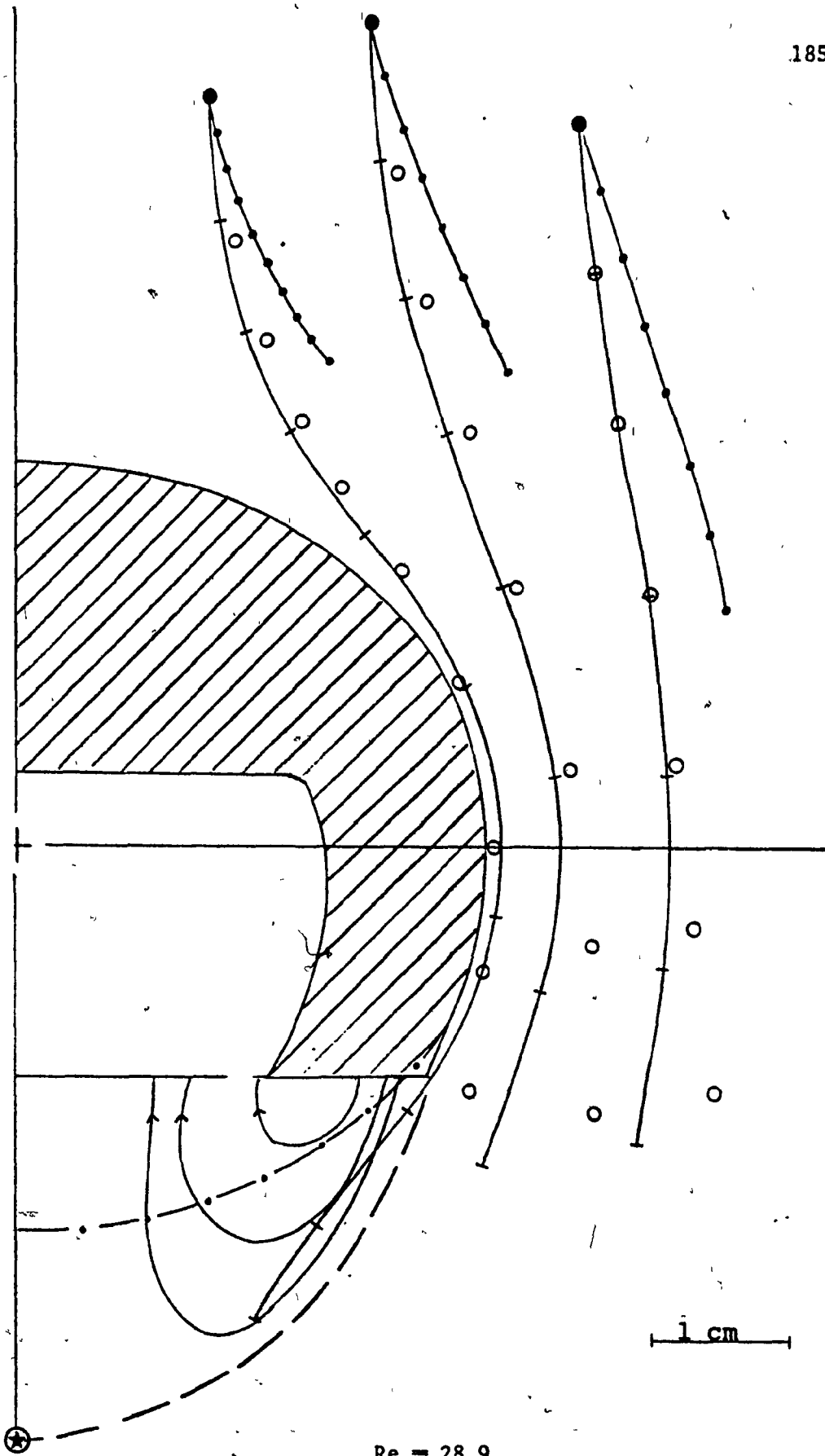
are confined to a thin boundary layer. Fig. 4.16 demonstrates that
Moore's boundary layer theory is successful in predicting the deviation
from potential flow. Further, the good agreement with Moore's theory
implies poor agreement with Parlange's (1970) version of the boundary
layer theory which is significantly different from Moore's over the
forward surface of the bubble.

4.5.2.6 Flow field around skirted bubbles

Fig. 4.17 compares the experimental and the theoretical
streamlines around oblate shaped skirted bubbles at Re — 17.2 and 28.9.
The experimental data for both cases are bracketed by the potential
flow and the creeping flow predictions, however, the potential flow model
shows the better agreement. The enclosed wake extends beyond the tip of
the skirt and is larger than the spheroid that fits the bubble.

4.5.2.7 Transition of closed toroidal wake to open unsteady wake

The critical Re at which the instability in the closed toroidal
wake sets in leading to an open unsteady wake with periodic vortex
shedding, was determined in five solutions. The results are tabulated
in Table 4.9, which shows that the transition occurs around Re — 110 ± 2.
This value is in favourable agreement with the critical value of Re $\sim$ 100,
estimated by Wegener and Parlange (1973).

4.5.2.8 Parameters of the closed toroidal wake

About 30 to 40 long-exposure wake photographs per bubble, some
of which have been presented in Section 4.5.2.3, were taken for about 45
different bubbles in seven different sugar solutions. These photographs

TABLE 4.9 Critical Condition for Transition to Open Unsteady Wake

Liquid Properties				Bubble Data			
μ (Poise)	ρ (g/cm³)	σ (dynes/cm)	M (-)	V (cm³)	U (cm/sec)	Re (-)	Eö (-)
0.615	1.301	76.7	2.39×10^{-4}	2.75	30.21	110.4	50.3
0.840	1.320	77.1	8.20×10^{-4}	4.6	33.95	109.9	71.5
1.00	1.320	77.1	1.62×10^{-3}	7.2	35.71	110.2	96.4
1.30	1.326	77.2	4.59×10^{-3}	11.6	37.94	108.7	133.0
1.36	1.325	77.2	5.50×10^{-3}	13.9	38.46	111.8	149.8

were analysed to obtain the wake shape, its size and the location of the vortex centre. For the case where the experimental conditions were identical, the detailed streamline results presented in Section 4.5.2.3 were used as a cross-check.

Fig. 4.18 shows the effect of Re on the wake width, on the wake height and on the location of the vortex centres all in dimensionless form. With increasing Re the size of the wake increases quite significantly (see Fig. 4.18(a) and (b)); the vortex centres move downstream (see Fig. 4.18(d)) and spread apart in the transverse direction (see Fig. 4.18(c)). Data obtained from Slaughter's (1967) Schlieren photograph of a bubble wake are also included in these figures. The agreement with the present data is fairly good. Available numerical solution results (Masliyah and Epstein 1970) and experimental data for solid spheres (Taneda 1956; Kalra and Uhlerr 1971) and for solid oblate ellipsoids (Masliyah 1972) of aspect ratio 0.5 and 0.2 are also shown for comparison. The experimental data of the present study are well bracketed by the results for solid oblate ellipsoids of aspect ratio 0.5 and 0.2. Moreover, the data show better agreement with the results for solid oblate ellipsoids of aspect ratio 0.2 as Re tends to 100. This is explained by the fact that as Re tends to 100 bubbles become spherical-caps with aspect ratio, i.e. height/width of about 0.223 (see Chapter 3, Fig. 3.8).

The experimental data are fairly well correlated by the following expressions:

$$\frac{w_w}{d_e} = 0.794 \log Re - 0.032 \quad \text{for} \quad 4 \leqslant Re \leqslant 110 \quad (4.5)$$

$$\frac{h_w}{d_e} = 2.303 \log Re - 1.792 \quad \text{for} \quad 8 \leqslant Re \leqslant 110 \quad (4.6)$$

FIGURE 4.18 Effect of Re on the Shape Parameters
of Closed Toroidal Wake

(a) wake width   (b) wake height

(c) & (d) the location of the vortex centres

Present Experiments

Symbol	μ (Poise)	ρ (gm/cc)	σ (dynes/cm)	M (-)
$\diamond$	20.80	1.389	80.0	2.58×10^2
$\blacktriangleright$	13.10	1.378	78.8	4.35×10
$\triangledown$	7.40	1.370	78.7	4.41
$\circ$	5.00	1.359	77.7	9.62×10^{-1}
$\triangle$	3.10	1.349	77.6	1.44×10^{-1}
$\square$	1.30	1.326	77.3	4.58×10^{-3}
$\times$	0.84	1.315	76.8	8.20×10^{-4}

Previous Work

$\odot$ bubble,   Slaughter (1967)

$\bullet$ bubbles,   Hnat & Buckmaster (1976)

— — — solid oblate ellipsoide AR = 0.5 -Masliyah & Epstein (1970),
numerical solution
Masliyah (1972), experimental

——— solid oblate ellipsoide AR = 0.2 -Masliyah & Epstein (1970),
numerical solution
Masliyah (1972), experimental

--------- solid spheres   Taneda (1956), experimental
Kalra & Uhlerr (1972), experimental

FIG. 4.18(a)

FIG. 4.18(b)

FIG. 4.18(c)

FIG. 4.18(d)
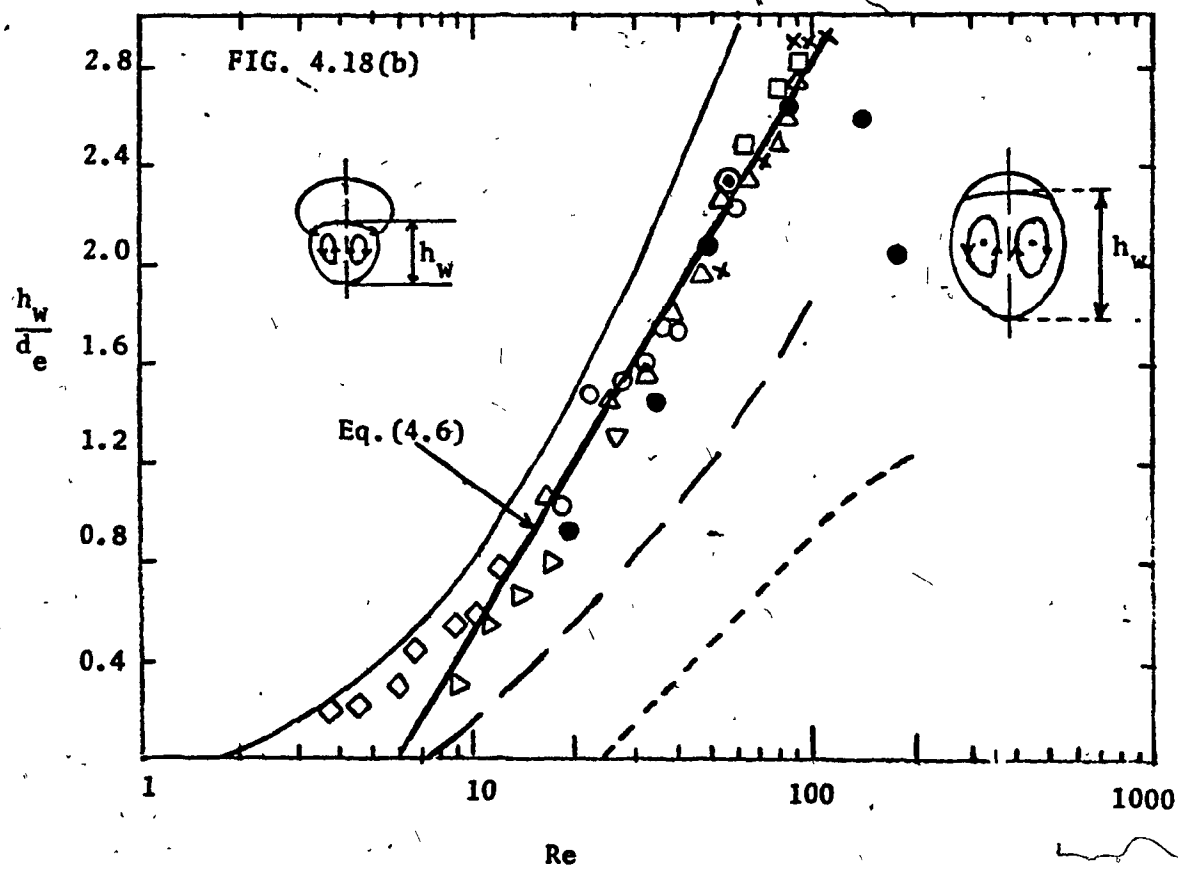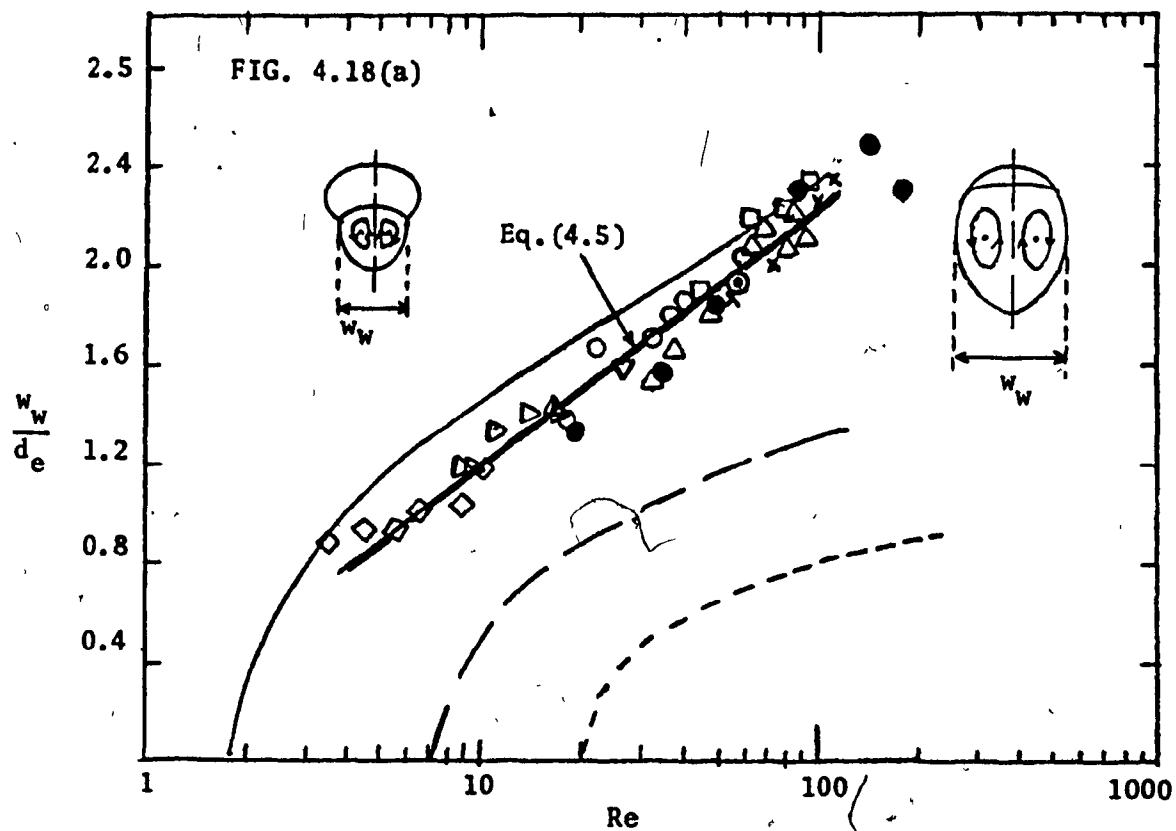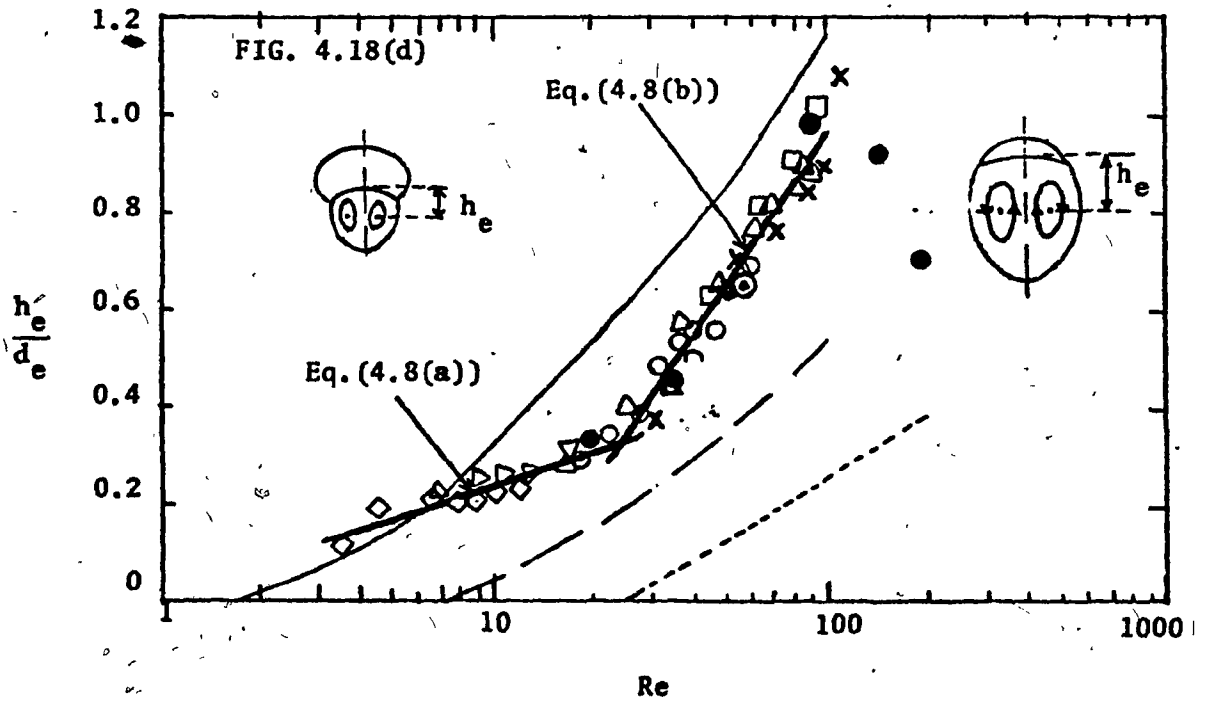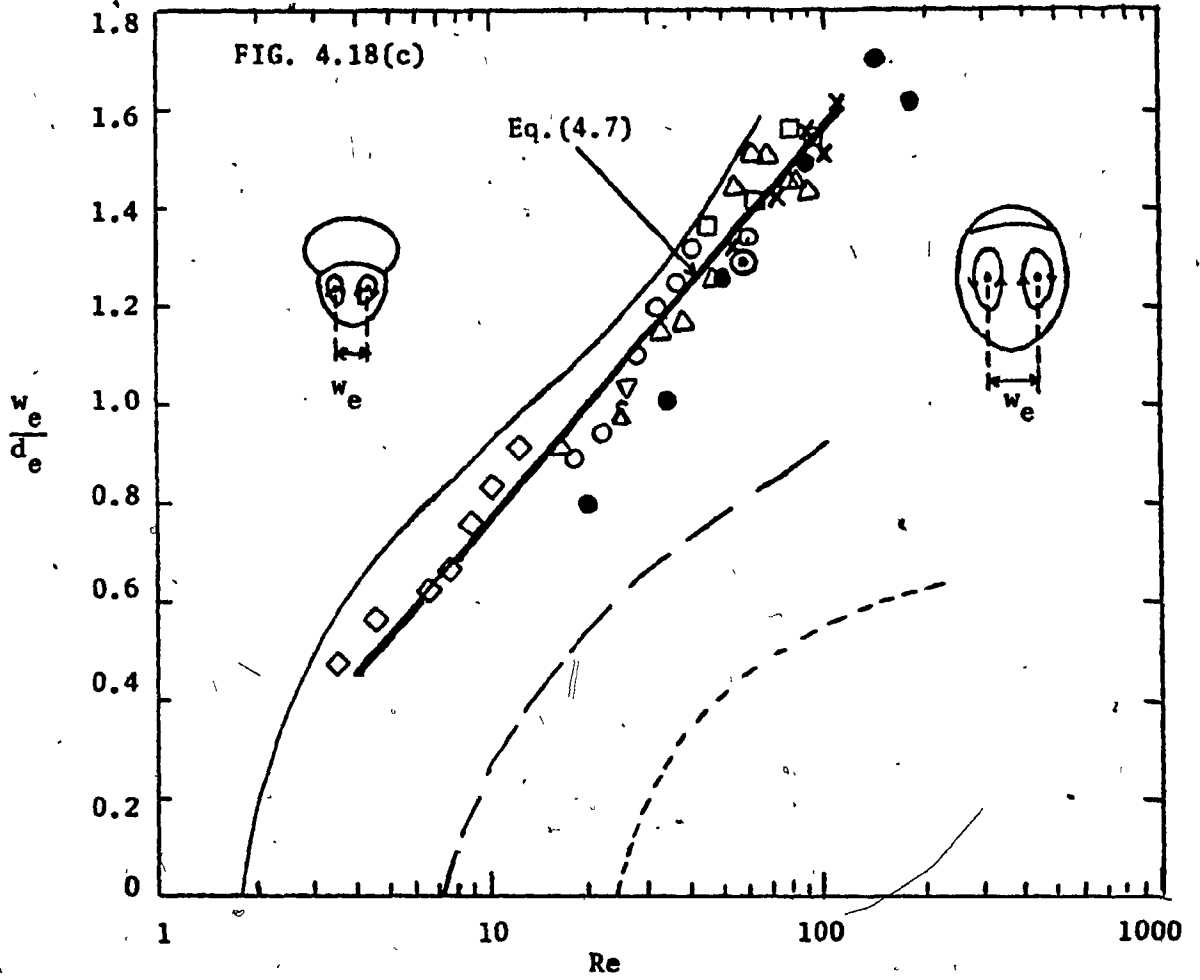
$$\frac{w_e}{d_e} = 0.801 \log Re - 0.049 \quad \text{for} \quad 4 \leqslant Re \leqslant 110 \quad (4.7)$$

$$\frac{h_e}{d_e} = \begin{cases} 0.237 \log Re - 0.003 & \text{for} \quad 3 \leqslant Re \leqslant 25 \quad (4.8(a)) \\ 1.037 \log Re - 1.116 & \text{for} \quad 25 \leqslant Re \leqslant 110 \quad (4.8(b)) \end{cases}$$

Finally, it is of interest to note that the maximum width of the toroidal wake was almost always found to be at the horizontal plane that contained the vortex centres. Further, the distance between the vortex centres when made dimensionless with respect to the width of the wake was found to be constant at 0.7 (± 10%). Surprisingly, this value compares well with the theoretical value of 0.707 for both the Hadamard's spherical vortex and the Hill's spherical vortex.

A sixth order polynomial fitted to the wake boundary was used to calculate the volume of the visible wake assuming axial symmetry. The total wake volume was obtained by adding volume of the indentation* in the base of the bubble to the visible wake volume. The wake volume so obtained was rendered dimensionless with respect to bubble volume and plotted versus Re in Fig. 4.19. Similarly, the volume of the bubble wake observed by Slaughter (1967) was calculated from his Schieren photograph. The result is in agreement with the present data. The experimental data are fairly well correlated by the relationship:

$$\frac{V_w}{V} = 0.04 \, Re^{1.35} \quad \text{for} \quad 3 \leqslant Re \leqslant 110 \quad (4.9)$$

---

* The volume of indentation was estimated using the method described in Chapter 3.
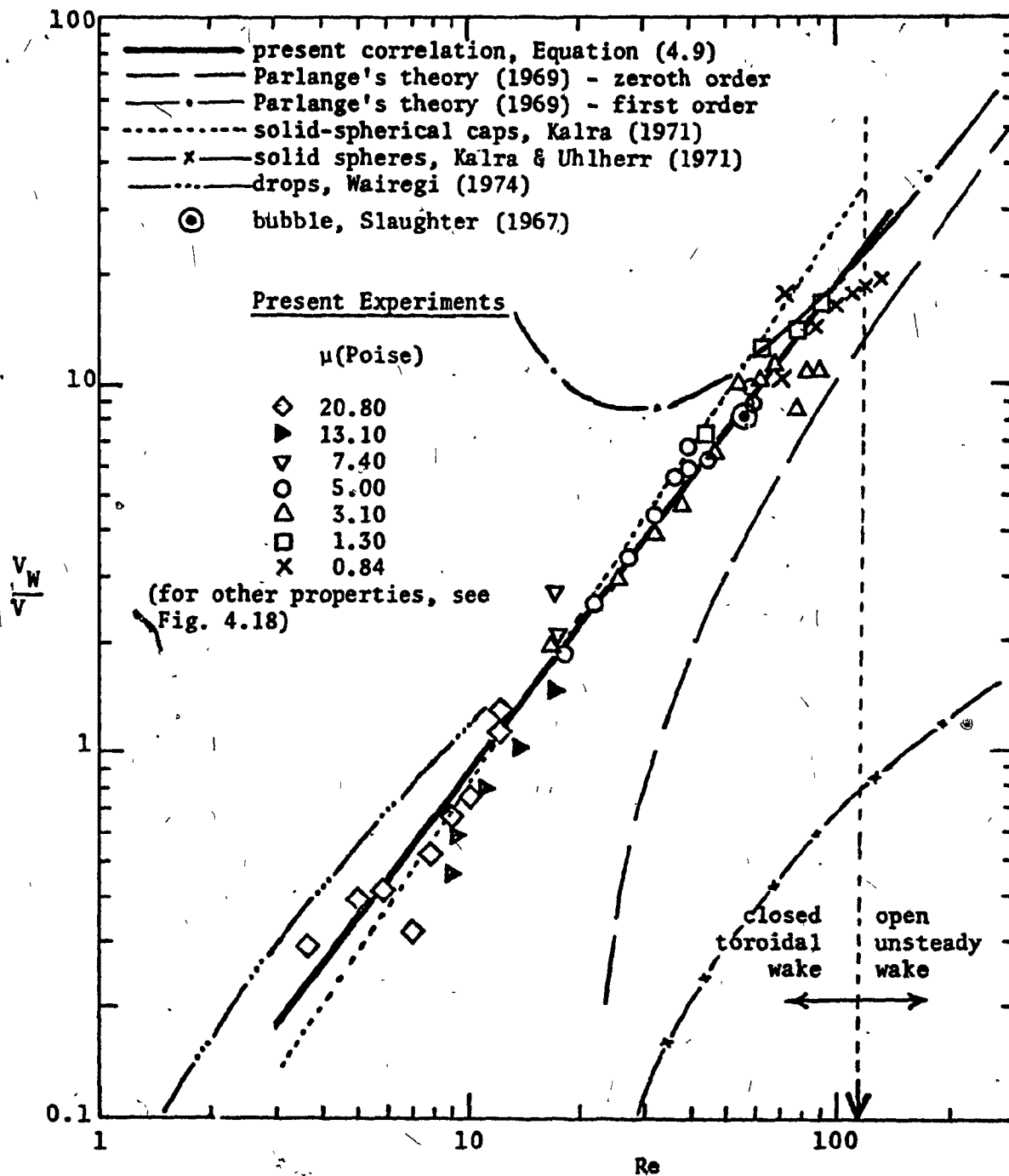
FIGURE 4.19   Effect of Re on Volume of Closed Toroidal Wake

Parlange's (1969) zeroth order theory, Equation (3.26), can be used to predict the rise velocity of the bubble which in turn can be used in Davies and Taylor's equation, Equation (3.22), to predict the radius of curvature of the bubble. By subtracting the bubble volume from the volume of the sphere of this radius we find a zeroth order of prediction of the wake volume. Similarly, another estimate of the wake volume can be obtained from Parlange's first order theory, Equation (3.27), which incorporates Harper and Moore's (1968) boundary layer correction in predicting the bubble rise velocity. These predictions of wake volume are also shown in dimensionless form in Fig. 4.19. The predictions were found to be independent of liquid properties and are only functions of Re. The experimental data lie between the predictions of the two models. At lower Re the assumptions inherent in the Parlange's theory are violated and the predictions diverge from the data, but as Re is increased the agreement improves. An important point worth noting is that at Re $\approx$ 110 a bubble can carry with it as much as 20 times its own volume of liquid in the toroidal wake. Above Re $\geq$ 110 the wake is open and unsteady and the term "wake volume" is meaningless.*

Recently, Kalra (1971) has measured the volume of the closed toroidal wake behing solid spherical-caps of varying aspect ratios (height/base — 0.180 to 1.266). The values of Re at which the gas bubbles

---

* Nonetheless, very recently, Kojima et al (1975) claim to have measured the volume of wake region for turbulent wakes behind air bubbles in water for Re — 2000 to 5000. The wake region was defined as: "a region immediately below the bubble in which the trajectory of a tracer particle was definitely disturbed and the angle between a trajectory and the main flow was almost rectangular." The value of V_w/V exhibited a rather large scatter, owing to difficulty in determining the wake region boundary. The averaged value of V_w/V — 4.7 ± 2 was reported.

have aspect ratios identical to Kalra's solid spherical-caps were
obtained from our shape study results reported in Chapter 3 (see Section
3.4.2.3). The dimensionless wake volumes which a solid spherical-cap
would have at these Re were then obtained from a graph of Karla's data
plotted as dimensionless wake volume versus Re with the aspect ratios of
the cap as a parameter. The results of these computations are also shown
in Fig. 4.19. The agreement with the present data is excellent. The
reason for this agreement is that for a spherical-cap body with aspect
ratio ≤ 0.6 the separation always occurs at the sharp rear edge (Kalra
and Uhlherr 1971) and is thus independent of the boundary conditions at
the frontal surface which are usually different for the solid cap and
the gas cap. _

The data of wakes behind oblate-ellipsoidal-cap drops of
chloroform falling in 26.5 Poise sugar solution (Wairegi 1974) are included
in Fig. 4.19 for comparison. The agreement with present data is quite
good bearing in mind that for the case of drops the physical properties
of the dispersed phase would effect the size of the wake to some extent.

For comparison, the wake volume data for solid spheres (Karla
and Uhlherr 1971) are also shown in Fig. 4.19. The present data for
bubbles are well above the solid sphere data, undoubtedly, due to the
considerable deformation from the spherical shape of bubbles in high M
liquids at these values of Re.

4.5.2.9 Circulation within the closed toroidal wake

From the experimental streamlines within the closed toroidal
wake and around its immediate surroundings, the velocity distribution
along the equator containing the vortex centres was obtained. Results

of five different experiments for a spherical-cap bubble at Re $-$ 94.0
are shown in dimensionless form in Fig. 4.20. The reproducibility of
the data is well demonstrated in this figure. Half the width of the
wake was selected as the most logical length scale for making the hori-
zontal distance from the axis of symmetry dimensionless, since it marks
the boundary between the closed toroidal wake and the external flow.
Theoretical predictions of Hill's spherical vortex (see Table 4.6),
Hadamard's spherical vortex (see Table 4.1), Harper and Moore's boundary
layer correction to Hill's spherical vortex (see Equation (4.1)), and
Parlange's boundary layer correction to Hill's spherical vortex (see
Equation (4.2)) are also compared in this figure. Within the closed
toroidal vortex the data lie between the Hadamard's and Hill's spherical
vortex. The agreement with Harper and Moore's correction is remarkably
good if one considers that the shape of the toroidal wake is not exactly
spherical and that the top part of the sphere is occupied by the gas
bubble. Parlange's boundary layer correction somewhat overpredicts the
circulation within the wake. Just outside the toroidal wake the experi-
mental dimensionless velocity exceeds unity in absolute value and
approaches the potential flow prediction from above. For a dimension-
less distance, $2x/w_w$, greater than about 1.5, the potential flow model
represents the data very well.

Fig. 4.21 shows the variation of the experimental dimension-
less velocity profiles with Re for six bubbles with Re ranging from 13.3
to 94.0. Within the closed toroidal vortex increasing deviation from
the Hill's spherical vortex is observed with decreasing Re, as expected.
For the external flow the deviation from the potential flow extends to
a larger distance as Re is decreased, indicating an increase in the
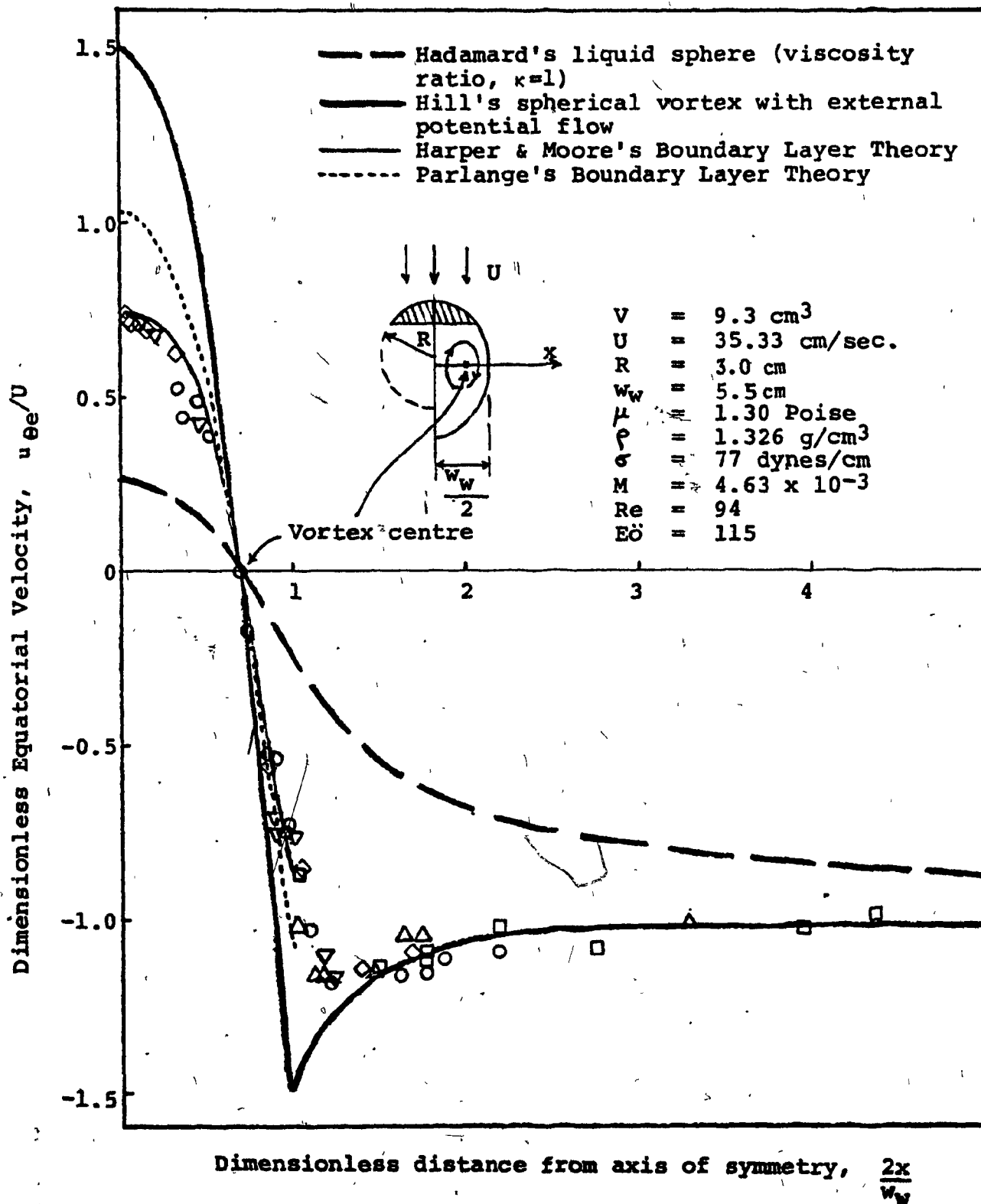
FIGURE 4-20: <u>Equatorial velocity distribution for closed toridal wake</u>

thickness of the liquid boundary layer around the closed toroidal wake. The boundary layer thickness ranges from approximately 0.2 semi-wake widths at Re = 94.0 to 2.5 semi-wake widths at Re = 13.3.

Following Huong and Kintner (1969) we define the volumetric circulation rate, Q, as the volumetric flow through the stagnation ring:

$$Q = \int_0^{R_W/\sqrt{2}} 2\pi r u_{\theta e} \, dr \qquad (4.10)$$

where R_W is the radius of the wake at the stagnation ring and $u_{\theta e}$ is the equatorial velocity. For a fully circulating Hadamard fluid sphere it can be shown that the circulation rate is given by:

$$Q_{Ha} = \frac{\pi R_W^2}{8} \frac{U}{1+\kappa} \qquad (4.11)$$

Similarly, for Hill's spherical vortex,

$$Q_{Hi} = \frac{3\pi R_W^2 U}{8} \qquad (4.12)$$

A sixth order polynomial was fitted through the experimentally measured equatorial wake velocity profiles for several bubbles with Re ranging from 13.3 to 94.0, and was subsequently used to find the experimental values of volumetric circulation rate by integration assuming axial symmetry. Two separate estimates of the circulation rate were made; one by integrating the velocity profile from the axis to the vortex centre and the other by integrating the velocity profile from the vortex centre to the outer boundary of the toroidal wake. Excellent agreement was found between the two estimates. This provides further evidence of the
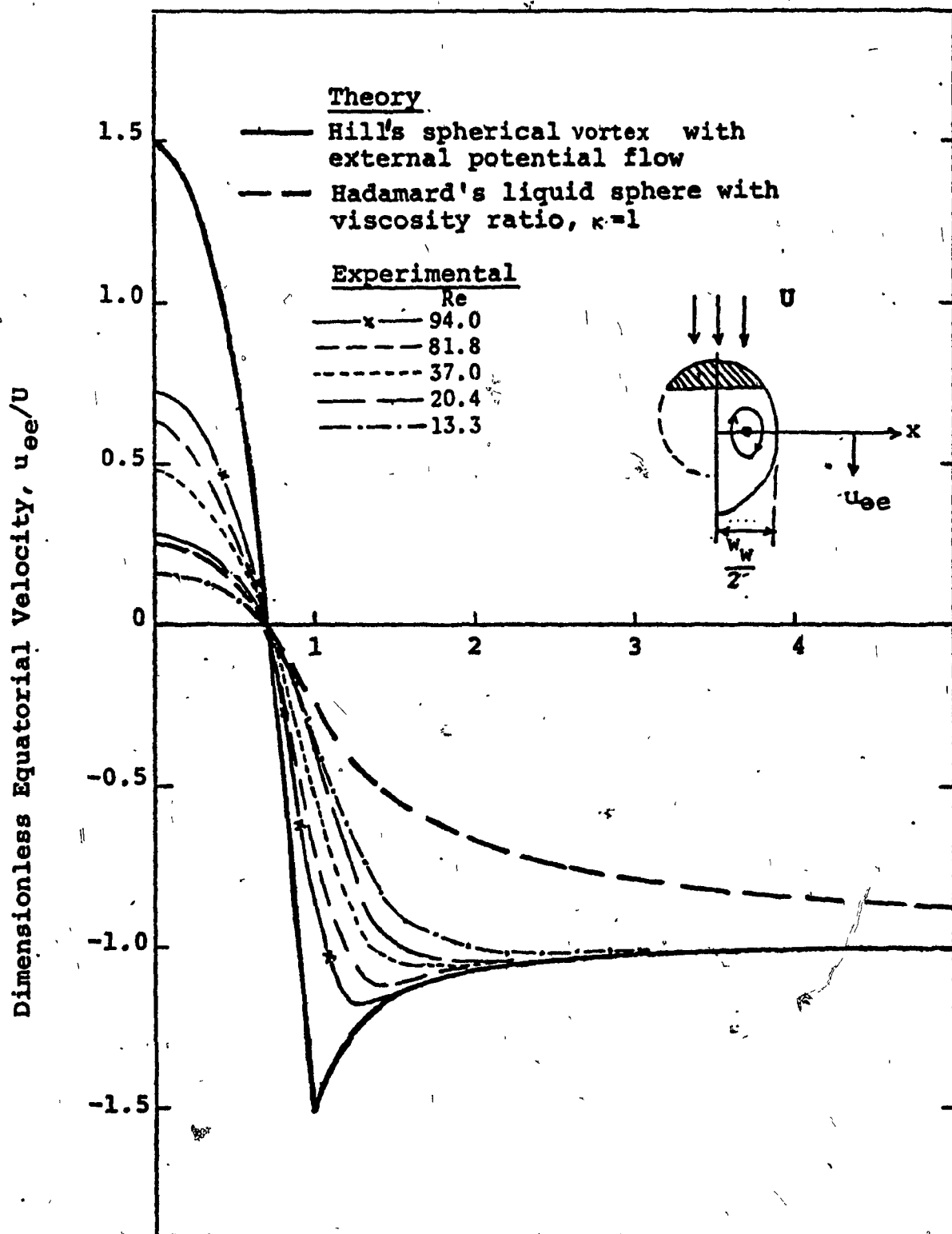
FIGURE 4-21 : **Variation of equatorial velocity distribution for closed toroidal wake with Re**

accuracy of the experimental technique for measurement of velocities.

The volumetric circulation rates so obtained were made dimension-less with respect to the circulation rate of Hadamard spherical vortex, Equation (4.11), with the viscosity ratio, $\kappa = \frac{\mu'}{\mu} = 1$. The results are plotted versus Re in Fig. 4.22. The theoretical predictions of the models cited earlier in Section 4.4 are also shown. The data are well bracketed by Hill's and Hadamard's spherical vortex. Harper and Moore's correction to Hill's spherical vortex shows good agreement at Re $\geq$ 45, while Parlange's correction overpredicts the circulation rate.

4.5.3 Liquid flow field far away from a bubble

4.5.3.1 Drift of liquid caused by a rising bubble

When a bubble moves through an incompressible liquid, it induces a drift* in the liquid, such that the final positions of small elements of the liquid are different from the initial positions. This phenomena is well illustrated by the two photographs in Fig. 4.23, taken with a stationary camera. A row of hydrogen tracer bubbles generated before the passage of the bubble (see Fig. 4.23(1)) is stretched out showing the drift of the liquid caused by the passage of the bubble (see Fig. 4.23(2)). It is this row of hydrogen tracers that appear as a tail

---

* The "drift" has a very important significance in hydrodynamics in that the drift-volume enclosed between the initial and final positions of the fluid particles, is equal to the volume corresponding to the well known "hydrodynamic mass" or the "added mass" of the body, i.e. the mass of fluid to be added to that of the body in calculating its kinetic energy. An excellent exposé of the concept of drift has been presented by Darwin (1952) and Lighthill (1956). The practical aspects of drift have been discussed for a fluidized bed by Rowe and Partridge (1963) and for a liquid column by Vickery (1965).
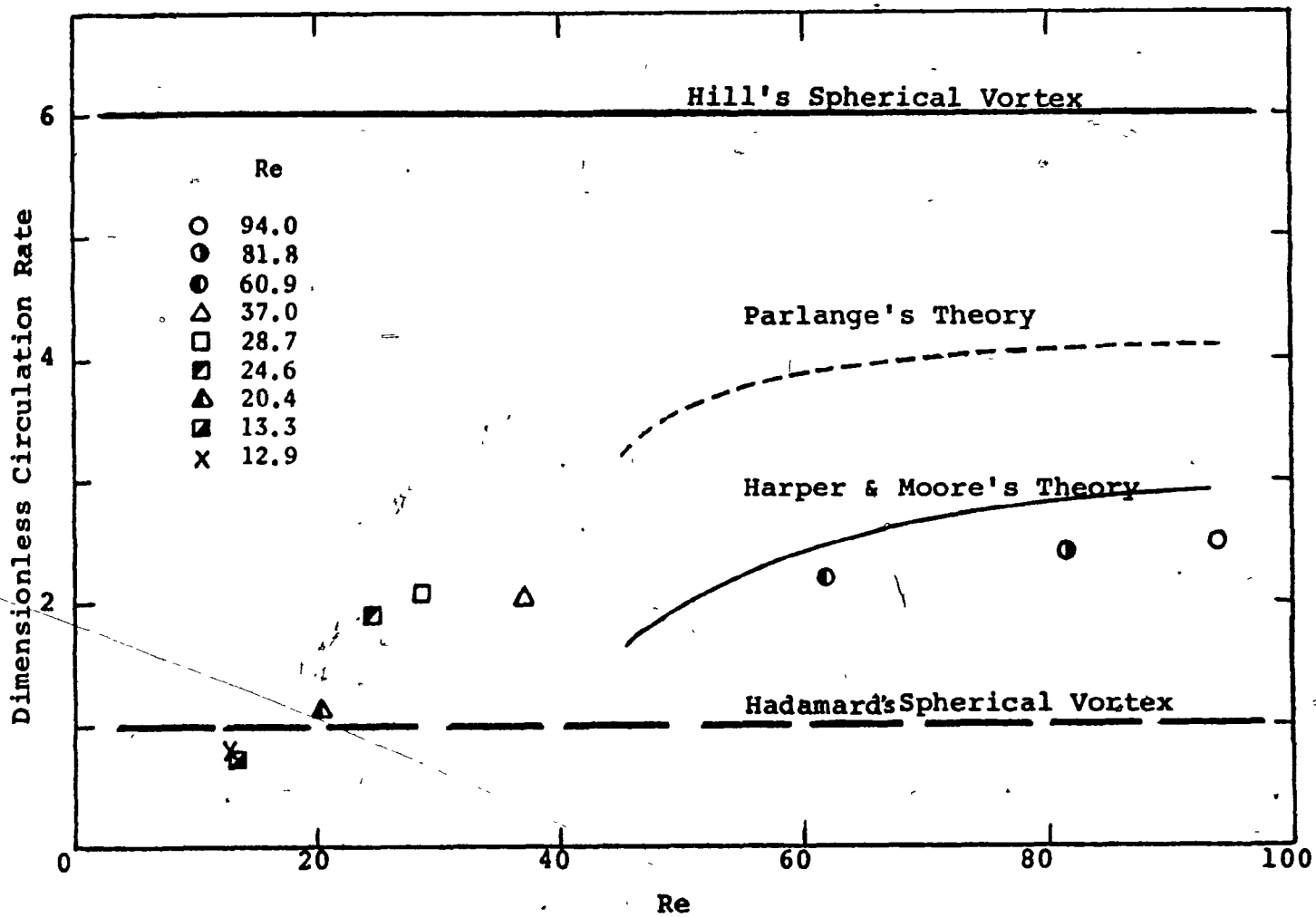
FIGURE 4-22: Comparison of experimental circulation rate in the closed toroidal wake with theory.

FIGURE 4.23 The Drift of Liquid Caused by
the Passage of a Bubble

Bubble Data: V $=$ 55.5 cm^3

U $=$ 36.6 cm/sec

Re $=$ 11.7

$E\ddot{o}$ $=$ 383

Liquid Properties: μ $=$ 20.60 Poise

ρ $=$ 1.383 g/cm^3

σ $=$ 79.5 dynes/cm

M $=$ 2.54x10^2
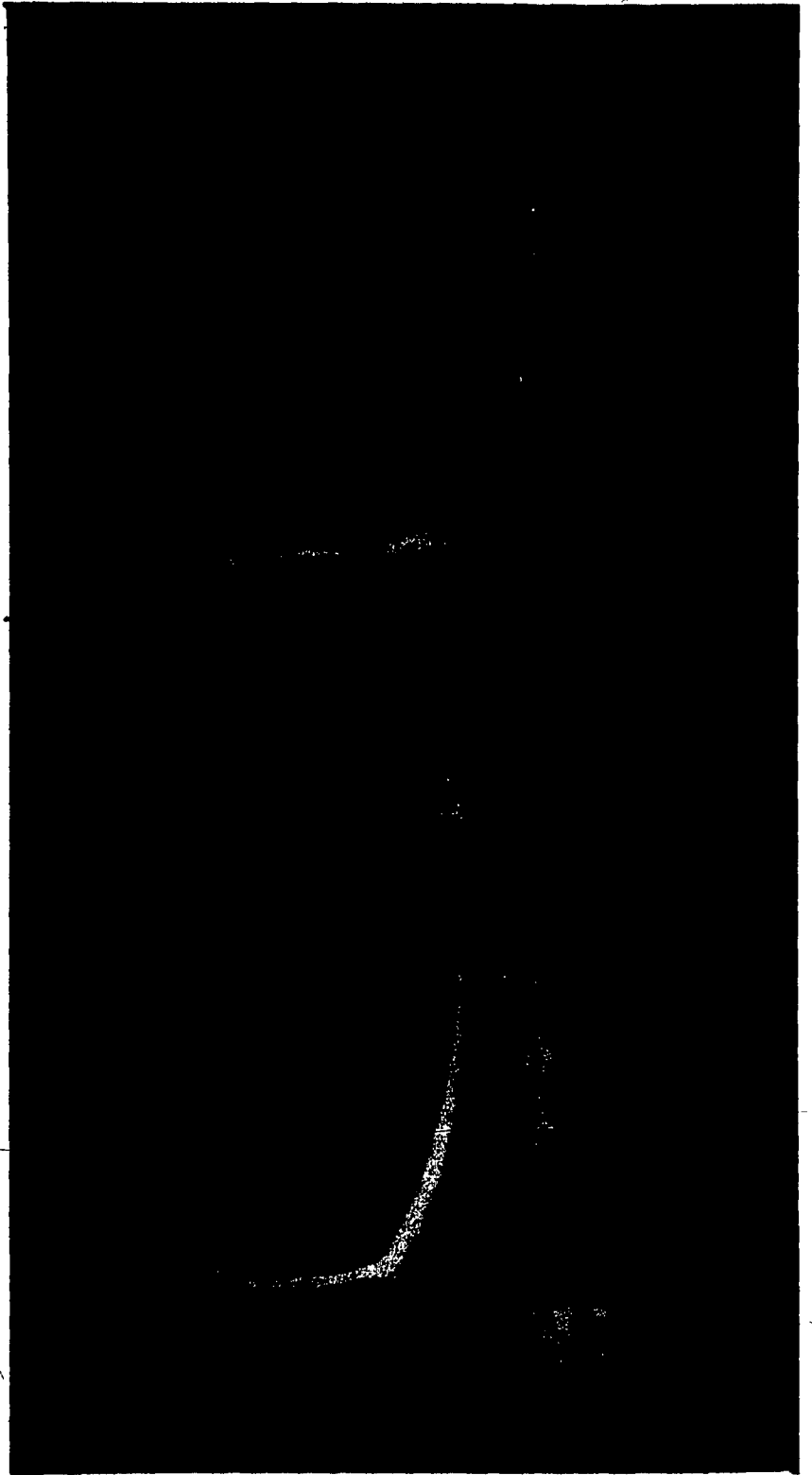
(or two tails) in some of the wake photographs (for example, see Fig. 4.5(1)). presented in Section 4.5.2.3. Note that most of the upward drift occurs directly behind the bubble, while the extent of upward motion decreases rapidly in the horizontal direction. In a finite container, continuity considerations dictate that there should be a negative (or downward) drift equal in magnitude to the central positive (or upward) drift and Darwin (1952) pointed out that this downward flow occurred near the walls of the container. This is clearly shown in Fig. 4.23(2) where a slight downward peak is seen at about 3 cm. from the inside wall of the column.*

Figs. 4.24(a) and 4.25(a) show a detailed quantitative measurement of upward drift of liquid for a 9.3 cm^3 bubble in two sugar solutions at Re = 2.47 and 94.0, respectively. The following points are noteworthy.**

(i) The influence of a bubble on the liquid in the horizontal direction decreases as Re increases.

(ii) Except at very low Re where the bubble is spherical and follows the Hadamard-Rybczynski theory, fore and aft symmetry is never observed. This asymmetry increases as Re increases.

(iii) The liquid motion induced by a rising bubble is considerably stronger behind it than ahead of it.

(iv) When a bubble plus its toroidal wake passes a horizontal plane the maximum horizontal displacement of the liquid

---

* Here the left end of the probe just touches the inner wall so that the end of the row of tracer bubbles marks the position of the inner wall. The horizontal bars on the vertical scale are 2 cm. apart.

** Many experiments of this type were conducted but only two of them are reported here in detail for illustrative purpose. However, the general conclusions mentioned here are based on more than the data presented in Figs. 4.24(a) and 4.25(a).

position of tracer bubbles
at frame no.

40
35
30
25
20
15

Position of bubble nose
at frame no.

$V = 9.3 \text{ cm}^3$
$\mu = 28.23 \text{ Poise}$
$\rho = 1.384 \text{ g/cm}^3$
$\sigma = 80.0 \text{ dynes/cm}$
$M = 8.48 \times 10^3$
$U = 19.10 \text{ cm/sec}$
$Re = 2.47$
$Eo = 116$
$S = 35.0 \text{ frames/sec}$

40
35
30
25
20
15
10
5

boundary of ellipsoide
that fits the bubble

boundary of closed
toroidal wake

-10
-15
-20
-40

-10

-15
-20
-40

1 cm

● indicates position of tracer bubble at frame no. zero

⊗ vertex centre and stagnation point

FIGURE 4.24(a) Experimental Pathlines for an Oblate-Ellipsoidal-Cap Bubble

Position of bubble
nose at frame no. ————→ 20

○   experimental data

——•—— prediction - potential flow
        around oblate ellipsoide

——•—— prediction - creeping flow
        around oblate ellipsoide

Frame no. is indicated beside
the points.

For experimental conditions see
Fig. 4.24(a)

1 cm
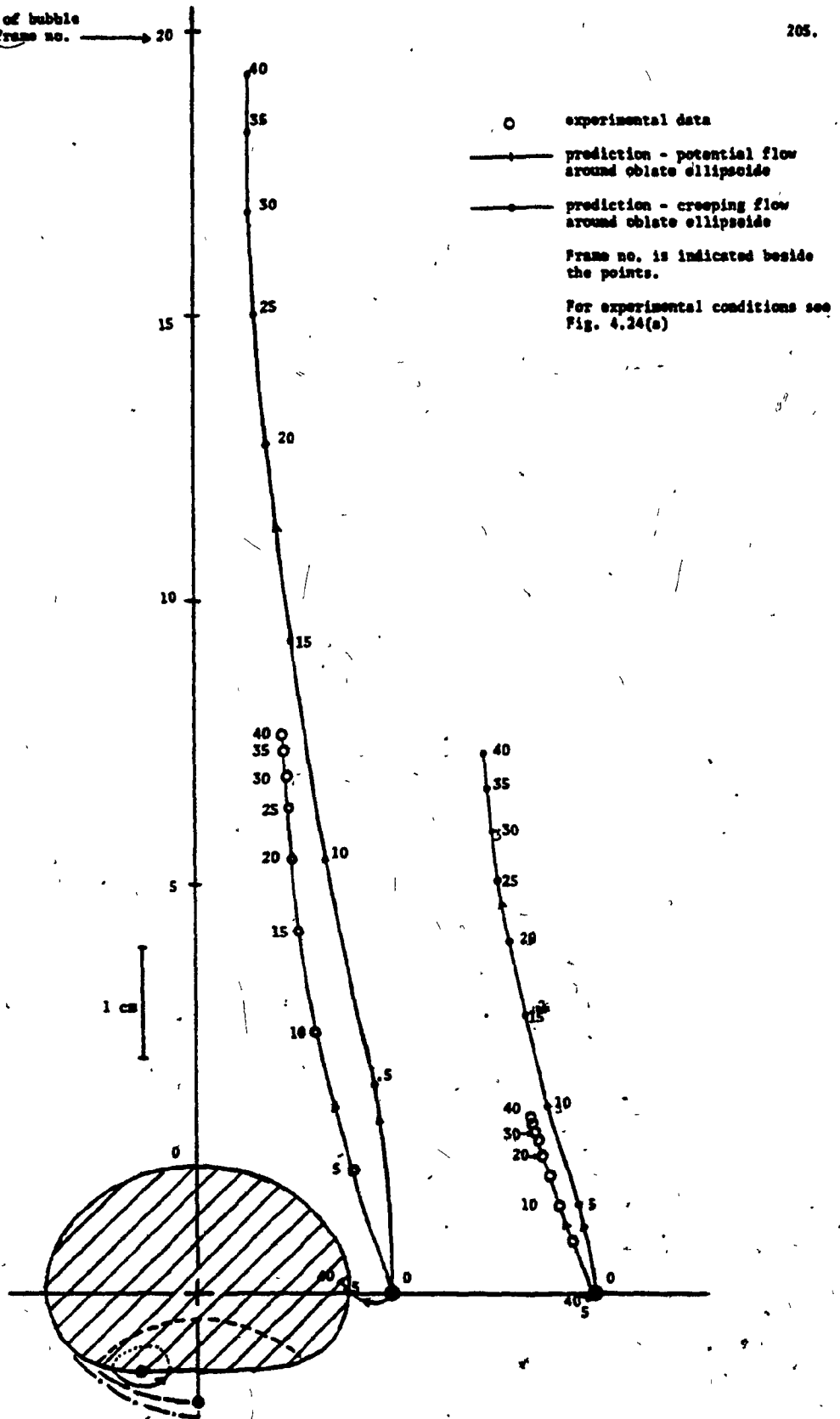
FIGURE 4.24(b)   Comparison of Experimental and Theoretical Pathlines for an
Oblate Ellipsoidal-cap Bubble

occurs when the maximum width of the moving unit, i.e. the bubble plus its toroidal wake, passes this plane.

(v) The scale of disturbance decreases with increasing Re in agreement with the theoretical predictions of the low Re viscous flow equations such as Stokes, Hadamard-Rybczynski and Oseen equations in contrast to the high Re potential (or inviscid) flow equation.

(vi) For low Re the pathlines are not looped (see Fig. 4.24(a)) as opposed to high Re where they exhibit looping (see Fig. 4.25(a)). This is in agreement with the creeping flow theories such as Stokes and Hadamard-Rybczinski in which the velocity component in vertical direction, u_y, is always positive (see Table 4.1) and thus no looping is predicted. For potential flow, however, u_y, is negative in some portion of the flow field, thus looping is predicted.

(vii) For bubbles with an unsteady open wake (i.e. Re $\gg$ 110) essentially steady pathlines are observed ahead of the bubble but behind it the pathlines are unsteady.

In Fig. 4.24(b) the experimental pathlines are compared with the predictions of potential flow and creeping flow around a solid oblate ellipsoid that fits the bubble cap. The data lie between these two models as expected.

Fig. 4.25(b) compares the experimental pathlines with the predictions of potential flow and Hadamard-Rybczinski flow around the sphere that fits the cap. In the latter model the presence of the gas cap was neglected and it was assumed that the sphere consisted of the same liquid as the external liquid, i.e. $\mu'/\mu = 1$. The data are bracketed by these

Positions of tracer bubble ● at frame no.

Position of bubble nose at frame no.

40

35

5

30

4

25

3

2

20

1

15

0

-1

10

boundary of sphere that fits the cap

-2

-3

-4

-5

boundary of closed toroidal wake
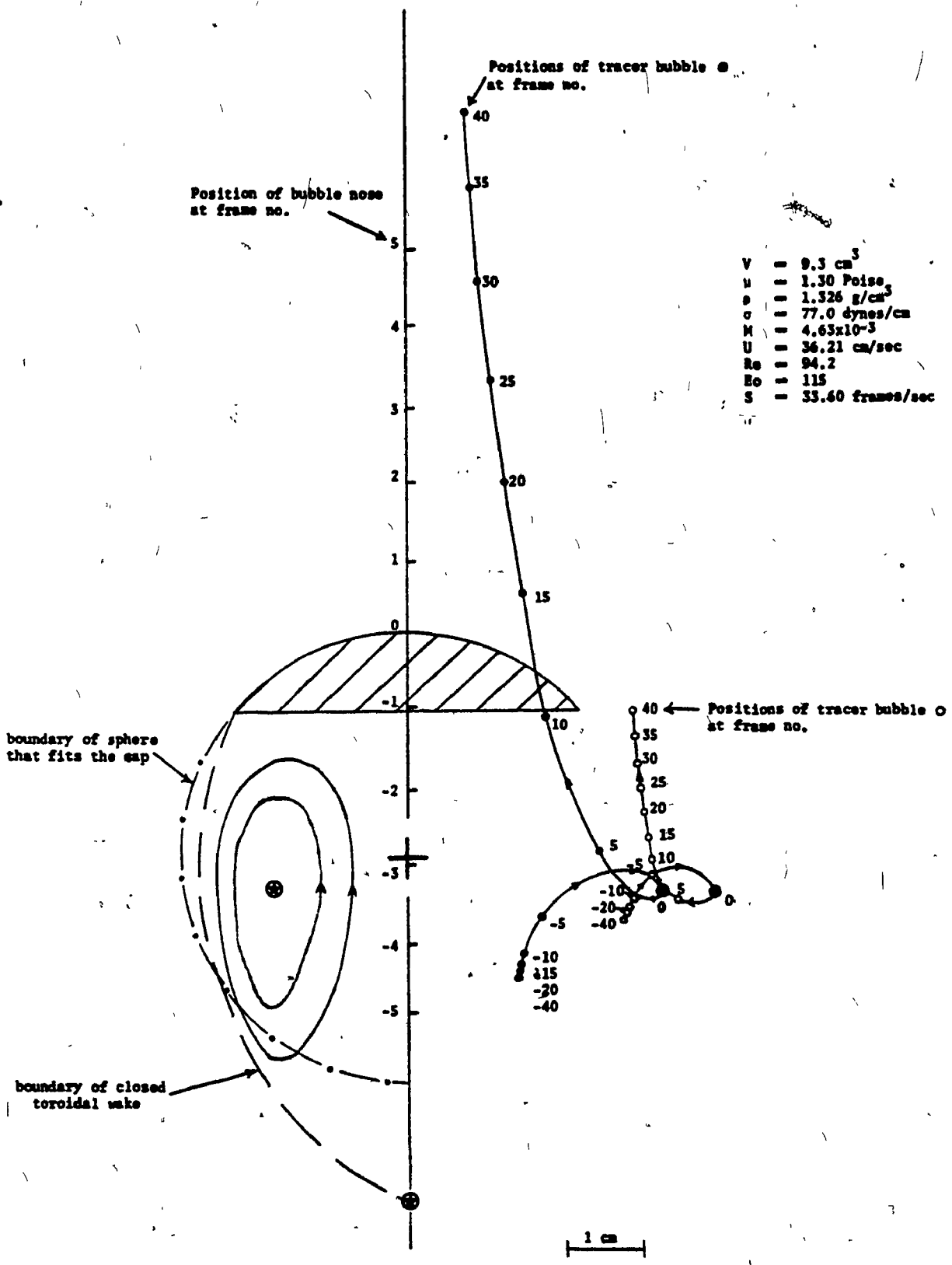
V = 9.3 cm^3
μ = 1.30 Poise
ρ = 1.326 g/cm^3
σ = 77.0 dynes/cm
M = 4.63x10^{-3}
U = 36.21 cm/sec
Re = 94.2
Eo = 115
S = 33.60 frames/sec

40 ← Positions of tracer bubble ○ at frame no.

35

30

25

20

15

10

5

5

10

-5

-10

-20

-40

0

-5

-10

15

-20

-40

1 cm

● indicates position of tracer bubble at frame no. zero;

⊕ vortex centre and stagnation point

FIGURE 4.25(a) Experimental Pathlines for a Spherical-cap Bubble

Position of bubble
nose at frame No.

⊚ indicates position of the tracer bubble
at frame no. zero

● ; ○ experimental data

prediction - potential flow around a sphere

prediction - Hadamard liquid sphere with $\kappa = 1$

Frame no. is indicated beside the points.

1 cm
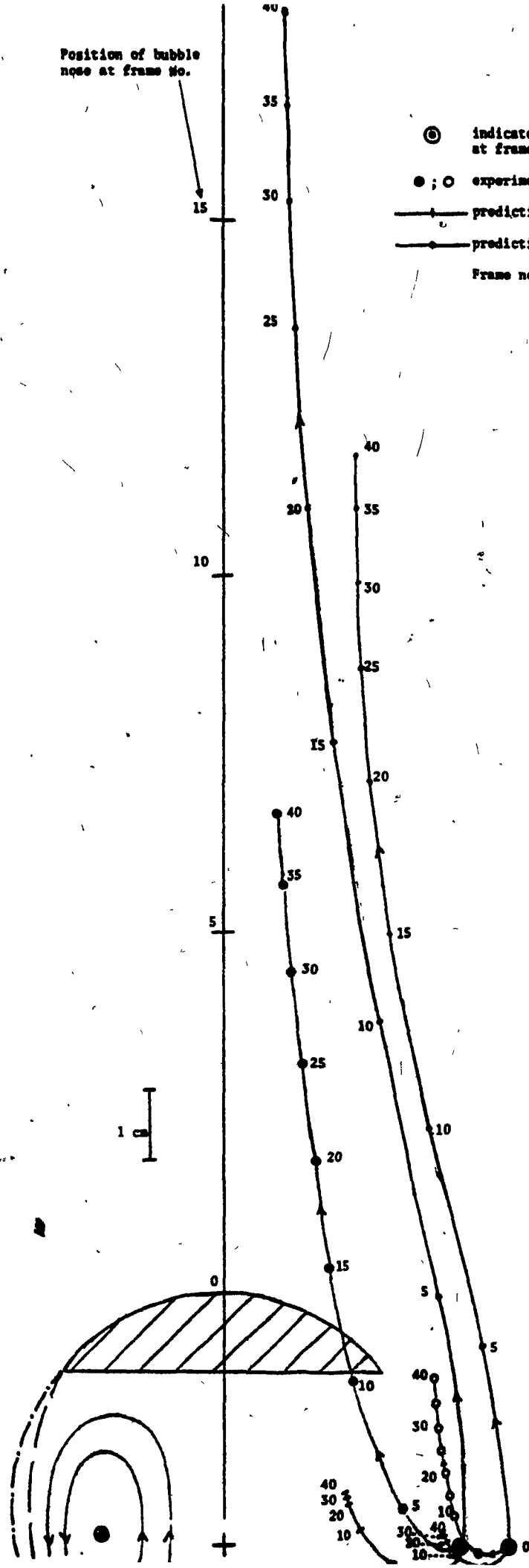
FIGURE 4.25(b) Comparison of
Experimental and
Theoretical pathlines
for a spherical-cap
bubble

two models but show favourable agreement with neither. The Hadamard-Rybczynski theory overpredicts the liquid motion even if the sphere was gas.* Similar results were obtained for many other spherical-cap bubbles. Thus, no simple model satisfactorily describes the flow downstream from the bubble. This will be further demonstrated in the next section.

4.5.3.2 Liquid velocity downstream of the bubble

The following method was used to measure the centre-line wake velocity downstream of the closed toroidal wake. The ciné-film taken with a stationary camera recorded the motion of the tracer bubbles induced by the passage of a bubble. These images were analysed frame by frame. From several repeated experimental runs it was possible to find a tracer bubble that moved behind the bubble along the axis of rise. Typical results are presented in Fig. 4.26 which shows the position of the bubble nose, X_B, as well as the position of a tracer particle, X_p, measured from a common reference point as a function of time. The bubble position data are well represented by a straight line confirming the constancy of the rise velocity. The tracer bubble falls farther behind with time which implies decreasing velocity in the wake with the distance downstream from the bubble.

The centre-line wake velocity, W, and the downstream distance, L, measured from the nose of the bubble are given by:

---

* To preserve clarity the theoretical prediction of this case is not shown.
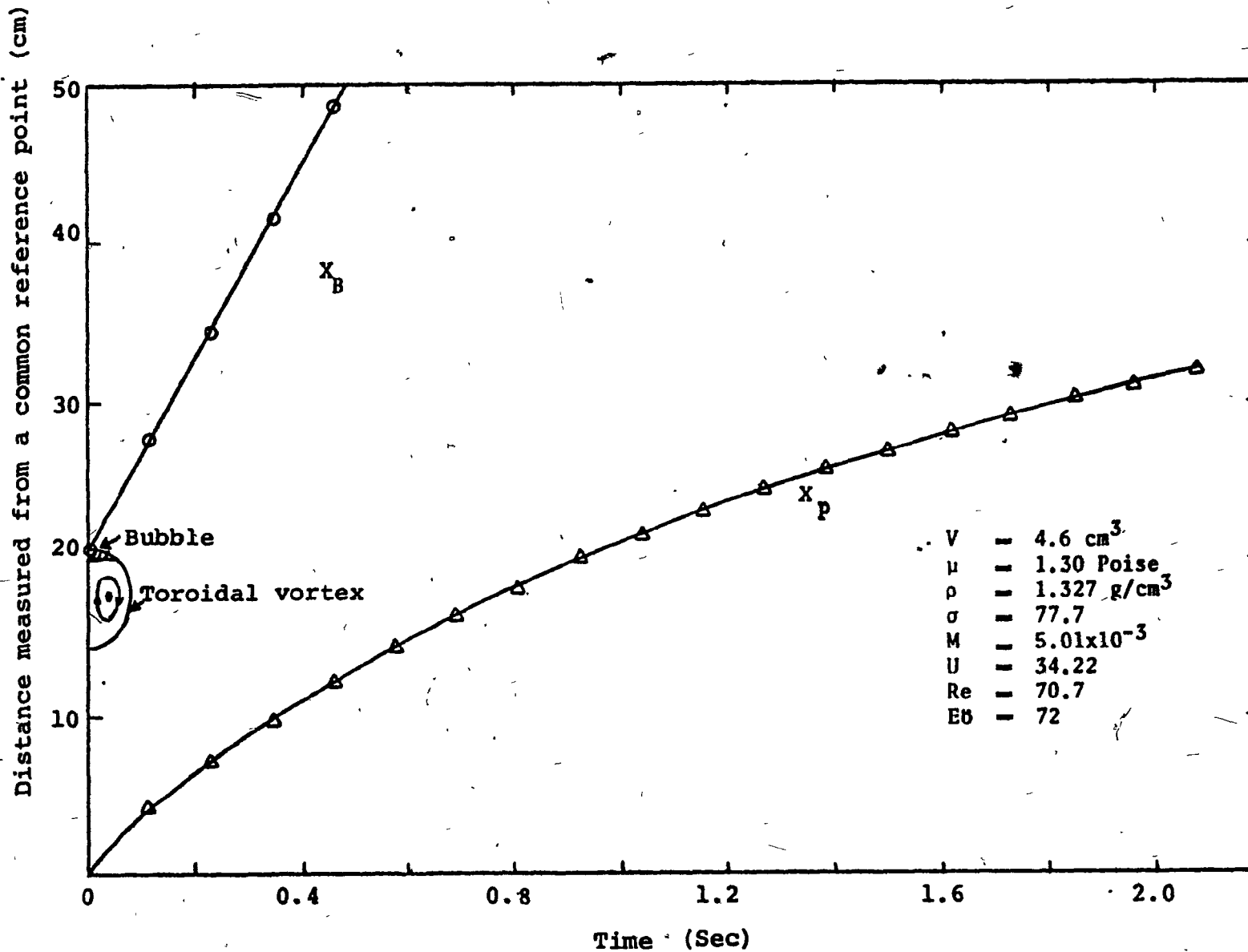
FIGURE 4-26 : Displacement versus time for a bubble and a tracer particle located in the wake along the centre-line.

$$W = \frac{dX_p}{dt} \qquad (4.13)$$

and

$$L = X_B - X_p \qquad (4.14)$$

In order to determine the centre-line wake velocity, the experimental position-time data were differentiated numerically by the "moving strip technique" (Hershey et al 1967). The details of this technique are presented in Appendix D. The results of this computation are presented in Fig. 4.27. The centre-line wake velocities inside the toroidal vortex and just below it were obtained from the moving camera experiments reported in Section 4.5.2. The data from these two types of experiments are in good agreement. The velocity at stagnation points C and B (see Fig. 4.27) is equal to the rise velocity (34.22 cm/sec) of the bubble. The velocity inside the toroidal vortex is greater than the bubble rise velocity, with its maximum value (52.2 cm/sec) occurring at point F located in the same horizontal plane as the stagnation ring of the toroidal vortex. Below the stagnation point B the centre-line wake velocity gradually decays.

Fig. 4.28 shows some of the centre-line wake velocity results for bubbles having Re from 14.9 to 70.7 in dimensionless form. The dotted portions of the curves going up to $W/U = 1$ were obtained from the moving camera experiments. Data for other bubbles (not shown) of different sizes and in sugar solutions of different physical properties but having almost the same Re were in excellent agreement, which imply that the dimensionless wake velocity is only a function of Re just like the bubble shape (see Chapter 3) and the wake parameters (see Section 4.5.2.8). As Re is increased the viscous effects downstream of the bubble and its toroidal

Point F

50

X Data from moving camera experiments
O Data from stationary camera "

$V = 4.6 \ cm^3$
$U = 34.22 \ cm/sec.$
$Re = 70.7$
$E\ddot{o} = 72$
$M = 5.01 \times 10^{-3}$

Stagnation Point A
Stagnation Point C
Stagnation Point B

40

Centre-line wake velocity, W (cm/sec.)

30

Closed Toroidal Vortex

20

10

0   20   40   60   80

Distance from Nose, L (cm)
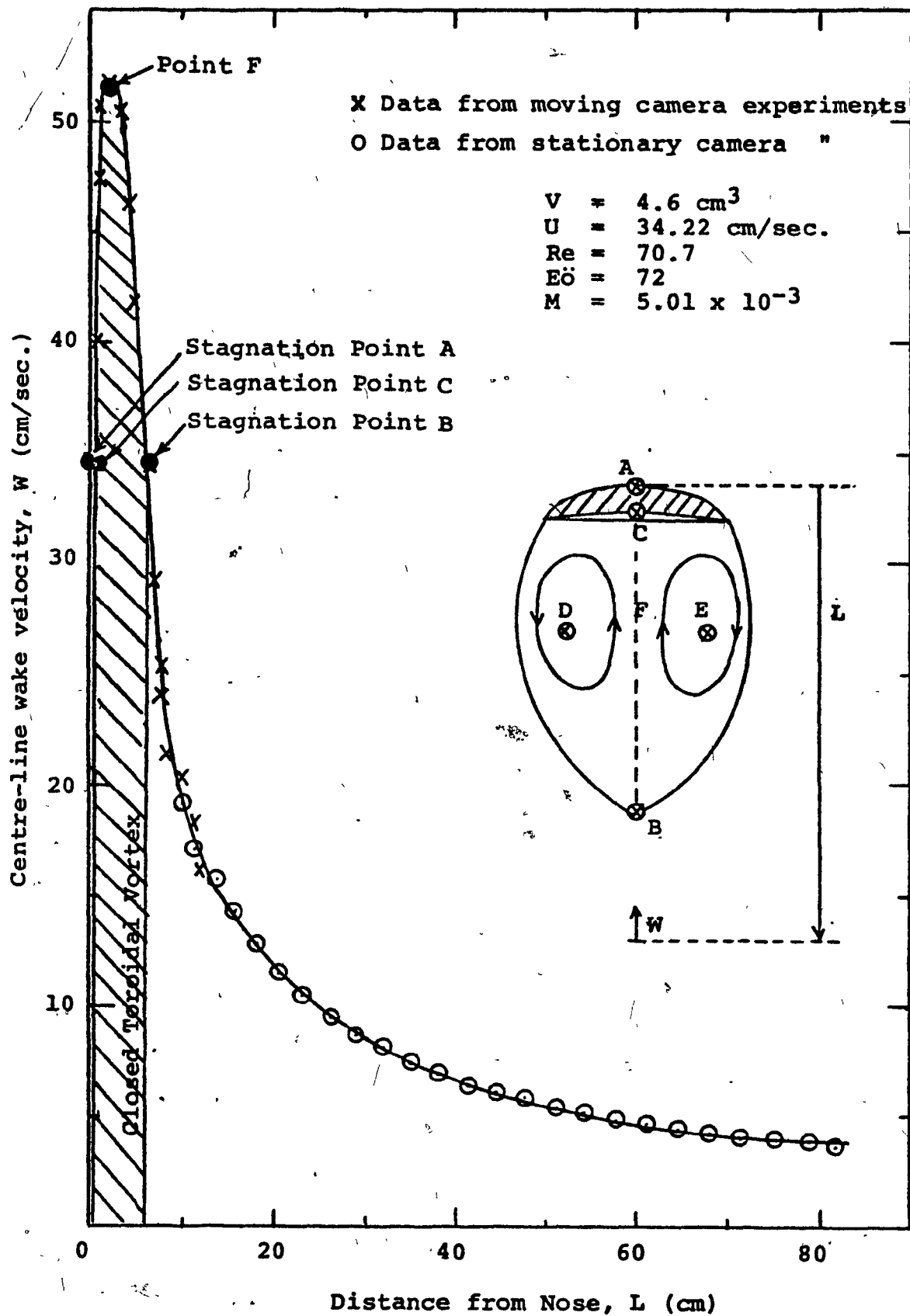
FIGURE 4-27: <u>Measured centre-line wake velocity behind a spherical-cap</u>
<u>bubble.</u>

FIGURE 4.28   Measured Dimensionless Centre-line Wake Velocity
Behind Oblate-Ellipsoidal-Cap and Spherical-Cap Bubbles

	μ (Poise)	ρ (g/cm^3)	σ (dynes/cm)	M (-)	V_3 (cm^3)	d_e (cm)	U (cm/sec)	Re (-)	Eδ (-)
$\triangledown$	13.00	1.378	78.8	4.16×10	27.8	3.76	37.23	14.9	242
$\diamondsuit$	7.50	1.370	78.7	4.65	13.9	2.98	35.27	19.2	152
$\triangle$	5.00	1.357	77.7	9.63×10^{-1}	9.3	2.61	32.62	23.1	116
$\triangledown$	7.50	1.370	78.7	4.65	27.8	3.76	42.55	29.2	241
$\bigcirc$	5.00	1.357	77.7	9.63×10^{-1}	18.5	3.26	38.62	34.4	185
$\square$	1.30	1.327	77.3	5.01×10^{-3}	4.6	2.06	34.22	70.7	72

Dimensionless centre-line wake velocity, W/U
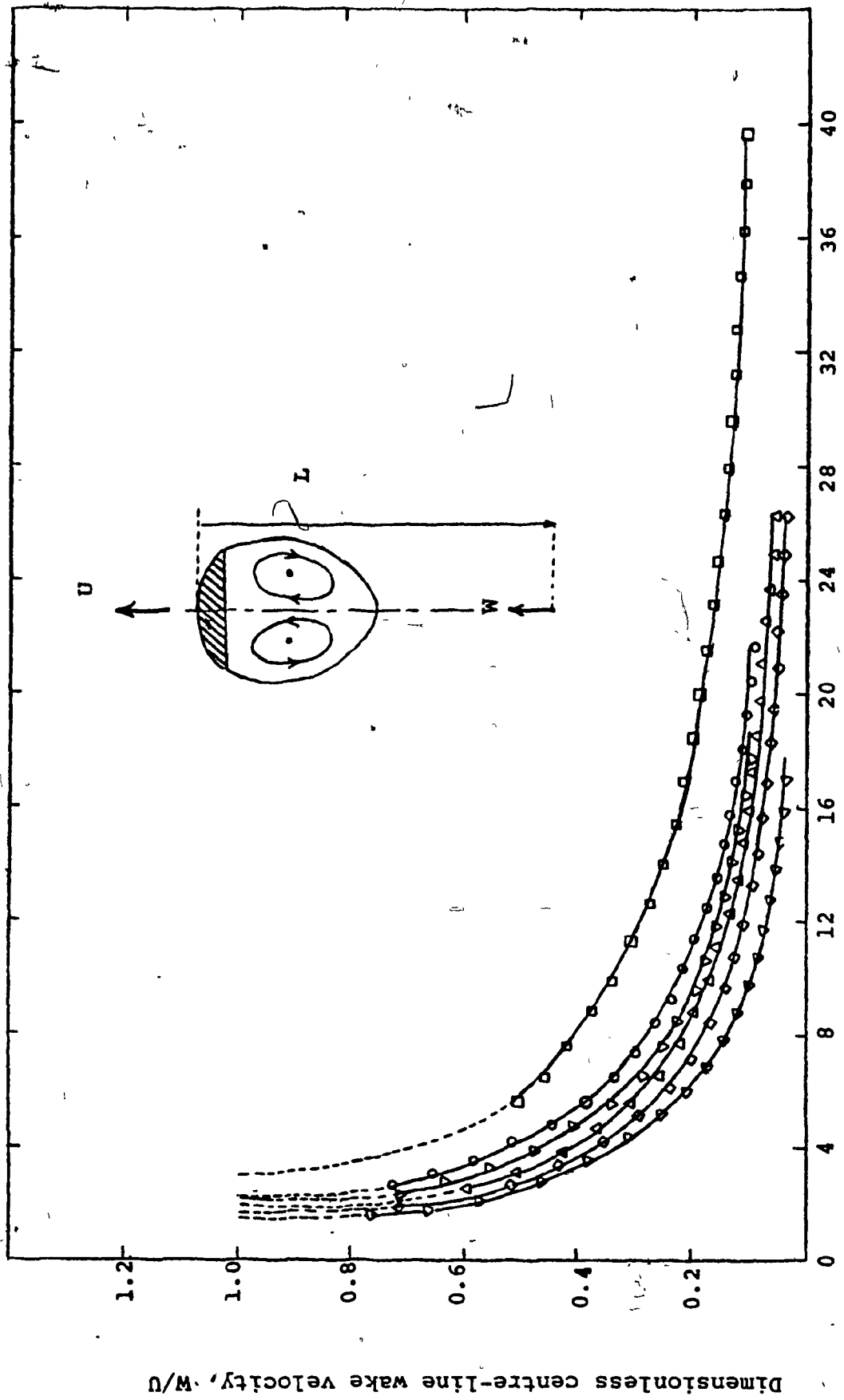
Dimensionless Downstream Distance from the Bubble-nose, L/d_e

wake become confined to smaller regions around the axis of the bubble
rise. Consequently, at fixed dimensionless downstream distance, L/d_e,
the axial wake velocity increases with Re as is evident in Fig. 4.28.
Note that even as far downstream as $L/d_e = 40$ the liquid motion is
quite significant. This, of course, plays an important role in bubble
interaction leading to coalescence of bubbles as shown in Chapter 5.

In Figs. 4.29(a), (b) and (c) the measured centre-line velocity
is compared for bubbles at Re = 14.8, 29.2 and 70.7, respectively, with
four theoretical predictions: the asymptotic wake velocity model,
Stoke's flow around a solid sphere, Hadamard-Rybczynski flow around a
liquid sphere of the same viscosity as the external liquid, and potential
flow around a sphere. Because the motion of the liquid downstream of the
closed toroidal wake will be largely determined by the flow behaviour of
the toroidal wake and to a lesser extent by the gas cap, it seems logical
to base the size of the sphere on the volume of the toroidal wake.* We
hypothesize that the bubble plus the closed toroidal wake can be replaced
by a sphere of volume equivalent to the volume of the toroidal wake, and
positioned such that the rear stagnation point of the toroidal wake and
that of the sphere coincide (see sketch below).

oblate ellipsoidal-cap bubble
and its wake

spherical-cap bubble and its wake

sphere
of equivalent
volume as closed toroidal wake

---
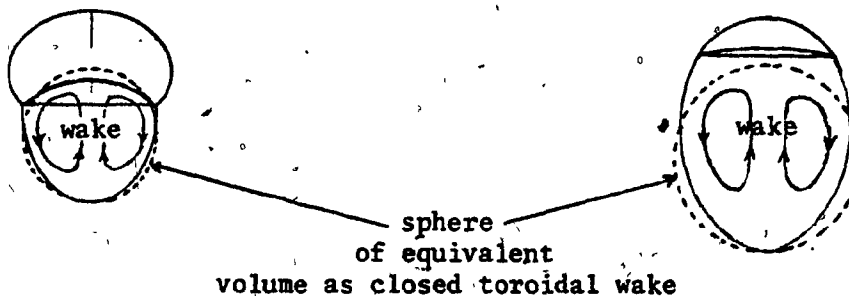
* See footnote on page 220.

FIGURE 4.29 Comparison of Experimental Centre-line Wake
Velocity with Theoretical Predictions

No.	μ (Poise)	ρ (g/cm³)	σ (dynes/cm)	M (-)	V (cm³)	U (cm/sec)	Re (-)	Eö (-)
a	13.00	1.378	78.8	4.16×10	27.8	37.23	14.8	242
b	7.50	1.370	78.7	4.65	27.8	42.55	29.2	241
c	1.30	1.327	77.3	5.01×10^{-3}	4.6	34.22	70.7	72

————— experimental

—— —— asymptotic wake model

— — — — Stokes flow around solid sphere

—·—·— Hadamard liquid sphere model with viscosity ratio, $\kappa = 1$

·········· potential flow model

Re=14.8

Dimensionless Downstream Distance, L/d_e

FIGURE 4-29(a)

Dimensionless Centre-line Wake Velocity, W/U

dimensionless downstream distance, L/d_e

Re = 29.2

dimensionless centre-line wake velocity, W/U

FIGURE 4.29(b)

Re=70.7

Dimensionless Downstream Distance, L/d$_e$

Dimensionless Centre-line Wake Velocity, W/U
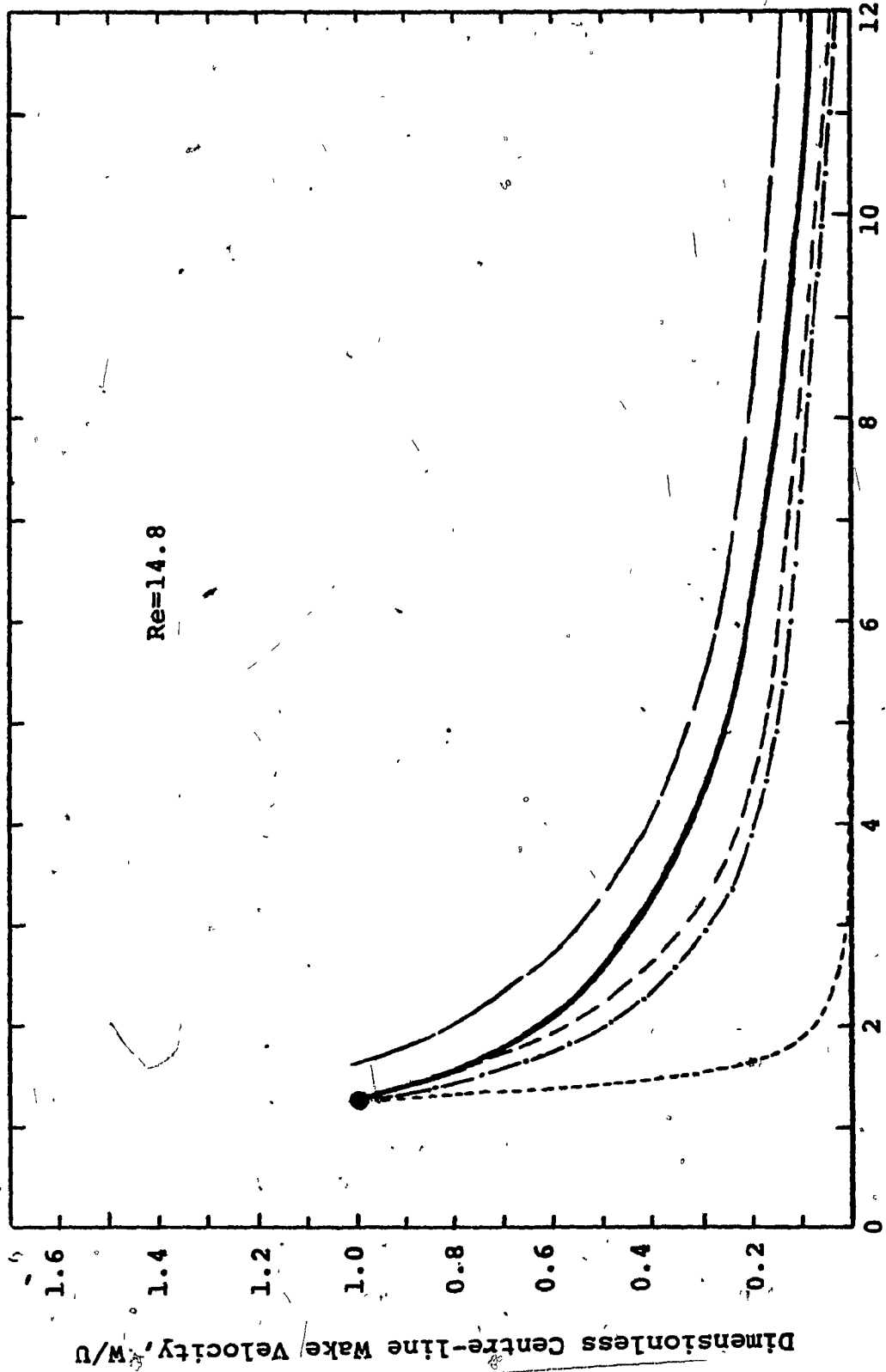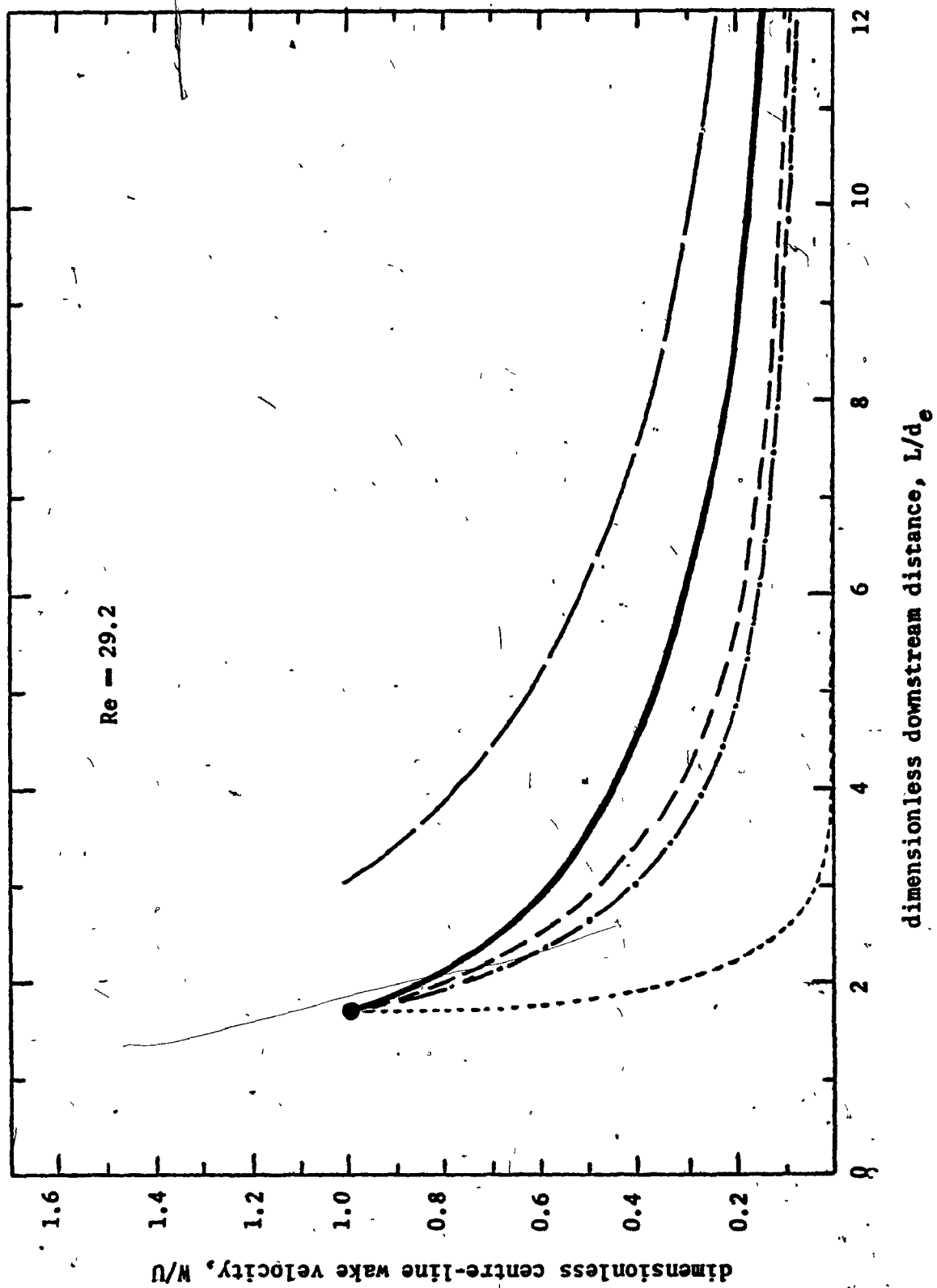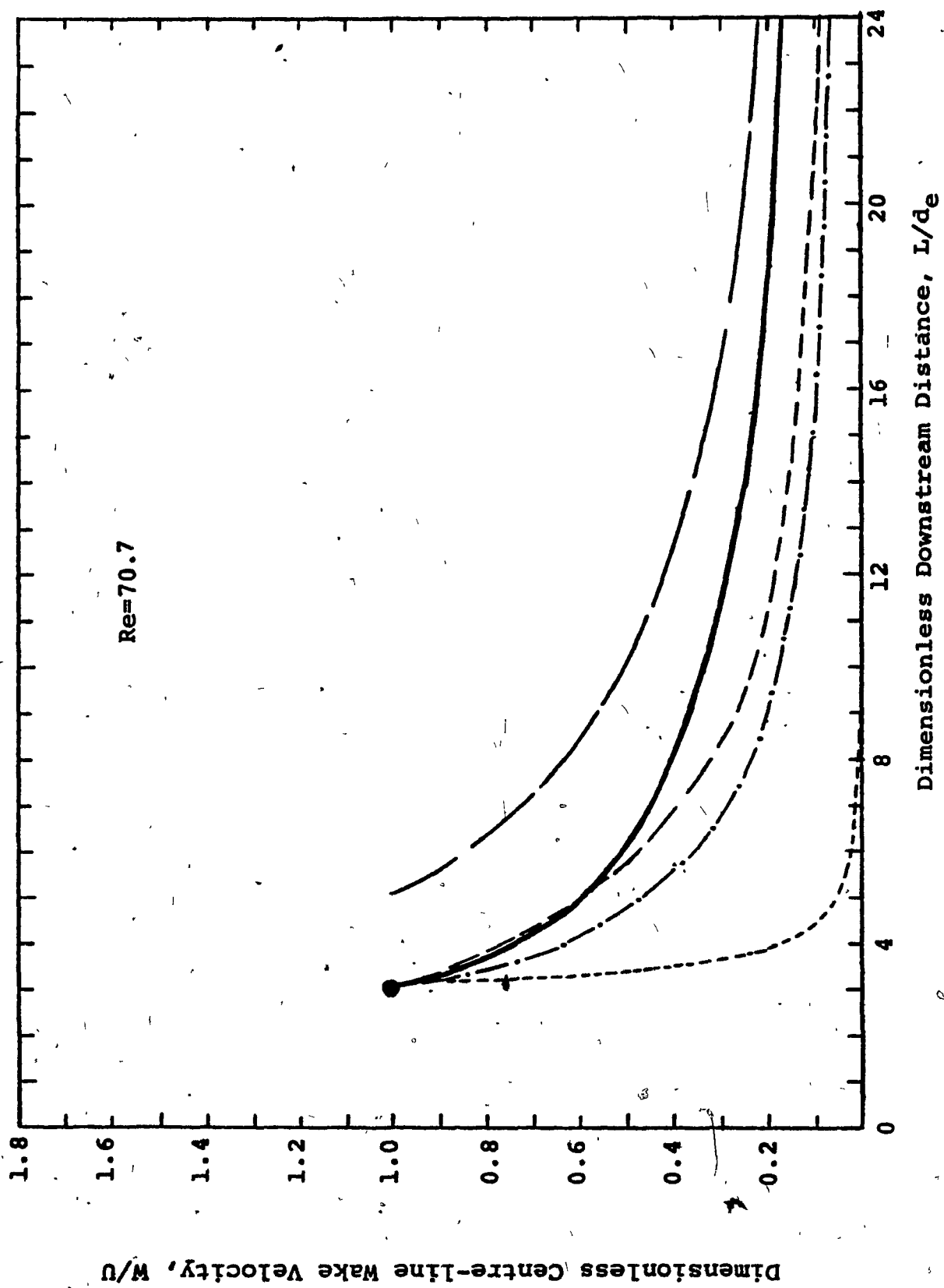
FIGURE 4-29 (c)
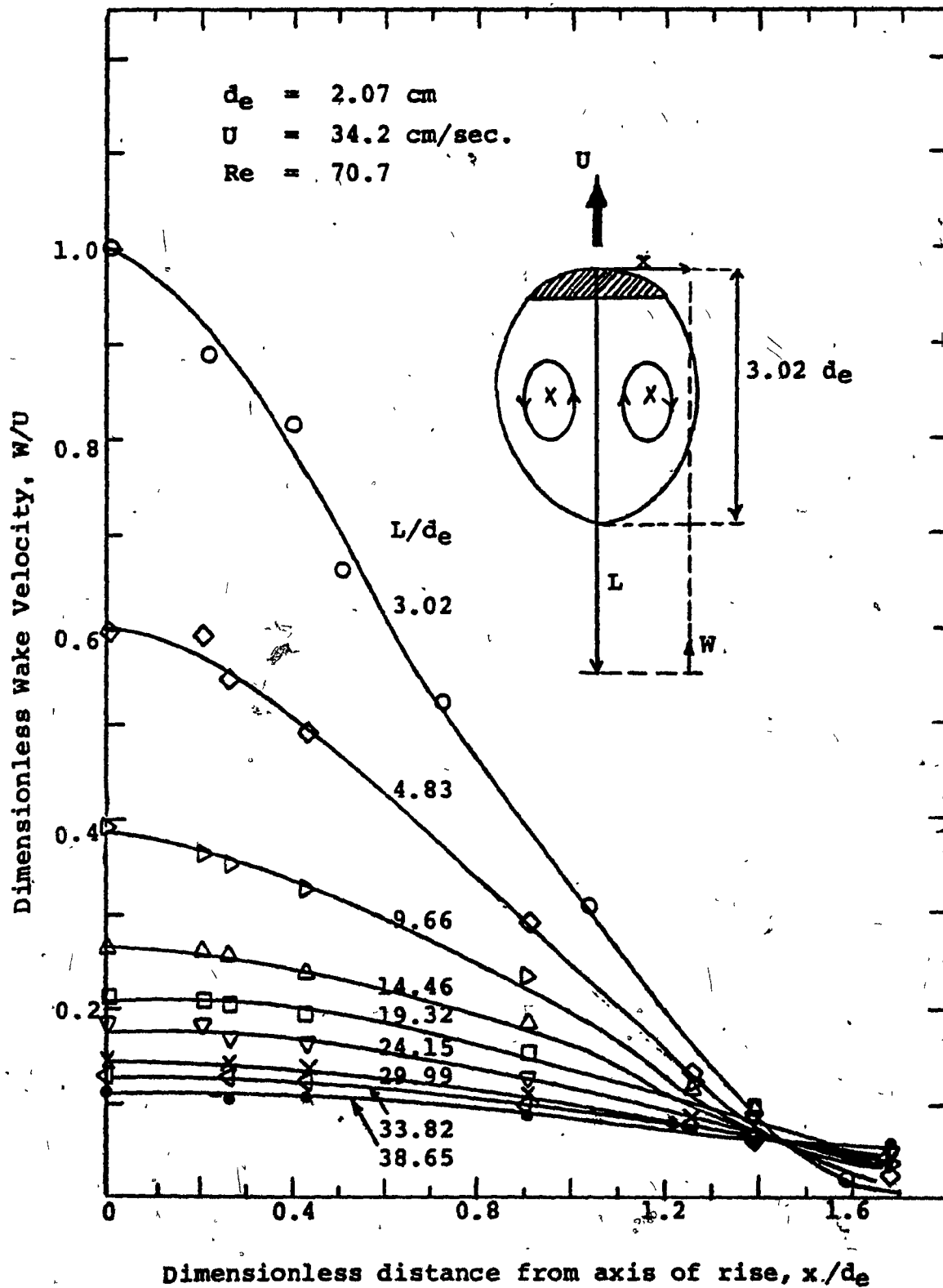
FIGURE 4-30: Profile of the axial velocity behind a spherical-cap bubble.

Fig. 4.29(a), (b) and (c) show that the data for all those cases are between the asymptotic wake model and potential flow model. In the entire range the potential flow model shows extremely poor agreement with the data, even at reasonably high value of Re — 70.7. The asymptotic wake velocity prediction shows somewhat better agreement with the data at lower Re and at larger downstream distances where the key assumption of the model, namely w/U << 1, is justified. The experimental data for all three cases are higher than both the Stokes model* and the Hadamard-Rybczynski model.*

Finally, in Fig. 4.30 a typical distribution of the axial velocity behind a spherical-cap bubble at Re — 70.7 is presented at different dimensionless downstream distances ranging from L/d_e — 3.02 to 38.65. It is seen that the velocity profile becomes more flat but extends further into the tranverse direction as L/d_e increases.

4.6 Addendum

While the final preparation of this thesis was underway two papers (Collins 1974; Hnat and Buckmaster 1976), relevant to this work, were published.

Collins (1974) concludes that the free-streamline models (Temberley and Chambers 1945; Moore 1959; Rippin and Davidson 1967), which assume that a spherical-cap bubble is followed by an infinite axi-symmetric wake, do not provide an acceptable description of the

---

* Even if we assume the gas bubble plus the toroidal wake to be sphere of the same radius as the bubble cap we arrive at essentially the same conclusions.

real flow. He further contends that at high values of Re ($\sim 10^4$) the turbulent wake is closed and consists of a symmetric primary wake vortex followed by a secondary wake. In the wake immediately behind a spherical-cap bubble, Collins observed a structured flow on a scale larger than the scale of the turbulence; however, it does not necessarily follow that the wake is closed as Collins claims. The present data show that for Re > 110 the spherical-cap bubble has an open, unsteady, asymmetric wake. Eddies or vortices of scale similar to the bubble do follow the bubble for a short period during which the vortices grow. However, the flow in the wake is essentially unsteady since the vortices do not stay attached to the bubble for long. The present experiments on spherical-caps with an open unsteady wake (Re $\simeq$ 110 to 296) are believed to be in the transition region between laminar and fully turbulent flow in the wake.

Hnat and Buckmaster (1976) published excellent shadowgraphs of wakes behind spherical-cap and skirted bubbles.* Their wake shapes are comparable to those presented in this chapter. The wake parameters calculated from their photographs are included in Fig. 4.18 and compare favourably with the present data for Re $\leq$ 110. The transition region where vortex shedding occurs was not clearly defined in their work. Bubbles with "perfectly formed wakes" were observed with Re as high as 220 while vortex shedding was observed for Re as low as 140. In contrast, in the present study the transition point was more closely defined at

---

* The findings of these authors on skirted bubbles are discussed in Chapter 6, Section 6.6.

Re $\approx$ 110. This discrepancy is probably due to the different methods of observation (the bubble was followed with a moving camera here while Hnat and Buckmaster used a stationary camera) and of bubble release. Their measurements of the extent of indentation are in good agreement with the present work although the variation of indentation with Re differs somewhat from the present data. Their measurements of the semi-included angle, θ_m, are also in good agreement with those reported in Chapter 3.

4.7 Conclusions

1. The flow field around a spherical bubble at Re << 1 is in agreement with the Hadamard-Rybczynski (1911) analysis for creeping flow. For a slightly deformed spherical bubble the theory of Taylor and Acrivos (1964) describes the external flow field.

2. At higher Re (Re > 1)* a closed axi-symmetric laminar toroidal wake develops behind the bubble, the base of the bubble becomes indented and the fore and aft symmetry in the liquid flow field is destroyed. With increasing Re, the size of the toroidal wake grows in both the transverse and streamwise directions until for Re $\approx$ 110 the wake becomes open, unsteady and asymmetric with periodic vortex shedding. The bubble base oscillates as the vortices are shed, but the bubble rises rectilinearly.

---

* This description is restricted to bubbles in high-M liquids. Bubbles in low-M liquids exhibit rather different behaviour (Rosenberg 1950; Haberman and Morton 1953,1956; Lindt 1971 ; Lindt and De Groot 1974).

3.   For spherical-cap bubbles (Re $\gtrsim$ 45) the flow field up to the bubble base is in good agreement with the potential flow around a sphere. Slight deviations from the potential flow near the bubble surface are due to the development of a boundary layer as proposed by Moore (1963). Below the bubble base the agreement with potential flow is poor for streamlines close to the toroidal wake because the wake shape does not coincide with the sphere that fits the cap. However, at horizontal distances from the axis of rise greater than about $2d_e$ the influence of the wake shape on the flow field diminishes and the potential flow prediction is in accord with the experimental data. For spherical-cap bubbles with an open unsteady wake (i.e. Re $\gtrsim$ 110) the liquid flow field is unsteady below the base of the bubble, while above the bubble base the flow field is essentially steady and in agreement with potential flow.

4.   For oblate ellipsoidal-cap (Re $\lesssim$ 45) and skirted bubbles (Re > 12) the liquid flow field up to the bubble base is between the predictions of potential flow and creeping flow around an oblate ellipsoid with potential flow showing better agreement. The deviation from potential flow diminishes with increasing Re. The dimensionless equatorial velocity at the surface of an ellipsoidal-cap bubble is considerably below unity at low Re and increases with Re. The velocity profile far away from the bubble approaches potential flow rather than creeping flow.

5.   The volume of the liquid carried by a bubble in its toroidal wake can be as large as 20 times the volume of the bubble at Re $\approx$ 110, beyond which the wake becomes open and unsteady. The wake volume data are well correlated with Re (Eq. (4.9)) and compare favourably with wake volume data of solid spherical-caps and drops. The data are

also consistent with the predictions of Parlange's (1969) theory. The parameters describing the geometry of the closed wake are only functions of Re and can be predicted using Eqs. (4.5) to (4.8).

6. The velocity distribution within the closed toroidal wake is between the theoretical predictions of Hadamard's (1911) and Hill's (1894) spherical vortex. At high Re (Re $\geq$ 45) the circulation within the toroidal vortex agrees favourably with the predictions of Harper and Moore's (1968) correction to Hill's spherical vortex, whereas Parlange's (1970) correction overpredicts the circulation rate. The external streamlines in the neighbourhood of the toroidal wake show the existence of a liquid boundary layer with a thickness decreasing as Re increases.

7. For skirted bubbles the liquid in the wake enclosed by the skirt moves as a toroidal wake which extends beyond the end of the skirt. The circulation rate is somewhat slower than that of a wake in the absence of the skirt.

8. When a bubble moves through a liquid, it induces considerable upward drift in the liquid in a region near the axis of rise. The extent of upward motion decreases rapidly in the horizontal direction. Except at Re $\ll$ 1, the induced motion of liquid behind the bubble is significantly greater than ahead of it. Even as far downstream as $L/d_e = 40$ the upward liquid motion is significant. As Re is increased the centre-line wake velocity increases and the influence of the bubble on the liquid in the horizontal direction diminishes. For Re $>$ 1 the experimental velocities behind the bubble are bracketed by the asymptotic wake theory and the potential flow theory, but no simple model satisfactorily describes the flow.

CHAPTER 5

INTERACTION AND COALESCENCE OF BUBBLES

5.1 Introduction

When a gas is bubbled into a viscous liquid, coalescence of the bubbles inevitably occurs, except at very small gas hold-up. This, in turn, influences the bubble size distribution, interfacial area, gas residence time and bubble induced liquid flow. Thus, coalescence plays a vital role in determining the efficiency of gas-liquid contacting devices as well as gas-liquid separating devices (Jackson 1964; Calderbank et al 1964; Valentin 1967). In a contactor coalescence is undesirable because it reduces the interfacial area, whereas in a separator coalescence is desirable because by increasing the bubble sizes and hence their rise velocity it speeds up the separation.

In order to elucidate the mechanisms that govern coalescence this chapter focusses on the interaction of two vertically aligned bubbles.

5.2 Literature Review

The complex problem of bubble interaction and coalescence in viscous liquids has received relatively little attention until recently. Early investigations were confined to the interaction of solid spheres and are summarised by Happel and Brenner (1965), Steinberger et al (1968) and Lin et al (1970). The theoretical treatment of the interaction of solid spheres involves great mathematical difficulties, even for two spheres in unbounded fluid media, hence, the problem has been solved analytically only when certain simplifying assumptions are made. Recently similar theoretical approaches have been reported for the interaction of

spherical bubbles at low Re (Gailhbaud and Zortea 1969; Morrison 1973; Rushton and Davies 1973; Haber et al 1973) and also for spherical bubbles at high Re (Harper 1970).

Narayanan et al (1974) compared their experimental data on the in-line interaction of two spherical bubbles of equal size with the existing theories and concluded that the analysis of Stimson and Jeffery (1926) for solid spheres and that of Morrison (1973) for fluid spheres adequately described bubble interaction in the creeping flow for bubbles with rigid interfaces* and for freely circulating bubbles, respectively.

The interaction problem becomes even more complex at higher Re, where the bubbles are deformed and trail extensive wakes behind them. For this situation many authors have resorted to the "principle of super-position" to predict the motion of interacting bubbles or drops (Harrison and Leung 1962; Slaughter 1967; Clift and Grace 1969, 1970, 1971; Lin 1970; Crabtree and Bridgewater 1971; Wah-on 1971; Wairegi 1974; Narayanan et al 1974). The "principle of superposition" assumes that a bubble or drop moves with a velocity equal to the sum of its terminal velocity in isolation and the velocity which the continuous phase would have at the position of the nose if the bubble or drop were absent.

In their analysis of coalescing bubbles in a fluidized bed, Clift and Grace (1969, 1970, 1971) assumed the gas bubble and its associated wake to be a spherical body and the surrounding flow field to be potential flow. Good agreement with the experimental data was

----

* Bubble interfaces exhibit rigid behaviour when surface active impurities are present in quantities sufficient to prohibit internal circulation (Levich 1962).

demonstrated. Because fluidized beds have many properties analogous to liquid beds (Davidson and Harrison 1963) and because large gas bubbles in liquids are known to be associated with toroidal wakes which __approximately__ complete the sphere of which the bubble forms the cap, these authors suggested that the same method of predicting the motion of interacting bubbles might apply to bubbles in liquids.

Slaughter (1967) found that there was a marked increase in the terminal velocity of a large spherical-cap bubble when it is part of a stream of bubbles, even when separated by large distances from its nearest neighbors.* The relationship between the increase in terminal velocity and the distance of separation of the bubbles was independent of the bubble size. A semi-empirical model was formulated for a chain of bubbles by assuming potential flow around the bubble and its wake, but agreement with the data was poor.

Crabtree and Bridgewater (1971) applied the principle of super-position to coalescence of two vertically aligned spherical-cap bubbles in a viscous liquid (M — 0.02887; Re — 40 to 86). They found that the assumption of an asymptotic wake velocity profile (see Chapter 4, Section 4.4) behind the leading bubble could explain the coalescence phenomenon better than the assumption of potential flow for the flow field. However, considerable deviation from the theory was observed at small downstream distances. This led them to conclude that ...."Deviation from the theoretical prediction suggests the importance of obtaining

---

* Such enhancement of terminal velocity for bubbles rising in a chain has also been observed for bubbles of other shapes (Hoefer 1931; Owens 1921; O'Brien and Gosline 1935; Datta __et al__ 1950; Crabtree and Bridgewater 1969).

direct measurements of bubble wake velocities and of the deformation and flow of bubbles in a liquid velocity gradient."

Wah-on (1971) applied the potential flow equation, the Batchelor asymptotic wake velocity equation, the Hadamard-Rybczynski equation and the Oseen equation, in turn, to describe the velocity field around bubbles (Re $\sim$ 3) in viscous liquids and predicted coalescence of two in-line bubbles. He concluded that none of these models was completely satisfactory in describing the coalescence process.

Wairegi (1974) extended the Clift and Grace model to oblate ellipsoidal-cap bubbles and drops, and concluded that the potential flow model did not agree with the experimental data.

De Nevers and Wu (1971) proposed a coalescence model in which the wake behind the leading bubble was assumed to have a linearly or an exponentially decreasing width and the same velocity as the leading bubble. It was further assumed that the only significant forces acting on the trailing bubble were its buoyancy force and the drag. The latter force decreases as the bubble enters the upward moving wake of the preceeding bubble. Consequently, the trailing bubble accelerates and coalesces with the leading one. Since this model does not represent the actual wake observed in practice (see Chapter 4), it has limited utility.

Narayanan et al (1974) made an extensive study of two bubbles of equal size rising in-line at low Re (0.8 to 80) in glycerine (μ = 0.9, 2.4 and 9.0 Poise). They classified the bubbles having different wake structure at different Re. The mode of coalescence was found to depend upon the wake structure. The bubbles with Re < 7 followed the analysis of weightless solid spheres whereas for bubbles having toroidal wakes (Re $\geq$ 7), the trailing bubble was assumed to move with two additional

velocities imparted due to the wake structure of the leading bubble; namely that due to the toroidal vortex and that due to the wake behind the toroidal vortex. Equations correlating these velocity contributions with Re and dimensionless downstream distance were presented.

5.3 Objectives

The above review reveals that many attempts to predict coalescence of bubbles in viscous liquids using the principle of superposition and various velocity field assumptions were unsuccessful. It was not clear before the present work whether the principle of superposition or the assumed flow field or both were incorrect. In Chapter 4 it was shown that potential flow is a poor model for the velocity field behind a rising spherical-cap or an oblate ellipsoidal-cap bubble although quite acceptable in front of it. Other velocity fields, e.g., Stokes and Hadamard-Rybczynski, are also poor representations of the velocity field behind the bubble. Therefore, the main objective of this chapter is to test the validity of the principle of superposition directly using the measured velocity field behind an isolated bubble.

5.4 Experimental Results and Discussion

The interaction and coalescence of two vertically aligned bubbles rising in viscous liquids were studied using the experimental technique described in Chapter 2. The physical properties of the liquids and data for the bubbles employed in the experimental runs are summarized in Table 5.1. Various combinations of the bubble sizes were used so that $V_A > V_B$, $V_A - V_B$ and $V_A < V_B$, where V_A and V_B are the volumes of the leading bubble and trailing bubble, respectively.

TABLE 5.1   Summary of Experimental Conditions for Coalescence Runs

Sugar Solution	Liquid Properties				Bubble Data			
	μ (Poise)	ρ (g/cm^3)	σ (dynes/cm)	M (-)	V (cm^3)	U (cm/sec)	Re (-)	Eö (-)
B	13.00	1.378	78.8	4.16×10	27.8	37.23	14.8	242
					18.5	33.66	11.7	185
					13.9	31.27	9.9	153
C	7.50	1.370	78.7	4.65	27.8	42.55	29.2	241
					18.5	37.84	22.7	184
					13.9	35.27	19.2	152
					9.3	30.75	14.6	116
D	5.00	1.357	77.7	9.63×10^{-1}	18.5	38.62	34.4	185
					13.9	37.12	30.1	152
					9.3	32.62	23.1	116
F	1.30	1.327	77.3	5.01×10^{-3}	9.3	39.09	102	115
					4.6	34.22	70.7	72
G	0.85	1.314	76.8	7.45×10^{-4}	9.3	37.55	151	114
					4.6	33.95	110	72

5.4.1 Qualitative observations of bubble coalescence

The level in the column at which coalescence took place
depended on the size of the two bubbles and the initial separation
distance between them. If the separation was too large or if the
trailing bubble was too small compared to the leading bubble, the
height of the column was insufficient for the coalescence to occur.
Nonetheless, the trailing bubble was found to accelerate due to the
wake velocity of the leading bubble in all the cases. The bubbles
studied were of oblate ellipsoidal-cap and spherical-cap shape with
Re ranging from 10 to 151. Two different modes of interaction were
observed depending on the nature of the wake of the leading bubble.
When the leading bubble had a closed, laminar axisymmetric toroidal
wake ($Re_A \lesssim 110$), the bubbles remained in-line and the coalescence
sequence was reproducible, but when the leading bubble trailed an un-
steady, asymmetric open wake accompanied by vortex shedding ($Re_A \gtrsim 110$),
the trailing bubble wandered and the coalescence sequence was not
reproducible. The two modes of interaction are illustrated in Figs. 5.1
and 5.2, respectively.

Fig. 5.1 shows the in-line interaction of two bubbles of equal
size ($V = 9.3$ cm^3). In photograph 1 they are about 20.2 cm apart and are
practically identical in shape. Photographs 2 to 10 show the final
stages of coalescence of these bubbles at intervals of 0.056 sec. Note
that the shear field created by the passage of the leading bubble deforms
the trailing bubble axisymmetrically with its aspect ratio (height/width)
increasing as it catches up to the leading bubble. The trailing bubble
assumes a bullet-like shape with its frontal surface approximately para-
bolic. The shape of the leading bubble remains unchanged until the point

FIGURE 5.1 Coalescence Sequence where the Leading Bubble
Trails a Steady, Axisymmetric, Toroidal Wake

(The two bubbles are of equal volume.)

$V(cm^3)$	9.3
U (cm/sec)	32.62
Re	23.10
Eö	116

μ = 5.00 Poise

ρ = 1.357 g/cm^3

σ = 77.7 dynes/cm

M = 0.963

Note: (1) Time interval between each stage was 0.056 sec., except
between the first two stages for which the time interval
was 1.346 sec.

(2) The vertical scale shows horizontal markings at distances
of 2 cm.
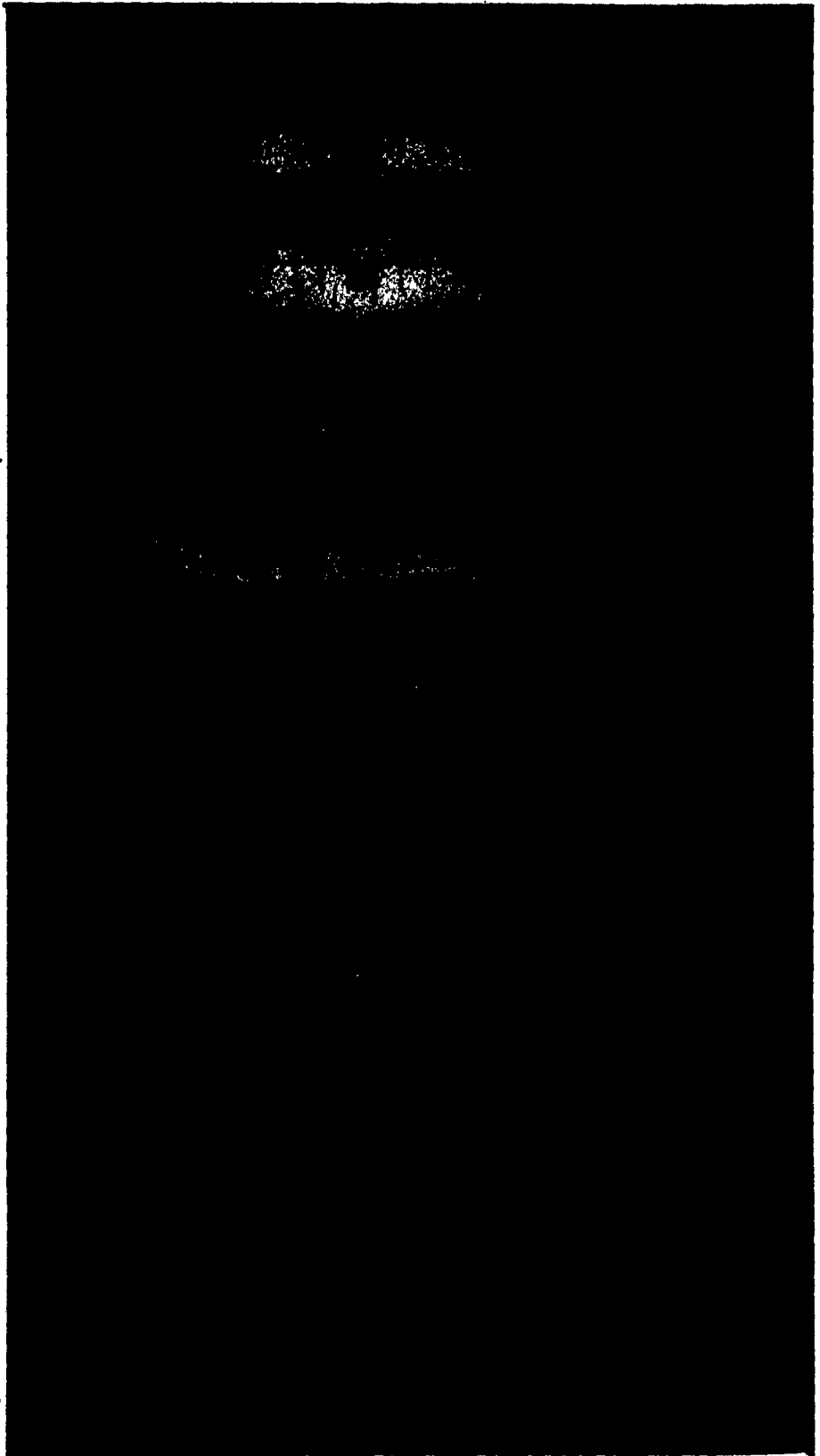
FIGURE 5.2 Coalescence Sequence where the Leading Bubble
Trails an Unsteady, Asymmetric, Open Wake

	Leading Bubble	Trailing Bubble
$V(cm^3)$	9.3	4.6
$U(cm/sec)$	37.55	33.95
Re	151	110
Eö	114	72

μ = 0.85 Poise

ρ = 1.314 g/cm^3

σ = 76.8 dynes/cm

M = 7.45x10^{-4}

Note: (1) Time interval between stages was 0.057 sec. except between
the first two stages for which the time interval was 1.143 sec.

(2) The vertical scale shows horizontal markings at distances of
2 cm.
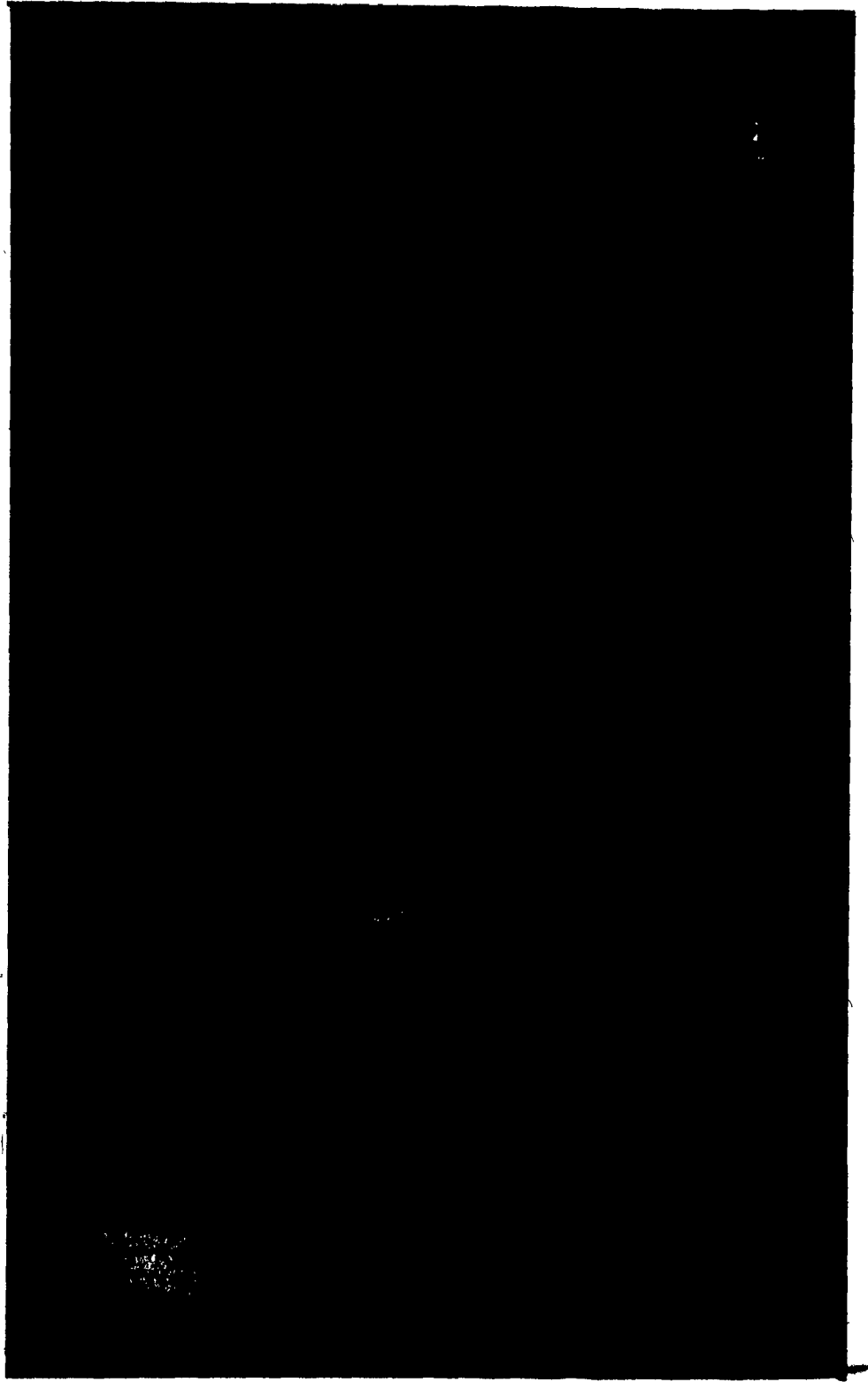
of coalescence, which suggests that the effect of the trailing bubble on the leading one can safely be ignored when formulating a predictive coalescence model (see Section 5.4.3).

The series of photographs in Fig. 5.2 shows the sequence of events for the second mode of coalescence. Here the asymmetric unsteady wake of the leading bubble ($Re_A - 151$) deforms the trailing bubble asymmetrically, forces it to move sideways erratically and makes it impossible to reproduce the motion of the trailing bubble.

The behavior of the bubbles formed by coalescence in both modes of coalescence depended on the viscosity of the liquid as well as on the size of the bubbles. Bubbles of small volumes coalesced to form a single large bubble. When larger bubbles coalesced the bubble so formed immediately disintegrated violently into several bubbles, especially in the lower viscosity liquid.

5.4.2 Analysis of coalescence data

The motion of the interacting bubbles as recorded on ciné films was analysed by projecting the film onto the lower surface of a ground-glass screen. The position of the nose of each bubble was measured relative to a reference grid fixed to the back surface of the column. Fig. 5.3 shows the positions of two bubbles with time during a typical coalescence sequence. The effect of the leading bubble on the trailing bubble is quite evident. As the trailing bubble moves toward the leading one it accelerates and finally coalesces.(see point C in Fig. 5.3). The trailing bubble has little or no influence on the leading bubble until just before coalescence, when the leading bubble accelerates slightly. Similar behaviour has been reported by others (Clift and Grace 1970; De Nevers
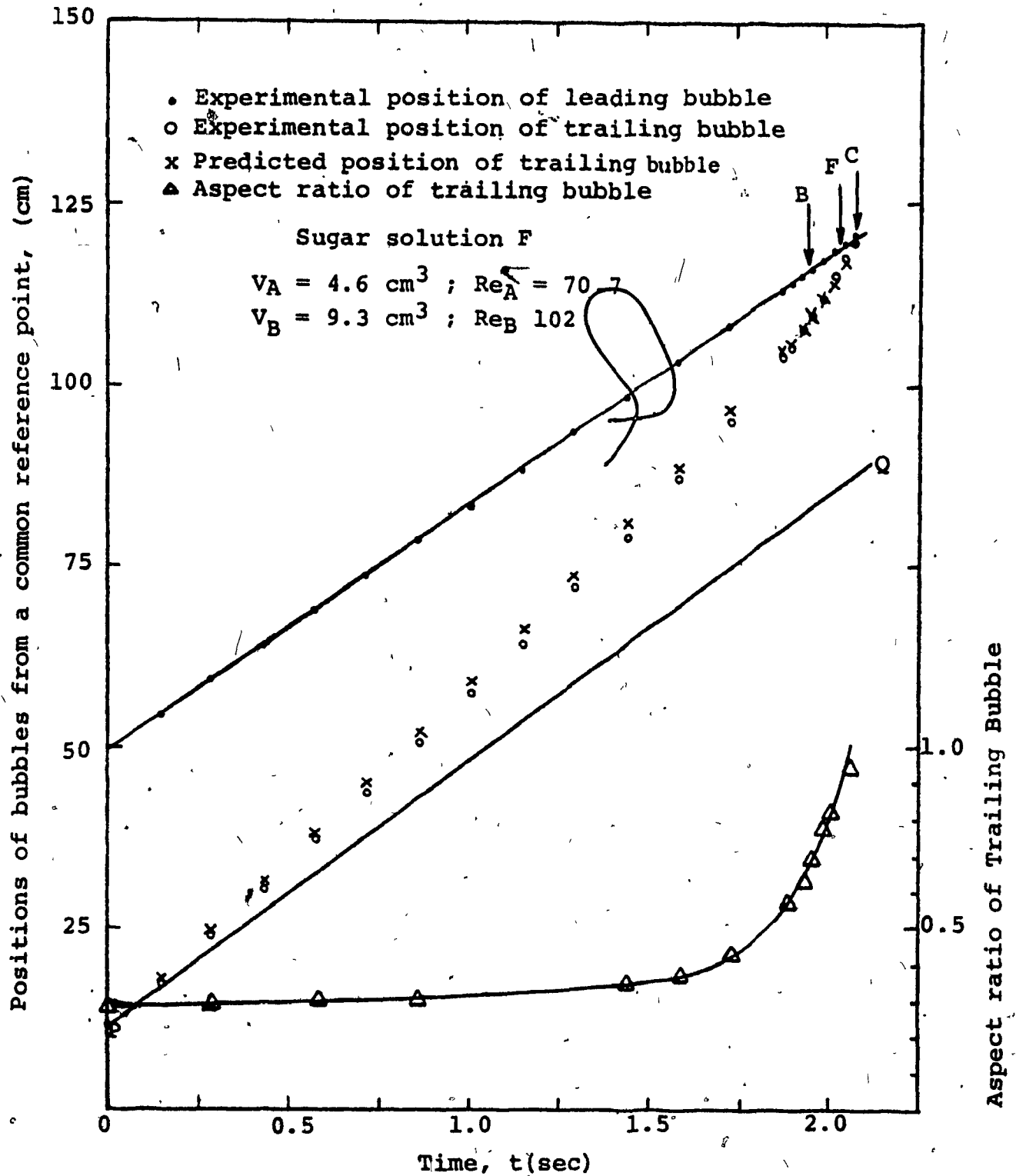
FIGURE 5-3 : In-line coalescence of Two Bubbles

and Wu 1971; Crabtree and Bridgewater 1971; Wah-on 1971; Wairegi 1974).
The variation of the aspect ratio of the trailing bubble is also shown
in Fig. 5.3. Considerable deformation and the largest acceleration of
the trailing bubble occur just before coalescence when it is moving
through the toroidal wake of the leading bubble (point B in Fig. 5.3 indi-
cates the condition when the trailing bubble enters the toroidal wake of
the leading bubble). The line $\overline{PQ}$ in Fig. 5.3 shows the trajectory the
trailing bubble would have if it were rising in isolation. Comparison
of the line $\overline{PQ}$ with the observed trajectory demonstrates the long range
effect of the wake of the leading bubble.

5.4.3 Test of the principle of superposition

The principle of superposition (see Section 5.2) can now be
tested directly, since the wake velocities have already been reported
in the previous chapter. The principle of superposition will be tested
only for coalescence between bubbles with steady, closed toroidal axi-
symmetric wakes. With open unsteady wakes no test is possible since the
velocity at a fixed position behind the leading bubble is not steady.

Consider the following model for coalescence of two vertically
aligned bubbles in an unbounded fluid. Label the leading bubble A and
the trailing bubble B, and at time t let X_j be the vertical position of
bubble j measured from a fixed reference point. If we assume the principle
of superposition, then with respect to a stationary observer bubble j will
rise at a velocity U_j given by the sum of (i) its terminal velocity in
isolation, U_{ji}; and (ii) any enhancement in velocity due to the presence
of the other bubble.

Since the trailing bubble has relatively little influence on the leading bubble (see previous two sections) we can write for the leading bubble

$$U_A = U_{Ai} \tag{5.1}$$

or

$$\frac{dX_A}{dt} = U_{Ai} \tag{5.2}$$

The trailing bubble is strongly affected by the leading bubble and thus

$$U_B = U_{Bi} + W \tag{5.3}$$

or

$$\frac{dX_B}{dt} = U_{Bi} + W \tag{5.4}$$

where W is the velocity in the wake of bubble A at the location of the nose of bubble B. Since only in-line interactions are considered, W is the centre line wake velocity. It varies with the nose-to-nose separation distance between the bubbles, L:

$$L = X_A - X_B \tag{5.5}$$

The validity of the proposed model which invokes the principle of superposition is tested as follows. The experimentally measured centre-line wake velocity for the leading bubble of the coalescence sequence shown in Fig. 5.3 was presented in Chapter 4. (see Fig. 4.27). A sixth order polynomial was fitted to these data to represent the variation of W with L

between point F* and G shown in Fig. 4.27. Using this information, Equations (5.2) and (5.4) were integrated numerically using the fourth-order Kutta-Merson technique (Lance 1960). The predicted trajectory of the trailing bubble, shown in Fig. 5.3,** is found to be in excellent agreement with the experimental data-thus supporting the principle of superposition.

A further test of the principle of superposition is shown in Fig. 5.4 where the measured centre-line wake velocity behind the leading bubble (see Chapter 4, Section 4.5.3.2) is plotted against downstream distance in dimensionless co-ordinates and compared with the apparent wake velocity as experienced by the trailing bubble. The apparent wake velocities were determined from ciné films of 23 coalescence sequences with various combinations of leading and trailing bubbles by the following method. The position versus time data of the trailing bubble were differentiated numerically by the "moving strip technique" (Hershey et al 1967; see Appendix D for details) to obtain, $\frac{dX_B}{dt} = U_B$, the effective rise velocity of the trailing bubble. Subtracting from this the rise velocity of the trailing bubble in isolation, U_{Bi}, the apparent wake velocity, W_{app}, was obtained (see Equation (5.4)). The apparent wake velocity was rendered dimensionless with respect to the rise velocity of the leading bubble in isolation, U_{Ai}, and then plotted versus the dimensionless downstream distance, L/d_e, where d_e is the equivalent sphere diameter of the leading bubble. The results for Re_A ranging from 14.6 to 70.7 and Re_B ranging from 9.9 to 102 are shown in series of Figs. 5.4(a)

---

* Point F in Fig. 4.27 shows the position of the horizontal plane that contains the stagnation ring of the toroidal wake of the leading bubble. The time when the nose of the following bubble reaches this point is also indicated on Fig. 5.3 by point F.

** Similarly, predictions for coalescence were also obtained for all the other coalescence experiments and fairly good agreement with the experimental data was observed.

FIGURE 5.4 <u>Comparison of the Apparent Wake Velocity</u>
<u>as Experienced by the Following Bubble with</u>
<u>the Measured Centre-line Wake Velocity</u>
<u>Behind the Leading Bubble</u>

No.	Re_A
a	70.7
b	34.4
c	29.2
d	23.1
e	22.7
f	19.2
g	14.8
h	14.6

———— measured centre-line wake velocity outside toroidal wake ⎱ (see

——— ——— measured centre-line wake velocity inside toroidal wake ⎰ Section 4.5.3.2)

- - - - - - - - Narayanan et al (1974)

———— Crabtree and Bridgewater correlation (1971)

Note: Experimental position of the stagnation points B and C as well as

point F indicating the position of the stagnation ring, are also

shown in each figure.

Sugar Solution F

$V_A = 4.6\ cm^3;$ $Re_A = 70.7$

$V_B = 9.3\ cm^3;$ $Re_B = 102$

The four different symbols indicate four different runs with identical conditions.

Dimensionless centre-line & apparent wake velocity

Dimensionless Downstream Distance, L/d_e

FIGURE 5-4(a)

240.

Sugar Solution D

V_A = 18.5 cm³; Re_A = 34.4

	V_B (cm³)	Re_B
O	9.3	23.1
□	13.9	30.1
△	18.5	34.4

Dimensionless centre-line & apparent wake velocity

Dimensionless Downstream Distance, L/d$_e$

FIGURE 5-4(b)

241.

Sugar Solution C

$V_A = 27.8 \text{ cm}^3$, $Re_A = 29.2$

	V_B (cm^3)	Re_B
△	9.3	14.6
◇	13.9	19.2
□	18.5	22.7
○	27.8	29.2

Dimensionless centre-line & apparent wake velocity

Dimensionless Downstream Distance, L/d_e

FIGURE 5-4(c)

Sugar Solution D

V_A = 9.3 cm³; Re_A = 23.1

	V_B (cm³)	Re_B
◻	9.3	23.1
△	13.9	30.1
○	18.5	34.4

Dimensionless centre-line & apparent wake velocity

Dimensionless Downstream Distance, L/d_e

FIGURE 5-4(d)

Sugar Solution C

V_A = 18.5 cm^3; Re_A = 22.7

$V_B(cm^3)$		Re_B
□	13.9	19.2
○	18.5	22.7
◇	27.8	29.2

Dimensionless centre-line & apparent wake velocity

Dimensionless Downstream Distance, L/d_e

FIGURE 5-4(e)

FIGURE 5-4(f)

DIMENSIONLESS DOWNSTREAM DISTANCE, L/d_e
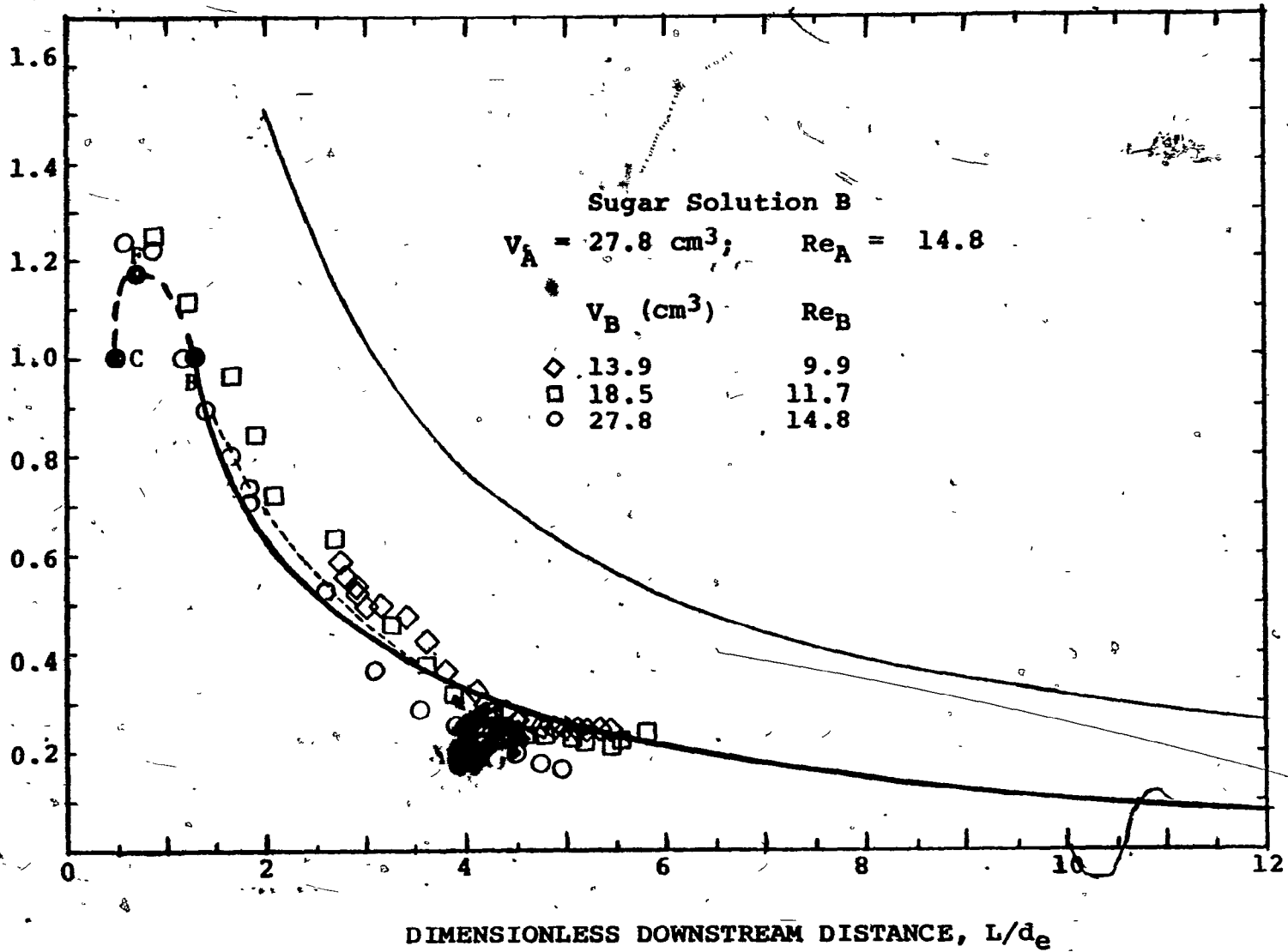
FIGURE 5-4(g)

246.

FIGURE 5-4(h)

Sugar Solution C

$V_A = V_B = 9.3 \text{ cm}^3$

$Re_A = Re_B = 14.6$

Dimensionless centre-line & apparent wake velocity

Dimensionless Downstream Distance, L/d_e

247.
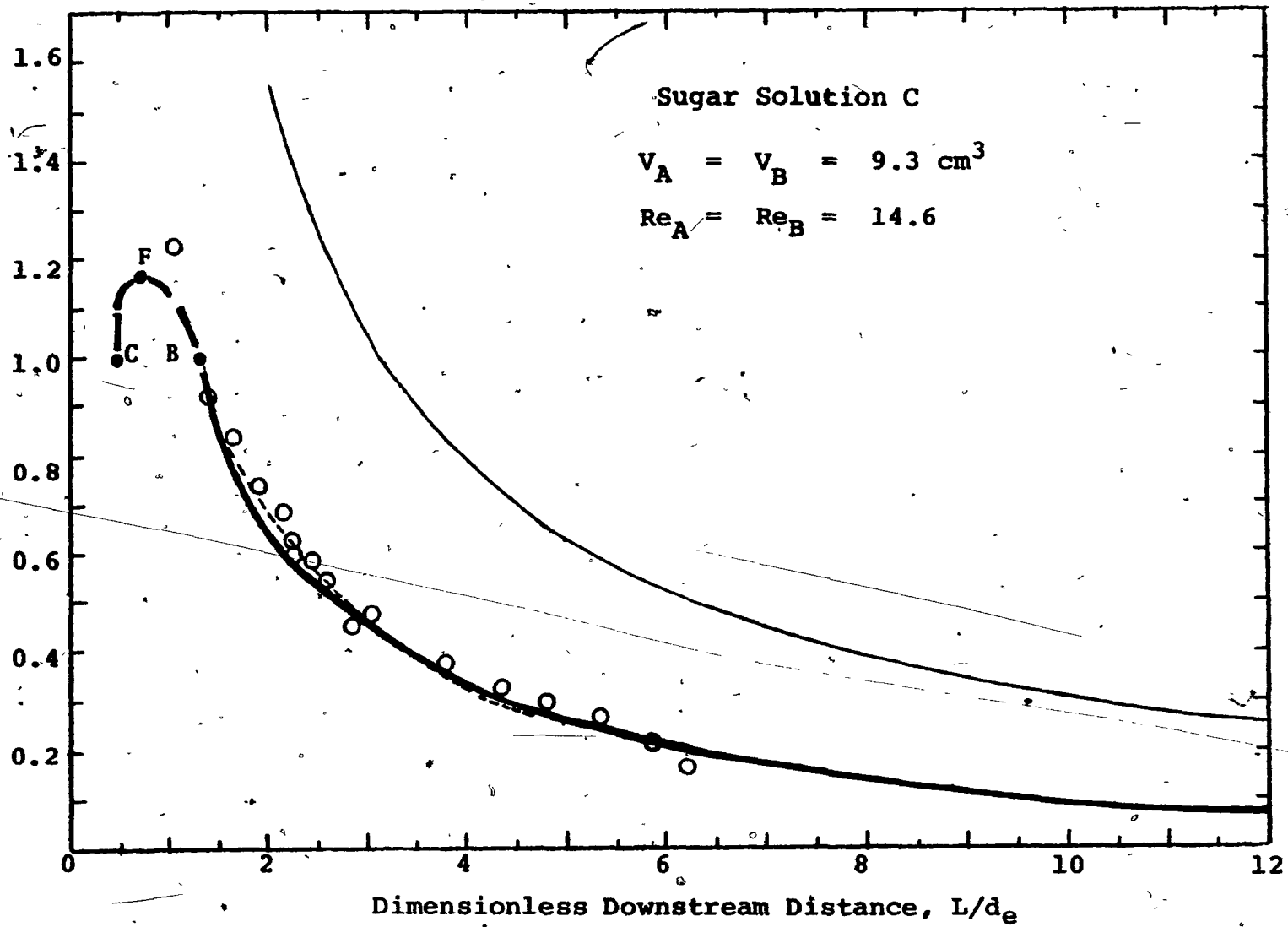
to 5.4(h).

Fig. 5.4(a) includes the results of four repeated coalescence experiments and demonstrates the reproducibility of the data. The scatter is due to errors which are inherent in any analysis which involves differentiation of experimental data. From Fig. 5.4(b) to (h) it is observed that within the scatter of the data there is no effect of the size of the trailing bubble on the apparent wake velocity. The finding of Crabtree and Bridgewater (1971) that the apparent wake velocity is greater for larger trailing bubbles is not substantiated. By comparing the results of Fig. 5.4(d) to (e) and Fig. 5.4(g) to (h) where the Reynolds number of the leading bubble is almost identical we conclude that the apparent wake velocity experienced by the trailing bubble is only a function of the Reynolds number of the leading bubble.

Narayanan et al (1974) presented their coalescence results for equal size bubbles in graphical form (see their Fig. 7). These data were interpolated at the appropriate Reynolds number and the results are included in Fig. 5.4. Their results compare quite well with the present experimental data.

Crabtree and Bridgewater (1971) correlated their data on coalescence of spherical-cap bubbles with Re = 40 to 90 by

$$\frac{W_{app}}{U_{Ai}} = 3.1 \frac{d_e}{L} \tag{5.6}$$

which they claim is valid for $L/d_e = 2.5$. This correlation is also included in Fig. 5.4. It shows good agreement with the present data at Re = 70.7 (See Fig. 5.4(a)) but overpredicts the apparent wake velocity at lower Re, the overprediction increasing with decreasing Re.

The above results provide ample evidence for the validity of the simple principle of superposition for the interaction of two in-line bubbles. Predictive coalescence models using this principle will be in good agreement with the data if a realistic velocity field is used. A more complete coalescence model should account for the effect of the deforma- tion of the trailing bubble on its rise velocity and the changes in the flow field when the trailing bubble approaches the wake of the leading bubble, but in view of the present findings the additional complexity may not be justified.

5.5 Conclusions

1. Two different modes of bubble interaction are observed depending on the nature of the wake of the leading bubble. When the leading bubble has a closed, steady, axisymmetric, toroidal wake (Re $\leq$ 110) the bubbles remain in-line and the coalescence is reproducible, but when the leading bubble trails an open, unsteady, asymmetric wake accompanied by vortex shedding (Re $\gtrsim$ 110) the trailing bubble wanders and the coales- cence sequence is not reproducible.

2. The trailing bubble has relatively little influence on the velocity and the shape of the leading bubble, but the wake of the leading bubble has a significant effect on the velocity and deformation of the trailing bubble. The simple principle of superposition (neglecting deformation of the trailing bubble) gives a good description of the inter- action of two in-line bubbles with $Re_A \leq 110$. Predictive coalescence models using this principle will be in good agreement with the data if a realistic velocity field is used.

3.   The apparent wake velocity experienced by the trailing bubble is only a function of the Reynolds number of the leading bubble.

4.   The behaviour of the bubble formed by coalescence depends on the viscosity of the liquid as well as the size of the interacting bubbles.

CHAPTER 6

SKIRTED BUBBLES AND DROPS

6.1 Introduction

Bubbles rising in highly viscous liquids have been reported to
trail very thin sheets of gas, often referred to as "skirts", from the
periphery of their rear surfaces (Jones 1965; Angelino 1966; Davenport
et al 1967; Guthrie and Bradshaw 1969; Calderbank et al 1970; Wegener
et al 1971; Wairegi 1974). Similar observations have also been made for
liquid drops rising or falling in viscous liquids (Thomson and Newall
1885; Shoemaker and Chazal 1969; Wairegi 1972, 1974). The existence of
skirts has a strong effect on heat and mass transfer processes because
the contact area between the dispersed phase and the continuous phase is
markedly increased and because the flow conditions behind the bubble (or
drop) are changed. Three aspects of skirts are considered in this chapter:
(i) incipience of skirts, (ii) skirt thickness, and (iii) skirt length.

6.2 Literature Review

The work of Guthrie and Bradshaw (1969) was the first theoretical
treatment of skirts. The thickness of the skirt was predicted by assuming
viscous flow inside the skirt and then by equating the hydrostatic pressure
increase in the liquid outside the skirt to the pressure increase inside
the skirt due to the gas motion. The gas in the skirt was treated as a
two-dimensional Poiseuille flow, i.e. the skirt was idealized as a slab.
The skirt thickness, Λ, was shown to be:

$$\Delta \cdot = \sqrt{\frac{12\mu'U}{\rho g}} \qquad\qquad (6.1)$$

or

$$\Delta = \sqrt{\frac{6\mu'U}{\rho g}} \qquad\qquad (6.2)$$

Equation (6.1) is applicable where the wake enclosed by the skirt is stagnant while Equation (6.2) assumes a recirculating wake with the liquid velocity down the inside surface of the skirt being equal to that of the liquid flowing down the outer surface of the skirt. By ingeniously trapping the gas skirts they found the skirts to be extremely thin, of order 40 μm, in reasonable agreement with the theoretical values pre-dicted by Equations (6.1) and (6.2). Wairegi and Grace (1974) modified the Guthrie and Bradshaw treatment by taking the skirt to be an annular cylindrical shell. For physically realistic cases their prediction is not significantly different (less than 1%) from that of Guthrie and Bradshaw.

A criteria for the incipience of skirts behind spherical-cap bubbles was proposed by Wegener et al (1971). The pressure due to the flow at the rim of the bubble was estimated by assuming a two-dimensional creeping flow at the corner formed by the bottom surface of the bubble and the boundary of the circulating wake at the rim of the bubble. This flow was matched at the bubble edge to the outer flow velocity given by potential flow (see Fig.6.1). It was postulated that a skirt is formed when the normal viscous force at the rim of the bubble cannot be balanced by the surface tension force. Application of this criteria gave the critical bubble rise velocity for the onset of a skirt, U_c, as

$$U_c \quad \blacksquare \quad \frac{}{3\mu}) \frac{(\pi-\theta_m) + \sin\theta_m \cos\theta_m}{\sin^2\theta_m \tan(\theta_m/2)} \qquad\qquad (6.3)$$

where θ_m is the semi-included angle. This equation was tested for bubbles in mineral oil over a small range of viscosity (μ — 2.05 P to 2.59 P) and favourable agreement was shown. Wairegi and Grace (1974) applied the theory of Wegener et al in terms of the corner angle, ϕ, and the velocity at the bubble surface, q_o. Unfortunately, they made an error in equating the forces at the corner and were led to propose an empirical expression for q_o to bring their predictions into agreement with the experimental data.

Wairegi (1972, 1974) made experimental observations of skirted drops in a large number of systems of varying physical properties. The onset of the skirt was found to depend upon a dimensionless number called the "skirt number", $Sk = \mu U/\sigma = We/Re^*$, and the Reynolds Number, Re. The existence of flow in the liquid skirt was confirmed by observation of the motion of solid tracer particles dispersed in the drop phase; however, complete flow patterns inside the skirt and accurate velocity measurements were not possible. A theoretical treatment of the transition from a stable to a wavy skirt was also initiated and reasonable qualitative agreement with the theory was demonstrated.

6.3 Objectives

It is obvious from the above review that our understanding of the skirt phenomena is far from complete. The theory of Wegener et al

---

* The skirt number is a measure of the relative magnitude of viscous and interfacial tension forces. It has been referred to as the capillary number, Ca., in the literature dealing with free coating of flat plates (White and Tallmadge 1965) and petroleum recovery problems (Scriven 1974).

(1971) can explain the occurence of skirts behind spherical-cap bubbles at high Re (Re $\gtrsim$ 45) but fails to explain the incipience of skirts behind the oblate-ellipsoidal-cap bubbles observed in relatively high M liquids at low Re (Re $\lesssim$ 45) (see Section 6.5.1). The first objective of the work reported in this chapter was to extend this skirt incipience model to an oblate-ellipsoidal-cap bubble (or drop) with an indented base, and to use this model to explain the experimental data.

The second objective was to explain why the skirts behind bubbles appear to be quite thick and of almost constant thickness in contrast to the skirts behind drops which appear to be comparatively thin and which exhibit decreasing thickness with length (compare, for example, the photograph in Fig.6.10(2) with that in Fig.6.17(2)).

Thirdly, the factors that control the length of the skirt were to be explored.

The final aim was to collect more experimental data and to test the theories and hypotheses proposed in the present work.

6.4 Theory

6.4.1 Skirt incipience theory

The co-ordinate system is taken to be fixed to the moving bubble or drop, thus the continuous liquid appears to be moving downward with a velocity U equal to the terminal rise velocity (see Fig.6.1(a)). Consider the flow in the corner formed by the lower surface, OA, of a bubble or a drop and the wake boundary, OS (see Fig.6.1(b)). Inside this corner in the neighbourhood of O, the flow is assumed to be two-dimensional and inertial forces are neglected compared to viscous forces. The flow in
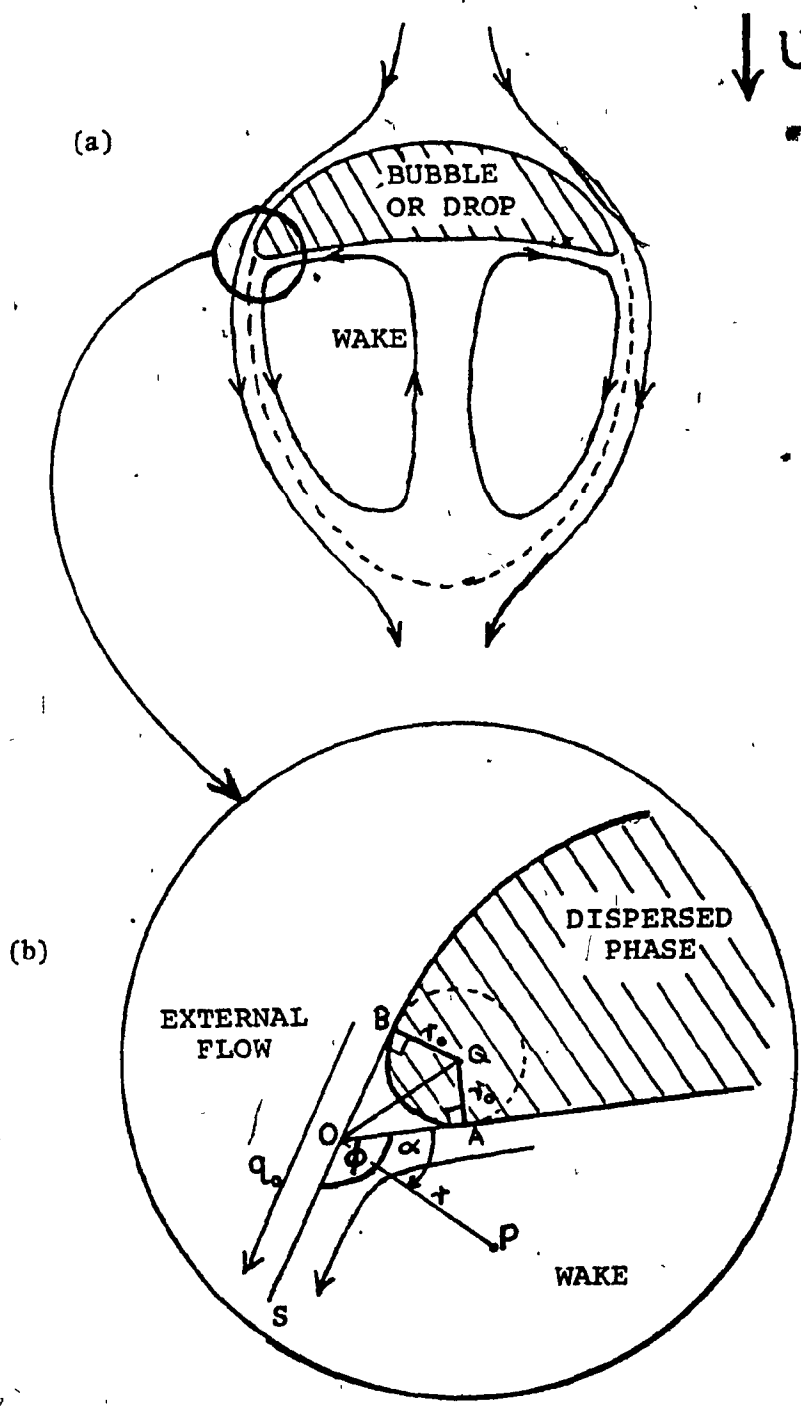
FIGURE 6-1: Co-ordinate system for the flow around the
edge at the point of skirt formation.

such a corner can be described by a stream function of the form (Moffatt 1964; Batchelor 1967):

$$\psi = rf(\alpha) \qquad (6.4)$$

which must satisfy

$$\nabla^2(\nabla^2\psi) = 0 \qquad (6.5)$$

where

$$\nabla^2 = \frac{\partial}{\partial r^2} + \frac{1}{r}\frac{\partial}{\partial r} + \frac{1}{r^2}\frac{\partial^2}{\partial \alpha^2} \qquad (6.6)$$

hence, we require

$$f''''(\alpha) + 2f''(\alpha) + f(\alpha) = 0 \qquad (6.7)$$

The solution of Equation (6.7) is of the form

$$f(\alpha) = (c_1\alpha + c_2)\cos\alpha + (c_3\alpha + c_4)\sin\alpha \qquad (6.8)$$

where c_1, c_2, c_3 and c_4 are the constants to be determined from the following boundary conditions.

(i)   Since $\alpha = 0$ is a streamline

$$f(0) = 0 \qquad (6.9)$$

(ii)   Since $\alpha = \phi$ is a streamline separating the outside flow and the wake

$$f(\phi) = 0 \tag{6.10}$$

(iii) For the cases where the dispersed phase viscosity, $\mu' <<$ the continuous phase viscosity, μ, the tangential stress along the base OA, i.e. along $\alpha = 0$, is negligible. Hence,

$$f''(0) = 0 \tag{6.11}$$

(iv) Along the streamline, OS, the external flow imposes a velocity, q_o, on the liquid in the wake, hence

$$f'(\phi) = q_o \tag{6.12}$$

With these four boundary conditions the constants in Equation (6.8) are determined giving:

$$f(\alpha) = -\frac{q_o(\alpha\cos\alpha\sin\phi - \phi\cos\phi\sin\alpha)}{\phi - \sin\phi\cos\phi} \tag{6.13}$$

From the streamfunction, the normal stress on the bottom surface, $\alpha = 0$, can now be obtained as

$$P_{\alpha\alpha}\Big|_{\alpha = 0} = \frac{2\mu q_o\sin\phi}{r(\phi - \sin\phi\cos\phi)} \tag{6.14}$$

This normal stress must be balanced by the surface or interfacial tension stress, σ/r_o, hence

$$\frac{\sigma}{r_o} = \frac{2\mu q_o \sin\phi}{r(\phi - \sin\phi\cos\phi)} \qquad (6.15)$$

where σ is the surface or interfacial tension and r_o is the radius of curvature of the interface.

From Equation (6.15) we see that as the edge is approached (i.e., $r \to 0$) the radius of curvature, r_o, decreases. A skirt will appear if the radius of curvature becomes so small that it is not possible to join the base and the frontal part of the bubble (or drop). Thus, the limiting condition for the appearance of a skirt is achieved when the base and the front can just be joined by a circular arc BA (see Fig.6.1(b)) so that

$$r_o = r \tan Q\widehat{O}A = r \tan(\tfrac{1}{2}B\widehat{O}A) = r \tan(\tfrac{\pi-\phi}{2})$$

$$\therefore \ r_o = r \cot(\phi/2) \qquad (6.16)$$

Combining Equation (6.15) and (6.16) we get

$$\frac{\mu q_o}{\sigma} = \frac{\phi - \sin\phi\cos\phi}{2\sin\phi\cot(\phi/2)} \qquad (6.17)$$

At the volumes for which skirts first appear bubbles and drops have been observed to be spherical-cap or oblate-ellipsoidal-cap in shape (see Fig.6.10). For these shapes the surface velocity at the edge of the bubble or drop may be given by:

$$q_o = K_o C_f U \tag{6.18}$$

where K_o = shape-dependent surface velocity coefficient for potential flow (see Table 6.1) and C_f = correction factor for departure from potential flow.

Combination of Equations (6.18) and (6.17) yields

$$\frac{\mu U}{\sigma} = \frac{\phi - \sin\phi\cos\phi}{2 C_f K_o \sin\phi \cot(\phi/2)} \tag{6.19}$$

Because of refraction of light at the outer surface it is not possible to observe the exact shape of the indentation, especially near the bubble rim (see Fig.6.10). Hence, it is practically impossible to determine the corner angle, ϕ, with acceptable accuracy. To circumvent this problem three simple shapes for the bubble base are proposed which permit calculation of values of the corner angle, ϕ, and hence, Sk. These idealized shapes and the corresponding equations for ϕ are summarised in Tables 6.3 and 6.4.

From Tables 6.1 to 6.4 it is clear that $\phi = f(\theta_m, b/a, \text{shape of the indentation})$ and $K_o = f(\theta_m, b/a)$. It was demonstrated in Chapter 3 that the shape parameters θ_m, and b/a as well as the size of the indentation are a function of Reynolds Number, Re. It is also reasonable to assume that the correction factor, C_f, is a function of Re with $C_f < 1$ for low Re and C_f approaching unity at high Re. (This is shown to be true in Section 6.5.1.) Thus we expect the right-hand side of Equation (6.19) to be function of Re, whereas the left-hand side is simply the skirt number, Sk.

TABLE 6.1 Surface Velocity, q_o, for Potential Flow Past Bodies of Various Shapes

$$q_o = C_f K_o U$$

where U = free stream velocity
  K_o^* = shape-dependent surface velocity coefficient for potential flow
  C_f = correction factor for departure from potential flow ($C_f = 1$ for potential flow)

Shape	K_o	Reference
spherical	$K_o = \dfrac{3}{2}\sin\theta$	Davies & Taylor (1950)
oblate ellipsoid	$K_o = \dfrac{e^3\sin\eta}{(\sin^{-1}e - e\sqrt{1-e^2})\{(1-e^2)\sin^2\eta\,\cos^2\eta\}^{1/2}}$	Wairegi & Grace (1976)
prolate ellipsoid	$K_o = \dfrac{e^3\sin\eta}{(e-(1-e^2)\tanh^{-1}e)\{\sin^2\eta\,(1-e^2)\cos^2\eta\}^{1/2}}$	Grace & Harrison (1967)

where $e = \sqrt{1 - \left(\dfrac{b}{a}\right)^2}$

  a = semi-major axis

  b = semi-minor axis

For definitions of θ and η see Table 6.2.

TABLE 6.2 Relationship between Eccentric Angle, η, and the Angle
Measured from the Front Stagnation Point, θ
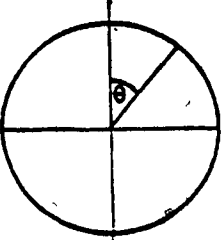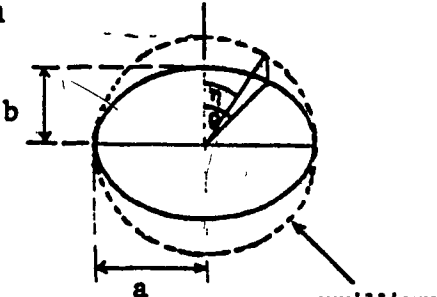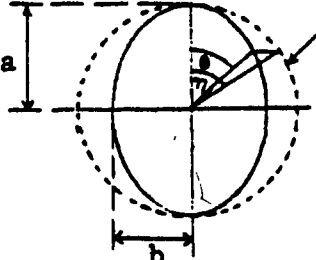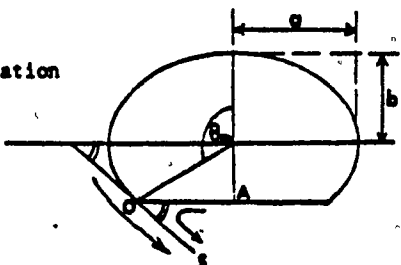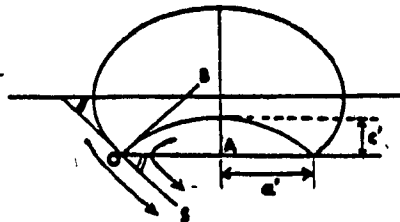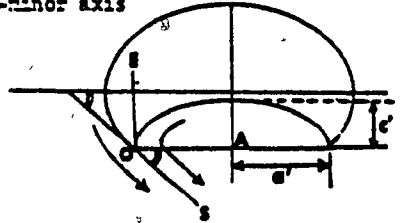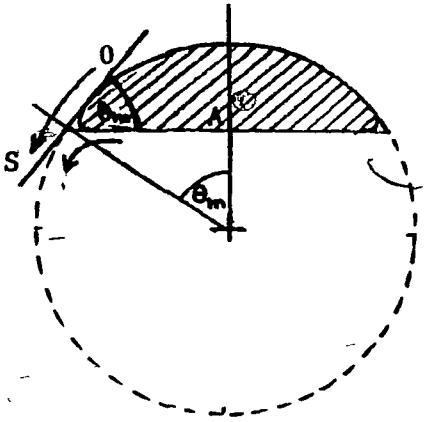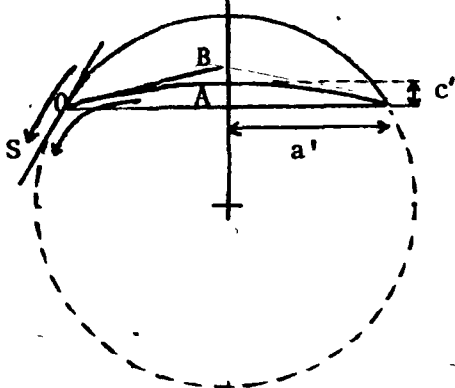
Shape	η
(a) spherical	$\eta = \theta$ for all θ
(b) oblate ellipsoidal	$\eta = \tan^{-1}(\frac{b}{a}\tan\theta)$ for $\theta < 90^{\circ}$ $\eta = \pi - \tan^{-1}\left[\frac{b}{a}\tan(\pi-\theta)\right]$ $\theta > 90^{\circ}$
(c) prolate ellipsoidal	$\eta = \tan^{-1}(\frac{a}{b}\tan\theta)$ for $\theta < 90^{\circ}$ $\eta = \pi - \tan^{-1}\left[\frac{a}{b}\tan(\pi-\theta)\right]$ $\theta > 90^{\circ}$

TABLE 6.3 Corner Angle, ϕ, for Oblate Ellipsoidal Cap at Onset of Skirt

Shape of the Base	ϕ
(a) Flat i.e. no indentation 	Since OS is a tangent to the elliptical surface at the bubble or drop edge, 0, it follows from geometrical property of ellipse: $\phi = A\hat{O}S = \phi_f$ where $\phi_f = \tan^{-1}(-\frac{b}{a}\tan n)$* for $n > 90$ $\phi_f = \pi - \tan^{-1}(\frac{b}{a}\tan n)$ for $n < 90$
(b) Spherical indentation 	$\phi = B\hat{O}S = A\hat{O}S + B\hat{O}A$ $= \phi_f + \sin^{-1}\left[\frac{2(c'/a')}{1+(c'/a')^2}\right]$
(c) Semi-ellipsoidal** indentation with a' = semi-major axis c = semi-minor axis 	$\phi = E\hat{O}S = A\hat{O}S + E\hat{O}A = \phi_f + \pi/2$

* eccentric angle n is related to the semi-included angle, θ_m, by equations listed in Table 6.2(b)
** indentation of this shape is impossible for $\theta_m < 90°$

TABLE 6.4   <u>Corner Angle,ϕ,for Spherical Cap</u>

Shape of the Base	ϕ
(a) Flat base	$\phi = \widehat{AOS} = \pi - \theta_m$
(b) Spherical indentation	$\phi = \widehat{BOS} = \widehat{AOS} + \widehat{BOA}$ $\phi = \pi - \theta_m + \sin^{-1}\left[\dfrac{2(c'/a')}{1+(c'/a')^2}\right]$

263.

If the bubble (or drop) is a spherical-cap with a flat base and the external flow is potential flow, then

$$\phi = \pi - \theta_m \qquad\qquad (6.20(a))$$

$$C_f = 1 \qquad\qquad (6.20(b))$$

and

$$K_o = 3/2 U \sin\theta_m \qquad\qquad (6.20(c))$$

On substituting these three equations into Equation (6.19) we recover Equation (6.3) which was derived by Wegener et al (1971).

6.4.2 Skirt thickness theory

Consider a skirted bubble or drop, the outer surface of which can be represented by a spheroid. We introduce a curvilinear system of co-ordinates on the outer surface as shown in Fig.6.2. The velocity components parallel and normal to the surface are denoted by u and v, respectively. Let the terminal velocity, U, and the maximum width of the bubble or drop, w, be the characteristic velocity and the characteristic length, respectively. Since the non-dimensional skirt thickness is expected to be very small, i.e. $\frac{\Delta}{w} \ll 1$ (Guthrie and Bradshaw 1969) and hence the velocity gradient normal to the surface, $\frac{\partial u}{\partial y}$, is very large, the flow of the dispersed phase inside the skirt is described by the following boundary layer equations, which are identical to those for a boundary layer on a body of revolution (Schlichting 1968).

$$\Delta \ll w$$

Note: (1) Skirt is present for $\theta_s > \theta > \theta_c$.

(2) The most probable direction of the flow is shown on the left half.

FIGURE 6.2   Co-ordinate System for Skirt Thickness Theory

$$\frac{\partial u}{\partial t} + u\frac{\partial u}{\partial x} + v\frac{\partial u}{\partial y} = \frac{1}{\rho'}\frac{\partial P}{\partial x} + \frac{\mu'}{\rho'}\frac{\partial^2 u}{\partial y^2} \tag{6.21}$$

and

$$\frac{\partial}{\partial x}(ur(x)) + \frac{\partial}{\partial y}(vr(x)) = 0 \tag{6.22}$$

Here the contour of the body of revolution is specified by the radius $r(x)$ of the section taken normal to the axis of symmetry, and ρ' and μ' are the density and the viscosity of the dispersed phase, respectively.

An order of magnitude estimate of terms in the equation of motion in the y-direction shows that the pressure gradient in the y-direction is negligible compared to that in the x-direction and thus the external fluid pressure is imposed on the dispersed phase fluid in the skirt.

If the flow is steady and fully developed within the skirt (the latter is an approximation at either end of the skirt) and inertia terms are neglected, Equation (6.21) simplifies to:

$$\frac{dP}{dx} = \mu'\frac{d^2 u}{dy^2} \tag{6.23}$$

The velocity profile for the viscous flow within the skirt, and the corresponding skirt thickness may now be obtained by solving Equation (6.23) using appropriate boundary conditions.

Fig.6.3(a) shows an enlarged cross-section of the skirt. The skirt is assumed to enclose a recirculating wake with the liquid velocity down the inside surface of the skirt being, q_i, and the velocity of the liquid flowing down the outer surface of the skirt being, q_o. Since there is no net flow down the skirt if the skirt is not growing, the velocity near the center of the skirt is directed upward. The boundary conditions are: (i) at $y = 0$, $u = q_o$; (ii) at $y = -\Delta$, $u = q_i$

(a) <u>Most likely velocity profile</u> $(0 < q_i < q_o)$

dispersed
fluid

external liquid

$y = -\Delta$

q_i

wake

q_o

y

x

(b) <u>Recirculating wake</u> $(q_i = q_o)$

dispersed
fluid

external liquid

$y = -\Delta$

wake

q_i

q_o

y

x

(c) <u>Stagnant wake</u> $(q_i = 0)$

dispersed
fluid

external liquid

$y = -\Delta$

wake

q_o

y

x
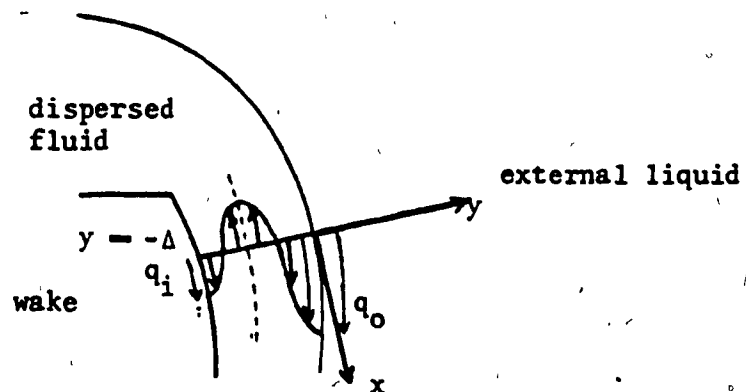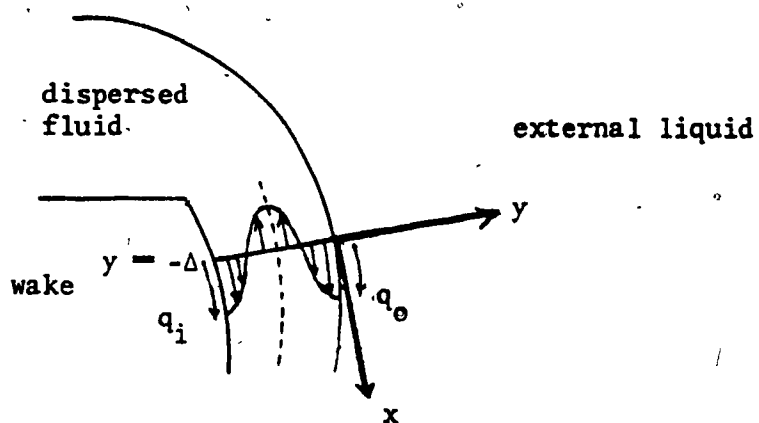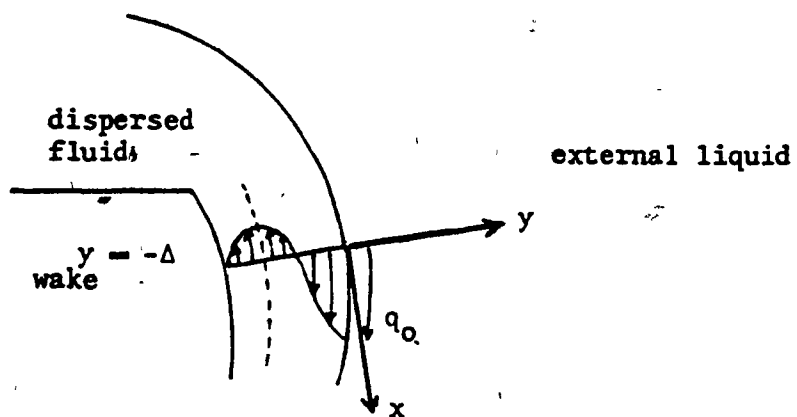
FIGURE 6.3 <u>Velocity Profiles for Dispersed Phase Flow
Within Skirt</u>

Integrating Equation (6.23) twice with respect to y and using the above boundary conditions gives the velocity profile in the skirt:

$$u = \frac{1}{2\mu'} \frac{dP}{dx}(y^2 + y\Delta) + \frac{y}{\Delta}(q_o - q_i) + q_o \qquad (6.24)$$

Under steady state conditions, the net flow rate across any cross-section of the skirt is zero, i.e.

$$\int_{-\Delta}^{o} u\,dy = 0 \qquad (6.25)$$

Substituting for u from Equation (6.24) and integrating we obtain the skirt thickness, Δ.

$$\Delta = \sqrt{\frac{6\mu'(q_o + q_i)}{\frac{dP}{dx}}} \qquad (6.26)$$

Since it would be extremely difficult to measure, q_i, we consider two limiting conditions which should bracket the actual case.

For the recirculating wake with $q_i = q_o$ (see Fig.6.3(b)), the skirt thickness is given by:

$$\Delta = \sqrt{\frac{12\mu'q_o}{\frac{dP}{dx}}} \qquad (6.27)$$

For the stagnant wake, $q_i = 0$ (see Fig.6.3(c)), hence the skirt thickness reduces to:

$$\Delta = \sqrt{\frac{6\mu'q_o}{\frac{dP}{dx}}} \qquad (6.28)$$

We will now consider the various shapes for the skirted bubbles and drops that are encountered in practice (see Fig.6.4) and show how the shape affects the predicted thickness through the terms q_o and $\frac{dP}{dx}$.
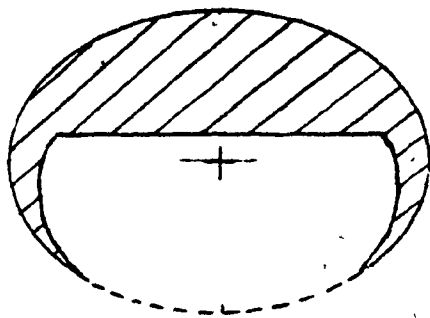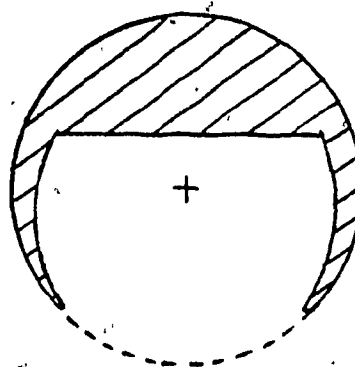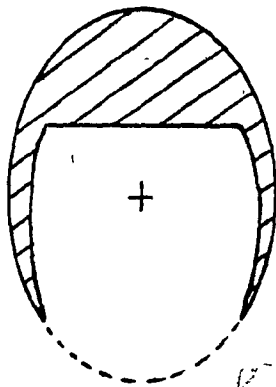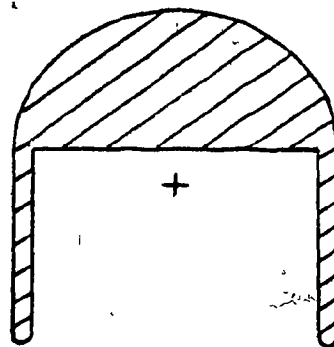
FIGURE 6.4 Various Shapes for Skirted Bubbles and Drops

Consider first the oblate ellipsoidal skirted bubble or drop shown in Fig.6.2. If the flow external to the skirt,is taken to be potential flow, Bernoulli's equation may be applied between the front stagnation point, S, and any other point, A, on the outer surface to give:

$$P = P_S + \rho g h_o - \frac{\rho q_o^2}{2} \tag{6.29}$$

where P and q_o represent the total pressure and the surface velocity, respectively, at a vertical distance, h_o, below the front stagnation point where $h_o = 0$, $P = P_S$ and $q_o = 0$.

Note that the pressure, P, in Equation (6.23) is the modified pressure such that

$$P = p' - h_o \rho' g \tag{6.30}$$

where p' and ρ' are the total pressure and the density of the dispersed phase, respectively.

Since the radius of curvature of the outer surface of the bubble or drop is quite large, the pressure difference due to interfacial tension can be ignored giving $P = p'$. Combination of Equation (6.29) and (6.30) yields

$$P = P_S + h_o(\rho - \rho')g - \frac{\rho q_o^2}{2} \tag{6.31}$$

From the geometry of the ellipse (see Fig.6.2),

$$h_o = b(1 - \cos\eta) \qquad (6.32)$$

The surface velocity, q_o, for a potential flow around the oblate ellipsoid is related to the terminal velocity by the equation listed in Table 6.1. The terminal velocity, U, of the bubble or drop is in turn related to its shape as shown in Table 6.5.

Substituting the appropriate relations for q_o, U and Equation (6.32) in Equation (6.31) yields the pressure distribution inside the skirt (i.e. for $\theta_c < \theta < \theta_s$):

$$P = P_s + (\rho - \rho')(1 - \cos\eta)bg - \frac{(\rho-\rho')\sin^2\eta bg}{2\{(1-e^2)\sin^2\eta + \cos^2\eta\}}$$
$$\ldots\ldots(6.33)$$

For the ellipsoidal co-ordinate system it can readily be shown that

$$\frac{\partial\eta}{\partial x} = \frac{1}{a\left[(1-e^2)\sin^2\eta + \cos^2\eta\right]^{1/2}} \qquad (6.34)$$

Noting that the pressure gradient tangential to the outer surface is given by:

$$\frac{dP}{dx} = \frac{\partial P}{\partial\eta} \cdot \frac{\partial\eta}{\partial x} \qquad (6.35)$$

we finally obtain

$$\frac{dP}{dx} = \frac{(\rho-\rho')g\sqrt{1-e^2}\sin\eta}{\left[(1-e^2)\sin^2\eta + \cos^2\eta\right]^{1/2}}\left[1 - \frac{\cos\eta}{\left[(1-e^2)\sin^2\eta + \cos^2\eta\right]^2}\right]$$
$$\ldots\ldots(6.36)$$

TABLE 6.5 Relationship between Terminal Velocity of Bubble or Drop and its Shape

Shape	Terminal Velocity, U	Reference
(a) Spherical cap	$U = \frac{2}{3}\sqrt{\frac{(\rho-\rho')}{\rho}gR}$	Davies and Taylor (1950) for bubbles where $(\rho-\rho') \approx \rho$ Harrison et al. (1961) for drops
(b) Oblate ellipsoidal cap	$U = \frac{\sin^{-1}e - e\sqrt{1-e^2}}{e^3}\sqrt{\frac{(\rho-\rho')}{e}gb}$	Wairegi and Grace (1976)
(c) Prolate ellipsoidal cap	$U = \frac{\sqrt{1-e^2}\,e - (1-e^2)\tanh^{-1}e}{e^3}\sqrt{\frac{(\rho-\rho')}{\rho}ga}$	Simple extension of treatment by Grace and Harrison (1967) for bubbles

Here $e = \sqrt{1-\left(\frac{b}{a}\right)^2}$

Substituting for q_o from Table 6.1 and $\frac{dP}{dx}$ from Equation (6.36) into Equations (6.27) and (6.28) we get the skirt thickness

$$\Delta = F\sqrt{\frac{12\mu'U}{(\rho-\rho')g}} \tag{6.37}$$

and

$$\Delta = F\sqrt{\frac{6\mu'U}{(\rho-\rho')g}} \tag{6.38}$$

for the recirculating wake and the stagnant wake, respectively.

Here the "shape dependent thickness coefficient", F, is

$$F = \left[\frac{e^3}{\sqrt{1-e^2}(\sin^{-1}e - e\sqrt{1-e^2})\{1 - \frac{\cos\eta}{\left[(1-e^2)\sin^2\eta + \cos^2\eta\right]^2}\}}\right]^{1/2}$$

$$\cdots\cdots(6.39)$$

The potential flow assumption for the external flow is expected to give the upper limit for the actual flow. Hence, if we introduce the correction factor, C_f, which corrects for the deviation from potential flow, the skirt thickness for the recirculating wake and the stagnant wake are given by:

$$\Delta = F\sqrt{\frac{12C_f\mu'U}{(\rho-\rho')g}} \tag{6.40}$$

and

$$\Delta = F\sqrt{\frac{6C_f\mu'U}{(\rho-\rho')g}} \tag{6.41}$$

respectively.

By applying a similar theoretical treatment to prolate and spherical shape skirted bubbles or drops, we can obtain equations analogous to those obtained above. The resulting equations are summarized in Table 6.6.

TABLE 6.6 <u>Summary of Relations used to find Skirt Thickness for Various Shapes</u>

	oblate ellipsoidal	prolate ellipsoidal	spherical
h_o	$b(1-\cos\eta)$	$a(1-\cos\eta)$	$R(1-\cos\eta)$
$\dfrac{\partial\eta}{\partial x}$	$\dfrac{1}{a\left[(1-e^2)\sin^2\eta+\cos^2\eta\right]^{1/2}}$	$\dfrac{1}{a\left[\sin^2\eta+(1-e^2)\cos^2\eta\right]^{1/2}}$	$\dfrac{1}{R}$
P	$p_s+(\rho-\rho')(1-\cos\eta)bg$ $-\dfrac{bg(\rho-\rho')\sin^2\eta}{2\{(1-e^2)\sin^2\eta+\cos^2\eta\}}$	$p_s+(\rho-\rho')(1-\cos\eta)ag$ $-\dfrac{ag(\rho-\rho')\sin^2\eta}{2\{\dfrac{1}{(1-e^2)}\sin^2\eta+\cos^2\eta\}}$	$p_s+(\rho-\rho')(1-\cos\eta)Rg$ $-\dfrac{Rg(\rho-\rho')\sin^2\eta}{2}$
$\dfrac{dP}{dx}$	$\dfrac{A(\rho-\rho')g\sqrt{1-e^2}\sin\eta}{\left[(1-e^2)\sin^2\eta+\cos^2\eta\right]^{1/2}}$	$\dfrac{B(\rho-\rho')g\sin\eta}{\left[\sin^2\eta+(1-e^2)\cos^2\eta\right]^{1/2}}$	$(\rho-\rho')g(1-\cos\eta)\sin\eta$
F	$\left[\dfrac{e^3}{\sqrt{1-e^2}(\sin^{-1}e-e\sqrt{1-e^2})A}\right]^{1/2}$ where $A=1-\dfrac{\cos\eta}{\left[(1-e^2)\sin^2\eta+\cos^2\eta\right]^2}$	$\left[\dfrac{e^3}{\left[e-(1-e^2)\tan\eta^{-1}e\right]B}\right]^{1/2}$ where $B=1-\dfrac{\cos\eta}{\left[\dfrac{1}{1-e^2}\sin^2\eta+\cos^2\eta\right]^2}$	$\left[\dfrac{3}{2(1-\cos\eta)}\right]^{1/2}$

The relationships for the oblate and for the prolate shape, reduce to those for a sphere when $a = b = R$ and $e = 0$.

The theory of Guthrie and Bradshaw (1969) is a special case of the present theory. They assumed the bubble skirt to be a vertical slab (see Fig.6.4(d)). For this case $q_o = U$ and $\frac{dP}{dx} = \rho g$; hence, the skirt thickness equations (6.27) and (6.28) simplify to Guthrie and Bradshaw's results, Equations (6.1) and (6.2), respectively.

For a drop with straight skirt, $q_o = U$ but $\frac{dP}{dx} = (\rho - \rho')g$. Substitution of these values in Equation (6.28) gives

$$\Delta = \sqrt{\frac{6\mu'U}{(\rho-\rho')g}} \qquad (6.42)$$

which has recently been used by Wairegi (1974) for skirted drops.

The skirt thickness coefficient, F, is a measure of the variation of skirt thickness with angular position or length. It is clear from Table 6.6 that F is a function of the shape that fits the outer surface of the skirted bubble or drop. The skirt thickness coefficient for different shapes is plotted in Fig.6.5 for $50^\circ < \theta < 140^\circ$. This range of θ, the angle measured from the vertical axis, covers the values of θ for which skirts have been observed for bubbles and drops (see Fig.6.20 and Fig.6.21). It is important to note that in all three cases where the outer surface is curved (i.e. for sphere, oblate and prolate shape) the skirt thickness coefficient decreases. This implies that skirts become thinner, with increasing skirt length, which is in agreement with experimental observations (see Fig.6.17(2)).

Shape

AR < 1	Oblate ellisoid
AR = 1	Sphere
AR > 1	Prolate ellipsoid
AR = ∞	Straight skirt
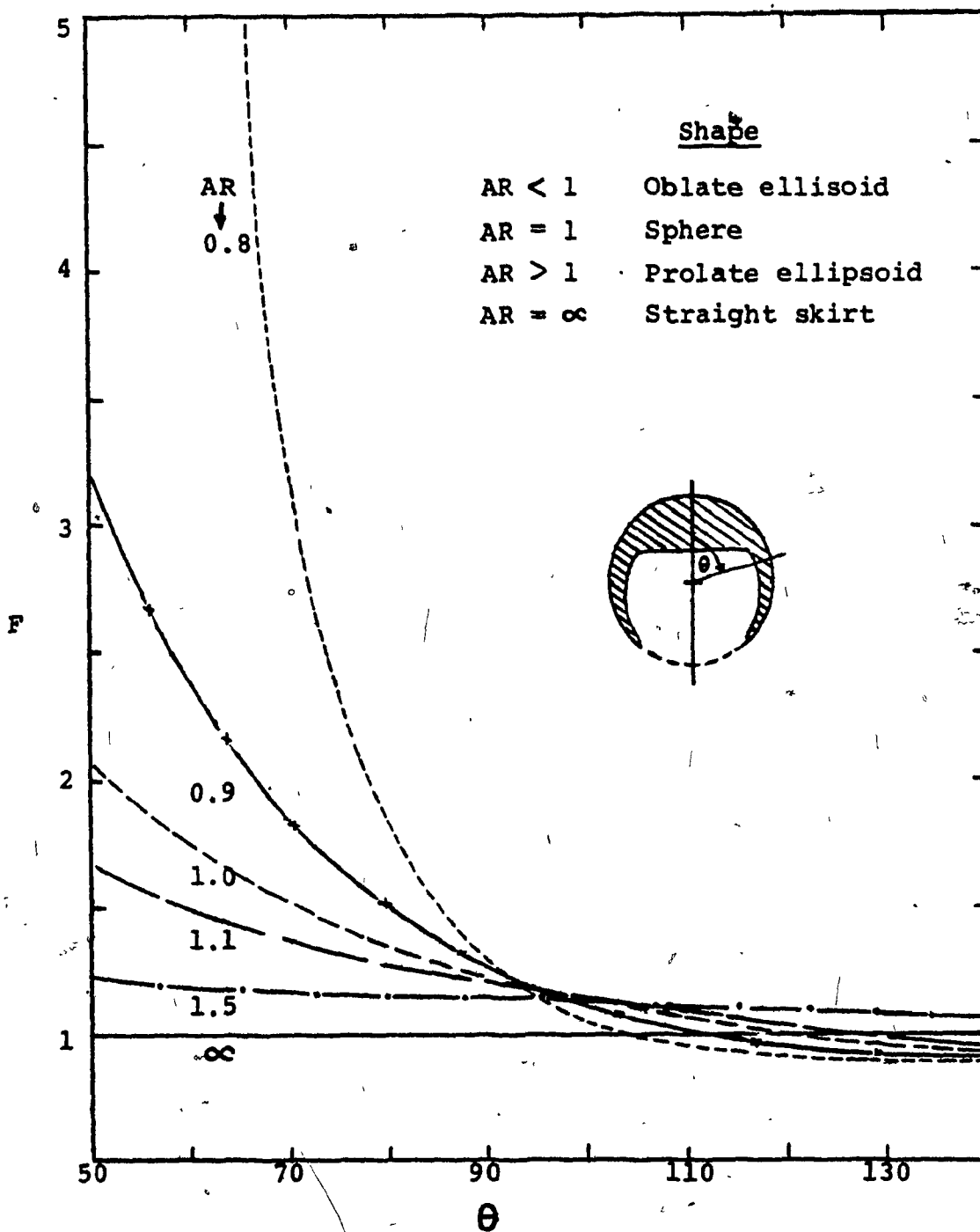
FIGURE 6-5: <u>Theoretical predictions of skirt thickness coefficient, F, for various shapes of bubbles or drops.</u>

The rate of decrease in F and hence the rate at which the skirt thins is greater at smaller θ and levels off at larger θ. The skirt thinning rate is quite high for oblate spheroid of low aspect ratio, AR*. It becomes progressively smaller with increasing AR and in the limit as AR $\to \infty$, i.e. for a straight skirt, the value of F is constant at unity indicating that the skirt thickness remains constant. This latter conclusion is in accord with the simple theory of Guthrie and Bradshaw (1969).

6.4.3 Skirt length theory

It has been observed experimentally that stable skirts always extend below the equator; thus the angle measured to the end of the skirt, θ_s is greater than 90°. We postulate that the length of the skirt is determined by the forces acting at the end of the skirt. For increasing θ_s when $\theta_s > 90^o$, the surface velocity decreases and hence the viscous force decreases. On the other hand the surface tension force increases with increasing θ_s because of the decrease in the skirt thickness. The length attained by a stable skirt is that where these forces are balanced.

Consider a skirted bubble or drop, the outer surface of which is a spheroid. A simple geometrical model for the end of the skirt is shown in Fig.6.6(b). Locally the flow in the corner AES (corner angle $= \phi$) is assumed to be two-dimensional creeping flow. Along the surface BS, the external flow imposes its velocity, q_o, on the liquid in the wake. Thus,

*. The aspect ratio, AR, is defined as the ratio of vertical semi-axis to horizontal semi-axis, i.e. AR $=$ b/a.
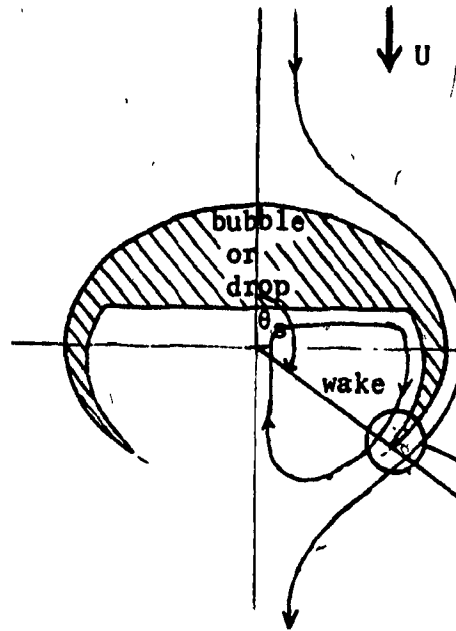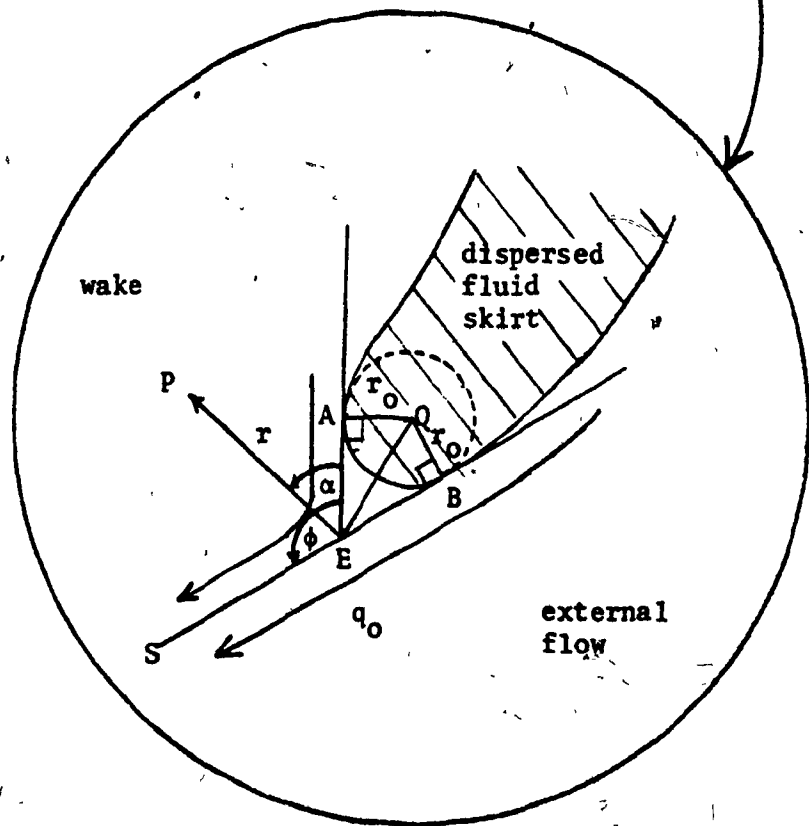
FIGURE 6.6 Co-ordinate System for the Flow Around the End of the Skirt

the situation is very similar to that for the onset of the skirt depicted in Fig.6.1 and discussed in Section 6.4.1. By applying a similar theoretical treatment the skirt length criterion can be shown to be:

$$\frac{\mu U}{\sigma} = \frac{\phi - \sin\phi\cos\phi}{2C_f K_0 \sin\phi\cot(\phi/2)} \qquad (6.43)$$

which is identical to that for skirt formation, Equation (6.19). The value of K_0 for various shapes is given by the equations listed in Table 6.1.
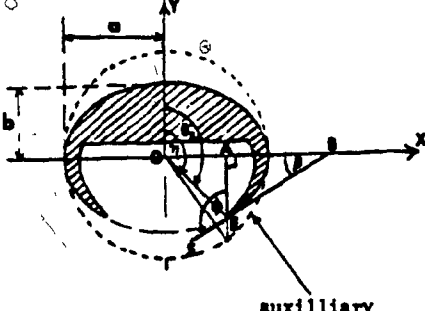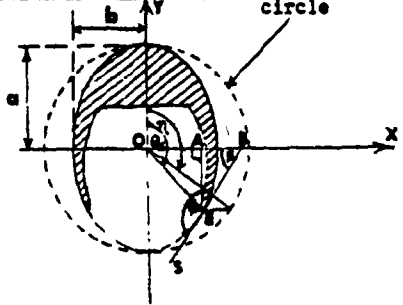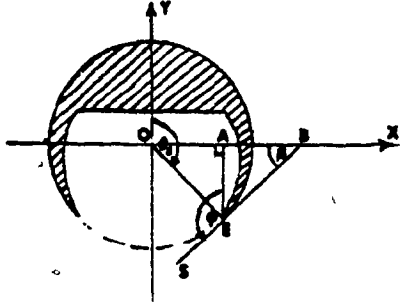
We assume a rather simple geometry for the end of the skirt which enables us to relate the corner angle, ϕ, to the skirt termination angle, θ_s. The tangent ES to the outer skirt surface at the end of the skirt, E, and the vertical line EA that is parallel to the vertical axis are taken to be the two sides of the corner so that $\phi = \widehat{AES}$ (see Fig.6.6 and the sketches in Table 6.7). The relations between ϕ and θ_s for the different shape skirted bubbles or drops are listed in Table 6.7, and are self-explanatory.

From Tables 6.1, 6.2 and 6.7 it is clear that both K_0 and ϕ are related to b/a and θ_s. By substituting these relations into the general skirt length relationship, Equation (6.43), and putting $C_f = 1$, i.e. assuming the external flow to be potential flow, we can find the skirt termination angle, θ_s, at a given skirt number, Sk, for different aspect ratio, AR. The results of such computations are plotted in Fig.6.7 for the range of aspect ratio 0.6 to 1.4 that covers the shapes for skirted bubbles and drops encountered in practice.

For any given bubble or drop the presence of a skirt does not change the terminal velocity (see Section 6.5.1.1). Consider a bubble released from the bottom of the column. If it is large enough a skirt will start to grow. Since the rise velocity is not affected by the

TABLE 6.7 Corner Angle, ϕ , for Predicting Skirt Length

(Note: SEB is tangent to the skirt outer surface at E where the skirt ends; EA is perpendicular to the horizontal axis.)

Shape	ϕ
(a) oblate	From geometrical property of ellipse: $\eta = \pi - \tan^{-1}\frac{b}{a}(\pi-\theta_s)$ $\beta = \tan^{-1}(-\frac{b}{a}\tan\eta)$ From $\triangle AEB$: $\phi = \pi/2 + \beta$
(b) prolate	From geometrical property of ellipse: $\eta = \pi - \tan^{-1}\frac{a}{b}(\pi-\theta_s)$ $\beta = \tan^{-1}(-\frac{b}{a}\cot\eta)$ From $\triangle AEB$: $\phi = \pi/2 + \beta$
(c) spherical	Since $O\hat{E}B = 90°$ $\beta = \pi - \theta_s$ From $\triangle AEB$: $\phi = \pi/2 + \beta = \frac{3\pi}{2} - \theta_s$
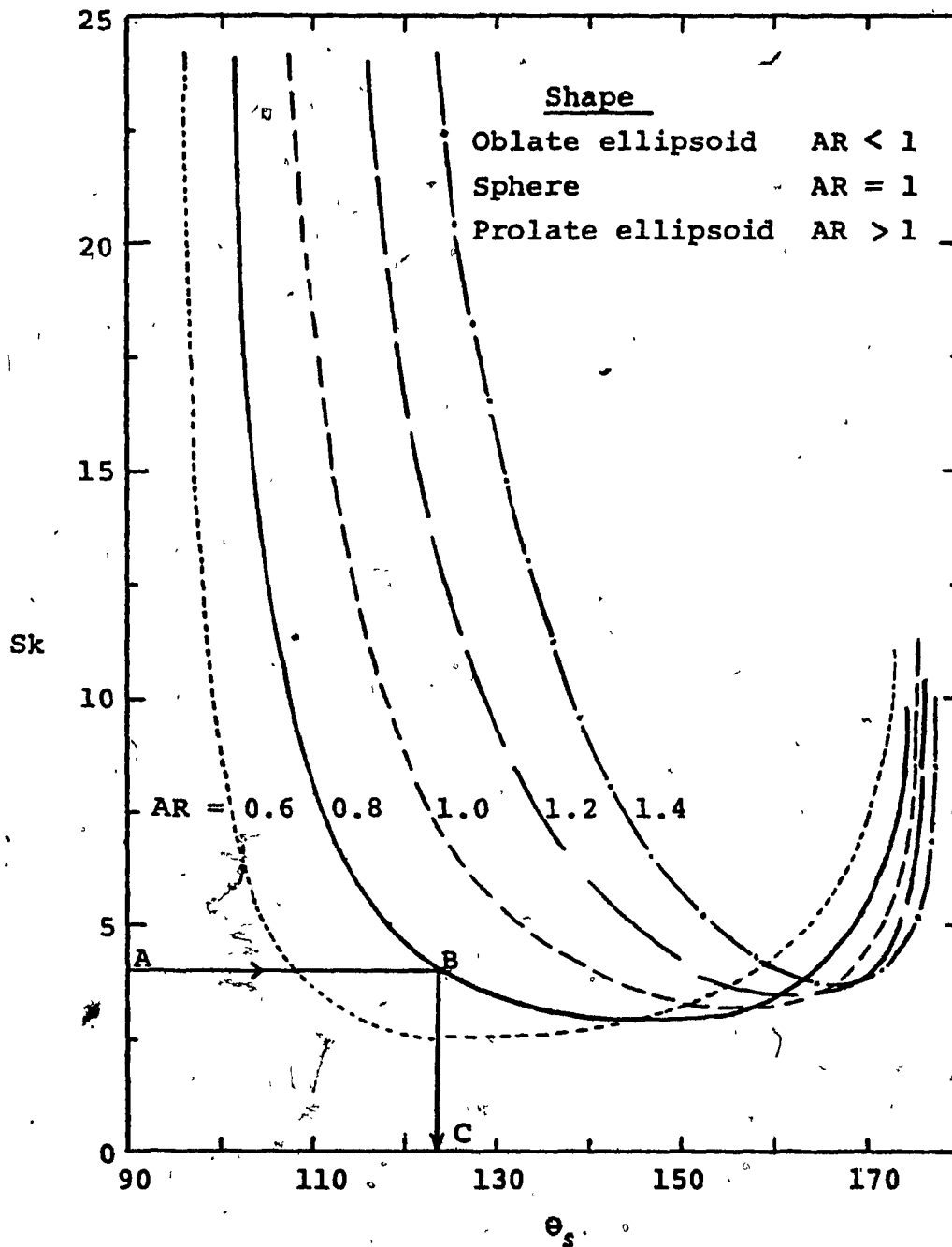
FIGURE 6-7: <u>Theoretical prediction of skirt termination angle, θ_S,</u>

<u>for skirted bubble or drop of different shapes.</u>

presence of the skirt, the skirt number, Sk, remains constant as the skirt grows. The skirt will grow until the surface tension force at the end of the skirt becomes large enough to balance the viscous force which is trying to lengthen it. This critical condition is given in Fig.6.7 by that portion of the curves to the left of the minimum.* For example, the theory predicts a skirt termination angle of 124° for an oblate shaped bubble or drop of AR = 0.8 and Sk = 4 (see Fig.6.7).

An important implication of the theory is that skirts should exist only for bubbles or drops with Sk $\geqslant$ 2.5. It is encouraging to find that all the skirted bubbles and drops reported to date have Sk $\geqslant$ 2. (see Fig.6.9).

6.5 Experimental Results and Discussion

6.5.1 Skirt incipience results

The critical bubble volume at which stable skirts first appear was determined for aqueous sugar solutions with viscosities from 4.6 P to 28.3 P. The results are presented in Fig.6.8, which shows that the critical volume above which skirts exist is strongly dependent on the liquid viscosity. These same results are plotted as skirt number, Sk, versus the Reynolds Number, Re, in Fig.6.9. Data from earlier studies are also included for comparison. The physical properties of the liquids, the column size and other pertinent data are listed in Table 6.8. The experimental data are all well ordered with data for higher M liquids

---

* From the above reasoning it is concluded that the region to the right of the minimum is physically impossible.
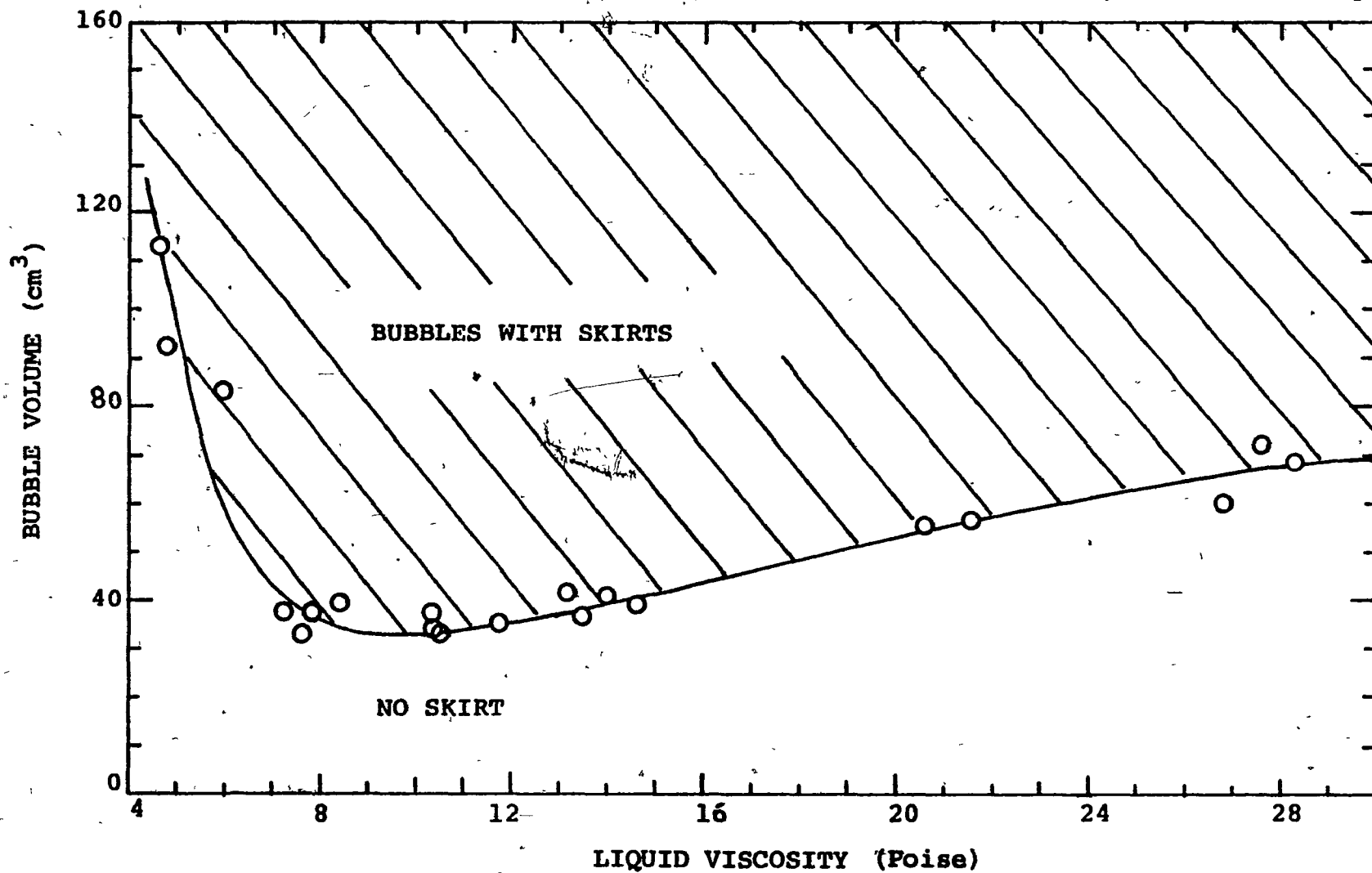
FIGURE 6-8: Critical bubble volume for skirt incipience in sugar solutions.

TABLE 6.8 Critical Conditions for Incipience of Skirts for Bubbles

Author	Column Size	Liquid	Temp. (°C)	M (Poise)	ρ (g/cm³)	σ (dynes/cm)	V (cm³)	U (cm/sec)	M (-)	Re (-)	Sk (-)	EO (-)
Present work	29.2 cm I.D.	sugar solution	20.3	28.28	1.390	80.0	68.6	38.50	8.82×10^2	9.61	13.61	440
"	"	" "	20.5	27.60	1.390	80.0	72.4	37.30	8.00×10^2	9.71	12.87	456
"	"	" "	20.8	26.80	1.390	80.0	59.4	35.40	7.11×10^2	8.89	11.86	399
"	"	" "	25.5	21.60	1.388	79.8	56.4	37.52	3.03×10^2	11.47	10.16	386
"	"	" "	25.5	20.60	1.390	80.0	55.6	36.60	2.48×10^2	11.70	9.42	382
"	"	" "	22.4	14.60	1.382	79.3	38.9	37.70	6.45×10	15.00	6.94	302
"	"	" "	19.3	13.98	1.379	78.8	40.8	37.60	5.55×10	15.84	6.67	313
"	"	" "	25.1	13.44	1.387	79.8	36.1	36.91	4.54×10	15.62	6.22	287
"	"	" "	19.9	13.15	1.378	78.8	41.6	38.00	4.35×10	17.12	6.34	317
"	"	" "	25.9	11.71	1.385	79.3	35.2	37.88	2.67×10	18.21	5.59	283
"	"	" "	25.9	10.42	1.382	79.3	32.9	38.04	1.68×10	20.05	5.00	270
"	"	" "	25.7	10.36	1.383	79.3	33.8	37.88	1.63×10	20.28	4.95	275
"	"	" "	25.1	10.30	1.382	79.3	37.0	39.95	1.60×10	22.16	5.19	292
"	"	" "	20.1	7.81	1.370	78.7	37.1	39.70	5.47	28.82	3.92	292
"	"	" "	25.0	7.69	1.372	78.6	32.4	40.32	5.15	28.46	3.94	268
"	"	" "	20.5	7.20	1.370	78.7	37.1	39.70	3.95	31.26	3.63	292
"	"	" "	21.2	5.92	1.358	77.7	83.5	50.90	1.89	63.32	3.88	504
"	"	" "	25.0	4.72	1.363	78.1	92.7	49.44	0.75	80.15	2.99	540
Davenport (1964)	15 cm I.D.	PVA solution	17.0	2.16	1.000	46.2	15.0	30.20	2.17×10^{-1}	42.78	1.41	199
Jones (1965)	45 cm x 45 cm	glycerol	16.0	16.70	1.260	62.5	35.0	36.00	2.48×10^2	11.02	9.62	326
"	"	"	19.6	12.00	1.261	62.5	20.0	44.00	6.6×10	15.57	8.45	224
Angelino (1966)	29 cm I.D.	glycerine oil	18.0	14.40	1.260	63.72	55.0	35.00	1.29×10^2	14.45	7.91	432
"	"	" "	18.0	7.40	0.882	31.85	25.0	32.50	1.03×10^2	14.05	7.55	358
Guthrie (1967)	45 cm I.D.	PVA solution	18.3	7.35	1.02	46.0	20.0	30.5	2.88×10	14.39	4.92	247
Calderbank et al (1970)	10.6 cm I.D.	99% glycerol	25.0	7.75	1.256	62.5	28.7	32.0	1.15×10	19.71	3.97	285
Wegener et al (1971)	30 cm I.D.	mineral oil	varied	~2.0 to 2.5	0.89	32.0	~25 to 50	~40 to 50	~1.33 to 0.53	~50 to 90	~3.2 to 2.8	~350 to 550
Wairegi (1974)	32 cm x 39 cm	sugar solution	29.0	14.72	1.392	79.1	50.0	33.60	6.69×10	14.52	6.25	361
"	"	" "	28.5	13.35	1.392	79.1	45.0	33.41	4.52×10	15.54	5.70	336
"	"	" "	27.0	3.4	1.366	50.2	45.0	45.71	7.57×10^{-1}	81.04	3.09	519
"	"	paraffin oil	19.5	2.0	0.883	37.5	25.0	41.74	3.37×10^{-1}	67.42	2.25	303
Hnat & Buckmaster (1976)	150 cm I.D.	mineral oil	varied	1.10 to 2.12	0.874 to 0.880	32.0 to 33.1	?	?	~0.52 to 0.05	~50 to 500	~2.2 to 2.45	?
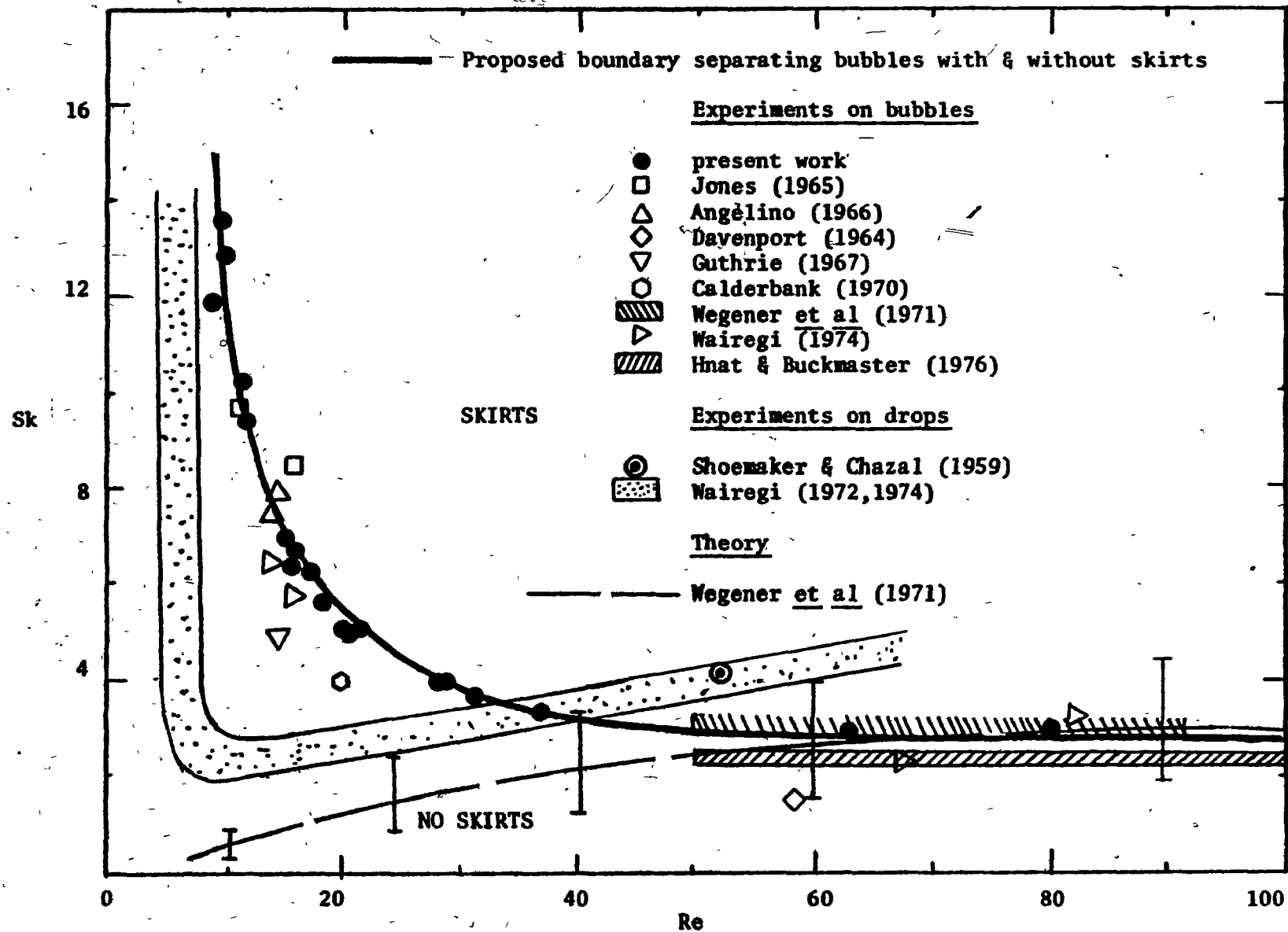
FIGURE 6.9 Variation of skirt number with Reynolds number at skirt incipience for bubbles & drops

being progressively further to the left and higher up on the curve.

From this figure we conclude that skirts do not exist for bubbles having Re less than about 9 or Sk less than about 2.

Data on the incipience of skirts for drops are also shown in Fig.6.9 for comparison. These results differ somewhat from those for bubbles, possibly because the variation of the shape of drops with Re may be different from that of bubbles and also because the internal flow of the higher density and viscosity dispersed phase liquid may be important.

These data were also used to map the skirted bubble region on the Reynolds Number versus Eötvos Number plot of Fig.3.13. Using this latter figure it is possible to predict either the critical bubble volume or the rise velocity for the appearance of a skirt in any liquid.

The theoretical equation of Wegener et al (1971), Equation (6.3), relates Sk to the semi-included angle, θ_m, for spherical-cap bubbles. In Chapter 3 the experimental relationship between θ_m and Re was presented graphically in Fig.3.12. These values were combined with Equation (6.3) to give a theoretical prediction of Sk shown by the dashed line in Fig.6.9. The range of the theoretical prediction of Sk, indicated by the vertical bars reflects the scatter in the measured values of θ_m at a given Re. The agreement with the experimental data at large Re is excellent since the potential flow assumption for the external flow (see Chapter 4) and the assumption of spherical-cap shape with a flat base (see Chapter 3) are both justified at high values of Re. At lower Re where the shape changes to oblate cap with a considerable indentation of the base, and where the external flow diverges from potential flow, the theory of Wegener et al falls below the data.

The effect of the liquid properties on the bubble shape at the skirt incipience condition is illustrated in Fig.6.10. For each pair of photographs, the one on the left shows a bubble just before the skirt begins to form, whereas that on the right shows the same bubble after a rise of about 40 to 50 cm. when the skirt had appeared. The bubble shape just before the skirt appears is oblate-cap with semi-included angle, $\theta_m > 90^O$, and a significantly indented base in very high M liquids; with decrease in M, both θ_m and the indentation decrease and the bubble tends towards a spherical-cap shape. At the incipience condition the outer boundary of the skirted bubble is oblate in high M liquids; is spherical in intermediate M liquids and tends to become prolate in low M liquids. The skirts appear to be of constant thickness of about 1 to 1.5 cm. This is an optical illusion due to the difference in the refractive index of air and sugar solution. Similar observations are also reported by other workers (Jones 1965; Angelino 1965; Guthrie 1967; Wairegi 1974). The volume of gas in the skirt is extremely small as can readily be verified by comparing the volume of any pair of bubbles both of which are shown at the same magnification.

The four photographs on the left clearly demonstrate how the refraction at the outer surface of the bubble distorts the shape of the base and prevents us from seeing the intersection of the base and the outer surface. Since this information is lacking, idealized models of the bubble base (see Tables 6.3 and 6.4) are used to permit the computation of the limiting values of the corner angle, ϕ, and hence Sk. The experimentally measured values of b/a, θ_m, c'and a' with $C_f = 1$ were used in the appropriate equations presented in Section 6.3.1 (Equation (6.19) and the equations listed in Tables 6.1 to 6.4) to predict the variation

FIGURE 6.10 Effect of Liquid Properties on Shape of Bubbles at Incipience of Skirt

No.*	Liquid Properties			M	V_3 (cm³)	U (cm/sec)	Re	Eö	Sk
	μ (Poise)	ρ (g/cm³)	σ (dynes/cm)						
1 & 2	7.81	1.370	78.5	5.51	37.1	39.70	28.8	293	3.95
3 & 4	15.15	1.378	78.8	4.35x10	41.6	38.00	17.1	317	6.34
5 & 6	20.60	1.384	79.5	$2.54x10^2$	55.5	36.60	11.7	383	9.48
7 & 8	27.60	1.390	80.8	$7.80x10^2$	72.4	37.30	9.71	456	12.87

* For each pair, the photograph on the left shows a bubble just before the skirt begins to form, whereas that on the right shows the same bubble after a rise of about 40 to 50 cm. by when the skirt had grown; each pair of bubbles is shown at the same magnification.
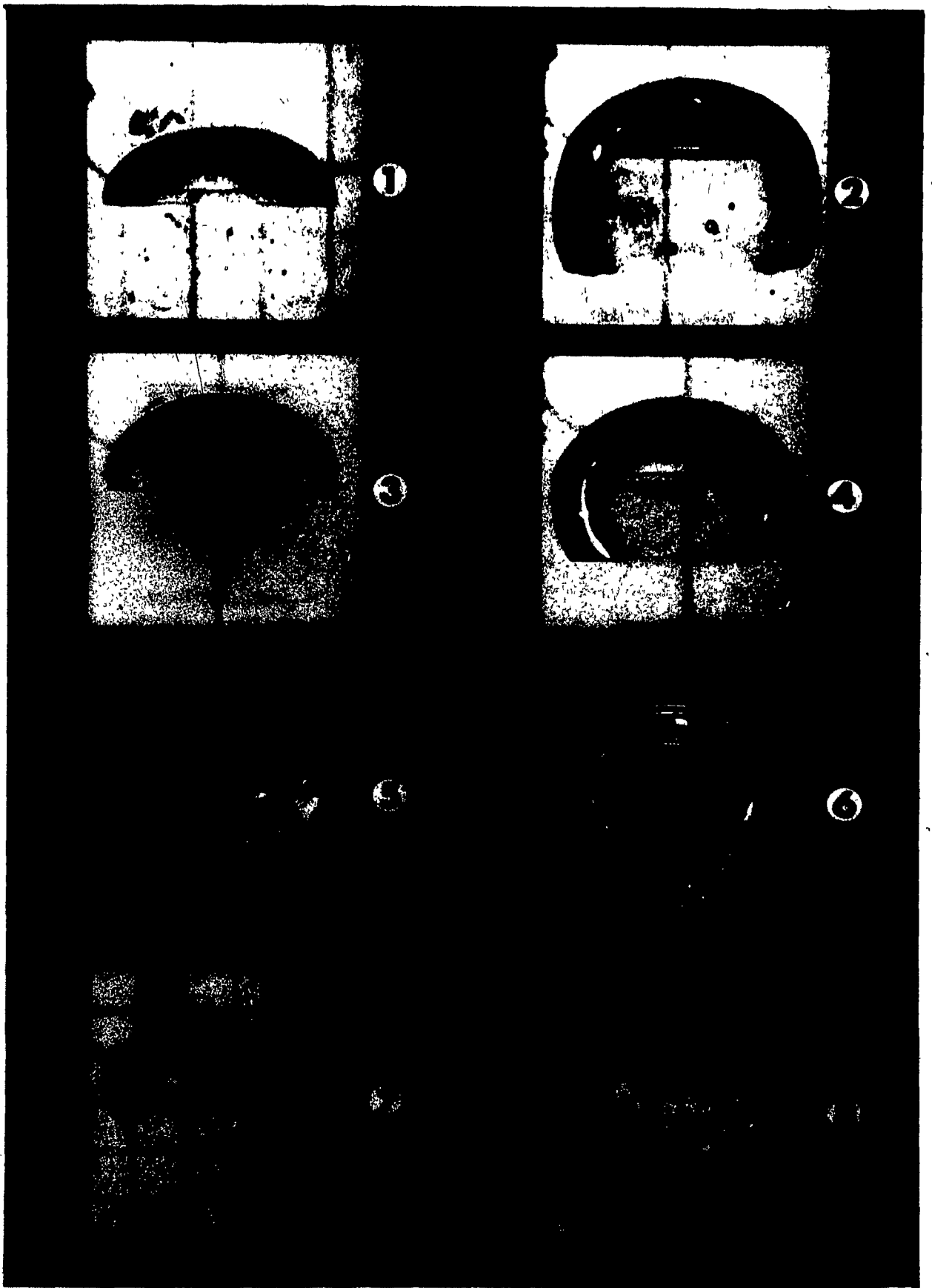
of Sk versus Re. These predictions are represented by curves ①, ②
and ③ in Fig.6.11.

The dimensionless velocity at the bubble edge, q^*_{oe}, defined by

$$q^*_{oe} = \frac{\text{measured velocity of external liquid at the bubble edge}}{\left(\begin{array}{l}\text{local velocity at the bubble edge predicted from poten-}\\\text{tial flow around the spheroid that fits the bubble}\end{array}\right)}$$

was calculated from the experimentally measured surface velocity data
(see Chapter 4) and is presented in Fig.6.12. As this dimensionless
velocity, q^*_{oe} is equivalent to the correction factor, C_f, we can incorporate
this additional information to get a better prediction of Sk versus Re,
the deviation from potential flow being accounted for by C_f. These pre-
dictions are displayed by the curves ①c , ②c and ③c in Fig.6.11.

Comparison of the experimental data with these theoretical
curves suggests the following shapes for the bubble base when skirts
first form:

Re	Predicted Shape for the Bubble Base
low ($9 \leqslant Re \leqslant 43$)	— between semi-ellipsoidal and spherical
intermediate ($43 \leqslant Re \leqslant 62$)	— between spherical and flat
high ($62 \geqslant Re \geqslant 168$)	— flat base

These predicted shapes for the base of the bubble are plausible and lend
support to the present theory. A more stringent test should be carried
out as data for drops on systems having similar refractive indices become
available. For the case of drops an accurate measurement of the corner

FIGURE 6-11: <u>Comparison of theoretical predictions</u>
<u>for skirt formation for bubbles with</u>
<u>experimental data</u>

Oblate cap   Spherical cap

① Flat base model

② Spherical indentation model

③ Semi-ellipsoidal indentation model

① c, ② c, ③ c represent above models incorporating measured values of correction factor C_f, taken from Fig. 6-14.

E experimental results (see Fig. 6.9)
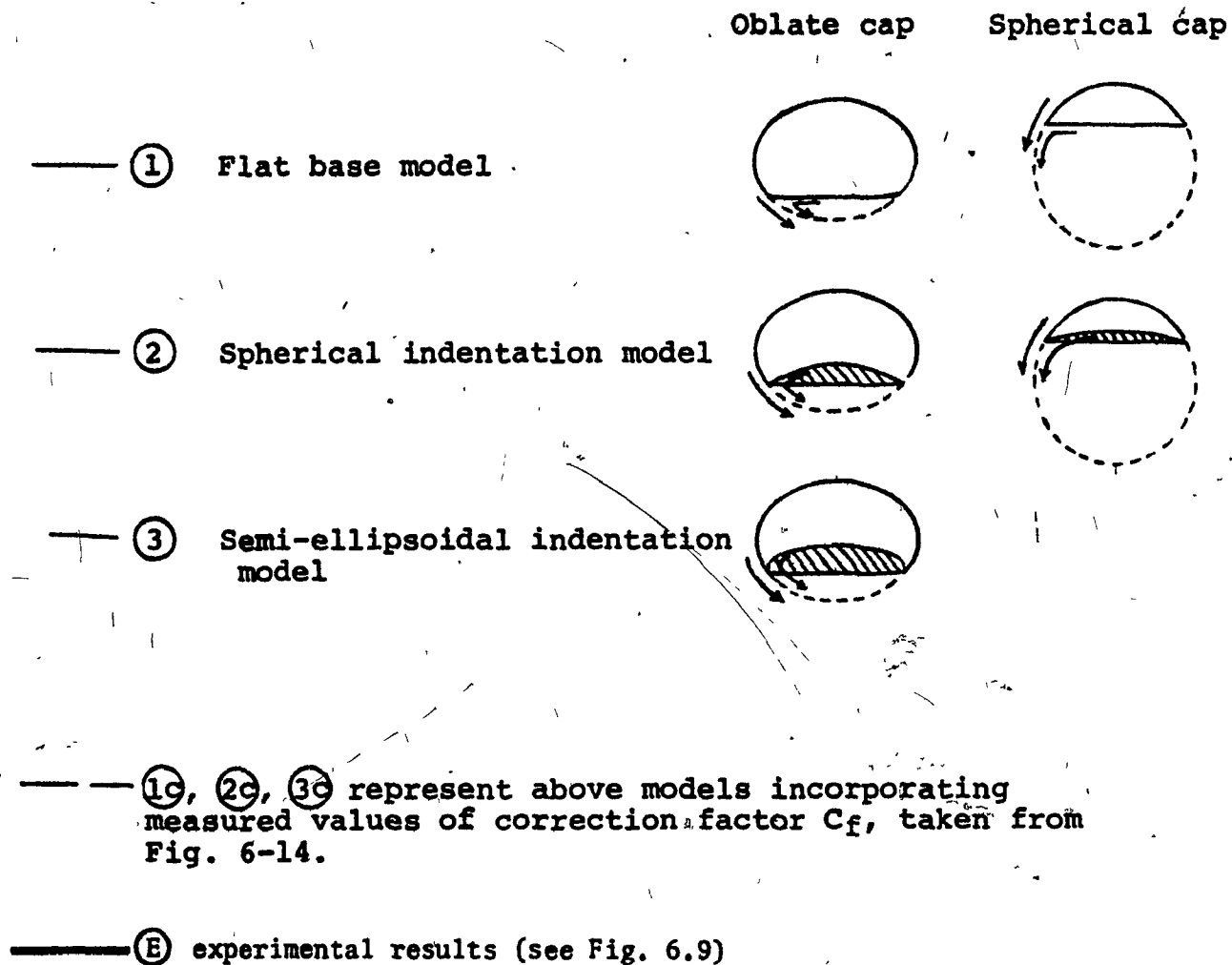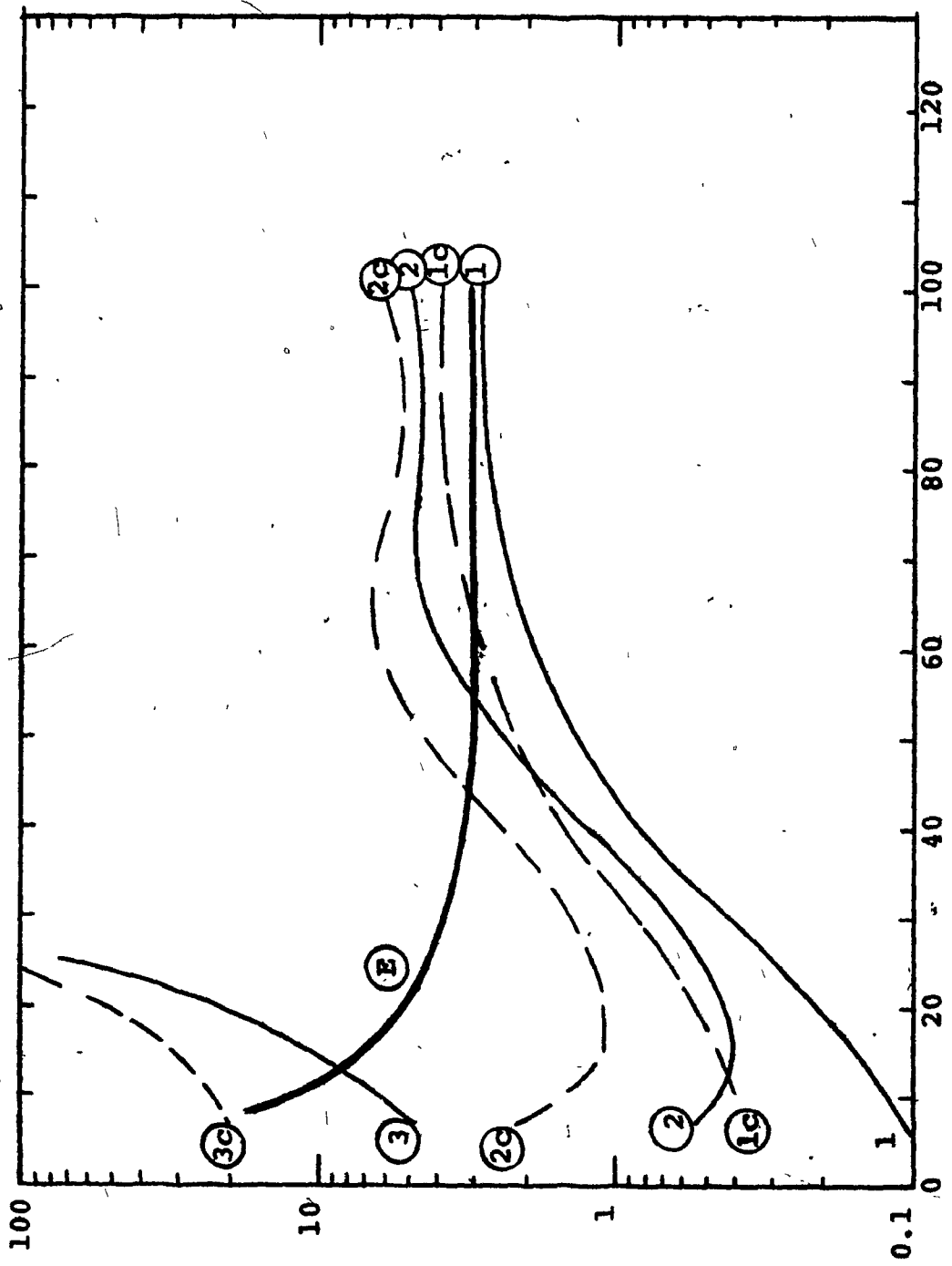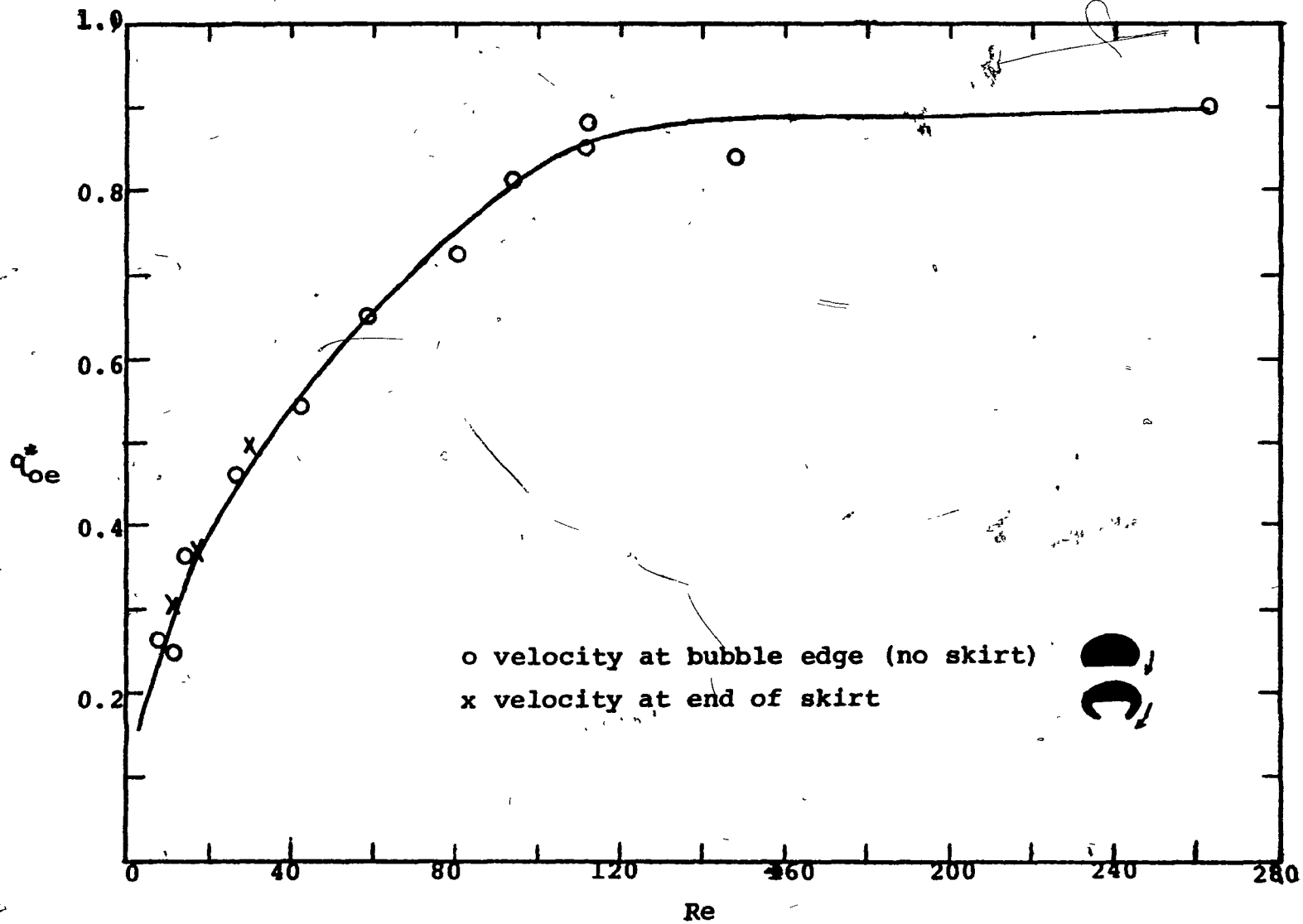
FIGURE 6-12: Dependence of dimensionless surface velocity at bubble edge on Re.

angle, ϕ, would be possible as can be seen from Fig.6.17(1) showing a typical photograph of a 50 cs silicone oil drop rising through 8.86 Poise sugar solution.*

6.5.1.1 Skirt growth and its effect on the rise velocity

The growth of the skirt behind bubbles in three different sugar solutions of viscosity 27.60, 13.15 and 7.81 Poise is illustrated in Figs.6.13(a), (b) and (c), respectively. A rise of more than about 50 cm. is required for the bubbles to attain a steady skirt length once the skirt starts to form. The distance travelled for the completion of the growth process seems to increase slightly with decreasing liquid Morton Number, M.

Fig.6.14 shows the variation of the vertical distance travelled with time for these same skirted bubbles. The time is taken to be zero at the instant the complete bubble first comes into the field of view which covered the upper 140 cm. of the column. The data for all three cases are well described by a straight line showing that the rise velocity is not affected by the formation and the subsequent growth of the skirt.

The rise velocity for skirted bubbles can be predicted using Fig.3.13. However, because we have used equations (see Table 6.5) relating the shape of the bubble or drop to its rise velocity in the formulation of the skirt thickness theory, it is worth testing these equations to see if they are indeed applicable. In Fig.6.15 the experimental velocities are compared with those predicted from the shape for spherical, oblate and prolate shape skirted bubbles as well as drops. The agreement is excellent, hence, we may conclude that the velocity of skirted bubbles and drops can be

---

* The author is grateful to Drs. T. Wairegi and J. Grace for their kind permission to reproduce the two drop photographs of Fig.6.17.

FIGURE 6.13 Stages of Skirt Growth for Air Bubbles
in Three Sugar Solutions

	Liquid Properties								
No.	μ (Poise)	ρ (g/cm^3)	σ (dynes/cm)	M (-)	V (cm^3)	U cm/sec	Re (-)	Eö (-)	Sk (-)
a	27.60	1.390	80.0	8.00×10^2	72.4	37.30	9.71	456	12.87
b	13.15	1.378	78.8	4.35×10	41.6	38.00	17.12	317	6.34
c	7.81	1.370	78.7	5.47	37.1	39.70	28.82	292	3.92

distance from the
bottom of the
column (cm)

↓

80

90

100

110

120

distance from
the bottom of
the column (cm)

↓

130

140

150

160

170

FIGURE 6.13(a)

distance from the
bottom of the
column (cm)

80

90

100

110

120

distance from
the bottom of
the column (cm)

130

140

150

160

170

FIGURE 6.13(b)

distance from the
bottom of the
column (cm)

distance from the
bottom of the
column (cm)

80

90

100

110

120

130

140

150

160

170
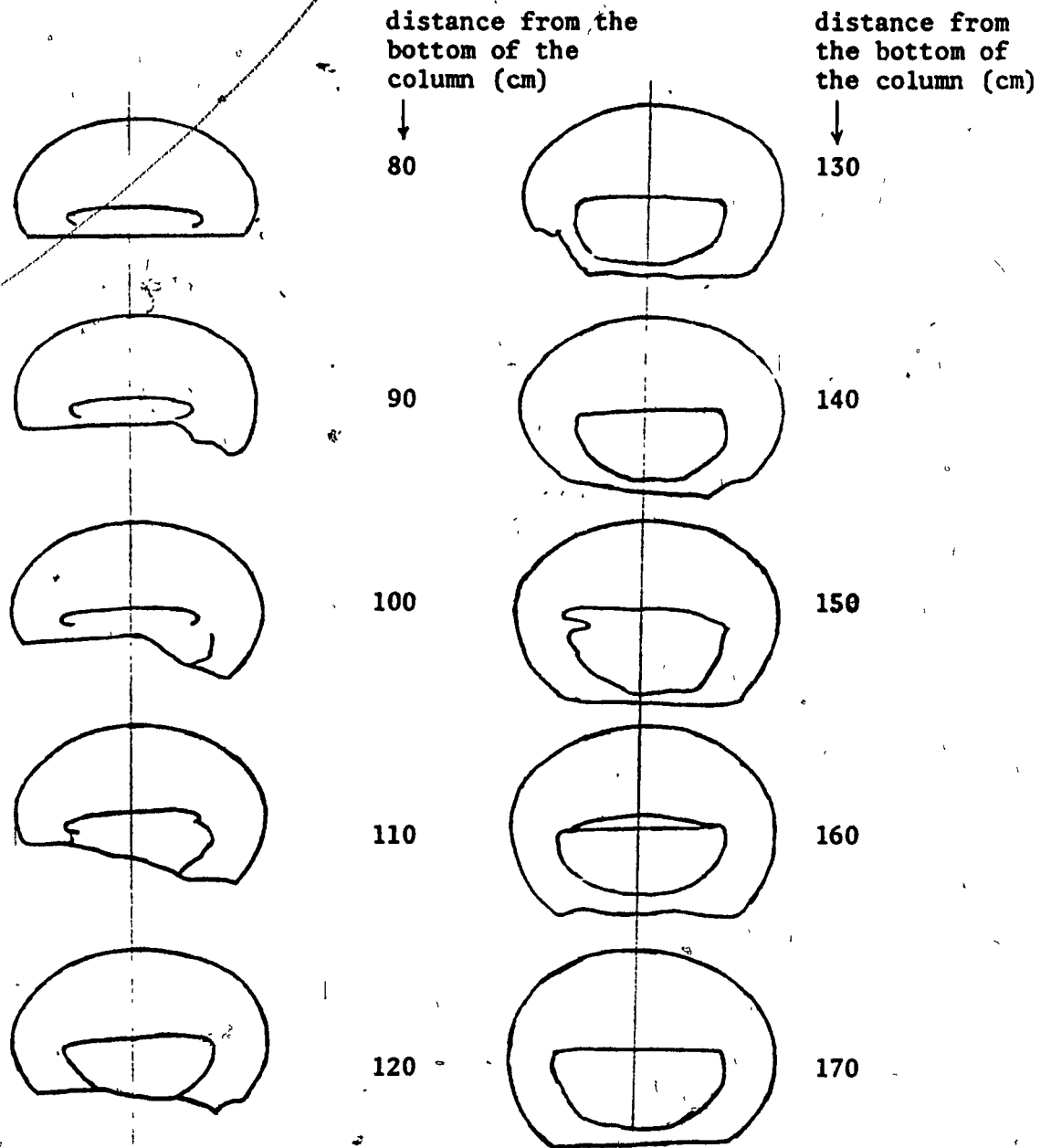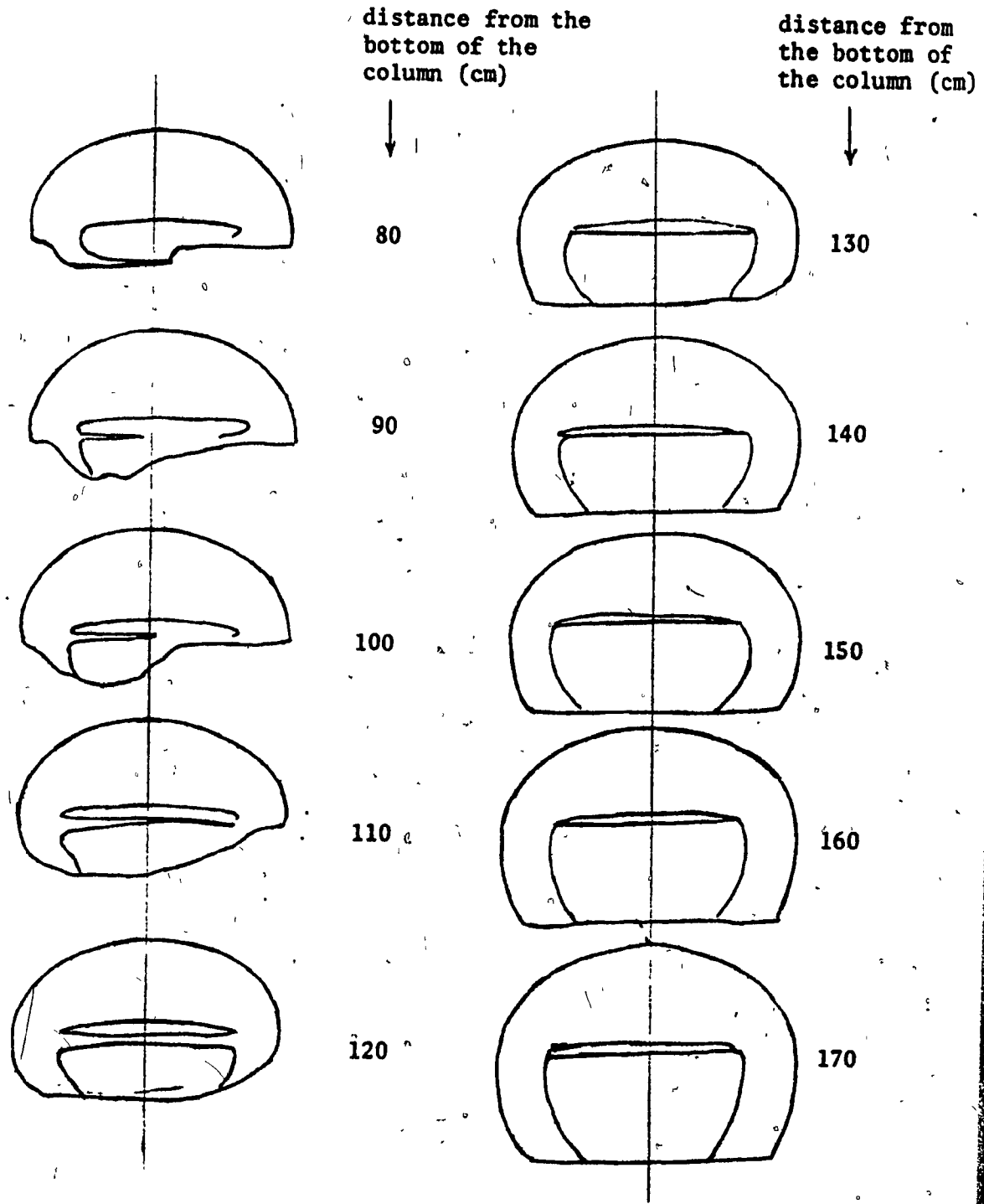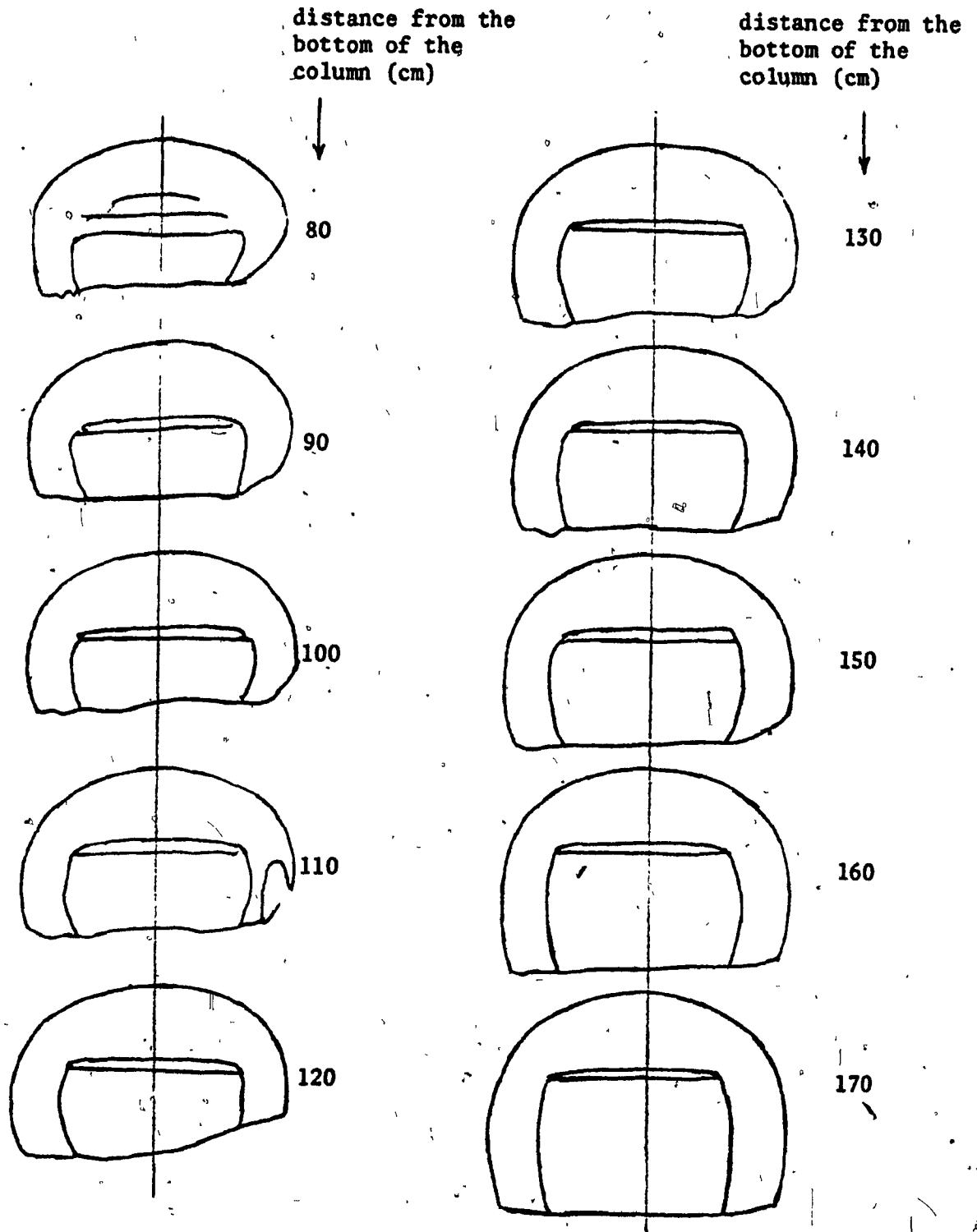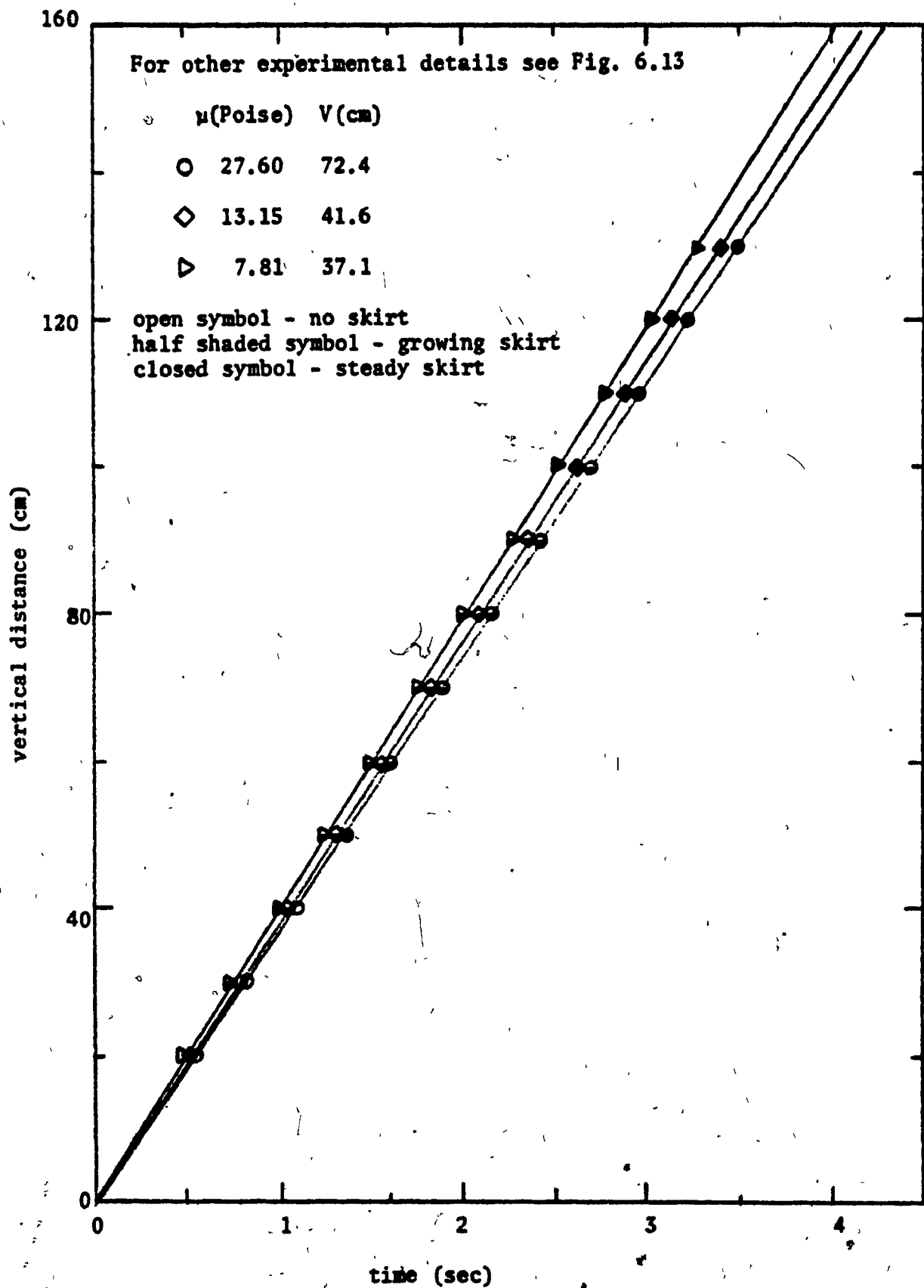
FIGURE 6.13(c)

FIGURE 6.14 Displacement versus time curve deduced from ciné-film of bubbles with growing skirts
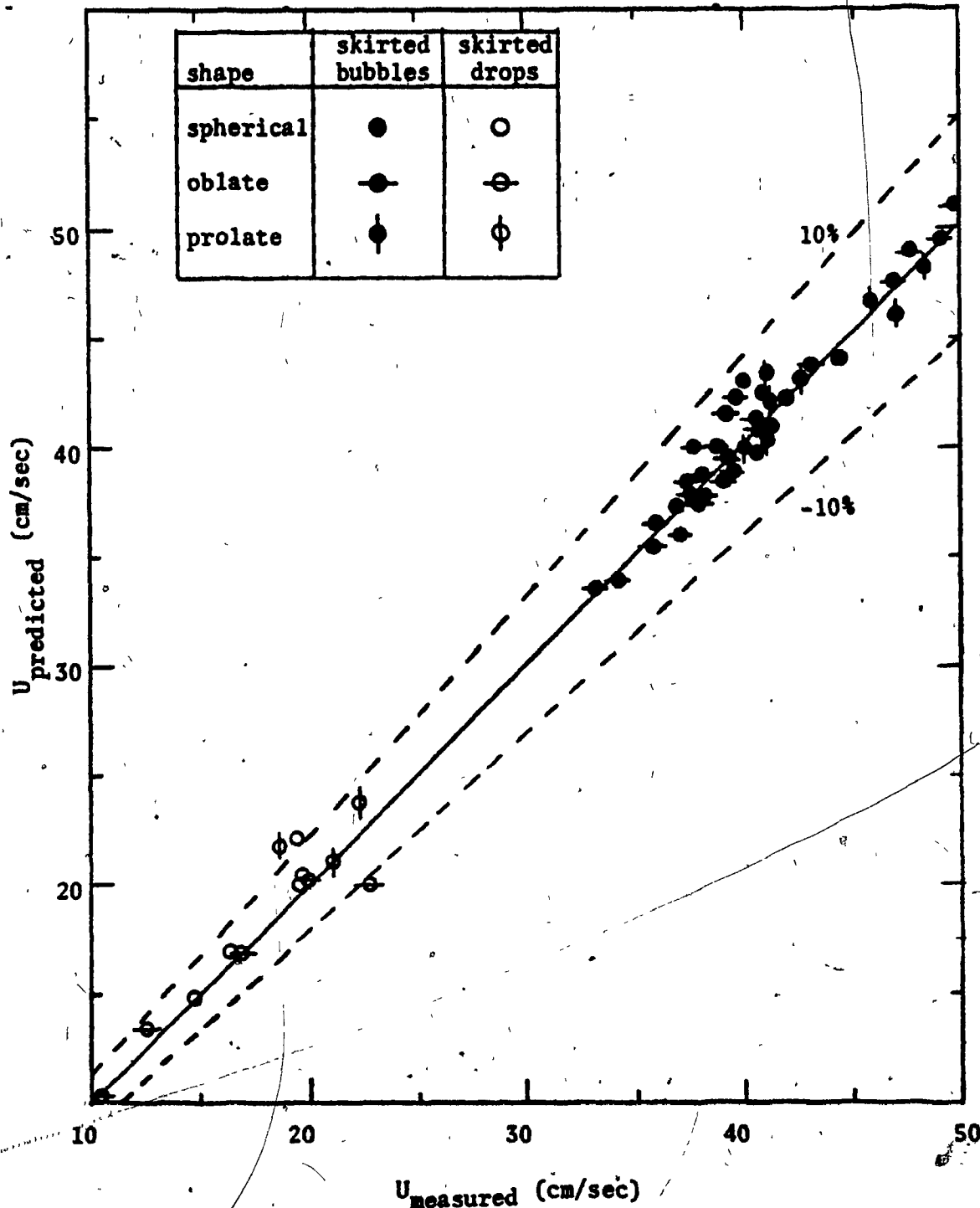
FIGURE 6-15: Comparison of terminal velocity predicted from the shape of the skirted bubbles and drops.

predicted from the shape of the cap.

6.5.1.2 Effect of bubble volume on the shape of skirted bubbles and transition to wavy skirts

The effect of bubble volume on the shape of skirted bubbles is illustrated in Fig.6.16 for a 13.44 Poise sugar solution. All the bubbles shown were photographed near the middle of the column and are presented here at the same magnification. The shape of the skirt is strongly affected by the bubble volume; for a given liquid skirted bubbles can be spherical, oblate or prolate in shape depending on their volumes.

The length of the skirt increases with bubble volume and above a certain volume the skirt becomes wavy and its bottom edge becomes unstable, with fragments of the skirt breaking off into small bubbles. Table 6.9 shows the conditions at which the transition from a stable-laminar skirt to a wavy skirt occurs. To enable the prediction of the incipience of waves, these data were used to delineate a region of wavy skirt on the Re versus Eö plot of Fig.3.13. Some of these data may be affected by the presence of the column wall, hence the boundary should be regarded as a tentative one and it may be modified as further information on skirted bubbles becomes available.

6.5.2 Skirt thickness results

6.5.2.1 Measuring local skirt thickness

In order to test the present theoretical model of skirt thickness the local variation in skirt thickness must be measured. Guthrie and Bradshaw's (1969) technique was unsuitable because it gives only an

FIGURE 6.16   Effect of Bubble Volume on Shape of Skirted Bubbles

No.	V (cm^3)	U (cm/sec)	Re	Eö	We	Sk
1	35.2	36.46	15.3	282	93.9	6.14
2	36.1	36.91	15.6	287	97.1	6.22
3	37.0	37.55	16.0	292	101	6.32
4	37.9	38.04	16.4	297	105	6.41
5	38.9	38.38	16.6	301	108	6.46
6	41.6	39.41	17.5	315	116	6.64
7	92.5	46.05	26.7	537	207	7.76
8	138.8	54.34	36.0	704	330	9.15

All bubbles shown at same magnification. The grid in the background is approximately 2 cm x 2 cm.

Liquid properties: $\mu = 13.44$ Poise
$\rho = 1.387$ g/cm^3
$\sigma = 79.8$ dynes/cm
$M = 45.4$

TABLE 6.9 Onset of Waves on Bubble Skirts

Reference	System	Column Size	Liquid Properties				Critical Condition				
			μ (P)	ρ (gm/cm^3)	σ (dynes/cm)	M (-)	V_3 (cm^3)	U cm/sec	Re (-)	Sk (-)	Eö (-)
Present work	air-sugar solution	29.2 cm I.D.	13.7	.1.375	78.8	55.5	83.4	44.26	24.2	7.39	505
	"	"	7.3	1.370	78.7	4.17	65.3	45.27	42.4	4.20	426
	"	"	5.09	1.358	77.7	1.03	92.7	51.00	76.4	3.34	540
Wairegi (1974)	"	35.5 cm I.D.	13.4	1.39	79.1	45.98	50.0	34.6	16.5	5.86	365
	"	"	14.7	1.35.	79.1	66.59	51.0	33.6	14.6	6.24	365
	"	"	3.4	1.366	50.2	0.759	90.0	53.3	119.9	3.61	837

estimate of the _average_ skirt thickness. The method used here was based upon photographic measurements using a refractive index correction. The fact that the refractive index of the dispersed phase is different from that of the continuous phase enables one to see the inner surface of the skirt on a photograph taken with backlighting. However, there is considerable distortion which must be corrected to obtain the actual value of the thickness from the apparent thickness measured on a photograph. In Appendix E a corrective procedure for a spherical shape skirted bubble (or drop) is presented and approximate methods of correction for oblate and prolate shape skirts are given.

6.5.2.2 Skirt_thickness_results_for_bubbles

Table 6.10(a) lists the angular variation of the theoretical prediction of the actual skirt thickness for a spherical skirted air bubble in sugar solution. These predictions were obtained using Equations (6.37) and (6.38). The angular variation in apparent thickness (the thickness that would be observed on a photograph taken with backlighting) was computed using the correction procedure for refraction described in Appendix E.

It should be noted that the theory predicts appreciable thinning (as much as about 38%) of the skirt over its length which extends from $\theta_c = 62$ to $\theta_s = 116^o$. In contrast, over the same skirt length the apparent skirt thickness is predicted to decrease only about 0.24%. Similar results are obtained for a nitrogen skirted bubble in glycerol observed by Guthrie and Bradshaw (1969) (see Table 6.10(b)). The reason for the large apparent thickness for gas bubbles can be seen by rearranging Equation (E-4) to give:

TABLE 6.10 (a) Theoretical Prediction of Skirt Thickness for Spherical Skirted Bubble

PRESENT WORK: Air bubble in sugar solution

V (cm^3)	U (cm/sec)	μ (Poise)	μ' (Poise)	ρ (g/cm^3)	ρ' (g/cm^3)	Refractive n	Index n'	σ (dynes/cm)	M (-)	Re (-)	Eo (-)	Sk (-)
41.68	41.07	7.3	1.83×10^{-4}	1.37	1.8×10^{-4}	1.475	1.000	78.7	4.17	33.16	.316	3.81

Radius of cap, $R = 3.89$ cm

Polar angle at which skirt begins, $\theta_c = 62°$

Polar angle at which skirt ends, $\theta_s = 116°$

Predicted Skirt Thickness (cm)

| | Actual Thickness, $\Delta(\theta)$ | | | Apparent Thickness as Would Appear on Photograph, $\Delta'(\theta)$ | | |
| | Assuming Circulating Wake $q_i = q_o$ | Assuming Stagnant Wake $q_i = 0$ | | Assuming Circulating Wake $q_i = q_o$ | | Assuming Stagnant Wake $q_i = 0$ |
θ			α		α	
60.0	0.014189	0.010033	47.2	1.263137	46.6	1.260319
65.0	0.013204	0.009337	54.8	1.262468	54.4	1.259847
70.0	0.012369	0.008746	62.2	1.261903	61.8	1.259446
75.0	0.011654	0.008241	69.3	1.261417	69.0	1.259104
80.0	0.011037	0.007805	76.2	1.261000	76.1	1.258808
85.0	0.010501	0.007426	83.1	1.260636	83.1	1.258551
90.0	0.010033	0.007095	90.0	1.260319	90.0	1.258327
95.0	0.000623	0.006804	96.9	1.260040	97.0	1.258130
100.0	0.009261	0.006549	103.8	1.259795	104.0	1.257957
105.0	0.008943	0.006323	110.9	1.259580	111.1	1.257804
110.0	0.008661	0.006124	118.2	1.259389	118.5	1.257668
115.0	0.008412	0.005948	125.7	1.259220	126.1	1.257539

TABLE 6.10 (b) Theoretical Prediction of Skirt Thickness for Spherical Skirted Bubble

GUTHRIE (1967): Nitrogen bubble in glycerol

V (cm³)	U (cm/sec)	μ (Poise)	μ' (Poise)	ρ (g/cm³)	ρ' (g/cm³)	Refractive n	Index n'	σ (dynes/cm)	M (-)	Re (-)	Eo (-)	Sk (-)
53.0	34.0	12.3	1.76×10^{-4}	1.26	1.74×10^{-4}	1.474	1.00	63.0	71.27	16.23	426	6.64

Radius of cap, R — 3.11 cm

Polar angle at which skirt begins, θ_c — 88°

Polar angle at which skirt ends, θ_s — 145°

Predicted Skirt Thickness (cm)

θ	Actual Thickness, Δ(θ) Assuming Circulating Wake $q_1 - q_o$	Assuming Stagnant Wake $q_1 - 0$	θ	Apparent Thickness as Would Appear on Photograph, Δ'(θ) Assuming Circulating Wake $q_1 - q_o$	θ	Assuming Stagnant Wake $q_1 - 0$
80.0	0.010270	0.007262	76.3	1.005031	76.2	1.002990
85.0	0.009771	0.006909	83.2	1.004692	83.1	1.002750
90.0	0.009335	0.006601	90.0	1.004397	90.0	1.002542
95.0	0.008953	0.006331	96.9	1.004138	96.9	1.002359
100.0	0.008617	0.006093	103.8	1.003909	103.9	1.002196
105.0	0.008321	0.005884	110.8	1.003708	111.0	1.002054
110.0	0.008058	0.005698	118.0	1.003581	118.3	1.001928
115.0	0.007827	0.005534	125.5	1.003373	125.9	1.001818
120.0	0.007622	0.005390	133.5	1.003234	134.0	1.001719
125.0	0.007442	0.005262	142.2	1.003112	142.9	1.001613
130.0	0.007284	0.005150	152.3	1.003004	153.4	1.001556
135.0	0.007145	0.005052	167.1	1.002911	169.8	1.001491

$$\Delta'(\alpha) \ = \ R(1 - \frac{n'}{n}) + \frac{n'}{n}\Delta(\theta) \qquad\qquad (6.44)$$

For a typical skirted bubble: $R(1 - \frac{n'}{n}) \approx 4(1 - \frac{1}{1.47}) \approx 1.28$ cm. and $\frac{n'}{n}\Delta(\theta) \approx \frac{1}{1.47} \times 70 \times 10^{-4} \approx 0.00475$ cm.; i.e. the first term on the right-hand side of Equation (6.44), which is independent of the actual skirt thickness, $\Delta(\theta)$, is the dominant one, hence the predicted variation in the actual skirt thickness is not reflected in the apparent skirt thickness, $\Delta'(\alpha)$. Consequently, the skirt would appear to be of nearly constant thickness. This is indeed the case for all of the bubbles observed in the present work (see Fig.6.10 and Fig.6.16) as well as those reported by other workers.

From the above discussion it is clear that a reliable test of the present skirt thickness theory cannot be made using skirt thickness data of bubbles. Fortunately, for liquid-liquid systems n'/n can be close to unity so that the second term on the right-hand side of Equation (6.44) is the dominant one or at least is comparable to the first term. Consequently the thinning of the skirt for a drop can be seen quite clearly as shown in the photograph of a skirted drop of silicone oil rising through sugar solution, Fig.6.17(2).

6.5.2.3 Skirt thickness results for drops

The original photographs of skirted drops taken by Wairegi (1972,1974) were projected at high magnification and traced. From these tracings the apparent skirt thickness, $\Delta'(\alpha)$, was measured at different angles, α, from the front stagnation point. The actual skirt thickness, $\Delta(\theta)$, and the corresponding angle, θ, were then obtained by applying the appropriate refraction correction described in Appendix E. The results

FIGURE 6.17(1). The Shape of a Drop at Skirt Incipience Showing the Shape of the Indentation

(2) The Shape of a Skirted Drop Showing Skirt Thinning

No.	Reference	System	Viscosity (Poise)		Density (g/cm³)		Refractive Index		σ (dynes/cm)	V_3 (cm³)	U (cm/sec)	Re (-)	Eö (-)	Sk (-)
			μ	μ'	ρ	ρ'	n	n'						
1	Wairegi (1972)	silicone oil B drop in sugar solution	14.60	0.465	1.385	0.958	1.456	1.404	53.9	33.8	18.85	7.18	125	5.00
2	Wairegi (1974)	silicone oil drop in sugar solution	8.86	0.465	1.392	0.958	1.470	1.400	53.9	47.7	22.80	16.1	513	3.75
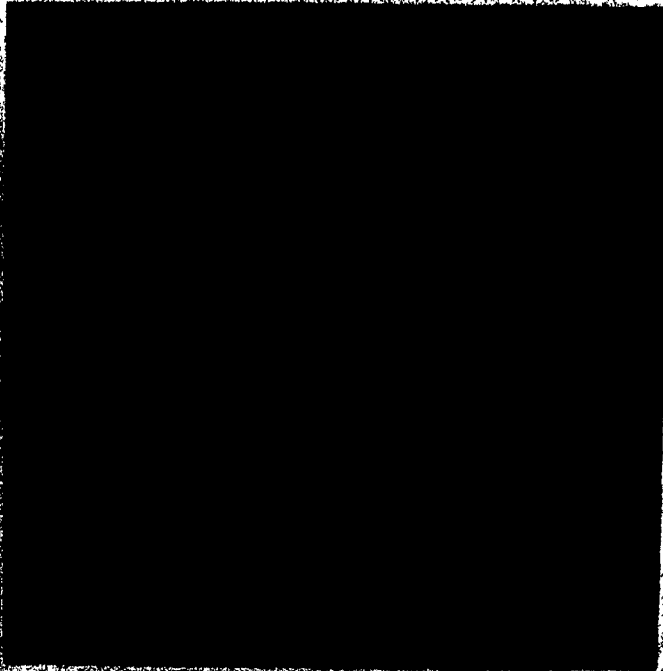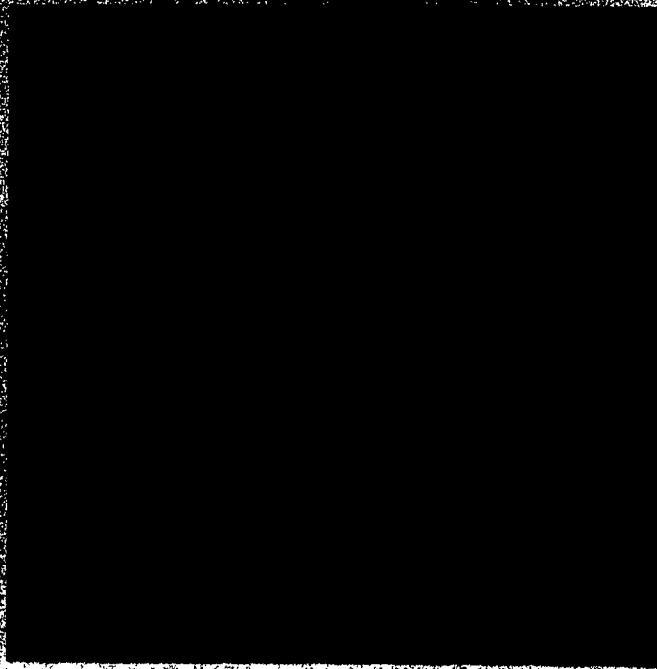
are presented in Figs. 6.18(a) to (f). The expected error in the measured thickness is indicated in each figure by a vertical bar. The positions of the beginning and the end of the skirt are shown by θ_c and θ_s, respectively. The thickness predicted from Equations (6.40) and (6.41), assuming potential flow for the external liquid, i.e. putting $C_f = 1$, are shown by the dotted curves ① and ② for circulating and stagnant wake, respectively.

The deviation from potential flow around these skirted drops is not known. The best we can do at present is estimate it from the present experimental data on the velocity field around skirted bubbles at similar values of Re. Fig. 6.19 shows the variation of the dimensionless velocity, q_{os}^*, at the outer surface of the skirted bubble with the angle θ measured from the nose for three skirted bubbles at Re = 11.45, 17.21 and 30.21. Here q_{os}^* is defined as:

$$q_{os}^* = \frac{\text{(experimental velocity of external liquid at the bubble surface measured tangentially to the surface)}}{\text{(surface velocity at same } \theta \text{ predicted from potential flow around the spheroid that fits the bubble)}}$$

Note that the dimensionless surface velocity, q_{os}^*, is equivalent to the correction factor, C_f, included in the skirt thickness Equations (6.40) and (6.41); it decreases with decrease in Re and increase in θ and is significantly lower than 1.

Assuming that at a given Re the deviation from potential flow for a drop is the same as for a bubble at the same Re, the value of the correction factor, C_f, was estimated from Fig. 6.19 for all the skirted drops used in Fig. 6.18(a) to (f). These values of C_f were then used to give improved predictions which are shown in Fig. 6.18 by the solid curves ①c and ②c for the circulating and the stagnant wake, respectively.

FIGURE 6.18 Comparison of Skirt Thickness Results of Drops* with Theoretical Predictions

Details of Skirted Drops and Physical Properties of Liquids

No.	Dispersed Liquid**	μ (Poise)	μ' (Poise)	ρ (g/cm^3)	ρ' (g/cm^3)	Refractive Index n	n'	σ (dynes/cm)	μ'/μ	V_3 (cm^3)	U (cm/sec)	Re (-)	AR***
a	silicone oil	8.86	0.465	1.392	0.958	1.470	1.400	53.90	5.25×10^{-2}	48.67	22.86	16.27	0.83
b	o-diethyl phthalate	11.20	0.089	1.385	1.115	1.465	1.502	29.40	7.95×10^{-3}	35.57	16.30	8.23	0.88
c	silicone oil-B	14.60	0.465	1.385	0.958	1.456	1.404	53.90	3.18×10^{-2}	45.74	19.79	8.33	1
d	paraffin oil-A	13.00	0.385	1.385	0.859	1.465	1.471	53.41	2.96×10^{-2}	30.49	19.46	8.04	1
e	silicone oil-AB1	11.20	0.232	1.385	0.944	1.465	1.403	53.50	2.07×10^{-2}	42.35	18.48	9.88	1.13
f	silicone oil-B	14.60	0.465	1.385	0.958	1.456	1.404	53.90	3.18×10^{-2}	60.98	21.10	9.78	1.29

* All data from Wairegi (1972) except for silicone oil drop (No.a) which is from Wairegi (1974).

** Continuous liquid in all cases was aqueous sugar solution. Physical properties of continuous phase are indicated by μ, ρ and n. Physical properties of dispersed phase are indicated by μ', ρ' and n'.

*** For aspect ratios, AR < 1 → oblate shape;
     AR = 1 → spherical shape;
     AR > 1 → prolate shape.
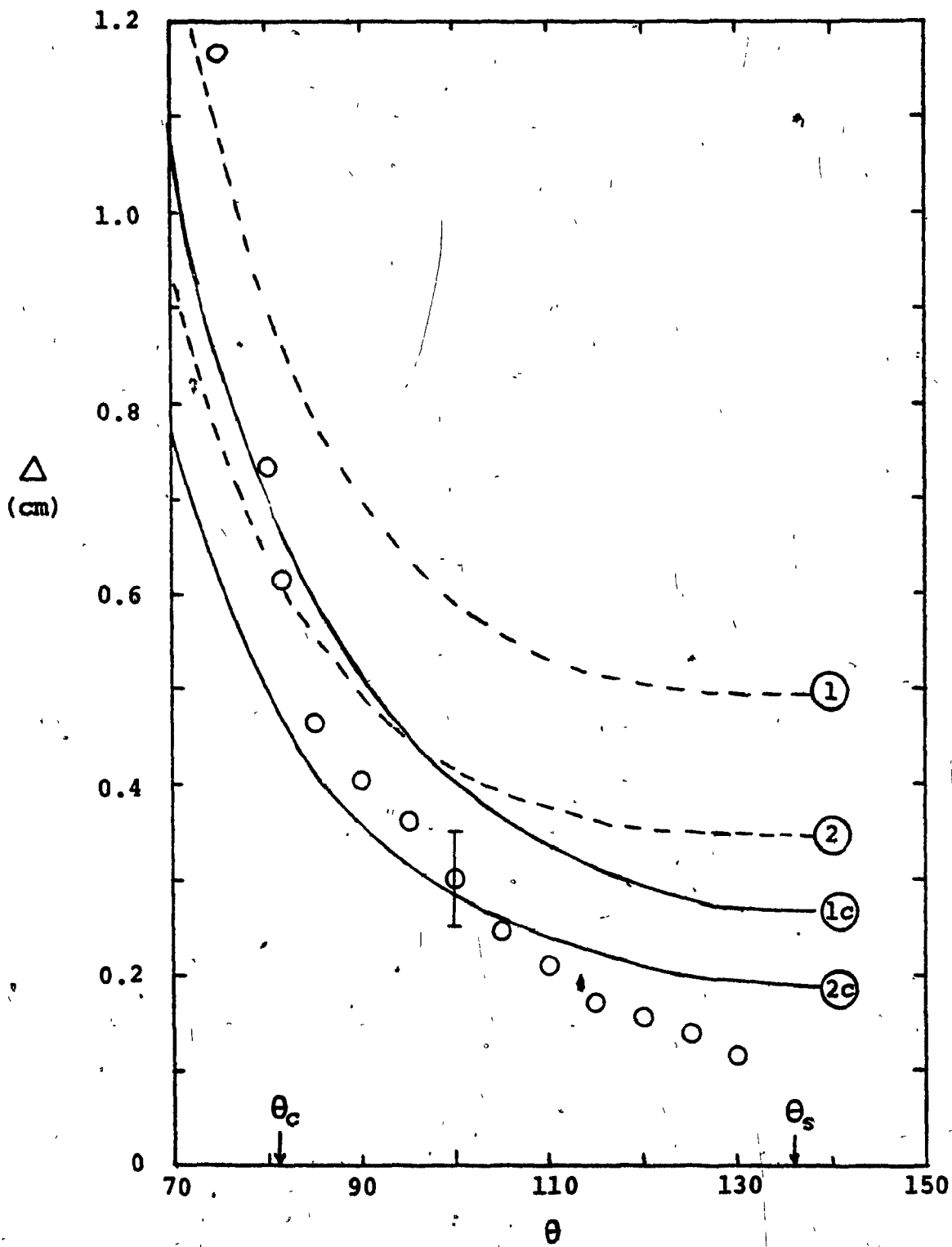
FIGURE 6-18(a): **Skirt thickness for oblate skirted drop of silicone oil in sugar solution.**
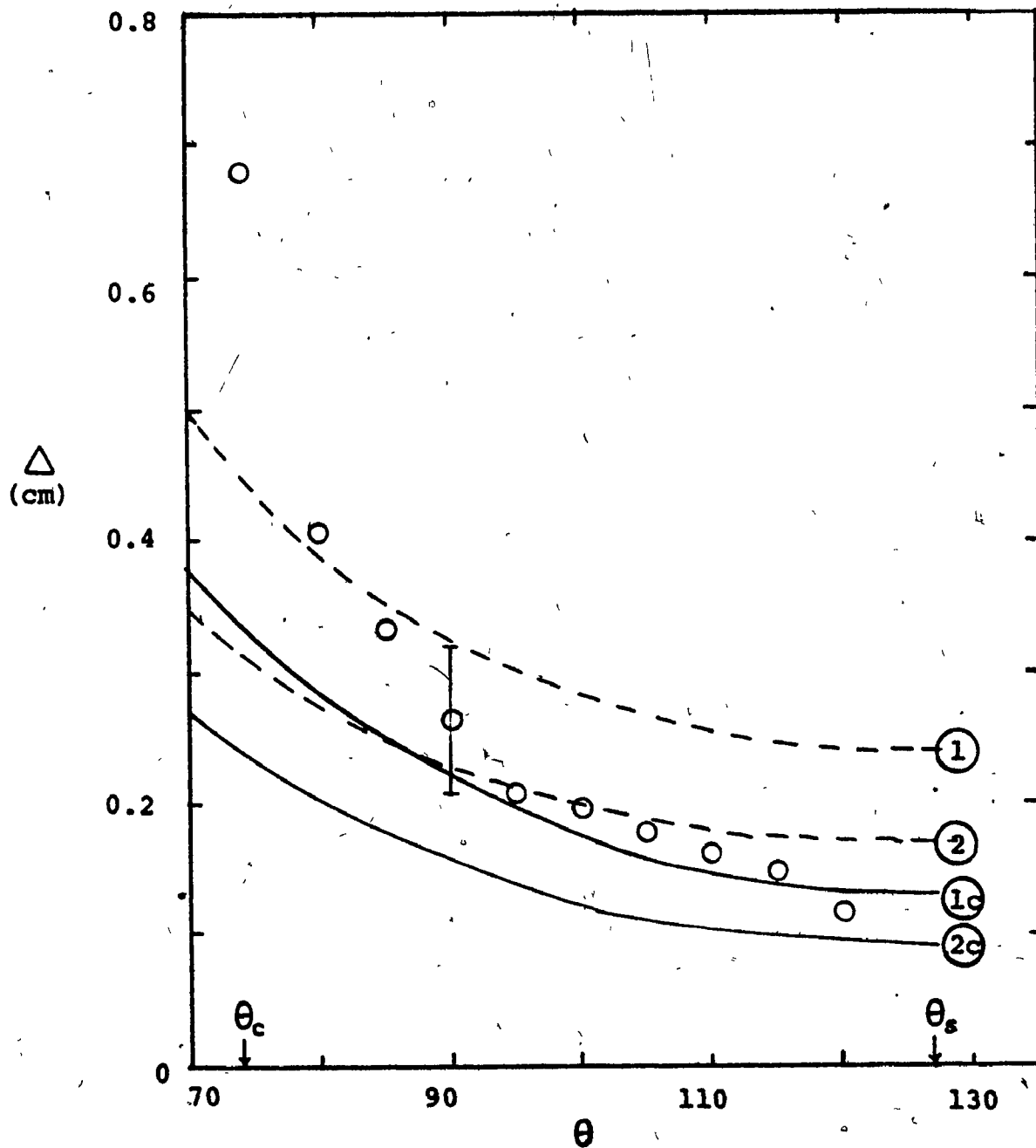
FIGURE 6-18(b): Skirt thickness for oblate skirted drop of o-diethyl phthalate in sugar solution.
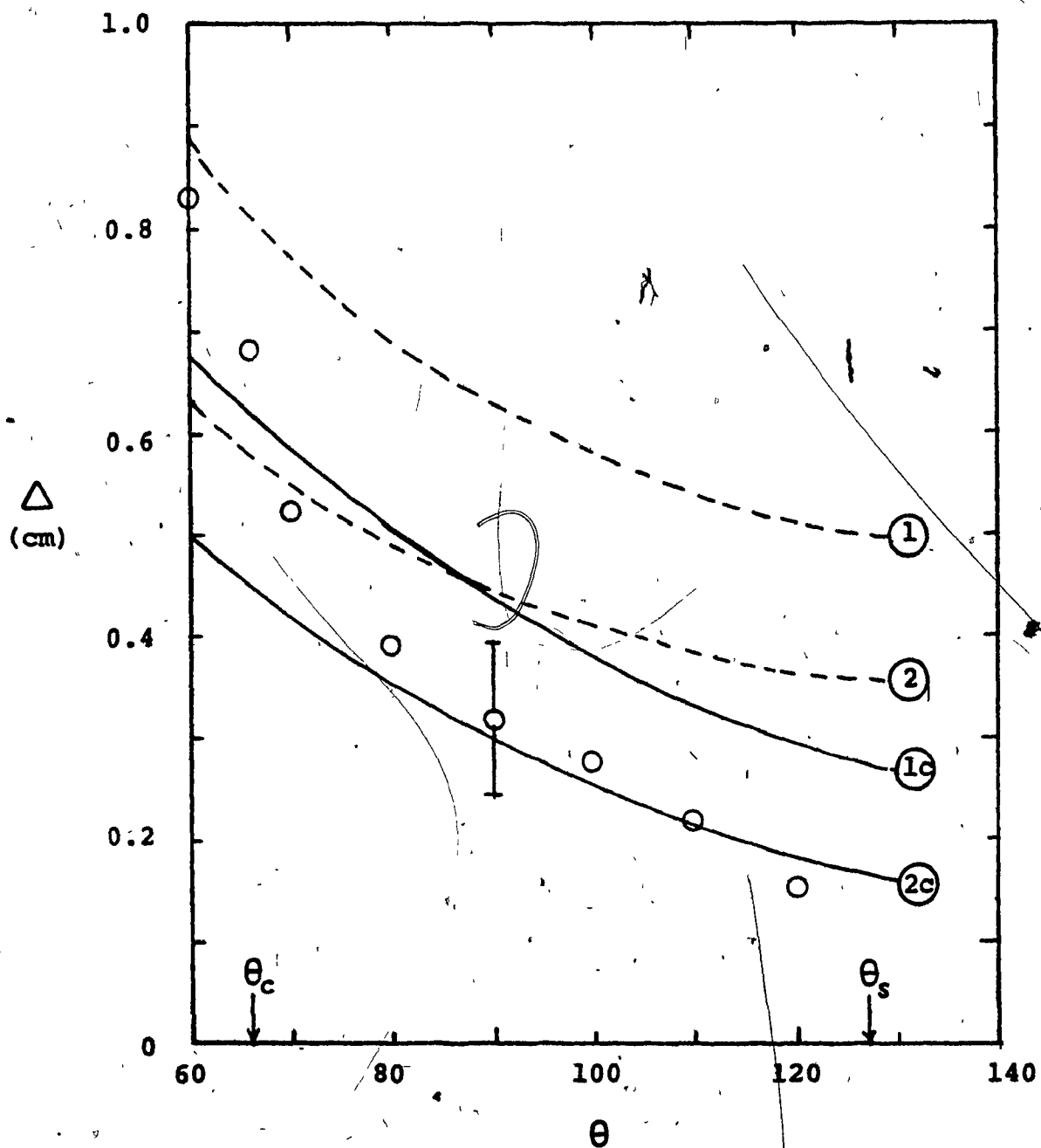
FIGURE: 6-16(c): <u>Skirt thickness for spherical skirted drop of silicone oil-B in sugar solution.</u>
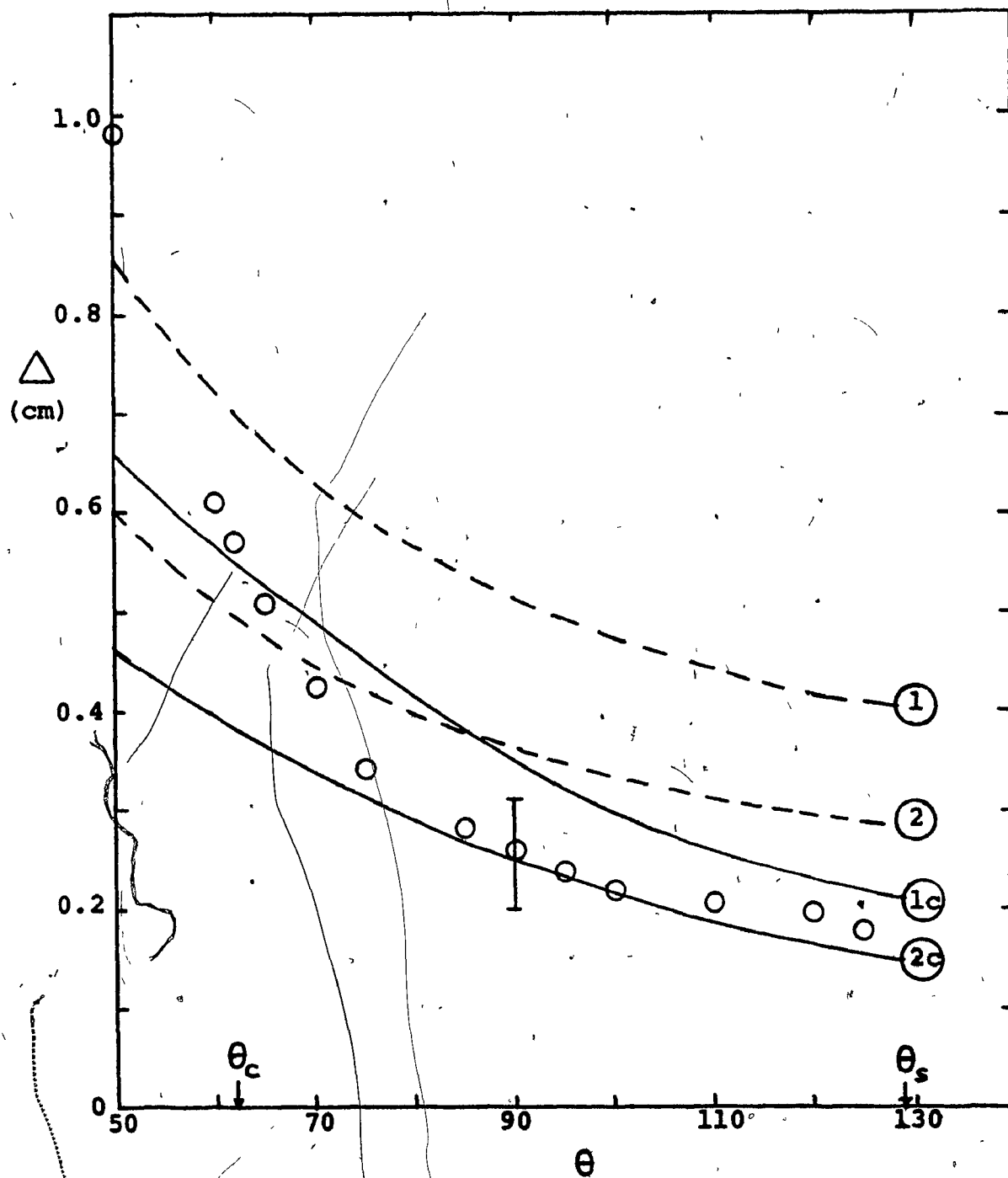
FIGURE 6-18(d): Skirt thickness for spherical skirted drop of paraffin oil-A in sugar solution.
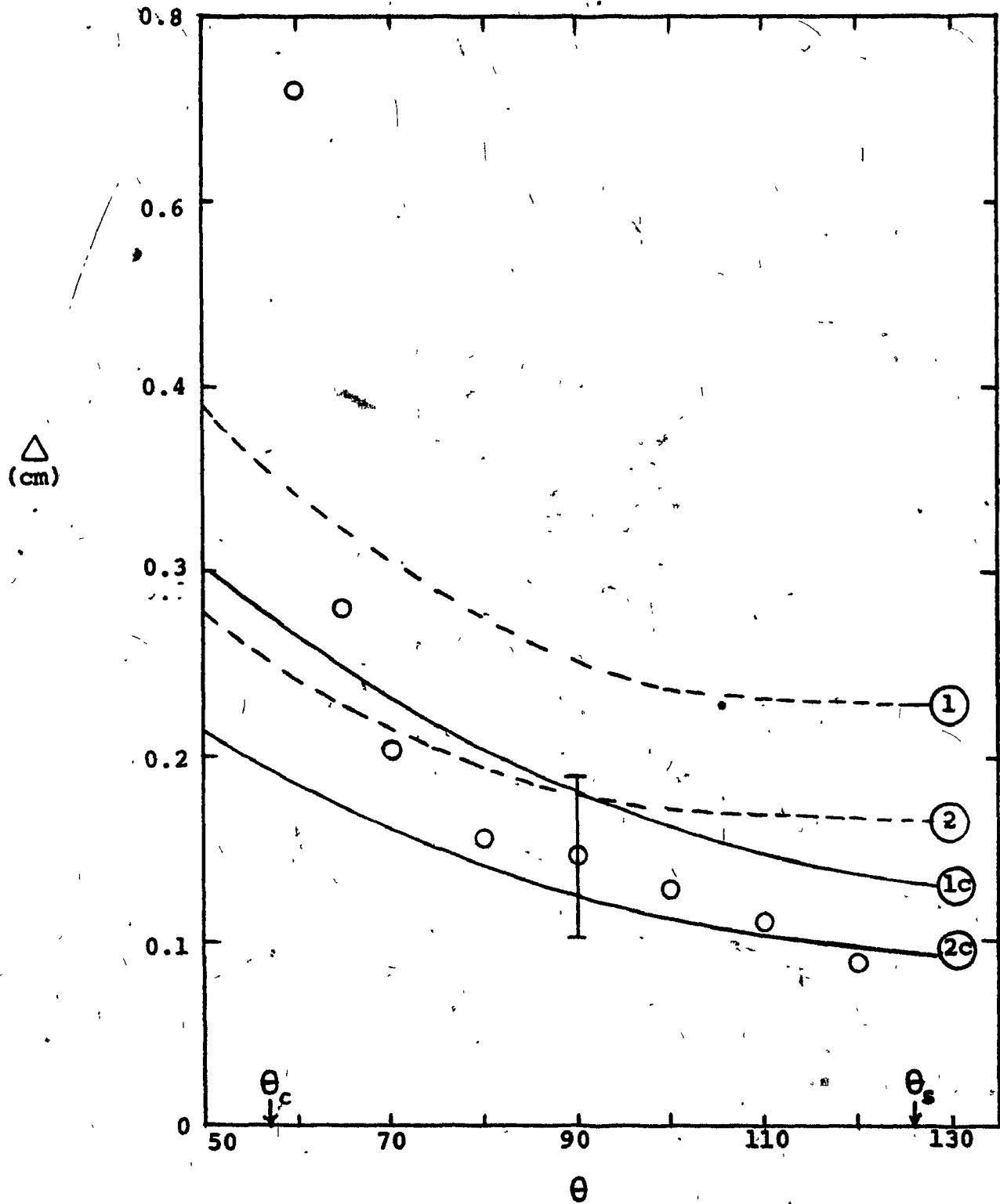
FIGURE 6-18(e): **Skirt thickness for prolate skirted drop of silicone oil-AB1 in sugar solution.**
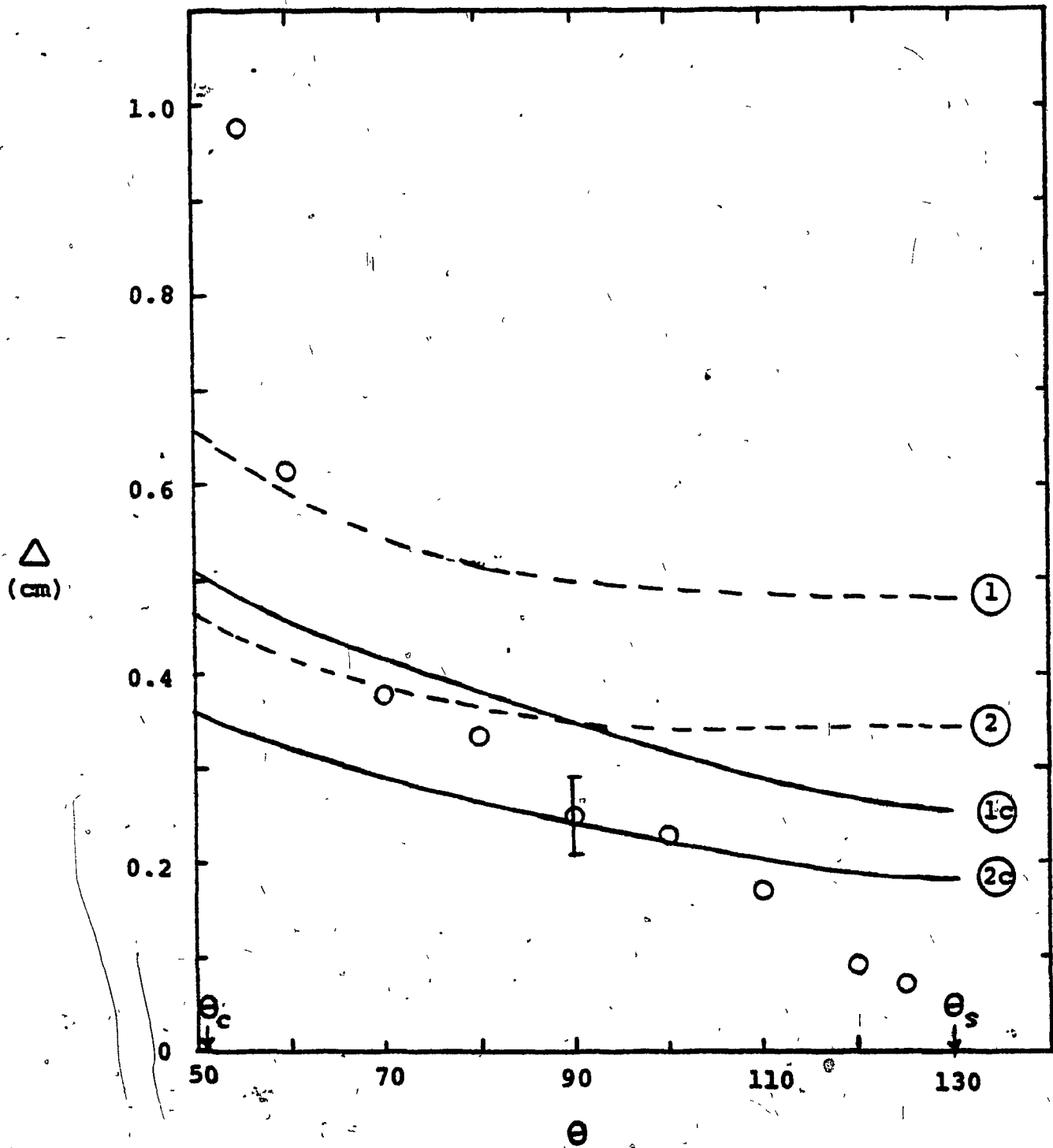
FIGURE 6-18(f): __Skirt thickness for prolate skirted drop of__
__silicone oil-B in sugar solution.__
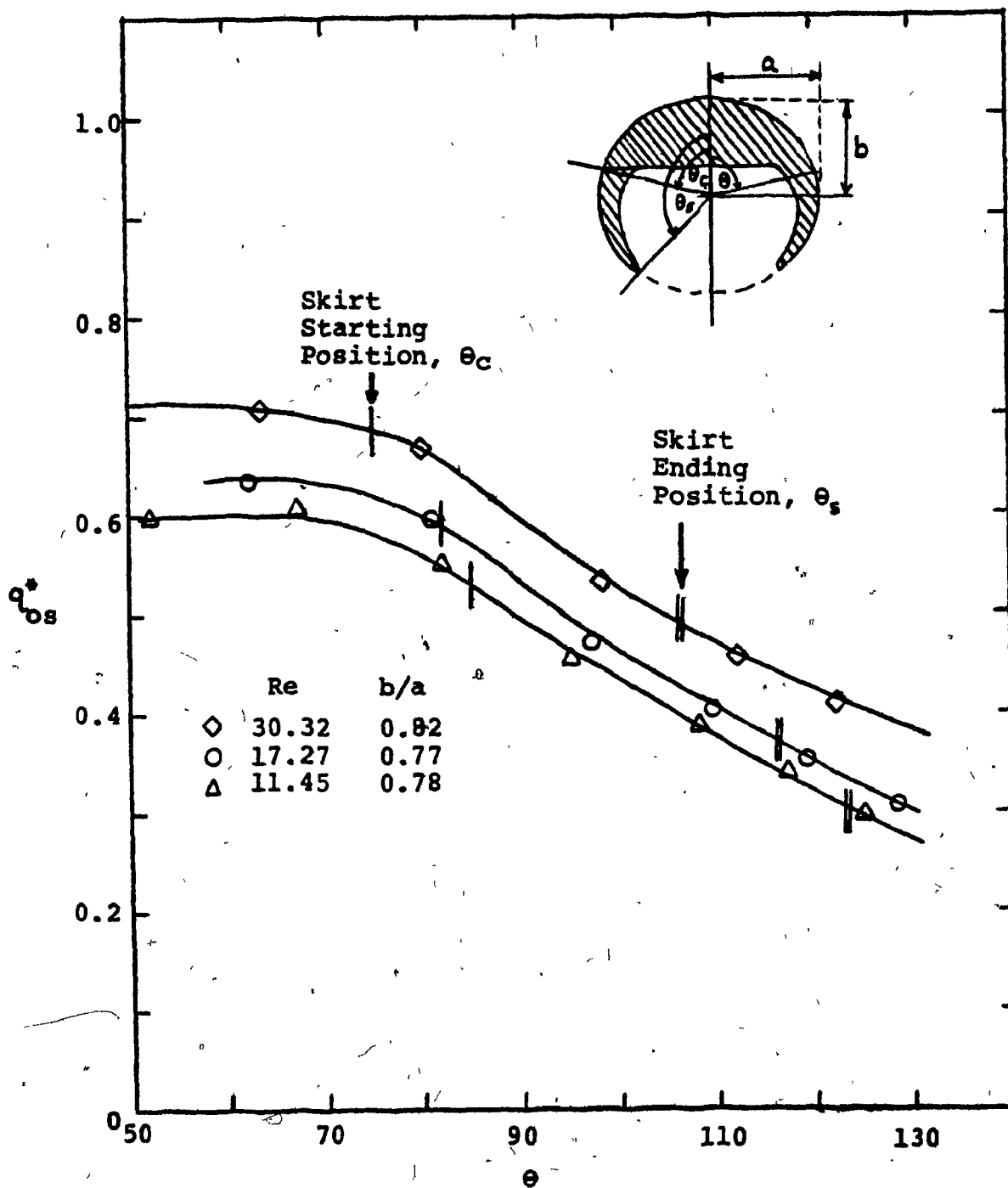
FIGURE 6-19: Measured dimensionless velocity at the outer surface of skirted bubbles.

For all three shapes (spherical, oblate and prolate) the agreement between the experimental thickness and the theoretical prediction is favourable. The discrepancy between the theory and the experiments near the beginning and the end of the skirt is to be expected because end effects are not included in the theory.

6.5.3 Skirt length results for bubbles and drops

The experimental skirt lengths are compared with the theoretical predictions in Figs. 6.20 and 6.21 for bubbles and drops, respectively. Available data of other experimenters are included. The theoretical predictions were obtained assuming potential flow for the external liquid, and using the theoretical equations presented in Section 6.4.3. The agreement is surprisingly good. It may be noted that the theory predicts that the skirt will always end for $\theta_s < 180$, i.e. the skirt never completely encloses the wake. This is confirmed by all the skirt experiments reported to date.

The potential flow assumption should result in an underprediction of skirt length. On the other hand, the idealized geometry for the end of the skirt adopted in the theory gives the lower limit of the corner angle, ϕ, (the actual value of ϕ is expected to be somewhat larger as shown in Fig. 6.22) which should result in an overprediction of the skirt length. These factors have partially compensated each other yielding reasonably good agreement between the theory and the experiments.

6.6 Addendum

* While this chapter was being proofread Hnat and Buckmaster's (1976) work on spherical-cap bubbles and skirt formation was published.
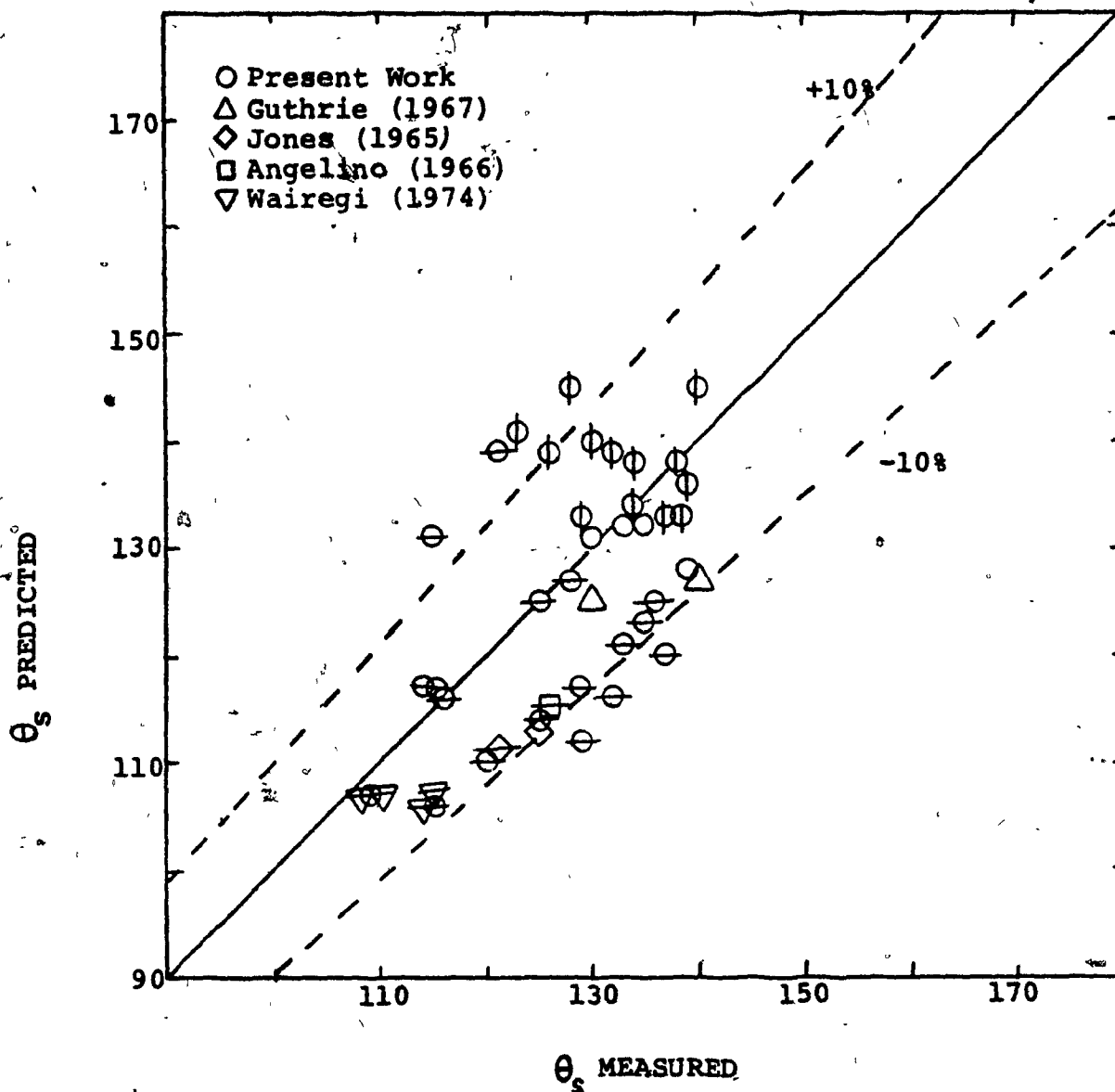
FIGURE 6-20: Comparison between measured and predicted skirt termination angle for skirted bubbles.

Shape	Indicated By
Spherical	No bar on the symbol
Oblate	Horizontal bar on the symbol
Prolate	Vertical bar on the symbol

FIGURE 6-21:   Comparison between measured and predicted skirt termination angle for drops.

Wairegi's (1972) Data

○ Silicone oil-B drops in sugar solution
◊ Paraffin oil-A   "   "   "   "
□ Silicone oil-AB1 "   "   "   "
△ O-diethyl phathalate drops in sugar solution
◁ Silicone oil-A   "   "   "   "
◊ 1.2 - dichloroethane "   "   "   "
○ Trichloroethane   "   "   "   "
◇ dichlorobenzene   "   "   "   "
△ 1.2-dichloroethane   "   "   "   "

Wairegi's (1974) Data

▽ Silicone oil drops in sugar solution

Shoemaker & Chazal's (1969)Data
▽ 2-butanone drops in glycerol solution

Shape   Indicated by

Spherical ⟶ No bar on the symbol
Oblate   ⟶ Horizontal bar on the symbol
Prolate   ⟶ Vertical bar on the symbol
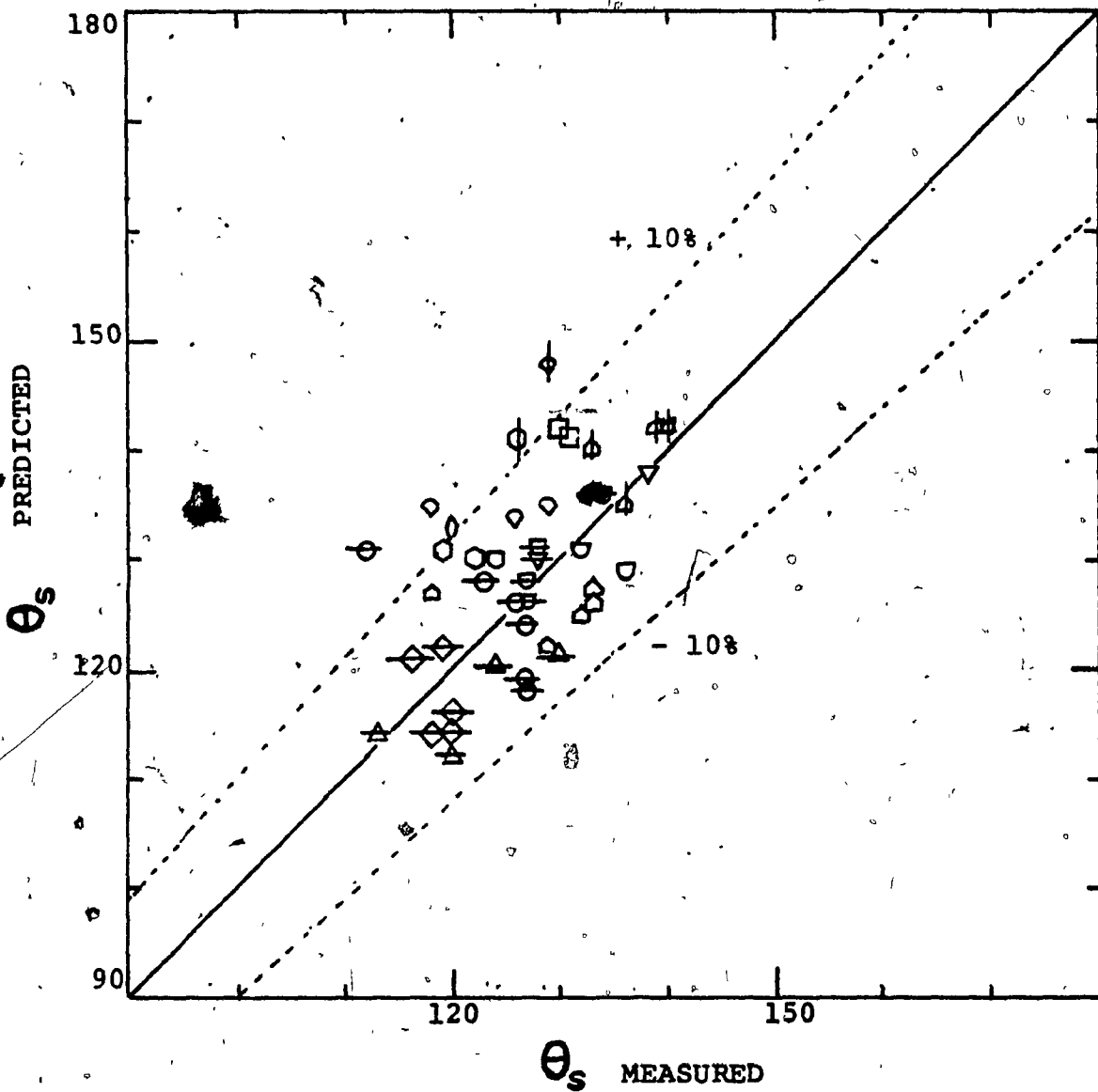
In both figures, SEB is a tangent to the outer surface of the skirt at B where the skirt ends.

(a) <u>idealized geometry for skirt end</u>
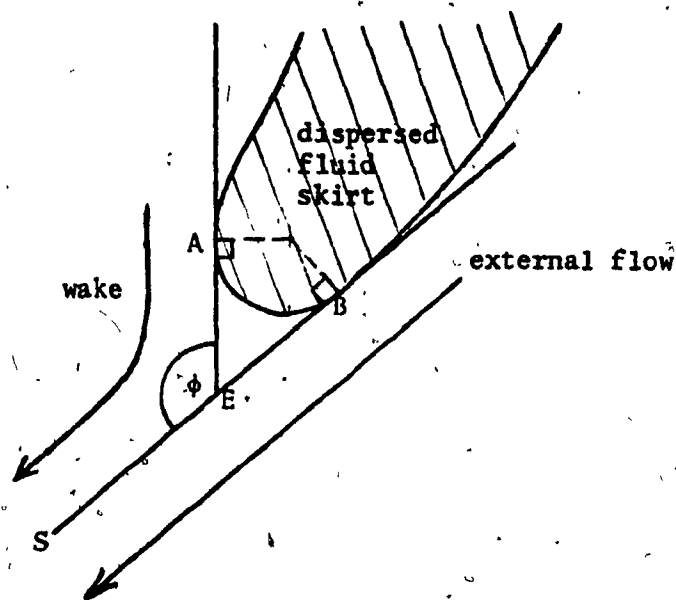
Here EA is taken to be a vertical line touching the inner surface of the skirt so that the corner angle, ϕ, can be related to the skirt termination angle, θ_s, by geometry (see Table 6.7).

(b) <u>actual geometry for skirt end</u>
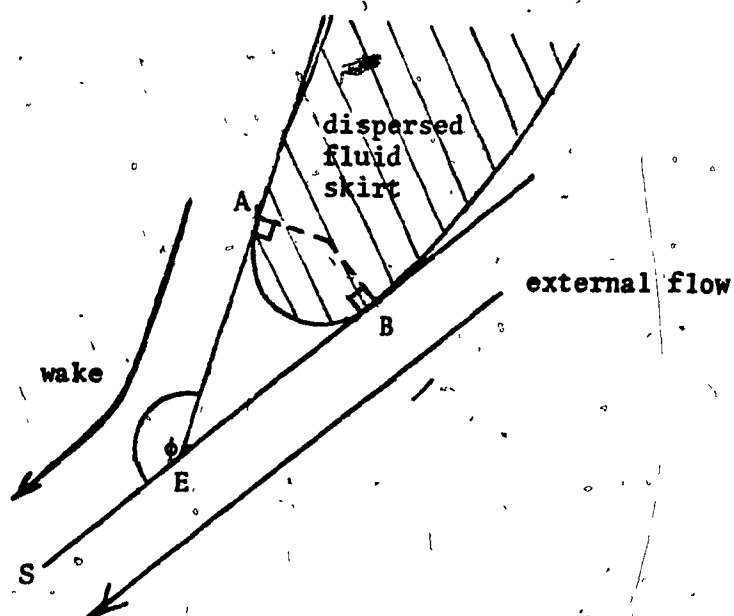
Here EA is a tangent to the inner surface of the skirt at A where the skirt ends.

FIGURE 6.22 <u>Geometry of skirt end</u>

Their shadowgraphs of skirted bubbles confirm the conclusion of the present study that the wake enclosed by the skirt is not stagnant. Their data on the incipience of skirts are included in Fig. 6.9 and are in good agreement with present and previous data. It is noteworthy that these authors observed skirts in mineral oil with M as low as 0.05 and Re as high as 500. Thus skirt appearance did occur for bubbles whose wakes were quite unstable. This led them to conclude that....."skirts have a stabilizing effect on the wake in that the vortex shedding appears to be restrained." Like the present study, these authors also support the theoretical views of Wegener et al (1971) that a skirt is formed when the viscous forces at the lower edge of the bubble cap overcome the surface tension forces. Their theoretical analysis of skirt thickness for a spherical shape is in agreement with the present, more general, approach; however, no experimental evidence was provided to test the conclusion that the skirt thins with increasing length. Their finding - that the appearance of the skirt does not affect the bubble rise velocity - is in accord with the present finding. Finally, these authors applied Helmholtz stability analysis to explain the appearance of waves on the skirts.

6.7 Conclusions

1. Skirts will appear for bubbles having Re greater than about 9 and Sk greater than about 2. The limiting values for drops are slightly different (see Fig. 6.9).

2. Just prior to formation of a skirt in a high-M liquid, the bubble shape is oblate-cap with a significant indentation of the base. With decreasing M, the indentation decreases and the bubble tends towards spherical-cap shape.

3.   The shape of the outer surface of a skirted bubble is strongly dependent on the bubble size and the physical properties of the liquid. At the skirt incipience condition the outer boundary of a skirted bubble is oblate in high-M liquids, spherical in intermediate-M liquids and tends to become prolate in low-M liquids.

4.   The rise velocity of the bubble is not affected by the appearance of the skirt and the velocity can be predicted from the shape of the cap.

5.   The Wegener et al (1971) skirt incipience theory for a spherical-cap bubble with a flat base has been extended to an oblate-ellipsoidal-cap bubble with an indented base. This extended theory explains why the critical value of Sk goes up with decreasing Re, and lends support to the hypotheses of Wegener et al that a skirt is formed when viscous shear forces at the lower edge of the bubble cap overcome surface tension forces.

6.   A method is developed to correct for the optical distortion (due to difference in refractive indices of the two phases) of the skirt thickness for spherical, oblate and prolate skirted bubbles or drops. The actual thickness of skirts behind gas bubbles varies from about 0.01 to 0.005 cm. In contrast, for liquid skirts trailed behind drops the thickness varies from about 0.6 to 0.1 cm.

7.   A theoretical model for the skirt thickness is developed which predicts decreasing skirt thickness with increasing skirt length. Experimental data from the literature on skirted drops support the theory. The results of all the previous analyses (Guthrie and Bradshaw 1967; Wairegi 1974; Hnat and Buckmaster 1976) are recovered as special cases of the present more general theory.

8. Stable skirts always extend below the equator but never completely enclose the wake.

9. As the skirt grows it becomes progressively thinner and terminates when the surface tension force at the end of the skirt becomes large enough to balance the viscous shear force. A simple theoretical model based upon the above hypothesis is found to be in good agreement with the experimental data on skirt lengths of bubbles and drops.

10. The length of the skirt increases with bubble volume (or Re); above a certain volume the skirt becomes wavy, its bottom edge becomes unstable with fragments breaking off to form small bubbles.

CHAPTER 7

EFFECTS OF CONTAINER WALLS ON BUBBLE MOTION

7.1 Introduction

Since the continuous medium in which a bubble rises is never
infinite in extent, it is important to know the effect of container
walls on the behaviour of bubbles. In this chapter we consider how the
presence of the container walls effects the bubble rise velocity, its
shape, its wake and the surrounding flow field. The wall effect on skirted
bubbles is also explored.

7.2 Literature Review

The literature contains extensive work on low Reynolds number
motion of solid spheres in a bounded fluid. Most of this work is reviewed
by Happel and Brenner (1965), Salami et al (1965), Sutterby (1973) and
very recently by Clift et al (1976).

Haberman and Sayre (1958) have given a theoretical treatment
for rigid spheres as well as freely circulating spheres. moving in
creeping flow along the axis of cylindrical containers. The terminal
velocity was found to decrease as the ratio of sphere diameter to tube
diameter, d_e/D, increased. The velocity retardation was less for circu-
lating spheres than for a rigid particle with the same diameter ratio.
The theory accurately predicted the wall correction factor for the rise
velocity of bubbles and drops with d_e/D up to about 0.5 despite the fact
that significant deformation from spherical shape was observed at larger d_e/D.*

---

* As the ratio d_e/D increased, the presence of the wall was found to deform
the spherical droplets into prolate ellipsoidal shapes. The ratio of the
major to minor axis of up to 1.5 was observed without noticeably affecting
the wall correction factor.

Fidleris and Whitmore (1961) provided extensive experimental data on the wall effect for solid spheres for a wide range of Re (0.05 to 20000). They compared their data with all the then-existing wall correction formulae and also presented a useful correlation of U/U_∞ versus Re_∞ with d_e/D as a parameter, where U_∞ is the terminal velocity in a liquid of infinite extent and $Re_\infty = \dfrac{\rho U_\infty d_e}{\mu}$.

Uno and Kintner (1956) reviewed the literature on wall effects for solid spheres and concluded that the presence of the container wall could be accounted for by the general equation

$$\frac{U}{U_\infty} = f(1 - \frac{d_e}{D})^{n_1} \tag{7.1}$$

By assuming that Equation (7.1) would apply equally well to bubbles, they were able to correlate their data on bubbles in low-M liquids ($1.4 \times 10^{-11} < M < 2.9 \times 10^{-5}$) with the following expression:

$$\frac{U}{U_\infty} = \frac{1}{B}(1 - \frac{d_e}{D})^{0.765} \tag{7.2}$$

where B was a factor which depended on column diameter and surface tension. This dependence was presented graphically. Unfortunately, this widely used empirical correlation suffers from a serious deficiency in that it predicts a zero value for the terminal velocity for $d_e = D$, i.e. for bubbles or slugs which are large enough to fill the tube. It is well known, however, that except for tubes of very small diameters, slugs have a finite rise velocity (Harmathy 1960; White and Beardmore 1962; Wallis 1969). Uno and Kintner also presented a graphical correlation relating U/U_∞ to d_f/D where d_f is the frontal diameter (basal diameter

or maximum width) of the bubble. Unfortunately, they did not once measure d_f, but calculated values using their own measurements of volume and a "compromise curve" relating $d_{f/2}$ to $d_{e/2}$ which was drawn to link up Rosenberg's (1950) data for spherical-cap bubbles with his data for ellipsoidal bubbles. This curve was employed by Uno and Kintner for all six columns (diameters ranging from 2 to 15 cm.) used in their experiments, so that there was no allowance made for the effect of the column size on the shape adopted by a gas bubble of given volume.*

Strom and Kintner (1958) have shown that the wall correction equation of Uno and Kintner (1956) is not entirely satisfactory for liquid-liquid systems, and developed another empirical equation:

$$\frac{U}{U_\infty} = \left[1 - \left(\frac{d_e}{D}\right)^2\right]^{1.43} \tag{7.3}$$

Harmathy (1960) correlated the effect of d_e/D on the terminal velocities of rigid and fluid particles for $Re > 500$. He improved Uno and Kintner's correlation by expressing the surface tension effect in terms of Eotvos number based on column size ($E\ddot{o}' = \frac{\rho g D^2}{\sigma}$), and proposed the following correlation:

$$\frac{U}{U_\infty} = \frac{1 - \left(\frac{d_e}{D}\right)^2}{\sqrt{1 + \left(\frac{d_e}{D}\right)^4}}\left[1 - \frac{2}{3}\frac{E\ddot{o}'}{1 + E\ddot{o}'}\left(\frac{d_e}{D}\right)\right]^{3/2} \tag{7.4}$$

---

* Collins (1967) criticized Uno and Kintner on this point but when comparing his wall effect theory for spherical cap bubbles with Uno and Kintner's data (see Collins' Fig.10) he misinterpreted the frontal radius, r_f, (i.e. half of the maximum width of bubble) employed by Uno and Kintner as the radius of the spherical cap, $\bar{R}$. Note that r_f is only equal to $\bar{R}$ when the spherical cap bubble is a perfect hemisphere.

A more general graphical correlation of U/U_∞ versus Eo' with d_e/D as a parameter was presented by Salami et al (1965) for liquid drops.

Angelino (1966) conducted wall effect experiments for bubbles in three liquids (M = 2.39×10^{-2}, 103 and 133) in four columns (10.2, 18.5, 29.0 and 40.0 cm. I.D.). He plotted U/U_∞ versus (1 - d_f/D) and compared his data with results of Uno and Kintner (1956) and Fidleris and Whitmore (1961). Referring to Angelino's thesis (1964) from which the above paper originated, it has been found that Angelino measured the diameter of the bubble, d_f, only in the 29.0 cm. I.D. column and that he assumed the same value for the other columns. This is wrong because the shape of the bubble is strongly dependent on the size of the column, as will be demonstrated later in this chapter.

Maneri and Mendelson (1968) extended Mendelson's (1967) analogy between the propagation of waves and the rise velocity of bubbles. From the effect of finite depth on the velocity of waves they proposed the following equation for bubbles in low-M liquids:

$$\frac{U}{U_\infty} = \left\{ \tanh\left[C\ \frac{D}{d_e} + \frac{12}{Eo'}(\frac{D}{d_e} - 1) \right] \right\}^{1/2} \tag{7.5}$$

where

$$C = \tanh^{-1}\left[\frac{0.245(1 - \exp\frac{3.37 - Eo'}{10})}{1 + \frac{4}{Eo'}} \right]^2 \tag{7.6}$$

In Equation (7.5), the constant C, was determined such as to yield the limiting slug velocity at d_e = D, and the Eotvos number dependent term was added to account for the damping effect of the column on the oscillating and spiralling bubbles. Good agreement between Equation (7.5) and published data for bubbles in low-M liquids was demonstrated.

Tasuge and Hibino (1975) extended the correlations of Fujita et al (1950) and Tadaki and Maeda (1961) on dimensional grounds to take into account the retardation of rise velocity of bubbles due to the tube walls. They experimented on bubbles in low-M liquids and also compared their correlations with the existing literature data (O'Brien and Gosline 1935; Peebles and Garber 1953; Uno and Kintner 1956) of bubbles in low-M liquids and found satisfactory agreement.

For spherical-cap bubbles in confined vessels, an excellent theoretical and experimental study was carried out by Collins (1967a, 1967b). He considered the flow around a spherical cap bubble and its associated spherical wake to be given by a doublet at the centre of the sphere. From the stream function for the potential flow of a uniform stream past a doublet at the axis of a cylindrical column (Lamb 1926) he was able to predict values of U/U^*_∞ and $U/(gR_c)^{1/2}$ as functions of $\bar{R}/R_c$. Here U is the observed rise velocity of a spherical cap bubble in the column, U^*_∞ is the rise velocity the bubble of the same shape would have in an infinite liquid, $\bar{R}$ is the average radius of the bubble cap measured over ± 37.5° from the front stagnation point, and R_c is the radius of the column. The theory was found to be in excellent agreement with his own data and those of other workers for bubbles in low-M liquids. Collins was unable to predict from the theory the velocity of the bubble in terms of its volume; however, he found that the experimental results were correlated by the equation:

$$\frac{\bar{R}}{R_c} = 0.71 \tanh^{1/2}\{4.25\,(V^{1/3}/R_c)^2\} \qquad (7.7)$$

which had no theoretical basis except for the fact that it possessed the correct asymptotes.

From this equation and Davies and Taylor's equation for the velocity in terms of the volume of the bubble (see Equation (3.25)), it was possible to cast the theory into a semi-empirical form:

$$\frac{U}{U_\infty^*} = (\frac{\bar{R}}{R_c})^{1/2} (\frac{R_c}{V^{1/3}})^{1/2} \left[0.734 + 0.092 \tanh^{1/2}\left(\frac{0.71 - \bar{R}/R_c}{0.45}\right)^2\right]$$

$$\ldots\ldots(7.8)$$

The asymptote at the slug limit was obtained by combining the theoretical slug velocity with Davies and Taylor's semi-empirical equation relating the velocity to the volume of the bubble:

$$\frac{U}{U_\infty^*} = 0.62(R_c/V^{1/3})^{1/2} \tag{7.9}$$

Collins found the last two equations to be in good agreement with the experimental data in low-M liquids.

The wall effect for bubbles at large Re has also been treated theoretically by Lin (1967) using a slightly different model than Collins. In Lin's model, the bubble shape was assumed to be spherical and the flow field was described by the stream function for potential flow of a uniform stream past a sphere in a circular cylinder (Smythe 1961,1964). With this known velocity field Lin applied Bernoulli's equation around the bubble boundary and forced the pressure around the front stagnation point to be constant to get the bubble velocity in the confined vessel. Lin claimed that his theory gave better results than Collins' theory for small

bubble-to-column diameter ratios, but this claim is not justified considering the extent of scatter in his experimental data.

For values of d_e/D in excess of about 0.5 a bubble becomes greatly elongated; its rise velocity becomes independent of the size* and the limiting rise velocity is determined by the column diameter. The behaviour of these bubbles which are often referred to as "slugs" has been reviewed by Brown (1965), Zukoski (1966), Wallis (1969) and Govier and Aziz (1972).

For the case where viscous forces and interfacial tension can be neglected (i.e. $M \leqslant 10^{-5}$, $Eö' \geqslant 100$), theoretical derivations of the rise velocity of a slug yield

$$U = k\sqrt{gD} \tag{7.10}$$

where k values of 0.35 (Dumitrescu 1943), 0.33 (Davies and Taylor 1950) and 0.36 (Layser 1955, Nicklin 1961) have been proposed. The slight differences in k are due to the different shapes and flow models used in the theoretical analysis. Experimental results favour $k = 0.35$ (White and Beardmore 1962; Stewart 1965).

Brown (1965) extended the inviscid flow model by considering the effects of the viscosity only in the annular film. The slug velocity was shown to depend only on the frontal radius of curvature which is influenced in a minor way by the fluid properties through their control of the thickness of the annular film.

---

* Slug velocity is essentially independent of slug length as long as it exceeds 1.5 D (Laird and Chisholm 1956; Griffith and Wallis 1961; Nicklin et al 1962; Zukoski 1966).

For the case where the surface tension is dominant ($E\delta' \leq 3.4$) several workers (Hattori 1935; Bretherton 1961; White and Beardmore 1962) have shown that the slug remains motionless with its shape determined by a balance between hydrostatic and capillary forces.

For the slugs where the viscous forces are dominant (i.e. $M \gg 10^5$, $E\delta' \gg 100$ and $k \leq 0.05$) Goldsmith and Mason (1962) applied creeping flow equations to the annular liquid film and found slug velocity as a function of liquid film.

When none of the above conditions apply the rise velocity of slugs may be estimated quite accurately using a very general graphical correlation presented by White and Beardmore (1962). These authors made exhaustive study of the literature on slug velocity and correlated data of previous investigators as well as their own as k versus Eo' with Morton number, M, as a parameter.

Alternatively, one could use general relations for k, presented by Wallis (1969) together with Equation (7.10) to predict the rise velocity of a slug in any liquid. Wallis has shown that his relations for k represent the graphical correlation of White and Beardmore (1962) fairly well.

7.3 Objectives

From the preceeding review it is clear that most of the early experimental work was on bubbles rising in low-M liquids; the emphasis being placed on the reduction in rise velocity due to the presence of the container walls. In recent years it has been recognized that the containing walls tend to alter bubble shape and to suppress secondary motion as well. None of the studies reported to date has dealt with the effect of walls on the wakes of bubbles and on the behaviour of skirted

bubbles.

In view of this, in the present experimental program, the behaviour of large bubbles (> 1 cm^3) in high-M liquids was studied in columns of 7.06 cm, 14.4 cm and 29.2 cm I.D. to determine:

    (i)   the wall effect on the rise velocity, the shape and the wake of bubble;

    (ii)   the influence of walls on the skirted bubbles; and

    (iii)   how the wall effects for bubbles in high-M liquids differ from those reported for bubbles in low-M liquids, and from those for solid spheres.

Collins (1967b) discussed the application of his wall effect theory for spherical cap bubbles in liquids to gas bubbles in fluidized beds which are known to possess high apparent viscosity (Davidson and Harrison 1963; Stewart 1968; Grace 1970) giving Re $<$ 100, and which exhibit bubble shapes similar to those in viscous liquids (Rowe and Patridge 1965; Jones 1965). Collins concluded that "before applying the wall correction derived here to the fluidized bubble, its validity at a Reynolds number of order 30 would need to be demonstrated". One of the objectives of the present experiments was to provide this demonstration, thus permitting the effect of the container walls to be evaluated for large bubbles at low Re in viscous (or high-M) liquids as well as in fluidized beds.

7.4 Experimental Results and Discussion

The physical properties of the liquid used in the wall effect experiments are listed in Table 7.1. In some cases the experimental data points were too numerous to place on the graphs hence only representation data are displayed to preserve clarity.

TABLE 7.1 <u>Physical Properties of Liquids used in Wall Effect Experiments</u>

Author	Liquid		μ (Poise)	ρ (g/cm^3)	σ (dynes/cm)	M (-)
present work	sugar solution	B	13.98	1.379	78.8	5.55×10
"	"	C	7.30	1.370	78.5	4.20
"	"	D	5.09	1.358	77.7	1.30
"	"	E	2.89	1.347	77.6	1.09×10^{-1}
"	"	F	1.36	1.325	77.3	5.48×10^{-3}
"	"	G	1.00	1.320	76.8	1.64×10^{-3}
Davenport (1974)	PVA solution		2.16	1.00	46.2	2.16×10^{-1}
"	"		1.15	1.00	46.9	1.66×10^{-2}
"	"		0.54	1.00	47.0	8.03×10^{-4}
Guthrie (1967)	PVA solution		7.35	1.02	46.0	2.88×10
"	"		1.30	1.01	46.5	5.61×10^{-1}
"	"		0.46	1.01	47.7	4.01×10^{-4}
	water		0.01	1.00	73.0	3.69×10^{-11}
Guthrie and Bradshaw (1969)	glycerol		12.3	1.26	63.0	7.13×10

7.4.1 Evaluation of measuring technique

The volumes, shapes and velocities of the bubbles rising in the two small column were measured using the same methods as those used for the larger column. The accuracy of these methods has already been discussed in Chapter 3, Section 3.4.1. The wake volumes were determined using the procedure outlined in Chapter 4, Section 4.5.2.8.

Because the plexiglass has a refractive index fairly close to that of sugar solutions used, no noticeable radial optical distortion was observed, even when the smaller column inserts were present. This was verified by photographs of an accurate scale placed inside the small columns in the central plane containing the axis of bubble rise.

7.4.2 Wall effect on rise velocity

Figure 7.1 illustrates a typical effect of wall proximity on rise velocity. The approach to the slug flow condition for large bubbles is clearly seen for the smallest column. The upper curve with its straight line extrapolation beyond a bubble volume of about 45 cm^3 is considered to represent the relationship in an infinite medium.*

7.4.3 Wall effect on bubble shape

The effect of the column wall on typical bubble shapes encountered in the present work is illustrated in the photographs of Figures 7.2 and 7.3 for a bubble volume of 27.8 cm^3 (Re — 9.61 to 217) and 92.6 cm^3 (Re — 15.3 to 369), respectively. The left, the middle and the right columns in both figures show bubbles in three columns of different internal diameters,

---

* See Chapter 3, Section 3.4.3.4, for more discussion on this matter.

29.2 cm, 14.4 cm and 7.06 cm, respectively. The top, the middle and
the bottom rows show the bubbles in sugar solutions of viscosity 1.00,
7.30 and 13.98 Poise, respectively. All the bubbles are shown at the
same magnification to enable easy visual comparison. A strong influence
of the wall proximity on bubble shape is observed. The decrease in
column diameter tends to cause elongation of bubbles in the vertical
direction. Note that the extent of the change in bubble shape brought
about by the presence of the container walls is greatly influenced by
the original shape of the bubble in an unbounded fluid as well as by
the size of the bubble and by the physical properties of the liquid.
The change in the shape of the bubble base (see for example Figure 7.2(1)
to (3), Figure 7.3(1) to (3) and Figure 7.3(4) to (6)) indicates that the
wake structure of the bubble is also altered by the walls. Further, it
is noted that the size of the column affects the onset of waves or
skirted bubbles (see Figure 7.3(4) to (6), for example).

The right column in Figure 7.3 shows slug-like bubbles with
$d_e/D = 0.795$. It is evident from these photographs that the shape of
the slug is strongly influenced by the physical properties of the liquid.
The thickness of the annular liquid film seem to increase with the
increase in viscosity of the liquid.*

The wall effect on the maximum width of the bubble is presented
in Figure 7.4 for a 13.98 Poise sugar solution. Similar trends were
observed for the other liquids. These data confirm the findings of
others (Collins 1967; Guthrie 1967) that the shape is strongly affected

---

*. The two closely spaced parallel vertical lines on either side of the
slugs in Figure 7.3(4), (6) and (9) indicate the walls of the 7.06 cm I.D.
column insert.
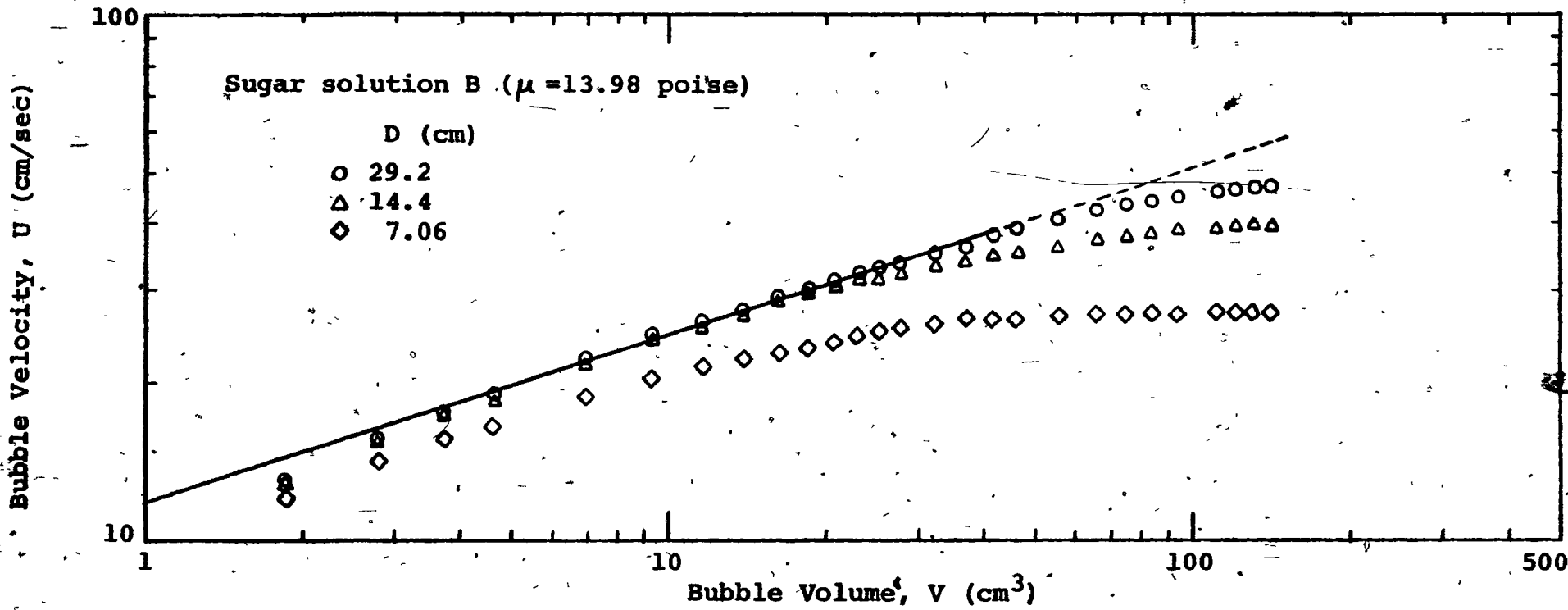
FIGURE 7-1 : Effect of column diameter on bubble rise velocity

FIGURE 7.2 Wall Effect on the Shape of a Bubble in Three Different Sugar Solutions

$$V = 27.8 \text{ cm}^3; \; d_e = 3.76 \text{ cm}; \; E\acute{o} = 242$$

No.	Liquid Properties			M	Column dia.,D (cm)	de/D	U (cm/sec)	Re
	μ (Poise)	ρ (g/cm³)	σ (dynes/cm)					
1	1.00	1.320	76.8	1.64×10^{-3}	29.2	0.129	43.77	217
2	1.00	1.320	76.8	1.64×10^{-3}	14.4	0.261	38.67	192
3	1.00	1.320	76.8	1.64×10^{-3}	7.06	0.533	28.18	140
4	7.30	1.370	78.5	4.20	29.2	0.129	37.38	26.4
5	7.30	1.370	78.5	4.20	14.4	0.261	34.53	24.4
6	7.30	1.370	78.5	4.20	7.06	0.533	27.21	19.2
7	13.98	1.379	78.8	5.55×10	29.2	0.129	33.85	12.6
8	13.98	1.379	78.8	5.55×10	14.4	0.261	32.15	12.2
9	13.98	1.379	78.8	5.55×10	7.06	0.533	25.41	9.61

All bubbles shown at same magnification. The grid in the background is
approximately 2 cm x 2 cm.

FIGURE 7.3 <u>Wall Effect on the Shape of a Bubble in Three Different Sugar Solutions</u>

$V = 92.6 \text{ cm}^3$; $d_e = 5.61 \text{ cm}$; $E\ddot{o} = 540$

No.	Liquid Properties			M	Column dia.,D (cm)	de/D	U (cm/sec)	Re
	μ (Poise)	ρ (g/cm³)	σ (dynes/cm)					
1	1.00	1.320	76.8	1.64×10^{-3}	29.2	0.192	49.79	369
2	1.00	1.320	76.8	1.64×10^{-3}	14.4	0.390	41.78	310
3	1.00	1.320	76.8	1.64×10^{-3}	7.06	0.795	28.44	211
4	7.30	1.370	78.5	4.20	29.2	0.192	48.36	50.9
5	7.30	1.370	78.5	4.20	14.4	0.390	41.51	43.7
6	7.30	1.370	78.5	4.20	7.06	0.795	28.01	29.5
7	13.98	1.379	78.8	5.55×10	29.2	0.192	45.09	25.1
8	13.98	1.379	78.8	5.55×10	14.4	0.390	40.52	22.4
9	13.98	1.379	78.8	5.55×10	7.06	0.795	27.14	15.3

All bubbles shown at same magnification. The grid in the background is approximately 2 cm x 2 cm.

6"-insert   2¼"-insert
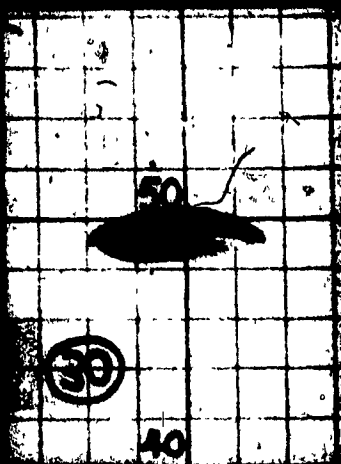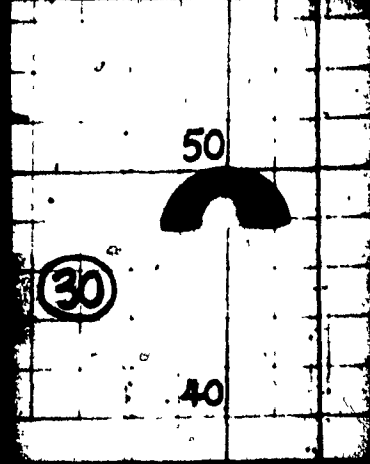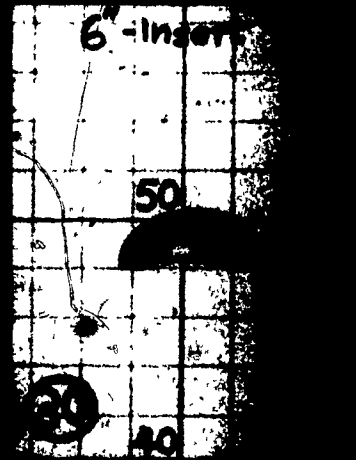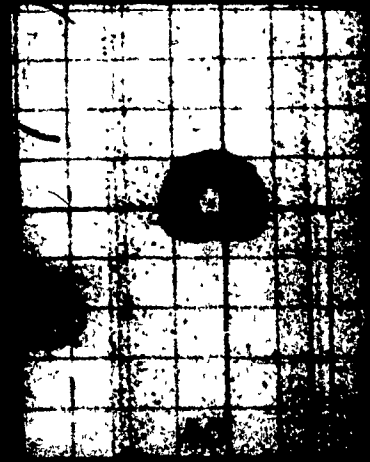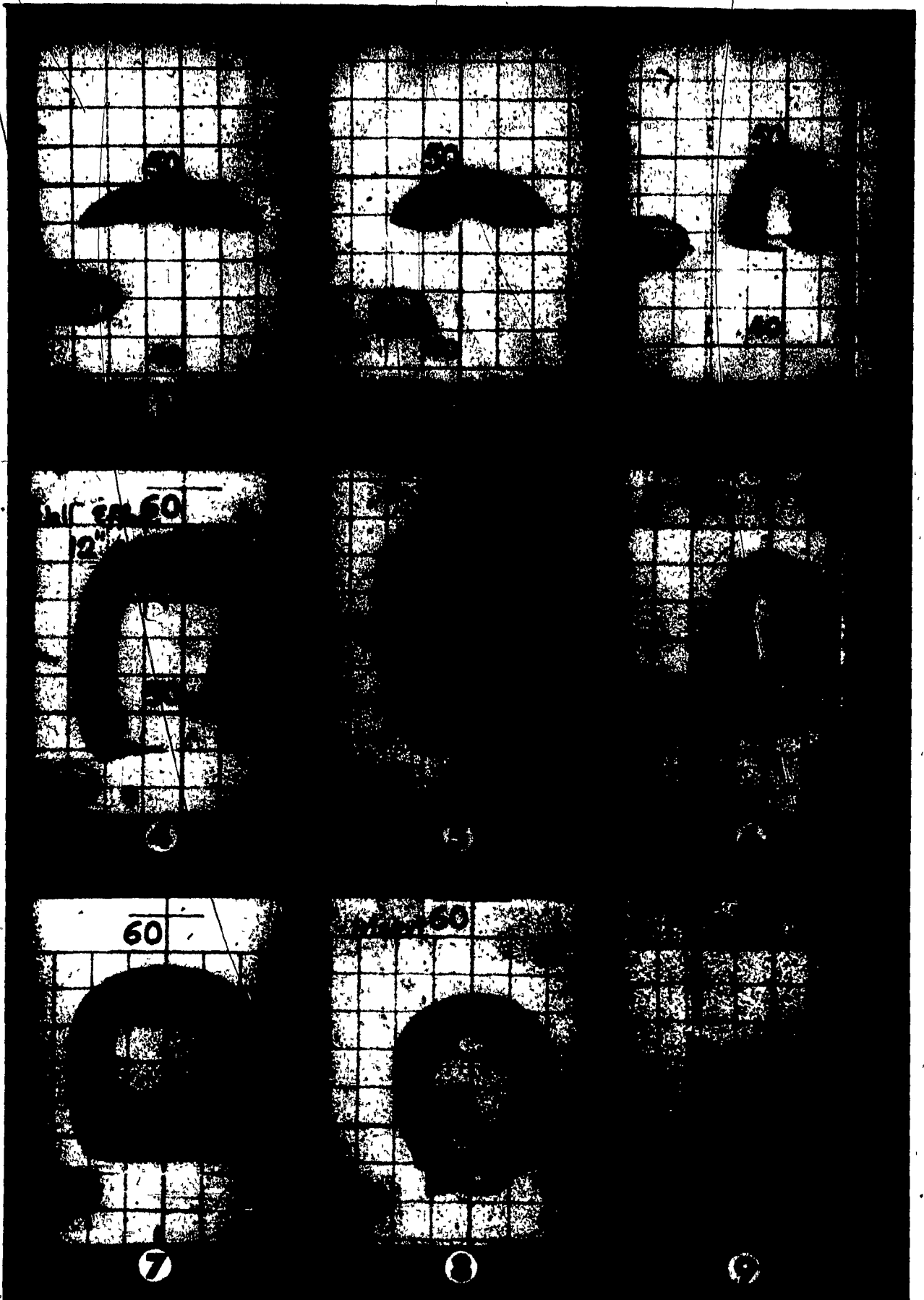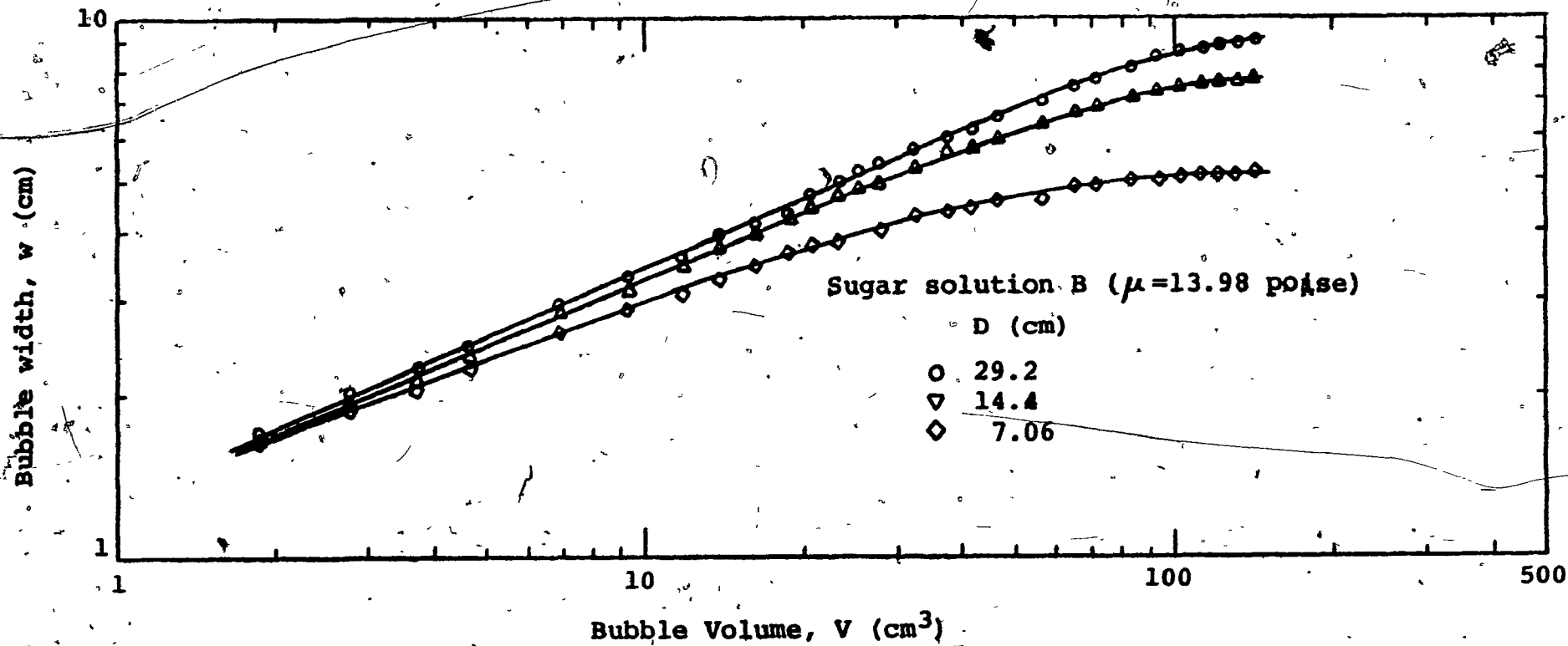
FIGURE 7-4 : Effect of column diameter on bubble shape

The figure plots Bubble width, w (cm) versus Bubble Volume, V (cm³) on log-log axes, showing:

Sugar solution B (μ=13.98 poise)

D (cm)
○ 29.2
▽ 14.4
◇ 7.06

by the wall proximity and further supports the contention that Figure 10 of Uno and Kintner (1956) and Figures 11 and 12 of Angelino (1966) which neglect the wall effect on shape are invalid.

7.4.4 Comparison with wall effect theories and correlations

7.4.4.1 Spherical-cap bubbles

In Figures 7.5 to 7.7 the effect of the wall on the velocity of spherical-cap bubbles in viscous liquids is compared with Collins' theory (1967). The range of d_e and Re for the data are indicated on the figures. The Reynolds number range for the present data span 10 to 421 compared to Collins' Re range of 1600 to 58,000. The good agreement with the theory observed at these lower Re is due to the fact that the potential flow assumption near the nose of the bubble is still reasonable, as shown in Chapter 4. In addition, the experimental rise velocities are also in good agreement with the inviscid models for spherical cap bubbles and for slugs which constitute the asymptotes of Collins' theory. The experimental data of Davenport (1964), Guthrie (1967) and Guthrie and Bradshaw (1969) are plotted in the same form in Figure 7.8. The physical properties of the liquids used by these authors are listed in Table 7.1. The data of these workers also agree well with the theory.

Lin's theory (1967) is also shown for comparison in Figures 7.5 to 7.8. Up to $\overline{R}/R_c \approx 0.3$ Lin's theory essentially coincides with Collins' theory and with the experimental data. However, at larger values of $\overline{R}/R_c$ Lin's theory falls below the experimental data and the theoretical predictions of Collins. Further, unlike Collins' theory, Lin's theory does not approach the asymptotic slug limit. Lin's claims that his theory should be used up to $\overline{R}/R_c \approx 0.6$ and that his theory gives better predic-
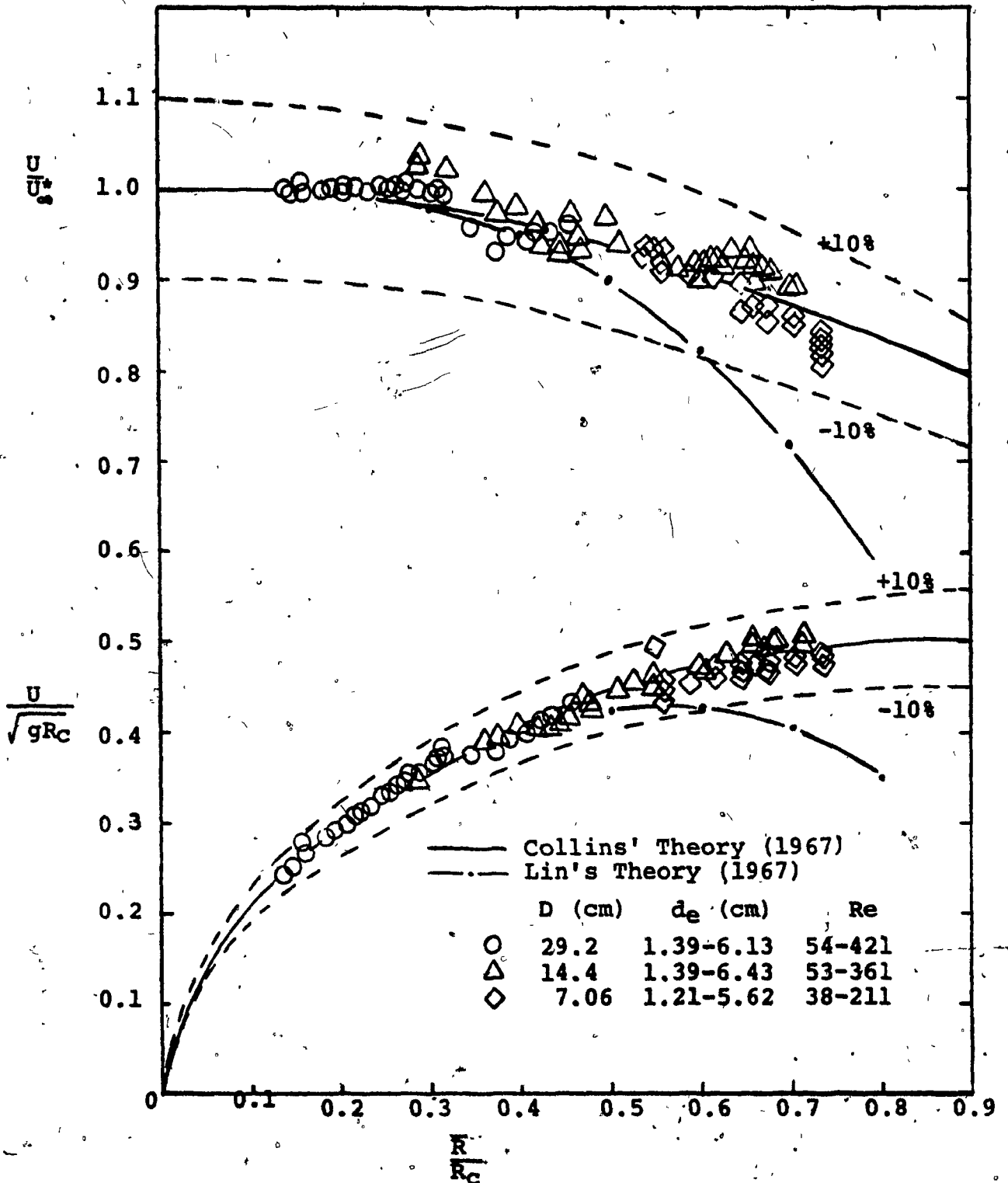
FIGURE 7-5: Comparison between wall effect theories and experimental data for spherical-cap bubbles in 1.00 poise sugar solution.
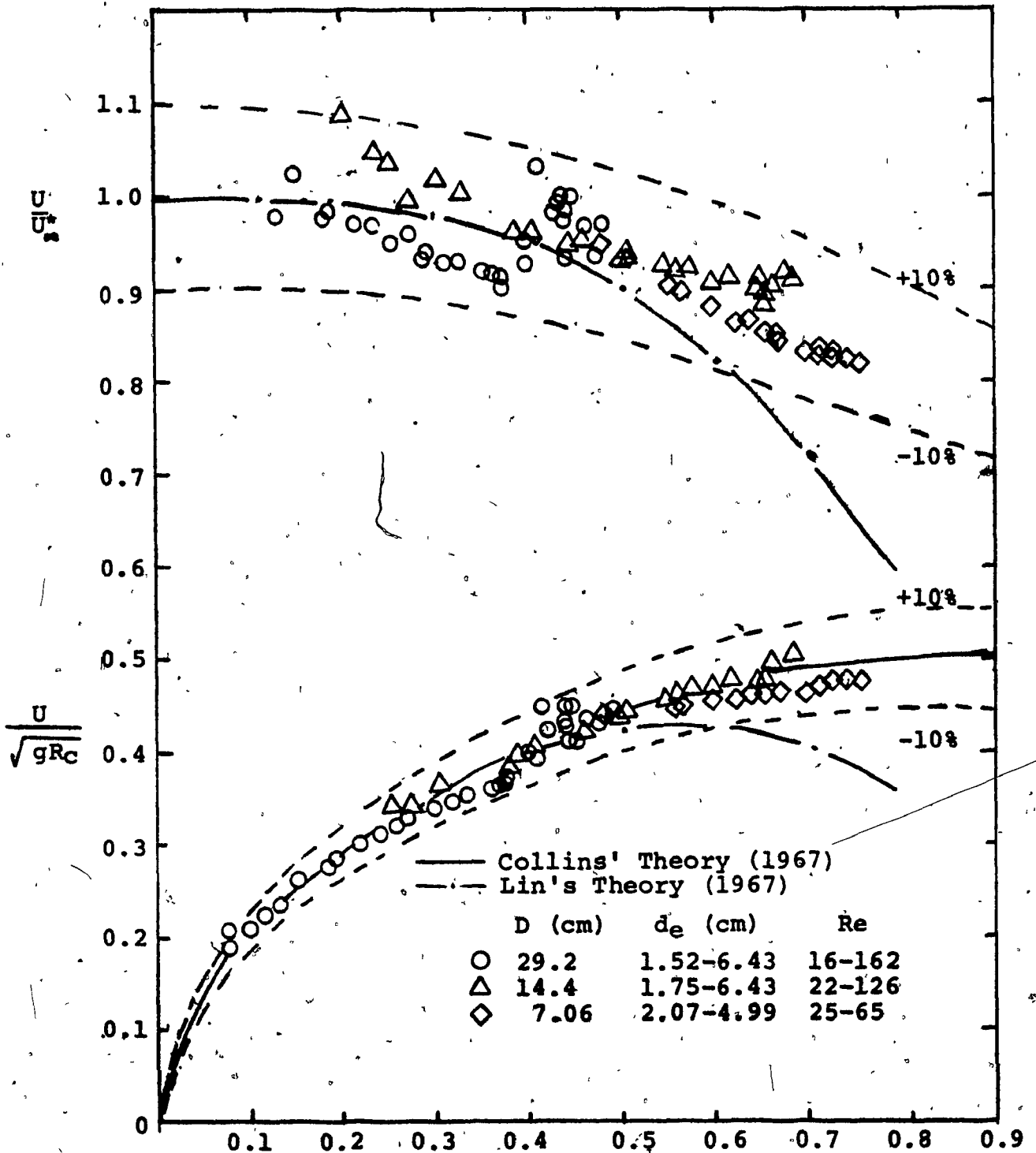
FIGURE 7-6: Comparison between wall effect theories and experimental data for spherical-cap bubbles in 2.89 Poise sugar solution.
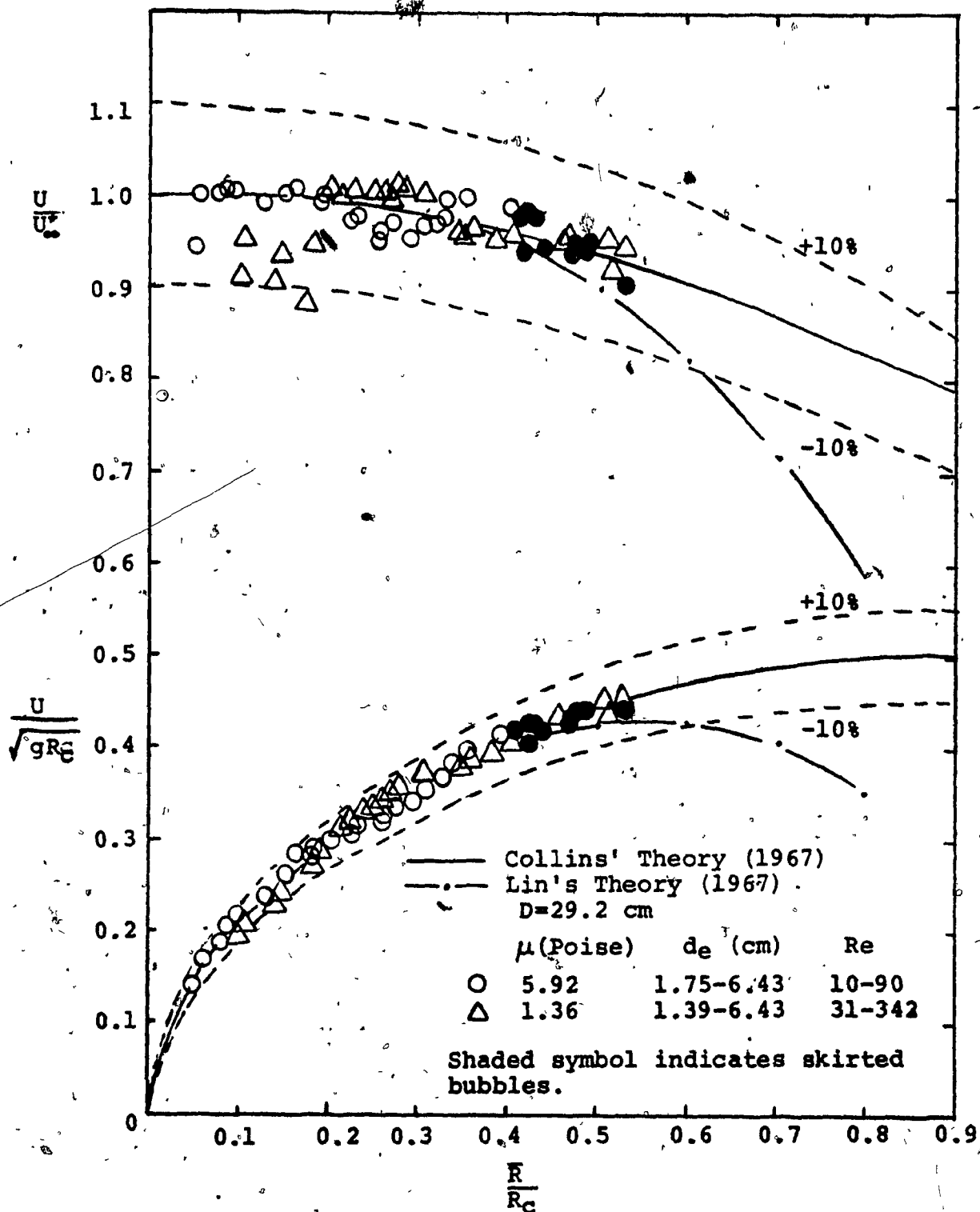
FIGURE 7-7: Comparison between wall effect theories and experimental data fo[r] [sphe]rical-cap and skirted bubbles in sugar solution of 1.36 and 5.92 Poise.

FIGURE 7.8 Comparison between wall effect theories and
experimental data of other workers for spherical-
cap and skirted bubbles

Davenport's (1964) Data in 6" x 6" Column *

	μ(Poise)	d_e (cm)	Re	
●	2.16	1.30-3.80	12-64	
◆	1.15	1.32-4.48	28-150	
▲	0.54	1.38-4.48	67-324	
◐	2.16	4.06-4.28	70-75	(skirted bubbles)

Guthrie's (1967) Data in 18" I.D. Column

	μ(Poise)	d_e (cm)	Re	
○	7.35	3.28-5.91	16-42	
◇	1.30	2.83-5.20	77-203	
△	0.4	2.26-5.18	164-572	
◁	0.01	2.58-2.92	9291-11290	

Guthrie and Bradshaw (1969) Data in 4" x 4" Column *

	μ(Poise)	d_e (cm)	Re	
⊗	12.3	4.66	23	(skirted bubble)

* For the square column, the radius of a circle having the same
cross-sectional area was selected as the equivalent column radius,
as suggested by Collins (1967).

Figure showing $\frac{U}{U^*}$ (top) and $\frac{U}{\sqrt{gR_C}}$ (bottom) versus $\frac{\overline{R}}{R_C}$.

- Collins' Theory (1967)
- Lin's Theory (1967)

Top curves labeled +10% and −10%; bottom curves labeled +10% and −10%.
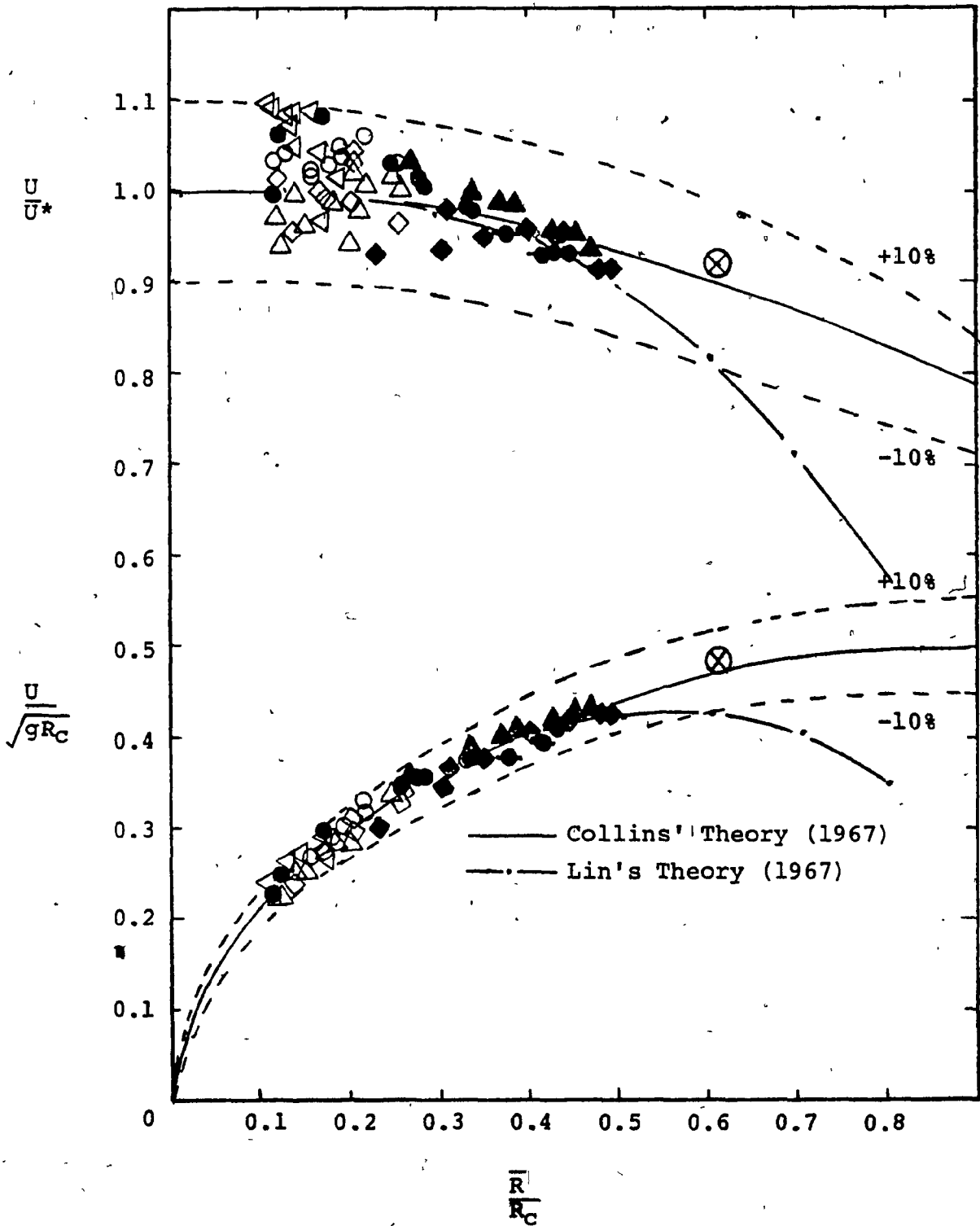
tions than Collins' for $0.3 < \bar{R}/R_c < 0.6$ are not valid.

Data for skirted bubbles are also presented in Figures 7.7 and 7.8. It is clear that the wall effect is the same for both skirted and unskirted bubbles at the same value of $\bar{R}/R_c$. The data for skirted bubbles also show excellent agreement with Collins' theory.

From the above discussion it is concluded that Collins' wall effect theory for spherical-cap bubbles in non-viscous (or low-M) liquids can safely be applied in viscous (or high-M) liquids and in fluidized beds to predict the shape from the observed velocity or vice-versa for Re greater than about 10.

Collins' semi-empirical correlation relating the bubble shape to its volume, Equation (7.7), is compared with the present data in Figures 7.9 and 7.10. For 1.00 Poise sugar solution (see Figure 7.9) the agreement is fairly good whereas for a higher viscosity (2.89 Poise) solution (see Figure 7.10) the experimental data lie below the curve, the discrepancy increasing at lower Re. Similar trends (not shown) were also observed for 1.36 Poise and 5.09 Poise solutions and also for the data of Davenport and Guthrie. This is not surprising since it is well known that for a given volume of gas the radius of curvature of the bubble decreases as the viscosity is increased for Re < 100. (see Chapter 3; also Davenport 1964; Guthrie 1967).

The variation of U/U_∞ with $V^{1/3}/R_c$ for spherical cap bubbles is shown in Figure 7.11 For convenience the bubble size is also shown as d_e/D on the upper abscissa. Collins used the value of U_∞ obtained from the Davies and Taylor semi-empirical Equation (3.25) which is applicable only for dynamically similar spherical cap bubbles that are encountered at Re > 100 with $\theta_m \approx 50°$. For spherical cap bubbles in viscous liquids
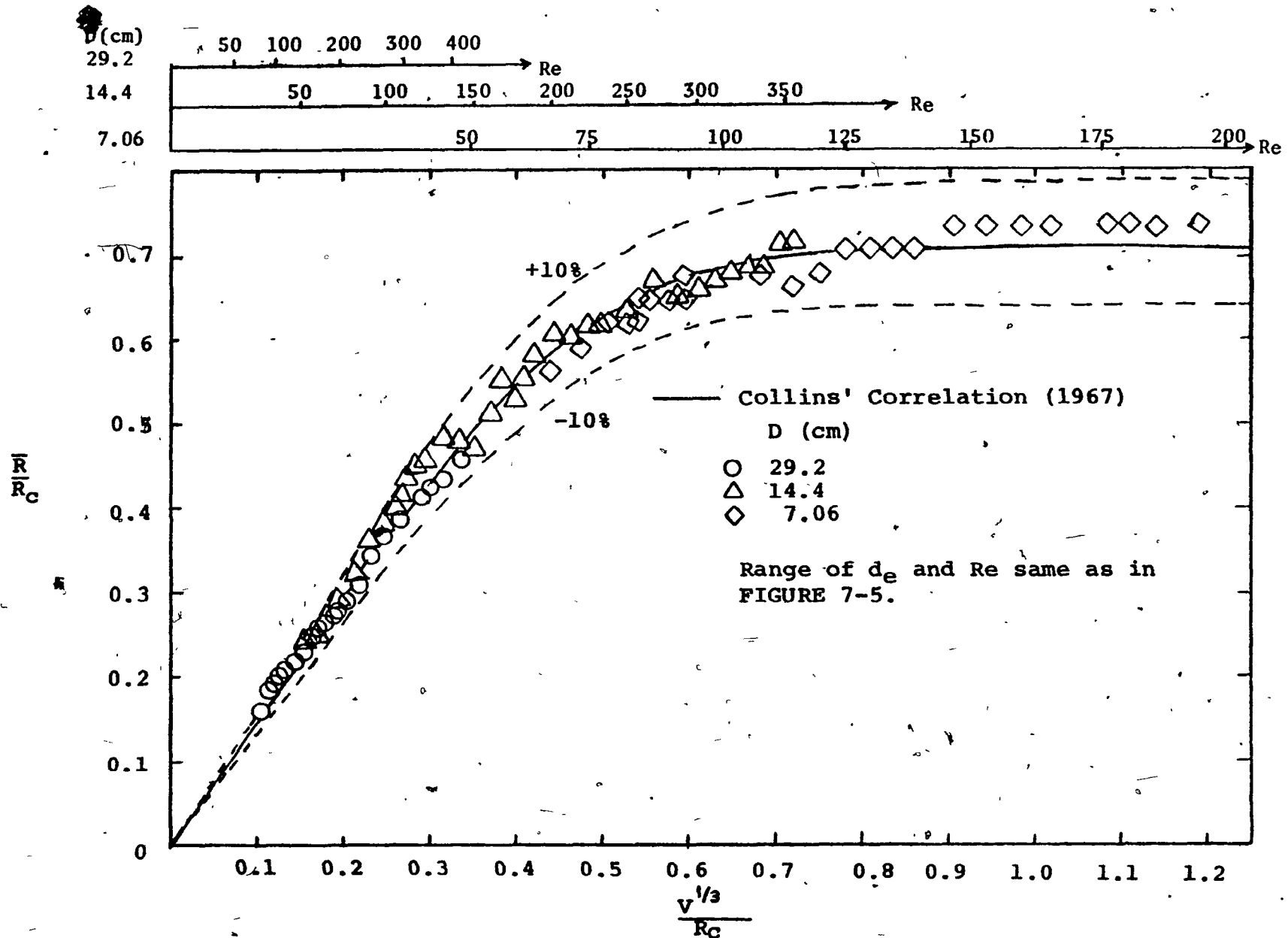
FIGURE 7-9: Comparison of Collins' correlation for shape of spherical-cap bubbles in confined medium (1.00 Poise sugar solution).
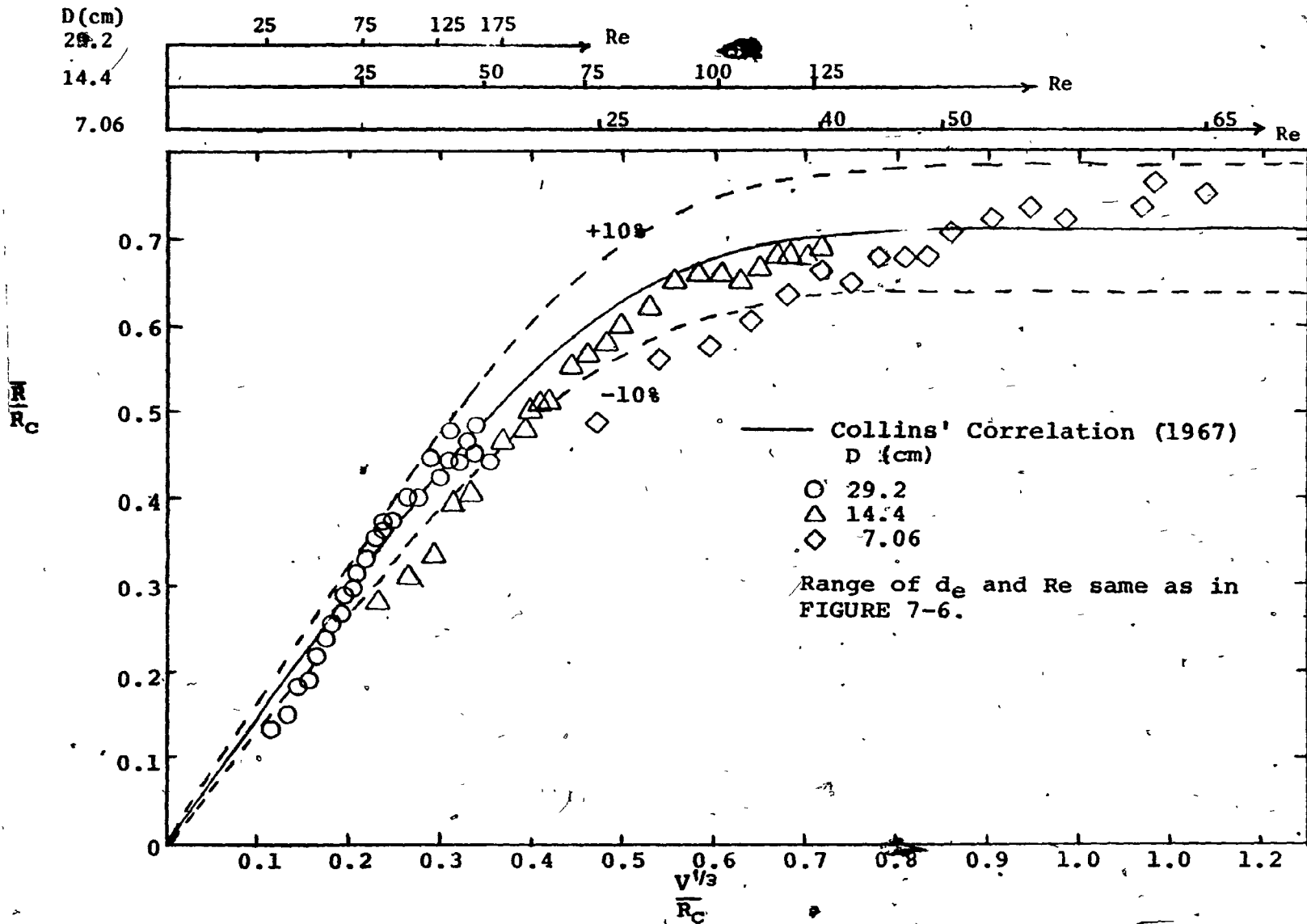
FIGURE 7-10: Comparison between Collins' correlation for shape of spherical-cap bubbles in confined medium (2.89 Poise sugar solution).

346.

FIGURE 7.11 <u>Comparison of various wall correction models</u>

<u>Present Experiments</u>

μ(Poise)	D (cm)
□ 5.09	29.2
◇ 2.89	29.2
◑ 2.89	10.4
◆ 2.89	7.06
△ 1.36	29.2
○ 1.00	29.2
◑ 1.00	14.4
● 1.00	7.06

<u>Previous Theories & Correlations</u>

————	Collins (1967), semi-empirical theory	(bubbles)
▬ ▬	Collins (1967), asymptote at slug limit	(bubbles)
—x—	Maneri & Mendelson (1968), wave analogy	(bubbles)
⫫⫫⫫	Uno & Kintner (1956), correlation	(bubbles)
·············	Harmathy (1960), correlation	(bubbles, drops & solid spheres)
——HSB	Haberman & Sayers (1958), theory	(bubbles)
——HSS	Haberman & Sayers (1958), theory	(solid spheres)
——FW	Fidleris & Whitmore (1961), correlation	(drops)
—·—	Strom & Kintner (1958), correlation	(drops)
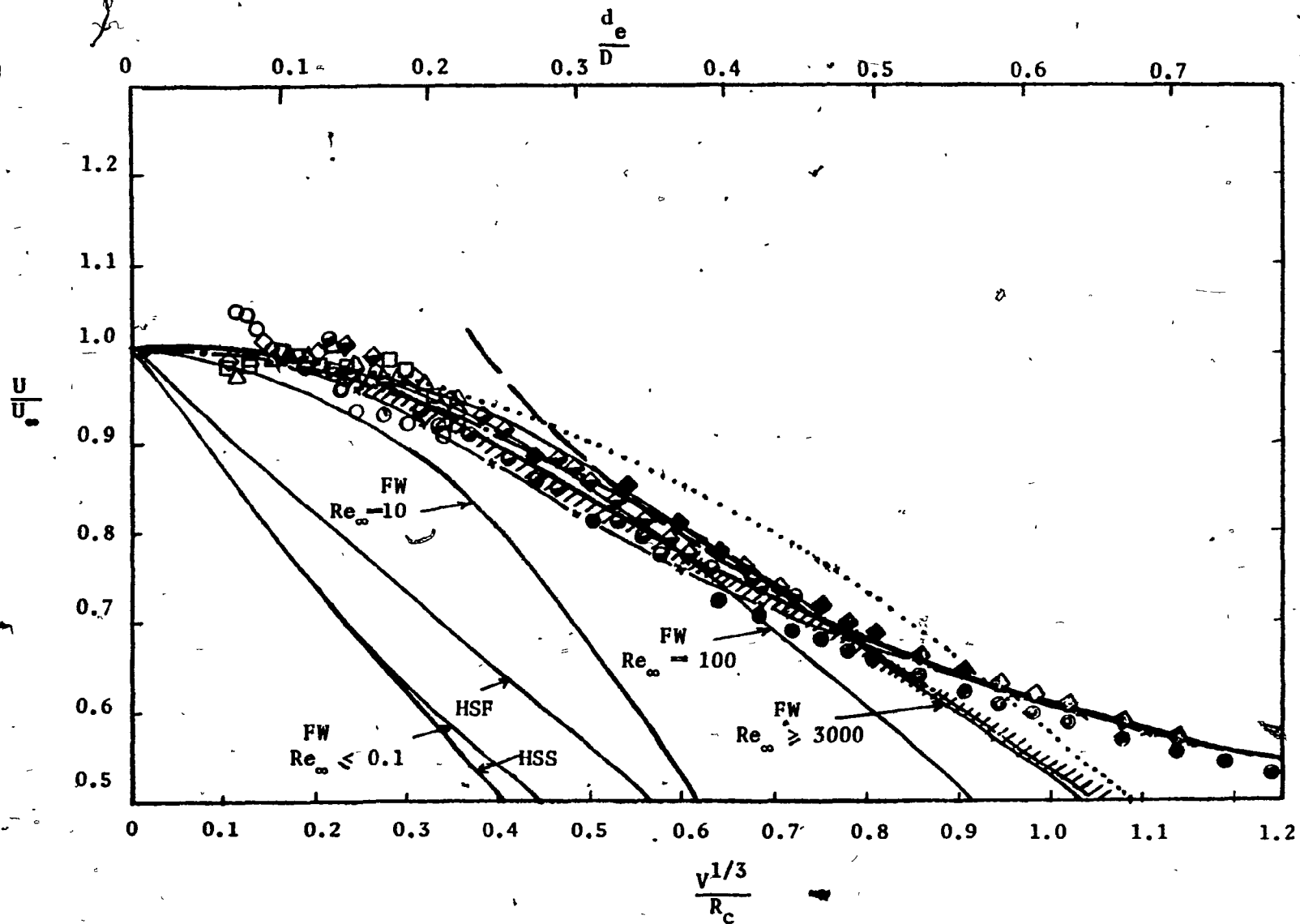
FIGURE 7.11 Comparison of various wall correction models

with Re $\leqslant$ 100 it was shown in Chapter 3, Section 3.4.2.3 that with
decreasing Re, θ_m decreases and the Davies and Taylor semi-empirical
equation[*] does not hold. Therefore, the value of U_∞ was obtained from
$U_\infty = KV^m$ where the values of K and m were determined as mentioned in
Section 3.4.3.4. This further illustrates the usefulness of the cor-
relation for K and $\overset{o}{n}$ that was developed in the present work.

The wall correction models reviewed in Section 7.2 are compared
with the data in Figure 7.11. On the whole the experimental data show
excellent agreement (within ± 5%) with Collins' semi-empirical equation
over the entire range of d_e/D.

Maneri and Mendelson's wave analogy, Equation (7.5), also
conform to the experimental data at high and low values of d_e/D or
$V^{1/3}/R_c$ but at the intermediate values their model slightly underpredicts
the value of U/U_∞. The value of C in the Equation (7.5) was determined
by using Wallis' equation for the slug velocity and was found to be
insensitive to the physical properties and the values of Eö' = 849 to
14519 that were encountered for the data plotted on Figure 7.11.

For Uno and Kintner's correlation (Equation (7.2)) the value
of B was obtained from their Figure 9 by extrapolation. A range of pre-
dicted values of U/U_∞ for the present experimental conditions show
reasonably good agreement with the data up to $d_e/D \approx 0.05$ beyond which
their correlation begins to underpredict U/U_∞, as was found for bubbles
in low-M liquids by these authors as well as Maneri and Mendelson (1968).
This divergence obviously stems from the solid sphere analogy that was
used by Uno and Kintner in obtaining the form of the correlation which
requires the terminal velocity at $d_e = D$ to be zero as the sphere fills
the tube.

---

[*] Relating bubble velocity to its volume (Equation (3.25)).

Similar trends to Uno and Kintner's correlation are observed for Strom and Kintner's correlation, Equation (7.3), with the latter being slightly above the former, for d_e/D between 0.2 and 0.5.

The general experimental correlations of Harmathy (1960) for $Re_\infty > 500$, Equation (7.4) with $E\ddot{o}' = \infty$ and Fidleris and Whitmore (1961) for various Re are also shown in Figure 7.11. These curves demonstrate that the wall retardation effect for solid spheres is not the same as that for bubbles since the flow induced deformation of a fluid particle is not accounted for in the rigid particle correlations, nor is the mobility of the surface. Haberman and Sayre (1958) demonstrated the importance of the latter factor in creeping flow where they showed that wall correction is significantly different for circulating spheres than for solid spheres. Their theoretical predictions for solid spheres and for freely circulating spherical gas bubbles are also shown in Figure 7.11.

7.4.4.2 Ellipsoidal-cap bubbles

In high-M (or high viscosity) liquids bubbles adopt oblate ellipsoidal-cap shapes for $Re \lesssim 45$ (see Chapter 3, Section 3.4.2.3). The deformation of such bubbles by the column walls is illustrated in Figure 7.2 (see for example Figs. 7.2(7) to (9)). Because of its success for spherical-caps at low Re, the theory of Collins' relating bubble shape to rise velocity was applied for ellipsoidal-cap bubbles with the following modifications:

(i)   The major semi-axis, a, was substituted for $\overline{R}$ as the
      representative shape parameter; and

(ii) The value of U^{*}_{∞} was obtained by means of Equation (3.30)
      due to Wairegi & Grace (1976) for oblate ellipsoidal-cap
      bubbles and a similar equation (see Table 6.5(c)) due to
      Grace and Harrison (1967) for prolate ellipsoidal-cap
      bubbles.

Collins' theory in this modified form is compared with the
experimental data on ellipsoidal-cap bubbles in Figs. 7.12 and 7.13.
The prevalent Re are also indicated on the graph. We observe that for
about Re $\gtrsim$ 5 the modified theory agrees reasonably well with the experi-
ments while at lower Re it underpredicts both U/U^{*}_{∞} and $U/\sqrt{gR_{c}}$, especially
the former.

The velocity retardation, U/U_{∞}, for these bubbles is displayed
in Fig. 7.14. The value of U was obtained as before using $U_{\infty} = KV^{m}$.
The data lie well above the semi-empirical equation of Collins. The data
for the higher viscosity liquid seem to lie above those for the lower
viscosity liquid. In order to arrive at an explanation of this observa-
tion the following factors are considered:

(i)   For a bubble of given volume in a given column (i.e. for
      fixed d_{e}/D) as the viscosity is increased the bubble
      shape changes and the maximum width of the bubble
      decreases. (see Figs. 7.2 and 7.4) Thus, one would
      expect the velocity retardation to decrease with increasing
      viscosity at constant d_{e}/D.

(ii) On the other hand, Re for a given bubble decreases with
      increase in viscosity and the velocity retardation would
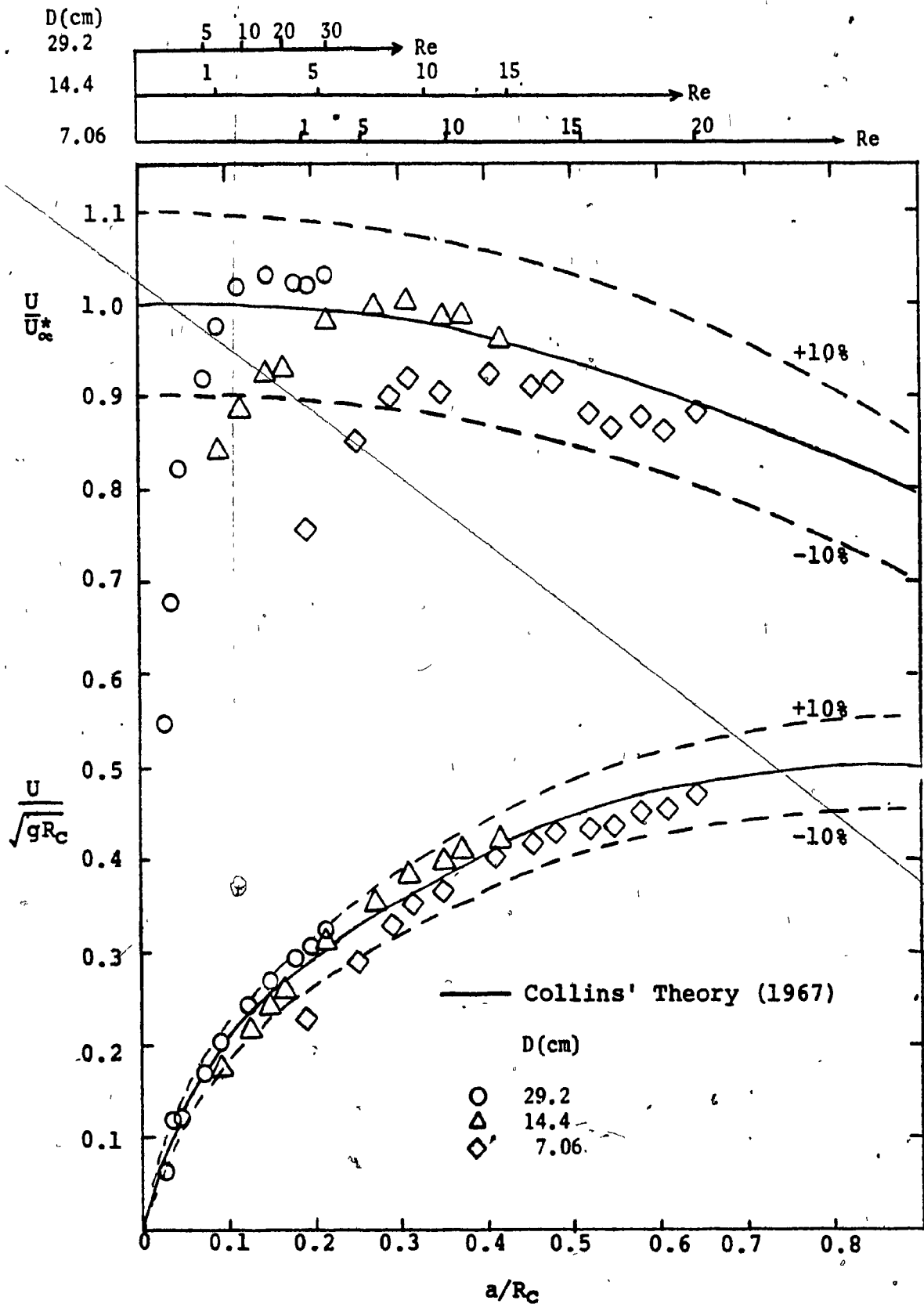
FIGURE 7-12: Application of Collins' wall effect theory to ellipsoidal-cap bubbles in 7.30 Poise sugar solution.
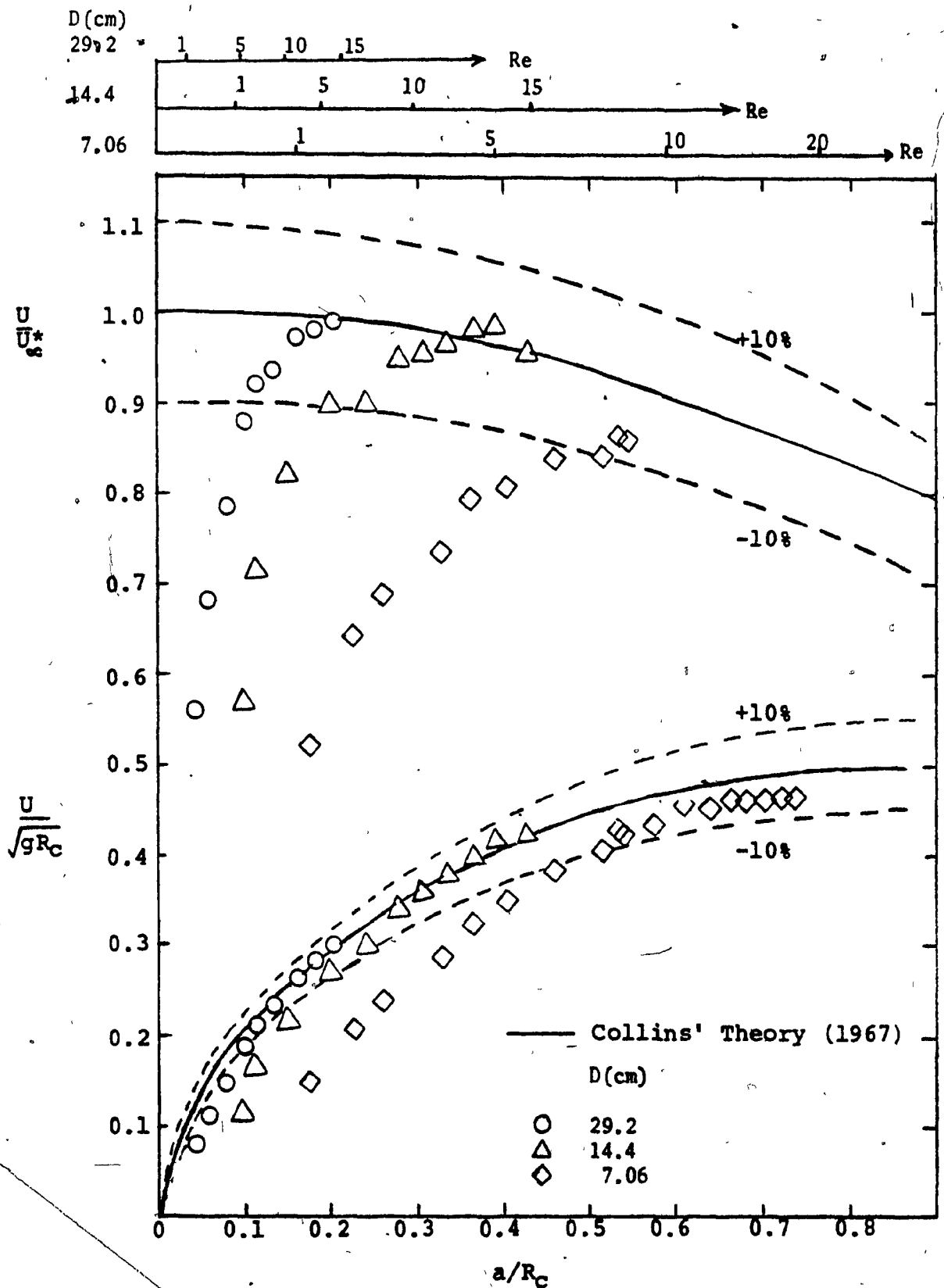
FIGURE 7-13: Application of Collins' wall effect theory to ellipsoidal-cap bubbles in 13.98 Poise sugar solution.
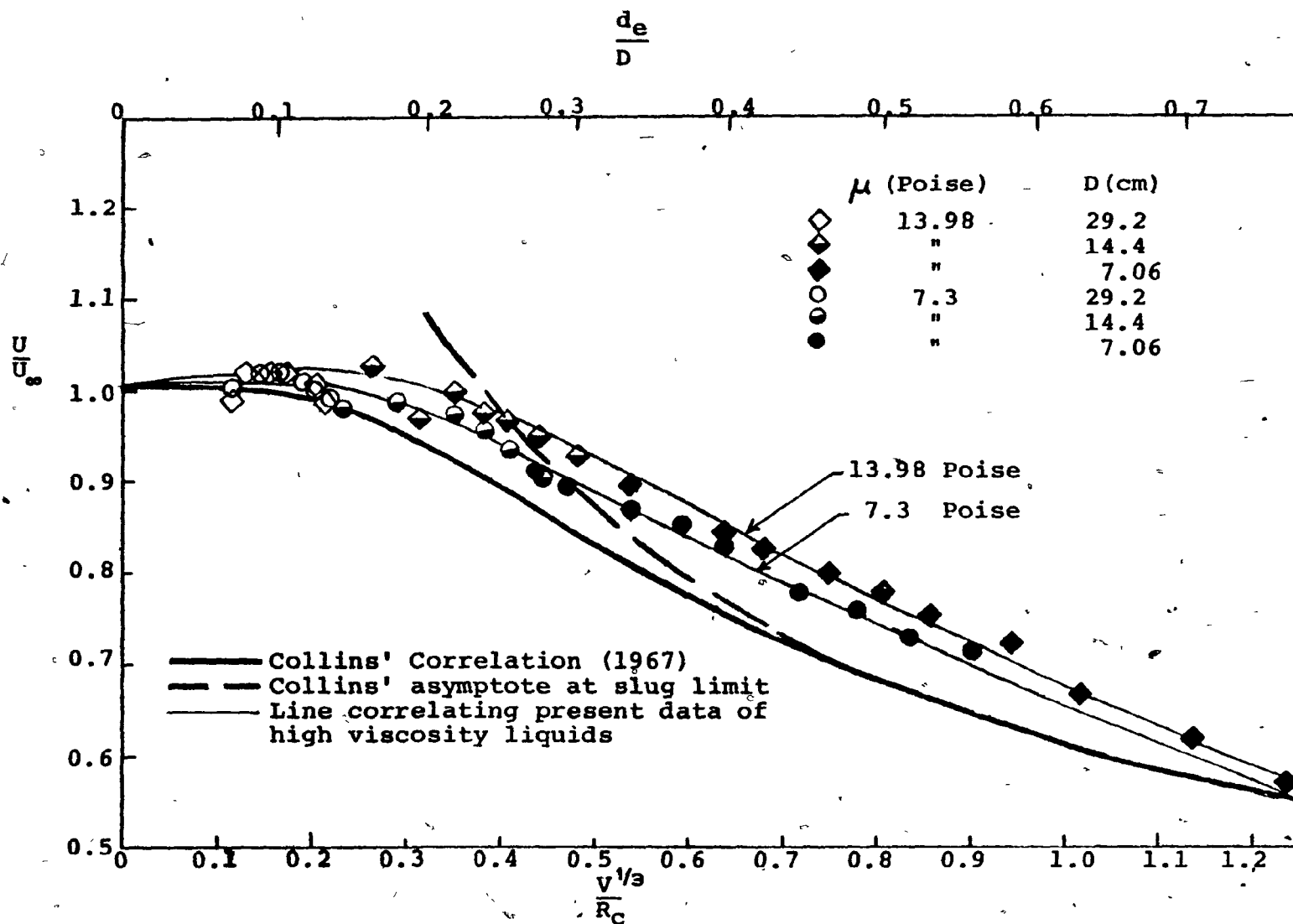
FIGURE 7-14: Comparison of Collins' correlation for velocity retardation with experimental data for ellipsoidal-cap bubbles in viscous liquids.

be expected to increase as was observed for solid spheres

by Fidleris and Whitmore (1961).

Although it is impossible to estimate the magnitude of change in rise

velocity brought about by these two opposing factors, factor (i) seems

to play an increasingly important role as the viscosity of the liquid

is increased.

7.4.4.3 Slugs

In Table 7.2 the experimental rise velocities of slugs are

compared with those predicted by various theoretical and empirical models

that were reviewed in Section 7.2. The value of the dimensionless number

k (which is often referred to as Froude number based on column diameter)

and hence the rise velocity is found to increase with decreasing liquid

viscosity.* As expected, with decreasing liquid viscosity, the value of

k approaches the theoretical predictions of the potential flow models.

Brown's model which accounts for the viscous effects in the liquid

annulus underpredicts the rise velocity by about 2.9 to 6.2%. The values

predicted by the empirical equation of Wallis and the graphical correla-

tion of White and Beardmore are in fairly good agreement with the experi-

mental data.

---

* As can be seen in Table 7.2, a 14-fold increase in viscosity of the
liquid was accompanied by only 4.46% increase in density and 2.6% increase
in the surface tension, hence the variation of density and surface tension
can be neglected compared to the variation in the viscosity.

TABLE 7.2 Comparison of Rise Velocity of Slugs

Bubble volume — 139 cm^3

Column diameter, $D - 7.06$ cm., $d_e/D - 0.91$

					Eö'	Re'	$k - \dfrac{U}{\sqrt{gD}}$			
μ (Poise)	ρ (g/cm^3)	σ (dynes/cm)	M	U (cm/sec)	$-\dfrac{\rho g D^2}{\sigma}$	$-\dfrac{\rho UD}{\mu}$	Experimental	Wallis	White and Beardmore	Brown
7.00	1.320	76.8	1.64×10^{-3}	28.47	840.4	17.8	0.342	0.345	0.343	0.326
2.89	1.347	77.6	1.09×10^{-1}	28.12	848.8	36.4	0.338	0.345	0.335	0.317
7.30	1.370	78.7	4.17	27.50	851.2	92.6	0.330	0.331	0.318	0.306
13.98	1.379	78.8	555	25.50	855.7	265.4	0.306	0.281	0.275	0.297

Theoretical predictions by potential flow models of Dumitrescu   : $k - 0.35$
Davies and Taylor : $k - 0.33$
Layser
Nicklin$^}$: $k - 0.36$

7.4.5 Wall effect on flow fields and wakes

Typical long-exposure photographs of bubble wakes, taken using the experimental technique described in Chapter 2, are reproduced at the same magnification in Fig. 7.15 to demonstrate the profound effect of the container walls on bubble shape and its associated toroidal wake in a liquid of viscosity 2.89 Poise. The top, the middle and the bottom row show the bubbles in columns of internal diameters 29.2, 14.4 and 7.06 cm, the size of the left and the right bubble in each row being 18.6 cm^3 and 9.27 cm^3, respectively. The wake volumes for these bubbles were determined using the technique described in Chapter 4, Section 4.5.2.8. The results are tabulated in the far right-hand column of the legend for Fig. 7.15. The reduction of the wake volume due to the walls is quite remarkable.

Figs. 7.16(a), (b) and (c) illustrate the change in the velocity field around a bubble of 27.8 cm^3 in 13.98 Poise sugar solution in columns of 29.2, 14.4 and 7.06 cm I.D., respectively. The spacing between the dots on a streamline indicate the distance travelled in a fixed time.

The following points should be noted:

(i)   The reduction in column size tends to straighten the streamlines and the bubble elongates. This is readily apparent in Fig. 7.16(c) where the location of the wall with respect to the bubble is also shown.

(ii) Comparing Fig. 7.16(a) and (b) we find that the effect of the wall on the bubble wake seems to be stronger than on the bubble shape. The streamlines tend to curve more behind the bubble with the smaller wake.

FIGURE 7.15 Wall Effect on the Shape, Velocity and Wake of Bubbles

Liquid Properties: μ = 2.89 Poise
ρ = 1.347 g/cm^3
σ = 77.6 dynes/cm
M = 0.109

No.	V (cm^3)	Column Dia. D (cm)	d_e/D (-)	U (cm/sec)	Re (-)	Eö (-)	Wake Volume (cm^3)
1	18.6	29.2	0.112	38.20	58.5	184	187.1
2	18.6	14.4	0.228	35.57	54.4	184	129.2
3	18.6	7.06	0.468	27.08	41.5	184	28.2
4	9.27	29.2	0.089	33.10	40.2	116	55.6
5	9.27	14.4	0.181	32.04	38.9	116	46.8
6	9.27	7.06	0.369	26.45	32.1	116	20.2

All bubbles shown at same magnification.

FIGURE 7.16 Effect of Walls on Bubble Shape and the
Associated External Flow Field

Liquid Properties: μ = 13.98 Poise
ρ = 1.379 g/cm^3
σ = 78.8 dynes/cm
M = 55.5

No.	V (cm^3)	Column Dia. D (cm)	d_e/D	U (cm/sec)	Re	Eö	S frame/sec
a	27.8	29.2	0.129	33.85	12.6	242	34.00
b	27.8	14.4	0.261	32.15	12.2	242	34.00
c	27.8	7.06	0.532	25.41	9.61	242	34.00

For legend see Table 4.8.

All three bubbles shown at same magnification.

1 cm.

Re = 12.6

FIGURE 7.16(a)

1 cm.

Re = 12.2

FIGURE 7.16(b)

1 cm

Re = 9.61

FIGURE 7.16(c)

(iii) The presence of the wall decreases the circulation velocity in the wake (compare for example Figs. 7.16 (a) and (c)).

(iv) Although the terminal velocity of bubble has decreased in the presence of the container walls, the liquid velocity in the annulus formed by the bubble and the container wall increases (compare Figs. 7.16(a) and (c)) owing to the superimposed downward flow of liquid in the annulus.

7.4.6 Wall effect on skirted bubbles

In the preceeding sections we have seen that the proximity of the container walls effects the bubble rise velocity, its shape and the surrounding flow field. Since the incipience of a skirt is dependent upon all these factors (see Chapter 6, Section 6.4.1) the presence of wall should have an effect on the critical condition for this phenomenon. The volumes for which skirts first appear and the corresponding Re, and Sk for two sugar solutions in three columns of different diameters, are tabulated in Table 7.3. It is clear that as the column diameter is decreased the critical volume increases while the critical velocity, Re and Sk all decrease. This finding also explains why, in Fig. 6.9, the data of Calderbank et al (1970) for a 10 cm diameter column and Davenport (1964) for a 15 cm x 15 cm column lie to the left of and below the curve, representing the other skirt incipience data which were taken in larger columns.

The effect of the container walls on the onset of waves on the skirted bubble is illustrated in Table 7.4, where transition conditions

TABLE 7.3 Wall Effect on Skirt Incipience Condition

Liquid Properties				Critical Condition for Skirt Incipience						
μ (Poise)	ρ (g/cm^3)	σ (dynes/cm)	M (-)	Column I.D. D(cm)	V (cm^3)	d_e/D	U (cm/sec)	Re	Sk	Eö
13.93	1.379	78.8	54.74	29.2	41.7	0.147	37.94	16.2	6.71	318
"	"	"	"	14.4	41.7	0.301	35.64	15.2	6.21	323
"	"	"	"	7.06	92.6	0.795	26.14	14.8	4.72	541
7.30	1.370	78.7	4.17	29.2	35.2	0.139	39.43	30.1	3.66	282
"	"	"	"	14.4	37.1	0.287	35.88	27.9	3.33	292
"	"	"	"	7.06	38.0	0.591	28.40	22.2	2.63	297

TABLE 7.4 <u>Wall Effect on the Incipience of Waves on Bubble Skirts</u>

Liquid Properties				Critical Condition for Onset of Waves						
μ (Poise)	ρ (dynes/cm)	σ (dynes/cm)	M (-)	Column I.D, D(cm)	V (cm^3)	d_e/D	U (cm/sec)	Re	Sk	Eö
13.70	1.375	78.8	55.5	29.2	83.4	0.186	44.26	24.2	7.69	505
"	"	"	"	14.4	64.9	0.346	37.31	18.7	6.49	427
"	"	"	"	7.06	120.5	0.868	27.20	16.8	4.73	645
7.30	1.370	78.7	4.17	29.2	65.3	0.171	45.27	42.4	4.20	426
"	"	"	"	14.4	83.9	0.377	41.35	42.2	3.84	504
"	"	"	"	7.06	56.0	0.672	27.52	24.5	2.55	385

364.

for two sugar solutions in three columns of different diameters are tabulated. The data show that the critical value of the velocity, Re and Sk are decreased with the decrease in the column diameter. Note that the critical Re for skirt incipience approaches the critical Re for onset of waves for high d_e/D, thus smooth steady skirts without waves are observed in smaller columns only over a small Re range.

In the previous section we have seen that in the presence of the container walls the liquid velocity near the bubble interface is larger than that in an unbounded fluid. Because both the incipience of skirts (see Chapter 6, Section 6.4.1) and the onset of waves (Wairegi 1974) are enhanced by higher liquid velocity at the bubble interface, the presence of the wall lowers the critical value of Re and Sk for both these phenomena.

7.5 Conclusions

1. A decrease in column diameter reduces the bubble rise velocity, elongates the bubble in the vertical direction, alters the liquid flow field, reduces the circulation rate and the volume of the closed wake and lowers the critical value of Re and Sk for the incipience of skirts and the onset of waves on the skirts.

2. The velocity retardation of bubbles ($V \geq 1$ cm^3) is independent of the physical properties of the liquid for $M \leq 1.3$ and is in good agreement with Collins' semi-empirical equation (Equation 7.8). For higher-M liquids the retardation decreases with increasing M (or viscosity). The retardation effect of walls on bubbles is significantly different from that for solid spheres.

3. The extent of the change in bubble shape induced by the container walls is greatly influenced by the original shape of the bubble in an unbounded fluid as well as by the ratio of the sphere equivalent diameter to the column diameter, d_e/D, and by the physical properties of the liquid. Some of the results of previous workers (Uno and Kintner 1956; Angelino 1966) in which the effect of the wall on bubble shape was neglected are of limited value.

4. For spherical-cap bubbles Collins' theory (1967) can be applied to predict the shape from the observed velocity or vice-versa for Re greater than about 10.* For $\bar{R}/R_c < 0.3$ Lin's theory (1967) coincides with Collins' theory. Lin claims that his theory should be used up to $\bar{R}/Re \approx 0.6$ and that his theory gives better predictions than Collins' for $0.3 < \bar{R}/R_c < 0.6$ are not valid. Collins' correlation relating the radius of curvature of the spherical-cap to its volume breaks down for $Re \lesssim 110$ when the bubbles are no longer dynamically similar.

5. For ellipsoidal-cap bubbles ($Re \lesssim 45$) the modified version of Collins' theory as outlined in Section 7.4.4.2 conforms to the data provided $Re \gtrsim 5$.

---

* See footnote on page 98.

CHAPTER 8

CONCLUSIONS

This work originated with a broad desire to expand the knowledge of bubble behaviour in relatively viscous Newtonian liquids. The following aspects of bubble motion were investigated: the bubble shape; the bubble rise velocity; the liquid motion induced by a rising bubble; the structure of the bubble wake; the interaction of two vertically aligned bubbles; the formation, the thickness and the termination of skirts trailed behind bubbles and drops; and the effect of the container wall on bubble and liquid motion. The detailed conclusions of this investigation have been presented at the end of each of the previous five chapters. This chapter summarizes the important contributions and offers suggestions for future work.

8.1 Contributions to Original Knowledge

The following elements of this thesis are original contributions to knowledge:

(1) Development of a technique for measurement of the liquid velocity field around a rising bubble and collection of comprehensive experimental data on the velocity field around bubbles of the different shapes encountered in viscous liquids.

(2) Detailed classification of bubble shape regimes and formulation of a method for predicting bubble shape, its wake and liquid circulation within the wake.

(3) Resolution of uncertainty regarding the nature of the bubble wake and determination of the critical point for the transition from a closed axisymmetric toroidal wake to an open unsteady wake.

(4) Verification of the principle of velocity superposition directly using the measured velocity field.

(5) Extension of existing skirt incipience theory (Wegener et al 1971) to shapes other than spherical cap and accounting for the reduction in the surface velocity occurring at lower Re.

(6) Development and verification of theoretical models for the thickness and length of skirts trailed behind bubbles and drops.

(7) Demonstration that the presence of the container walls not only reduces the rise velocity and changes the shape of a bubble, but also alters the liquid flow field, reduces the volume of the toroidal wake and the rate of circulation within it, and delays the skirt formation and promotes the formation of waves on the skirt.

(8) Verification of Collins' (1967) wall effect theory for bubbles with Re as low as 10 in viscous liquids.

8.2 Recommendations for Future Work

In view of the present findings, the following recommendations are made for future work:

(1) The influence of the container walls on the Reynolds number for transition from closed to open wakes should be determined.

(2) Further experimental and theoretical work should be undertaken to determine why disc-like bubbles, which are found in liquids having M close to the critical M separating high-M and low-M liquids (see Section 4.5.2.3(A)), wobble despite the fact that no wake shedding takes place.

(3) A stringent test of the present skirt theory using liquid-liquid systems, where the lower edge of the bubble is easier to view experimentally, would be valuable.

(4) Further study of the mechanics of bubble coalescence is of great interest, especially for bubbles which are not in vertical alignment. For the latter case the principle of velocity superposition should be tested and used as a building block for bubble interaction and coalescence for swarms of bubble.

(5) For a bubble of known shape, numerical techniques should be applied to predict the liquid velocity field and the results tested with the data of this work. If successful the calculations should be extended to include the calculation of the bubble shape.

(6) The experimental data of this work on the bubble shape and the associated liquid flow field should be used to predict liquid phase controlled mass transfer behaviour.

(7) The present technique for measuring the liquid velocity field could be used for bubbles in non-Newtonian liquids and possibly even for drops.

NOMENCLATURE

Note: Some symbols defined in the Appendices and used only once are not listed.

a semi-major axis

a' basal radius (see Fig. 3.1)

AR   aspect ratio $= b/a$

b semi-minor axis

B factor used in Equation (7.2)

c focal length $= \sqrt{a^2 - b^2}$

c' indentation (see Fig. 3.1)

c_1, c_2, c_3, c_4 constants in Equation (6.8)

C constant in Equation (7.6)

Ca   capillary number $= \mu U/\sigma$

C_f correction factor for departure from potential flow

C_D drag coefficient $= 4gd_e/3U^2$

d_e equivalent sphere diameter (i.e. diameter of a sphere having a volume equal to the bubble volume) $= (6V/\pi)^{1/3}$

d_f frontal (or basal) diameter of spherical-cap bubble

D column inside diameter

D' drag force

e eccentricity $= \sqrt{1 - (b^2/a^2)}$

erfc   complementary error function, i.e. erfc $= 1$-error function

exp   exponential

Eö   Eötvos Number $= gd_e^2\rho/\sigma$

Eö'   Eötvos Number based on column diameter $= gD^2\rho/\sigma$

$f(\alpha)$ function of α

f', f'', f''', f'''' first, second, third and fourth derivatives of function $f(\alpha)$ with respect to α

F	shape dependent thickness coefficient defined in Equation (6.39)
Fr	Froude Number $= U^2/gd_e$
g	acceleration of gravity
h	bubble height
h_e	height of vortex centre (see Fig. 4.18)
h_o	vertical distance below the front stagnation point
h_w	height of wake (see Fig. 4.18)
$h(\theta)$	function of θ defined in Table 4.7
$h'(\theta)$	derivative of $h(\theta)$ with respect to θ
$\hat{i}$	angle of incidence
k	square root of Froude Number based on column diameter $= U/\sqrt{gD}$
k'	constant in Equation (3.37)
K	constant in the velocity correlation, $U = KV^m$
K_o	shape dependent surface velocity coefficient for potential flow (see Table 6.1)
L	vertical downstream distance from bubble nose (in Chapter 4) nose to nose separation distance between two bubbles (in Chapter 5)
m	constant in the velocity correlation, $U = KV^m$
M	Morton Number $= g\mu^4/\rho\sigma^3$
n	refractive index of continuous phase
n'	refractive index of dispersed phase
n_1	constant in Equation (7.1)
p	function defined in Table 4.7
p'	total pressure in the dispersed phase
P	total pressure in the continuous phase
$P_2(\cos\theta)$, $P_3^2(\cos\theta)$	Legendre polynomials of 2nd and 3rd order, respectively

$P_{\alpha\alpha}\big|_{\alpha=0}$	normal stress, $P_{\alpha\alpha}$ at $\alpha = 0$
P_s	pressure at the stagnation point
q	function defined in Table 4.7
q_i	liquid velocity at inner surface of the skirt
q_o	liquid velocity at outer surface of the skirt
q^*_{oe}	dimensionless velocity at bubble edge as defined in Section 6.5.1
q^*_{os}	dimensionless velocity at outer surface of skirted bubble as defined in Section 6.5.2.3
Q	volumetric circulation rate defined in Equation (4.10)
Q_{Ha}	volumetric circulation rate for Hadamard fluid sphere
Q_{Hi}	volumetric circulation rate for Hill's spherical vortex
r	radial coordinate
r_e	equivalent sphere radius $= d_e/2$
r_f	frontal radius of bubble (or half maximum width of bubble)
r_o	radius of curvature of interface at bubble edge (see Fig. 6.1)
$\hat{r}$	angle of refraction
$r(x)$	radius of the section taken normal to the axis of symmetry
R	radius of sphere
$\overline{R}$	average radius of curvature over $\pm 37.5^\circ$ around front stagnation point of spherical bubble as defined by Collins (1967)
R^*	dimensionless radial distance $= r/r_e$
R_1 & R_2	distances defined in Table 4.5
R_c	inside radius of bubble column
R_o	radius of curvature at bubble nose
R_w	radius of wake at stagnation ring $= w_w/2$ (see Fig. 4.20)
Re	Reynolds Number $= d_e\rho U/\mu$
Re'	Reynolds Number based on column diameter $= D\rho U/\mu$

Re_D	Reynolds Number based on diameter of sphere $= 2R_0U/\mu$
Re_o	Reynolds Number based on $2R_0$ and $U_0 = 2R_0\rho U_0/\mu$
Re_∞	Reynolds Number, $d_e\rho U_\infty/\mu$
s	variable defined in Table 4.7
S	film speed
Sk	Skirt Number $= \mu U/\sigma = We/Re = Ca$
t	time
u	velocity component parallel to the outer surface of a bubble or drop (see Fig. 6.2)
u_r	velocity in r direction
u_θ	velocity in θ direction
u_x	velocity in x direction
u_y	velocity in y direction
u_η	velocity in η direction
u_ξ	velocity in ξ direction
u'_r, u'_θ	perturbation velocity components defined in Table 4.7
$\overline{u}_r, \overline{u}_\theta$	velocity components for boundary layer theory in Table 4.7
$u_{\theta e}$	equatorial velocity
U	bubble rise velocity
U_A, U_B	rise velocity of bubbles A and B, respectively
U_{Ai}, U_{Bi}	rise velocity of isolated bubbles A and B, respectively
U_c	critical bubble rise velocity for onset of skirt
U_o	bubble rise velocity given by zeroth order theory of Parlange Equation (3.26)
U_∞	bubble rise velocity in infinite medium
U^*_∞	rise velocity which the bubble of the <u>same shape</u> would have in an infinite liquid
v	velocity component normal to outer surface of a bubble or drop (see Fig. 6.2)
V	bubble volume
V_A, V_B	volume of leading bubble A and trailing bubble B, respectively

V_C	volume of the cap
V_i	volume of the indentation defined by Equation (3.41)
V_w	volume of the toroidal wake
V_{EC}	volume of the ellipsoidal-cap given by Equation (3.38)
V_{SC}	volume of a spherical-cap given by Equations (3.39) and (3.40)
w	bubble width
w_e	width of stagnation ring of distance between eyes of the vortex (see Fig. 4.18)
w_w	wake width (see Fig. 4.18)
W	centreline wake velocity
W_a	assymptotic wake velocity defined by Equation (4.3)
W_{app}	apparent wake velocity
We	Weber Number $= \rho U^2 d_e / \sigma$
x	horizontal coordinate
X_A, X_B	displacement of bubble A and B respectively from a fixed reference point
X_P	displacement of tracer bubble P from a fixed reference point
$X(\theta)$	function of θ defined in Table 4.7
y	vertical coordinate
z	variable used in Table 4.7

GREEK SYMBOLS

α	polar angle (see Fig. E.1)
β	azimuthal angle (see Fig. E.1)
γ	ratio of density of dispersed phase to that of continuous phase $= \rho' / \rho$

δ	variable defined in Table 4.7 $= 2/\sqrt{Re}$
Δ	skirt thickness
$\Delta(\alpha)$	actual skirt thickness at polar angle, α
$\Delta(\theta)$	actual skirt thickness at polar angle, θ
$\Delta'(\alpha)$	apparent thickness measured on photograph at polar angle, α
$\Delta_n(\theta)$	actual normal skirt thickness at angle θ
$\Delta_h(\theta)$	actual horizontal skirt thickness at angle θ
$\Delta'_h(\theta)$	apparent horizontal skirt thickness measured at angle θ
η	elliptical coordinate
θ	polar angle measured from bubble nose
θ_c	polar angle at which skirt begins (see Fig. 6.2)
θ_m	semi-included angle (see Fig. 3.1)
θ_s	polar angle at which skirt ends (see Fig. 6.2)
κ	ratio of dispersed phase viscosity to that of continuous phase $= \mu'/\mu$
λ	$\sinh \xi$
λ_o	$\sinh \xi_o$
μ	viscosity of continuous phase
μ'	viscosity of dispersed phase
ξ	elliptical coordinate
ξ_o	variable describing spheroid surface $= \tanh^{-1}(b/a)$
π	pi $= 3.14159.....$
ρ	density of continuous phase
ρ'	density of dispersed phase
σ	surface (or interfacial) tension
ϕ	corner angle ϕ (see Figs. 6.1 and 6.6)
ψ	Stokes stream function

REFERENCES

Ackeret, J., "Uber exakte Lösungen der Stokes-Navier-Gleichungen inkompressibler Flüssigkeiten bei veranderten Grenzbedingungen", Z. Agnew. Math. Phys., 3, 259 (1952).

Al Dimian and Ruckenstein, E., "A note on the wakes behind drops", Chem. Eng. Sci. 25, 1821 (1970).

Angelino, H., "Etude du comportement des bulles gazeuses dans des liquides et dans les lits fluidisés", Ph.D. Thesis, la Faculté des sciences de l'Université de Toulouse (1964).

Angelino, H., "Hydrodynamique des grosses bulles dans les liquides visqueux", Chem. Eng. Sci., 21, 541 (1966).

Angelino, H., Charzat, C. and Williams, R., "Evolution de bulles de gaz dans des liquides et des systèmes fluidisés", Chem. Eng. Sci., 19, 289 (1964).

Asanuma, T. and Takeda, S., "A study on the flow visualization by the hydrogen-bubble method", Bulletin. of JSME, 8 (32), 599 (1965).

ASME, "Symposium on Flow Visualization", ASME Symposium Volume (1960).

Astarita, G. and Apuzzo, G., "Motion of gas bubbles in non-Newtonian liquids", AIChE J., 11, 815 (1965).

Aybers, N.M. and Tapucu, A., "Studies on the drag and shape of gas bubbles rising through a stagnant liquid", Warme-und Stoffübertragung Bd. 2, S 171 (1969).

Baird, M.H.I. and Davidson, J.F., "Gas absorption by large rising bubbles", Chem. Eng. Sci., 17, 87 (1962).

Batchelor, G.K., "An Introduction to Fluid Dynamics", Cambridge University Press (1967).

Bischoff, K.B. and Himmelblau, D.M., "Mass transfer", Ind. & Eng. Chem., 60 (1), 66 (1968).

Blandamer, M.J., et al, "Effect of added solutes on the size of hydrogen bubbles liberated from a cathodic wire in aqueous solution", Nature, 216, 783 (1967).

Bonato, L.D.M., "Sulla forma di bolle di aeriforme iniettate in liquidi in quiete e correlazione della variabili", Thermotechnica Richerche, 20, 11 (1971).

Bretherton, F.P., "The motion of long bubbles in tubes", J. Fluid Mech., 10, 166 (1961).

Brignell, A.S., "The deformation of a liquid drop at small Reynolds number", Quart. J. Mech. and Appl. Math., 26, 99 (1973).

Brignell, A.S., "Mass transfer from a spherical cap bubble in laminar
         flow", Chem. Eng. Sci., 29, 135 (1974).

Brown, R.A.S., "The mechanics of large gas bubbles in tubes", Can. J.
         Chem. Eng. 43, 217 (1965).

Calderbank, P.H., "Review series No.3: Gas absorption from bubbles",
         The Chemical Engineer, 212, CE 209-33 (1967).

Calderbank, P.H., Johnson, D.S.L. and Loudon, J., "Mechanics and mass
         transfer of single bubbles in free rise through some Newtonian
         and non-Newtonian liquids", Chem. Eng. Sci. 25, 235 (1970).

Calderbank, P.H., Lochiel, A.C., "Mass transfer coefficients and shapes
         of carbon dioxide bubbles in free rise through distilled water",
         Chem. Eng. Sci., 19, 485 (1964).

Calderbank, P.H., Moo-Young, M.B. and Bibby, R., "Coalescence in bubble
         reactors and absorbers", Chem. Eng. Sci., 19, 91 (1964).

Chan, B.K.C. and Prince, R.G.H., "Distillation studies - viscous drag
         on a gas bubble rising in a liquid", AIChE J., 11, 268 (1965).

Clayton, B.R. and Massey, B.S., "Flow visualization in water: A review
         of techniques", J. Sci. Instrum., 44, 2 (1967).

Clift, R. and Grace, J.R., "Bubble interaction in fluidized beds",
         AIChE Symposium - Fluidization Fundamentals No.39a, 1, (1969).

Clift, R. and Grace, J.R., "Bubble interaction in fluidized beds",
         Chem. Eng. Prog. Symposium Series No.105, 66, 14 (1970).

Clift, R. and Grace, J.R., "Coalescence of bubbles in fluidized beds",
         AIChE Symposium Series No.116, 67, 23 (1971).

Clift, R., Grace, J.R. and Weber, M.E., "Bubbles, Drops and Particles",
         Academic Press, New York (in press 1976).

Clutter, D.W. and Smith, A.M.O., "Flow visualization by electrolysis of
         water", Aerospace Eng., 20 (1), 24 (1961).

Clutter, D.W., Smith, A.M.O. and Brazier, J.G., "Techniques of flow
         visualization using water as the working medium", Douglas
         Aircraft Co. Report No.ES 29079 (1959).

Collins, R., "Structure and behaviour of wakes behind two-dimensional
         air bubbles in water", Chem. Eng. Sci., 20, 851 (1965).

Collins, R., "A second approximation for the velocity of a large bubble
         rising in an infinite liquid", J. Fluid Mech. 25, 469 (1966).

Collins, R., "Experiments on large bubbles in liquids", A.E.R.E. Rept.
         No.5402, Atomic Energy Research Establishment, Harwell, U.K.
         (1967a).

Collins, R., "The effect of a containing cylindrical boundary on the velocity of a large gas bubble in a liquid", J. Fluid Mech., 28, 97 (1967b).

Collins, R., "Models of spherical-cap bubbles", Proc. of Intn. Colloquium on bubbles and drops, California Inst. Tech. Vol.2, 414 (1974).

Crabtree, J.R., "Chain bubbling and coalescence in liquids", Ph.D. Thesis, Chemical Eng. Dept., Cambridge Univ. (1969).

Crabtree, J.R. and Bridgewater, J., "The wakes behind two-dimensional air bubbles", Chem. Eng. Sci., 22, 1517 (1967).

Crabtree, J.R. and Bridgewater, J., "Chain bubbling in viscous liquids", Chem. Eng. Sci., 24, 1755 (1969).

Crabtree, J.R. and Bridgewater, J., "Bubble coalescence in viscous liquids", Chem. Eng. Sci., 26, 839 (1971).

Darwin, C., "Note on hydrodynamics", Proc. Cambridge Phil. Soc., 49, 342 (1953).

Davenport, W.G., "Bubbles in liquids including liquid metals", Ph.D. Thesis, Imperial College, London (1964).

Davenport, W.G., Richardson, F.D. and Bradshaw, A.V., "Spherical cap bubbles in low density liquids", Chem. Eng. Sci., 22, 1221 (1967).

Davidson, J.F., Cambridge University - private communication (1974).

Davidson, J.F. and Harrison, D., "Fluidised Particles", Cambridge University Press (1963).

Davidson, J.F. and Kirk, F.A., "Holding a bubble fixed by downward flow", Chem. Eng. Sci., 24, 1529 (1969).

Davis, W. and Fox, R.W., "An evaluation of the hydrogen bubble technique for the quantitative determination of fluid velocities within clear tubes", ASME Paper No.66-WA/FE-21 (1966).

Davies, R.M. and Taylor, G.I., "The mechanics of large bubbles rising through extended liquids and through liquids in tubes", Proc. Roy. Soc. A200, 375 (1950).

Datta, R.L., Napier, D.H. and Newitt, D.M., "The properties and behaviour of gas bubbles formed at a circular orifice", Trans. Instn. Chem. Engrs., 28, 14 (1950).

De Nevers, N. and Wu, J.L., "Bubble coalescence in viscous liquids", AIChE Journal, 17, 182 (1971).

Dumitrescu, D.T., Z. Ang. Math. Mech. 23, 139 (1943).

379.

Edge, R.M. and Grant, C.D., "The terminal velocity and frequency
        of oscillation of drops in pure systems", Chem. Eng. Sci.,
        26, 1001 (1971).

El Sawi, M., "Distorted gas bubbles at large Reynolds number", J. Fluid
        Mech., 62, 163 (1974).

Elzinga, E.R. and Banchero, J.T., "Some observations on the mechanics
        of drops in liquid-liquid systems", AIChE J., 7, 394 (1961).

Fararoui, A. and Kintner, R.C., "Flow and shape of drops in non-Newtonian
        fluids", Trans. Soc. Rheol., 5, 369 (1961).

Fidleris, V. and Whitmore, R.L., "Experimental determination of the wall
        effect for spheres falling axially in cylindrical vessels",
        Brit. J. Appl. Phys., 12, 490 (1961).

Filla, M., Davidson, J.F., Bates, J.F. and Eccles, M.A., "Gas phase
        controlled mass transfer from a bubble", Chem. Eng. Sci., 31,
        359 (1976).

Gailhbaud, J. and Zortea, M., "Recherches sur la coalescence des bulles
        dans un liquide visqueux", Revue Gen. Therm., 89, 433 (1969).

Gal-or, B., Klinzing, G.E. and Tavalarides, L.L., "Bubble and drop
        phenomena", Ind. & Eng. Chem., 61 (2), 21 (1969).

Garner, F.H. and Hammerton, D., "Circulation inside gas bubbles",
        Chem. Eng. Sci., 3, 1 (1954).

Garner, F.H. and Haycock, P.J., "Internal circulation in liquid drops",
        Proc. Roy. Soc., A252, 457 (1959).

Garner, F.H., Mathur, K.D. and Jenson, V.G., "Distortion of fluid drops
        in the Stokesian region", Nature, 180, 331 (1957).

Garner, F.H. and Skelland, A.H.P., "Some factors affecting droplet
        behaviour in liquid-liquid systems", Chem. Eng. Sci. 4, 149
        (1955).

Garner, F.H. and Tayeban, M., "The importance of the wake in mass
        transfer from both continuous and dispersed phase systems -I",
        Anales de Fisica Y Quimica, LV1-B, 479 (1960).

Geller, E.W., "An electrochemical method of visualizing the boundary
        layer", M.Sc. Thesis, Aero. Engg. Dept., Mississippi State
        College (1954).

Gerrard, J.H., "Velocity measurement in water using flow visualization
        by tracers produced at a wire", ASME Paper No.72-FE-3 (1972).

Gill, W.N., Cole, R., Estrin, J. and Nunge, R.J., "Fluid dynamics:
        Annual review", Ind. & Eng. Chem., 61 (1), 41 (1969).

Gill, W.N., Cole, R., Davis, E.J., Estrin, J., Nunge, R.J. and Littman, H., "Fluid dynamics: Annual review", Ind. & Eng. Chem. 62 (4), 49 (1970).

Gill, W.N., Cole, R., Davis, E.J., Lin, S.P. and Nunge, R.J., "Fluid dynamics: Annual review", Ind. & Eng. Chem., 62 (12), 108 (1970).

Goldburg, A. and Florsheim, B.H., "Transition and Strouhal number for the incompressible wake of various bodies", Phys. Fluids, 9, 45 (1966).

Goldsmith, H.L. and Mason, S.G., "The movement of single large bubbles in closed vertical tubes", J. Fluid Mech., 14 (1), 42 (1962).

Golovin, A.M. and Ivanov, M.F., "Motion of a bubble in a viscous liquid", J. of Appl. Mech. and Tech. Phys., 12 (1), 91 (1973).

Gomezplata, A. and Regan, T.M., "Mass transfer", Ind. & Eng. Chem., 60 (12), 53 (1968).

Govier, G.W. and Aziz, K., "The Flow of Complex Mixtures in Pipes", Van Nostrand-Reinhold, New York (1972).

Grace, J.R., "The viscosity of fluidized beds", Can. J. Chem. Eng., 48, 30 (1970).

Grace, J.R., A letter to the Editor, C.J.Ch.E., 50, 440 (1972).

Grace, J.R., "Shapes and velocities of bubbles rising in infinite liquids", Trans. Instn. Chem. Engrs., 51, 116 (1973).

Grace, J.R. and Harrison, D., "The influence of bubble shape on the rising velocities of large bubbles", Chem. Eng. Sci., 22, 1337 (1967).

Grace, J.R., Wairegi, T. and Nguyen, T.H., "Shapes and velocities of single drops and bubbles moving freely through immiscible liquids", accepted for publication in Trans. Instn. Chem. Engrs., 54, 167 (1976).

Griffith, R. and Wallis, G.B., "Two-phase slug flow", J. Heat Transf. - Trans. ASME Ser.C, 83, 307 (1961).

Guthrie, R.I.L., "Dynamic mass transfer phenomena of spherical capped bubbles", Ph.D. Thesis, Imperial College, London (1967).

Guthrie, R.I.L. and Bradshaw, A.V., "The stability of gas envelopes trailed behind large spherical cap bubbles rising through viscous liquids", Chem. Eng. Sci. 24, 913 (1969).

Guthrie, R.I.L. and Bradshaw, A.V., "Spherical capped gas bubbles rising in aqueous media", Chem. Eng. Sci., 28, 191 (1973).

Haber, S., Hetsroni, G. and Solan, A., "On the low Reynolds number motion of two droplets", Int. J. Multiphase Flow, 1, 57 (1973).

Haberman, W.L. and Morton, R.K., "An experimental investigation of the drag and shape of air bubbles rising in various liquids", David Taylor Model Basin Rept. No.802, U.S. Navy Dept., Washington (1953).

Haberman, W.L. and Morton, R.K., "An experimental study of bubbles moving in liquids", Trans. Amer. Soc. Civ. Eng., 121, 227 (1956).

Haberman, W.L. and Sayre, R.M., "Motion of rigid and fluid spheres in stationary and moving liquids inside cylindrical tubes", David Taylor Model Basin Rept. No.1143, U.S. Navy Dept., Washington (1958).

Hadamard, J., "Mouvement permanent lent d'une sphère liquide et visqueuse dans un liquide visqueux", C.R. Acad. Sci., 152, 1735 (1911).

Hama, F.R., "Streaklines in a perturbed shear flow", Physics of Fluids, 5 (6), 644 (1962).

Hama, F.R. and Nutant, J., "Detailed flow-field observations in the transition process in a thick boundary layer", Proc. of Heat Trans. and Fluid Mech. Inst., 77 (1963).

Hamielec, A.E., Hoffman, T.W. and Ross, L.L., "Numerical solution of the Navier-Stokes equations for flow past spheres", AIChE J., 13, 212 (1967).

Hansen, E.O., "Investigation of the hydrogen-bubble flow-visualization technique in high-speed two-dimensional steady flow", Naval Ship R & D Center Report No.2626 (1968).

Happel, J. and Brenner, H., "Low Reynolds Number Hydrodynamics", Prentice Hall Inc., Englewood Cliffs, NJ (1965).

Harmathy, T.Z., "Velocity of large drops and bubbles in media of infinite or restricted extent", AIChE J., 6 (2), 281 (1960).

Harper, J.F., "On bubbles rising in line at large Reynolds numbers", J. Fluid Mech., 41 (4), 751 (1970).

Harper, J.F., "The motion of bubbles and drops through liquids", Advances in Applied Mechanics, 12, 59 (1972).

Harper, J.F. and Moore, D.W., "The motion of a spherical liquid drop at high Reynolds number", J. Fluid Mech. 32, 367 (1968).

Harrison, D., Davidson, J.F. and de Kock, J.W., "On the nature of aggregative fluidization, Trans. Instn. Instn. Chem. Engrs., 39, 202 (1961).

Harrison, D. and Leung, L.S., "Symposium on Interaction between Fluids and Particles", Instn. Chem. Engrs., London, 127 (1962).

Hartunian, R.A. and Sears, W.R., "On the instability of small gas
    bubbles moving uniformly in viscous liquids", J. Fluid Mech.
    3, 27 (1957).

Hattori, S., Rep. Aeronaut. Res. Inst., Tokyo Imp. Univ., No.115 (1935).

Hayashi, S. and Matunobu, Y., "Experimental study on a deformed drop
    moving through viscous media", Physical Soc. of Japan J., 22
    (1), 905 (1967).

Hershey, H.C., Zakin, J.L. and Simha, R., "Numerical differentiation of
    equally spaced and not equally spaced experimental data",
    Ind. & Eng. Chem. Fundamentals, 6 (3), 413 (1967).

Hill, M.J.M., "On a spherical vortex", Phil. Trans. Roy. Soc. London,
    Ser. A185, 213 (1894).

Hnat, J., Yale University - private communication (1973).

Hnat, J.G. and Buckmaster, J.D., "Spherical cap bubbles and skirt
    formation", Phys. Fluids, 19, 192 (1976), see also: "Erratum",
    Phys. Fluids, 19, 611 (1976).

Hoefer, K., Z. ver. Deut. Ing., 57 (2), 987 (1913).

Huang, W.S. and Kintner, R.C., "Effects of surfactants on mass transfer
    inside drops", AIChE J., 12, 10 (1966).

Hyzer, W.G., "Flow visualization", Research/Development, 25 (8), 26 (1974).

Jackson, M.A., "The formation and coalescence of drops and bubbles in
    liquids", Industrial Research Fellow Report No.1, The Chemical
    Engineer, May, CE 107 (1964).

Jones, D.R.M., "The steady rise of air bubbles in viscous liquids", Ph.D.
    Thesis - Chemical Eng. Dept., Cambridge Univ. (1965).

Kalra, T.R., "Bluff body wakes - geometry and mass transfer", Ph.D.
    Thesis, Chem. Eng. Dept., Monash University, Melbourne (1971).

Kalra, T.R. and Uhlherr, P.H.T., "Properties of bluff body wakes", paper
    presented at Fourth Australian Conf. on Hydraulics and Fluid
    Mech., Monash University, Melbourne (1971).

Kline, S.J., "Flow visualization", p.34, Illustrated Experiments in
    Fluid Mechanics, published by National Committee on Fluid
    Mechanics Films, MIT Press, Cambridge, Massachusetts (1972).

Kojima, E., Akehata, T. and Shirai, T., "Rising velocity and shape of
    single air bubbles in highly viscous liquids", J. of Chem. Eng.
    Japan, 1 (1), 45 (1968).

Kojima, E., Akehata, T. and Shirai, T., "Behaviour of single air bubbles held stationary in downward flows", J. of Chem. Eng. Japan, **8** (2), 108 (1975).

Kubota, M., Akehata, T. and Shirai, T., Kagaku Kogaku, 31, 1074 (1967).

Laird, A.D.K. and Chisholm, D., "Pressure and forces along cylindrical bubbles in a vertical tube", Ind. Eng. Chem., **48**, 1361 (1956).

Lamb, H., "Hydrodynamics", Cambridge University Press (1945).

Lance, G.N., "Numerical Methods for High-Speed Computers", Liffe and Sons Ltd., London (1960).

Layser, D., "On the instability of superposed fluids in a gravitational field", Astrophys.J., **122**, 1 (1955).

Lazarek, G.M. and Littman, H., "The pressure field due to a large circular capped air bubble rising in water", J. Fluid Mech., **66**, 673 (1974).

Le Clair, B.P. and Hamielec, A.E., "Viscous flow through particle assemblages at intermediate Reynolds numbers - a cell model for transport in bubble swarms", Can. J. Chem. Eng., **49**, 713 (1971).

Lennemann, E. and Howard, J.H.G., "Unsteady flow phenomena in rotating centrifugal impeller passages", ASME Paper No.69-GT-35 (1969).

Levich, V.G., "Motion of gaseous bubbles with high Reynolds numbers", (in Russian), Zhu. Eksp. Teor. Fiz., **19**, 18 (1949).

Levich, V.G., "Physicochemical Hydrodynamics", Prentice-Hall Inc., Englewood Cliffs, NJ (1962).

Lighthill, M.J., "Drift", J. Fluid Mech., **1**, 31 (1956).

Lin, C.J., Lee, K.L. and Sather, N.F., "Slow motion of two spheres in a shear field", J. Fluid Mech. **43** (1), 35 (1970).

Lin, S.P., "Velocity of a bubble rising in liquid along the axis of a circular tube", Phys. Fluids, **10**, 2283 (1967).

Lindt, J.T., "Time dependent mass transfer from single bubbles", Ph.D. Thesis, Technische Hogeschool, Delft, The Netherlands (1971a).

Lindt, J.T., "Note on the wake behind a two-dimensional bubble", Chem. Eng. Sci., **26**, 1776 (1971b).

Lindt, J.T. and De Groot, R.G.F., "The drag on a single bubble accompanied by a periodic wake", Chem. Eng. Sci., **29**, 957 (1974).

Lippisch, A.M., "Flow visualization", Aeronautical Eng. Review, 17 (2), 24 (1958).

Lochiel, A.C. and Calderbank, P.H., "Mass transfer in the continuous phase around axisymmetric bodies of revolution", Chem. Eng. Sci. 19, 471 (1964).

Lukasik, S.J. and Grosch, C.E., "Velocity measurements in thin boundary layers", Stevens Inst. of Tech. Memo No.122 (1959).

Macagno, E.O., "Flow visualization in liquids", Iowa Inst. of Hydraulic Research Report No.114 (1969).

Magarvey, R.H. and Bishop, R.L., "The wake of a moving drop", Nature, 188, 735 (1960).

Magarvey, R.H. and Bishop, R.L., "Transition ranges for three-dimensional wakes", Can. J. Phys. 39, 1418 (1961).

Magarvey, R.H. and Bishop, R.L., "Wakes in liquid-liquid systems", Phys. Fluids, 4 (7), 800 (1961a).

Magarvey, R.H. and Maclatchy, C.S., "Mass transfer and wake phenomena", AIChE J., 14, 260 (1968).

Maneri, C.C. and Mendelson, H.D., "The rise velocity of bubbles in tubes and rectangular channels as predicted by wave theory", AIChE J., 14, 295 (1968).

Masliyah, J.B., "Steady wakes behind oblate spheroids: flow visualization", Phys. Fluids, 15, 1144 (1972).

Masliyah, J.B. and Epstein, N., "Numerical study of flow past spheroids", J. Fluid Mech., 44, 493 (1970).

Mattingly, G.E., "The hydrogen-bubble, flow-visualization technique", David Taylor Model Basin Report 2146 (1966).

Mattingly, G.E. and Chang, C.C., "Unstable waves on an axisymmetric jet column", J. Fluid Mech., 65 (3), 541 (1974).

Mattingly, G.E. and Criminale, W.O., "The stability of an incompressible two-dimensional wake", J. Fluid Mech., 51 (2), 233 (1972).

Maxworthy, T., "A note on the existence of wakes behind large rising bubbles", J. Fluid Mech., 27, 367 (1967).

Maxworthy, T., "The flow created by a sphere moving along the axis of a rotating, slightly-viscous fluid", J. Fluid Mech., 40 (3), 453 (1970).

Mendelson, H.D., "The prediction of bubble terminal velocities from wave theory", AIChE J., 13, 250 (1967).

Merzkirch, W., "Flow Visualization", Academic Press, New York (1974).

Milne-Thomson, L.M., "Theoretical Hydrodynamics", 5th Edition, MacMillan, New York (1968).

Miyagi, O., "The motion of an air bubble rising in water", Phil. Mag. S.6, 50 (295), 112 (1925).

Moffatt, H.K., "Viscous and resistive eddies near a sharp corner", J. Fluid Mech., 18, 1 (1964).

Moore, D.W., "The rise of a gas bubble in a viscous liquid", J. Fluid Mech., 6, 113 (1959).

Moore, D.W., "The boundary layer on a spherical gas bubble", J. Fluid Mech., 16, 161 (1963).

Moore, D.W., "The velocity of rise of distorted gas bubbles in a liquid of small viscosity", J. Fluid Mech., 23, 749 (1965).

Moo-Young, M., Fulford, G. and Cheyne, I., "Bubble motion studies in a countercurrent flow apparatus", Ind. Eng. Chem. Fundamentals, 10, 157 (1971).

Morrison, F.A., Jr., "Breakup of bubble chain", Chem. Eng. Sci., 28, 1115 (1973).

Narayanan, S., Goosens, L.H.J. and Kossen, N.W.F., "Coalescence of two bubbles rising in line at low Reynolds numbers", Chem. Eng. Sci., 29, 2071 (1974).

Nicklin, D.J., Ph.D. Thesis - Chemical Eng. Dept., Cambridge Univ. (1961).

Nicklin, D.J., Wilkes, J.O. and Davidson, J.F., "Two-phase flow in vertical tubes", Trans. Instn. Chem. Engrs., 40, 61 (1962).

Nowell, R.W., "An investigation of fluid motion with variable viscosity", M.Sc. Thesis, Princeton University (1965).

O'Brien, M.P. and Gosline, J.E., "Velocity of large bubbles in vertical tubes", Ind. Eng. Chem., 27, 1436 (1935).

Offen, G.R. and Kline, S.J., "Combined dye-streak and hydrogen-bubble visual observations of a turbulent boundary layer", J. Fluid Mech., 62 (2), 223 (1974).

Oseen, C.W., "Über die Stokes' sche Formel, und über eine verwandte Aufgabe in der Hydrodynamik", Ark. f. Mat. Astr. och Fys., 6, 29 (1910).

Owens, J.S., Engineering, 112, 458 (1921).

Pan, F.Y. and Acrivos, A., "Shape of a drop or bubble at low Reynolds number", Ind. & Eng. Chem. Fundamentals, 7 (2), 227 (1968).

Parlange, J.Y., "Spherical bubbles with laminar wakes", J. Fluid Mech. 37, 257 (1969).

Parlange, J.Y., "Motion of spherical drops at large Reynolds numbers", Acta Mechanica, 9, 323 (1970).

Parlange, J.Y., a letter to the Editor, CJChE, 50, 439 (1972).

Peebles, F.N. and Garber, H.J., "Studies on the motion of gas bubbles in liquids", Chem. Eng. Progr. 49, 88 (1953).

Proudman, I. and Pearson, J.R.A., "Expansion at small Reynolds numbers for the flow past a sphere and a circular cylinder", J. Fluid Mech., 2, 237 (1957).

Pruppacher, H.R. and Piffer, R.L., "A semi-empirical determination of the shape of cloud and raindrops", J. Atm. Sci., 28, 86 (1971).

Ralston, A., "First Course in Numerical Analysis", McGraw-Hill, New York (1965).

Redfield, J.A. and Houghton, G., "Mass transfer and drag coefficients for single bubbles at Reynolds number of 0.02 - 5000", Chem.. Eng. Sci., 20, 131 (1965).

Regan, T.M. and Gomezplata, A., "Mass transfer", Ind. & Eng. Chem., 62 (2), 41 (1970).

Reinhart, A., "Das verhalten fallender tropfen", (The behaviour of falling drops), Chem. Ing. Tech., 36, 740 (1964).

Rice, J.C. and Thomas, W.C., "Application of hydrogen-bubble technique for velocity measurements in thin liquid films", J. of App. Mech., 40 (E1), 321 (1973).

Rippin, D.W.T. and Davidson, J.F., "Free streamline theory for a large gas bubble in a liquid", Chem. Eng. Sci., 22, 217 (1967).

Rivkind, V.Y., Ryskin, G.M. and Fishbein, G.A., "A motion of a spherical drop in the flow of a viscous fluid", Fluid Mech. Soviet Research, 1 (1), 141 (1972).

Rosenberg, B., "The drag and shape of air bubbles moving in liquids", David Taylor Model Basin Rept. No.727, U.S. Navy Dept., Washington (1950).

Rosenhead, L., editor, "Laminar Boundary Layers", Oxford University Press, London (1963).

Rowe, P.N. and Partridge, E.A., "Gas flow through bubbles in a fluidized bed - I", Chem. Eng. Sci., 18, 511 (1963); see also AERE Report No.R4108 (1963).

Rowe, P.N. and Partridge, B.A., "An X-ray study of bubbles in fluidized beds", Trans. Instn. Chem. Engrs. 43 (5), 157 (1965).

Rubczynski, W., "On the translatory motion of a fluid sphere in a viscous medium (in German", Bull. Int. Acad. Pol. Sci. Leff. Cl. Sci. Math. Natur., Ser.A, 40 (1911).

Rushton, E. and Davies, G.A., "The slow unsteady settling of two fluid spheres along their line of centres", Appl. Sci. Res. 28, 37 (1973).

Saffman, P.G., "On the rise of small air bubbles in water", J. Fluid Mech., 1, 249 (1956).

Saito, S., "On the shape of the nearly spherical drop which falls through viscous media", Sci. Rep. Tôhoku Imp. Univ., Sendai, Japan, 2, 179 (1913).

Salami, E., Vignes, A. and Le Goff, P., "Hydrodynamique des dispersions: II - Effect de paroi", Genie Chimique, 94 (3), 67 (1965).

Satapathy, R. and Smith, W., "The motion of single immiscible drops through a liquid", J. Fluid Mech., 10, 561 (1961).

Savic, P., "Circulation and distortion of liquid drops falling through a viscous medium", Natl. Res. Council, Canada, Rept. No.NRC-MT-22 (1953).

Schlichting, H., "Boundary-layer Theory", McGraw-Hill (1968).

Schmidt, E., "Ahnlichkeitstheorie der Bewegung von Flussigkeitsgasgemischen", VDI-Forchungsheft, S.1-3, 365 (1934).

Schraub, F.A., Kline, S.J., Henry, J., Runstadler, P.W., Jr., and Littell, A., "Use of hydrogen bubbles for quantitative determination of time-dependent velocity fields in low-speed water flows", J. of Basic Engg., Trans. ASME, Series D, 87, 429 (1965).

Scriven, L.E., University of Minnesota - private communication (1974).

Seeley, L.E., "An experimental investigation of laminar and turbulent flow around a sphere at intermediate Reynolds number", Ph.D. Thesis, University of Toronto (1972).

Shoemaker, P.D. and Chazal, L.E., "Dimpled and skirted liquid drops moving through viscous media", Chem. Eng. Sci., 24, 797 (1969).

Sideman, S., Hortascu, O. and Fulton, J.W., "Mass transfer in gas-liquid contacting systems", Ind. & Eng. Chem., 58 (7), 32 (1966).

Siemes, W., "Gasblasen in Flussigkeiten. Teil II: Der Aufstieg von Gasblasen in Flussigkeiten", Chemie. Ing. Techn., 26, 614 (1954).

Simmons, H.P., Ind. Eng. Chem. Anal. Ed., 13, 536 (1941).

Slaughter, I., "The motion of gas bubbles rising singly and in streams through liquids", Ph.D. Thesis, Dept. of Metallurgy, Univ. of Newcastle upon Tyne (1967).

Slaughter, I. and Wraith, A.E., "The wake of a large gas bubble", Chem. Eng. Sci., 23, 932 (1968).

Smyth, W.R., "Flow around a sphere in a circular tube", Phys. Fluids, 4, 756 (1961).

Smyth, W.R., "Flow around a spheroid in a circular tube", Phys. Fluids, 7, 633 (1964).

Somerscales, E.F.C., "Bubble motion as a factor in hydrogen bubble technique of flow visualization", ASME Paper No.71-EA-6 (1971).

Soo, S.L., "Fluid Dynamics of Multiphase Systems", Blaisdell Publishing Co., Waltham, Massachusetts (1967).

Steinberger, E.H., Pruppacher, H.R. and Neiburger, M., "On the hydro-dynamics of pairs of spheres falling along their line of centre in a viscous medium", J. Fluid Mech., 34 (4), 809 (1968).

Stewart, P.S.B., "Isolated bubbles in fluidised beds - theory and experi-ments", Trans. Instn. Chem. Engrs., 46, T60 (1968).

Stimson, M. and Jeffery, G.B., "The motion of two spheres in a viscous fluid", Proc. Roy. Soc. London, A111, 110 (1926).

Stokes, G.G., "On the effect of the internal friction of fluids on the motion of pendulum", Trans. Camb. Phil. Soc., 9, 8 (Mathematical and Physical Papers, 3 (1) (1851).

Strom, J.R. and Kintner, R.C., "Wall effect for the fall of single drops", AIChE J., 4 (2), 153 (1958).

Subramanian, G. and Tien, C., "Mixing in liquid phase due to bubble motion", Paper 43d presented at AIChE 63rd Annual Meeting, Chicago (1970).

Sundell, R.E., "An experimental investigation of spherical cap bubbles in liquids", Ph.D. Thesis, Yale University (1971).

Sutterby, J.L., "Falling sphere viscometry: I - wall and inertial corrections to Stokes' law in long tubes", Trans. of the Soc. of Rheology, 17 (4), 559 (1973).

Tadaki, T. and Maeda, S., "On the shape and velocity of single air bubbles rising in various liquids", Kagaku Kōgaku 25, 254 (1961).

Tadaki, T. and Maeda, S., "On the shape and velocity of single air bubbles rising in various liquids", Kagaku Kōgaku (Chem. Eng. Japan), 25, 254 (1964).

Taneda, S., "Experimental investigation of the wake behind a sphere at low Reynolds numbers", J. Phys. Soc. Japan, 11, 1104 (1956).

Tasuge, H. and Hibino, S., "Effect of column wall on the ascending velocity of gas bubbles in various liquids", Intl. Chem. Eng., 15 (1), 186 (1975).

Tavlarides, L.L., Coulaloglon, C.A., Zeitlin, M.A., Klinzing, G.E. and Gal-or, B., "Bubble and drop phenomena", Ind. & Eng. Chem., 62 (11), 6 (1970).

Taylor, T.D. and Acrivos, A., "On the deformation and drag of a falling viscous drop at low Reynolds number", J. Fluid Mech., 18, 466 (1964).

Thomas, J.J. and Newall, H.F., "On the formation of vortex rings by drops falling into liquids, and some allied phenomena", Proc. Roy. Soc., 39, 417 (1885).

Tory, A.C. and Haywood, K.H., "The hydrogen bubble technique of flow visualization: factors affecting bubble size and buoyancy", ASME Paper No. 71-Fe-36 (1971).

Uno, S. and Kintner, R.C., "Effect of wall proximity on the rate of rise of single air bubbles in a quiescent liquid", AIChE J., 2, 420 (1956).

Valentin, F.H.H., "Absorption in gas-liquid dispersions: some aspects of bubble technology", E. & F.N. Spon Ltd., London (1967).

Van Dyke, M., "Perturbation Methods in Fluid Mechanics", Academic Press (1964).

Vickery, L., "Drift", Research Project Report, Chem. Eng. Dept., Univ. of Cambridge (1965).

Wah-on, H.C., "Bubble coalescence in viscous liquids", technical report McGill University, Dept. of Chem. Eng. (1971).

Wairegi, T., "The behaviour of dimpled drops", M. Eng. Thesis, Chemical Eng. Dept. McGill University (1972).

Wairegi, T., "The mechanics of large drops and bubbles moving through extended liquid media", Ph.D. Thesis, Chemical Eng. Dept., McGill University (1974).

Wairegi, T. and Grace, J.R., "The mechanics of fluid skirts", Can. Sym. of Fluid Dynamics, Univ. of Western Ontario, 156 (1974).

Wairegi, T. and Grace, J.R., "The behaviour of large drops in immiscible liquids", Int. J. Multiphase Flow, 3, 67 (1976).

Wallis, G.B., "One-Dimensional Two-Phase Flow", McGraw-Hill, New York (1969).

Wallis, G.B., "The terminal speed of single drops or bubbles in an infinite medium", Int. J. Multiphase Flow, 1, 499 (1974).

Wegener, P.P. and Parlange, J.-Y, "Spherical cap bubbles", Annual Review of Fluid Mechanics, 5, 79 (1973).

Wegener, P.P., Sundell, R.E. and Parlange, J.-Y, "Spherical cap bubbles rising in liquids", Z. Flugwiss., 19, 347 (1971).

Weinberg, S.L. and Heiser, W.H., "Use of hydrogen bubble technique in observing unsteady boundary layers", Paper presented at Symposium on Unsteady Flow at the Fluids Engineering Conference, Philadelphia (1968).

Wellek, R.M., Agrawal, A.K. and Skelland, A.H.P., "Shape of liquid drops moving in liquid media", AIChE J., 12, 854 (1966).

Werlé, H., "Hydrodynamic flow visualization", Annual Review of Fluid Mechanics, 5, 361 (1973).

White, E.T. and Beardmore, R.H., "The velocity of rise of single cylindrical air bubbles through liquids contained in vertical tubes", Chem. Eng. Sci., 17, 351 (1962).

White, D.A. and Tallmadge, J.A., "Theory of drag out of liquids on flat plates", Chem. Eng. Sci., 20, 33 (1965).

Winnikow, S. and Chao, B.T., "Droplet motion in purified systems", Phys. Fluids, 9, 50 (1966).

Wortmann, F.X., "Eine Method zur Beobachtung und Messung von Wasserströmungen mit Tellur", Z. Angew. Physik, 5 band, 6 heft, S201 (1953).

Zukoski, E.E., "Influence of viscosity, surface tension and inclination angle on motion of long bubbles in closed tubes", J. Fluid Mech., 25, 821 (1966).

APPENDIX A

DAVIDSON'S DERIVATION OF THE RISE VELOCITY EQUATION
FOR SPHERICAL-CAP BUBBLES (USED IN CHAPTER 3)

Davidson (1974) attempted to incorporate viscous correction
to Davies and Taylor's (1950) theoretical treatment of rise velocity
for spherical-cap bubbles. Since this work has not been published
elsewhere and is referred to in the published literature (Guthrie 1967),
a brief outline of his derivation is presented and discussed below.

A spherical-polar co-ordinate system fixed to the sphere
which fits the cap (see Table 4.6) and the potential flow velocity
distribution is used to calculate the velocity gradients. The normal
stress, P_{rr}, and the tangential stress, $P_{r\theta}$, at the bubble surface are
then obtained as:

$$P_{rr} = - p - \frac{6\mu U\cos\theta}{R_o} \tag{A.1}$$

$$P_{r\theta} = - \frac{3\mu U\sin\theta}{R_o} \tag{A.2}$$

The condition of constant pressure inside the bubble requires
that the normal stress at the bubble surface be constant

$$\therefore - P_s - \frac{6\mu U}{R_o} = - p - \frac{6\mu U\cos\theta}{R_o} \tag{A.3}$$

where p_s and p are the pressures at the front stagnation point and at a
point θ (measured from the front stagnation point) on the bubble surface.

Assuming the flow to be irrotational application of
Bernoulli's equation along the bubble surface gives

$$p_s = p + \frac{\rho u_\theta^2}{2} - \rho g R_o(1 - \cos\theta) \qquad (A.4)$$

where the tangential velocity at the bubble surface, u_θ, for potential
flow, is given by

$$u_\theta = \frac{3}{2} U\sin\theta \qquad (A.5)$$

Equations (A.3), (A.4) and (A.5) are combined and rearranged
to yield

$$(gR - \frac{6\mu U}{\rho R_o}) \frac{1 - \cos\theta}{\sin^2\theta} = \frac{9U^2}{8} \qquad (A.6)$$

Around the stagnation point where θ is small, $(\frac{1 - \cos\theta}{\sin^2\theta}) \to 1/2$ and
Equation (A.6) simplifies to

$$U = \frac{2}{3} \sqrt{gR_o - \frac{6\mu U}{\rho R_o}} \qquad (A.7)$$

This is the equation quoted by Guthrie (1967), except he has left out ρ
in the second term under the square root. Notice that when $\mu = 0$ the
above expression simplifies to Davies and Taylor's relationship,
Equation (3.22). Rearrangement of Equation (A.7) also gives Equation (3.28)
which was quoted by Guthrie (1967).

Discussion

The boundary condition at the bubble surface requires the tangential stress, $P_{r\theta}$, to be zero since viscosity of the gas is negligible. Note that for inviscid liquid $P_{rr} = p$ and $P_{r\theta} = 0$. Thus Davies and Taylor's derivation satisfies the stress boundary condition at the surface. For a liquid of finite viscosity, Equation (A.2) does not give vanishing tangential stress. Davidson has thus included the viscous correction in the normal stress by an amount which is of the same order of magnitude as that which he has neglected in the tangential stress. Despite this error, the experimental data seem to conform to his theory (see Chapter 3, Section 3.4.3.5). The correct way to account for the vanishing tangential stress, however, is to use the boundary layer method of Moore (1968).

APPENDIX B

DERIVATION OF RELATIONSHIPS BETWEEN VELOCITY COMPONENTS
u_x, u_y, u_η AND u_ξ (USED IN CHAPTER 4)

The velocities u_x, u_y, u_ξ and u_η (see Table 4.5) are all related to the velocity potential, ϕ, by (Batchelor 1967):

$$u_x = \frac{1}{h_x} \frac{\partial \phi}{\partial x} \tag{B.1}$$

$$u_y = \frac{1}{h_y} \frac{\partial \phi}{\partial y} \tag{B.2}$$

$$u_\xi = \frac{1}{h_\xi} \frac{\partial \phi}{\partial \xi} \tag{B.3}$$

and $\quad u_\eta = \frac{1}{h_\eta} \frac{\partial \phi}{\partial \eta}$ $\hfill$ (B.4)

where h_x, h_y, h_ξ, and h_η are the inverse of the metric coefficients and are given by (Happel and Brenner 1965):

$$h_x = h_y = 1 \tag{B.5}$$

$$h_\xi = h_\eta = c\left[\cosh^2\xi \, \cos^2\eta + \sinh^2\xi \, \sin^2\eta\right]^{1/2} \tag{B.6}$$

Now $\quad \phi = f(x,y)$ $\hfill$ (B.7)

with $\quad x = c \cosh\xi \, \sin\eta$

$\quad\quad\quad y = c \sinh\xi \, \cos\eta$ $\qquad$ (see Table 4.5) $\qquad$ (B.8)

$$\therefore \quad \frac{\partial \phi}{\partial \xi} = \frac{\partial \phi}{\partial x} \cdot \frac{\partial x}{\partial \xi} + \frac{\partial \phi}{\partial y} \cdot \frac{\partial y}{\partial \xi} \qquad (B.9)$$

Substitution of Equations (B.1) to (B.8) in Equation (B.9) yields

$$u_\xi h_\xi = \left[u_x c \sinh\xi \sin\eta + u_y c \cosh\xi \cos\eta \right] \qquad (B.10)$$

Similarly

$$\frac{\partial \phi}{\partial \eta} = \frac{\partial \phi}{\partial x} \cdot \frac{\partial x}{\partial \eta} + \frac{\partial \phi}{\partial y} \cdot \frac{\partial y}{\partial \eta} \qquad (B.11)$$

$$\therefore \quad u_\eta h_\eta = \left[u_x c \cosh\xi \cos\eta - u_y c \sinh\xi \sin\eta \right] \qquad (B.12)$$

Multiplying Equations (B.10) and (B.12) by $\cosh\xi \cos\eta$, adding and rearranging, yields

$$u_x = \frac{u_\xi \sinh\xi \sin\eta + u_\eta \cosh\xi \cos\eta}{(\cosh^2\xi \cos^2\eta + \sinh^2\xi \sin^2\eta)^{1/2}} \qquad (B.13)$$

and

$$u_y = \frac{u_\xi \cosh\xi \cos\eta - u_\eta \sinh\xi \sin\eta}{(\cosh^2\xi \cos^2\eta + \sinh^2\xi \sin^2\eta)^{1/2}} \qquad (B.14)$$

APPENDIX C

METHOD FOR OBTAINING THEORETICAL STREAMLINES AND PATHLINES

(USED IN CHAPTER 4)

The instantaneous components of velocity with respect to the sphere or ellipsoid that fits the bubble surface were obtained from the stream functions corresponding to the theoretical models describing the flow field. The results are summarised in Tables 4.1 to 4.4, 4.6 and 4.7. The relationships of the velocity components in the spherical polar co-ordinate system and in the oblate ellipsoidal co-ordinate system to those in the Cartesian co-ordinate system are given in Tables 4.1 and 4.5, respectively. The starting position (x_o, y_o) of the hydrogen tracer bubble provided the initial conditions for the pair of differential equations giving the position in terms of the velocity components.

i.e.
$$\frac{\partial u_x}{\partial t} = u_x \tag{C.1}$$

$$\frac{\partial u_y}{\partial t} = u_y \tag{C.2}$$

B.C. At $t = 0$, $x = x_o$ and $y = y_o$

The two differential equations were integrated numerically using the fourth order Runge-Kutta-Merson technique (Lance 1960) to give the theoretical streamlines.

The pathline predictions, i.e. motion of the tracer particle as seen by a stationary observer, were obtained by subtracting the vertical displacement in a given time due to the bubble rise velocity, U, from the above computation.

APPENDIX D

NUMERICAL DIFFERENTIATION OF EQUALLY SPACED EXPERIMENTAL DATA
(USED IN CHAPTERS 4 AND 5)

The derivatives of the measured displacement versus time data required in Sections 4.5.3.2 and 5.4.2 were computed using a numerical differentiation method called the "movable strip (or arc) technique" (Hershey et al 1967).

The use of the "optical" method proposed by Simmons (1941) to find the derivative was ruled out because it is often unintentionally biased as well as tedious. The simple difference technique (Ralston 1965) is also unsatisfactory since the experimental data are always subject to some error. In contrast, the numerical differentiation used here gives unbiased and fairly accurate values of the derivates. This method is based on fitting an orthogonal least-square polynomial through a small, odd number of data points, evaluating the slope at the mid-point and proceeding stepwise through the data. For the few points at each end of the range the slopes are obtained by a similar procedure using off-centre formulae. The method is most convenient for evenly spaced data, and it is often desirable to smooth the data (Ralston 1965) sufficiently to eliminate random errors and yet maintain the basic shape and character of the data unaltered.

In the present work a third-degree, five-point orthogonal polynomial was chosen for the smoothing operation. No significant improvement was found after the smoothing had been applied more than twice. Then, second-order, seven-point sloping formulae were used to obtain the derivatives. The orthogonal least square coefficients for the smoothing and sloping formulae were obtained from Hershey et al (1967).

APPENDIX E

REFRACTION CORRECTION FOR SKIRT THICKNESS

(USED IN CHAPTER 6)

E.1. Spherical Skirted Bubble or Drop

Let n and n' be the refractive index of the continuous phase and the dispersed phase, respectively. The refraction correction for the skirt thickness depends on the relative magnitude of n and n' as shown below:

(I) For n > n'

Consider an axisymmetric spherical skirted bubble (or drop) rising in vertical direction OS (see Fig.E.1(a)). Let AOQ be a plane inclined at angle α from the vertical (see Fig.E.1(b)). This figure shows a section of this plane viewed from a direction perpendicular to it for $\alpha < 90^o$. This section is an annulus of variable thickness because the skirt thickness decreases with angle measured from the front stagnation point S, as shown in Section 6.3.2.1.

Consider what happens to the rays of light travelling in the above plane (see Fig.E.1(b)). Let the camera be focussed on the median plane containing line AOQ, this plane being perpendicular to the normal to the camera lens. The light rays emerging from the median plane will be refracted at the interfaces and upon crossing the outer surface of the bubble (or drop) can be assumed to follow paths parallel to the normal to the camera lens, if the camera is sufficiently far away. No additional distortion is introduced by the container walls if the bubble or drop is viewed through flat walls. The ray TP that just grazes the inner surface is the limiting ray coming from the light source. It would therefore
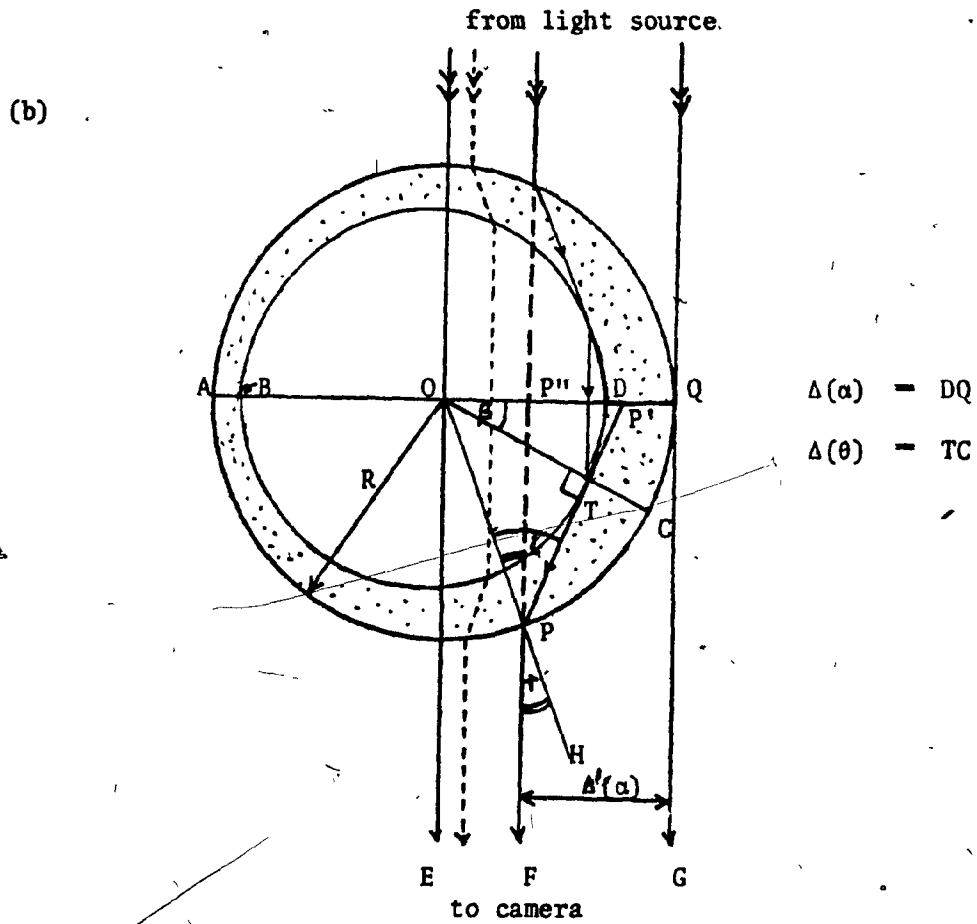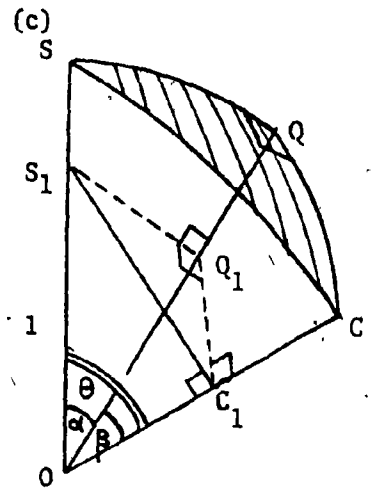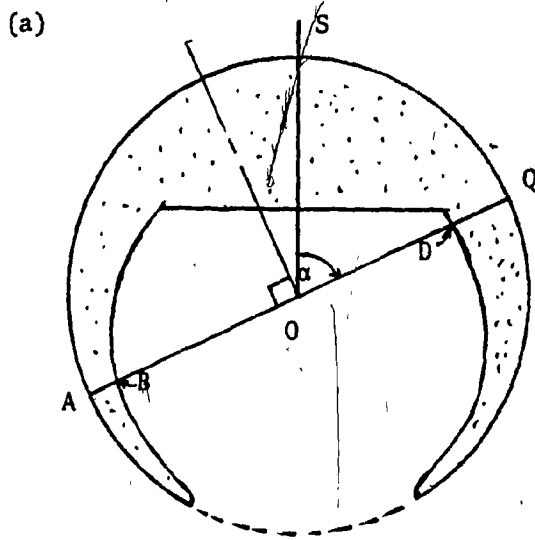
(a)

(c)

from light source.

(b)

$\Delta(\alpha) = DQ$

$\Delta(\theta) = TC$

$\Delta'(\alpha)$

E   F   G

to camera

FIGURE E.1   Refraction Correction for Skirt Thickness when $n > n'$

appear as a point on the inner surface of the skirt at an angle α measured from the front stagnation point on a photograph taken with backlighting.

Now, let

$\hat{i} = \widehat{OPT} = $ angle of incidence

$\hat{r} = \widehat{FPH} = \widehat{OPP''} = $ angle of refraction

$R = $ radius of outer surface of bubble or drop

$\alpha = $ polar angle for line OQ

$\beta = $ azimuthal angle for line OC

$\theta = $ polar angle for line OC

$\Delta(\alpha) = $ true thickness at polar angle, $\alpha = DQ$

$\Delta(\theta) = $ true thickness at polar angle, $\theta = TC$

$\Delta'(\alpha) = $ apparent thickness measured on photograph at polar angle α

From geometry of Fig.E.1(b)

$$\sin \hat{r} = \frac{OP''}{OP} = \frac{R - \Delta'(\alpha)}{R} \tag{E.1}$$

By Snell's law of refraction

$$\frac{\sin \hat{i}}{\sin \hat{r}} = \frac{n}{n'} \tag{E.2}$$

Since TP is a ray just grazing the inner surface, $\widehat{OTP} = 90^{\circ}$

$$\therefore \sin \hat{i} = \frac{OT}{OP} = \frac{R - \Delta(\theta)}{R} \tag{E.3}$$

Upon substituting Equations (E.2) and (E.3) in Equation (E.1) and re-arranging, we obtain

$$\Delta(\theta) = R\left[1 - \frac{n}{n'}(1 - \frac{\Delta'(\alpha)}{R})\right] \qquad (A.4)$$

The relationship between angles α and θ is now obtained from geometry as follows.

In Fig.E.1(c), let $OS_1 = 1$; then

$$OQ_1 = \cos\alpha; \quad Q_1S_1 = \sin\alpha; \quad OC_1 = \cos\alpha \text{ and } C_1S_1 = \sin\theta$$

from $\triangle OC_1Q_1$

$$OC_1 = OQ_1\cos\beta$$

$$\therefore \cos\theta = \cos\alpha\cos\beta \qquad (E.5)$$

From $\triangle OTP'$ in Fig.E.1(b)

$$\cos\beta = \frac{OT}{OP'} = \frac{R-\Delta(\theta)}{OP'' \ P''P'} \qquad (E.6)$$

But $\qquad OP'' = R \sin\hat{r} \qquad (E.7)$

and $\qquad P''P' = P''P \tan(\hat{i}-\hat{r})$

$$= R \cos r \tan(\hat{i}-\hat{r}) \qquad (A.8)$$

Substituting Equations (E.7) and (E.8) into (E.6) we obtain

$$\cos\beta = \frac{R-\Delta(\theta)}{R\left[\sin\hat{r}+\cos\hat{r} \ \tan(\hat{i}-\hat{r})\right]} \qquad (E.9)$$

where angles $\hat{r}$ and $\hat{i}$ can be obtained from Equation (E.1) and (E.2), respectively.

The above set of equations suggests the following procedure to obtain actual skirt thickness $\Delta(\theta)$ at an angle θ:

(i) From a photograph of the skirted bubble or drop we measure R and the apparent skirt thickness $\Delta'(\alpha)$ at an angle measured from the front stagnation point.

(ii) The actual skirt thickness $\Delta(\theta)$ is obtained from Equation (E.4). And, finally

(iii) The angle θ is calculated using Equations (E.1), (E.2), (E.5) and (E.9).

Note that when $\alpha = 90^{\circ}$, β reduces to zero and $\alpha = \theta$ as it should. For this case the Fig.E.1(b) reduces to an annulus of equal thickness and

$$\Delta(\theta) = R\left[1 - \frac{n}{n'}(1 - \frac{\Delta'(\theta)}{R})\right] \tag{E.10}$$

(II) **For $n = n'$**

When $n = n'$ we find $\theta = \alpha$ and $\Delta(\theta) = \Delta'(\alpha)$ which imply that there is no distortion. For this case, however, it would be difficult to observe the boundary of the dispersed phase unless the dispersed phase were dyed.

(III) **For $n < n'$**

When $n < n'$ we find that $\beta = 0$ and $\alpha = \theta$ for all values of α. For this case the limiting ray passes through D, and the skirt appears thinner than it really is as shown in Fig.E.2.

As before

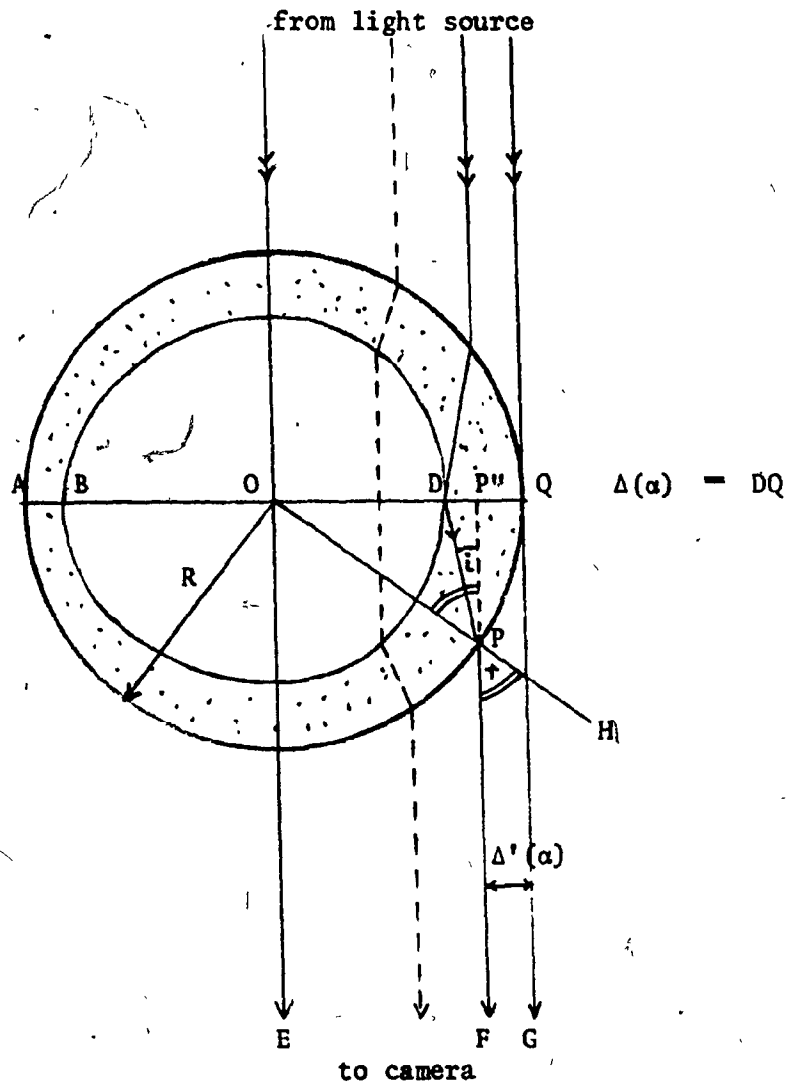$$\sin \hat{r} = \frac{OP''}{OP} = \frac{R - \Delta'(\theta)}{R} \tag{E.11}$$

FIGURE E.2 Refraction Correction for Skirt Thickness when n < n'

From Snell's law,

$$\frac{\sin \hat{i}}{\sin \hat{r}} = \frac{n}{n'} \tag{E.12}$$

From $\Delta DPP''$,

$$\tan(\hat{r}-\hat{i}) = \frac{DP''}{Pp''} = \frac{\Delta(\alpha)-\Delta'(\alpha)}{R\cos \hat{r}} \tag{E.13}$$

$$\therefore \Delta(\alpha) = \Delta'(\alpha) + R\cos r \, \tan(\hat{r}-\hat{i}) \tag{E.14}$$

E.2. Oblate Skirted Bubbles or Drops

For oblate shape skirts the geometry for the optical correction is so complex that it was not possible to devise a precise corrective procedure. However, since the skirts usually appear for $50^{\circ} < \theta < 140^{\circ}$ (see Section 6.5.3) we can find the sphere that fits as much of the skirt as possible and then apply the spherical correction to estimate the thickness. Provided that the aspect ratio of the spheroid is not too small and the difference between the refractive indices is not too large, this procedure should be adequate.

E.3. Prolate Skirted Bubbles or Drops

For prolate shapes an approximate method of correction is as follows. The distortion occurring due to curvature in vertical direction is neglected and a correction is applied for the curvature in horizontal direction using Equation (E.10) which is applicable for a cylindrical annulus of equal thickness. Thus, from the apparent horizontal thickness,

$\Delta'_h(\theta)$, measured at angle θ from the front stagnation point on a photo-graph we can obtain the actual experimental horizontal thickness, $\Delta_h(\theta)$. The skirt thickness theory presented in Section 6.4.2 allows the prediction of the thickness normal to the outer surface, $\Delta_n(\theta)$. However, we require the prediction of the horizontal skirt thickness, $\Delta_h(\theta)$, to effect the comparison with the experimentally obtained horizontal thickness. The relationship between $\Delta_h(\theta)$ and $\Delta_n(\theta)$ is derived as follows.

The geometry of an oblate skirted bubble (or drop) to be considered is sketched in Fig. E.3. Let $P(x_1, y_1)$ be a point on the ellipse; then the equation of the tangent to the ellipse at point P (i.e. line TP) is given by:

$$\frac{xx_1}{b^2} + \frac{yy_1}{a^2} = 1 \tag{E.15}$$

hence

$$OT = y_{x=0} = \frac{a^2}{y_1} = \frac{a}{\cos\eta} \tag{E.16}$$

$$MT = OT - OM = \frac{a\sin^2\eta}{\cos\eta} \tag{E.17}$$

$$MP = b\sin\eta \tag{E.18}$$

and

$$\tan\phi = \frac{MP}{MT} = \frac{b}{a}\cot\eta \tag{E.19}$$

Now

$$SP = MM' = a(\cos\eta - \cos\beta) \tag{E.20}$$

FIGURE E.3 The Geometry of an Oblate Skirted Bubble or Drop

Further, from the congruency of triangles QPS and PP'S

$$SP = QP\sin\phi = \Delta_n(\theta)\sin\phi \qquad (E.21)$$

where $\Delta_n(\theta)$ is the skirt thickness at P measured normally to the ellipsoidal surface.

Combining Equations (E.20) and (E.21) and rearranging yields

$$\beta = \cos^{-1}\left[\cos\eta - \frac{\Delta_n}{a}\frac{1}{\sqrt{1 + (\frac{b}{a})^2\cot^2\eta}}\right] \qquad (E.22)$$

The horizontal thickness at point P' on the ellipse, $\Delta_h(\theta)$, is then found to be

$$\Delta_h(\theta) = b(\sin\beta - \sin\eta) + \frac{\Delta_n(\theta)\frac{b}{a}\cot\eta}{\sqrt{1 + (\frac{b}{a})^2\cot^2\eta}} \qquad (E.23)$$

since $\qquad \Delta_h(\theta) = QP' = MP' - MQ' \qquad (E.24)$

The following procedure is recommended to obtain $\Delta_h(\theta)$ and the corresponding angle θ (consult Fig. E.3).

(i)   Select θ_p;

(ii)   Find corresponding eccentric angle η_p since b/a is known;

(iii)   Find $\Delta_n(\theta_p)$ from the skirt thickness theory for prolate shape;

(iv)   Find β from Equation (E.22);

(v)   Find $\Delta_h(\theta_{p'})$ from Equation (E.23); and

(vi)   Find $\theta_{p'}$ using value of β.

- THE END -